U.PORTO

FEUP FACULDADE DE ENGENHARIA
UNIVERSIDADE DO PORTO

NUMERICAL SIMULATION OF THE STRUCTURAL BEHAVIOUR OF CONCRETE SINCE ITS EARLY AGES

A thesis submitted for the degree of Doctor of Philosophy in Civil Engineering
at the Faculty of Engineering of the University of Porto

by

Miguel Ângelo Dias Azenha

Supervisor
Prof. Rui Faria (University of Porto - FEUP)

Co-Supervisor
Prof. Koichi Maekawa (University of Tokyo – School of Engineering)

September 2009
(Thesis defence on the 4th December 2009)

To my dear friend Bernardino Dias

Abstract

Concrete is a composite material whose stress history assumes relevance since the early ages. Soon after concrete casting important exothermic cement hydration reactions take place, ensuring the development of an internal porous structure responsible for the material strength growth. Simultaneously, chemical and physical processes driven by early cement hydration and by concrete interactions with the surrounding environment are responsible for load-independent volumetric changes of thermal and shrinkage origins (autogenous or drying). Under partial or total restraints these volumetric changes lead to an initial stress state build-up, which may either limit concrete ability to carry further tensile stresses, or generate cracks during service life operating conditions. In order to predict these load-independent stresses in concrete, advanced simulation tools are necessary for computing the time and space distributions of temperature and moisture, which are driving potentials for the material self-induced stresses.

The purpose of this thesis is to contribute to the up-to-date knowledge on early age concrete performance in a twofold manner: (i) on one hand, establishing the grounds for a macro-scale numerical simulation framework suitable for thermo-hygro-mechanical analysis of real sized applications; (ii) on the other hand, supporting the parameter estimation for numerical models on easily manageable and comprehensive experimental campaigns, conducted to the farthest possible extent. The work is structured according to the layout of the numerical framework, focusing aspects related to the thermal, moisture and mechanical models.

With regards to the research concerned to the thermal model, the following items are highlighted: an extensive characterization campaign of the heat generation associated to hydration of several cements available in Portugal; the use of thermography imaging for monitoring temperatures in the surfaces of a hydrating concrete cube; wind tunnel tests for identifying convective boundary coefficients and experiments evaluating the effect of solar radiation on concrete.

Regarding the moisture model, focus is centred on the choice of a field potential (water content *versus* relative humidity), with a detailed discussion on the relationship between moisture states in concrete and its corresponding tendency to shrink.

Special regard is given to the thermal and moisture boundary conditions, with the combined use of experimental research and the multi-scale simulation tool DuCOM (developed at the Concrete Laboratory of the University of Tokyo), encompassing aspects

as the environmental effects on moisture losses from cementitious materials and on the evaporative cooling phenomenon.
In parallel to the development of the thermo-hygro-mechanical numerical framework, it is worth mentioning the experiments conducted towards the implementation of a suitable procedure for monitoring concrete deformations at early ages using vibrating wire strain gages, the use of the concrete ring test to evaluate shrinkage behaviour under restrained conditions and the development of a new methodology for continuous monitoring of concrete E-modulus since casting.
At the end of this thesis, real field applications are presented encompassing both in-situ monitoring and numerical simulations of two Portuguese concrete structures at early ages: a wind tower concrete foundation with an embedded part of the steel mast, and a concrete gravity dam studied in a zone where several galleries exist.

Resumo

O betão é um material compósito cujo historial de tensões assume relevância desde as primeiras idades. Logo após a mistura iniciam-se reacções exotérmicas de hidratação que asseguram o desenvolvimento da estrutura porosa interna que é por sua vez responsável pela evolução da resistência. Simultaneamente, os processos químicos e físicos associados às reacções de hidratação, bem como as interacções do betão com o ambiente circundante provocam variações volumétricas de origem térmica ou associadas à retracção (autogénea ou de secagem). Quanto total ou parcialmente restringidas, estas variações volumétricas conduzem a estados de tensão inicial que podem limitar a capacidade do betão suportar tensões de tracção adicionais, ou até por si só conduzirem à fissuração em condições de serviço. Para prever estas tensões auto-induzidas são necessárias ferramentas avançadas de simulação que permitam calcular as distribuições temporais e espaciais de temperatura e humidade que estão directamente relacionados essas tensões.

Pretende-se com esta tese contribuir para o conhecimento actual do comportamento do betão desde as primeiras idades de duas formas: (i) por um lado, estabelecendo as bases para uma aplicação numérica de simulação (à macro-escala) que seja adequada para a análise termo-higro-mecânica de estruturas reais; (ii) por outro lado, suportar a estimativa de parâmetros para os modelos numéricos em campanhas experimentais levadas a cabo, tanto quanto possível, no âmbito desta tese. O trabalho está estruturado de acordo com o plano da ferramenta de simulação numérica, focando-se em aspectos relacionados com os modelos térmico, de humidade e mecânico.

No que diz respeito à pesquisa relacionada com o modelo térmico, enfatizam-se os seguintes itens: campanha alargada de caracterização do calor de hidratação de vários cimentos comercializados em Portugal; uso de imagem termográfica para monitorização de temperaturas superficiais de um cubo de betão durante a hidratação; testes em túnel de vento para estudo dos coeficientes de convecção para as fronteiras e experimentação relativa ao efeito da radiação solar sobre o betão.

Relativamente ao modelo de humidade, centra-se a atenção na escolha do potencial de campo (conteúdo em água *versus* humidade relativa), com discussão detalhada da relação entre os estados da humidade no betão e a consequente tendência para retrair.

É dada especial atenção às condições fronteira de temperatura e humidade, através do recurso combinado a trabalho experimental e a ferramenta de simulação numérica multi-escada DuCOM (desenvolvida no "Concrete Laboratory" da Universidade de Tóquio),

compreendendo aspectos como efeitos ambientais sobre as perdas de humidade de materiais cimentícios e o fenómeno do arrefecimento por evaporação.
Em paralelo ao desenvolvimento da ferramenta numérica de análise termo-higro-mecânica, é relevante mencionar as experiências conduzidas com vista à implementação de procedimentos adequados para monitorização de deformações no betão desde as primeiras idades com recurso a sensores de cordas vibrantes, o uso do ensaio do anel de betão para avaliar o comportamento do betão quando parcialmente impedido de retrair, bem como o desenvolvimento de uma nova metodologia para monitorização contínua do módulo de Elasticidade desde a betonagem.
No final da tese são apresentadas duas aplicações de campo que compreendem monitorização in-situ e simulação numérica desde as primeiras idades de duas estruturas localizadas em Portugal: a fundação de uma torre eólica com um troço do mastro em aço nela parcialmente embebido, e uma barragem gravidade em betão estudada numa zona onde existem diversas galerias.

Résumé

Le béton est une matière composite dont l'histoire de contraintes est essentielle depuis les jeunes âges. Immédiatement après le mélange commence la réaction exothermique d'hydratation assurant le développement de la structure poreuse interne qui est, à son tour, responsable par l'évolution de la résistance. Simultanément, les processus chimiques et physiques associés aux réactions d'hydratation et les interactions du béton avec le milieu environnant provoquent des variations de volumétrie d'origine thermique ou associées au retrait (autogène ou de séchage). Quand total ou partiellement empêchées, ces variations volumétriques conduisent à un état de tension initiale qui peut limiter la capacité du béton de supporter des contraintes de traction additionnelles, ou même conduire à la fissuration en conditions de service. Pour prévoir ces autocontraintes induites il y a besoin d'outils de simulation de pointe qui permettent de calculer des distributions spatiales et temporelles des températures et de l'humidité qui sont directement liées à ces contraintes.

L'objectif de cette thèse est de contribuer aux connaissances actuelles sur le comportement du béton depuis les jeunes âges de deux façons: (i) d'une part, établir la base pour une application de simulation numérique (en macro-échelle) qui soit appropriée pour les analyses thermo-hydro-mécaniques des structures réelles, (ii) d'autre part, d'appuyer l'estimation des paramètres pour les modèles numériques dans des campagnes expérimentales menées aussi loin que possible dans cette thèse. L'ouvrage est structuré en conformité avec le plan de l'outil de simulation numérique, en se concentrant sur certains aspects du modèle thermique, d'humidité et mécanique.

En ce qui concerne la recherche liée au modèle thermique, voici les éléments les plus importants ce qui suit: vaste campagne de caractérisation de la chaleur d'hydratation de 10 ciments en vente au Portugal ; l'utilisation d'images thermographiques sur un cube de béton en cours d'hydratation ; tests en tunnel de vent pour étudier les coefficients de convection, et l'expérience sur l'effet de la radiation solaire sur le béton.

Pour le modèle de l'humidité, l'attention est centrée sur le choix du champ de potentiel (teneur en eau versus humidité relative), avec une discussion détaillée de la relation entre les états d'humidité dans le béton et la tendance pour retraire.

Une attention particulière est accordée aux conditions limites de température et d'humidité, en utilisant un outil combiné expérimental et simulation numérique multi-échelle DUCOM (développé au "Concrete Laboratory" de l'Université de Tokyo), y

compris des aspects tels que les effets environnementaux sur la perte d'eau des matériaux cimentaires et le phénomène de refroidissement par évaporation.
En parallèle au développement de l'outil numérique d'analyse thermo-hydro-mécanique, il est pertinent de mentionner les expériences menées en vue de la mise en œuvre des procédures appropriées pour surveiller la déformation du béton dès les premiers âges en utilisant des senseurs de cordes vibrantes, l'utilisation du test de l'anneau de béton afin d'évaluer le comportement du béton lorsqu'il est partiellement empêché de retraire, et le développement d'une nouvelle méthodologie pour la surveillance continue du module d'élasticité depuis le bétonnage.
À la fin de la thèse deux applications réelles sur le terrain sont présentées qui incluent la surveillance in situ et la simulation numérique dès les jeunes âges de deux structures situées au Portugal: la fondation d'une colonne éolienne avec une section du mât en acier partiellement noyé dans la masse, et un barrage de gravité en béton étudié dans un domaine où il ya plusieurs galeries.

Acknowledgements

Most of the work in this thesis was conducted at the Faculty of Engineering of the University of Porto (FEUP - Portugal), within the research unit LABEST (Laboratory for the Concrete Technology and Structural Behaviour), whereas a period of the work (6 months) was conducted at the School of Engineering of the University of Tokyo (Japan), within the Concrete Laboratory research unit. The supervisors of this thesis are Prof. Rui Faria (University of Porto) and Prof. Koichi Maekawa (University of Tokyo).

Guidance provided by both supervisors has been of great importance and influence to the work conducted. Specifically, I would like to express my deepest gratitude to Prof. Rui Faria, whose professional and personal characteristics have led him to play several relevant roles in my life: as supervisor (by his constant availability and wise advice), as a research colleague (with much work being conducted jointly, particularly in writing papers) and as a friend. I also acknowledge the importance of the contribution of Prof. Koichi Maekawa, who kindly accepted to receive me in the Concrete Laboratory of the University of Tokyo, providing all the necessary conditions for access to laboratory facilities and using the DuCOM numerical framework, as well as his kind guidance throughout the conducted research.

I would also like to thank Prof. Joaquim Figueiras, Director of LABEST, who not only provided me with all the possible conditions for a feasible conduction of experimental work at FEUP, but also for establishing the initial contacts with the University of Tokyo.

I would also like to recognize the contribution of the colleagues with whom I had the pleasure of performing parts of the research work reported in this thesis: Carlos Sousa, Filipe Magalhães, Leonel Ramos, Helena Figueiras, Luís Silva, Denise Ferreira and Carlos Cardoso. The contribution of other colleagues, friends and co-workers at the University of Porto is also acknowledged, particularly to: Mário Pimentel, Pedro Costa, Miguel Ferraz, Topa Gomes, Miguel Castro, Sandra Nunes, Carlos Moreno, Hélder Silva, Diogo Ribeiro, Bruno Costa, Helder Sousa, José Matos, Lino Maia, Carlos Rodrigues and Filipe Cavadas. The helpful nature of the staff at the laboratory and secretary of the Structural Division of FEUP is gratefully acknowledged, namely Paula Silva, Amândio Pinto, Alberto Monteiro, Cecília Barbosa, Cláudio Ferraz, Cláudia Correia, Marta Poinhas, Maria Vitória, Joana Rodrigues and Elisabete Rosa.

During my stay in Japan, I had the pleasure of working and being helped by a very united research group, of which I would like to point out the names of Doctors Shingo Asamoto, Nobuhiro Chijiwa, Kenichiro Nakarai, Tetsuya Ishida, Bongochgetsakul

Nattakorn and Essayas Gebreyouhannes. In the period abroad, the discussions held remotely with Prof. Vitor Costa from University of Aveiro (Portugal) were very fruitful for a better understanding of moisture transport in concrete.
I also gratefully acknowledge the help of Teófilo Silva, Augusto and Vasco at the construction site of the dam studied in the context of this thesis.
Financial help by the Portuguese Foundation for Science and Technology is recognized both through the PhD grant (SFRH/BD/13137/2003 – POCI2010 "Formação Avançada para a Ciência – Medida IV.3") and the funding for the research project entitled "Early Age Concrete: Behavioural Prediction" (POCI/ECM/56458/2004).
As a consequence of my recent career shift towards the School of Engineering of the University of Minho, I wish to thank the Head of the Civil Engineering Department (and President of the ISISE research group) Prof. Paulo Lourenço for providing me with the necessary conditions for the final phase of writing of this thesis. The help of Prof. Joaquim Barros, Prof. José Sena Cruz and Cátia Valente in reviewing the thesis is also gratefully acknowledged.
I would also like to acknowledge the discussions with Prof. Daniel Cusson (NRC – Canada) and Prof. Folker Wittmann (AIF - Germany), which revealed quite fruitful and important for the validation of my research.
The help of my late friend, and grandfather Bernardino Dias with his great carpentry skills and wise advice proved quite fruitful in many of the woodcraft involved in the experiments reported in this thesis.
Finally, I would like to thank my family in general for their support, particularly my parents for all their selflessness with regards to me, and Lurdes for her love, care, companionship and patience during the obsessive times of this work.

Table of contents

List of symbols and abbreviations

For the sake of clarity, the description of each notation or symbol is made upon its first appearance in the text. The following list is presented in alphabetic order and does not include symbols or notations of a secondary nature (i.e. those whose concern is restricted to localized applications).

Roman Letters

A	Area through which a flux occurs
$A_{c,ef}$	Effective area of concrete around reinforcing bars
A_T	Proportionality constant for the Arrhenius Law
a_λ	Reflectivity of a given wavelength λ (radiation)
c	Specific heat
c_a	Specific heat capacity of air
D	Diffusion coefficient
D_1	Value of D_H (Bazant's approach) when H=1
D_0	Value of D_H (Bazant's approach) when H=0
D_H	Humidity diffusion coefficient
D_{H^*}	Diffusivity D_H lumped with moisture capacity
DFT	Discrete Fourier transform
DOH	Degree of hydration
d	Day cardinal within the year
E	voltage output of the heat flux sensor
E_a	Apparent activation energy
$\dot{E}_g$	Energy generation rate within the REV
E_c	Concrete Young's modulus
$\dot{E}_{in}$	energy input rate to the REV
$\dot{E}_{out}$	energy output rate from the REV
$\dot{E}_{st}$	Rate of energy storage within the REV
E_v	Evaporation coefficient
E_s	Moisture emissivity coefficient of water (vapour pressure formulation) E-modulus of steel
EA	Equivalent age

E_aI_a	Flexural stiffness of the acrylic tube
EI	Flexural stiffness of concrete tube
$\overline{EI}$	Distributed flexural stiffness of the composite beam
e_s	Saturation vapour pressure of water
e	Vapour pressure in the gas medium
FE	Finite element
f	Frequency
f_{ct}	Concrete tensile strength
f_c	Concrete compressive strength
f_{sy}	Steel yield stress
$f(\alpha_T)$	Normalized heat generation function
G_F	Fracture energy
g	Proportionality constant
H	Relative humidity (applicable to pores or environment)
H_C	relative humidity for which $D_H = 0.5 \times D_1$ (Bazant's approach)
H_{env}	Environmental relative humidity
H_{surf}	Relative humidity in the surface
H_S	Internal humidity decrease associated to cement hydration
H_{vap}	Evaporation heat of water at the reference temperature [$Jmol^{-1}$]
h	Solar elevation; Characteristic length
h_{cr}	Combined convective/radiation heat transfer coefficient
h_{eq}	Equivalent boundary transfer coefficient
h_l	Latent heat of vaporization of water [Jkg^{-1}]
h_{moist}	Moisture emissivity coefficient (formulation based on H)
h_T	Convective heat transfer coefficient
h_r	Longwave radiation heat transfer coefficient
i	Iteration number; angle of incidence of the sunbeam with respect to $\overline{n}$
J	Diffusion flux per unit area
$J(t,t')$	Creep compliance function at instant t for load applied at instant t'
K_1, K_2	Isothermal calorimeter constants
k	Thermal conductivity; Boltzman's constant
k_{duf}	Crossed proportionality heat conductivity due to moisture transport
L	Thickness, length
l, m, n	Direction cosines of the normal versor to Γ_q
M	Molar mass of water
M	Bending moment
M_{cr}	Cracking moment
$\overline{m}$	Uniformly distributed mass
m, n	Material parameters for DPL
$\boldsymbol{N}$	Interpolation matrix
$NPSD$	Normalized auto-spectrum
$\overline{n}$	Versor normal to the surface
n	Material property for calculation of: D_H (Bazant's approach) and DPL

P	Heat loss term; Total air pressure
PSD	Averaged auto-spectrum
p_v	Pressure of water vapour
p_0	Reference pressure
p_w	Pressure in water
$Q(t)$	Accumulated heat generated until a certain instant t
$\dot{Q}$	Rate of internal heat generation per unit volume
Q_{add}	Added energy flux associated to night cooling
Q_{total}	Asymptotic value of $Q(t)$ after heat liberation has ceased
q_i	Heat flux in direction i
q_h	Heat flux due to convection and longwave radiation (per unit area)
$q_{h,c}$	Heat flux due to convection (per unit area)
$q_{h,r}$	Heat flux due to longwave radiation (per unit area)
q_m	Solar radiation that reaches a surface
q_m , q_S	Moisture flux per unit area
$q_{S,concr}$	Solar radiation absorbed by a concrete surface
R	Ideal gas constant
REV	Representative elementary volume
RH	Relative humidity
r	Pore radius
s	Parameter that depends on type of cement
T	Temperature
$\boldsymbol{T}^e$	Nodal temperatures for a given FE
T_0	Reference temperature
$\overline{T}$	Average annual ambient temperature
T_{env}	Environmental temperature
T_{sample}	Temperature of the sample
T_{surf}	Temperature of a given surface
$TOLER$	Tolerance for convergence checking
t	Time; instant
t_λ	Transmissivity of a given wavelength λ (radiation)
t_e	Equivalent age
t_0	Time 0 (before which mechanical properties are considered null)
u	Specific heat of the sample container and contents (iso. calorimeter)
V	Wind speed velocity
v	Specific volume of water
W	Total water concentration
W_e	Evaporable water concentration
W_n	Non-evaporable water concentration
w	Mass of free water (not chemically bound) per unit volume of concrete; Angular frequency
X_{i1}	hypothetical value of X_i upon full hydration development (α=1)
$X_i(\alpha)$	Property X_i for degree of hydration α

$X_i(t_e)$	Property X_i for equivalent age t_e
x, y, z	Spatial coordinates in the reference axis
$Y(t)$	Amplitude of the transversal displacement as a function of time t

Greek Letters

α_s	Absorptivity of concrete (solar radiation)
α_{T}	Thermal dilation coefficient; Degree of heat development
α_λ	Absorptivity of a given wavelength λ (radiation)
α_0	Initial degree of hydration
α_{sh}	Coefficient of hygral expansion
α	Degree of hydration; surface angle relative to the horizontal plane
β_t	Factor for average tensile stress carried by the concrete between cracks
χ_m	Curvature
ΔT	Temperature difference
ΔT_{nsky}	difference between environmental and apparent sky temperature
δ	Declination of the sun
ε	Emissivity parameter (radiation); Total strain
ε^e	Elastic strain
ε^{cr}	Crack strain
ε_n	Strain perpendicular to the crack
ε_{yc}	Concrete strain at which steel yields in the crack section
ε_{sy}	Yield strain of steel
$\varepsilon_{sh,c,ult}$, $\varepsilon_{sh,\infty}$	Ultimate shrinkage in concrete
$\varepsilon_{sh,p,ult}$	Ultimate shrinkage in cement paste
ε_θ	Hoop strain
Φ_0	Molecular flux (number of molecular impacts per unit area of water surface and per unit time)
ϕ_1	Material parameter for DPL
$\phi(x)$	Vertical deflection mode
Γ_{q}	FE Boundary
γ	Surface tension of the water/water vapour interface
η_i	Parameter for estimation of $X_i(\alpha)$
$\eta_{\mathrm{max,i}}$	Cracking index at point i
φ	Latitude
λ	Wave length
ν	Poisson's coefficient
θ	Moistening angle
ρ	Specific mass (mass per unit volume)
ρ_{s}	Reinforcement ratio
σ_{ct}	Principal tensile stress
σ_θ	Hoop stress

σ_r	Radial stress
σ	Stefan-Boltzmann constant; Stress
σ_n	Normal stress perpendicular to the crack
$\boldsymbol{\sigma_x}$	Stresses in x direction
$\boldsymbol{\sigma_y}$	Stresses in y direction
$\boldsymbol{\sigma_z}$	Stresses in z direction
$\sigma_1, \sigma_2, \sigma_3$	Principal stresses
Ω	Hour angle of the sun; volume of a finite element
Ψ	Azimuth of projection of $\overline{n}$ on the horizontal plane

Chapter 1

Introduction

1.1 Scope and general remarks

Concrete is a composite material whose stress history begins at its early ages. Soon after being cast (fresh state) cement hydration reactions progressively take place, engendering a porous solid network responsible for the concrete mechanical strength enhancement. The chemical and physical processes involved, both due to early hydration and to interactions with the surrounding environment (in short and long term), are responsible for volume changes in concrete, usually termed as thermal, autogenous and drying shrinkage. Under the usual situation of partial or total restraint, these volume changes lead to a stress build-up, thus creating a state of residual stresses that may either limit the concrete's ability to carry further stresses, or even cause a state of cracking when the material tensile strength is reached. A good knowledge of the risk or extent of cracking in concrete structures since casting and throughout their lifetime is important in order to ascertain their serviceability and durability conditions.

However, it is known that design practices with basis on current regulations tend to simplify, or even disregard, some of the above mentioned phenomena, with the purpose of maintaining their practical application. The years have proven design codes to be quite satisfactory for the ultimate limit states, with adequately designed and built structures showing proper behaviour and safety margins. However, the case has not been the same with regards to the service life of structures, with frequent occurrence of crack widths larger than predicted in design, as well as the occurrence of cracks whose existence cannot be explained through the models available in the design codes. These cracks end up causing accelerated deterioration of structures, frequently demanding costly repairs, in order to maintain serviceability and durability at acceptable levels. It is therefore possible to conclude that service life models of design codes may, in some cases, be considered insufficient to predict the behaviour of concrete structures. Therefore, these considerations

have motivated the conduction of the research work presented in this thesis, aiming at a more consistent modelling of concrete behaviour. The fundamental purpose of the work undertaken was to establish a methodology for numerical modelling of the behaviour of concrete structures since early ages, with explicit account for a set of physical and chemical processes not usually put together in the analysis of the service life behaviour of real scale structures, together with a strong emphasis on the experimental characterization of the material to be actually used in the structure. One of the reasons for the feasibility of the research reported in this work is the availability of computational capacity for the intended simulations. According to Moore's Law (1965), the number of transistors that can be placed inexpensively on an integrated circuit doubles approximately every two years, with the consequent increase in computational capability. This increase causes the context of numerical simulation of whichever phenomenon to change dramatically through the decades, thus allowing for new generations of complexities in the numerical models to be applicable to real scale structures.
For a better understanding of the partial objectives and methods envisaged in the conducted research to be focused in Section 1.3, the following section introduces a set of quite relevant phenomena for concrete performance since the end of casting.

1.2 Concrete: from a solid suspension to a porous solid

In this section a group of physical/chemical characteristics and processes inherent to concrete are to be described. The descriptions will help in understanding that usual models used by designers reveal themselves as insufficient to describe the involved phenomena in stress generation, and thus justify the necessity of studying and implementing the models used in this thesis.
The composition of a concrete mix usually includes cement, water, aggregates and additions. Cement is the constituent responsible for bonding the components of the mix, therefore playing a central role in the behaviour of concrete. Portland cement, which is the most widely used in Civil Engineering construction, is obtained from calcareous materials (limestone being the most usual) and others such as alumina/silica (e.g., clay, shale). The raw materials for cement production are ground together in controlled proportions and fed to a kiln, enduring temperatures of approximately 1450°C, which is termed the sintering temperature of cement. At this temperature the raw materials partially fuse into ball shaped particles, called clinker. The resulting clinker is cooled and ground into a fine powder, to which some gypsum is added. After the described process, the final product is then considered as Portland cement (Neville 1995). From a chemical point of view, unhydrated cement is mainly composed of a group of oxides, such as SiO_2, Al_2O_3, Fe_2O_3, CaO, MgO and SiO_3. However, the interpretation of cement behaviour has been traditionally linked to its mineralogical composition, which corresponds to four main phases: tricalcium silicate ($3CaO\ SiO_2$), dicalcium silicate ($2CaO\ SiO_2$), tricalcium aluminate ($3CaO\ Al_2O_3$) and tetracalcium aluminoferrite ($4CaO\ Al_2O_3\ Fe_2O_3$). These four mineralogical compounds are usually termed in abbreviated form as C_3S, C_2S, C_3A and C_4AF, respectively. Both the chemical and mineralogical composition of cement can be

obtained experimentally. However, the methods used for the determination of the mineralogical composition are more expensive and demand greater operator skill, thus being less frequently adopted. For such reason, the most usual approach to obtain the mineralogical composition of cement is to extrapolate it from the known chemical composition, using an approximated method such as the Bogue's formula (Aldridge 1982, Neville 1995, Taylor 1989).

The reader is now referred back to the beginning of the previous paragraph, where concrete has been defined as a mix of cement, water, fine/coarse aggregates and additions. Immediately after mixing and casting, and depending on the actual mix proportions, the material may be thought as a concentration or suspension of rigid particles in water, or as a granular water-filled porous medium (Bentz 2008). The cement paste (water, cement) endures a set of complex physical/chemical processes, which are ultimately responsible for the transformation of the mix into a load-bearing durable solid. These processes are generally termed as hydration reactions, and commence as soon as water and cement come into physical contact, passing then through several stages that may be interpreted with basis on the cement mineralogical compounds, which exhibit distinct characteristics. It is usual to divide cement hydration reactions into three stages (Neville 1995) (even though some authors further sub-divide these stages), which are schematically represented in Figure 1.1, and whose evolution of hydration products is depicted in Figure 1.2:

- Stage I – Early stage – as soon as the contact between water and cement particles occurs, there is an immediate reaction between the surface ions of the clinker and water: C_3A reacts with water and gypsum to form ettringite, and the reaction of water with the calcium silicates results in some semi-stable hydrated calcium silicates. These early reactions are highly exothermic, and last for a few minutes (five or less), as seen in Figure 1.2, where the heat generation rate curve attains very high values (off-chart) during a very small period. This initial part of the early period is usually termed as pre-induction. After the pre-induction, there is a period of apparent inactivity, called induction or dormant period, which may last up to ~5h. A possible cause for this dormant period is the formation of a protective layer around cement particles, temporarily preventing further reactions (see Figure 1.1). During this period the material remains workable, i.e., it exhibits negligible mechanical stiffness.
- Stage II – Intermediate stage – initiated after disruption of the mechanism that prevented hydration during the dormant period. The cement particles (mainly C_3S and C_2S) hydrate at significant speed with the formation of amorphous calcium silicate hydrate (CSH) and crystalline calcium hydroxide ($Ca(OH)_2$), while aluminates react forming ettringite that is later converted into monosulphate (see Figure 1.2). During this stage the cement particles begin expanding, with the appearance of long fibres in the recently formed porous network (which results from the bridging between adjacent cement particles) - Figure 1.1. Due to the strong rate at which hydration reactions start occurring at this stage, together with their exothermic character, a heat generation rate peak occurs, followed by a period of deceleration that results from the layer of hydration products that is formed around the cement particles. This layer represents an obstacle to the access of water to the core unhydrated cement. The rates of reaction start becoming controlled by the diffusion rates of ions through the layers of hydrated products. Concomitantly with the sudden heat generation at

the beginning of this period, there is a sudden and strong increase in stiffness, with the transition of the material from a fluid-like behaviour to a porous solid, usually attaining stiffness (i.e., Young's modulus, also known as E-modulus) of over 50% of the value at 90 days by the end of this stage. During the whole process, porosity of the material starts diminishing in correspondence to the growing formation of solid material.

- Stage III – Late stage – This period corresponds to the continuing of the diffusion controlled hydration reactions that characterized the end of stage II, but with much lower reaction rates due to the progressive thickening of the hydrated products surrounding the cement particles (see Figure 1.1), which strongly reduce the heat generation rate (see Figure 1.2). The hydration products formed during this period are quite stable and occupy the voids between the thin fibres mentioned in stage II.

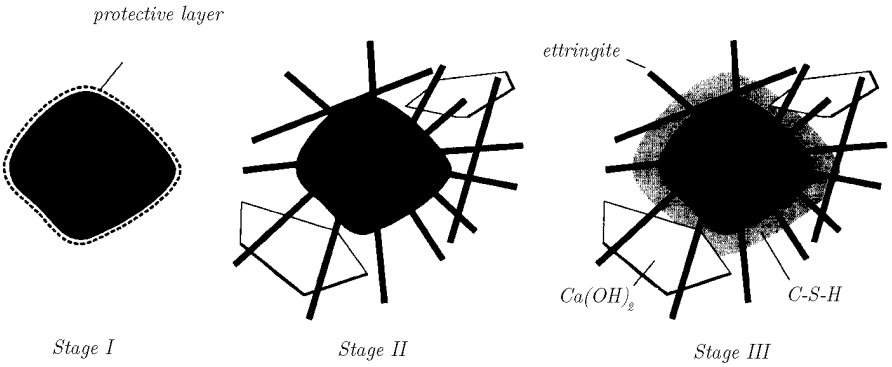

Figure 1.1: Hydration products through the three stages of hydration (adapted from Beek (2000))

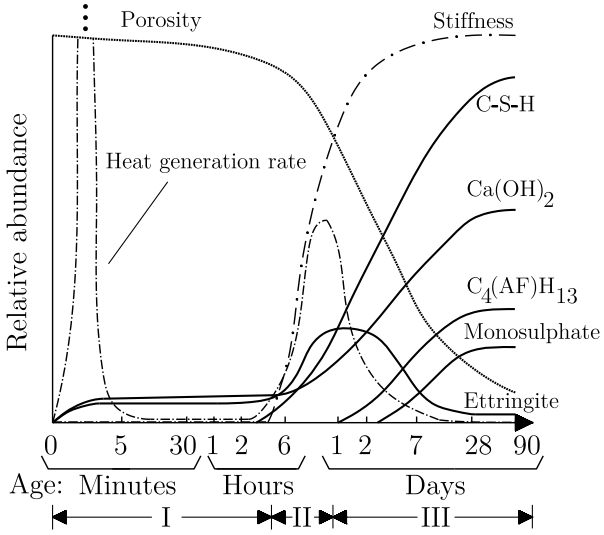

Figure 1.2: Formation of several hydration products with time, together with porosity and heat generation rate evolution (partially based on Lura (2000))

Still regarding the average timings for the hydration product formation, heat generation and porosity evolution depicted in Figure 1.2, it should be stressed that these are merely indicative for an ordinary Portland cement at a room temperature of ~20°C. In fact, the

set of chemical reactions involved in cement hydration are thermally activated, i.e., their rates of reaction are strongly influenced by temperature: the higher the temperature under which hydration occurs, the higher the rates of hydration.
The descriptions of hydration reactions that have been made allow for the conclusion that these are by no means simple processes, and that the concrete properties (thermal, hygral, mechanical) evolve dramatically during the several stages, as seen for example by the porosity decrease and the stiffness increase throughout time (Figure 1.2).
It must also be understood that this evolving concrete is interacting both internally with neighbouring parts of the material and externally with its surrounding environment in many ways, most of them directly or indirectly influencing the stress development. This range of interactions is to be covered here in a stepwise manner, dealing firstly with thermal issues, then with moisture transport issues, and finally the mechanical point of view, as referred to in the text that follows.

Thermal problem

Regarding thermal issues, it has been stated that the chemical reactions involved in cement hydration are exothermic. This heat generation engenders a temperature rise in concrete, which usually becomes higher than the surrounding environmental temperature. As a consequence of this thermal imbalance, heat transfer between concrete and the surrounding environment starts occurring, through the mechanism of convection (which becomes more effective in the presence of wind). During the period whilst the internal heat generation supersedes the heat fluxes towards the environment, the temperature within the concrete element keeps its rising tendency, with the core standing hotter than the external surfaces. Due to these temperature differences between the core and surfaces, and bearing in mind the thermally activated character of the chemical reactions involved, it is understandable that hydration reactions in core regions occur at higher rates than in the case near the surfaces. These differences in hydration rate between different regions of concrete also cause differences in the evolution of thermal properties (such as thermal conductivity and specific heat), which may influence the subsequent behaviour of the material. At some point in time, the heat liberation from the chemical reactions drops under the threshold at which the heat fluxes towards the environment supersede it. Since this instant the concrete element starts cooling until it attains thermal equilibrium with the environment, which represents the end of the non-negligible thermal processes associated to heat of hydration of cement, occurring at ages that depend on the structure size and shape, the concrete composition, the initial concrete temperature and the environmental temperature (among others). Depending on the factors that have just been mentioned, this so-called thermal equilibrium can occur as soon as 4-5 days for a thin slab, or as late as after several years for a large gravity concrete dam.
The description of the thermal processes given above was rather simplified, in order to provide a better understanding for the reader, since many phenomena other than convection contribute to the interactions between concrete and the environment. A brief enumeration of such additional phenomena concerns the radiation heat exchanges, which occur between the concrete surface and all the surrounding objects; the radiation intake to concrete that occurs during daylight due to the sun (whose intensity varies throughout the day, and depends on the season, the latitude, the inclination of the surface and on

shadowing effects, among others); the cooling of the concrete surfaces associated to the evaporation of water upon formwork removal; the strong night cooling associated to the radiation heat exchanges between the concrete surface and the deep night sky; and the thermal imbalances created by curing water, or even rain over concrete. The inconstant character of environmental temperature, together with the varying nature of the several thermal interactions between concrete and the environment that have just been enumerated, lead to the conclusion that concrete temperatures cannot be considered constant after heat of hydration release has ceased: in fact, particularly due to sun exposure and microclimatic effects, such as wind concentrations, the temperature inside concrete experiences non-negligible gradients throughout its lifetime.

Moisture problem

The freshly cast concrete is a solid suspension with liquid water occupying most of the voids between the solid components of the mix (the rest of which being occupied by particles of entrapped air). Due to cement hydration reactions, free water starts to become chemically combined with the cement particles, thus diminishing the volume of liquid water, and increasing the links between adjacent cement particles to form a porous network. Due to the fact that the reaction hydration products occupy less volume than the reactants (unhydrated components and water), this process may lead to a partial emptying of the porous network, and consequently an internal pore relative humidity (RH) decrease. This internal RH decrease is termed self-desiccation, or internal drying (Bentz 2008, Lim 2002, Neville 1995), and depends on the initial water to cement ratio of the mix (w/c): the lower the w/c, the higher will be the effect of self-desiccation. Thus, self-desiccation in Normal Strength Concrete (NSC) with w/c typically above 0.45 (i.e., with water in excess of the minimum necessary to assure the hydration of all cement particles) tends to be very low, with internal RH of sealed concrete specimens exhibiting values quite near 100% even after several days of age (since casting).

Water that has not been chemically combined with cement exists either in the liquid phase (physically bound or free) or in the vapour phase, being distributed among pores of several ranges of diameters within the pore network, which has intricate paths, tortuosities and discontinuities. It is therefore understandable that moisture transport within concrete has a great deal of specificities, such as the hysteretic water retention upon wetting/drying cycles.

A concrete element completely sealed externally during cement hydration, would only see its internal RH reduced due to the phenomenon of self-desiccation. However, real concrete structures are not sealed from the environment, but instead they have many moisture interactions during their service life. Usually, upon formwork removal, the saturated (or almost) concrete surface starts immediately exchanging moisture with the environment (usually at a lower humidity state) through the process of evaporation/drying. This process tends to empty the concrete pores (beginning with the larger ones), according to a drying process typical of porous media that starts on the cover and progresses inwards to the concrete core. Unlike which occurs in the case of the thermal equilibrium, hygral equilibrium between concrete and the surrounding environment may take several years to be attained, even in the case of a thin slab. An important consequence associated to the drying of concrete (either due to self-desiccation or to surface evaporation) is the

deceleration, or even stagnation of cement hydration reactions associated to the withdrawal of water from the porous network. Focusing particularly on the sudden surface drying, which occurs upon exposure of concrete to the environment, it has been acknowledged that the near surface cement hydration reactions almost cease, hindering the development of the surface concrete properties (mechanical strength, durability, permeability, etc.), contrarily to what happens to the core concrete that remains for a long time in near-saturated conditions. This fact points to an interaction that exists between the moisture and the thermal fields: if water is no longer available for hydration, heat generation also ceases. Another interaction between these two fields is due to the evaporation cooling phenomenon mentioned in the thermal problem, which is a consequence of moisture movements in concrete, and it affects the temperature on the concrete surfaces.

Moisture fields in concrete evolve along time as stated, but another important influence affects their evolution: rain. Every time rain falls over a concrete element, there is a partial re-wetting of the surface, with a strong effect in the retardation of the drying process as a whole.

Mechanical problem

As a consequence of the thermal and moisture distributions, internal stresses develop within concrete. Any variation in temperature within concrete causes a corresponding volumetric change, according to the material coefficient of thermal expansion. Also, it has been acknowledged that internal moisture losses in concrete, due to self-desiccation or drying, lead to a tendency of the porous matrix to contract (even though the explanation of the physical mechanisms that drive moisture related contraction are still a subject of discussion and disagreement in the scientific community (Wittmann 2008)). Therefore, with knowledge of the driving potentials (temperature and moisture), and a good correlation between each driving potential and the inherent volumetric variation, it is possible to provide a good estimation of the tendency of concrete to shrink. This allows the phenomena of thermal, autogenous and drying shrinkage to be explicitly estimated, thus allowing knowledge of their non-uniform character along space and time in concrete elements. The stresses associated to thermal and hygral phenomena that are developed in a given part of a concrete element are naturally linked to the restraint to deformation: if deformations are not restrained at all, the envisaged part of the concrete element only suffers dimensional variation without any stress development. Nonetheless, restraint always exists in real structures, be it at a cross-sectional level, or at a global structural level. The cross-sectional restraint can be easily explained by examining what occurs in a square concrete cross section under heat release associated to the heat of hydration: during the temperature rise in concrete the inner core attains higher temperatures than the surface, thus the tendency to expand is higher in the core than in the surface. As a consequence the core endures compressive stresses and the surface is under tension. Similar reasoning could be used to explain the influence of this restraint during the cooling phase, or even during drying shrinkage associated to evaporation (which is stronger near the surface). The other kind of restraint that has been mentioned refers usually to the constraints to structural deformation imposed by external supports or connections, for which a beam fixed at both ends can be used as an example: during the

heat liberation associated to cement hydration, all parts of the beam endure a temperature rise (even though not uniform along the cross section), with the corresponding tendency of the element's length to increase. The restraint to longitudinal deformation caused by the supports provides the necessary conditions for the beam to become longitudinally compressed (or conversely stressed in tension, upon temperature decay).

The development of stresses in concrete structures due to thermal and moisture self-induced effects, which start occurring since very early ages (particularly the thermal ones), must further take into account the marked evolution that during this stage occurs for the following material properties: E-modulus E_c, tensile strength f_{ct}, thermal dilation coefficient α_T and Poisson's coefficient ν. Regarding this evolution, a very important issue should be addressed: the mechanical threshold (often referred to as *time0*), i.e., the instant at which the solid skeleton of the cement matrix starts to be able to bear stresses. Before *time0*, whatever volumetric variations occur (either due to thermal effects or self-desiccation) do not cause stresses, and can thus be disregarded by the structural engineer. Also, viscoelastic behaviour of concrete plays an important role in the relaxation of stresses driven by the thermal and moisture volume changes, which occur in a rather progressive fashion. During this process of stress development in concrete, at some part of the structure tensile stresses may reach the instantaneous tensile strength of the material, and cause cracks to occur, with the corresponding redistribution of stresses and restraint alleviation. The effect of reinforcement, both as a restraining element to shrinkage deformation, and as a stabilizing component after crack initiation, is also of relevance in the study of concrete since early ages.

Concomitantly with the self-induced stresses that have been mentioned, one has also to be aware of the external loads applied to the structure. The analysis of the actual stresses development on a structure during its service life should therefore take into account the simultaneous existence of self-induced stresses and externally applied loads. Engineering experience throughout the years has taught that the so-called residual stresses due to the self-induced effects can sometimes play an important role in the overall behaviour of the structure when subject to its design service loads.

1.3 Research objectives, methods and chapter outline

The previous section highlighted a set of relevant phenomena for stress development in concrete structures since the early ages, and throughout service life. The main purpose of the research conducted during this thesis is to establish a numerical framework to predict the thermal, moisture and mechanical fields in concrete since casting, with particular attention to a sound choice of phenomenological models, supported on an adequate experimental evaluation of the material model parameters. The final goal of the developed methodologies is to provide feasible numerical models and approaches to allow better predictions of concrete behaviour since early ages, in order to avoid problems that otherwise would not be identified in design stage (such as early age cracking or drying shrinkage), or even grant relevant financial savings in design by allowing bold decisions to be made with proper scientific background.

The conducted research reported in this thesis is organized in a total of 7 Chapters (including the present introduction).

Chapter 2 is focused on the thermal problem, with initial considerations about the governing phenomena and material properties, and with special regard to the heat generation potential of cement and concrete. By using the isothermal conduction calorimetry technique, an extensive campaign of cement heat of hydration characterization involving the most common cements in Portugal is described, conducting to the proposal of a set of reference parameters for numerical simulation. Issues regarding the estimation of boundary transfer coefficients are tackled, with consideration of several phenomena such as natural and forced convection, and radiation heat transfer (body-to-body, solar radiation and night sky radiation). Then a brief discussion follows, regarding the adopted strategies in the implementation of a 3D MATLAB finite element model for transient heat transfer in concrete structures, accounting for heat of hydration. The chapter extends further with a set of numerical simulations and experiments regarding the use of the developed simulation tool, including thermography imaging of a hardening concrete cube (for validation of numerical predictions), sensitivity analyses pertaining the effect of reinforcement and variable thermal properties of concrete at early stages of hydration, experimental verification of the feasibility of implemented solar radiation models and wind tunnel testing to back choices regarding heat transfer coefficients.

The moisture problem is dealt with in Chapter 3, focusing on the involved mechanisms and governing equations for moisture transport in concrete. A detailed description is made, pertaining to several parameters involved in the numerical modelling of this problem, particularly in what regards to the choice of the driving potential, the sorption and desorption isotherms and the moisture diffusion coefficient. Strong emphasis is given to the possibility of establishing a relationship between the moisture variations and the potential volumetric changes of concrete. Several descriptions are made regarding the adopted simplifications for the implementation made in this PhD work. The chapter ends with a description of the moisture model implemented in MATLAB (that works together with the thermal model described in Chapter 2), a validation example of its performance against experimental results reported by Kim and Lee (1999) and the moisture analyses of concrete prisms and a reinforced concrete (RC) slab (to be used further in Chapter 5 within the complete thermo-hygro-mechanical analysis framework).

The research documented in Chapter 4 focused specifically on several interactions between concrete and the environment, particularly in what regards to moisture losses from concrete. This part of the work was performed during the stay at the University of Tokyo, with support on the numerical framework DuCOM from the Concrete Laboratory of that university (Maekawa *et al.* 1999). Experiments are reported, focusing on aspects such as the effect of wind speed, curing periods of concrete, environmental temperature and relative humidity on moisture losses from cementitious materials. A new formulation for moisture boundary conditions that uses the water vapour pressure as driving potential for moisture exchanges between concrete and the environment is proposed, implemented in DuCOM and validated against experimental results. The effect of evaporative cooling upon formwork removal in concrete elements is also studied, both experimentally and numerically. Sensitivity numerical analyses are conducted, in regard to several possible situations for environmental exposure of cementitious materials. Also, the ability of

DuCOM to predict the hydration reaction hindering induced by concrete drying is checked against the experimental results obtained by Patel *et al.* (1988). Chapter 4 ends with final remarks regarding the lessons learned from the experiments and conducted simulations, given the fact that the DuCOM framework is not used throughout the other chapters. However, several findings concerning this part of the research are used to back models and simplifications adopted for the thermo-hygro-mechanical framework envisaged in this thesis.

Following the description made in Section 1.2, the next logical issue in the study of concrete performance since early ages is the mechanical problem, which is dealt with in Chapter 5. After a brief review on relevant topics regarding modelling of concrete stresses since early ages (creep, properties evolution, etc.), a description of the overall numerical framework to be used is made, which includes the thermal and hygral sub-models described in Chapters 2 and 3 (implemented in a MATLAB finite element code), the outputs of which are thereafter transferred to the DIANA software (developed by TNO DELFT) for stress field estimation. A pilot experiment for monitoring strains and temperatures in a concrete prism since early ages is presented, with the purpose of better understanding early age strain measurement, and to work as a rehearsal for the choices to be made in the real-scale monitoring necessary in Chapter 6. Also, laboratory experiments regarding the restrained concrete ring test (which allows for measurement of concrete stresses since the early ages) are reported, showing that adequate material characterization, together with a proper choice of numerical models, can lead to reasonable numerical predictions of the stresses that are actually measured in the ring experiment. Finally, a new methodology for quantifying the E-modulus of concrete or cement paste since casting, based on monitoring the evolution of the 1st resonance frequency of a composite beam is proposed and validated. This measuring technique seems quite promising, as it combines the advantages of both ultra-sound and classic resonant frequency methods, without having their specific limitations. A set of several sensitivity analyses is also reported, aimed at checking the influence of the accuracy of mechanical parameters estimation on the quality of concrete stress predictions obtained with the adopted numerical models. Chapter 5 ends with a demonstration of the feasibility and capabilities of the adopted thermo-hygro-mechanical numerical framework, by using it to analyze the behaviour of a free shrinkage prism and a RC slab. The internal stresses developed in the prism due to thermal and drying shrinkage volumetric variations are calculated and thoroughly discussed. Regarding the RC slab, studied under the combined effect of self-induced stresses and external loading, it is shown that the thermo-hygro-mechanical framework allows for interesting insights on the actual stress profiles that develop in the slab, as well as on the influence of cracking.

Applications of the tools developed and described throughout the thesis are presented in Chapter 6. The first application in Chapter 6 relates to the thermo-mechanical analysis of a massive reinforced concrete foundation of a steel wind tower (turbine), for which thermal cracking risk is evaluated. This real-size application involved the monitoring of the actual concrete temperatures developed in-situ, to check the quality of the numerical temperature predictions. The conducted numerical simulations for the stress field aimed at checking the cracking risk in the area where the owner feared thermal stresses: the stretch of the steel tower embedded into the concrete foundation. The second application

in Chapter 6 concerns the stress analysis of a concrete gravity dam during the construction phase, which involved an extensive monitoring campaign (for measurement of early age concrete temperatures and strains) and complementary laboratorial characterization of concrete properties (calorimetric and mechanic). The numerical simulation of the thermal problem involved several complexities, such as the effect of solar radiation (which was explicitly modelled), the contribution of night cooling and the thermal exchanges induced by cleaning water jets during construction. The numerically calculated temperatures and strains are compared to the monitored ones.
The main conclusions of this thesis are summarized in Chapter 7, together with some suggestions for possible extensions to the performed research.

Chapter 2

Thermal problem

2.1 Introduction

The exothermic character of the cement hydration reactions is the reason for the heat liberation that occurs within the first days after casting of concrete structures. Due to the thermal properties of concrete, the released cement hydration heat does not dissipate easily to the environment, causing temperature within concrete to rise up to values as high as 60°C. These temperature changes cause concrete volumetric variations, which are partially hindered by either external or internal restraints. These restrained deformations lead to the occurrence of early age thermal stresses, capable of inducing premature cracks in concrete, or at least to create a stress state of imminent cracking. Most commonly, early age thermal cracking poses durability problems, related to an increased susceptibility of concrete to degradation phenomena (such as corrosion or carbonation), rather than causing structural concerns. An accurate estimation of the concrete stresses caused by the heat of hydration induced volumetric changes calls for a numerical prediction of the temperature field along the early ages.

In the present chapter, the governing equation for heat transfer in homogeneous solids is applied with regards to concrete. Special attention is paid to the thermal properties of concrete at the early ages. The heat generation potential associated to the exothermic nature of cement hydration reactions is thoroughly discussed, both in terms of its experimental determination and its mathematical formulation. The phenomena involved in the boundaries between concrete and its surrounding environment are discussed, along with their numerical formulation, concerning the following topics: natural/forced convection, long-wave radiation, solar radiation and night cooling effects. The numerical implementation in MATLAB of a 3D thermal field simulation software is described, along with its validation. Furthermore, sensitivity analyses are conducted with regards to the effect of reinforcement in the temperature distribution and evolution in concrete

structures, as well as to the simplification of considering thermal properties of concrete as being constant throughout the cement hydration process. With the aid of the developed FE code, experiments are conducted to better clarify issues regarding the numerical modelling of solar radiation and convective heat transfer coefficients.

2.2 General remarks about heat transfer

2.2.1 Modes of heat transfer

Heat transfer occurs through three main mechanisms, as summarized in Figure 2.1: conduction, convection and radiation. Conduction is the process of heat transfer in which the thermal energy transport is performed by the random vibratory motion of molecules, or by the movement of free electrons; it is the typical energy transfer within solids. Convection relies on the motion of fluids to transfer heat; in a typical convective transfer a hot surface heats the surrounding fluid, which is then carried away by fluid movement such as wind. The warm fluid is replaced by cooler fluid, which can draw more heat away from the surface. Since the heated fluid is constantly replaced by cooler fluid, the rate of heat transfer is enhanced. Radiation heat transfer is related to the energy emission from a body as a consequence of its temperature. Radiation heat transfer is argued to be made through electromagnetic waves (according to Maxwell Classic Theory), or through discrete photons (Planck's hypothesis).

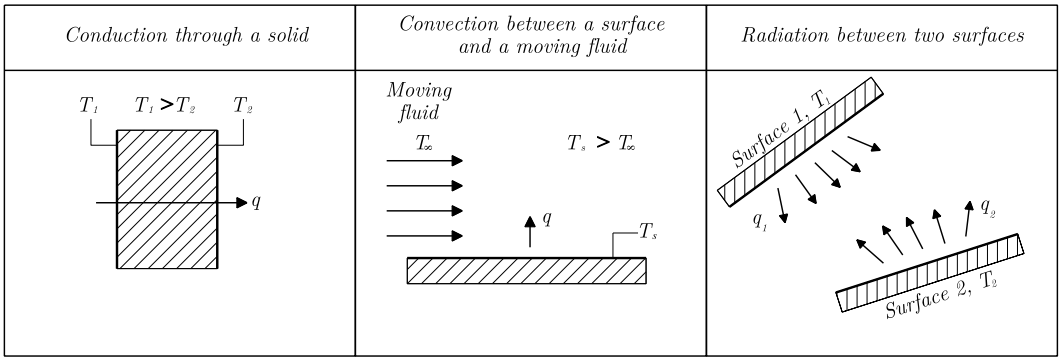

Figure 2.1: Modes of heat transfer

2.2.2 Averaging procedures – REV concept

At several scales, concrete may be considered as a heterogeneous porous material with inclusions (aggregates). However, when an overall temperature distribution is envisaged in a concrete structure, there is no special need to know how temperatures are distributed within the scale of the cement paste and aggregates. Rather, a macro-scale approach is preferable, in which the spatially averaged energy balances of the solid, liquid and gas phases of concrete can be characterized over a specified representative elementary volume (REV). So, concrete is assumed as being a homogeneous isotropic porous medium at a macro scale, even though it is known that at the micro-scale it is quite inhomogeneous and non isotropic. This approach facilitates the deduction of the governing energy balance equation for the temperature field in concrete. In fact, even though many of the

phenomena that occur at a microscopic scale are identified and the modelling is possible, the transposition of results to a real-scale structure would yield unbearable calculations, thus making this approach impossible. The averaging approach for the heterogeneous domain assumes that all phases (solid, gas and liquid) that occupy the porous network are considered to be present at the same time at every point of the REV (overlapping continua). However, care should be taken when choosing possible sizes for the REV: it should be large enough for heterogeneities to have a negligible effect (i.e., it should be larger than pores or aggregates), but it should be small enough to be considered infinitesimal in relationship to the whole medium to be simulated (Mainguy *et al.* 1999). An interesting graphical representation of this concept in regard to acceptable values of the REV volume dv can be observed in Figure 2.2 (adapted from Lewis and Schrefler (2000)).

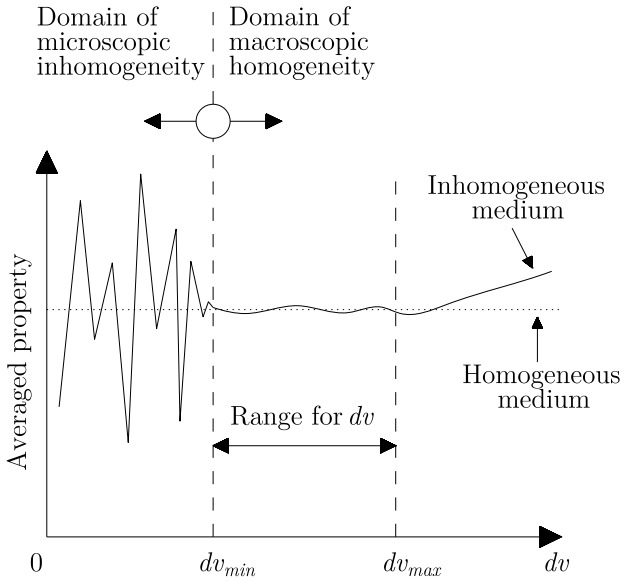

Figure 2.2: Averaged value of a property as a function of the average volume dv

2.3 Heat conduction equation

The rate equation for conduction in solids is known as Fourier's Law, and it is expressed for one dimension as

$$q_x = -k\,A\frac{\partial T}{\partial x} \tag{2.1}$$

where q_x is the heat flux (W) through area A (m^2), k is the thermal conductivity ($Wm^{-1}K^{-1}$), T is the temperature (K) and x is the spatial coordinate (m).
It is known, however, that in porous media such as concrete heat may also be transmitted due to moisture transport (Bazant *et al.* 1978). Equation (2.1) earns a new parcel pertaining to this additional flux, the Dufour effect, which can be defined as the heat flux produced by a concentration gradient (Nield *et al.* 2006)

$$q_x = -k\,A\frac{\partial T}{\partial x} - k_{duf}\,A\frac{\partial w}{\partial x} \tag{2.2}$$

where k_{duf} is the crossed proportionality heat conductivity due to moisture transport ($Wm^{-1}kg^{-1}$) and w is the mass (kg) of free water (not chemically bound) per unit volume of concrete. The Dufour effect, however, has been recognized as playing a negligible role on concrete heat transfer near room temperatures (Bazant and Thonguthai 1978), and therefore will be disregarded in the present research.

The macroscopic energy balance equation in cartesian coordinates may be stated with regards to the REV as represented in Figure 2.3.

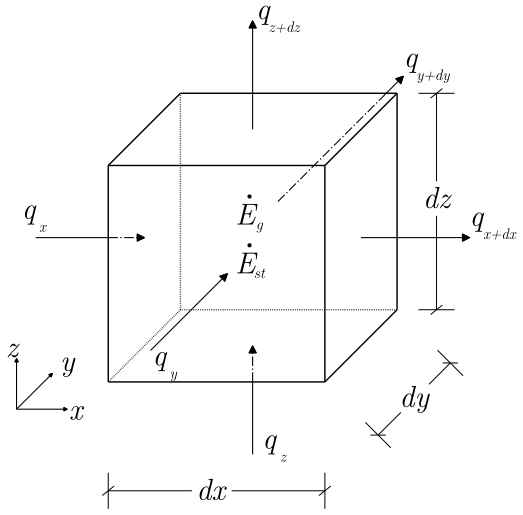

Figure 2.3: Heat conduction in REV

In the presence of thermal gradients, heat conduction occurs through the REV surfaces, perpendicularly to them. In three of the surfaces, heat fluxes may be represented by q_x, q_y and q_z, whereas in the opposite surfaces, heat fluxes may be represented according to a Taylor series expansion (neglecting second and higher order terms) as:

$$q_{x+\partial x} = q_x + \frac{\partial q_x}{\partial x}\partial x \quad q_{y+\partial y} = q_y + \frac{\partial q_y}{\partial y}\partial y \quad q_{z+\partial z} = q_z + \frac{\partial q_z}{\partial z}\partial z \tag{2.3}$$

Denoting by $\dot{Q}$ (Wm^{-3}) the rate of internal heat generation (e.g., due to cement hydration) per unit volume, the energy generation rate within the REV is

$$\dot{E}_g = \dot{Q}\,\partial x\,\partial y\,\partial z \tag{2.4}$$

The rate of energy storage within the REV, $\dot{E}_{st}$ (W), can be expressed as a function of the derivate of temperature in regard to time $\dot{T}$, the specific heat of the material c ($Jkg^{-1}K^{-1}$) and the specific mass ρ (kgm^{-3}):

$$\dot{E}_{st} = \rho\, c\, \dot{T}\, \partial x\, \partial y\, \partial z \tag{2.5}$$

Considering the energy input and output rates $\dot{E}_{in}$ and $\dot{E}_{out}$ in the REV, the energy balance according to the First Law of Thermodynamics in a closed system may be stated as

$$\dot{E}_{in} + \dot{E}_{g} - \dot{E}_{out} = \dot{E}_{st} \tag{2.6}$$

By also introducing the energy fluxes depicted in Figure 2.3, and substituting equations (2.4) and (2.5) into equation (2.6), the following is obtained:

$$q_x + q_y + q_z + \dot{Q}\, \partial x\, \partial y\, \partial z - q_{x+\partial x} - q_{y+\partial y} - q_{z+\partial z} = \rho\, c\, \dot{T}\, \partial x\, \partial y\, \partial z \tag{2.7}$$

Furthermore, by introducing equation (2.3) into (2.7) one arrives at:

$$-\frac{\partial q_x}{\partial x}\partial x - \frac{\partial q_y}{\partial y}\partial y - \frac{\partial q_z}{\partial z}\partial z + \dot{Q}\, \partial x\, \partial y\, \partial z = \rho\, c\, \dot{T}\, \partial x\, \partial y\, \partial z \tag{2.8}$$

According to the principle stated in (2.1), the heat transfer at the surfaces of the REV may be expressed by:

$$q_x = -k\, \partial y\, \partial z \frac{\partial T}{\partial x} \qquad q_y = -k\, \partial x\, \partial z \frac{\partial T}{\partial y} \qquad q_z = -k\, \partial x\, \partial y \frac{\partial T}{\partial z} \tag{2.9}$$

Thus, the general transient heat conduction equation (2.8) becomes:

$$\frac{\partial}{\partial x}\left(k\frac{\partial T}{\partial x}\right) + \frac{\partial}{\partial y}\left(k\frac{\partial T}{\partial y}\right) + \frac{\partial}{\partial z}\left(k\frac{\partial T}{\partial z}\right) + \dot{Q} = \rho\, c\, \dot{T} \tag{2.10}$$

Finally, for the cases in which thermal conductivity is spatially constant during the period of analysis, it is usual to represent the equation (2.10) as

$$k\left(\frac{\partial^2 T}{\partial x^2} + \frac{\partial^2 T}{\partial y^2} + \frac{\partial^2 T}{\partial z^2}\right) + \dot{Q} = \rho\, c\, \dot{T} \tag{2.11}$$

2.3.1 Material properties involved in the heat conduction equation

Concrete is a composite material, defined at the macro-scale as containing cement, water (free or combined), aggregates and partial substitutions of cement (such as fly ash, blast furnace slag or other). Because of that, thermal properties of concrete are greatly influenced by the properties and proportions of its constituents. The following sections deal with the thermal conductivity and the specific heat of concrete.

2.3.1.1 Thermal conductivity

Thermal conductivity of concrete is known to be influenced by several parameters such as: age, w/c ratio, types of admixtures, aggregate volume fraction, fine aggregate fraction, temperature and saturation (because conductivity of air is lower than that of water) (Kim *et al.* 2003). For hardened concrete at room temperature (~20°C), several ranges of variation for this thermal property have been put forward, like 1.2 to 3.5 $Wm^{-1}K^{-1}$ according to Breugel (1980, 1998), 2.5 to 2.9 $Wm^{-1}K^{-1}$ according to the Japanese Concrete Institute (1985), 1.4 to 3.6 $Wm^{-1}K^{-1}$ according to Neville (1995) or 1.2 to 2.4 $Wm^{-1}K^{-1}$ according to Silveira (1996). The relatively wide range of these values can be mainly attributed to the aggregate volume fraction and to the moisture condition of concrete (Kim *et al.* 2003), as well as to the nature of the aggregates (Breugel 1998). Since the aggregate volume fraction in concrete is mostly situated around 80%, the thermal conductivity of concrete is then mostly influenced by the nature of the aggregates. Typical values of concrete thermal conductivity as a function of the aggregate type are reproduced in Table 2.1. Another important issue, particularly for thermal analyses in concrete at early ages, is the temperature dependency of thermal conductivity within the range 5-50°C, which not only encompasses cold concreting, but also frequently reached temperatures in structures due to the heat of hydration. Based on experimental results, both Morabito (2001b) and Kim *et al.* (2003) have reported a linear tendency of concrete thermal conductivity to decrease with T, with a variation of ~5% within the range of temperatures 5-50°C. Therefore, for the applications envisaged in this thesis, it is deemed that within this temperature range it is reasonable to consider that thermal conductivity is constant, with its reference value at ~20°C.
Exceptionally low values of k can be found in lightweight concretes, namely those obtained with the use of expanded shale, having values as low as 0.85 $Wm^{-1}K^{-1}$ (Neville 1995).

Table 2.1: Thermal conductivity of concrete (Breugel 1998)

Type of aggregate	**Thermal conductivity of concrete ($Wm^{-1}K^{-1}$)**
Quartzite	3.5
Dolomite	3.2
Limestone	2.6 - 3.3
Granite	2.6 - 2.7
Rhyolite	2.2
Basalt	1.9 - 2.2

If experimental determination of this property – e.g. the two linear parallel probe method (Morabito 2001b) or the guarded hot plate (Zarr 2001) - is not available, it is possible to conduct estimates of k for hardened concrete (Bentz 2007, Lura *et al.* 2001). Lura and Breugel (2001) provide an estimation of thermal conductivity of concrete based on a ponder average of the thermal conductivities of the components of the mix (cement k_{cem},

aggregates k_{agg} and water k_w) with the ponder factor being the component's content (weight) in the mix per cubic metre (W_{cem}, W_{agg} and W_w):

$$k = \frac{W_{cem}\, k_{cem} + W_{agg}\, k_{agg} + W_w\, k_w}{W_{cem} + W_{agg} + W_w} \tag{2.12}$$

Reference values for thermal conductivities of the components are summarized in Table 2.2 (Breugel 1980), whereas an extensive review on k for rock-forming minerals can be found in Horai and Simmons (1969). It is noteworthy to mention that the small dependency of k with regards to temperature, within the range 5-50°C, can be partially confirmed by application of equation (2.12) with values taken from Table 2.2.

Table 2.2: Thermal conductivity of several materials at four reference temperatures (Breugel 1980)

Material	Thermal conductivity ($Wm^{-1}K^{-1}$)			
	21.1°C	32.2°C	43.3°C	54.4°C
Water	0.60	0.60	0.60	0.60
Cement	1.23	1.27	1.31	1.35
Quartz	3.09	3.08	3.07	3.06
Basalt	1.91	1.90	1.90	1.90
Dolomite	4.31	4.23	4.17	3.98
Granite	3.03	2.90	2.90	2.88
Limestone	4.03	3.94	3.86	3.79
Quartzit	4.69	4.65	4.61	4.57
Rhyolite	1.88	1.89	1.90	1.91

An alternative for estimating the thermal conductivity of concrete has recently been applied by Bentz (2007), who used the Hashin-Shtrikman (H-S) bounds (Christensen 1979, Hashin *et al.* 1962) applied to concrete as a two-phase composite material (cement paste and aggregates). By considering cement paste as phase 1 and aggregates as phase 2 (with thermal conductivities k_1 and k_2), the lower and upper bounds for thermal conductivity of concrete (k_l and k_h respectively) are obtained with basis on the volume fractions of phase 1 and 2 (x_1 and x_2):

$$k_l = k_1 + \frac{x_2}{\dfrac{1}{k_2 - k_1} + \dfrac{x_1}{3\,k_1}} \qquad k_h = k_2 + \frac{x_1}{\dfrac{1}{k_1 - k_2} + \dfrac{x_2}{3\,k_2}} \tag{2.13}$$

For application of this set of equations (2.13) Bentz (2007) recommends a nominal value of $1.0 Wm^{-1}K^{-1}$ for the thermal conductivity of hardened cement paste. The practical application of equations (2.12) and (2.13) provides final values for the thermal conductivity of concrete that are fairly coherent with each other.

A further important issue that needs to be addressed is the evolution of thermal conductivity of concrete since the fresh state and along its hydration process. Since the

free moisture content changes with the progress of cement hydration reactions, and bearing in mind that conductivity is influenced by the moisture content, it is plausible to expect changes in concrete thermal conductivity at early ages. Taking into account that higher moisture content leads to higher values of k (Kim *et al.* 2003), the expectable tendency would be higher initial thermal conductivity in freshly cast concrete, with a propensity to lower down to a stabilized value after hydration completion. Contradictory results are reported on this subject (Breugel 1998, De Schutter 2001), with some authors claiming the aforementioned tendency, and others, such as Morabito (2001b), claiming opposite trends. By performing measurements on hydrating cement pastes, Bentz (2007) concluded that there is little variation (within +/-5%) of k with the degree of hydration.
In the scope of those who acknowledge relevant early changes of k, equations have been proposed that relate this parameter linearly with the degree of hydration (De Schutter 2002, De Schutter *et al.* 1995b, Ruiz *et al.* 2001). De Schutter and Taerwe (2002, 1995b) propose a linear decrease of k from its original value (considered 110% of the final value) as a function of the degree of hydration α, according to

$$k(\alpha) = k(1.10 - 0.10\,\alpha) \tag{2.14}$$

while Ruiz *et al.* (2001) use a very similar formulation, but instead consider the initial k as being 133% of its final value.
As a final remark on the variation of k along hydration, a sensitivity analysis will be presented at the end of this chapter in Section 2.8.1, where further considerations may be found regarding the plausibility of considering k as being constant along early periods of concrete.
Aside from early reactions that occur usually within the first three days after casting, it is however generally agreed that thermal conductivity of concrete is not influenced by age, as confirmed by Kim *et al.* (2003) on tests performed at the ages of 3, 7, 14 and 28 days.

2.3.1.2 Specific heat

Specific heat of hardened concrete has been found to be influenced by several factors, such as the aggregate volume ratio, the w/c ratio, type of aggregates, temperature and moisture state (De Schutter 2001). The mineralogical composition of the aggregate has small importance on the specific heat of concrete, while an increase in moisture content has considerable influence on c (Neville 1995), leading to variations of about 16% between the dry and saturated states (Breugel 1980). Based on experimental results, specific heat has been reported to increase linearly with temperature, with less than 10% variation in the interval 5-50°C (Breugel 1998, Morabito 2001b). The range of variation of this parameter in hardened concrete has been stated as 850-1150Jkg^{-1}K^{-1} (Breugel 1998) or 840-1170Jkg^{-1}K^{-1} (Neville 1995, Silveira 1996). Experimental determination of c is usually made with recourse to similar equipments to the ones that have been mentioned previously for k.
Prediction formulas also exist for specific heat of concrete, which are based on the mass fraction of the constituents of the mix (Bentz 2007, Breugel 1980, Lura and Breugel 2001, Ruiz *et al.* 2003). Breugel (1980), Lura (2001) and Ruiz *et al.* (2003) use an equation

similar to (2.12), and perform a ponder average of the specific heat of concrete constituents (cement c_{cem}, aggregates, c_{agg} and water c_w), which is claimed valid during hydration by comprising a term related to the influence of chemically and physically bonded water in the specific heat (coefficient c_{bindW}=0.2) and degree of hydration α:

$$c = \frac{W_{cem}\, c_{cem} + W_{agg}\, c_{agg} + W_w\, c_w - c_{bindW}\, W_{cem}\, \alpha\, c_w}{W_{cem} + W_{agg} + W_w} \tag{2.15}$$

In this equation the following dependencies on T are considered

$$c_{cem} = 0.1812\sqrt{T} + 2.618\,T + 431 \quad (\mathrm{Jkg^{-1}K^{-1}}) \tag{2.16}$$

$$c_{agg} = 0.0604\sqrt{T} + 0.468\,T + 662 \quad (\mathrm{Jkg^{-1}K^{-1}}) \tag{2.17}$$

and

$$c_w = 4186 \quad (\mathrm{Jkg^{-1}K^{-1}}) \tag{2.18}$$

Alternatively, equation (2.15) may also be used with recourse to the reference values for specific heat of constituents shown in Table 2.3 (Breugel 1980). Even though the temperature dependency of c_{cem} is relatively important, its relevancy is secondary in the final value of the concrete's specific heat, given the fact that the aggregates, whose c_{agg} temperature dependency is slighter, usually represent ~80% of the concrete weight, thus contributing most to the final value of c according to equation (2.15).

Table 2.3: Specific heat of several materials at four reference temperatures

Material	Specific heat ($\mathrm{Jkg^{-1}K^{-1}}$)			
	21.1°C	32.2°C	43.3°C	54.4°C
Water	4187	4187	4187	4187
Cement	456	536	662	825
Quartz	699	745	795	867
Basalt	766	758	783	837
Dolomite	804	821	854	888
Granite	716	708	733	775
Limestone	749	758	783	821
Quartzit	691	724	758	791
Rhyolite	766	775	800	808

The approach forwarded by Bentz (2007) is similar to the one that has been stated in equation (2.15), and can be expressed as

$$c = c_{paste}\, M_{paste} + c_{fineagg}\, M_{fineagg} + C_{crseagg}\, M_{crseagg} \tag{2.19}$$

where M_i stands for mass ratio of the i-th mix component, and the considered components are cement paste ($_{paste}$), fine aggregates ($_{fineagg}$) and coarse aggregates ($_{crseagg}$). This approach also allows for the estimation of the evolution of c along hydration, once a model for the evolution of c_{paste} is associated, as it may be confirmed in Bentz (2007).

The issue of evolution of the specific heat of concrete since the fresh state has been the subject of several research works, and the overall tendency is to acknowledge that c at the beginning of hydration is slightly higher than at its final value. However, some disagreements between different researchers exist with regard to the amplitude of this decrease in specific heat (De Schutter 2001). Lura and Breugel (2001) mention variations from 902Jkg^{-1}K^{-1} for fresh concrete to 804Jkg^{-1}K^{-1} for hardened concrete (a decrease of ~12%), whereas Morabito (2001b) indicates the decrease of specific heat at this stage as being negligible. With regards to the same subject, Breugel (1980) reports a decrease of ~5%, whereas the review conducted by DeSchutter (2001) on this matter states a decrease that ranges from 0% to 20%.

Regarding the same matter, and using the experimental results reported by Bentz (2007), a small sensitivity analysis is conducted with regards to the predictable change in c during hydration. The highest specific heat drop during hydration reported for the cement pastes studied by Bentz (2007) was of about 27%, from ~1720Jkg^{-1}K^{-1} at the beginning, to ~1350Jkg^{-1}K^{-1} at an advanced stage of hydration. By applying the equation (2.19) to an hypothetical paste mass ratio of 0.21 and a mass ratio of 0.79 for granitic aggregates (with a specific heat of 716Jkg^{-1}K^{-1}), one obtains the two limit values for concrete of 928Jkg^{-1}K^{-1} and 850Jkg^{-1}K^{-1}, which actually only show a difference of ~9%. As it can be directly realized from the used equation, this attenuation is related to the superiority of the mass ratio of aggregates (which do not endure any kind of change during cement hydration) as compared to the one concerning hydrating cement paste.

DeSchutter (2002) and DeSchutter and Taerwe (1995b) consider the decrease in the concrete's specific heat to be linear with regards to the degree of hydration α, forwarding an equation similar to (2.14):

$$c(\alpha) = c(1.15 - 0.15\,\alpha) \tag{2.20}$$

The small variations of c during cement hydration, together with the dispersion of proposals with regards to the magnitude of such variation, lead many authors to consider this parameter constant in this context. Nonetheless, a numerical sensitivity analysis is conducted in the scope of this thesis and presented in Section 2.8.1.2 analyzing the impact of considering variable c along hydration in the estimated temperatures for concrete.

2.4 Heat generation potential

2.4.1 Adopted mathematical formulation

The chemical reactions involved in cement hydration are known to be exothermic, with energy outputs of up to ~500kJkg^{-1} (Neville 1995). Hydration heat liberation is not constant and endures several stages, as referred to in Section 1.2. Also, hydration

reactions are thermally activated, with increased rates of reaction when subject to higher temperatures.

The present section aims to describe the numerical model for the heat generation rate $\dot{Q}$ in equation (2.10), which must be capable of translating the exothermic and thermally activated nature of the chemical reactions involved. The adopted formulation was originally proposed by Reinhardt *et al.* (1982), and it is still widely used nowadays. The methodology can be described with basis on the experimentally obtained thermal energy output of a given cement paste, when hydrating under distinct temperatures (20, 30 and 40°C), as depicted in Figure 2.4a (expressed in W per kg of cement). It can be seen that higher temperatures lead to higher heat generation rates from the paste, thus confirming the thermally activated nature of hydration reactions. Another important conclusion is drawn from Figure 2.4b, where integrals of the curves of heat generation rate are depicted, resulting in the evolution of the accumulated heat of hydration Q. It is clear for the three tested temperatures that the final accumulated Q tends to an asymptotic value, here termed as Q_{total}.

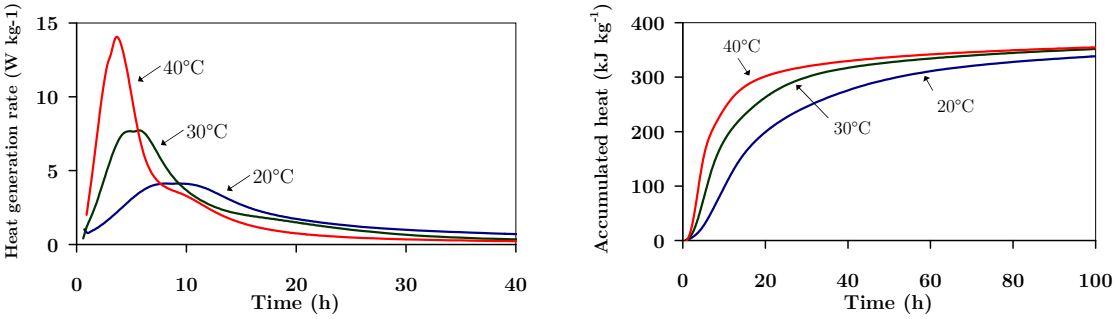

a) $\dot{Q}$ b) Q

Figure 2.4: a) Heat generation rate of a cement paste under three isothermal conditions; b) corresponding accumulated heat of hydration

Let's consider a parameter called degree of heat development α_T, defined as the ratio between $Q(t)$, the accumulated heat generated until a certain instant t and Q_{total}:

$$\alpha_T = \frac{Q(t)}{Q_{total}} \tag{2.21}$$

If the heat generation rate $\dot{Q}$ is plotted against α_T, one arises to Figure 2.5a, where shape resemblance of the curves for the distinct temperatures is striking. Further, if $\dot{Q}(\alpha_T)$ is now divided by the corresponding peak heat generation rate $\dot{Q}_{peak}$, Figure 2.5b is obtained, where the three curves become almost coincident to a single one, termed normalized heat generation rate and represented by the symbol $f(\alpha_T)$.

The mathematical formulation proposed by Reinhardt *et al.* (1982) relies on one basic assumption corroborated by the reasoning conducted above: the rate of heat generation may be described by the product of two independent functions, one taking account of the degree of heat development - $f(\alpha_T)$ - and the other reproducing the influence of temperature - $g(T)$.

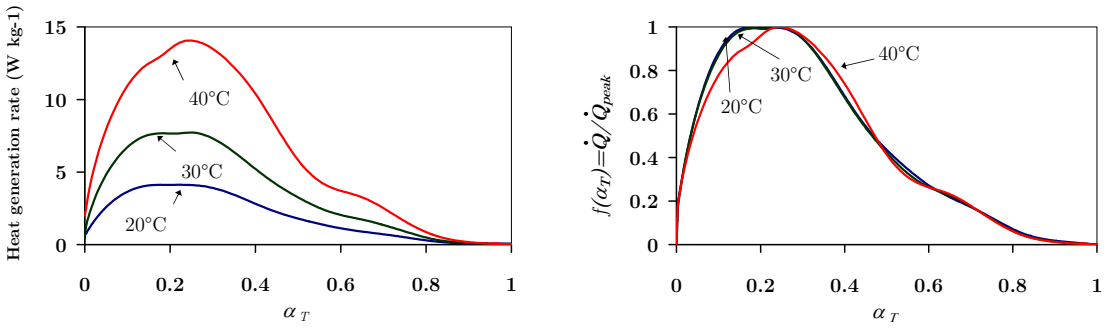

a) b)

Figure 2.5: a) Heat generation rate as a function of α_T; b) normalized heat generation rate $f(\alpha_T)$

Function $f(\alpha_T)$ is directly obtained from experiments, while $g(T)$ is formulated with an Arrhenius-type law as follows, devised originally to describe the kinetics of simple chemical thermally activated reactions:

$$g(T) = A_T \, e^{\frac{-E_a}{RT}} \tag{2.22}$$

where A_T is a rate constant, R is the ideal gas constant (8.314Jmol^{-1}K^{-1}) and E_a is the apparent activation energy (Jmol^{-1}). The exponential involved is based on collision probabilities, thermodynamics and statistical mechanics for homogenous gas and liquid single-phase reactions, which clearly is not the case in cement hydration, where a set of distinct chemical reactions are occurring at the same time or in sequence, with interaction with each other. This is the reason why E_a is termed as an 'aparent' activation energy, since it does not apply to a chemical reaction in particular, as was the case in the original derivation of the Arrhenius law. E_a represents the energy that a molecule in the initial state of the process must acquire before it can take part in a reaction. $g(T)$ expresses the maximum expectable heat generation rate per kg of cement(Wkg^{-1}) for the hydration reaction at temperature T, so the value of $g(293.15)$ should equal the peak of the isothermal 20°C curve in Figure 2.4a which in turn should be conveniently multiplied by the volumetric cement mass content in the concrete mix, VC_{cement} (kgm^{-3}) in order to obtain $\dot{Q}$ for concrete (Wm^{-3}).

The resulting formulation for $\dot{Q}$ is then:

$$\dot{Q} = f(\alpha_T) \, A_T \, e^{\frac{-E_a}{RT}} \tag{2.23}$$

A similar mathematical formulation also based on the Arrhenius law, and involving the product of temperature and hydration dependent factors has been devised by Ulm and Coussy (1995), with a similar performance as equation (2.23):

$$\dot{Q} = Q_\xi \, \tilde{A}(\alpha) \, e^{\frac{-E_a}{RT}} \tag{2.24}$$

where Q_ξ is a material constant, α is the degree of hydration and $\tilde{A}(\alpha)$ is the normalized affinity.

Degree of hydration and its relationship to the degree of heat development

The concept of degree of hydration is frequently used to describe the advancement of the chemical reactions involved in cement hydration. In fact, due to the amount and diversity of chemical reactions involved (namely the several clinker phases C_3S, C_2S, C_3A, C_4AF), it is unfeasible to characterize the actual state of reactions, which is diverse at each instant for each reactant. Nonetheless, it has been consensual to consider that for practical applications the degree of hydration $\alpha(t)$ may be defined as the ratio between the amount of cement that has reacted, i.e., that has been dissolved at time t, and the original amount of cement (Breugel 1991):

$$\alpha(t) = \frac{amount\ of\ cement\ that\ has\ reacted\ at\ time\ t}{total\ amount\ of\ cement\ at\ time\ t = 0} \tag{2.25}$$

The degree of hydration as just defined is quite practical to express material property dependency on the state of reaction advancement, particularly at early ages (De Schutter 2002). However, the direct determination of the degree of hydration is not possible; hence indirect methods by measuring related properties must be used. A review of the many methods used for this purpose (liberated heat of hydration, amount of chemically bound water, chemical shrinkage, amount of $Ca(OH)_2$, specific surface of the cement paste, strength and dielectric properties of cement, compressive strength) can be found in Breugel (1991) and Parrott *et al.* (1990). In this paragraph, however, attention is drawn to the correspondence that exists between the degree of heat development α_T (defined in equation (2.21)) and the degree of hydration. Within the scope of cement hydration at early ages, several studies have been conducted with regards to the relationship between the degrees of hydration measured through different techniques. In particular, with regards to the relationship of the heat liberation with other techniques that indirectly measure the degree of hydration, quite linear relationships have been obtained, as may be confirmed by the results of Lerch and Ford (1948), which compare non-evaporable water with liberated heat of hydration (see Figure 2.6a), as well as by the results of Parrot *et al.* (1990), in which the degree of hydration calculated from quantitative X-ray diffraction analysis (QXRD) is compared with the liberated heat of hydration (see Figure 2.6b).

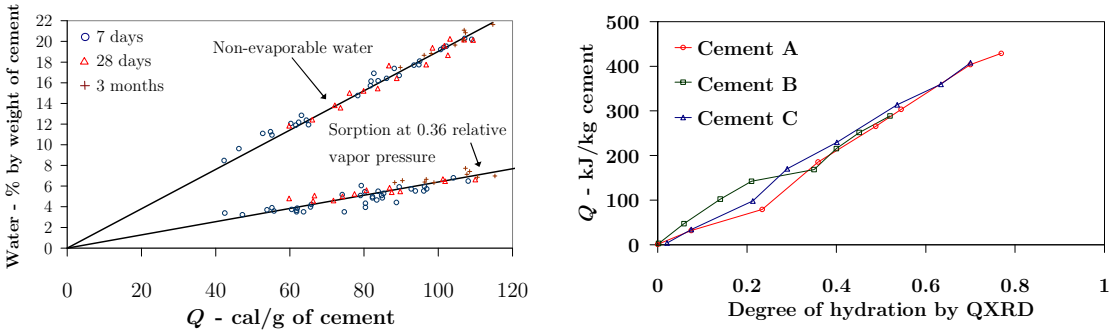

a) b)

Figure 2.6: a) Relationship between Q and non-evaporable water at normal curing conditions; b) Relationship between Q and degree of hydration measured by QXRD

However, this acknowledged linear relationship between heat liberation and degree of hydration for pure Portland cements at early ages has not been verified for the cases where puzzolanic materials are added (Hedlund *et al.* 2000), thus limiting its applicability. Furthermore, another complication arises when trying to use degree of heat liberation as an indication of degree of hydration: knowing the maximum degree of hydration and its relationship to the total generated heat. On one hand, regardless of the composition used (in regard to w/c ratio or inclusion of additions), the degree of heat development α_T after a few days always reaches values very near 1, which is an indication that almost all the heat that can be generated by the mix has been released. On the other hand, the degree of hydration α only seldom, and at very particular conditions, reaches values near 1 (Bentz *et al.* 2005, Breugel 1991, Neville 1995); measurement of heat does not account for this fact, and in case it is used for estimating α, it should be corrected in order to avoid overcoming the actual maximum degree of hydration. This kind of approach has been followed by authors like Cervera *et al.* (2002) and Prato (1999), but still the maximum value of α has to be either experimentally determined or numerically predicted. Several prediction formulae exist for this purpose, usually relating the maximum degree of hydration to the w/c ratio of concrete (Bentz *et al.* 2005, Breugel 1991, Pantazopoulou *et al.* 1995), but even these are relatively inconsistent with each other. For example: according to Bentz *et al.* (2005), for w/c ratios higher than 0.36, the maximum expected degree of hydration can be estimated as 1, whereas using the mathematical formulation proposed in Pantazopoulou and Mills (1995), the corresponding maximum degree of hydration is 0.67.
Bearing this in mind, it was decided to maintain the degree of heat development α_T as the state variable for heat generation, and not computing the degree of hydration α since it is unnecessary for the models in use. Regarding the possible use of the degree of hydration concept in the stress field simulations, further remarks will be made in Chapter 5.

2.4.2 Experimental methods to determine the heat generation potential

The present section provides a brief review of available experimental methods to assess the heat generation from cementitious materials. The review includes four mainstream calorimetric methods: heat of solution, adiabatic, semi-adiabatic and isothermal.

2.4.2.1 Heat of solution calorimetry

Heat of solution calorimetry allows for the measuring of the total heat produced by a cement sample during a given period, with its experimental procedure being regulated by CEN (2003a) and ASTM (2005). Its basic principle relies on the Hess's law, which states that the total energy change for a chemical reaction is independent of the route by which it takes place, provided initial and final conditions are the same. The method relies on using two samples of a given cement: one with hydrated cement (with a certain age t_{test}) – sample *a* - and the other composed of the same cement in unhydrated state – sample *b*. Each of the samples is individually dissolved in a mixture of nitric and hydrofluoric acids inside a Dewar flask (also known as thermos flask), and the heat release is measured with basis on the temperature evolution of the samples (through a process similar to that of

semi-adiabatic calorimetry). The difference in thermal output of the two samples a and b upon dissolution in acid (to the same completely dissociated condition) represents the heat evolved during the hydration of cement.
This method only allows for the measuring of heat generated until a discrete point in time, not allowing a continuous monitoring of heat evolution (unless a series of dozens of experiments are conducted simultaneously for the same mix). Also, this experimental technique is limited to certain types of cement, since some components or additions may be insoluble in the nitric/hydrofluoric acid solution.

2.4.2.2 Adiabatic calorimetry

The principle of adiabatic calorimetry consists of placing the freshly cast sample to be tested in a closed system, which guarantees that no heat energy exchanges occur between the sample and the surrounding environment (adiabatic conditions). As a consequence of these experimental conditions, all the heat produced within the sample due to the exothermic character of the cement hydration reactions is converted into temperature rise, which in turn is uniform within the sample. Temperature rises from an initial value until a plateau is attained, in correspondence to the end of relevant heat generation by the hydration reactions. Because of its characteristics, adiabatic calorimetry is suitable for characterizing cement paste, mortar or even concrete (i.e., large samples are allowable).
The measured output of an adiabatic test is the temperature rise of the sample, therefore, it is necessary to conduct conversion procedures in order to obtain a measure of the generated heat. If one takes the simplifying assumption that both thermal conductivity and specific heat are constant during hydration, then equation (2.11) holds valid for the temperature field within the adiabatic chamber. Furthermore, given the fact that no spatial temperature gradients exist inside the adiabatic chamber, the conductivity k-related terms cancel out, with the resulting field equation being

$$\dot{Q} = \rho\, c \frac{\partial T}{\partial t} \tag{2.26}$$

From this equation it can also be observed that knowledge of the volumetric specific heat (ρc) of the sample is indispensible for computing the heat rate generation. This is frequently considered a downside of this kind of calorimetric technique, since it requires the previous experimental determination of ρc, or alternatively an estimation, which may induce errors in the heat generation assessment. Also, estimation of the apparent activation energy by using adiabatic calorimetry is difficult, when compared to the case of isothermal calorimetry, which will be dealt with in detail further on this document (see Section 2.4.3).

2.4.2.3 Semi-adiabatic calorimetry

Semi-adiabatic calorimetry, which is regulated in EN196-9 (CEN 2003b), basically consists of placing the freshly cast cementitious material sample into a container (usually a Dewar flask), allowing some limited heat exchanges between the sample and the outer environment to occur. According to EN 196-9 the coefficient of total heat loss of the

calorimeter shall not exceed $100 Jh^{-1}k^{-1}$ for a temperature rise of 20K. Samples tested by this technique may be as heavy as 10kg, therefore concrete samples may be tested.
Heat generated by the sample up to a given instant is calculated by summing up the heat calculated from the temperature rise in the sample and the calculated heat loss from the container. The required calculations necessary for this kind of experiment, may also be obtained from analysis of equation (2.11); however, two assumptions are necessary: a) spatial temperature gradients within the sample are small enough to be considered negligible (condition assured by limiting the total heat loss of the calorimeter as stated above); b) a term pertaining to the heat losses P is added to the equation. The resulting basic equation to compute $\dot{Q}$ is thus

$$\dot{Q} = \rho\, c \frac{\partial T}{\partial t} + \frac{\partial P}{\partial t} \tag{2.27}$$

Apart from the difficulties that this calculation procedure shares with that of adiabatic calorimetry (necessity of measuring or estimating ρc), semi-adiabatic calorimetry calls for the necessity of calibrating coefficients for the determination of P and its sensitivity to the temperature of the sample.

2.4.2.4 Isothermal calorimetry

Isothermal calorimetry, which is also called conduction calorimetry, consists of measuring the thermal heat output directly from the reacting sample. The basic principle of this experimental technique relies on maintaining the sample under study at constant temperature during the whole test, measuring the thermal output of the sample using heat flux sensors. The necessity of assuring isothermal conditions within cement based materials requires that only small samples of ~45g cement paste (or mortar) are used, thus not allowing direct tests on concrete. Anyway, this is not considered to be a significant drawback, since the responsible part for heat generation in concrete is in fact the cement paste. So, upon knowledge of the volumetric content of cement paste within concrete, it is possible to obtain the expectable heat generation from concrete by extrapolating the corresponding cement paste results. Of course, this extrapolation is only valid in the cases that the aggregates do not affect the hydration kinetics of cement, which is usually the case for the great majority of concretes (Wadsö 2003). Difficulties in this extrapolation have however been reported by Morabito (1998), who mentions kinetics in concrete to be different from those of cement paste due to buffering effects of the aggregates. Nonetheless, the simplification of ignoring this buffering effect has been adopted in the work developed for this thesis. The reasonable temperature prediction coherences obtained point to a probable small or negligible buffering effect of aggregates.
The main advantage of isothermal conduction calorimetry in regard to the experimental techniques reported previously relies in the fact that it allows direct measurement of heat Q (the desired entity), whereas the other methods require indirect measurement of it through temperature monitoring, and require estimation of ρc. Furthermore, isothermal conduction calorimetry allows for direct estimation of the apparent activation energy of the hydration reaction by using the results of isothermal tests conducted at distinct

temperatures, as documented in Section 2.4.3. These were the main reasons for the purchase of an isothermal conduction calorimeter within the LABEST research unit.
Given the fact that extensive results obtained with an isothermal calorimeter are to be presented in this thesis, a general description of the equipment used, as well as its basic working principles, are described in the following. The equipment used is a JAF60 calorimeter, which allows performing isothermal tests from room temperature until 60°C. The basic equipment core is the calorimetric unit to be placed inside a constant temperature bath, which is represented schematically in Figure 2.7. Within this unit, the cement paste or mortar sample is placed inside a small plastic bag, which in turn is placed inside a brass container in the lower part of the unit, in direct contact with a heat sink. Except for the contact with the heat sink, all surfaces of the sample container are thermally insulated from the effects of the surrounding bath as much as possible, with recourse to polystyrene elements. As soon as exothermic hydration reactions start to take place, most of the generated heat is conducted to the constant temperature bath through the heat sink. Heat flux sensors, which are placed between the sample brass container and the heat sink, generate an output voltage proportional to the flow of heat $\dot{Q}$ through the sensor from the reaction vessel to the heat sink.

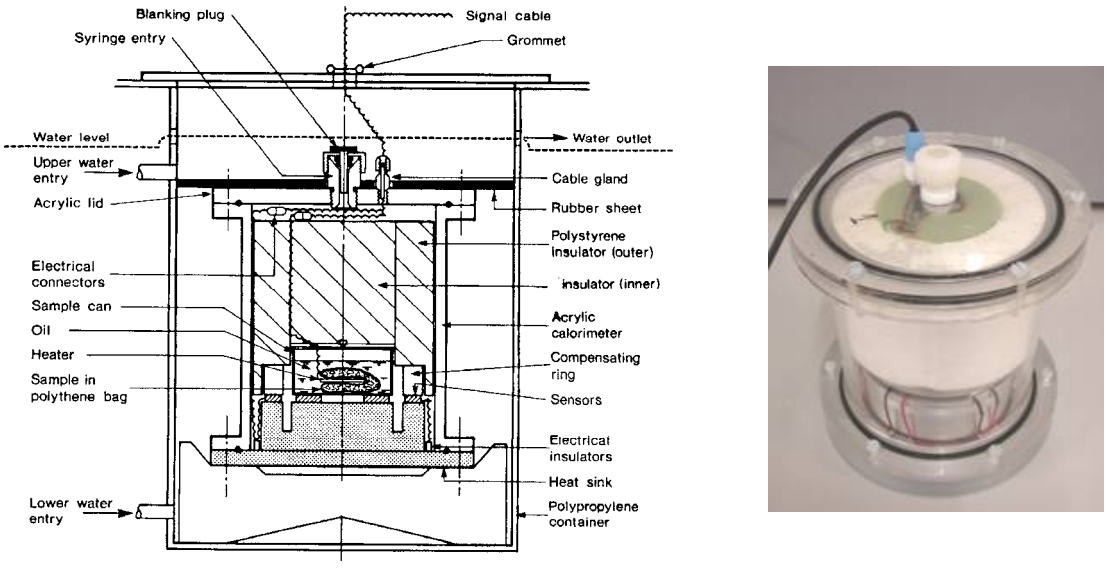

a) b)

Figure 2.7: Calorimeter basic unit: a) Scheme (Wexham 1998); b) Photo

Working equations for the isothermal calorimeter

Assuming that the heat sink is at the same constant temperature of the water bath T_{sink}, when the sample generates a small quantity of heat dQ in a short interval of time dt, there is a slight rise in temperature in the sample (reaching temperature $T_{sample} > T_{sink}$, with the temperature difference $\Delta T = T_{sample} - T_{sink}$) before heat is actually conducted to the heat sink. Labelling the specific heat of the sample container and its contents as u, this internal heating absorbs energy at a rate $u \times \partial T \times \partial t$. The remaining heat is conducted through the heat sink, which means that it is proportional to the temperature difference by a rate constant, here considered p. The heat balance equation can then be formulated as:

$$\frac{\partial Q}{\partial t} = p\,\Delta T + u\frac{\partial T}{\partial t} \tag{2.28}$$

Given the fact that voltage output E of the heat flux sensor is proportional to ΔT (E=$g\Delta T$, being g a proportionality factor), equation (2.28) may be rewritten as follows, usually termed Tian-Calvet equation (Mulligan 2002),

$$\frac{\partial Q}{\partial t} = \frac{p}{g}E + \frac{u}{g}\frac{\partial E}{\partial t} \quad \Leftrightarrow \quad \frac{\partial Q}{\partial t} = K_1\,E + K_2\,\frac{\partial E}{\partial t} \tag{2.29}$$

where K_1 and K_2 are the calorimeter constants. As the sample's ρc may vary from case to case, as well as other variables may, this calorimetry technique requires a calibration at the end of every experiment (when the heat generated by the sample becomes null or negligible), using the obtained calorimeter constants for analysis of results. The process of obtaining K_1 and K_2 consists of generating a known heat source within the sample container (and before removing the sample) with a known electrical resistance. The experimental setup is left undisturbed for ~1/2 hour (with the heat source turned on), and the measured output from the heat flux sensors is registered in regular intervals. The result of the calibration experiment may be plotted in the form of a $\partial E/\partial t$ *versus* E curve, as depicted in Figure 2.8.

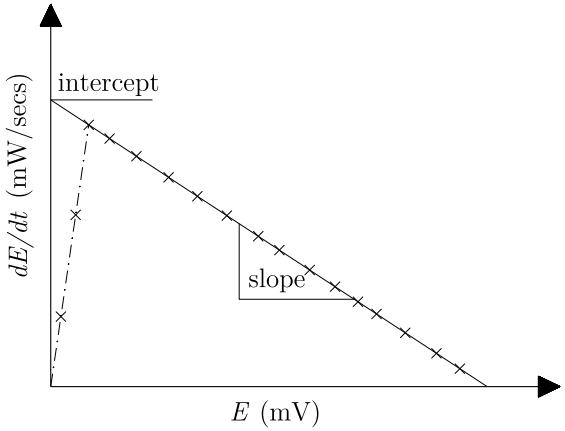

Figure 2.8: Typical graph of $\partial E/\partial t$ *versus* E

By solving equation (2.29) in order to $\partial E/\partial t$, the following equation is obtained

$$\frac{\partial E}{\partial t} = -\frac{K_1}{K_2}E + \frac{1}{K_2}\frac{\partial Q}{\partial t} \tag{2.30}$$

Equating K_1/K_2 and $(1/K_2)\times(\partial Q/\partial t)$ to the slope and intercept values in Figure 2.8, respectively, the calorimeter constants K_1 and K_2 are then obtained.

2.4.3 Characterizing heat generation of cement paste using isothermal calorimetry

The presented isothermal JAF60 calorimeter was used for an extensive campaign, centred on the experimental evaluation of concrete mix calorimetric properties, for application to

numerical modelling in the format of equation (2.23). In the text that follows, the used procedure for implementation to obtain the many entities involved in calorimetric characterization is outlined, in view of an automatic data processing routine implemented in MATLAB.

The data provided by the isothermal calorimeter for a given isothermal testing temperature is the time evolution of $\dot{Q}(t)$ - as seen in Figure 2.4a - and of the generated heat $Q(t)$ – as seen in Figure 2.4b. The calculation procedures to be described in the following are fully based in the aforementioned set of data.

2.4.3.1 Computation of $f(\alpha_T)$

The general description of how $f(\alpha_T)$ can be obtained has been given in Section 2.4.1. However, the actual detailed process used is explained here, which starts by estimating the asymptotic value of Q_{total}. To this purpose, curve $Q(t)$ of Figure 2.4b is plotted as $Q(1/t)$, resulting in a plot similar to the one depicted in Figure 2.9a. The least square method is used to get the best fit of an equation $l(x)$ of type

$$l\left(\frac{1}{t}\right) = a\, e^{b\frac{1}{t}} \tag{2.31}$$

where a and b are the fitting parameters. The data used for the fitting corresponds to 1/t values lower than 0.02 – see Figure 2.9 -, which is the same as saying that experimental results obtained earlier than 50h are being disregarded. This option of not using values $1/t$>0.02 has proved to be consistently robust for all the experimental data studied within the present research work. Function $l(1/t)$ is then solved for $1/t \sim 0$, providing $l(\sim 0) = Q_{total}$.

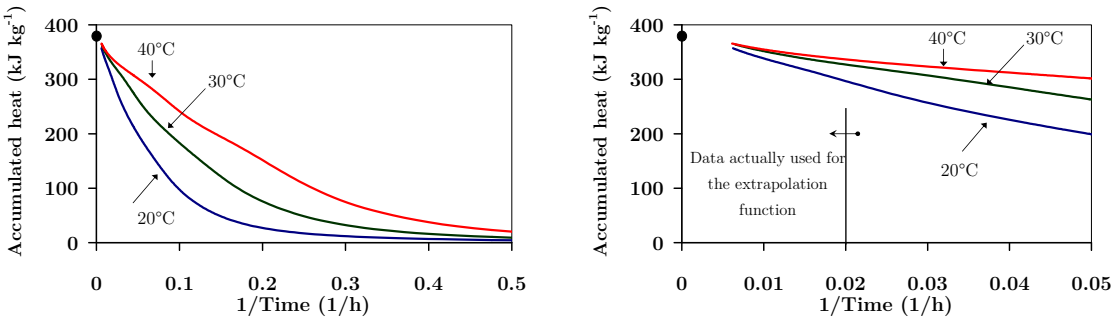

Figure 2.9: Extrapolation procedure for Q_{total} – diagram for: a) 1/t < 0.5; b) 1/t<0.05

Upon knowledge of Q_{total}, $\alpha_T(t)$ is calculated using equation (2.21). The combined information of $\alpha_T(t)$ and $\dot{Q}(t)$ allows obtaining $\dot{Q}(\alpha_T)$. From $\dot{Q}(\alpha_T)$, the maximum $\dot{Q}_{peak}$ is numerically detected and used for computing $f(\alpha_T) = \dot{Q}(\alpha_T)/\dot{Q}_{peak}$. It should be noted, however, that detection of this maximum should be directed to the first local maximum that is preceded by a local minimum, due to the possible disturbances to the automatic process that might arise associated to residual heat generation caused by early reactions, as schematically shown in Figure 2.10.

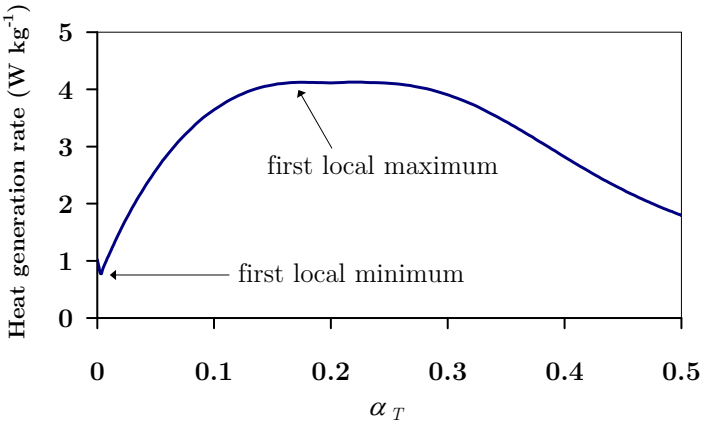

Figure 2.10: Schematic representation of the methodology to determine $\dot{Q}_{peak}$

2.4.3.2 Computation of E_a and A_T

Two alternatives for the calculation of E_a were adopted in the present thesis: the speed method and its variant, the derivative of the speed method. Both methods are described in detail by D'Aloia (2001) and D'Aloia and Chanvillard (2002) and are based on the determination of E_a in a temperature range limited by two tested temperatures in the isothermal calorimeter.

The speed method

Formulation of α_T given in equation (2.21) can be differentiated with regards to time to render

$$\dot{\alpha}_T = \frac{\dot{Q}(t)}{Q_{total}} \tag{2.32}$$

Therefore, based on equations (2.23) and (2.32) it may be stated that:

$$\dot{\alpha}_T = \frac{f(\alpha_T) A_T}{Q_{total}} e^{\frac{-E_a}{RT}} \tag{2.33}$$

For a given fixed degree of heat development $\alpha_{T\text{-}ref}$ and referring to two isothermal calorimetry tests $C1$ and $C2$ of the same mix conducted at distinct temperatures T_{C1} and T_{C2}, equation (2.33) holds true for both of them as:

$$\left[\dot{\alpha}_T\left(\alpha_{T-ref}\right)\right]_{C1} = \frac{f\left(\alpha_{T-ref}\right) A_T}{Q_{total}} \exp\left(\frac{-E_a}{R\,T_{T_{C1}}}\right) \tag{2.34}$$

$$\left[\dot{\alpha}_T\left(\alpha_{T-ref}\right)\right]_{C2} = \frac{f\left(\alpha_{T-ref}\right) A_T}{Q_{total}} \exp\left(\frac{-E_a}{R\,T_{T_{C2}}}\right) \tag{2.35}$$

Considering that E_a does not depend on T within the considered range, and dividing equation (2.34) by equation (2.35), one obtains

$$\left[\dot{\alpha}_T\left(\alpha_{T-ref}\right)\right]_{C1} = \left[\dot{\alpha}_T\left(\alpha_{T-ref}\right)\right]_{C2} \exp\left(\frac{-E_a}{R}\left(\frac{1}{T_{C1}} - \frac{1}{T_{C2}}\right)\right) \tag{2.36}$$

By solving this equation for E_a, one finally gets

$$E_a\left(\alpha_{T-ref}\right)\Big|_{T_{C1}}^{T_{C2}} = \frac{-R\left(T_{C1} \times T_{C2}\right)}{T_{C2} - T_{C1}} \ln\left[\frac{\left[\dot{\alpha}_T\left(\alpha_{T-ref}\right)\right]_{C1}}{\left[\dot{\alpha}_T\left(\alpha_{T-ref}\right)\right]_{C2}}\right] \tag{2.37}$$

The speed method allows for computation of E_a along all stages of hydration, which varies considerably in most cases. This is consistent with the fact that hydration reactions are initially reaction-rate-limited, and become diffusion-limited as hydration products form. Nonetheless, for α_T between 0.1 and 0.6 the E_a values computed from the use of (2.37) exhibit relatively low variations, which makes it feasible to adopt these values for heat of hydration estimation, since it is also within this range of α_T that the heat generation rates are higher. A typical result of the speed method can be found in Figure 2.11.

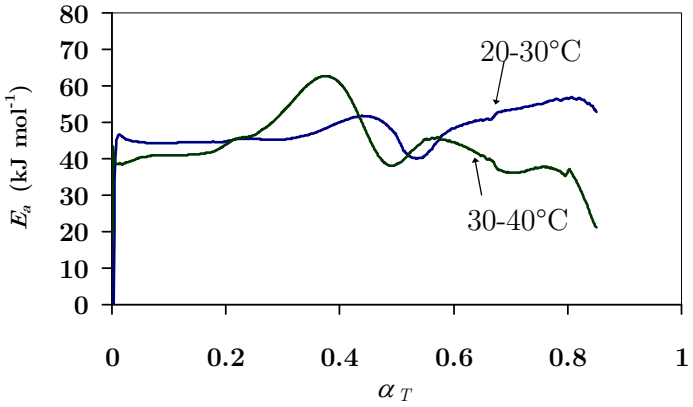

Figure 2.11: Typical E_a evolution using the speed method

The derivate of the speed method

This alternative way for calculation of the apparent activation energy derives from the methodology proposed by ASTM (1987). It consists of applying Nepper logarithms to both terms of equation (2.23) for a given isothermal heat conduction experiment temperature T_{Ci}, and at a degree of heat development $\alpha_{T\text{-}ref}$:

$$\ln\left(\dot{Q}_{Tsti}\left(\alpha_{T-ref}\right)\right) = \ln\left(f\left(\alpha_{T-ref}\right)A_T\right) - \frac{E_a}{R\,T_{Ci}} \tag{2.38}$$

This equation may be interpreted as a line of the type Y=mX+b in a graphic whose Y axis is $\ln\left(\dot{Q}_{Tsti}\left(\alpha_{T-ref}\right)\right)$ and X is the reciprocal of the absolute temperature $1/T_{Ci}$, where m= - E_a/R and b=ln($f(\alpha_{T\text{-}ref})A_T$). Therefore, for the reference degree of heat development

$\alpha_{T\text{-}ref}$, a point pertaining to each *i*-th isothermal temperature experiment may be plotted independently, allowing for a best-fit line to be assessed for the group of points. From the obtained fitting parameters, both E_a and A_T may be obtained directly. Repeating this procedure for distinct degrees of heat development, it is possible to obtain the relationship between E_a and α_T. However, it has been proposed by Wadso (2003) to consider a unique reference value of α_T corresponding to the peak value of heat generation rate $\dot{Q}_{peak}$ (that roughly occurs at the same degree of heat development for the range of temperatures usually studied in cement calorimetry), which in turn corresponds to $f(\alpha_T)=1$. This allows obtaining a single value of E_a for the whole hydration reaction, which is representative of the instant at which heat generation rate is most significant, having thus better precision at such stage of the reaction. An example of the application of this method can be seen in Figure 2.12, where each square represents the information of an isothermal calorimetry test at its highest heat generation rate, and the black line is the best fit line. The fact that all squares are very well aligned confirms the validity of the apparent activation energy concept for the studied degree of hydration.

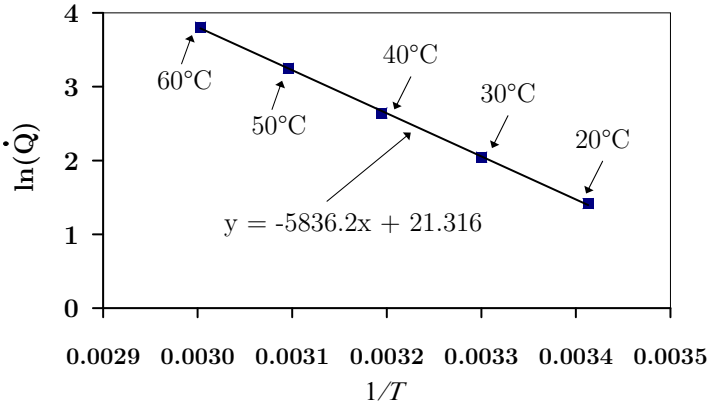

Figure 2.12: Application of the derivate of the speed method

2.4.3.3 Experimental campaign over commercially available cements in Portugal

With the purpose of creating a wide collection of data pertaining to the heat development characteristics of a representative group of cements commercially available in Portugal, isothermal conduction calorimetry tests at several temperatures were conducted. This experimental campaign intended to create a database in a format suitable for input to numerical models concerning thermal analysis of concrete structures at early ages. The two main Portuguese cement selling companies, named here as Company A and Company B, were selected for the sake of representativeness, with the selection of five cements from each (designation according to EN197-1 (2000) and chemical composition of the studied cements given in Table 2.4). Bearing in mind that each isothermal calorimetric test was conducted for no less than 72h (reaching 186h for the tests at lower temperatures), and that all cements were studied for no less than 4 distinct temperatures, the present experimental campaign corresponds to no less than 120 days of continuous operation of the isothermal calorimeter. The actual experimental campaign took almost two years to be concluded.

Table 2.4: Chemical composition and fineness of the cements

	Cement type	SiO2	Al2O3	Fe2O3	CaO (Total)	MgO	SO3	K2O	Free CaO	Loss on ignition	Blaine (cm^2/g)
Company A	CEM I 52.5R	18.98	5.43	3.57	64.03	1.6	3.31	1.03	1.12	2.13	3880
	CEM I 42.5R	18.26	5.47	3.32	63.89	1.86	2.75	1.08	1.29	2.6	2950
	CEM II/A-L 42.5R	16.82	5.11	3.11	62.31	1.78	3.2	1	1.12	6.39	3830
	CEM II/B-L 32.5N	12.74	4.17	2.31	59.75	1.47	3.04	0.79	0.73	14.54	4060
	CEM IV/B(V) 32.5N	31.73	12.67	6.88	39.85	1.69	2	1.06	0.84	3.02	3630
Company B	CEM I 52.5R	20.16	4.35	3.48	62.97	2.33	3.4	-	-	-	4914
	CEM I 42.5R	19.82	4.22	3.4	62.66	2.21	3.47	-	-	-	4112
	CEM II/A-L 42.5R	18.58	4.18	3.22	62.02	2.09	3.35	-	-	-	4494
	CEM II/B-L 32.5N	18.02	3.86	2.52	59.7	1.79	2.61	-	-	-	4433
	CEM II/B-L 32.5R (w)	17.29	2.38	0.17	64.58	0.5	2.48	-	-	-	5019

In the present section, discussions are conducted with regard to the results obtained directly from the isothermal conduction calorimeter - $\dot{Q}(t)$ and $Q(t)$ -, as well as to the corresponding parameters for numerical implementation according to equation (2.23). Cements from Company A were experimentally studied at the temperatures of 20°C, 30°C, 40°C, 50°C and 60°C. Cements from Company B were studied for the same temperatures, except for 60°C.

Almost half of the tests were conducted twice, with very coherent results between pairs: the worst deviation in terms of generated heat rate was of about 2.6%. Therefore, in this thesis only the results concerning one specimen per studied situation are presented.

The experimental procedure consisted of preparing 30g samples of cement in a small plastic bag, to which 15g of de-ionized water were added (previously conditioned at the same temperature of the isothermal test to be performed), resulting in a mix with w/c=0.5. Within a period of less than 10 minutes the mixing was performed, and the sample was put on the calorimeter unit inside the thermostatic bath (heat sink) at the predefined test temperature. This time lapse of not more than 10 minutes between mixing and the beginning of the measurements causes this test to be unable to capture the very early heat release that occurs immediately after mixing. These early reactions have negligible influences on the heat generation in real concrete applications, and therefore they were disregarded in this study (De Schutter *et al.* 1995a).

Results and discussion

Heat generation rate

The curves regarding the heat generation rate $\dot{Q}$ (expressed in W per kg of cement) as a function of time are depicted in Figure 2.13a (Company A) and in Figure 2.14a (Company B) for the studied cements, with cements labelled with a prefix regarding their corresponding company: CA or CB. The expectable increase of $\dot{Q}_{peak}$ with T was observed (see also Table 2.5), as well as the tendency of this maximum to occur sooner for higher isothermal curing temperatures. These observations confirm the thermally activated nature of the chemical reactions involved in cement hydration. The mentioned heat

generation peak has been reported as motivated by C_3S hydration; some of the cements exhibited a secondary peak, which is usually assigned to hydration of C_3A (Bensted 1987). The information provided in Table 2.5 also allows observing that even though $\dot{Q}_{peak}$ tends to occur sooner for higher isothermal test temperatures, the corresponding degree of heat development remains relatively consistent around a certain value for each cement (exception for CA CEM II A L 42.5R and CB CEM I 42.5R). However, for the highest testing temperatures of 50°C and 60°C this coherent tendency was disturbed.

Total heat of hydration

Integration of each heat generation rate curve of Figure 2.13a and Figure 2.14a allows obtaining the corresponding accumulated heat generation Q *versus* t plotted in Figure 2.13b and in Figure 2.14b. There is a general tendency of reaching the end of each test with higher values of Q as the experiment temperature increases, meaning that the extent of hydration at the end of the experiment was higher for higher testing temperatures (as expectable). This tendency was only clearly disrupted for CA CEM II/B-L 32.5N.

In Table 2.6 the extrapolated values of the total heat Q_∞ for the analyzed range of cements and temperatures are presented. For a given cement, the calculated values of Q_∞ seem to be reasonably homogeneous, even in the case in which deviations are larger: in CA CEM IV B(V) 32.5N the largest deviation in regard to the average was observed in the isothermal test at 20°C, were a ~10% higher value was obtained. Contrarily to what was observed at the end of each test and reported in the previous paragraph, there seems to be no observable pattern for the dependency of Q_∞ on the testing temperature.

If one focuses on the average values of Q_∞ for the different cements, several comparisons can be made. Even though CA CEM I 52.5R and CA CEM I 42.5R have very similar chemical compositions, and therefore should be expected to have similar values of total heat, the fineness of CA CEM I 52.5 R is clearly higher than that of CA CEM I 42.5 R (see Table 2.4), thus justifying the higher value of Q_∞ for the former cement. CA CEM II/A-L 42.5R has an average Q_∞ very similar to that of CA CEM I 42.5 R: this was a rather unexpected result, as the partial substitution of Portland clinker by limestone in the case of CA CEM II/A-L 42.5R would lead to a prediction of the heat liberation to become smaller than the one of the ordinary Portland CEM I 42.5R. The reason for such difference may be attributable also to the higher fineness of CA CEM II/A-L 42.5R. Apart from this unexpected tendency, the overall results were rather predictable: ordinary Portland cements have more total heat liberation than limestone cements, and the fly ash cement (CA CEM IV B (V) 32.5N) had the lowest total heat of all.

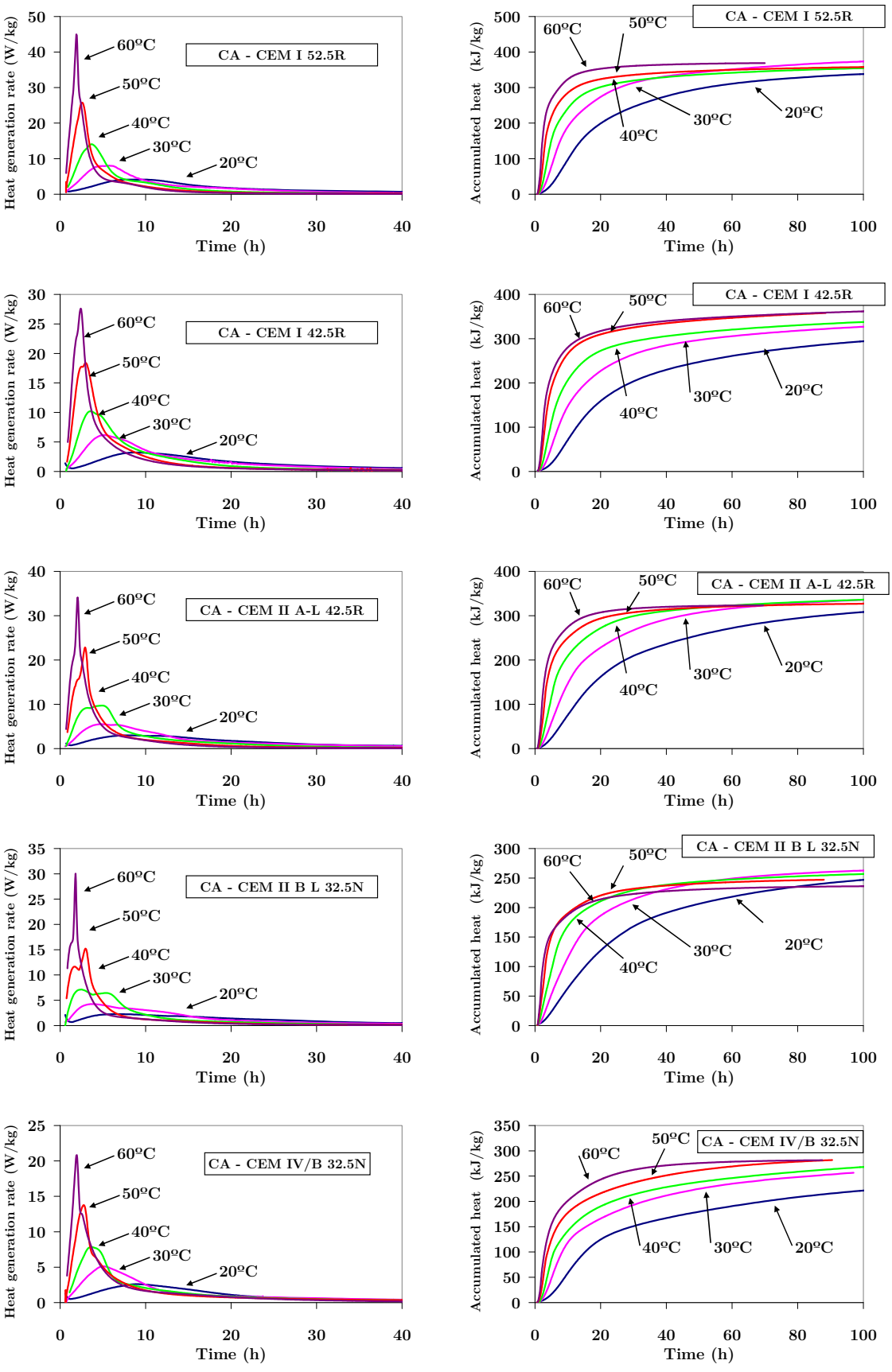

a) b)

Figure 2.13: Company A cements: a) Heat generation rate and b) total heat of hydration

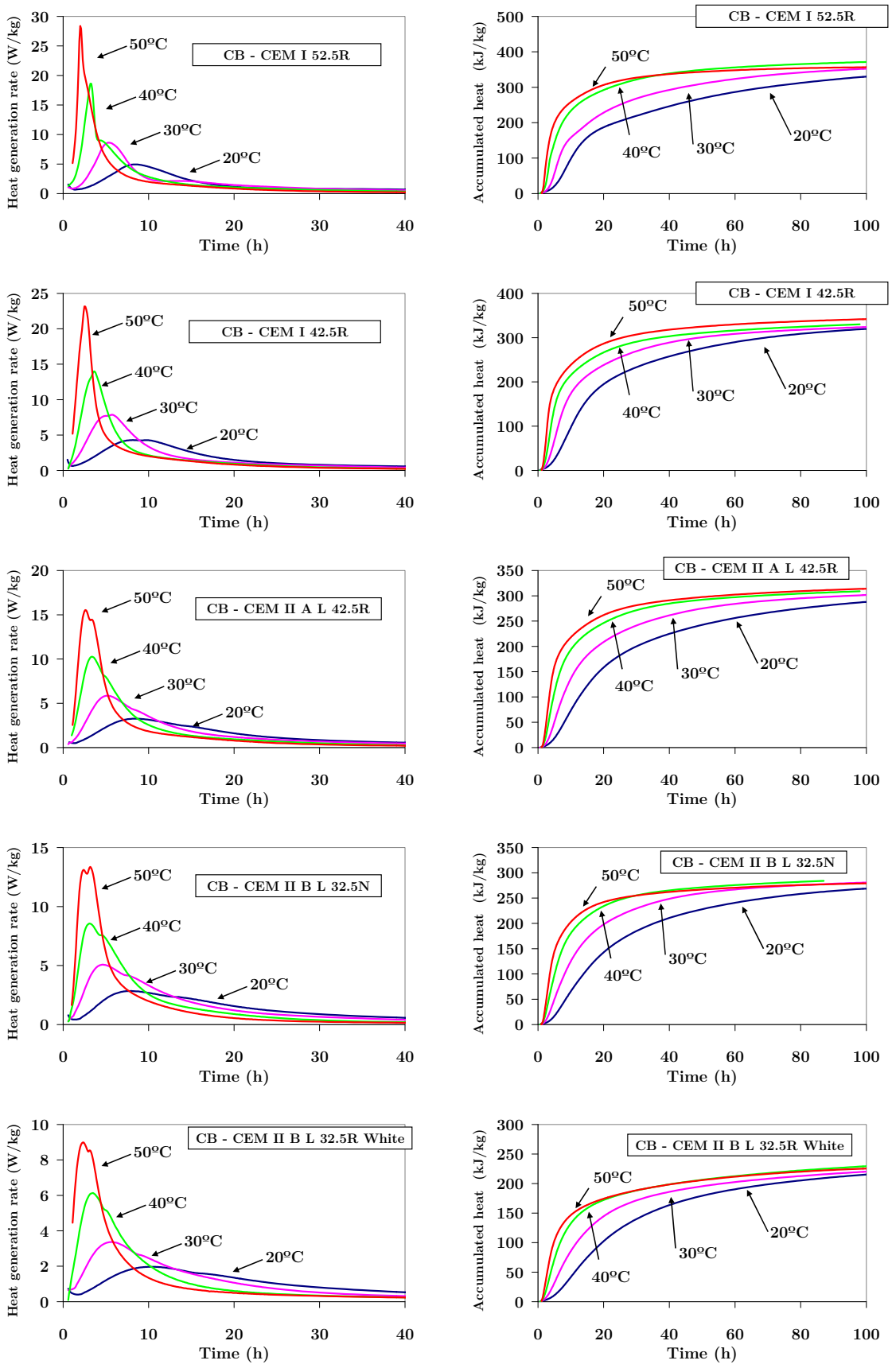

a) b)

Figure 2.14: Company B cements: a) Heat generation rate and b) total heat of hydration

Table 2.5: Heat generation for several cement pastes: peak values and corresponding α_T and instants of occurrence

		20°C	**30°C**	**40°C**	**50°C**	**60°C**
CA CEM I 52.5R	$\dot{Q}_{\max}$ (W/kg)	4.13	8.05	14.07	25.76	44.96
	$\alpha_T\left(\dot{Q}_{\max}\right)$	0.22	0.24	0.25	0.28	0.27
	$t\left(\dot{Q}_{\max}\right)$ (h)	9.2	5.7	3.7	2.6	1.9
CA CEM I 42.5R	$\dot{Q}_{\max}$ (W/kg)	3.21	6.16	10.20	18.41	27.60
	$\alpha_T\left(\dot{Q}_{\max}\right)$	0.17	0.16	0.17	0.25	0.26
	$t\left(\dot{Q}_{\max}\right)$ (h)	8.9	5.1	3.6	3.0	2.4
CA CEM II A L 42.5R	$\dot{Q}_{\max}$ (W/kg)	2.99	5.51	9.71	22.83	34.13
	$\alpha_T\left(\dot{Q}_{\max}\right)$	0.15	0.15	0.32	0.31	0.27
	$t\left(\dot{Q}_{\max}\right)$ (h)	8.0	4.8	5.0	2.9	2.1
CA CEM II B L 32.5N	$\dot{Q}_{\max}$ (W/kg)	2.27	4.26	7.14	15.22	30.03
	$\alpha_T\left(\dot{Q}_{\max}\right)$	0.11	0.12	0.13	0.35	0.26
	$t\left(\dot{Q}_{\max}\right)$ (h)	6.3	3.8	2.5	3.0	1.8
CA CEM IV 32.5N	$\dot{Q}_{\max}$ (W/kg)	2.60	5.11	7.84	13.77	20.84
	$\alpha_T\left(\dot{Q}_{\max}\right)$	0.18	0.16	0.15	0.20	0.18
	$t\left(\dot{Q}_{\max}\right)$ (h)	9.1	5.0	3.6	2.8	2.0
CB CEM I 52.5R	$\dot{Q}_{\max}$ (W/kg)	4.93	8.63	18.63	28.39	-
	$\alpha_T\left(\dot{Q}_{\max}\right)$	0.17	0.17	0.18	0.13	-
	$t\left(\dot{Q}_{\max}\right)$ (h)	8.4	5.4	3.2	2.0	-
CB CEM I 42.5R	$\dot{Q}_{\max}$ (W/kg)	4.29	7.86	14.00	23.17	-
	$\alpha_T\left(\dot{Q}_{\max}\right)$	0.18	0.25	0.23	0.21	-
	$t\left(\dot{Q}_{\max}\right)$ (h)	8.1	5.7	3.6	2.5	-
CB CEM II AL 42.5R	$\dot{Q}_{\max}$ (W/kg)	3.26	5.86	10.26	15.54	-
	$\alpha_T\left(\dot{Q}_{\max}\right)$	0.16	0.16	0.17	0.16	-
	$t\left(\dot{Q}_{\max}\right)$ (h)	8.5	5.1	3.4	2.6	-
CB CEM II B L 32.5N	$\dot{Q}_{\max}$ (W/kg)	2.85	5.07	8.55	13.36	-
	$\alpha_T\left(\dot{Q}_{\max}\right)$	0.14	0.14	0.15	0.28	-
	$t\left(\dot{Q}_{\max}\right)$ (h)	7.9	4.6	3.1	3.2	-
CB CEM II B L 32.5R White	$\dot{Q}_{\max}$ (W/kg)	1.97	3.37	6.13	8.99	-
	$\alpha_T\left(\dot{Q}_{\max}\right)$	0.16	0.15	0.16	0.13	-
	$t\left(\dot{Q}_{\max}\right)$ (h)	10.2	5.6	3.5	2.3	-

Table 2.6: Potential heat generation for each cement paste

	Q_∞ (kJ/kg)					
	20°C	30°C	40°C	50°C	60°C	Average
CA CEM I 52.5R	386.3	409.6	378.2	370.5	374.9	383.9
CA CEM I 42.5R	355.2	364.5	369.0	379.9	383.7	370.5
CA CEM II A L 42.5R	370.6	368.7	359.5	336.1	327.4	352.5
CA CEM II B L 32.5N	296.2	285.0	273.1	255.9	241.5	270.3
CA CEM IV 32.5N	279.5	294.0	310.2	309.0	289.4	296.4
CB CEM I 52.5R	414.0	399.0	397.4	368.1	-	394.6
CB CEM I 42.5R	370.3	350.4	350.9	361.7	-	358.3
CB CEM II AL 42.5R	343.1	331.2	327.0	334.4	-	333.9
CB CEM II B L 32.5N	315.8	304.3	302.0	291.8	-	303.5
CB CEM II B L 32.5R White	261.6	253.7	262.3	246.9	-	256.1

Degree of heat development

The degree of heat development was computed for all cements and tested temperatures. For the sake of conciseness, only the two extreme scenarios of 20°C and 60°C for the CA cements are presented in Figure 2.15. The evolution of α_T was quite coherent for all cements. Furthermore, configurations of the obtained curves α_T *versus* t agree with existing predictive equations for the degree of hydration evolution, like the ones reviewed by Mjörnell (1997), which do not consider the type of cement.

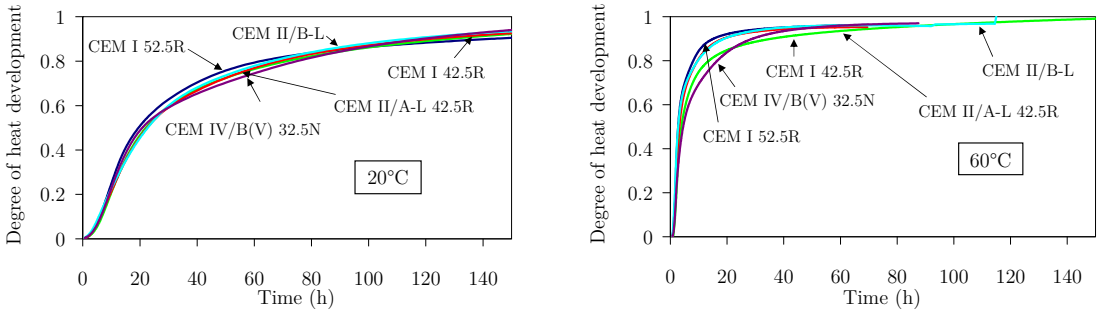

a) b)

Figure 2.15: Evolution of degree of heat development for the studied mixes of Company A at 20°C and 60°C

Normalized heat generation rate

One of the basic assumptions of equation (2.23) is that $f(\alpha_T)$ is independent of temperature (Reinhardt *et al.* 1982). However, it has been recognized that such an assumption is not entirely realistic, particularly in the case of slag cements, in which the heat generation of the secondary slag hydration reaction has a strong influence in the overall reaction kinetics (De Schutter and Taerwe 1995a). The results obtained for $f(\alpha_T)$ in this experimental campaign are depicted in Figure 2.16a and Figure 2.17a, for cements from Companies A and B, respectively. For the ordinary Portland cements, it is clear that $f(\alpha_T)$ can be considered almost independent of T within the studied range of temperatures (20°C-60°C). However, as depicted in Figure 2.16a, the blended cements with limestone

and fly ash (CA CEM II/A-L 42.5R and CA CEM II/B-L 32.5N) exhibit remarkably distinct evolutions of $f(\alpha_T)$ for the higher temperatures of 50°C and 60°C, when compared to the ones for 20°C, 30°C and 40°C. Nonetheless, if the relatively homogeneous values for $f(\alpha_T)$ at temperatures under 40°C are used in numerical models the error in the results might not be serious, as those high temperatures of 50°C and 60°C are not attained in regular concrete structures for long periods (D'Aloia 2001). However, in the case of massive structures where blended cements might be used, the issue of non-uniqueness of $f(\alpha_T)$ should be addressed with care, eventually by adopting functionals of the form $f(\alpha_T, T)$ that account for influences of both the degree of heat development and temperature.

Apparent activation energy

The values of E_a computed according to the speed method are depicted in Figure 2.16b and Figure 2.17b for the studied cements, and for the temperature intervals of [20°C-30°C], [30°C-40°C], [40°C-50°C] and [50°C-60°C] (with this last interval considered only for the case of Company A). It can be observed that E_a is not constant along the hydration reaction, but instead it oscillates around an average value for most cements. However, it is noticeable that the average value of the activation energy clearly drops for values of α_T higher than 0.6, which confirms findings of previous researchers (Breugel 2001, D'Aloia 2001). It is evident that higher temperatures yield more variable values of E_a, and that blended cements exhibit higher variations in the apparent activation energy, as it is particularly evident for the case of CA CEM IV/B (V) 32.5N. These increased inconstancies in E_a for α_T>0.6 , and for higher temperatures, may not necessarily cause significant errors in heat of hydration development predictions, as the value of $f(\alpha_T)$ that represents the relative heat liberation is low for such range of values of α_T (see Figure 2.16a and Figure 2.17a). Also, and as already stated, the higher temperatures of 50°C and 60°C are seldom achieved (at least for long periods) on practical applications of non massive structures, and thus the variations in E_a at higher T are not bound to be so influent in the temperatures to be expected on a real structure.

In view of the obtained results, reference values of E_a to be used in numerical thermal analyses of young concrete are proposed in Table 2.7 for the cements under study. These recommendations were essentially obtained by averaging the E_a values of the studied temperatures in the range of degree of heat development between 0 and 0.6 (in some cases the results for the temperature range 50°C-60°C were disregarded, due to their erratic pattern). The corresponding averaged values for A_T are also shown in the same table.

The values of E_a and A_T pertaining to the use of the derivate of the speed method are also shown in Table 2.7. The good performance of the recommended parameter values can be confirmed in Figure 2.18, where the experimentally measured heat generation rates are compared with the predictable ones upon usage of the parameters proposed in Table 2.7 together with equation (2.23) for the case of CA – CEM I 52.5R.

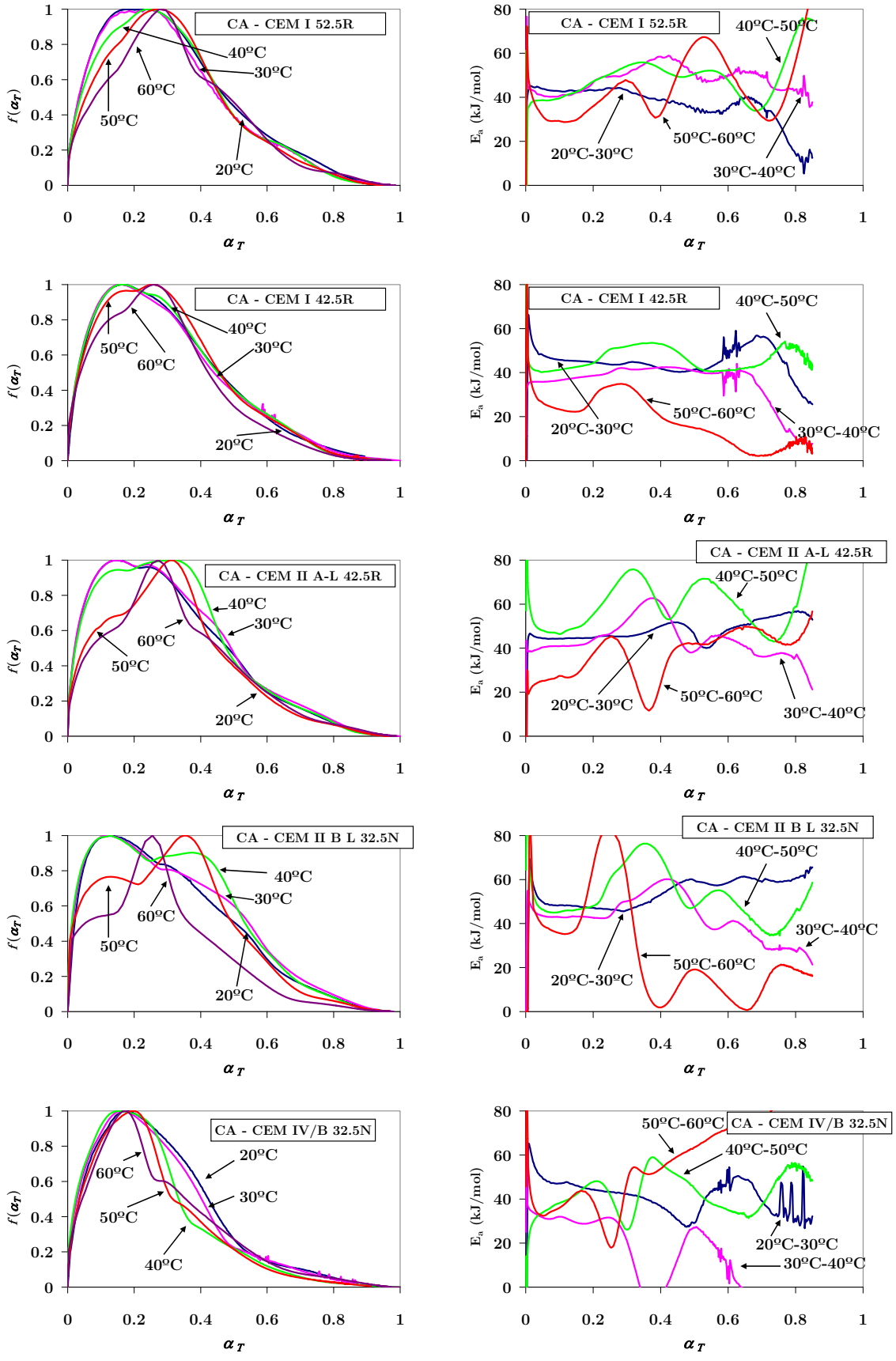

a) b)

Figure 2.16: Company A cements: a) $f(\alpha_T)$; b) E_a

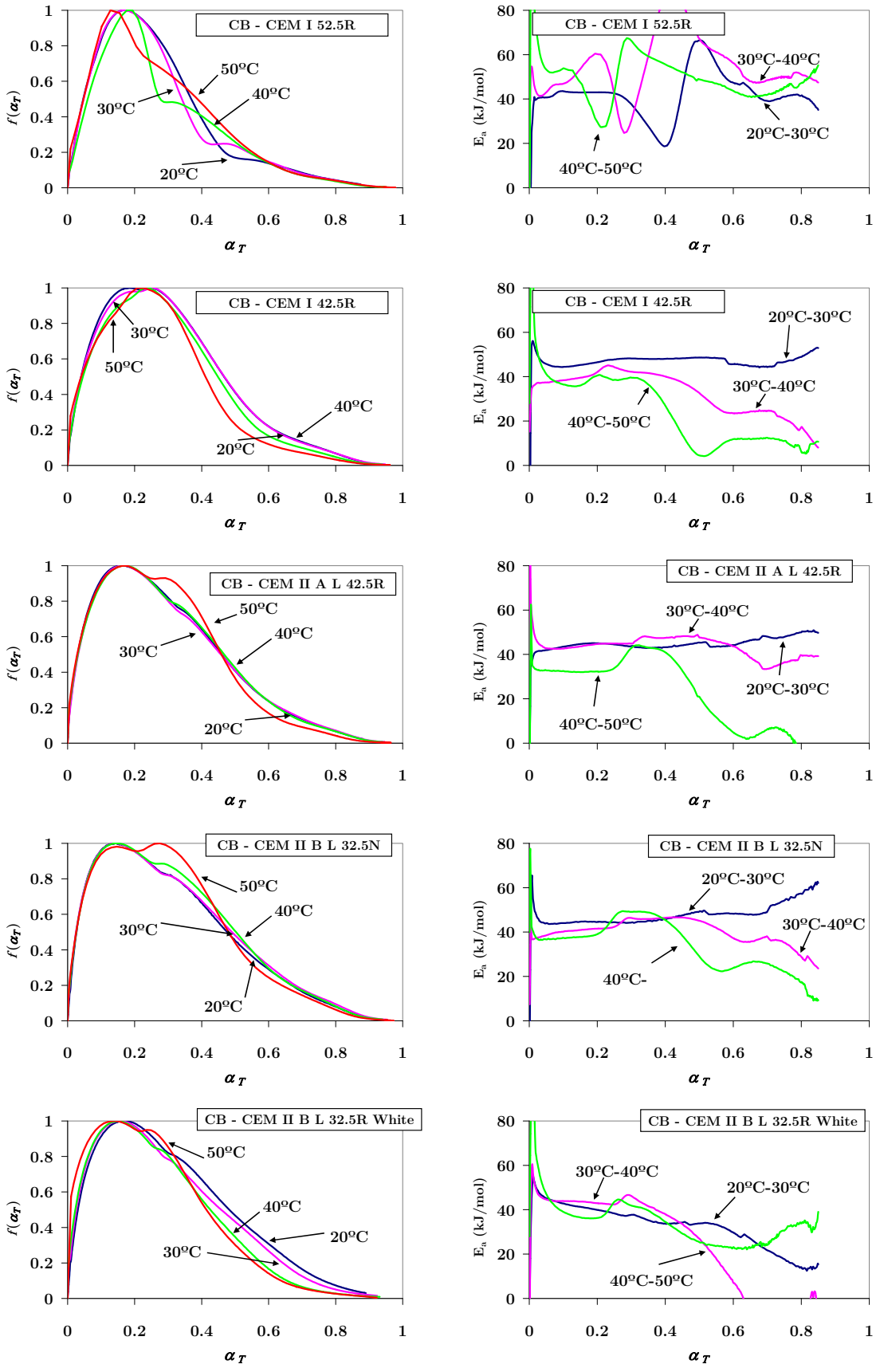

a) b)

Figure 2.17: Company B cements: a) $f(\alpha_T)$; b) E_a

Table 2.7: Parameters to be adopted in numerical modelling (per kg of cement)

	CA CEM I 42.5R	CA CEM I 52.5R	CA CEM II A L 42.5R	CA CEM II B L 32.5N	CA CEM IV 32.5N	CB CEM I 42.5R	CB CEM I 52.5R	CB CEM II AL 42.5R	CB CEM II B L 32.5N	CB CEM II B L 32.5R White
Derivate of the Speed Method A_T	2.150E+08	1.607E+09	3.553E+09	4.096E+09	7.807E+07	3.522E+08	1.374E+09	7.683E+07	5.128E+07	3.423E+07
Derivate of the Speed Method E_a (kJ/mol)	43.83	48.19	51.02	52.10	41.84	44.38	47.40	41.30	40.66	40.59
Speed Method A_T	2.645E+07	7.400E+08	1.054E+09	7.083E+08	1.831E+07	2.227E+07	5.118E+09	5.205E+07	1.178E+08	4.642E+06
Speed Method E_a (kJ/mol)	38.38	46.18	47.85	47.52	38.07	37.31	50.76	40.31	42.79	35.47
Q_∞ (kJ/kg)	355.2	386.3	327.4	296.2	279.5	370.3	414.0	343.1	315.8	261.6
α_T	$f(\alpha_T)$	$f(\alpha_T)$	$f(\alpha_T)$	$f(\alpha_T)$	$f(\alpha_T)$	$f(\alpha_T)$	$f(\alpha_T)$	$f(\alpha_T)$	$f(\alpha_T)$	$f(\alpha_T)$
0.00	0.00	0.00	0.00	0.00	0.00	0.00	0.00	0.00	0.00	0.00
0.05	0.65	0.62	0.75	0.83	0.62	0.58	0.53	0.68	0.74	0.68
0.10	0.91	0.88	0.95	0.99	0.85	0.85	0.83	0.92	0.96	0.91
0.15	1.00	0.99	1.00	0.99	0.98	0.98	0.99	1.00	1.00	0.99
0.20	0.98	1.00	0.97	0.95	0.99	1.00	0.98	0.98	0.96	0.99
0.25	0.94	1.00	0.96	0.87	0.92	1.00	0.89	0.91	0.88	0.92
0.30	0.86	0.95	0.90	0.83	0.82	0.94	0.76	0.82	0.82	0.82
0.35	0.75	0.85	0.78	0.77	0.72	0.83	0.57	0.74	0.76	0.77
0.40	0.63	0.70	0.66	0.68	0.58	0.69	0.39	0.64	0.66	0.67
0.45	0.51	0.56	0.56	0.59	0.41	0.55	0.24	0.52	0.55	0.56
0.50	0.41	0.45	0.46	0.51	0.27	0.41	0.17	0.41	0.45	0.47
0.55	0.32	0.36	0.34	0.42	0.19	0.30	0.16	0.31	0.36	0.38
0.60	0.24	0.28	0.25	0.30	0.15	0.22	0.14	0.24	0.29	0.31
0.65	0.18	0.23	0.20	0.21	0.12	0.17	0.11	0.18	0.22	0.23
0.70	0.13	0.18	0.16	0.16	0.10	0.13	0.08	0.14	0.16	0.16
0.75	0.09	0.13	0.12	0.12	0.08	0.10	0.06	0.10	0.12	0.11
0.80	0.06	0.08	0.08	0.08	0.05	0.07	0.04	0.07	0.08	0.07
0.85	0.04	0.04	0.04	0.04	0.03	0.04	0.03	0.04	0.04	0.05
0.90	0.02	0.02	0.02	0.02	0.02	0.02	0.02	0.02	0.02	0.03
0.95	0.01	0.01	0.01	0.01	0.01	0.01	0.01	0.01	0.01	0.01
1.00	0.00	0.00	0.00	0.00	0.00	0.00	0.00	0.00	0.00	0.00

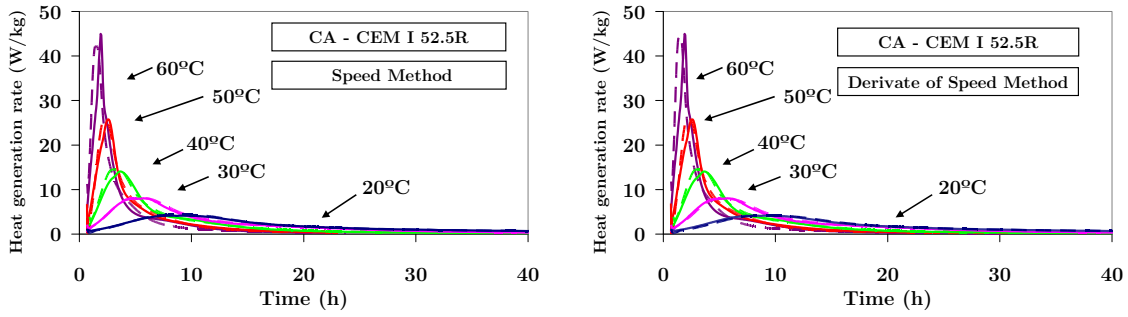

a) b)

Figure 2.18: Predicted (dashed lines) values of heat generation rates *versus* measured ones (full lines)

2.4.3.4 Extrapolation of cement paste thermal results to concrete

The wide range of heat generation results obtained for cement pastes cannot be directly applied to real concrete structures. However, by making the assumption that aggregates do not influence reaction kinetics, the expectable heat generation rates of the studied cement pastes (with w/c=0.5), whose units are expressed in W/(kg of cement content in the paste), may be extrapolated for a concrete with the same cement paste (i.e., same cement type and w/c ratio) through mere multiplication by the volumetric cement content in the concrete mix [kg of cement/m^3]. This results in an estimated heat generation in Wm^{-3}, suitable for application in numerical models based in equation (2.11). In case of a concrete with a w/c≠0.5, the extrapolation may increasingly lose validity as the deviation in the mix w/c ratio grows. Nonetheless, for w/c ratios between 0.4 and 0.6, the accuracy obtained by using the described methodology is likely to be more than satisfactory for heat generation prediction purposes. In cases where higher accuracy is demanded, a isothermal conduction calorimeter may be used to analyze the mortar contained in the concrete mix, with its actual w/c ratio and the actual fine aggregates or additions being included. In this case, extrapolation to concrete leads to a much smaller error margin associated to possible effects on the rates of hydration induced by coarse aggregates. A similar approach has been reported by D'Aloia (2001), with the equivalent mortar concept, following three main recommendations: (a) the w/c ratios of both concrete and equivalent mortar are equal; (b) equivalent mortar is composed of the same sand as concrete; (c) the specific surface of aggregates divided by the weight of cement is the same for both equivalent mortar and concrete.

A further remark is made regarding the presence of partial substitutions of cement, or even inclusion of admixtures (organic or mineral), which may alter hydration kinetics (Hewlett 2004, Lawrence *et al.* 2003, Neville 1995). The mortar to be tested in the isothermal calorimeter should therefore include all the components present in concrete that are expectable to change hydration kinetics. It is however considered that the errors induced by an equivalent mortar not satisfying the three recommendations are in fact masked in temperature rise estimation by the low conductivity of concrete, and its heat capacity, which, as long as the total generated heat is reasonably estimated, provide very similar results in terms of temperature development in real structures.

2.5 Boundary conditions of the thermal problem

After having presented the heat conduction equation and discussed the set of parameters involved in Sections 2.3 and 2.4, the next logical step to take is to deal with boundary conditions. In nature, heat transfer between a solid and the environment can occur in several ways (Figure 2.19):

- Natural convection – The heat exchange is caused by temperature difference between the bulk of air and the air neighbouring the solid (whose temperature is directly influenced by the solid onto which it is in contact). As a consequence, densities of the two mentioned air masses are different, and so an air movement is enforced. This movement causes a new air mass to get in contact with the solid,

and to become influenced by concrete temperature. This cycle may continue indefinitely while the temperatures of concrete and the bulk of air are different.

- Forced convection – When of one or more external sources of air movement over the solid exist, the natural convection heat exchanges are strongly intensified once the air near the solid is renovated at a higher rate. When this happens, heat transfer is said to occur due to mixed natural-forced convection.
- Long wave radiation – Thermal energy transmission due to radiation is related to energy emission of a body because of its temperature. According to Maxwell's Classic theory, this energy is emitted in the form of electromagnetic waves. While convection heat transfer requires a transmission medium such as air, radiation transmission can happen in vacuum conditions. Generally speaking, any solid is constantly emitting and receiving radiation from its surroundings.
- Short wave radiation – This kind of energy transmission occurs with very similar mechanisms to the ones described for long wave radiation. The main differences reside in the wave length of the involved electromagnetic waves, and that this kind of transmission is the one usually considered for energy emitted by the sun.

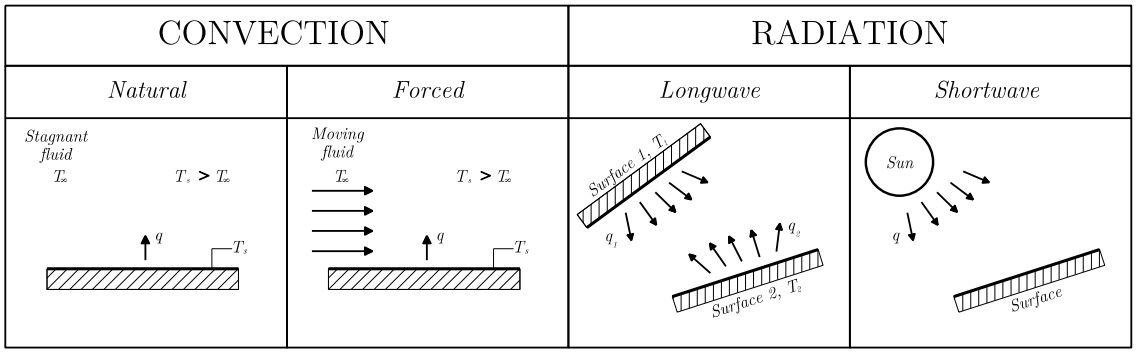

Figure 2.19: Modes of heat transfer between a solid and the environment

In the following sub-sections, some considerations will be made on how to account for the mentioned transfer modes in numerical calculations.
Note: Another mechanism of heat loss was considered in this research (evaporative cooling phenomenon), but due to its strong connection with the moisture boundary conditions, it is not addressed in this Chapter (see Chapters 3 and 4).

2.5.1 Convection

Numerically, natural and forced convection are usually dealt with as a unique phenomenon, because the mechanism of heat transfer is basically the same for both convection forms, being caused by air movement. Independently of the driving force for air movement, the convective heat transfer between concrete and the environment can be expressed by the Newton law of cooling (Incropera *et al.* 2001)

$$q_{h,c} = h_T \left(T_{surf} - T_{env} \right) \tag{2.39}$$

where $q_{h,c}$ is the heat flux at the surface [Wm^{-2}], h_T is the heat transfer coefficient [$Wm^{-2}K^{-1}$], and T_{env} and T_{surf} are the environment and the concrete surface temperatures [K].

Even though many theoretical efforts have been made in the past to establish predictive equations for the heat transfer coefficient, accurate predictions are only available for very simple geometries and carefully controlled environments. For any other situation, such as outdoor conditions and complex geometries such as civil engineering structures, predictions have been limited to empirical correlations, or in some cases based on computational fluid dynamics (CFD) approaches.

In the following, a brief review of some of the available equations for prediction of convection coefficients as a function of wind speed V (m/s) will be presented.

- Proposal from McAdams (1954) and Jonasson (1994):

$$\begin{cases} h_T = 4.3\,V + 6.2 & \text{if } V \le 5\text{m/s} \\ h_T = 7.6\,V^{0.78} & \text{if } V > 5\text{m/s} \end{cases} \tag{2.40}$$

- Proposal from Jayamaha *et al.* (quoted by Davies (2004)):

$$h_T = 1.444\,V + 4.955 \tag{2.41}$$

- Proposal from Silveira (1996):

$$h_T = 3.83\,V \tag{2.42}$$

- Proposal from Ruiz *et al.* (2001) (citing ASHRAE Hanbook 1993):

$$h_T = 1.06 \times 3.727\,C \times \left[0.9 \times \left(T_S + T\right) - 459.67\right]^{-0.181} \times \left(T_S - T\right)^{0.266} \sqrt{1 + 2.857 \times V}$$

$$C = \begin{cases} 1.79 & \text{for horizontal surfaces hotter than air} \\ 0.89 & \text{for horizontal surfaces cooler than air} \end{cases} \tag{2.43}$$

- Proposal from Branco *et al.* (1992)

$$h_T = 6.0 + 3.7\,\mathrm{V} \tag{2.44}$$

A comparative plot of the estimations provided by all these equations can be observed in Figure 2.20, where a significant scatter in predicted convection coefficients can be noticed. It must be stressed that these equations are based on experiments in which precision, purpose and procedures (such as the height of wind speed measurement, the kind of geometry of studied solid body, the turbulence of the air flow, the range in tested wind speeds) may widely vary from author to author. Since each one of these empirical equations is only applicable in the case of a perfect reproduction of the original experiments, under distinct situations they can only provide rough estimates for real applications. In spite of that, the empirical correlations play a very important role in sensitivity analyses and checking extreme scenarios.

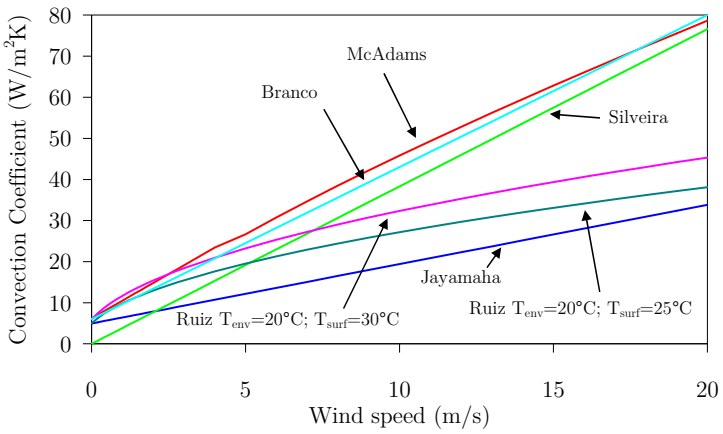

Figure 2.20: Comparative plot of empirical correlations for the convective heat transfer coefficient

2.5.2 Radiation

2.5.2.1 General remarks

Unlike conduction and convection, radiation is the only energy transfer mechanism that can take place without a material medium (air or solid). In fact radiation is best transferred in vacuum conditions, since it mobilizes photons that travel at the speed of light, and experience no scattering or absorption in such case. As a consequence of thermal agitations of its composing molecules, any body with temperature higher than 0°K, emits electromagnetic waves (mainly in the infrared region), which carry energy away from it. So, as all objects known to man exist at temperatures higher than 0°K, all bodies interact by emitting electromagnetic waves, thus promoting radiation heat transfer. Bodies behave differently when it comes to their capacity of absorbing incoming radiation from other objects. To radiation of a certain wavelength λ that hits an object, one or more of three things may happen:

- Part or all of it is reflected. The fraction of radiation reflected is named reflectivity a_λ. This part does not interact with the object, it is rejected.
- Part or all of it can be absorbed. The fraction of radiation absorbed is named absorptivity α_λ, and raises the object temperature.
- Part or all can be transmitted. The fraction of radiation transmitted is named transmissivity t_λ. This part does not interact with the object; it just passes through it.

Naturally, energy conservation dictates that:

$$a_\lambda + \alpha_\lambda + t_\lambda = 1 \tag{2.45}$$

A particular case regarding equation (2.45), occurs when the body absorbs all radiation incident on it (a_λ =1). If this is the case, the object is termed a black body. Even though this is an idealization, and no such object exists (at least for all wavelengths), many natural substances behave nearly like black bodies.

Regarding the capacity of emitting radiation, the emissivity parameter ε is used for characterizing different behaviours ($0<\varepsilon<1$). Black bodies are perfect emitters and have

ε=1, while in all the other cases when ε<1, they are termed grey bodies. The mathematical expression for the radiation emitted by a given body is provided by the Stefan-Boltzmann law, according to which a given substance emits radiation at a rate proportional to the 4th power of its absolute temperature T:

$$F_{tot} = \varepsilon \sigma T^4 \tag{2.46}$$

where F_{tot} is the total energy flux emitted (Wm^{-2}) and σ is the Stefan-Boltzmann constant (=5.67 x 10-8 W m^{-2} K^{-4}).
The energy balance of an object can be found by calculating the difference between the energy that is being emitted and the incident energy being absorbed from neighbouring bodies. Assuming two bodies A and B at different temperatures in an environment where no more entities exist, the energy balance E_{bal} on body A would be:

$$E_{bal} = \varepsilon_A \sigma T_A^4 - \alpha_A \varepsilon_B \sigma T_B^4 \tag{2.47}$$

In the particular case of black bodies, where ε=α=1, the former equation becomes:

$$E_{bal} = \sigma \left(T_A^4 - T_B^4 \right) \tag{2.48}$$

As mentioned before, transmission of energy by radiation occurs via electromagnetic waves, which may have a wide range of wavelengths and associated energies. The range of wavelengths of interest when it comes to thermal energy balances in concrete structures is the same as that of the meteorological sciences: the ultraviolet, the visible and the infrared radiations. Description of these categories of radiation is made in Table 2.8: it is seen that the sun's output is almost all within the wavelength under 1.5 μm, the range of shortwave radiation. On the other hand, earth's output lies over the wavelength of 1.5 μm, in correspondence to longwave radiation. The energy content of the sun's radiation as compared to that emitted by earth, is depicted in Figure 2.21: it is noticeable that the earth's energy output is lower than the sun's by several orders of magnitude.

Table 2.8: Radiation in the earth atmosphere system

	Ultraviolet radiation	**Visible radiation**	**Near infrared radiation**	**Far infrared radiation**
Wavelength	0.01-0.4μm	0.4-0.7μm	0.7-1.5μm	1.5-100μm
Effect	sunburn	"sunlight"	heat-radiation	heat-radiation
Class	----------shortwave radiation ----------			longwave radiation
Sun output	7%	43%	37%	11%
Earth output	0%	0%	0%	~100%

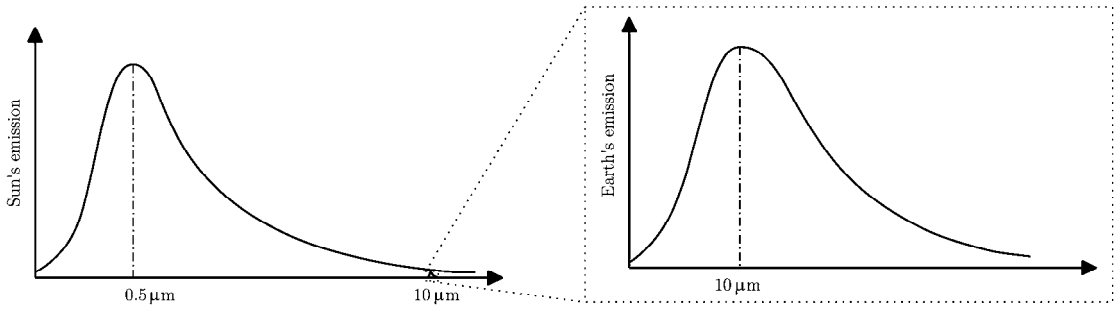

Figure 2.21: Energy content as a function of wavelength for sun and earth's radiation

2.5.2.2 Longwave radiation

The longwave radiation energy balance for concrete structures can be calculated through the use of equation (2.47), with consideration of the concrete's surface as body A and the surrounding environment (neighbouring objects, clouds, sky, i.e., virtually all objects except for the sun) as body B. It would not be practical to use such an approach, and simplifying equations exist, such as the one proposed by Branco *et al.* (1992), in which the energy balance for longwave radiation is made by an equation analogous to the boundary equation for convection, and using a radiation exchange coefficient h_r:

$$q_{h,r} = h_r \left(T_{surf} - T_{env} \right) \tag{2.49}$$

$$h_r = \varepsilon \left[4.8 + 0.075 \ \left(T_{env} - 278.15 \right) \right] \tag{2.50}$$

According to Branco *et al.* (1992), applicability of equations (2.49) and (2.50) is limited to the usual values of temperature difference between concrete and the environment. In order to get an actual idea of the differences between the two approaches (i.e. equations (2.47) and (2.50)), comparisons are made in Figure 2.22 for various scenarios of concrete surface temperatures (with consideration for a reference value ε=0.88, and α_A=1), and assuming an environmental temperature of 20°C. It can be concluded that it is quite feasible to use the simplified equations (2.49) and (2.50) for general applications.

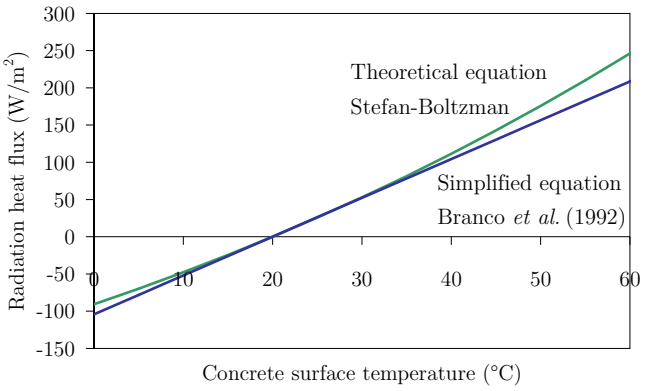

Figure 2.22: Comparison of theoretical and simplified approaches for the radiation flux at the surface (environmental temperature=20°C)

The calculated longwave radiation heat transfer coefficient h_r has the value of 5.2Wm^{-2}K^{-1} for an environmental temperature of 20°C and ε=0.88. Variation of this coefficient within the usual range of concrete casting environmental temperatures is observable in Figure 2.23 (for a surface at T=20°C): relatively low variations can in fact be detected between 5°C (~4Wm^{-2}k^{-1}) and 40°C (~7Wm^{-2}K^{-1}), which fairly represent extreme scenarios of environmental temperatures at which casting can usually take place. In view of this, it is considered feasible to adopt a constant value of h_r=5.2Wm^{-2}k^{-1} for practical applications.

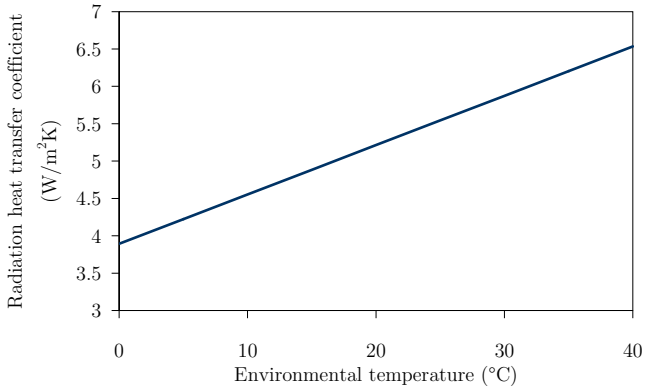

Figure 2.23: Evolution of h_r as a function of environmental temperature (radiating body at 20°C)

Bearing in mind the resemblance between equations (2.39) and (2.49) for the convective heat flux and for the longwave radiation heat flux, it is feasible to idealize a unique convection/radiation heat transfer coefficient h_{cr}=h_T+h_r that simultaneously accounts for the effects of both phenomena:

$$q_h = q_{h,c} + q_{h,r} = h_{cr}\left(T_{surf} - T_{env}\right) \tag{2.51}$$

The use of this h_{cr} coefficient brings simplification to the numerical simulation of boundaries for concrete. However, for the cases where formwork exists between concrete and the environment, a further simplification can be made that eliminates the necessity of explicitly accounting for formwork in the numerical model. In fact, as main heat fluxes through the concrete surface are perpendicular to it and as the thickness of the formwork is usually small, it is possible to lump the effect of conduction through formwork into the surface boundary coefficient by using an electrical analogy (Azenha 2004, Jonasson 1994). According to a scheme of n material layers between concrete and the environment, such as the one depicted in Figure 2.24, the heat transfer through these layers can be lumped into an equivalent boundary transfer coefficient h_{eq} as

$$h_{eq} = \left[\frac{1}{h_{cr}} + \sum_{i=1}^{n}\frac{L_i}{k_i}\right]^{-1} \tag{2.52}$$

where L_i and k_i are, respectively, the thickness and thermal conductivity of the i^{th} layer of material between concrete and the surrounding environment.

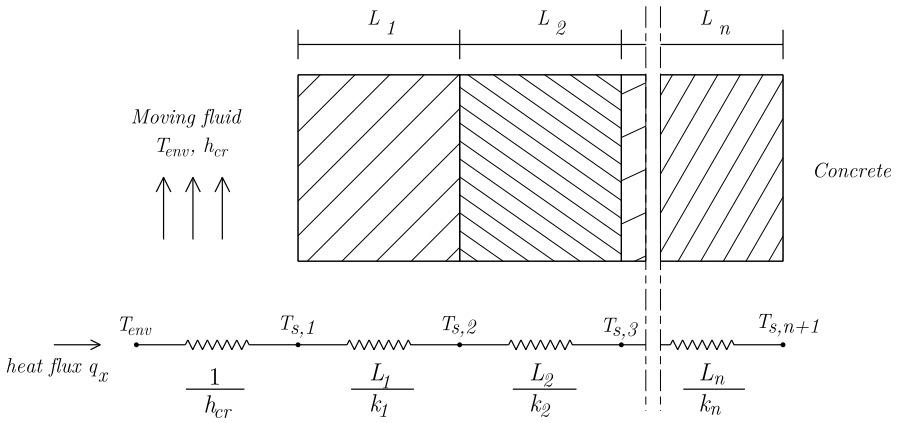

Figure 2.24: Electrical resistance analogy for boundary transfers

2.5.2.3 Night cooling effect

Radiation exchanges between bodies at the earth's surface and dark sky during the night usually cause frost to occur on objects, even though the environmental temperature remains well above the freezing point of water. Accordingly, the use of equation (2.47) for the predicting radiation heat fluxes between a given object - body A - at sea level and the surrounding hemisphere sky – body B - cannot consider the sky's temperature as being coincident with the environmental one: this would yield null heat fluxes from a body at the same temperature as the environment, which would not be accurate. Therefore, the computation of radiation fluxes between concrete and the surrounding environment during night time should consider temperature of the sky as different from the environmental one. It has been reported that during the night, in clear skies, this apparent sky temperature can be as low as 30°C under the environmental temperature (strongly dependent on dust existing on the air, as well as its relative humidity and cloud cover (Silveira 1996)). This results in an added energy flux Q_{add} from the concrete surface that can be accounted with:

$$Q_{add} = \varepsilon \, h_r \, \Delta T_{nsky} \tag{2.53}$$

where ΔT_{nsky} is the difference between the environmental and the apparent sky temperature, and ε is the emissivity of the night sky that may be computed with recourse to empirical formulations expressed in Chen *et al.* (1995). Determination of the apparent sky temperature may involve several degrees of complexity and methodologies, which often use empirical models derived from experiments; detailed information on this subject may be found in Parker (2005).

2.5.2.4 Solar radiation

A complete study of the temperature field evolution in a concrete structure cast in an outdoor environment should include the effect of solar radiation, as it may represent a significant heat input to the surface of concrete, and therefore have an important influence on the risk of surface thermal cracking. In massive structures such as dams, where heat of hydration may take several years to dissipate, the thermal input provided by solar radiation assumes considerable relevance, due to the repetitive action of every

solar day. On the other hand, for very slender elements, the solar radiation thermal input may play a role even more important than the one associated to the heat of hydration.
Predicting solar radiation incidence on a given surface is possible within certain accuracy limits, since two unpredictable main sources of error can occur: actual clouding conditions and atmospheric turbulence. Other than these two problems, it is actually possible to accurately predict the solar radiation incident at a given surface with arbitrary orientation and inclination, at any instant and any location. The models used for this purpose have been widely applied in several fields, such as meteorology, building physics, irrigation and solar energy harvesting among others.
Global solar irradiance is a measure of the rate of total incoming solar energy on a horizontal plane at the earth's surface, and it can be divided in two parts: the direct solar irradiance and the diffuse irradiance. Direct solar irradiance is a measure of the rate of solar energy arriving at the earth's surface from the sun's direct beam, on a plane perpendicular to the beam. Diffuse solar irradiance is a measure of the rate of incoming solar energy on a horizontal plane at the earth's surface, resulting from scattering of the sun's beams due to atmospheric constituents. Global and diffuse irradiance will be equal when direct solar irradiance is zero, that is, when the sun is obscured by thick clouds or the below the horizon. During clear days, the diffuse radiation is about 10 to 14% of the total solar radiation received at the earth's surface.

Incident direct radiation from the sun

The direct radiation energy flux from the sun that reaches the outer layers of the earth's atmosphere has an average value of 1367Wm^{-2} (known as solar constant). It is known that because of the elliptic earth orbit around the sun, and consequent varying distance to the latter, the direct radiation energy fluctuates by about 6.9% throughout the year (from 1412Wm^{-2} in January to 1321Wm^{-2} in July). This fluctuation is considered negligible in view of the necessary precision for concrete temperature estimation, therefore for the predictions made within this research the aforementioned value of the solar constant is to be used.
However, in order to reach a surface on earth (at sea level, for example), the sun's direct radiation has to travel through the atmosphere, experiencing absorption and scattering (even in a clear sky scenario). The actual radiation that reaches sea level q_m, may be estimated through the following empirical relationship derived in the Netherlands (Breugel *et al.* 2001):

$$q_m = q_0 \, e^{\frac{-T_l}{0.9+9.4\sin(h)}} \tag{2.54}$$

where q_0 is the solar constant, h is the solar elevation and T_l is the Linke turbidity factor. The T_l factor describes the optical thickness of the atmosphere due to both the absorption by the water vapour and the absorption and scattering by the aerosol particles relative to a dry and clean atmosphere. It summarizes the turbidity of the atmosphere, and hence the attenuation of the direct beam solar radiation (Kasten 1996, WMO 1981). The larger T_l, the larger the attenuation of solar radiation by the clear sky atmosphere, so T_l denotes the transparency of the cloudless atmosphere (if the sky was dry and clean, T_l would be

equal to 1). Common values of T_l range between 3 and 7, and in turbid atmosphere, like polluted cities, T_l is close to 6 or 7.
The solar elevation h is to be defined further in this section. For now, it is just worth mentioning that this parameter influences the length of atmosphere that sun beams have to cross. At midday this length is naturally smaller than that at sunset, so a higher attenuation of solar energy occurs for the latter.

Relevant geometric parameters
The analysis of the direct solar radiation flux on an arbitrarily inclined surface involves consideration of several geometric parameters, namely the following ones, depicted in Figure 2.25:

- α is the surface angle relative to the horizontal plane (°);
- $\overline{n}$ is a versor normal to the surface;
- Ψ is the azimuth of projection of $\overline{n}$ on the horizontal plane (°) - 0° means south; 90° means east; 180° means north; 270° means west;
- h is the solar elevation (°), and it corresponds to the angle between the direction of the sun and the (idealized) horizon;
- i is the angle of incidence of the sunbeam with respect to $\overline{n}$.

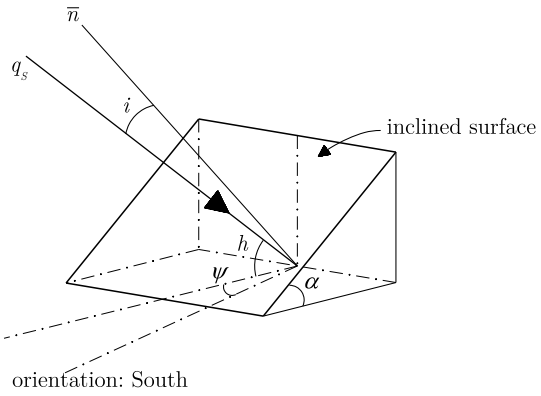

Figure 2.25: Arbitrarily inclined surface and incident sun beam

Calculation of the actual solar radiation incident on a surface at a given instant involves the necessity of knowing the value of several parameters beforehand, such as:

- The declination of the sun δ, which is the angle between the rays of the sun and the plane of the earth's equator. The earth's equator is tilted 23.44° with respect to the plane of the earth's orbit around the sun, so at various times during the year, declination varies from 23.44° North to 23.44° South. Several mathematical formulations exist for calculating this parameter, the one adopted in this research being (Breugel and Koenders 2001)

$$\sin(\delta) = 0.39782 \sin\left(4.871 + \frac{\pi}{180} d + 0.033 \sin\left(\frac{\pi}{180} d\right)\right) \tag{2.55}$$

  where d is the cardinal day within the year.
- The hour angle Ω of the sun describes the actual position of the earth in relationship to the sun. It is zero at solar midday (t=0 hours) and it varies

linearly between -180° at t=-12h and 180° at t=12h (rotation of the earth of 360° every 24 hours, meaning 15° per hour). Therefore, the definition of Ω (°) as a function of solar time t (in [h], ranging from -12 to 12) is

$$\Omega = 15\,t \tag{2.56}$$

Note that the solar noon does not usually coincide with the conventional 12h00m. Corrections have to be made if high precision is required. However, as this deviation in Portugal is usually in the order of 30 minutes (except for periods where the Daylight Saving Time is adopted), it was neglected in the applications of this thesis, more concerned with the global thermal input than with the exact time at which each value occurs.

- The solar elevation h may be computed with basis on δ, Ω and latitude φ (°) of the location, according to:

$$\sin(h) = \sin(\varphi)\sin(\delta) + \cos(\varphi)\cos(\delta)\cos(\Omega) \tag{2.57}$$

- The azimuth of projection of $\overline{n}$ on the horizontal plane can be computed with the expression:

$$\sin(\psi) = \frac{\cos(\delta)\sin(\Omega)}{\cos(h)} \tag{2.58}$$

- Finally, the angle of incidence with the normal to the surface i may be computed using:

$$\cos(i) = \cos(\alpha)\sin(h) + \sin(\alpha)\cos(h)\cos(\psi) \tag{2.59}$$

Actual radiation absorbed by a surface

The actual radiation $q_{S,concr}$ absorbed by a given concrete surface depends on the solar radiation q_m that reaches the surface (equation (2.54)), on the angle of incidence i of the sun beam (equation (2.59)) and on the absorvity of concrete α_s (which is a function of the surface colour, and usually ranges between 0.5 and 0.6 (Azenha 2004, Ruiz *et al.* 2001)):

$$q_{S,concr} = \alpha_S\, q_m \cos(i) \tag{2.60}$$

It should however be remarked that the present model does not account for shadowing effects caused by neighbouring obstacles. For such purpose, the most practical approach would be the conduction solar studies using Computer Aided Design (CAD) tools.

2.6 Numerical implementation with the finite element method

The heat field equation, together with a set of boundary conditions, was implemented through the use of the finite element method (FEM). The present section provides information on the adopted strategies for such goal.
As stated in section 2.3, the governing field equation for the relevant thermal problem in concrete since early ages is:

$$\frac{\partial}{\partial x}\left(k\frac{\partial T}{\partial x}\right)+\frac{\partial}{\partial y}\left(k\frac{\partial T}{\partial y}\right)+\frac{\partial}{\partial z}\left(k\frac{\partial T}{\partial z}\right)+\dot{Q}=\rho\, c\,\dot{T} \tag{2.61}$$

Considering Neumann conditions that apply in boundary Γ_q, where fluxes q_h expressed in equation (2.51) are to be accounted for, one has

$$-\left[k\frac{\partial T}{\partial x}l+k\frac{\partial T}{\partial y}m+k\frac{\partial T}{\partial z}n\right]=h_{cr}\left(T-T_{env}\right)=q_h \tag{2.62}$$

where l, m and n are direction cosines of the normal versor to Γ_q.
Following standard procedures in the FEM, an interpolation of the form

$$T=\boldsymbol{N}\,\boldsymbol{T}^e \tag{2.63}$$

is assumed where $\boldsymbol{N}$ denotes the interpolation matrix and $\boldsymbol{T}^e$ designates the nodal temperatures for a given finite element with volume Ω. Applying the Galerkin weighted residual method to the field equation (2.61), and to the boundary condition (2.62), thermal equilibrium over all volume Ω and boundary Γ_q, can be expressed in integral form as:

$$\begin{aligned}\int_\Omega \boldsymbol{N}^T\left[\frac{\partial}{\partial x}\left(k\frac{\partial T}{\partial x}\right)+\frac{\partial}{\partial y}\left(k\frac{\partial T}{\partial y}\right)+\frac{\partial}{\partial z}\left(k\frac{\partial T}{\partial z}\right)+\dot{Q}-\rho c\dot{T}\right]d\Omega+\\ \int_{\Gamma_q}\boldsymbol{N}^T\left[q_h-h_{cr}\left(T-T_{env}\right)\right]d\Gamma_q=\mathbf{0}\end{aligned} \tag{2.64}$$

A weak form for this equation may be obtained integrating by parts the first three terms of equation (2.64),

$$\begin{aligned}&-\int_\Omega\left[k\frac{\partial \boldsymbol{N}^T}{\partial x}\frac{\partial T}{\partial x}+k\frac{\partial \boldsymbol{N}^T}{\partial y}\frac{\partial T}{\partial y}+k\frac{\partial \boldsymbol{N}^T}{\partial z}\frac{\partial T}{\partial z}-\boldsymbol{N}^T\dot{Q}+\boldsymbol{N}^T\rho c\dot{T}\right]d\Omega\\ &-\int_{\Gamma_q}\boldsymbol{N}^T q_h\,d\Gamma_q+\int_{\Gamma_q}\boldsymbol{N}^T\left[q_h-h_{cr}\left(T-T_{env}\right)\right]d\Gamma_q=\mathbf{0}\end{aligned} \tag{2.65}$$

Simplifying equation (2.65) the following is obtained:

$$\int_{\Omega}\left[k\frac{\partial \boldsymbol{N}^T}{\partial x}\frac{\partial T}{\partial x}+k\frac{\partial \boldsymbol{N}^T}{\partial y}\frac{\partial T}{\partial y}+k\frac{\partial \boldsymbol{N}^T}{\partial z}\frac{\partial T}{\partial z}-\boldsymbol{N}^T\dot{Q}+\boldsymbol{N}^T\rho c\dot{T}\right]d\Omega+ \\ +\int_{\Gamma_q}\boldsymbol{N}^T h_{cr}\left(T-T_{env}\right)d\Gamma_q=\boldsymbol{0} \tag{2.66}$$

Introducing the approximation expressed in (2.63) into (2.66), a matrix format more convenient for numerical implementation can finally be obtained

$$\boldsymbol{C}^e\,\dot{\boldsymbol{T}}\;+\;\boldsymbol{G}^e\,\boldsymbol{T}\;=\;\boldsymbol{F}_T^e\;+\;\boldsymbol{F}_Q^e \tag{2.67}$$

where the elemental matrices and vectors (referenced by index 'e') are computed in accordance to the following (Faria *et al.* 2006):

$$\boldsymbol{C}^e\;=\;\int_{\Omega^e}\boldsymbol{N}^T\,\rho\,c\;\boldsymbol{N}\;d\Omega \tag{2.68}$$

$$\boldsymbol{G}^e\;=\;\int_{\Omega^e}\nabla\,\boldsymbol{N}^T\,k\,\nabla\,\boldsymbol{N}\;d\Omega\;+\;\int_{\Gamma_q^e}\boldsymbol{N}^T\,h_{cr}\;\boldsymbol{N}\;d\Gamma_q \tag{2.69}$$

$$\boldsymbol{F}_T^e\;=\;\int_{\Gamma_q^e}\boldsymbol{N}^T\,h_{cr}\;T_{env}\;d\Gamma_q \tag{2.70}$$

$$\boldsymbol{F}_Q^e\;=\;\int_{\Omega^e}\boldsymbol{N}^T\,\dot{Q}\;d\Omega \tag{2.71}$$

Implementing a time integration scheme, and assuming an unconditionally stable Euler approximation of the form

$$\dot{T}_{n+1}\;=\;(T_{n+1}\;-\;T_n)/\Delta t \tag{2.72}$$

with Δt=t_{n+1}-t_n and indexes "n" and "n+1" referring to two consecutive time steps t_n and t_{n+1}, equation (2.67) defined for instant t_{n+1} becomes

$$\frac{1}{\Delta t}\;\boldsymbol{C}_{n+1}^e\left(\boldsymbol{T}_{n+1}^e\;-\;\boldsymbol{T}_n^e\right)+\;\boldsymbol{G}_{n+1}^e\,\boldsymbol{T}_{n+1}^e\;=\;\boldsymbol{F}_{T,n+1}^e\;+\;\boldsymbol{F}_{Q,n+1}^e \tag{2.73}$$

Standard assembling procedures can now be invoked to constitute the global $\boldsymbol{C}_{n+1}$ and $\boldsymbol{G}_{n+1}$ matrices and the $\boldsymbol{F}_{T,n+1}$ and $\boldsymbol{F}_{Q,n+1}$ vectors required for the FE analysis of a thermal structural problem, that is,

$$\left(\frac{\boldsymbol{C}_{n+1}}{\Delta t}\;+\;\boldsymbol{G}_{n+1}\right)\boldsymbol{T}_{n+1}\;=\;\boldsymbol{F}_{T,n+1}\;+\;\boldsymbol{F}_{Q,n+1}\;+\;\frac{\boldsymbol{C}_{n+1}}{\Delta t}\;\boldsymbol{T}_n \tag{2.74}$$

Due to the necessity of calculating $\boldsymbol{F}_{Q,n+1}$ for step n+1, which according to equation (2.71) depends on T_{n+1} through $\dot{Q}_{n+1}$ (which expresses cement heat generation rate, and is computed with the Arrhenius law shown in equation (2.23)) a nonlinear dependence is

observed in equation (2.74). Accordingly, an incremental iterative procedure supported by the Newton-Raphson method is usually adopted to solve equation (2.74), towards extracting the nodal temperatures T_{n+1}.
The formulation that has been summarized can be implemented with 1D, 2D or 3D FE (isoparametric formulation), using different kinds of FE for the concrete itself and the boundaries (for example: if 3D bricks are being used for concrete, boundary elements are modelled with planar FE). Standard Gauss integration techniques are used for computing numerically the integrals involved in equations (2.68) to (2.71). Assembly of global matrices C and G as well as F_T and F_Q vectors is performed with implicit cycle formulations, taking advantage of MATLAB array handling (Alberty *et al.* 1999).
A brief outline of the overall procedure for conducting the thermal analysis of concrete since early ages is illustrated in Box 2.1, where the most relevant operations needed for evaluating the final temperature distribution are reproduced, with special regard to the application of the Newton-Raphson method in the iterative procedure.
For simplicity of interpretation, equation (2.74) was rewritten as

$$\hat{\boldsymbol{K}}_{n+1}\,\boldsymbol{T}_{n+1} = \hat{\boldsymbol{F}}_{n+1} \tag{2.75}$$

Where

$$\hat{\boldsymbol{K}}_{n+1} = \frac{\boldsymbol{C}_{n+1}}{\Delta t} + \boldsymbol{G}_{n+1} \tag{2.76}$$

$$\hat{\boldsymbol{F}}_{n+1} = \boldsymbol{F}_{T,n+1} + \boldsymbol{F}_{Q,n+1} + \frac{\boldsymbol{C}_{n+1}}{\Delta t}\,\boldsymbol{T}_n \tag{2.77}$$

2.7 Validation of the numerical model

The validation of the implemented code was conducted with recourse to several thermal field validation/benchmarking examples available in the literature provided by Manrique (1976). These examples included several situations, including steady state and transient problems, as well as situations in which non-linearity arose (thus testing the implemented Newton-Raphon algorithm). In order to validate the implemented code for the heat generation due to cement hydration, an experiment with a concrete cube was conducted, with detailed description as follows.

2.7.1 Hydration of a concrete cube

Prediction of temperature development in concrete structures at early ages, with due account for the exothermic hydration reactions, has been dealt with by several authors in recent years. Most authors use the finite element method for the resolution of the energy balance equation that allows computation of temperatures within concrete during hydration stages.

Box 2.1: Outline of the thermal model

INPUT: $n,\ \boldsymbol{T}_n,\ \Delta t\ ,\ t_{end},\ TOLER,\ Q_{total},\ \dot{Q}_n\ ,\ Q_n$

OUTPUT: $\boldsymbol{T}_{n+1}$

(i) Update time $t_{n+1} = t_n + \Delta t$.

Is $t_{n+1} > t_{end}$? NO: Go to step (ii).

YES: Go to step (x).

(ii) Initialize iteration counter i=0, set $\Delta \boldsymbol{T}_{n+1}^{i=0} = \mathbf{0}$ and $\dot{Q}_{trial} = \dot{Q}_n$.

(iii) Set $\boldsymbol{T}_{n+1}^{i} = \boldsymbol{T}_n + \Delta \boldsymbol{T}_{n+1}^{i}$.

(iv) Compute $\hat{\boldsymbol{F}}_{n+1}^{i}$ with basis on the following computed entities:

$$Q_{n+1}^{i} = Q_n + \dot{Q}_{trial}\,\Delta t$$

$$\alpha_{T,n+1}^{i} = \frac{Q_{n+1}^{i}}{Q_{total}}$$

$$\dot{Q}_{n+1}^{i}\left(\alpha_{T,n+1}^{i}, T_{n+1}^{i}\right)$$

Prepare $\dot{Q}_{trial}$ for next iteration $\dot{Q}_{trial} = \dot{Q}_{n+1}^{i}$.

If necessary, compute $\hat{\boldsymbol{K}}_{n+1}^{i}$.

(v) Compute the residuals vector $\boldsymbol{\psi}_{n+1}^{i} = \hat{\boldsymbol{F}}_{n+1}^{i} - \hat{\boldsymbol{K}}_{n+1}^{i}\boldsymbol{T}_{n+1}^{i}$.

(vi) Check convergence:

Is $\left\|\boldsymbol{\psi}_{n+1}^{i}\right\| \le TOLER$? NO: Go to step (vii).

YES: Go to step (ix).

(vii) Compute $\Delta \boldsymbol{T}_{n+1}^{i+1} = \Delta \boldsymbol{T}_{n+1}^{i} + \left[\ \hat{\boldsymbol{K}}_{n+1}^{i}\ \right]^{-1}\ \boldsymbol{\psi}_{n+1}^{i}$.

(viii) Update iteration counter i:=i+1. Go to (iii).

(ix) Update the step counter n:=n+1. Go to (i).

(x) End.

Validation of these models has been made by several authors with recourse to temperature measurement using embedded sensors (Azenha 2004, Branco *et al.* 1992, Gutsch 2002). Yet, in the review performed for this research no works were found that specifically focused on using both internal and surface measurements of temperature, to constitute a benchmark example for temperature fields in concrete at early ages. This is precisely the focus of the present section, in which the infrared thermography technology, together with embedded sensors, were used for monitoring the surface temperatures on a

$40\times40\times40\text{cm}^3$ concrete cube since casting. Also, the cement heat of hydration release is measured with the technique of isothermal conduction calorimetry, to obtain the relevant parameters for numerical simulation of the thermal problem involved. The measured temperatures are to be compared with those calculated using both the 3D finite element software developed within this thesis, and the DIANA software (TNO-DIANA-BV 2007). In this way, both numerical models are validated with regards to experiments, and performance of the developed software is compared to that of DIANA, the latter extensively tested worldwide.

2.7.1.1 Infrared thermography

Infrared thermography is a technique that may be used to measure surface temperatures of objects. It relies on the fact that all bodies with temperatures above the absolute zero (-273°C) continuously emit energy within the infrared wavelength band, i.e., thermal radiation. When captured by thermography cameras, this radiation is converted into an electric signal, allowing for the creation of images that represent the spatial distribution of temperature within the surface of the targeted body (NEC-SAN-EI-INSTRUMENTS 1991).

According to equation (2.46), the emitted thermal radiation does not only depend on the surface temperature of the body, but also on the material emissivity, i.e., the efficiency of the surface in acting as a radiator (Clark *et al.* 2003). The value of the emissivity coefficient depends upon the surface temperature T, the observation angle θ and the wavelength λ. In the particular case of solids, the spectral emissivity changes little with the wavelength, thus it is generally acceptable to assume a constant value for ε. Besides, for non-metallic bodies, when the interval of T is not wide, and the measurements are performed within an angle θ between 0° and 60° with the perpendicular to the surface, emissivity may also be considered constant (Barreira 2004).

There are many advantages in the use of infrared thermography for monitoring surface temperatures of solids, but the following are particularly relevant for the present study, as it allows: a remote and non-contact measurement, a great versatility in post-processing of results and a fast response (which makes it possible to monitor transient phenomena). However, obtaining reliable temperatures with this technique demands that caution measures are taken with regards to reflection of radiation coming from external sources, and to atmospheric absorption, and finally to the surface emissivity quantification (Maser *et al.* 1990).

It is here remarked that in the bibliographic review conducted for this research, no references to thermal imaging of concrete during the hydration period have been found.

2.7.1.2 Experimental campaign

Geometry, materials and procedure

One of the main requisites for the concrete specimen to be monitored in this experimental campaign was to endure a large enough hydration-induced temperature rise to be clearly identified with the thermographic technique. A cube with 40cm long edges was selected as a commitment between a reasonable temperature rise (the more volume, the higher temperature would be achieved) and a reasonable feasibility of the cube in terms of

concrete volume (due to mixer limitations) and the total weight (so as to be handled inside the lab). The concrete mix used for this experiment can be found in Table 2.9.

Table 2.9: Concrete mix used in the experiment

Constituents	**(kg/m³)**
Cement (Type I 52.5R)	430.0
Limestone filler	301.5
Sand 1 (finer)	339.7
Sand 2 (coarser)	335.0
Coarse aggregate	729.7
Water	193.4
Superplasticizer (liquid)	6.8

The experiment basically consisted of casting the specimen inside a climatic chamber (constant temperature T=20°C and relative humidity RH=50%), within the visibility field of a thermographic camera. The specimen was then left undisturbed for a period of 8.6h after casting, subsequent to which four lateral formwork panels were removed, resulting in five surfaces of the specimen in direct contact with the air.

Heat of hydration
The type I 52.5R cement used in the concrete mix was produced in the previously described Company A, and had already been characterized in Section 2.4.3.3 within the isothermal calorimeter campaign. The parameters for numerical modelling of a cement paste mix with 1kg of this cement (and w/c=0.5) are shown in Table 2.7, from which the data for the numerical model of the concrete cube were extrapolated (particularly by basing the extrapolation on the A_T and E_a values obtained from the "Derivate of the Speed Method"). It should be remarked that the A_T and Q_∞ values of this table were dully multiplied by 430kgm^{-3} to express the heat generation per cubic metre of the concrete mix, whereas $f(\alpha)$ and E_a were used directly from the table.

Monitoring of temperatures – thermography and temperature sensors
A 640×480 pixel infrared imaging resolution thermography camera was used, with an accuracy of ±2°C. The camera was placed at 2.5m from the concrete specimen, and 1m above its top surface, to allow three surfaces be totally visible simultaneously (Figure 2.26). Concrete emissivity was assumed constant with the value of 0.88 - calibrated to match thermography readings with thermocouple measurements, and lying within the ranges usually considered for concrete (Silveira 1996).

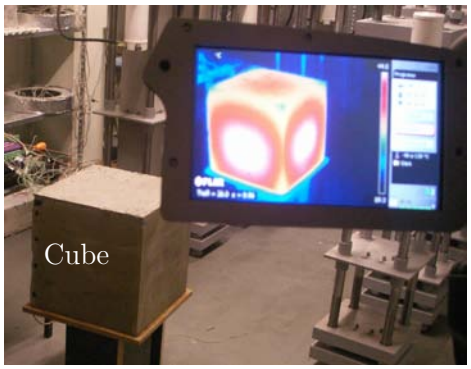

Figure 2.26: View of the camera image and specimen

Furthermore, temperature sensors were placed at several places within the cube, mainly in the neighbourhood of the surfaces shot by the thermography camera. Most sensors were thermocouples type K, but one PT100 sensor was placed in the cube centre, and another PT100 was used to monitor the environmental temperature. The overall arrangement of the sensors can be found in Figure 2.27, where thermocouples are labelled as TP1 to TP25.

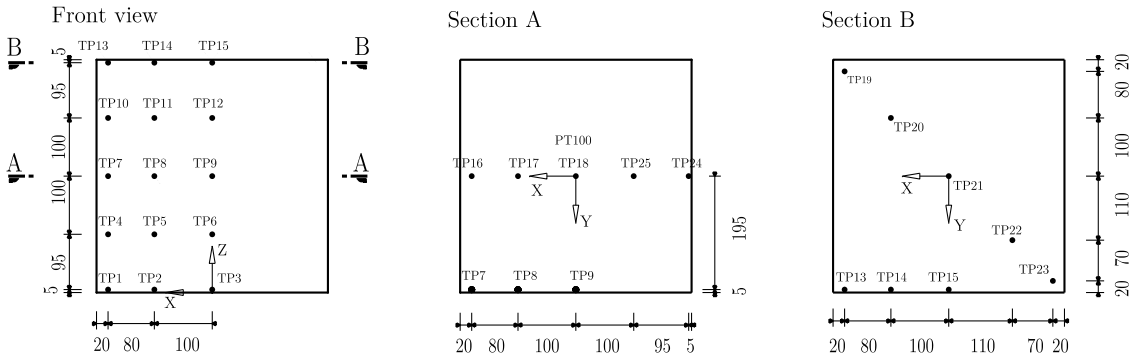

Figure 2.27: Three views of the temperature sensors arrangement (units in mm)

A 3D depiction of the placement of sensors can be seen in Figure 2.28a, where the same basic XYZ referential is used. The sensors were supported by thermally insulated wires, which in turn were attached to the wooden formwork of the specimen. The physical arrangement of this setup can be observed in Figure 2.28b. All sensors were connected to an automatic data acquisition system, one acquisition being made every 5 minutes.
Due to an unknown cause, the embedded sensors monitoring system yielded no results for the period between 0h15min and 3h40min after casting. Thus, all the plots for the temperature sensors to be presented are empty in such period (0.01-0.15 days); some temperature sensors had also further local disturbances, causing some periods to be absent of results in punctual cases.

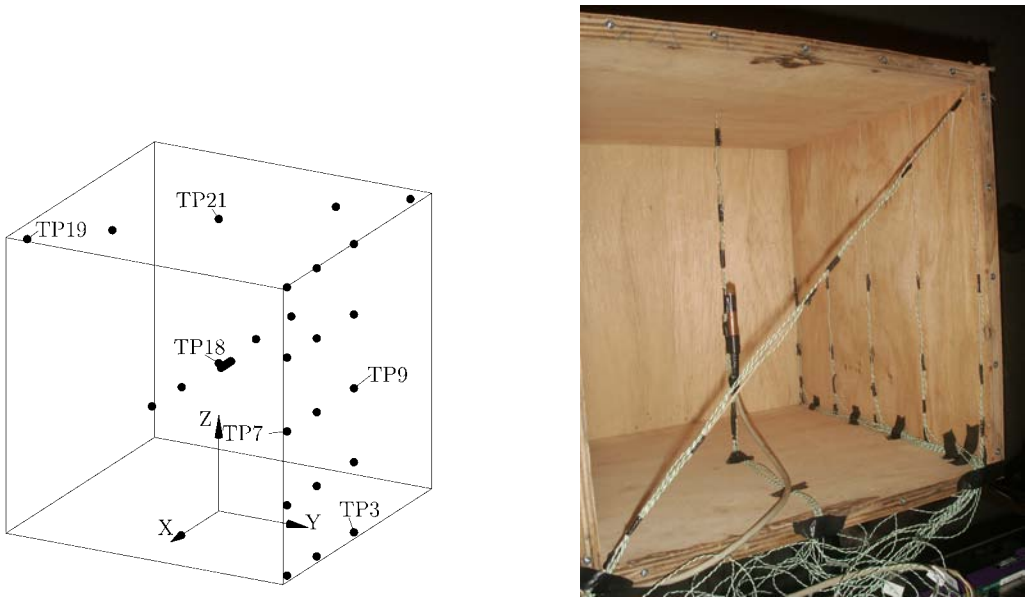

a) b)

Figure 2.28: a) Temperature sensors arrangement; b) Photo of the sensors and wooden formwork

Thermography technology allows plotting the temperature evolution at a given pixel of the image, providing the equivalent to hundreds of temperature sensors placed all along the visible specimen's surface. Bearing this capability in mind, two comparisons are now made regarding two temperature sensors placed near the surface, and their corresponding surface temperatures measured by the thermography camera. Lets start by sensor TP9, regarding the central point of one of the specimen's vertical surfaces at about 5mm depth (see Figure 2.28a), and whose temperature evolutions obtained using the two mentioned methodologies are depicted Figure 2.29a. Comments on this figure are divided in two phases:

- A first one, that pertains to the period before the formwork removal. While sensor TP9 is measuring temperature inside concrete, the thermography camera is measuring surface temperature on the formwork. Formwork is originally at 20°C, and even heating due to contact with concrete, it will be always colder than the latter, thus justifying a quite different evolution of the curves provided by thermography with respect to sensor TP9.
- The second one after formwork removal, when the thermography camera measures temperature at almost the same place as the sensor, yielding thus practically coincident curves.

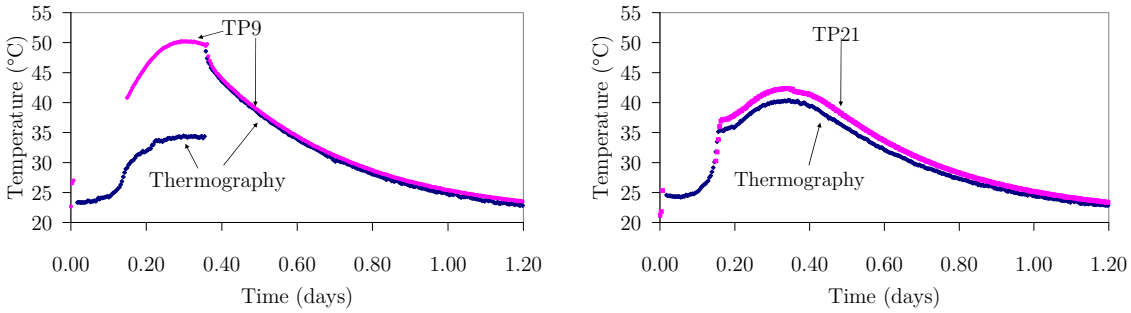

Figure 2.29: Temperature measurement at the location of: a) sensor TP9; b) sensor TP21

Regarding sensor TP21 (top surface), the temperature evolutions are presented in Figure 2.29b. In this case, since no formwork removal is involved, both techniques yield similar results. However, higher differences than it was observed for sensor TP9 occur, which could be related to a number of reasons, such a possible error in the sensor location (which may be slightly deeper than expected), errors in the measurement systems, or a change in the emissivity factor of concrete during hydration. In spite of all, these are, in fact, small differences, and so both measurement techniques validated each other, once similar conclusions as the ones presented in Figure 2.29 could be extracted for all the other near-surface temperature sensors (not included here for the sake of brevity).

2.7.1.3 Numerical simulation

For the numerical model of the 40×40×40 cm^3 concrete cube, and bearing in mind the existence of two symmetry planes, only one fourth of it was modelled. The 8 noded 3D FE mesh used in the discretization is shown in Figure 2.30.

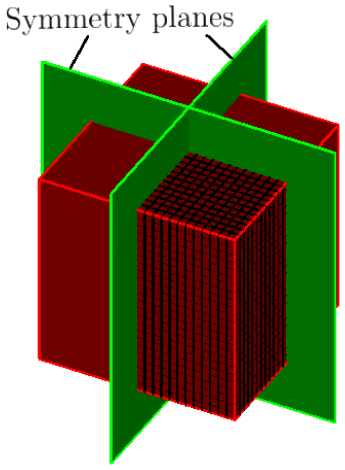

Figure 2.30: Planes of symmetry and the FE mesh adopted for the concrete cube

The thermal conductivity and specific heat of concrete were assumed as k=2.6$Wm^{-1}K^{-1}$ and ρc=2400$Jm^{-3}K^{-1}$. The initial temperature for concrete was considered to be 26°C, representative of the monitored temperatures during casting operations. The parameters

for simulation of heat of hydration release of the concrete mix using an Arrhenius-type law have already been described previously.

As far as boundary conditions are concerned, for concrete in direct contact with the environment a value of h_{eq}=10Wm^{-1}K^{-1} was considered, in correspondence to near stagnant air conditions (wind speed ~0m s^{-1}). At faces where wooden formwork exists between concrete and the environment, the electrical analogy for determination of h_{eq} was used, considering a thickness of 0.0185m for the formwork and k=0.20Wm^{-1}K^{-1} for the wood, according to

$$h_{eq} = \left(\frac{1}{10} + \frac{0.0185}{0.2} \right)^{-1} \approx 5.2 \, \mathrm{W \, m^{-1} \, K^{-1}} \tag{2.78}$$

The lateral boundaries were simulated with a h_{eq}=5.2Wm^{-1}K^{-1} until the age of 8.6h (to account for the wooden formwork), and h_{eq}=10Wm^{-1}K^{-1} from then onwards (reproducing direct contact of concrete with the air). In the symmetry planes, adiabatic boundaries were considered. Solar radiation and night cooling were disregarded, as the cube was placed inside an indoor climatic chamber without windows.

Numerical results and comparison with experiments

In Figure 2.31 temperatures predicted numerically are compared with the experimentally monitored ones at the locations of thermocouples TP3, TP7, TP9, TP18, TP19 and TP21. Generally speaking, the coherence between the experimental and numerical results is quite satisfactory. However, for sensors TP19 and TP21, some deviation is observed before formwork removal at the age of 0.36 days: these sensors are located in the vicinity of the top surface, which is horizontal and in direct contact with the air. It is known from heat transfer science that, in the absence of wind, the buoyancy forces (i.e., natural convection) can be of great importance when compared to the convective ones, as far as boundary transfers are concerned (Incropera and DeWitt 2001). In fact, for a horizontal surface the air right above is heated by the surface and rises, causing a renovation in the air, and therefore promoting continuation of the heat transfer mechanism. It is therefore understandable that higher surface temperatures will cause air to heat faster, and therefore to be renovated at a faster rate. This will engender higher transfer coefficients for the surface, leading to the conclusion that the boundary coefficient is dependent on the surface temperature. This dependence is not linear, and it has a strong interaction with the surface's size and the actual speed of air (regardless of the buoyancy mechanism). It is therefore quite difficult to predict and reasonable estimations can only be obtained by Computational Fluid Dynamics (or in a simplified manner by resemblance theories). This buoyancy phenomenon also occurs on vertical surfaces, and causes the transfer coefficient to be dependent of temperature, even though not as strongly as in the horizontal ones; furthermore, presence of a formwork on the vertical surfaces until the age of 0.36 days has also attenuated this phenomenon.

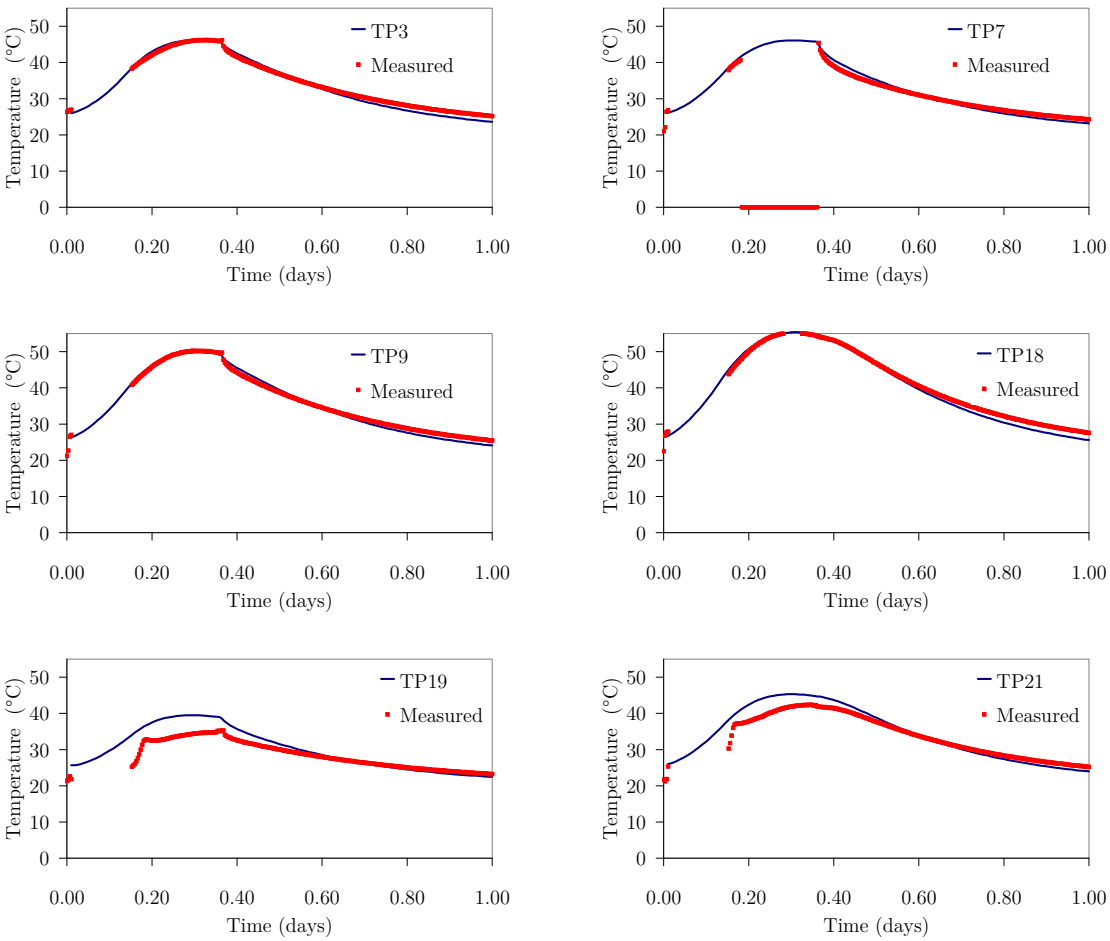

Figure 2.31: Comparison of temperatures: experimental (thermocouples) *versus* numerical results

Another possibility for explaining part of the difference between monitored and calculated temperatures near the top surface is the evaporative cooling phenomenon, a consequence of the additional heat that is removed from a surface from which evaporation is occurring. In this experiment, no curing membrane was used over the top surface of specimen, which may have created conditions for evaporation of water from the top surface concrete, and the corresponding heat removal.

Comparison of the temperatures predicted numerically against the thermography temperature contours, is made in Figure 2.32 for a set of relevant instants of time.

From the observation of this figure, it can be confirmed that all the instants plotted, an excellent coherence may be found for all vertical surfaces, while the top surfaces always exhibit larger deviations. This lesser coherence on the top surface confirms what had been observed previously for thermocouple results, leading thus to the confirmation of the difficulties of the used numerical models in correctly simulating the temperature development on the horizontal surfaces.

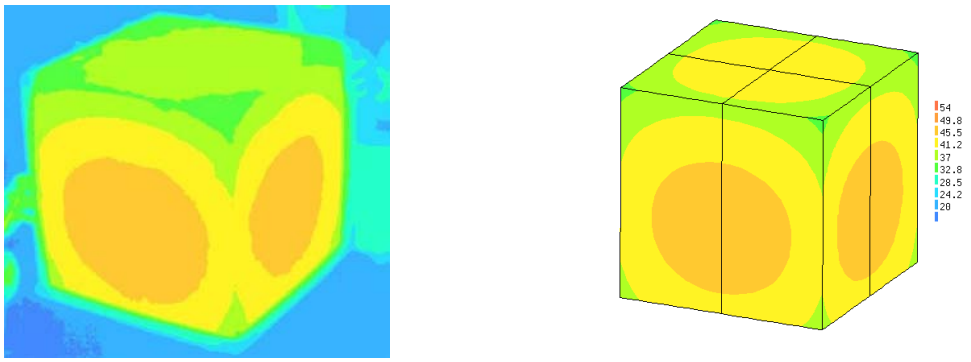

t=0.37 days

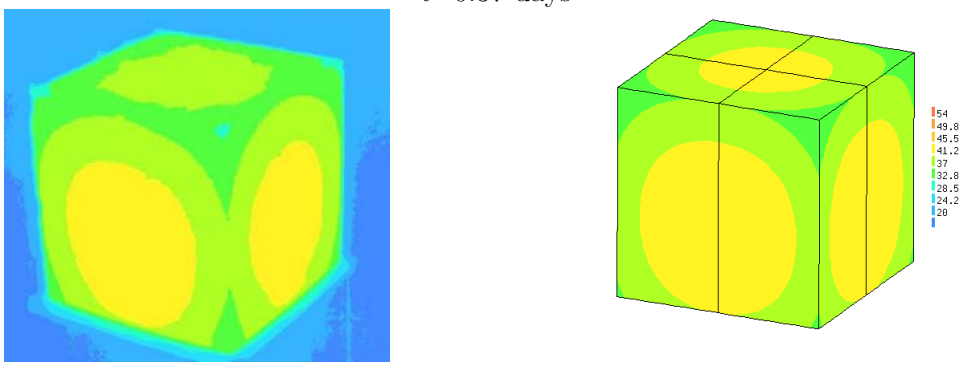

t=0.41 days

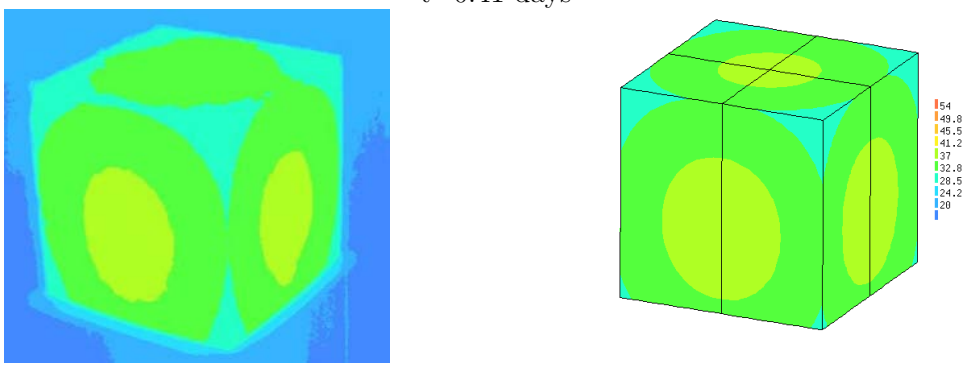

t=0.51 days

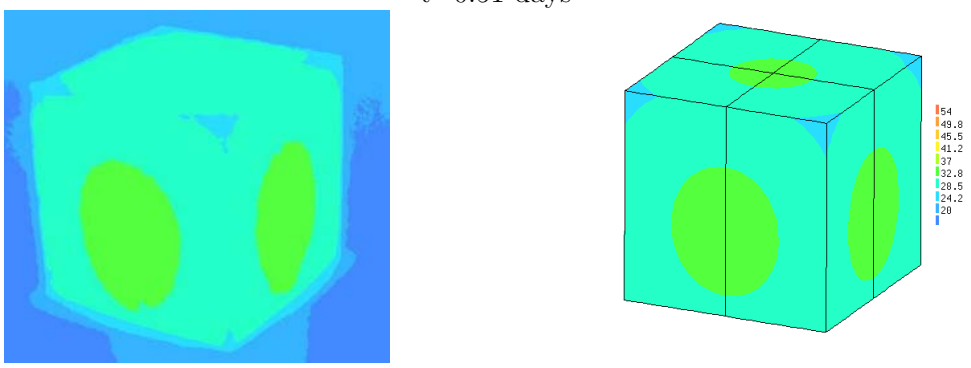

t=0.61 days

Figure 2.32: Comparison between thermography pictures (left) and temperature plots (right) of computed temperatures (in °C)

The numerical results obtained here were also replicated using DIANA, obtaining very similar computed temperatures, with differences lying under 0.2°C.
As a final remark, it can be said that the purpose of the present section has been achieved, in terms obtaining a validation example for hydrating concrete simulation (with

corresponding material characterization), and also in what regards to the capability of the FE software implemented in the scope of this thesis to reproduce the experiment.

2.8 Numerical sensitivity analyses

Numerical studies in regard to the importance of certain modelling options are performed in the present section. The selected examples are related to the variable character of properties k and ρc along hydration, as well as the presence of reinforcement and its effect on early age temperature development. These aspects, considered of significant importance, were not found to be covered in existing literature, thus motivating their relevance of study.

2.8.1 Variable thermal properties along hydration

Section 2.3.1 dealt with a literature review on thermal conductivity k and volumetric specific heat ρc, showing that some authors defend that these properties vary along the hydration process. As a simplification, the numerical models that have been presented so far considered these properties constant during hydration. However, clarification of the effects of considering these properties as being variable during hydration on the temperature development of concrete will be presented in the present section with recourse to numerical sensitivity analyses.

For the simulations envisaged, a very simple geometry was selected, involving a 1D – see scheme in Figure 2.33: a rectangular shape with boundaries *L3* and *L1* behaving as adiabatic, and *L2* and *L4* behaving as convective boundaries (thus promoting heat transfer only in the horizontal direction). No heat transfers occur in the plane perpendicular to the figure. The height of the model is 1m, and its width is variable, assuming the values of 1.0m and 0.3m in order to simulate a thick and thin concrete element respectively. Heat generation parameters are considered coincident to those of the simulation to be presented in Section 5.5. Boundary transfer coefficients for *L2* and *L4* were considered as h_{eq}=12Wm^{-2}K^{-1}, environmental temperature was considered constant at 20°C, and reference values for thermal conductivity and volumetric specific heat (when considered constant during the hydration process) were k = 2.674 Wm^{-1}K^{-1} and ρc = 2400 kJm^{-3}K^{-1}. Regardless of the geometry of the model, a 10×10 FE discretization was selected, with 4-noded elements. The 1.0m and 0.3m wide reference models will be named as 1ref and 0.3ref, respectively.

Two regions of the model are selected, where the corresponding average temperatures are to be analyzed: a core finite element, pertaining to the geometric centre of the FE model (termed with the suffix "-core"); and a surface FE, located at mid-height of *L4* (termed with the suffix "-surf").

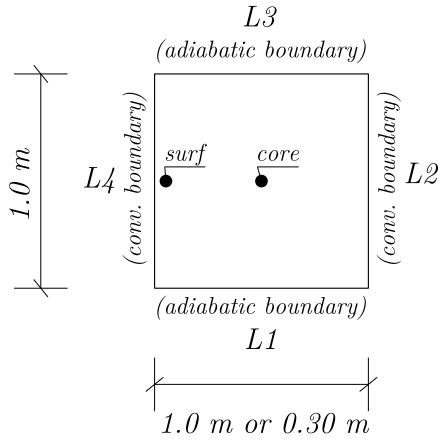

Figure 2.33: Scheme for the sensitivity analyses on variable k and ρc along hydration

The simulated temperatures corresponding to the two regions and reference situations are depicted in Figure 2.34. As expected, the differences in behaviour of the two models are remarkable, not only on the peak temperatures (~62.1°C for 1ref-core and ~39.3°C for 0.3ref-core), but also in the maximum temperature gradient between the surface and the core (~17°C for 1ref and ~3.9°C for 0.3ref). These reference situations will serve as starting points for the sensitivity analyses to be presented next.

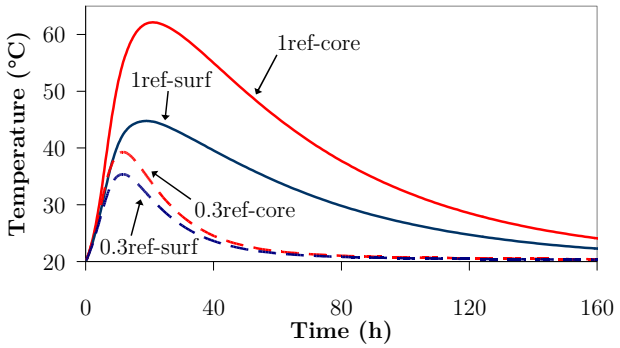

Figure 2.34: Simulated temperatures for the reference models 1ref and 0.3ref

2.8.1.1 Effect of variable k

Influence of varying the thermal conductivity along cement hydration was investigated by changing that property in the reference models 1ref and 0.3ref, so that it would evolve along hydration according to equation (2.14), duly adapted for the most dramatic scenario found in the literature, that is, with a 33% variation of k according to the formulation by Ruiz *et al.* (2001). The resulting numerical models are named 1kvar and 0.3kvar, and their outputs are compared to those of the reference models in Figure 2.35. It can be observed that in 1kvar and 0.3kvar models the use of an initially higher thermal conductivity led to a very slight decrease in the peak temperature (less than 0.8°C) in the calculated temperatures for both the studied situations (thick and thin element). Therefore, it can be concluded that the effect of variable k along hydration would generally have an almost negligible influence on temperatures, both in thin and thick concrete elements, and consequently it can be disregarded without significant detriment for the accuracy of results.

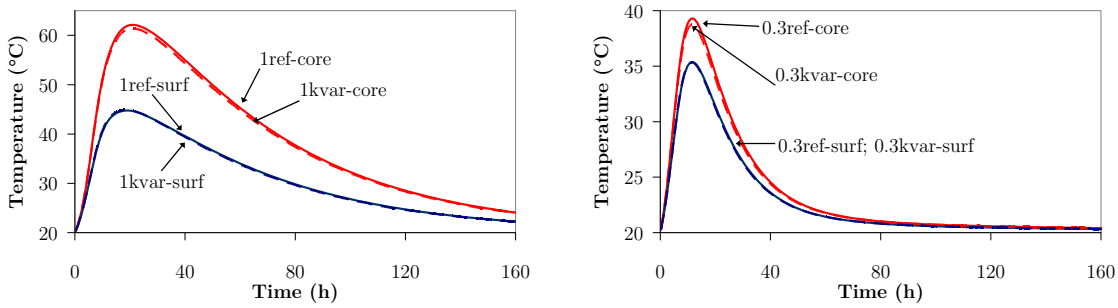

a) b)

Figure 2.35: Effect of variable k along hydration on calculated temperatures

2.8.1.2 Effect of variable ρc

The effect of variable volumetric specific heat along cement hydration was investigated by changing ρc in the reference models 1ref and 0.3ref, so that it would evolve along hydration according to equation (2.20). The resulting numerical models are named 1cvar and 0.3cvar, and their outputs are compared to those of the reference models in Figure 2.36. Consideration of variable ρc along hydration affected temperatures on both specimen geometries: peak temperature decreased 5°C in the 1m thick model, and 2°C in the 0.3m thick model. The diminishment of surface temperatures in comparison to the reference models was slightly smaller (2°C for the 1m model and 1.5°C for the 0.3m model). The overall conclusion is that varying ρc according to equation (2.20) produces non-negligible effects on the temperature development of both specimen geometries, with stronger emphasis on the wider one. This points to the necessity of further research regarding this matter.

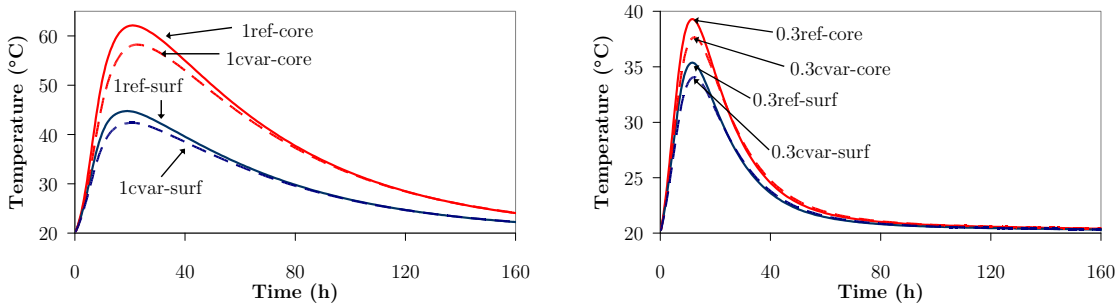

a) b)

Figure 2.36: Effect of variable ρc along hydration on calculated temperatures

2.8.2 Effect of reinforcement on the concrete temperature distribution

Calculation of temperatures within concrete at early ages, with consideration of heat generated due to cement hydration, is usually conducted disregarding the effect of steel reinforcement (Azenha 2004, Breugel 1998, Cervera *et al.* 2002, De Schutter 2002, Faria *et al.* 2006, Jonasson 1994, Maekawa *et al.* 1999, Nilsson 2003, Ruiz *et al.* 2001). This simplifying assumption is not usually explicitly justified, and no past research was found focusing on this particular issue. With this in mind a numerical exploratory analysis was conducted, with the purpose of checking the variation in temperatures on a concrete element with and without steel rebars.

Geometry and properties

For the intended numerical simulation, a hypothetical infinite length RC element was considered, with 12mm diameter steel rebars. The element is 0.40m thick and 1.60m tall, having 4 legs of 12mm diameter stirrups (with longitudinal spacing of 0.15m), two of which extend 0.40m outwards the element's surface – see sketch in Figure 2.37. All the four lateral surfaces are in direct contact with the environment since casting, as well as the salient reinforcement. No rebars were considered longitudinally, once these would have much less influence than the transversal ones. Another reference is made to a simplification pertaining the steel bars: instead of modelling them with a circular cross-section, they were considered with a square cross-section of 12mm×12mm.

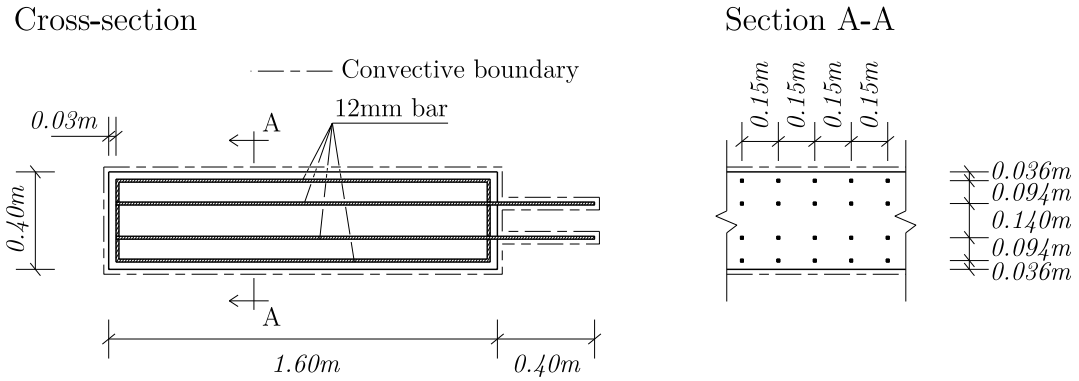

Figure 2.37: Schematic representation of the RC element

The thermal material properties for concrete were taken as: k=2.6Wm^{-1}K^{-1} and ρc=2400kJm^{-3}K^{-1}. The heat generation characteristics were considered coincident with those presented in Section 6.2.5 of this thesis. With regards to the steel thermal properties, k = 54Wm^{-1}K^{-1} and ρc = 3270kJm^{-3}K^{-1} were considered.

The boundary conditions were constant since casting with a surface convection coefficient h = 10Wm^{-1}K^{-1} being adopted.

A 3D FE model was considered, taking advantage of the symmetry at the cross sectional level, and the symmetry planes perpendicular to the longitudinal direction at a distance of 0.15m (in accordance to the repetition of reinforcement patterns that can be recognized in Section A-A of Figure 2.37). The selected FE for concrete and steel were 8-nodded bricks, with the mesh reproduced in Figure 2.38, where the three symmetry planes are identified, as well as the convective boundaries in concrete and the reinforcement elements (the exposed reinforcement elements also have convective boundaries in their surface, not represented in red for simplification). The reinforcement FE geometry is reproduced in Figure 2.39.

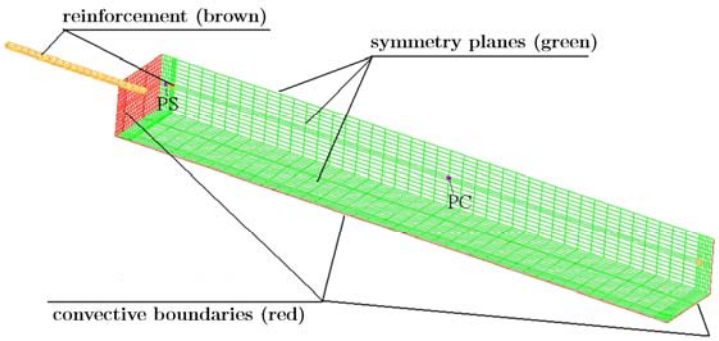

Figure 2.38: FE mesh for the RC element

Figure 2.39: FE mesh for the reinforcement

In order to assess the effect of reinforcement on the thermal field, a second model (named here as model 2, in opposition to the previous one, named as model 1) was created with the same FE mesh and geometry, except for the fact that all the FE are now considered as being concrete. The differences in the results will reflect the influence of reinforcement on the temperature distribution.
Both thermal analyses were conducted with a total of 168 time steps of 1 hour (7 days).

Results
The obtained results in the two models are presented simultaneously, providing grounds for the discussion of the influence of reinforcement. First, a plot of the temperature distribution in the models (at the instant when the maximum temperature is achieved – t=21 hours) is depicted in Figure 2.40: it is possible to observe that there was a slight effect of the reinforcement in the computed temperatures, once the maximum temperature of model 1 (33.8°C) is a little lower than that of model 2 (34.2°C). This 0.4°C peak temperature difference is accompanied by a subtle difference in the temperature distributions on the two models. However, there is no noticeable change in the temperature isolines, indicating that the effect of reinforcement proved to be quite small in this case.

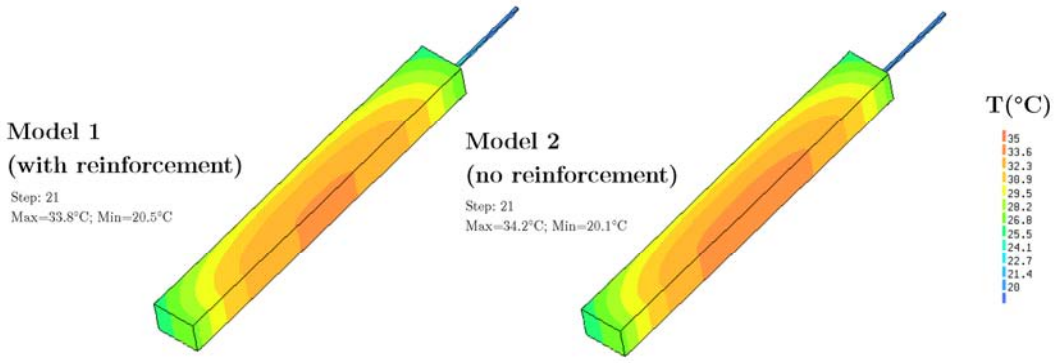

Figure 2.40: Temperature distribution at t=21 hours

The temperature development in points PS (1.5cm from the surface, located at the symmetry plane in line with the reinforcement – see Figure 2.38) and PC (geometrical centre of the modelled beam – see Figure 2.38) for both calculations is shown in Figure 2.41. The maximum temperature differences in the two control points occur at the instant of maximum temperature and nearby instants. Such difference never overcomes 0.5°C, and tends to be lower at other instants (both during heating and cooling phases). So, from the obtained results it is reasonable to postulate that for most applications the effect of reinforcement in the temperature distribution is of small importance, and may generally be neglected.

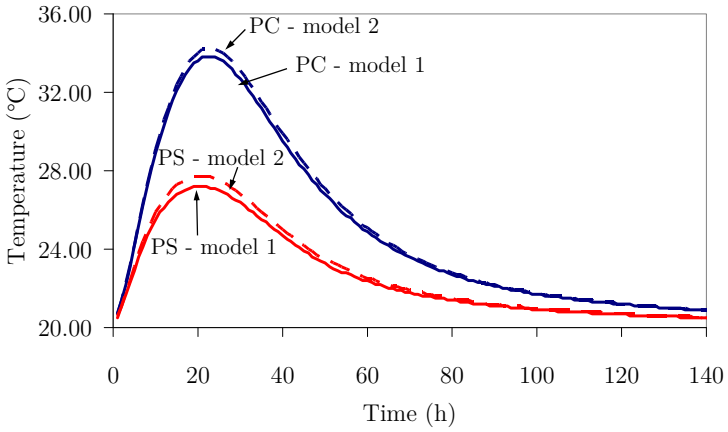

Figure 2.41: Temperatures in PS and PC – Models 1 and 2

2.9 Boundary conditions: experiments and simulations

Experimental work regarding thermal model boundary conditions was performed, aiming at two main points: (i) checking the capabilities of the solar radiation predictive models and the influence of considering solar radiation in the quality of numerical results; (ii) evaluation of convective heat transfer coefficients and their relationship to environmental wind speed.

2.9.1 Solar radiation

Bearing in mind that the intended application for the solar radiation model is the use on concrete structures, a simple experiment was conducted for validation purposes. On the roof of one of the buildings of the Faculty of Engineering of the University of Porto (tall enough to avoid any shadowing effects from neighbouring obstacles), two concrete cubes ($15\times15\times15cm^3$) were placed, with their lateral faces pointing to four cardinal directions, as represented in Figure 2.42.

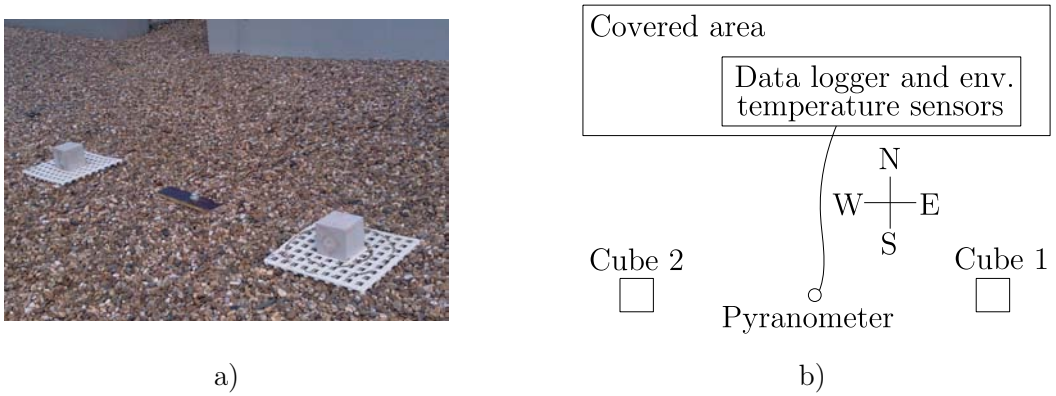

Figure 2.42: Cubic specimens for the solar radiation experiments: a) photo; b) scheme

The cubes with an age of ~2 years came from a climate controlled chamber, and can be considered to have an initial homogenous temperature of 20°C. No internal monitoring was considered necessary, as the most important results pertain to the surface temperature, which were monitored several times per day using a handheld infrared thermometer (see Figure 2.43a). This instrument has an accuracy of ±1°C within the range 10°C-30°C and ±1.5°C outside this range. It is also preset to an emissivity of 0.95, which is fairly consistent with the values of 0.85~0.95 usually considered for concrete (Silveira 1996). Even though it is not a high accuracy measuring instrument, it reasonably fits the needs for this particular research, where the numerical simulations usually deviate from real examples around ±2°C or even more.

Environmental temperature and solar radiation were measured continuously (in 5 minutes intervals) using a data logger – see Figure 2.43b. Environmental temperatures were continuously measured using a PT100 sensor (in a shadowed area between the data logger and the wall behind it, to minimize the effect of solar radiation in the temperature measurements). Solar radiation was measured using a low-cost pyranometer that uses a photodiode detector, which creates a voltage output that is proportional to the incoming radiation - Figure 2.43c.

a) b) c)

Figure 2.43: a) Infrared thermometer; b) Data logger and respective casing; c) Pyranometer

The experiment occurred between the 2nd June 2008 at 15h30m and the 3rd June 2008 at 20h20m. Surface temperatures had to be measured manually using the infrared thermometer at the geometrical centre of each exposed surface of each cube (North, South, East, West), at intervals rounding 1h during daytime.

The results collected with the data logger are depicted in Figure 2.44. Solar radiation reached peak values at the solar midday of about 1000Wm^{-2}. From the evolution of solar radiation input it can be seen that this was a sunny day, with some occasional clouds corresponding to the out-of-trend values. Environmental temperature had a maximum value of 23.4°C.

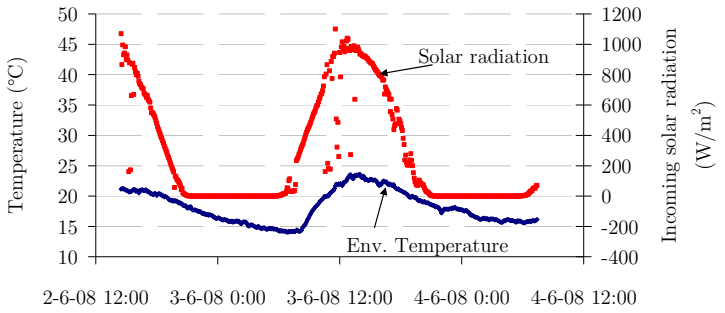

Figure 2.44: Results collected with the data logger – Environmental temperature and solar radiation

The measured temperatures at the surfaces of both cubes were quite coherent with each other, exhibiting maximum deviations that always remained below 10%. Thus, for the sake of brevity, only the data pertaining to the five surfaces of Cube 1 is shown in Figure 2.45. Centring attention on the results of the 3rd June 2008, it is pertinent to state that as expected, the orientation of the surface plays a role on the temporal distribution of temperatures: temperatures on the East surface are the highest during the morning (sun rises in the East), while the West surface has higher temperatures at the end of the afternoon (sun sets in the West). The highest temperatures are attained in the top surface. The lowest temperatures occur in the North surface which is the one less exposed to direct sunlight during the day.

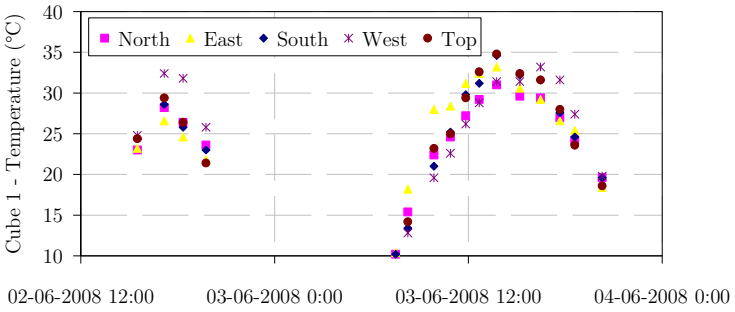

Figure 2.45: IR Temperature measurement results – Cube 1

By using the radiation models described in 2.5.2.4, the numerical simulation of the expectable solar radiation on a horizontal surface was conducted between the 2nd June at 15h30m and 3rd June at 23h59m. For best coherence, the Linke turbidity factor had to be adjusted by trial and error, obtaining a final value of T_l=2.5 (corresponding to a clear skies day, which was roughly the case). The other parameters considered were: α=0° (horizontal surface) and latitude=41.178° (the value of ψ is not relevant for a horizontal surface). The comparison between the numerical simulation and the actual measurements of incident solar radiation at a horizontal surface is depicted in Figure 2.46. It is clear that the numerical simulation matches the experimental values very well both in terms of amplitude of the day and shape of the curve. Most deviations are actually caused by partial shadowing due to passing clouds.

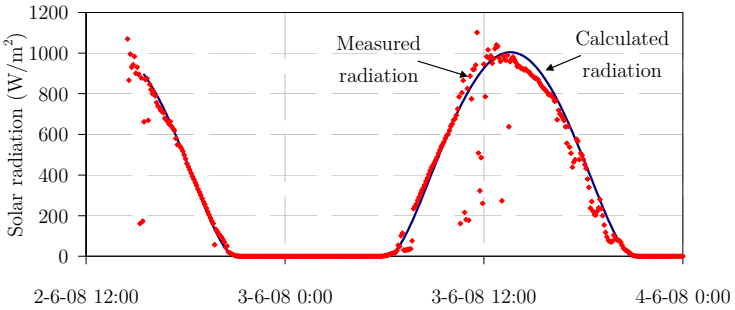

Figure 2.46: Measured solar radiation *versus* calculated solar radiation (horizontal surface)

Having validated the capabilities of the numerical model to simulate the incident radiation on a horizontal surface, the next step was to calculate the radiation that is actually absorbed by concrete on the five surfaces of the cube exposed to solar radiation. A value of 0.6 was adopted for the absorvity of concrete (α_S). The several vertical surface simulations considered α=90° and only differed in terms of the ψ value (that reflects the direction of the surface): ψ_{North}=180° ; ψ_{South}=0° ; ψ_{East}=90° ; ψ_{West}=270°. The simulation conducted to the results shown in Figure 2.47, where the relevancy of absorbed energy on each surface can be compared.

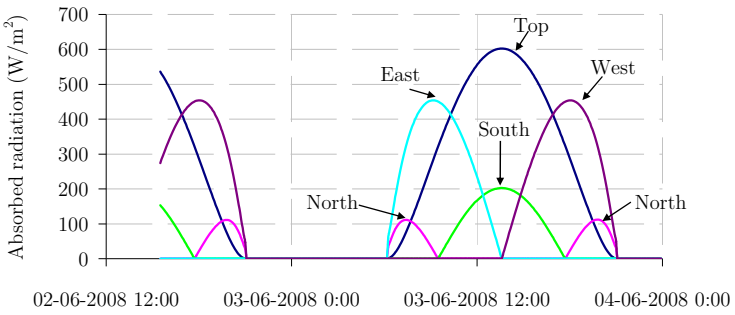

Figure 2.47: Computed absorbed radiation by concrete in the 5 relevant surfaces

For the FE simulation of the cube, two situations were simultaneously analyzed. Both of them have the exact same parameters, except for the fact that one considered the explicit contribution of solar radiation (through the input of the results depicted in Figure 2.47) and the other disregarded the solar radiation. The FE model comprised the three dimensional representation of a cube, using 8 nodded FE and a 2×2×2 Gauss quadrature (see Figure 2.48). All boundaries were considered to have a convection/radiation coefficient of 20$Wm^{-2}K^{-1}$, corresponding to a relatively windy situation on the roof top of the building. This is a rather simplifying assumption once the wind speed/direction was not constant, corresponding to varying transfer coefficients in time and space. As the purpose of this simulation was to compare the performance of the same numerical model with and without consideration of solar radiation, this simplification was considered acceptable. Regarding the thermal characteristics of concrete k=2.6 $Wm^{-1}K^{-1}$ and ρc=2400$kJm^{-3}K^{-1}$ were considered. External temperature was input with the measured values of the PT100 sensor. The analysis comprised 400 time steps of five minute duration each.

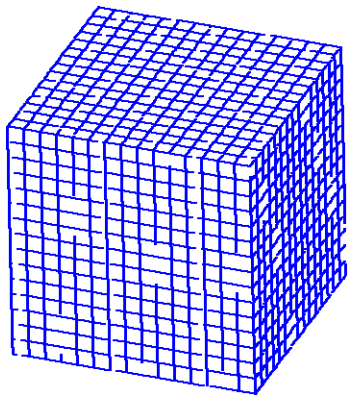

Figure 2.48: FE mesh adopted for the cube

The computed temperatures obtained from both numerical simulations in the centre point of the South and West surfaces, (with and without consideration of the effect of solar radiation), as well as the correspondent experimentally measured values are depicted in Figures 2.49 and 2.50. It becomes evident that even though the match of model including solar radiation effects is not perfect (simplifications exist in the convection coefficient and in the non-consideration of the effects of cloudiness, as well as the fact that night radiation cooling was not considered), it is much better than the model without

consideration of solar radiation, which fails to describe the differential behaviour between the several surfaces, as well as the large temperature increase due to solar exposure. Another important issue to be addressed regards the overestimation of temperatures on all surfaces at early morning: this is clearly related to the effect of night cooling which was disregarded in this study. Further experiments should be conducted in regard to this matter.

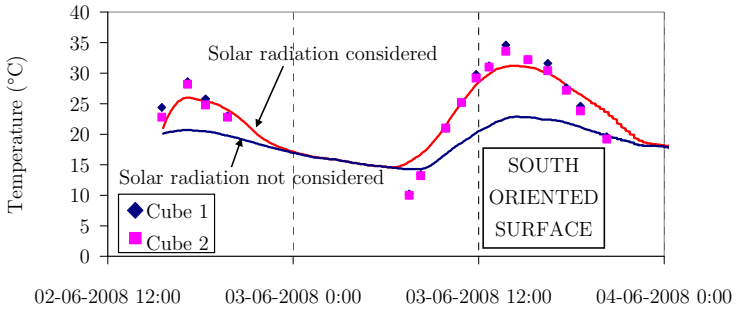

Figure 2.49: Experimental results (dots) and numerical results (lines) for the South oriented surface

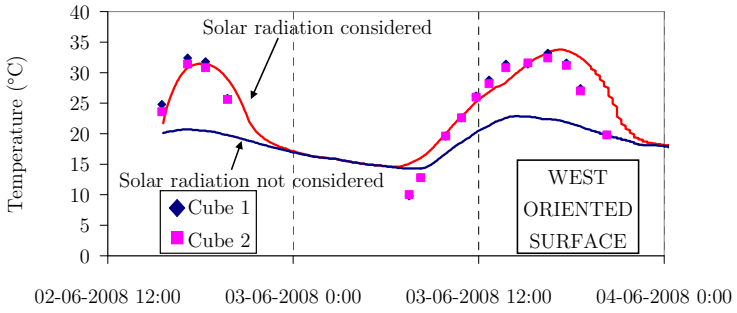

Figure 2.50: Experimental results (dots) and numerical results (lines) for the West oriented surface

2.9.2 Heat exchange coefficients for concrete – wind tunnel testing

One of the most important inputs necessary for the numerical simulation of temperature fields in concrete since early ages is the boundary transfer coefficient. The experimental campaign that is to be described in this section was essentially directed to the field of convection (both natural and forced). No experimental work was made in the field of long wave radiation transmission.

Natural convection tests are relatively easy to perform, once they are conducted in the absence of air movement. Nevertheless, in order to conduct a forced convection test, controlled conditions in terms of wind speed and turbulence are necessary, as well as specific monitoring devices. In this research, the Boundary Layer Wind Tunnel of the Bridge and Structure Laboratory of the University of Tokyo was used (see Figure 2.51). The wind tunnel has a cross section of 1.5m wide by 1.8m tall, and can easily deliver wind speeds until 30ms^{-1}, with turbulence intensities below 0.5%. Also, it is equipped with a high precision hot wire anemometer, which allows the measurement of both wind speed

and turbulence. With these characteristics, the wind tunnel fitted the requirements of the experiments that were to be carried out.

Figure 2.51: View inside the wind tunnel

Heat convection experiment – basic setup and experimental procedures

The basic idea of the heat convection experiment was to heat a prismatic concrete specimen from one surface and let it lose heat to the environment from the opposite surface, maintaining all the other faces as much thermally isolated as possible. The specimen size of 10cm×10cm×15cm was chosen in order to create a significant temperature gradient between the bottom surface and the top surface (separated by 15cm of concrete) - Figure 2.52.

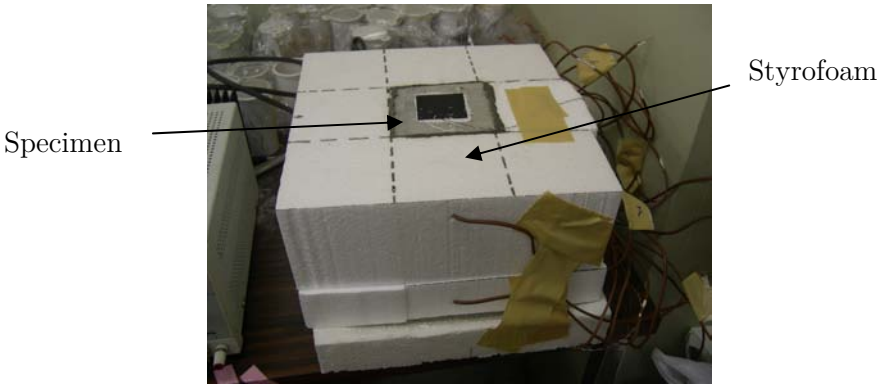

Figure 2.52: Specimen used for the heat convection test

The concrete mix used in this experiment had a w/c=0.53, and its composition is shown in Table 2.10.

Table 2.10: Concrete composition for the specimen

Constituent materials	Weight (kg m^{-3})
Water	175.6
Ordinary Portland cement	334.2
Sand	813.8
Small aggregate (5-13mm)	432.6
Coarse aggregate (13-20mm)	528.8

Three specimens were cast, each with three embedded thermocouples, even though only one specimen was to be tested (redundant specimens were cast in case of occurrence of any problem). The internal thermocouples were centred in the specimen, and placed at variable heights along the 15cm dimension: 2cm, 7.5cm and 13cm. With this setup temperature profiles along the height of the specimen could be established, and consequently internal heat fluxes could be calculated. In Figure 2.53 both temperature sensors (a) and photo of specimens in the formwork after casting (b) can be observed.

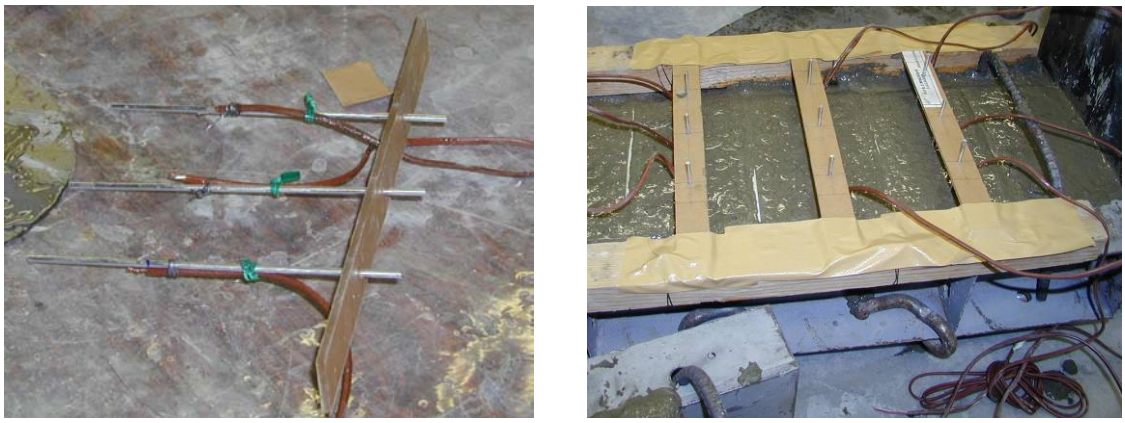

a) b)

Figure 2.53: a) Setup for temperature sensors; b) appearance after casting

After casting all specimens were covered with a plastic foil for a period of 24 hours, after which they were demoulded and placed inside a controlled environment room at a temperature of 20°C and a relative humidity (RH) of 60%.

The basic procedure of the experiment consisted of creating a heat source on the bottom 10cm×10cm face of the specimen, while keeping the four 10cm×15cm lateral faces thermally isolated with 10cm thick styrofoam blocks, and leaving the top surface in contact with the environment (in the presence or absence of wind). Besides the temperatures measured inside the specimen, the heat flux from the top surface was monitored using a 5cm×5cm heat flux sensor. The heat generation in the bottom surface was guaranteed by a 30cm×30cm heat mat placed under the specimen. This heat mat could be programmed to maintain temperature at a value defined by the user, heating and cooling according to a thermal sensor placed underneath it. The actual direct control of the heat generated by the mat was not possible under these conditions. Below the heat mat, a styrofoam base was used to minimize thermal losses downwards. The described system is depicted in Figure 2.54. With the above mentioned setup, heat transfer occurred mainly in 1D conditions (vertical direction).

For use in the wind tunnel, the mentioned setup required some adaptations: (*i*) to avoid flow disturbances caused by the boundary layer that is generated in the vicinity of the bottom slab of the wind tunnel, the specimen was placed over a 30cm tall table; (*ii*) to prevent strong disturbance of the flow due to the specimen geometry (such as flow separation and local turbulence effects), an aerodynamic appendix was placed in the upstream side of the setup, as depicted in Figure 2.55. This aerodynamic appendix had an elliptic shape to guarantee a smooth transition of the flow streamlines, staying parallel to

the top surface of the specimen in its neighbourhood. The whole setup inside the wind tunnel is reproduced in Figure 2.56.

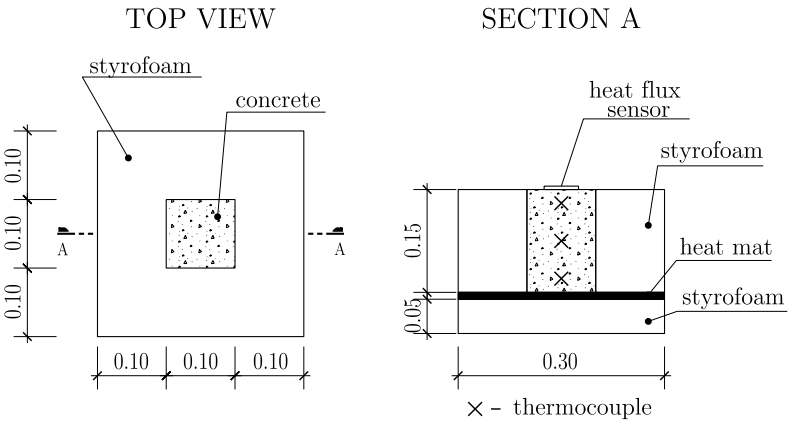

Figure 2.54: System for heat generation and temperature measurement in the concrete specimen (units: m)

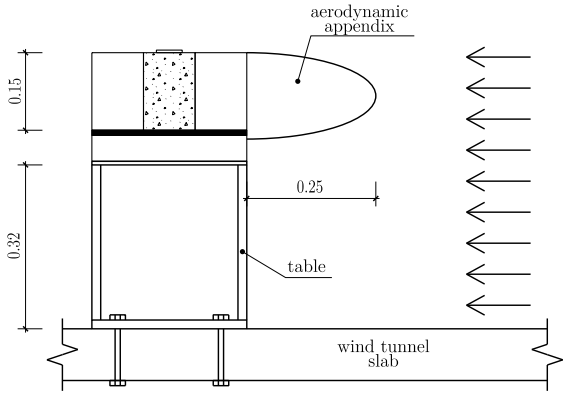

Figure 2.55: Setup of specimen in the wind tunnel (units: m)

Figure 2.56: Photo of experimental setup inside the wind tunnel (view from downstream)

Two kinds of tests were carried out in the wind tunnel:

- A **steady state test**: the specimen (initially at 20°C, the environment temperature inside the wind tunnel) was heated from the bottom surface to a prescribed temperature of 45°C, and thereafter the setup was submitted to a prescribed wind

speed until steady state heat transfer being reached. Such condition took 7-8 hours to be attained, due to the specimen geometry and the low heat conductivity of concrete. Such steady state conditions were obtained by observation of constancy in the output of both the core thermocouples and the top heat flux sensor for a period not less than 60 minutes.

- **Transient tests**: the specimen was required to be hot (top surface significantly hotter than the environment), and it was submitted to a succession of 5 minutes long cycles to a constant wind speed V (V was increased from a cycle to the succeeding one). The heat flux sensor output was recorded, as well as the surface temperature (the latter with the aid of an infrared thermometer).

To check the effect of turbulence on the heat transfer, some of the tests were conducted without any induced turbulence in the tunnel; other tests were conducted with induced turbulence, caused by a wooden grid placed upstream to the specimen.

Because of the limited time availability of the wind tunnel, only 4 steady state tests were conducted:

1. Without wind
2. With V=4.2m/s measured 200mm over the specimen, with induced turbulence
3. With V=3.4m/s measured 200mm over the specimen, with induced turbulence
4. With V=3.5m/s measured 200mm over the specimen, without induced turbulence

The transient tests were conducted for wind speeds between 0m/s and 8m/s (with steps $\Delta V \approx$1m/s), with and without induced turbulence.

Steady state tests

In steady state conditions, and assuming that the lateral heat flux across the styrofoam is negligible, the vertical heat flux inside the specimen is the same as the heat flux between the specimen and the environment. So, by monitoring temperatures inside the specimen and the flux through the top heat flux sensor, redundant data was obtained in regard to the evaluation of the heat flux between the specimen and the environment. That was the initial idea, but in fact the temperature profile (obtained by the measurements of the embedded thermocouples) in steady state conditions inside the specimen was not linear (as expected by application of the Fourier Law to 1D heat conduction), which revealed that some non-negligible heat flux was occurring across the styrofoam isolated surfaces. Therefore, in order to perform a mutual validation between the measurements of the thermocouples and the ones from the heat flux sensor, a 3D FE analysis was performed, accounting for realistic boundary conditions in the styrofoam. The numerical model took advantage of the two symmetry planes of the problem and it used 8-nodded prismatic FE; the adopted FE mesh, along with a temperature plot for one of the studied steady state conditions are shown in Figure 2.57. In this figure a small temperature drop near the lateral vertical edge can be observed, in correspondence to the already mentioned imperfect isolation provided by the styrofoam.

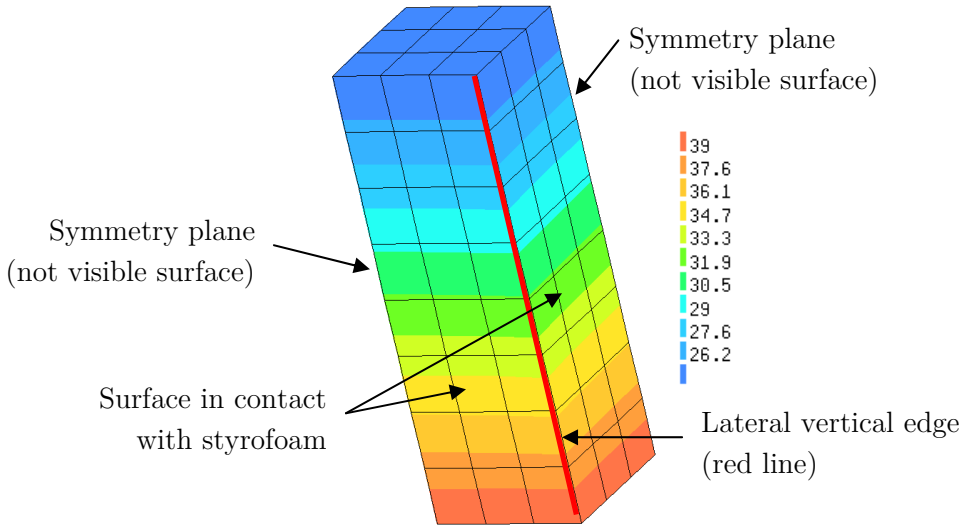

Figure 2.57: Temperature plot for one quarter of the specimen (°C)

Even though not shown here (for the sake of conciseness), the use of the mentioned numerical model combined with the results from thermocouples allowed computing the actual heat flux occurring in the top surface of the specimen. As this computed flux was coincident with the output of the heat flux sensor (which was being used for the first time), increased confidence was attained in the use of heat flux sensor.
For illustrative purposes, a typical output of the measurements made for the steady state tests is shown in Figure 2.58. It can be observed that the time to achieve almost steady state conditions in all sensors is of about 7 hours.

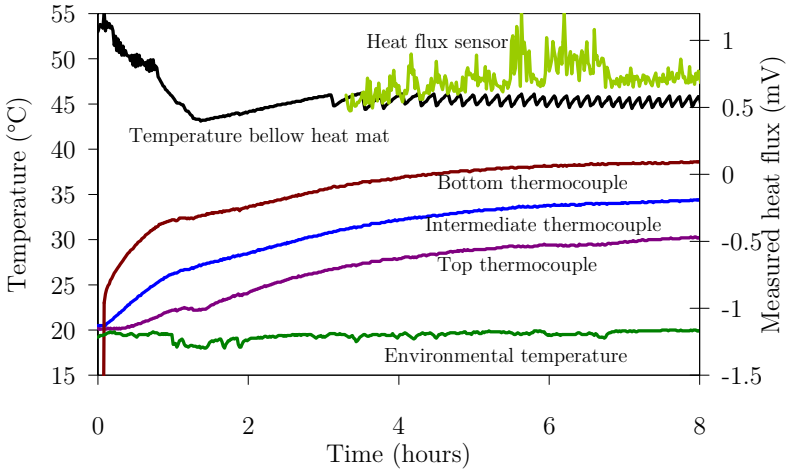

Figure 2.58: Typical output of the measurements in a steady state test

From the measured heat flux, the contribution of long wave radiation (according to the methods mentioned in section 2.5.2.2) was subtracted, so that the resulting values consisted of only convective heat losses. The heat transfer coefficient was computed according to equation (2.39), dividing the convective heat losses by the difference between the surface temperature of concrete (measured with an infrared sensor) and the environmental temperature.

The results of the four steady state tests that were performed are depicted in Figure 2.59. The expected tendency for higher convection coefficients for higher wind speeds was confirmed, yet the difference in the heat transfer coefficient between the two situations with 1% and 20% turbulence (for $V \approx 3.5$m/s) was smaller than expected.

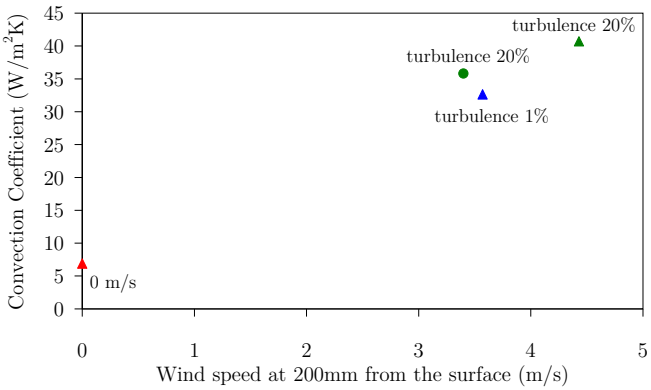

Figure 2.59: Results of the steady state tests: convection coefficients

Transient tests

For the transient tests measurements from the embedded thermocouples were not used. Only the heat flux sensor measurements, as well as the ones from the surface and environmental temperatures, were adopted. Due to the increasing wind speed, the top surface temperature of concrete decreased, even though the heat mat was constantly turned on. Due to this decrease, the heat flux also decreased during each wind speed step. A typical plot of the performed measurements is shown in Figure 2.60. In this particular test, the wind speed inside the wind tunnel was increased every 5 minutes: it can be observed that every time that V was changed there was a significant increase in the heat flux sensor output; yet, during the subsequent 5 minutes the heat flux diminished, in correspondence to the decrease in the surface temperature. As a consequence, the many instantaneous heat convection coefficients that were calculated during each 5 minutes interval were rather constant. This constancy reinforced the confidence on the experimental procedure and results.

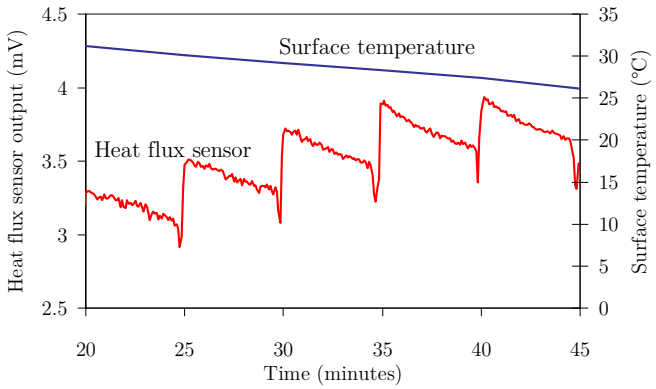

Figure 2.60: Typical output of the measurements in the transient test

As mentioned in the previous section, computation of the convective heat convection coefficient involved the deduction of the long wave radiation contribution to the heat flux

on the surface. The obtained results (and their comparison with the results obtained in the steady state tests) are summarized in Figure 2.61.

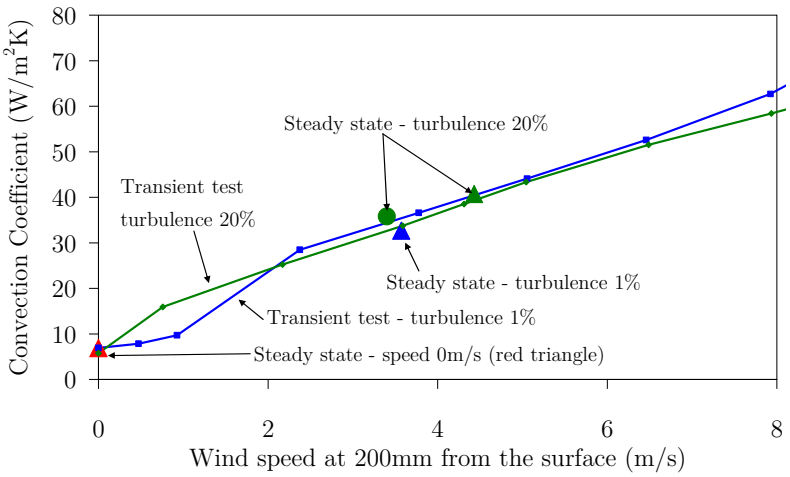

Figure 2.61: Results for both steady state and transient tests: heat convection coefficients

Coherence between the steady state and the transient tests appears to be reasonable. A great similarity between the results of high turbulence and low turbulence was also observed (except for very low wind speeds, where the high turbulence case yielded significantly higher convection coefficients). More research should be done to investigate this effect. Maybe it is related to the turbulence that is naturally caused by the presence of the specimen itself, which makes the basic turbulence of the flow less significant.
One further observation should be made at this point: from comparison of the results obtained in these experiments (Figure 2.61) with predictions from the empirical formulas mentioned in Section 2.5.1, it is noticeable that the increase of the heat convection coefficient for increasing wind speeds was far greater in the performed experiments than what would be expectable from the empirical equations. This fact is not surprising, as validity of the experimentally-based empirical equations is limited to the conditions for which they were established. As most of them were established for horizontal surfaces, where full development of the boundary layer is assumed to occur, they provide lower transfer coefficients than the ones obtained in the present experiments, where there is a strong edge effect (i.e., the point of interest for heat flux measurement is very near the edge where the boundary layer starts to be formed). It is known that near the edges, the heat transfer coefficients are higher than at some distance from the edge where the boundary layer can be said to be fully developed (Incropera *et al.* 1996, Masmoudi *et al.* 1991). The reader should therefore be aware that this kind of phenomenon and others may cause strong deviations between predictions of the heat transfer coefficient based solely on a free stream wind speed (and an hypothetically horizontal surface with a fully developed boundary layer) and the effective heat transfer coefficients that really occur because of the interaction between the free stream and the object in question.
For the case of no wind speed (predominance of natural convection), predictions of the empirical formulas for the heat convection coefficient range from $4.96 Wm^{-2}K^{-1}$ to $6 Wm^{-2}K^{-1}$; the experimental results of this research yielded values between $5.7 Wm^{-2}K^{-1}$ and $6.9 Wm^{-2}K^{-1}$. These results are rather coherent with each other, even though the

results from the performed experiments are a little higher than expectable from empirical predictions. Once again, there might be some differences between the experiments: the size and proportions of the surface from which natural convection happens is known to have some influence on the heat transfer coefficient (Incropera and DeWitt 1996). However, these verified deviations are very small when compared to the ones that could be observed for forced convection. Furthermore, attention must be drawn to the fact that natural convection performs differently for vertical or inclined surfaces (Incropera and DeWitt 1996), and that this research did not focus on such situations.

A very recent research work conducted by Lee *et al.* (2009) has used a wooden wind tunnel (similar to the one mentioned in Section 4.4.3 of this thesis) to study convective heat transfer on concrete during hydration. The study did not involve heat flux sensors, with the heat flux being estimated by embedded thermocouples. The work from Lee *et al.* (2009) revealed slightly lower convection coefficients than in this research, especially if it is beard in mind that the results reported in such paper included the contribution of radiation heat transfer. Nonetheless, the tendencies and overall magnitudes of convection coefficients are similar to those obtained in this research, which is a good indication in regard to the usability of such results.

A final remark on the issue of convective transfer coefficients is made: even though the differences in convection coefficients obtained from different researchers may strike the reader as very large, these results and their use for practical application should be looked at with caution. In fact, the environmental conditions that act on real in-situ concrete structures are usually (and mostly) related to outdoor applications, with great variations in wind and temperature within small distances over the structure. This reasoning shows that there is no point in trying to achieve a unified result for convection coefficients, given the fact that outdoor environments are characterized by great time and space microclimatic variability (Nilsson 1996), which is unfeasible to predict or even to fully characterize. It is considered that the available ranges of convective coefficients are good enough to provide engineers with guidance on probable values to use in numerical modelling, and to establish upper and lower bound scenarios for temperatures (and corresponding stresses) in concrete. In case the applications to be studied pertain to an indoor situation, with a relative constancy in temperature and wind situations (such as in pre-fabrication industry), it is considered advisable to perform preliminary testing on boundary conditions using monitored concrete specimens subject to known heat sources, thus allowing greater accuracy in subsequent numerical predictions.

Chapter 3

Moisture problem

3.1 Introduction

The necessity of knowing how moisture is distributed in concrete structures is justifiable by several reasons. This section intends to review some of those reasons and emphasize those that will be of particular interest for the present research.
Fresh concrete has an initial behaviour of suspended solid, with cement and aggregates in suspension in water. As hydration reaction occurs a solid skeleton (which can bear stresses) starts to be formed, and thus, beyond the thermal volumetric changes, a contraction due to the fact that reaction products occupy less volume than reactants leads to the build up of autogenous shrinkage stresses. These stresses are essentially related to the partial emptying of the pore structure due to consumption of the existing water, thus dropping humidity within the pores. It has been reported (Persson 1997) that this self-desiccation has significance only in concretes with w/c < 0.39.
Yet, another kind of shrinkage is well known: the drying shrinkage, which is a volumetric change driven by water loss from concrete to the environment, through evaporation. Concrete mixes with high w/c ratios have excedentary water that does not react with the cement, and thus remains in the pore structure. In fact the necessary water for cement hydration is only 20-30% of the cement weight. Thus, since early ages concrete is in a hygrothermal imbalance relatively to the surrounding environment. This excess water is therefore bound to be transported out of concrete by diffusion and evaporation.
As it has been stated, both autogenous and drying shrinkage are related to the moisture state within concrete. Neither of these phenomena occur uniformly in structures: chemical reactions are usually stronger in the core of elements, because of higher heat of hydration development, thus promoting higher autogenous shrinkage. Also, the drying front migrates gradually from the surface to the interior of concrete elements, justifying a non-uniform drying shrinkage field as well. For these reasons it can be argued that bulk

shrinkage values indicated in concrete codes (MC90, EC2) for autogenous and drying shrinkage are not strictly accurate in describing what happens at a cross sectional level in a concrete element. For example, supposing a concrete prism, and considering only the effect of drying shrinkage for the sake of simplicity, what happens is that upon onset of drying (from top and bottom surfaces as depicted in Figure 3.1) the near surface concrete tends to shrink to a certain extent; because of compatibility with the other cross section fibres the outer ones will not shrink as much as if they were totally free to contract, and the inner fibres that have no tendency for shrinking will contract to the compatibilized value. As a result, the outer fibres are in tension and the inner ones are in compression. So, it may be stated that each part of the specimen is subject to its own infinitesimal shrinkage (Wittmann 2008), with the macroscopic shrinkage measured in concrete and specified in codes resulting from the compatibilization of the several infinitesimal shrinkages of the layers of concrete, with corresponding self-equilibrated internal stresses (the infinitesimal shrinkage may also be termed as 'potential shrinkage' or 'local free shrinkage' in the sense that it represents the shrinkage that would occur in the material where it not totally or partially hindered).

Knowing these self-equilibrated stresses can be quite useful for assessing the service life conditions of a structure, particularly when it regards to cracking risk, crack width estimation, or even pre-stress losses. To know these stresses, it becomes necessary to compute moisture states within the concrete element. By using one of the available relationships between the moisture state and the potential shrinkage (reviewed in this Chapter), and applying structural analysis techniques, it is possible to achieve the aforementioned goal of internal stress determination.

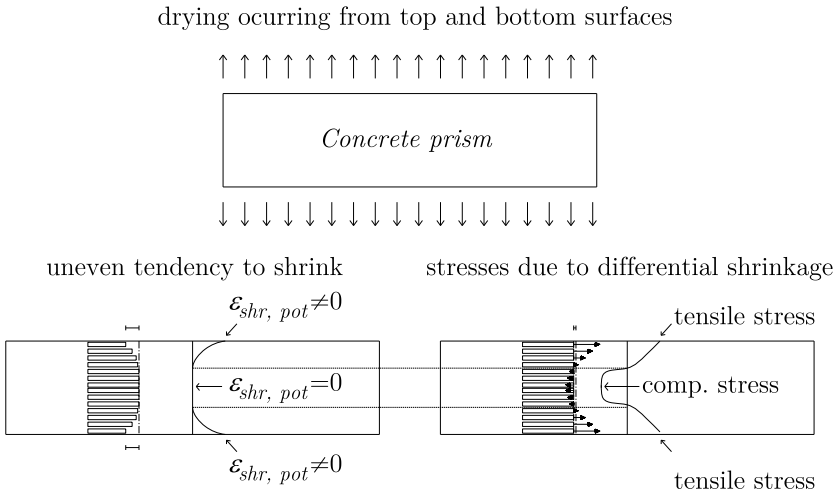

Figure 3.1: Differential drying shrinkage stresses within a cross-section

Research in concrete science has led to the conclusion that cement hydration only occurs normally under saturated conditions, i.e., 100% relative humidity (RH) (Neville 1995, Patel *et al.* 1988). When RH decreases, hydration reactions start to de-accelerate to such an extent that for RH<80% these chemical reactions occur at negligible rates. This is the reason why concrete curing is so important for the assurance of a good structural and durability performance of cover concrete. As soon as curing measures are interrupted, relative humidity in the near surface areas of concrete elements starts to decrease quickly, hindering the chemical reactions, and thus stagnating the development of the pore

structure and mechanical properties of concrete. Also, self-desiccation that occurs in concretes with low w/c can cause internal RH depressions to values as low as 72% (Persson 1997). For these reasons, knowledge of the moisture field, together with existing predictive tools that relate RH to cement hydration hindering (Maekawa *et al.* 1999, Mjörnell 1997), have paramount importance for predicting evolution of the pore structure development as well as relevant mechanical properties of concrete

Many other relevant phenomena can be related to the moisture states in concrete, as highlighted in the remainder paragraphs of this introduction that pertain respectively to evaporative cooling, concrete spalling due to high temperatures and durability performance.

Evaporation of a liquid from a porous solid involves the overcoming of an energy barrier named evaporation enthalpy. This means that the state change from liquid water to gas requires removal of heat from the porous solid from which it is evaporating. This phenomenon is known to occur in concrete right after formwork removal: the concrete surface is usually completely saturated, and a sudden high rate evaporation occurs during the first minutes after exposure. This evaporation causes the surface to have a sudden temperature decrease (which can have an amplitude as high as 8°C) (Azenha *et al.* 2007b, Kovler 1995), and consequently develop tensile stresses (associated to the hindered contraction), which can be the cause for cracking of the concrete surface. Knowledge of these sudden moisture fluxes from concrete to the environment is a fundamental tool for the prediction of the temperature drop and the depth of concrete that is affected, thus allowing the estimation of the corresponding tensile stresses.

The exposure of mature concrete to high temperatures is known to cause strong pressures in the water contained in pore structure, which in turn can cause spalling of the cover concrete, particularly in the case of high strength concrete. Knowledge of the moisture state of concrete is important for the prediction of how fire will affect it.

In what regards to durability performance of concrete, many phenomena are related to the moisture state in the pore structure: chloride ions require a liquid phase to penetrate and diffuse in concrete (Ababneh *et al.* 2003, Martin-Perez 1999); the chemical swellings of alkali silica reactions depend strongly on water content (Multon *et al.* 2004); carbon dioxide gas requires a connected gas phase to penetrate and diffuse in the material, and the presence of a liquid phase is needed for the carbonation chemical reactions themselves (Baroghel-Bouny 2007, Walton *et al.* 1990); upon freezing, water in the capillary pores of concrete expands in volume by approximately 9%, with the risk of deterioration of the pore structure (Walton *et al.* 1990).

All the above mentioned phenomena justify the necessity of modelling moisture fields in concrete. However, the review and proposals presented in this chapter are essentially centred in the effects of shrinkage (particularly the drying component) as well as the hindering of hydration reaction due to surrounding RH.

Regarding the structure of the chapter, it comprises a review on modelling moisture fields in concrete and corresponding parameter estimation. Relevance is given to the relationship between humidity in concrete and its tendency to shrink. The chapter ends with the description of the adopted numerical implementation, together with its validation and application examples (which are to be used in the thermo-hygro-mechanical analysis presented in Chapter 5).

3.2 Moisture movement mechanisms and water retention capacity

Concrete is a composite porous medium, with a large quantity of pores of different sizes and shapes, more or less connected to each other. Consequently, several mechanisms are involved in water transport. In this section a review of these mechanisms is carried out.

In a review about moisture transport mechanisms in concrete, performed by Xi *et al.* (1994a), three distinct mechanisms are identified to operate singularly or simultaneously: molecular diffusion, Knudsen diffusion and surface diffusion. Regarding molecular diffusion, which is believed to occur in macropores (50nm to 10μm in diameter), transport is dependent on the moisture concentration and occurs when the mean free path is relatively short compared to the pore size. At low RH, water molecules are captured by the pore walls and layers are formed that coat the pore walls while other water molecules that are not attracted to the wall manage to travel through the pore. As humidity increases, more layers coat the wall, thus the free space for water transport diminishes. However a contrary effect occurs, once the existing layers reduce the attractive forces exerted by the pore wall and the resistance to water transport diminishes. At even higher moisture content, the adsorbed water forms a meniscus at the necks of the pore, and the moisture transport is made by condensation at one meniscus and evaporation at the other.

Knudsen diffusion occurs in mesopores (25 to 500Å) and micropores (<25 Å) when the mean free path is relatively long compared to the pore size, so the molecules collide frequently with the pore wall (Malek *et al.* 2003). In this range of pores the main force that contraries the flow is the diameter of the pore: the smaller the pore, the higher the resistance.

Surface diffusion is used to explain a type of pore diffusion in which water molecules adsorb on the surface of the pore and hop from one site to another through interactions with the surface. This is a form of transport with negligible effect unless most of the water is adsorbed (case of very low humidity).

From what has been exposed it is understandable that the diffusion of water in concrete is highly dependent on the moisture content.

Defining internal relative humidity of concrete as the relative humidity (H) of the gaseous phase in equilibrium with the interstitial liquid phase in the pore network of the material (Baroghel-Bouny *et al.* 1999), it is possible to plot the relationship between internal H and the water content (in mass) for a given concrete at constant temperature: this plot is known as moisture sorption isotherm and it is qualitatively depicted in Figure 3.2a. It can be seen that the adsorption and desorption curves are different, highlighting the hysteretic behaviour concrete in regard to water retention. This hysteresis is usually explained with the so-called inkbottle effect, and it can be described with recourse to the states (i) to (v) as shown in the plot of Figure 3.2a and the schematic representation of a pore in Figure 3.2b: upon sorption from 0% RH (state labelled as (i)) pores start to become saturated in the order of their diameter (smaller pores saturate first, whereas larger ones only saturate at higher humidities) – state (ii) -, according to Kelvin's law. Water sorption continues until a fully saturated sate is reached (iii), with all pores completely filled with water (H=100%). Upon desorption the tendency becomes opposite:

de-saturation of larger pores occurs first, followed by smaller pores. However, some larger pores may be confined by smaller ones, as the example shown in Figure 3.2b: starting from total saturation of the large pore and the two adjacent smaller pores (iii), internal humidity decreases to a value at which the larger pore should become non-saturated (Kelvin's law). Yet, once it is connected to smaller pores that remain saturated, this larger pore's moisture cannot escape – state (iv) - until the instant when the smaller pores become also unsaturated, with final tendency to reach state (v) through a different path from that which could be observed in the adsorption process. This will cause the pore structure to hold more water for the same RH when in desorption than it does when in adsorption.

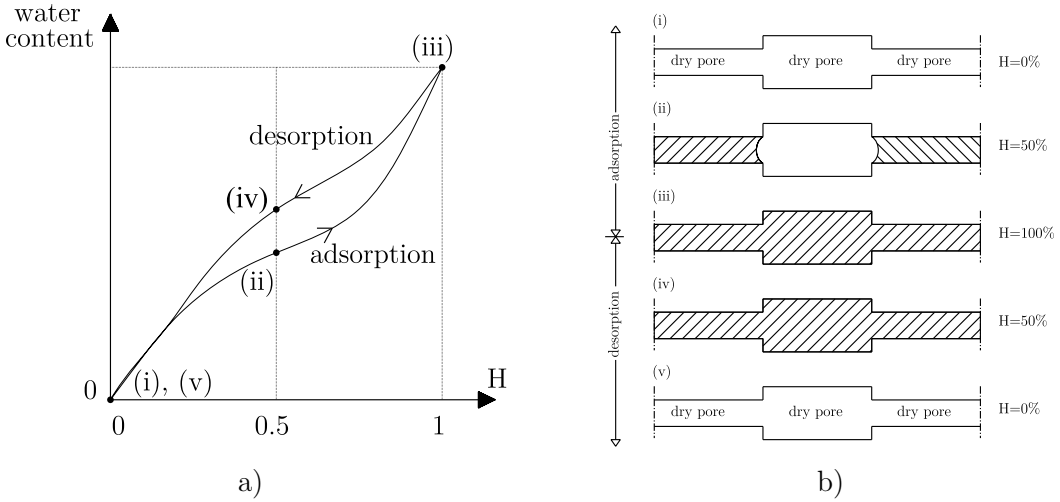

Figure 3.2: a) Typical shape of a moisture sorption isotherm for concrete; b) Schematic representation of the inkbottle effect

It should be stressed however, that concrete in civil engineering structures is rarely (or even never) subjected to continuous cycles of drying from 100% to 0% *H* or *vice versa*. In fact, relative humidity varies throughout the year and intermediate behaviours from those depicted in Figure 3.2a are observed. The resulting intermediate moisture retention curves are termed as scanning curves (Ishida *et al.* 2007).

Another important matter to be discussed is the physical interpretation of the slope changes in the sorption isotherms. Three phases may be identified (Xi *et al.* 1994a), as shown in Figure 3.3: a first phase that corresponds to very low humidities, in which the existing water is not enough to completely coat the pore structure. This coating occurs at the transition to the second phase (P1) that ends at a higher RH level that corresponds to the initial point of capillary condensation (P2), which in turn represents the onset of the third stage.

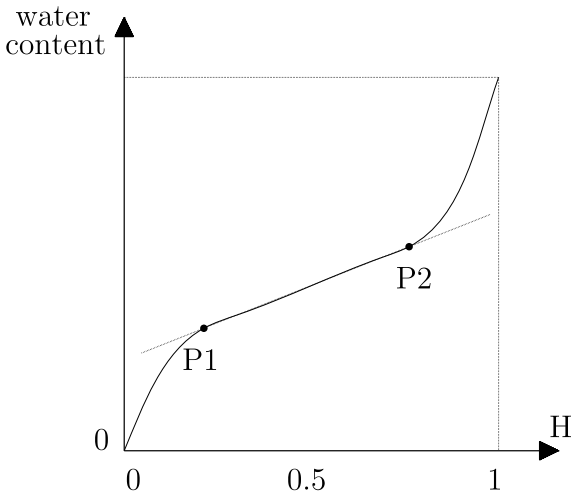

Figure 3.3: Slope changes in moisture sorption isotherms

Many factors affect the shape and maximum water retention capacity of moisture isotherms in concrete: the type of cement (chemical composition), the type of aggregates (and their interface with the matrix), the material porosity (which is age dependent), the w/c ratio, added ingredients and so on. Because of the complexity of the phenomena involved, there is no truly general model for concrete sorption isotherms. It can be measured with experiments, or merely estimated with recourse to empirical and semi-empirical models (Xi 1994a, Xi 1994b, Xi *et al.* 1994a) as will be presented in a following section.

At this time it is also convenient to make a differentiation on water classification in concrete. So far, one has been dealing with water that has the possibility of moving within the pore structure of concrete, regardless of the pore diameter and the mechanism of movement or attractive forces exerted. This water is usually defined as evaporable water, once its bound to the material is of weak to moderate physical nature. Evaporable water may be present as interlayer water between the layers of reacted material, as adsorbed water at the pore surfaces and as capillary condensed water in the pores. The rest of the water in concrete, which is either chemically combined or with strong physical bonds to concrete, is called non evaporable water (Neville 1995). Alternatively, the total non evaporable water in a given concrete corresponds to the residual water that remains after a complete desorption at RH=0% (Granger 1996). It is understandable that the moisture movement mechanisms are related to the evaporable water. Nevertheless it should be beard in mind that during cement hydration important transitions occur due to the chemical binding of evaporable water, which is thus transformed into non evaporable water. Mass balance equations for moisture content in concrete since early ages should therefore account for this phenomenon.

3.3 Formulation of moisture fields in concrete

3.3.1 Governing equation

Modelling of the moisture field in concrete can be made at several scales and levels of detail. Some authors who envisage the study of shrinkage cracking around aggregates have to use models with explicit consideration of the latter (Lopez *et al.* 2007, Roelfstra 1989, Roelfstra *et al.* 1985). Within this review, only macroscopic level approaches are considered in which the spatially averaged transport behaviours within concrete, which is constituted by various phases (solid, liquid and gas), can be characterized over a specified local volume (REV – Representative Elementary Volume – as defined in Section 2.2.2 of this thesis). With this averaging approach for the heterogeneous domain, all phases (gas and liquid) that occupy the porous network are considered to be present at the same time at every point of the REV (overlapping continua).

Most authors that deal with moisture transport in un-saturated concrete assume it as a non-deformable porous medium in isothermal conditions, and use the first Fick law as a basis for the mass balance equation. Also, it is considered that only the evaporable water is subject to actual transport, and it is used as a state variable, comprising both the liquid and the water vapour contents (Granger 1996). Mathematical diffusion theory in isotropic materials is based on the hypothesis that the rate of transfer of the diffusing substance through a unit area is proportional to the concentration gradient measured normal to the section, i.e.,

$$J = -D \quad grad(W_e) \tag{3.1}$$

where J is the diffusion flux [$kgm^{-2}s^{-1}$], D is the diffusion coefficient [m^2s^{-1}] and W_e is the evaporable water concentration [kgm^{-3}].

Let us consider a paralepipedic REV with dimensions $2dx$, $2dy$, $2dz$ (see Figure 3.4), with its sides parallel to the coordinate axes.

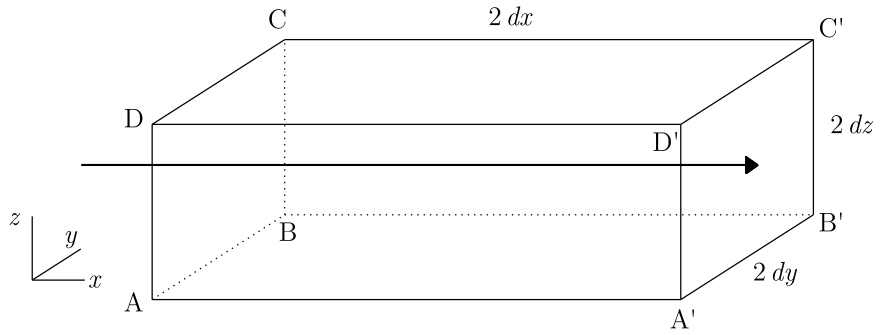

Figure 3.4: Water movement within the REV

The centre of the REV is $P(x,y,z)$, where the concentration of evaporable water is W_e. The water flux along axis X and through face ABCD can be expressed as

$$Q_1 = 4\ dy\ dz \left(J_x - \frac{\partial J_x}{\partial x} dx \right) \tag{3.2}$$

Based on a similar reasoning for the flux through face A'B'C'D', one gets

$$Q_2 = 4\ dy\ dz \left(J_x + \frac{\partial J_x}{\partial x} dx \right) \tag{3.3}$$

By using equations (3.2) and (3.3), contribution of these two faces on the increase of the diffusing substance in the REV can be obtained as:

$$Q_x = -8\ dx\ dy\ dz \left(\frac{\partial J_x}{\partial x} \right) \tag{3.4}$$

Contributions of the other four faces of the REV could be obtained analogously:

$$Q_y = -8\ dx\ dy\ dz \left(\frac{\partial J_y}{\partial y} \right) \tag{3.5}$$

$$Q_z = -8\ dx\ dy\ dz \left(\frac{\partial J_z}{\partial z} \right) \tag{3.6}$$

It must be kept in mind that concrete is a reacting porous medium, whose total water concentration W corresponds to the sum of W_e and the non evaporable water concentration W_n. So, the global rate of increase of water in the REV can also be expressed as a function of the variation in the total water concentration along time:

$$Q = 8\ dx\ dy\ dz \left(\frac{\partial \left(W_e + W_n \right)}{\partial t} \right) \tag{3.7}$$

So, the mass balance equation would become:

$$\dot{W}_e + \dot{W}_n + \frac{\partial J_x}{\partial x} + \frac{\partial J_y}{\partial y} + \frac{\partial J_z}{\partial z} = 0 \tag{3.8}$$

By using (3.1), (3.8) may be re-written as:

$$\dot{W}_e = div\left(D\ grad\left(W_e \right) \right) - \dot{W}_n \tag{3.9}$$

The last term of this equation reflects the consumption of water due to the chemical reactions, which reduces the available evaporable water in the pore structure. This term is obviously important at early ages, but its importance becomes negligible after some days as rates of hydration diminish.

Alternatively to the aforementioned formulation, based on water concentration, some authors defend formulations based on internal relative humidity H for the driving potential. According to this line of thought equation (3.1) may be rewritten as follows, provided a corresponding diffusion coefficient D_H is used:

$$J = -D_H \quad grad(H) \tag{3.10}$$

Equation (3.8) remains valid for this case and it may be rewritten as

$$\frac{\partial W}{\partial t} + \frac{\partial J_x}{\partial x} + \frac{\partial J_y}{\partial y} + \frac{\partial J_z}{\partial z} = 0 \tag{3.11}$$

where, the first term can be expressed as

$$\dot{W} = \frac{\partial W}{\partial H} \dot{H} \tag{3.12}$$

Nonetheless, the last factor of equation (3.12) - $\dot{H}$ - has two parts (considering isothermal conditions): the H changes due to drying $\left(\partial H/\partial t\right)_{drying}$, and the H changes due to internal water consumption in the chemical hydration reactions $\partial H_S/\partial t$:

$$\dot{H} = \left(\frac{\partial H}{\partial t}\right)_{drying} + \frac{\partial H_S}{\partial t} \tag{3.13}$$

So, combination of equations (3.10), (3.11), (3.12)and (3.13) leads to the final governing equation for the moisture field in concrete based on relative humidity:

$$\frac{\partial H}{\partial t} = \left(\frac{\partial W}{\partial H}\right)^{-1} div\left(D_H \ grad\left(H\right)\right) + \frac{\partial H_S}{\partial t} \tag{3.14}$$

Besides the driving potential itself, equations (3.9) and (3.14) have another important difference: when the driving potential is the relative humidity, a factor $\left(\partial W/\partial H\right)^{-1}$ appears at the right-hand side of equation (3.14). This factor is the reciprocal of the slope of the moisture isotherm $W=f(H)$ reproduced in Figure 3.2, that slope being also known as moisture capacity.

Some authors advocate that moisture capacity of cementitious materials at usual environmental relative humidity (H>50%) is fairly constant (Roncero 2000), thus motivating a further simplification on equation (3.14) by lumping the moisture capacity and the diffusivity D_H into a single coefficient D_{H^*}:

$$\dot{H} = div\left(D_{H^*} \ grad\left(H\right)\right) + \dot{H}_S \tag{3.15}$$

If the moisture state analysis is performed after most hydration reactions have occurred, or if influence of self-desiccation in the pore humidity is negligible (which is the case of high w/c ratio mixes (Baroghel-Bouny *et al.* 1999)), the last term in (3.15) can be

disregarded, thus yielding a simplified version of the moisture field equation, which corresponds to the approach that is put forward in Model Code 1990 (CEB-FIP 1993):

$$\frac{\partial H}{\partial t} = div\left(D_{H^*}\ grad\left(H\right)\right) \tag{3.16}$$

Authors that use H as the driving potential for modelling moisture fields in concrete, usually defend their option with the following arguments:

- For usual w/c ratios the drop in H due to chemical hydration of cement is relatively small (less than 3%), and thus it can be neglected even if hydration reactions have not ceased. This is not the case when W is used as a potential once W_n and W_e vary significantly during hydration.
- Boundary conditions are of easier expression in terms of H (Roncero 2000, Xi *et al.* 1994a).
- Generalization of the governing equation (derived for isothermal conditions) to situations under variable temperature is possible by using H as driving potential, in opposition to what occurs when W is used (Xi *et al.* 1994a).
- The use of H as driving potential is considered to be more practical when the solution of the drying problem is intended to serve as the base for rational analysis of creep and shrinkage effects (Bazant *et al.* 1971).

In an antagonist position, those who use the water concentration as the driving potential state that (Granger 1996, Granger *et al.* 1996):

- H cannot be considered a state variable, whereas W can.
- Experimental measurement of W is quite direct by weight measurements, whereas quantification of H is quite difficult.
- Limitation related to the non-negligible value of $\partial W_n/\partial t$ in equation (3.9) is overcome by performing calculations only after hydration has ceased.

It can be understood that the choice of the driving potential is clearly related to the purposes and means available to the analyst. For the applications of this chapter the approach based on relative humidity is considered preferable, as it provides easier modelling of concrete since early ages because of the small importance of $\partial H_S/\partial t$.

3.3.2 Boundary conditions

Most researchers follow the same approach for the boundary conditions in moisture field analysis in concrete science, irrespective to the selected driving potential. These conditions have a formal presentation quite similar to that adopted for the thermal field modelling (see equation – (2.39)), with its formulation in terms of pore relative humidity being:

$$q_m = h_m \cdot \left(H_{surf} - H_{env}\right) \tag{3.17}$$

where q_m is the moisture flux flowing through the boundary, h_{moist} is the moisture emissivity coefficient, and H_{surf} and H_{env} are respectively the values of H on the surface and on the surrounding environment.

A more general formulation for moisture boundary conditions, with the advantage of better handling non-isothermal conditions will be presented in the next chapter. Such formulation is not used for the present chapter as it would demand for the necessity of formulating the whole model by using pore water pressure as the driving potential. As applications envisaged for the model within this chapter concern isothermal water losses, the use of the simplified approach of equation (3.17) is considered enough.

3.3.3 Concrete weight loss computation

Regardless of the driving potential selected for the moisture field probem, one of the most easy and direct validation experiments that may be performed in concrete specimens is the weight loss evolution upon exposure to the environmental conditions.
When the driving potential is water concentration, a mere integration of the water content along the specimen allows for the direct evaluation of its global water loss, thus providing the necessary values for comparison between the numerically predicted and the experimentally observed weight losses. When the driving potential is H, the recourse to the sorption isotherm (which relates the local humidity to the moisture content) is necessary. Therefore, for a given instant t, upon knowledge of the local H in a given element (finite element method), the water content is computed through the moisture isotherm, and total weight loss corresponds to the sum of the weight losses of the FE of volume Ω_e (Roncero 2000).
Bazant and Najjar (1971) recommended another strategy that supposes that the slope of the desorption isotherm is constant. However, such approach has the downside of requiring the user to input the predicted total weight loss upon hygral equilibrium with the environment, which is often unknown or of difficult estimation.

3.4 Sorption-desorption isotherms

3.4.1 Experimental determination

The experimental determination of sorption-desorption isotherms for a given material involves weighting it at equilibrium with the surrounding environment (with a determined temperature and relative humidity). After having gone through weighting of the specimen for a wide range of environmental H (in both desorption and sorption processes), it is possible to plot the relationship water content *versus* relative humidity for the material. It is therefore understandable that these experiments require significant amounts of time, once it is necessary to assure equilibrium conditions with the environment, which in the case of diffusion is a quite lengthy process. This is especially the case for concrete specimens, whose large dimensions dictate that diffusion equilibrium for each H takes much longer than for small sized cement paste specimens. For this reason much data is available for cement paste and mortar, whereas very few exists for concrete.
Baroghel-Bouny *et al.* (1999) have specifically focused on quantification of moisture isotherms for both cement paste and concrete. They performed experiments by placing specimens (~1 year old) into sealed cells under controlled H, the latter varying by steps, with a constant temperature of 23°C. Specimens were discs with ~3mm thickness and

90mm diameter (in the case of concrete, with crushed aggregates). After placement into the sealed cells, specimens were then subjected to step-by-step desorption and sorption processes. Within each RH step, the weight equilibrium of the specimen took at least a few months, and even up to more than one year, confirming the unfeasibility of fast sorption/desorption of concrete characterization. All tests start with a desorption process in correspondence to what occurs in real structures that begin at high saturation states. The experimental results obtained for concretes are depicted in Figure 3.5 ("BO" – ordinary concrete with w/c=0.48; "BH" – high performance concrete with silica fume and w/c=0.26): it can be observed that the isotherms of high performance concrete exhibit lower water contents at high *H*. Further research on the same topic, but including more mixes, can be found in Baroghel-Bouny (2007).

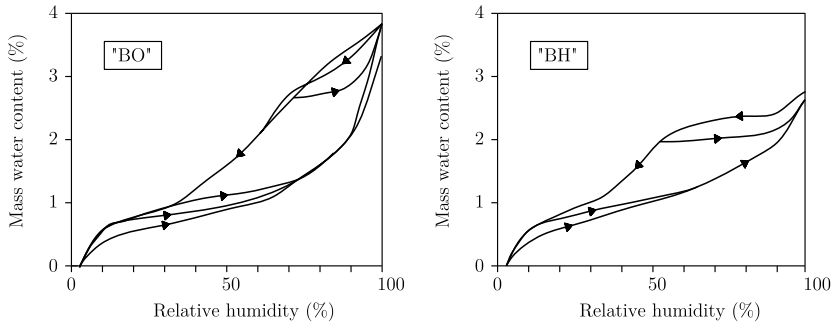

Figure 3.5: Sorption-desorption isotherms of "BO" and "BH" concretes – adapted from Baroghel-Bouny *et al.* (1999).

An alternative way of determining the adsorption isotherm, termed dynamic method, has been proposed by Tada and Watanabe (2005): it comprises the use of crushed specimens of concrete, mortar or cement paste (passing the 15mm sieve, but being fully retained by the 10mm one), which is in turn desiccated at 0% *H*, and then placed at a known stable RH for a given period (8 to 12 hours). From the resulting weight variation, it is possible to adjust theoretical solutions for the diffusion equation and then obtaining the equilibrium mass for the studied *H*. The method is very fast (once each *H* step characterization takes less than 12h, in opposition the several months in the previous conventional method) and is claimed to allow obtaining consistent results.

A further variant to this dynamic method is proposed by Anderberg and Wadso (2008), in which smaller specimens, with a better defined geometry 5.5mm diameter and 5mm long are used. The maximum aggregate size tolerated in this experiment is ~1mm, making it unsuitable for concrete specimens. Results obtained with this method are claimed to be reasonably coherent with traditional ones, and a complete sorption/desorption isotherm may be obtained in about 10 days.

Another important research that is worth mentioning is the one conducted by Mjornell (1997), where one of the main focus was to observe the changes in the moisture isotherms during early ages of concrete. An approach based the traditional stepwise weight measurement was used, but with slight adaptations: the saturated specimen (1 to 2mm thick) was placed in a controlled RH environment for 1 week. After that time, even though equilibrium with the environment had not been reached, the specimen would be

analyzed in terms of water content, and its internal RH would be measured. This allowed obtaining age dependent moisture isotherms for cement paste.

3.4.2 Numerical approaches

As stated previously, the existence of a general sorption isotherm formulation for concrete is far from being achieved, given the great amount of variables involved. However, many authors have put forward several approaches for the prediction of sorption isotherms for cement paste, mortar and concrete.

In an early publication by Bazant and Najjar (1971), and focusing particularly on hardened concrete, it was postulated that for dense cement pastes and concretes, moisture capacity is usually almost constant from H=0.95 down to about H=0.2. This simplification prevailed for some years, and in fact, it is recommended by Model Code 1990 (CEB-FIP 1993). In terms of the governing equation for moisture diffusion, this also was the approach adopted for the present thesis.

In Xi, Bazant and Jennings (1994a) a mathematical formulation for prediction of moisture sorption isotherms in cement pastes was put forward. This was a rather intricate model, with a great deal of input parameters, which were in turn derived and validated with basis on many existing experiments. A brief outline of the model is given here. The mathematical formulation of W=f(H) is

$$W = \frac{V_m \, C \, k \, H}{\left(1 - k \, H\right)\left[1 + \left(C - 1\right) k \, H\right]} \tag{3.18}$$

where

- V_m is the mass adsorbate required to cover the adsorbent with a single molecular layer. This parameter is obtained using a set of empirical equations that express the dependency of V_m on age, w/c ratio and cement type.
- C is a parameter that expresses the dependency of the adsorption isotherm on temperature.
- k is a constant.

This approach to the sorption isotherm failed to be applicable to concrete, and for such purpose Xi (1994a, 1994b) proposed a two phase composite model, with the cement as a matrix and the aggregate as an inclusion. However, probably due to its complexity and number of involved parameters, few further research works were found to actually use the model (namely Suwito *et al.* (2006)).

A quite simplified approach for concrete put forward by Bazant and Baweja (2000) consists of expressing the desorption moisture isotherm $W(H)$ as a function of the final water loss that would occur at environmental relative humidity 0% - $W(0)$ (similar to water lost by oven drying at a 105°C temperature):

$$\Delta W\left(H\right) = 0.75\left[1 - \left(\frac{H}{0.98}\right)^3\right]\Delta W\left(0\right) \tag{3.19}$$

Based on gravimetric technique measurements for several concrete mixes, Akita *et al.* (1996) proposed a polynomial with parameters a_1 to a_{10}, which allowed relating the relative water content R (ranging from R=0 in correspondence to totally dried concrete to R=1 for saturated conditions) with H as a function of the w/c ratio:

$$R = a_1 + a_2\,H + a_3\,w/c + a_4\,H^2 + a_5\,H\,w/c + a_6\left(w/c\right)^2 + a_7\,H^3 + a_8\,H^2\,w/c + a_9\,H\left(w/c\right)^2 + a_{10}\left(w/c\right)^3 \tag{3.20}$$

Finally, it is worth mentioning the work of Mjornell (1997), which devises a mathematical formulation for isotherms that accounts for early ages of exposure (while cement hydration has not ceased).

Within the scope of this thesis, no formulation for moisture isotherm was used, as its slope was considered constant and lumped into the diffusion coefficient according to the work of Bazant and Najjar (1972) mentioned in the beginning of this review and already expressed in equation (3.16).

3.5 Diffusion coefficient

3.5.1 Experimental determination

One of the most widely spread techniques to measure the moisture diffusion coefficient D_H is the "cup method". The experiment is conducted at constant temperature, and starts with an initial uniform moisture content of the cementitious material, the latter being placed as a cover of a cup containing a saturated salt-water solution. This solution keeps the relative humidity of the air inside the cup at a constant level (called cup climate). The covered cup is placed inside a climate chamber, where the air has a higher or lower H (called ambient climate) than inside the cup. During the experiment regular weighting of the cup is performed: the weight variation per unit time provides a measure of the moisture flux. At an initial stage a moisture gradient is built up in the specimen, before the process becomes steady-state and the moisture flux turns constant. Once a steady state is reached and both the flux J and the gradient of moisture between inside and outside the cup are known, the moisture diffusion coefficient can be obtained.

Perrin *et al.* (1998) conducted a set of distinct experiments regarding the moisture diffusivity of materials by using: (*i*) a similar method to the cup test by allowing steady state conditions to occur and extracting the correspondent coefficient (for a given H); (*ii*) a method based on using the results of equilibrium states obtained during the measuring of moisture isotherms; and finally (*iii*) a method based of computing the diffusion coefficients with basis on transient experiments of moisture movements in cementitious materials. They have shown that each of these methods induces a distinct hydric solicitation to the material, thus yielding dissimilar results.

Measuring diffusivity with basis on results collected during the steps involved in a sorption isotherm experiment has been carried out by Anderberg and Wadso (2008), with very reasonable coherence in regard to results obtained with the cup method.

With the special purpose of measuring diffusivity of concrete at early ages (1-7 days), Mjornell (1997) used a transient method by measuring weight losses from originally saturated specimens, in an arrangement similar to the cup test. From the information of the weight loss *versus* time curve, the diffusion coefficient was extracted with basis on analytical solutions for the diffusion equation.

3.5.2 Numerical approaches

The most widespread formulation for moisture diffusivity in concrete, using H as the driving potential, was proposed by Bazant and Najjar (1971), and it was included in Model Code 1990 (CEB-FIP 1993). The moisture diffusivity coefficient is expressed in the following manner:

$$D_H = D_1 \left[\alpha_H + \frac{1-\alpha_H}{1+\left[(1-H)/(1-H_C)\right]^n} \right] \qquad \text{with} \qquad \alpha_H = \frac{D_0}{D_1} \tag{3.21}$$

where D_1 and D_0 are, respectively, the values of D_H for $H = 1$ and $H = 0$, H_C is the relative humidity for which $D_H = 0.5 \times D_1$, and n is a material property. This is the formulation adopted for the calculations conducted within the present thesis.
In a later publication, Xi *et al.* (1994b) proposed a distinct formulation for the moisture diffusivity

$$D_H = \alpha_H + \beta_H \left[1 - 2^{-10\,\gamma_H (H-1)} \right] \tag{3.22}$$

where α_H, β_H and γ_H are coefficients to be calibrated upon test data. In that same reference, several equations are proposed for these three parameters as functions of w/c.
An approach based on capillary porosity of concrete P_{cap} is put forward by Mjornell (1997):

$$\begin{aligned} D_H(H) &= D^{60\%} + \left(D^{100\%} - D^{60\%}\right) \left(\frac{H-0.6}{0.4} \right)^k \\ D^{60\%} &= a + b\,P_{cap} \\ D^{100\%} &= c + d\,P_{cap}^2 \\ P_{cap} &= \frac{(w/c) - 0.39\,\alpha_C}{(w/c) + 0.32} \end{aligned} \tag{3.23}$$

where a, b, c, d and k are fitting parameters, and α_C is the degree of hydration.
The issue of the relationship between the diffusivity of cement paste and that of concrete was raised by Suwito *et al.* (2006). A model based on the approach for composite materials developed by Christensen (1979) was devised, accounting for the presence of aggregates

$$D_H = D_{Hcp}\left(1 + \frac{g_i}{\left[1 - g_i\right]/3 + 1/\left[\left(D_{Hagg}/D_{Hcp}\right) - 1\right]}\right) \tag{3.24}$$

where D_{Hcp} is the cement paste diffusivity, D_{Hagg} is the aggregates diffusivity and g_i is the aggregate volume fraction. However, it is stated by Suwito *et al.* (2006) that the D_{Hagg} term in concrete is very small, and can therefore be neglected.

Dependence of the diffusion coefficient in regard to the moisture potential has also been made with recourse to exponential functions by Mensi *et al.* (1988) (using W as the driving potential), and Martinola *et al.* (1998) and Sadouki *et al.* (1997) (using H as the driving potential). The mathematical formulation of the latter approach follows:

$$D_H(H) = a\, e^{b\,H} \tag{3.25}$$

where a and b are model parameters.

3.6 Measurement of moisture profiles in concrete

Modelling approaches of moisture content or relative humidity fields in cement based materials has been discussed in Section 3.3, and the relevant material characteristics (moisture isotherms and diffusivity) have been discussed in Sections 3.4 and 3.5. Validation of results obtained with the mentioned models has to be made with recourse to experimental techniques, to ascertain how moisture is distributed within the material.

One of the most straightforward laboratory approaches is the one used by Selih *et al.* (1996), who performed 1D moisture loss experiments in concrete cylinders (with the curved surface sealed), and checked moisture content profiles by cutting the specimens in parts and measuring their weight before and after oven drying, in order to obtain the evaporable water content.

An alternative non-destructive approach that also uses weighting was proposed by Sakata (1983), which consisted in casting several specimens enduring a 1D moisture loss from a single surface. Presuming that the distribution of moisture at a distance x from the drying surface is the same independently of the specimen height, the moisture content at a given time and depth could be mathematically computed with basis on the weight losses specimens with distinct heights.

The two methods just mentioned are suitable for water content measurement. However, if the adopted potential is H, gravimetric techniques (i.e., those based on weight measurements) are not suitable. In order to measure H within concrete, the most widespread technique is the relative humidity probe in a borehole: the method basically consists of drilling (or embedding) a sealing tube inside concrete with an opening at the desired depth. A humidity probe is placed in the vicinity of the open extremity, the tube is sealed, and the measurement may be carried out as soon as the air in the tube becomes in equilibrium with the pore H (this may take 1 day to 1 week). The use of humidity probes for profiling moisture has been widely used with reasonable results in concrete

science, and even in pavement construction (Baroghel-Bouny *et al.* 1999, Grasley *et al.* 2006, Jiang *et al.* 2006, Kim *et al.* 1998, Persson 1997, West *et al.* 2005, Ye *et al.* 2007).
Other methodologies have been used to a lesser extent: gammadensitometry (Mensi *et al.* 1988, Multon and Toutlemonde 2004); single point magnetic resonance (Cano-Barrita *et al.* 2004); ground penetrating radar (Klysz *et al.* 2007); neutron scattering (Parrott 1990), and others.
Recently, techniques based on Micro-Electro-Mechanical Systems (MEMS) sensors have arisen, with promising capacities in the measurement of internal H of concrete (Norris *et al.* 2008).

3.7 Relationship between humidity or moisture content and potential shrinkage

3.7.1 Shrinkage mechanisms

Shrinkage is the decrease in a linear dimension of a test specimen (mortar or concrete) caused by factors other than externally applied forces and temperature changes (ASTM 2006). Even though it is widely agreed that shrinkage is caused by water related mechanisms, several theories have been put forward to explain this phenomenon. Three main mechanisms are proposed in the literature that concerns this matter (Asamoto 2007, Baroghel-Bouny *et al.* 1999, Charron 2003, Grasley 2006, Han *et al.* 1995, Hansen 1987b, Hua *et al.* 1995, Neville 1995, Toma 1999, Wittmann 1973):

- **Capillary stress in capillary pores**. Capillarity is the ability of a substance to draw another substance (namely a liquid) into it, and it occurs when the adhesive intermolecular forces between the liquid and the substance (in this case, the pore walls) are stronger than the cohesive intermolecular forces inside the liquid. The effect causes a concave meniscus to form in capillary pores as depicted in Figure 3.6. As the cementitous material dries (from saturation), menisci are formed in the capillary pores, and their curvature radiuses progressively diminish in order to maintain equilibrium between gas and liquid. The pressure difference that occurs between liquid and gas at the menisci is intensified as drying advances. This pressure acts on the solid skeleton, promoting shrinkage. The effects of capillary pressure may be quantified based on the Laplace and Kelvin laws. The Laplace law describes the capillary pressure difference sustained across the interface between two static fluids (in the present case liquid water and water vapour) as follows

$$p_v - p_w = \frac{2\gamma}{r}\cos(\theta) \tag{3.26}$$

  where p_v is the pressure of water vapour, p_w is the pressure in water, γ is the surface tension of the water/water vapour interface, r is the radius of the pore and θ is the moistening angle (see Figure 3.6).
  The Kelvin Law relates the pressure difference between vapour and liquid with the relative humidity H:

$$p_v - p_w = \frac{R\,T}{M\,v}\ln(H) \tag{3.27}$$

where R is the ideal gas constant, M is the molar mass of water, v is the specific volume of water and T is temperature.

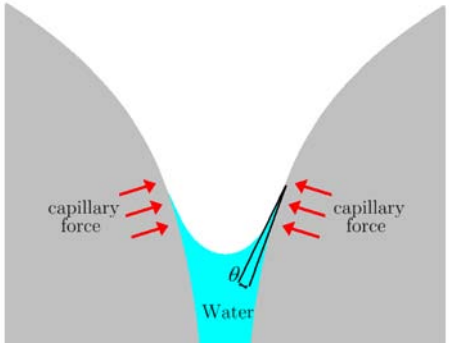

Figure 3.6: Schematic representation of the capillary stress mechanism

- **Disjoining pressure**. Consider two solid surfaces very near each other (see Figure 3.7): as water is progressively adsorbed in layers between these two surfaces (caused by an increase in pore H), a state is reached when no further adsorption is possible, since the two growing adsorbed layers join. If H increases further the adsorption of water tends to separate the two solid surfaces, so as to increase the thickness of the adsorbed layer, causing the so-called disjoining pressure. Therefore, an increase in H causes an increase in the disjoining pressure, which in turn generates expansion of the overall solid. Conversely, a decrease in H diminishes the disjoining pressure, and thus it induces shrinkage. According to Hua *et al.* (1995) disjoining pressure does not have relevant changes at H higher than 80%.

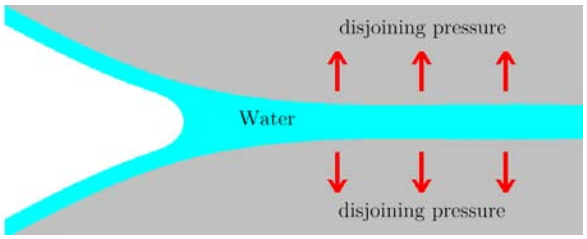

Figure 3.7: Schematic representation of the mechanism of disjoining pressure

- **Surface free energy**. The cohesive forces between liquid molecules are responsible for the phenomenon known as surface tension. The molecules at the surface do not have other similar molecules on all boundaries, and consequently they cohere more strongly to those directly associated with them on the surface: this is the reason why liquids adjust themselves naturally in a fashion that minimizes their exposed area. When water is adsorbed to the cementitious material, surface tension of the solid tends to lower progressively, resulting in an expansion. On the other hand, upon removal of water the surface tension forces increase, and the porous solid contracts. However, it has been postulated (Lura 2000) that the changes in surface tension of solids due to adsorption of water

molecules are of significance for the first three adsorbed layers only, causing influence of this phenomenon to be solely relevant for very low humidity states of the porous material (that is, H<50%).

It is commonly agreed that the shrinkage mechanism as a whole may include the three above mentioned contributions to some extent (Hansen 1987b, Wittmann 2008).

3.7.2 Shrinkage *versus* internal H: experiments

The example of a unrestrained concrete specimen discussed in Section 3.1 allowed demonstrating that upon beginning of drying shrinkage tensile stresses are induced in the external surfaces, whereas the inner core becomes compressed. The actual shrinkage of the specimen does not correspond to the free shrinkage of the concrete surface, nor to the zero shrinkage of the core at the beginning of the drying stage. Instead, a compatibilized shrinkage occurs with an intermediate value (Benboudjema *et al.* 2005a). So, it is worth mentioning that this kind of experiment is usually wrongly termed as a "free shrinkage test"; rather, it should be called shrinkage experiment on a specimen without external restraint.

For the numerical simulation of shrinkage stresses in concrete it is important to know how actual stress-free shrinkage, i.e., without any mechanical hindering, occurs in the material. The experimental determination of this shrinkage may only be performed in very thin cementitious specimens, so that the water potential within the material is uniform during the drying process (otherwise, moisture gradients would occur, and therefore stresses would build up). It has been reported (Bissonnette *et al.* 1999) that paste specimens with thickness in the range of 1 to 3mm can be considered to fully characterize free shrinkage without internal moisture gradients. This kind of experiment has been performed by Baroghel *et al.* (1999) on 3mm thick concrete disks (with crushed aggregates), starting at an H=90.4% on the specimen (1 year old), and progressively decreasing its relative humidity while recording shrinkage (in a set of several steps of H environments until equilibrium between the specimen and the environment is reached). The resulting plot of shrinkage strain *versus* H is depicted in Figure 3.8, where "BO" stands for ordinary concrete and "BH" stands for high performance concrete. For the two concretes it can be observed that there seems to exist an almost linear relationship between H and the free shrinkage strains from saturation down to H=50%, and below such value of H, shrinkage strains seem to stabilize (or at least be strongly decreased). Linear relationships between relative humidity and free shrinkage strains have also been reported by Baroghel-Bouny (1997) for self-desiccation, indicating that similar mechanisms to those of drying shrinkage also drive the autogenous shrinkage (with the difference residing in the fashion water is removed from the pore structure: evaporation to the environment *versus* autogenous consumption by hydration reactions, also known as internal drying). This similitude in origin mechanisms has been acknowledged also by Hua (1992, 1995), as well as by Song *et al.* (2001) and Oh and Choi (2006), whose numerical models devise a single equation for free shrinkage *versus* internal H, regardless of the shrinkage origin (drying or autogenous).

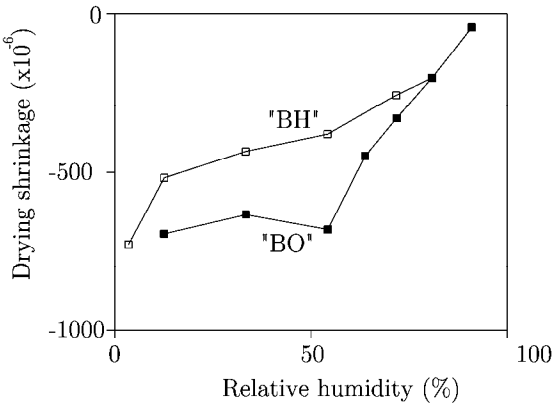

Figure 3.8: 1D free drying shrinkage on hardened concrete (Baroghel-Bouny *et al.* 1999)

Hansen and Almudaiheem (1987) performed experimental research on cement pastes and mortars, studying the quotient between actual shrinkage at a given H and ultimate shrinkage, which may also be referred to as relative shrinkage (K_H). They proposed bi-linear equation for the relationship between K_H and H (see equation (3.28)), confirming the previous finding of almost linear relationships between relative shrinkage and relative humidity for H>50%.

$$\begin{aligned} K_H &= 1.314 - 0.0083\,H \qquad for \;\; 11 \le H \le 50 \\ K_H &= 1.80 - 0.018\,H \qquad for \;\; 50 < H \le 100 \end{aligned} \tag{3.28}$$

Similar relationships to the one depicted in Figure 3.8 and expressed in equation (3.28) were reported by Gardner (2000), being shown in Figure 3.9. There is an interesting fact to pinpoint about this figure: rather than corresponding to free shrinkage measured in thin paste specimens, it reports the observations and equations appointed by many researchers that correspond to the ultimate shrinkage of concrete, and its relationship to the environmental relative humidity (note that the vertical axis of the figure reads as "relative shrinkage", as all shrinkage values of each author are divided by those obtained for H=0, motivating relative shrinkage of 1 for H=0, and relative shrinkage of 0 for H=100%). At this point, the moisture state in the solid can be considered homogenously distributed, leading to the absence of internal relative restraints (except for those provided by aggregates), which roughly corresponds to the conditions that are aimed in the thin paste specimens. This allows an important conclusion: regardless of a specimen's size, the ultimate relative shrinkage obtained is the same. This conclusion pertains to relative shrinkage in regard to the potential value that would occur upon drying at H=0%, rather than absolute values of shrinkage which vary between different concretes according to their type of cement, relative volume of paste/aggregates, elasticity modulus of paste and aggregates, etc. It is noteworthy to mention that the inexistence of size effects in relative shrinkage as a function of H has been previously reported by Hansen and Almudaiheem (1987), and Bazant and Panula (1982).

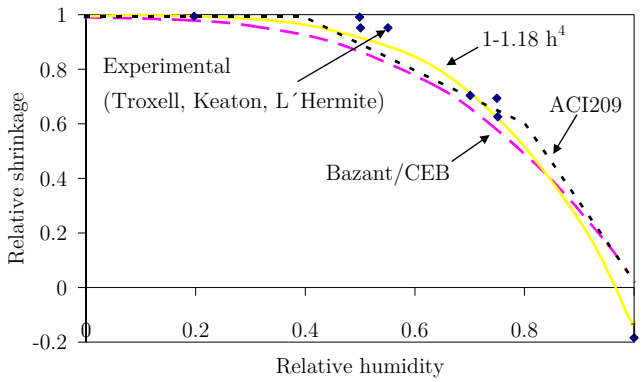

Figure 3.9: Relative shrinkage *versus* internal H (Gardner 2000)

There is a reasonable similarity between Figure 3.9 and the findings of Baroghel-Bouny *et al.* (1999): below H=50% shrinkage becomes negligible in concrete; also, in the range 50%<H<100%, which roughly includes the average H of most concrete structures built in the world, an almost linear relationship is observed. Therefore, in this research work no further attention is given to environmental humidities lower than 50%.

In view of this, and still focusing on experimentally obtained relationships between shrinkage and H, the results obtained by Bissonnette *et al.* (1999) are discussed. They performed shrinkage tests under several relative humidity environments (ranging from 48% to 100%) with two specimen geometries ($4\times8\times32mm^3$ and $50\times50\times400mm^3$), cast with two w/c ratios (w/c=0.35 – series 35; w/c=0.50 – series 50) and three sand/binder ratios (0 ratio for pastes "P" and ratios 1 and 2 for mortars "M"). The obtained results in terms of the relationship between H and relative shrinkage are depicted in Figure 3.10, where the absence of size effect can be confirmed, as well as the apparent independency of this relationship in regard to the w/c ratio of the mix. These are two fundamental cornerstones for the establishment of local shrinkage constitutive equations, which involve the multiplication of an hypothetical drying strain upon total drying (or a reference drying strain, such as H=50%) by a function that relates H to the relative local free shrinkage.

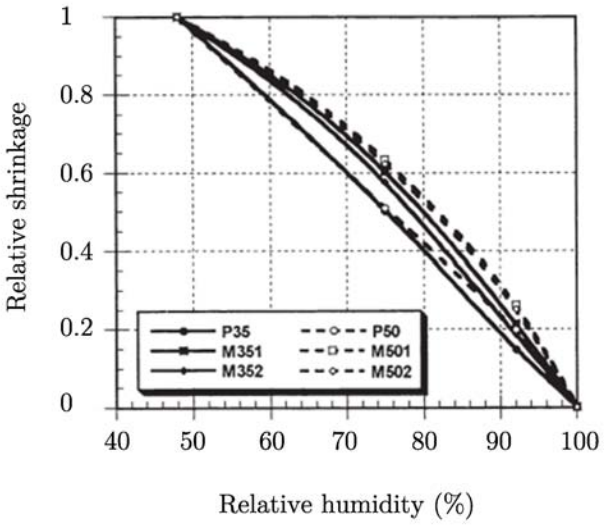

Figure 3.10: Shrinkage magnitude *vs* internal H for cement pastes and mortars (Bissonnette *et al.* 1999)

From a practical point of view, for a given concrete mix to be characterized, it is impossible to obtain reasonable estimates of the ultimate shrinkage of a specimen for application in the model here proposed (complete drying of a 15cm thick specimen could take years to happen, and such time is not available when decisions regarding the mix are to be taken quickly). Local free shrinkage measurement in concrete is also impossible, because of the size of the sample that would be needed (unless crushed aggregates were used, but then the mix would not actually be the real one). Therefore, a different strategy is proposed here: (i) to measure ultimate shrinkage in small specimens cast with the paste corresponding to the concrete under study (which may be obtained in much more feasible time windows than the case for concrete), (ii) to characterize the elasticity modulus of the aggregates under use, and (iii) to conduct an extrapolation for the expectable local free shrinkage in concrete. This extrapolation strategy is considered possible, given the experimental results obtained by Bissonnette *et al.* (1999): for two distinct w/c ratio concretes (and several aggregate/paste volume relationships), the relative concrete/paste shrinkage that expresses the relationship between the measured ultimate shrinkage in concrete $\varepsilon_{sh,c,ult}$ to the one that would be obtained in the corresponding cement paste $\varepsilon_{sh,p,ult}$ is plotted in Figure 3.11 as a function of the relative cement paste volume in the concrete mix. For the sake of clarity, the concept of relative concrete/paste shrinkage is shown in equation (3.29).

$$relative\,concrete\,/\,paste\,shrinkage = \frac{\varepsilon_{sh,c,ult}}{\varepsilon_{sh,p,ult}} \tag{3.29}$$

From Figure 3.11 it is apparent that an almost linear relationship may be established between the entities under observation: less paste volume in the concrete mix means that more aggregates are present to restrain deformation, thus ultimate shrinkage in concrete is smaller. The usual range of paste relative volume in concrete is usually between 25% and 35%, leading to a final concrete shrinkage of 15% to 25% of that which is obtained in the corresponding cement paste.

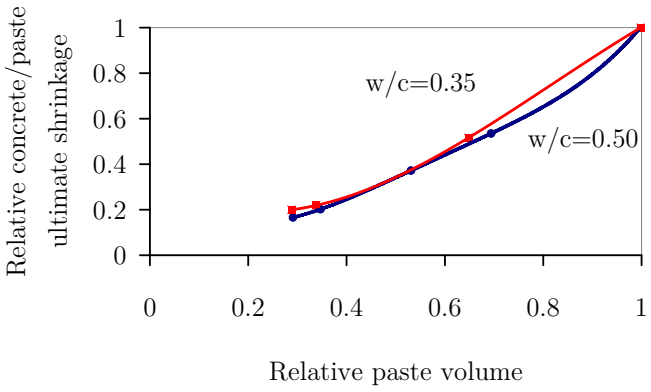

Figure 3.11: Relationship between relative concrete/paste ultimate shrinkage and relative paste volume (Bissonnette *et al.* 1999)

This kind of relationship between relative concrete/paste shrinkage and paste volume has also been acknowledged experimentally by Hansen and Almudaiheem (1987, 1987): by plotting Hansen's results in the same fashion as Bissonnette's, and comparing them,

Figure 3.12 is obtained. The reader should be reminded that even though the w/c ratios of Bissonnette's and Hansen's experiments were the same, the aggregate stiffness may have been dissimilar, so they would not have to yield coincident curves. The paramount conclusions to be taken from Figure 3.12 are: a) w/c ratio seems to affect this relationship in an almost negligible fashion; b) the tendency of the curves and values from both authors seem to be quite coherent, which is remarkable given the difference in the raw materials used.

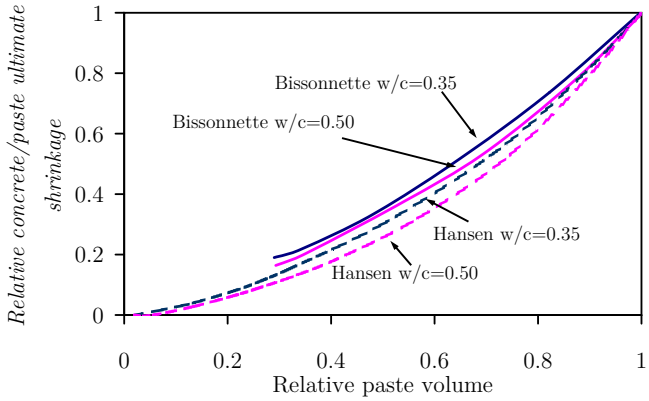

Figure 3.12: Relationship between relative concrete/paste ultimate shrinkage and relative paste volume

The mentioned experiments from Hansen and Almudaiheem (1987, 1987) resulted in the proposal of a numerical model, based on theory of elasticity and composite theory (Hansen 1987a). Accordingly concrete is idealized as a two-phase composite material, which consists of a shrinkage active matrix (the hydrated cement) and a non-shrinking particle phase (the aggregates and the unhydrated cement). The use of this model involves a two-step procedure, which firstly computes the ratio between the ultimate drying shrinkage of the paste and the ultimate shrinkage of the hydration products in the paste. In a second stage the relationship between the ultimate drying shrinkage of the concrete and the ultimate drying shrinkage of the hydration products in the paste is computed. From the results of these two computations the relationship between the ultimate drying shrinkage of the paste and the ultimate drying shrinkage of the concrete is obtained. A simplified application of the model, considering that the shrinkage of the paste equals the shrinkage of the hydration products, and assuming Poisson ratios of 0.26 for the fully hydrated paste and of 0.12 for the aggregates, leads to the following equation that relates the ultimate drying shrinkage of concrete to the ultimate shrinkage of its corresponding cement paste.

$$\frac{\varepsilon_{sh,c,ult}}{\varepsilon_{sh,p,ult}} = 0.5\left(1 - V_a\right)\left[\frac{1}{1 - V_a + 0.58\ m\ V_a} + \left(1 - V_a\right) + \frac{1.72}{m} V_a\right] \tag{3.30}$$

where V_a is the relative aggregate content by overall volume of concrete and m is the ratio of the elastic modulus of the aggregates and that of the cement paste (typical values for m are usually in the range of 4 to 7).

It is interesting to observe that a direct application of the simplified version of Hansen's model (Hansen 1987b) according to equation (3.30), with V_a adjusted to fit Bissonnette's

experiments for concrete and assuming m=4, provides a very good agreement with the experimental findings of Bissonnette, as it may be observed in Figure 3.13. This is a good indication about the capabilities and generality of the model, given the fact that it fits rather well to third party experimental results.

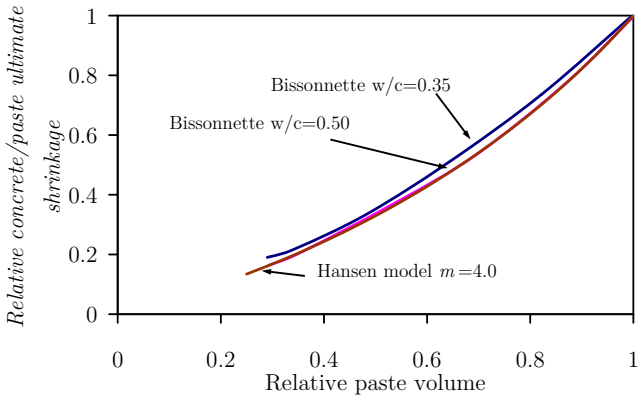

Figure 3.13: Relationship between relative ultimate shrinkage and relative paste volume: experimental results by Bissonnette *et al. versus* numerical model by Hansen

Bearing in mind the set of issues mentioned above, it is deemed feasible to devise a simplified procedure to obtain the constitutive equation for local unrestrained shrinkage to be applied in concrete. For a given concrete mix, such procedure would consist in characterizing the ultimate shrinkage of its constituting cement paste for a known constant H>50%. The obtained value can be extrapolated for concrete ultimate shrinkage by using Hansen's model (equation (3.30)). Together with the use of one of the models that relate the relative shrinkage with H as shown in Figure 3.9, it is possible to achieve the final goal of establishing the predictive equation of local shrinkage *versus H*.

3.7.3 Shrinkage *versus* internal moisture – numerical formulations

In regard to the numerical formulations relate the moisture potential (water content or relative humidity) with the free local shrinkage (unrestrained), a review follows on some of the most relevant cases found in the literature.

Maekawa *et al.* (Maekawa *et al.* 1999, Maekawa *et al.* 2003, Song *et al.* 2001) who use a field equation based on an equivalent liquid pore pressure, propose a relationship between concrete local shrinkage and pore humidity based on the assumption that capillary pressure is the main driving force, which after some mathematical handling (which involves the combination of the Laplace equation for meniscus curvature in pores with the Kelvin-Laplace equation for the relationship between internal H and the pore fluid pressure) results in

$$\varepsilon = A_S \frac{\sigma_S}{E_S} \qquad \text{with} \qquad \sigma_S = \frac{\rho R T}{M} \ln(H) \tag{3.31}$$

where ε is the free shrinkage strain, A_S is an area factor, E_S is the bulk elastic modulus on capillary tension, σ_s is the tensile stress due to the decrease in relative humidity of the

pores, ρ is the density of water, R is the universal gas constant and M is the molecular mass of water. Yuan and Wan (2002) applied this approach in their work.
A similar approach also based on the capillary tension as the main driving mechanism for shrinkage was proposed by Baroghel-Bouny *et al.* (1999)

$$d\varepsilon = \frac{\rho R T S_l}{K_0 M H} dH \tag{3.32}$$

where S_l is the liquid water saturation, and K_0 is the drained bulk modulus. Equation (3.32) almost corresponds to the derivate of equation (3.31), except for the presence of A_S in the latter, and of S_l in the former.
Another expression based on the same principles was derived by Grasley *et al.* (2006), who state that

$$\varepsilon = \frac{R T \ln(H) S_l}{v} \left(\frac{1}{3k} - \frac{1}{3 k_0} \right) \tag{3.33}$$

where v is the molar volume of water, k is the bulk modulus of the porous solid, and k_0 is the bulk modulus of the solid skeleton of the material.

On a numerical approach that uses the moisture content as driving potential, Torrenti *et al.* (1999) used a simplified formulation where the unrestrained concrete shrinkage is linearly related to the moisture content

$$\varepsilon = k_t \left(C(x,t) - C_0 \right) \tag{3.34}$$

where k_t is a proportionality constant, $C(x,t)$ is the instantaneous moisture content at point x and instant t and C_0 is the initial moisture content. In a publication that shares common authors, Granger *et al.* (1997) acknowledge the existence of a nonlinear relationship between humidity in pores and local unrestrained shrinkage, with the format

$$\varepsilon = \frac{3 \rho_l R T}{M (1 - \phi) k_0} \frac{C(H)}{\Omega_{tot}} \ln(H) \tag{3.35}$$

where ϕ is the porosity, $C(H)$ is the isothermal desorption curve relating water content and H and Ω_{tot} is the total concrete volume. Furthermore, they state that very good agreement is obtained when the product $C(H)\ \ln(H)$ is linearized and substituted by $a(1\text{-}H)$ for $H>50\%$, with a being a proportionality factor. The resulting equation for unrestrained shrinkage becomes:

$$\varepsilon = \left[\frac{3 \rho_l R T}{M (1 - \phi) k_0} a \right] (1 - H) \tag{3.36}$$

This approach corresponds to the consideration of a hygral expansion coefficient that is independent of H, such as the case of equation (3.34), through the use of k_t . This kind of strategy has also been adopted by Chen and Mahadevan (2007).

A linear relationship between the rates of unrestrained shrinkage strains and local H was proposed by Bazant and Xi (1994), who also accounted for material hardening through the evolution along time t of the concrete bulk elasticity modulus E with the function $g_s(t)=E(t=\infty)/E(t)$:

$$\dot{\varepsilon}_{sh} = k_{sh}\,\dot{H} \qquad \text{with} \qquad k_{sh} = -\varepsilon_s^0\, g_s\left(t\right) \tag{3.37}$$

where ε_s^0 is the value of final shrinkage. The same approach has been followed by Kim and Lee (1998).

Based on experimental results obtained for mortars, Martinola and Sadouki (1998) use a simple expression for the mortar unrestrained shrinkage as function of the relative humidity H that are related through a hygral shrinkage coefficient $\alpha_{sh}(H)$:

$$\Delta\varepsilon = \alpha_{sh}\left(H\right)\Delta H \tag{3.38}$$

However, unlike the findings of several other authors that have been mentioned above, the hygral coefficient has a strong dependency on H, as can be confirmed from observation of Figure 3.14 (two mortars were analyzed, named as optimized and standard).

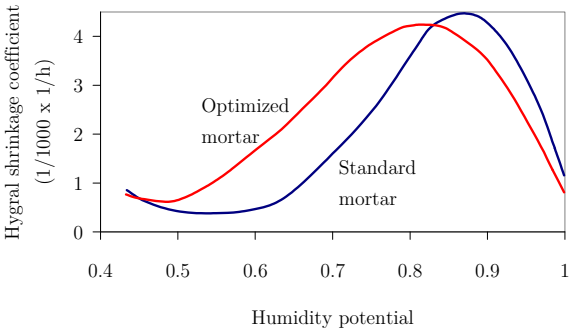

Figure 3.14: Hygral shrinkage coefficient as function of humidity (Martinola and Sadouki 1998)

The numerical model developed by Kwak *et al.* (2006b) expresses the relationship between moisture state and local unrestrained shrinkage of concrete as

$$\Delta\varepsilon_{sh} = \varepsilon_{sh,\infty}\left[\Delta f_s\left(H\right)\right] \qquad \text{with} \qquad f_s\left(H\right) = 0.97 - 1.895\left(H - 0.2\right)^3 \tag{3.39}$$

where $\varepsilon_{sh,\infty}$ is the ultimate concrete shrinkage. The outcome of this approach yields very similar results to the ones plotted in Figure 3.9, as well as to the MC90 equation that relates the extent of shrinkage β_{RH} with the environmental H:

$$\beta_{RH} = 1.55\left(1 - H^3\right) \quad \text{with} \quad 0.4 \le H < 0.99 \tag{3.40}$$

The similarity of the results of relative shrinkage computed from equations (3.39) and (3.40) can be observed in Figure 3.15, where the curves corresponding to the equation proposed by Gardner (2000) that had already been shown in Figure 3.9 are also represented, as well as the plot of the K_H correcting factor shown in equation (3.28). The similarity in results of all the plots in Figure 3.15, that have been derived in quite different contexts from each other, lead to the conclusion that there is a fairly reasonable consensus within the scientific community in regard to the issue of the relationship between relative shrinkage and relative humidity.

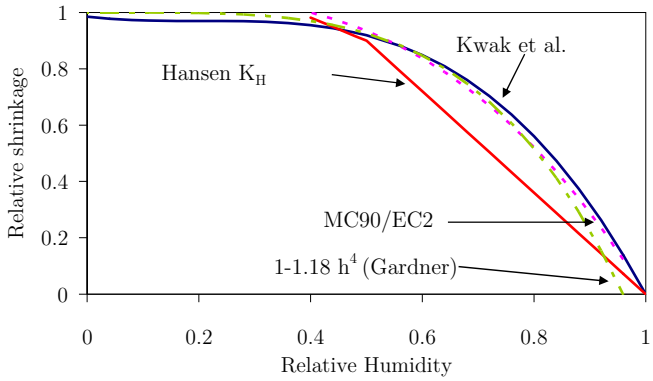

Figure 3.15 - Shrinkage magnitude vs internal RH – comparison

3.8 Relationship between local relative humidity and hindering of hydration reactions

Cement hydration reactions are strongly hindered, or even stopped, when the surrounding humidity (or pore humidity) drops below a threshold value (Azenha *et al.* 2007a, Neville 1995, Patel *et al.* 1988). This humidity drop may be caused either by self-desiccation (case of High Performance Concrete) or by evaporation to the surrounding environment (cover concrete). In both cases, numerical models should be able to cope with this phenomenon, and to simulate it accordingly.

Granger (1996) includes this effect of reaction hindering when computing local equivalent age of concrete, using a reduction variable β as proposed by Bazant (1988):

$$\beta = \left[1 + \left(5 - 5H\right)^4\right]^{-1} \tag{3.41}$$

This equation reproduces the well known perception that under H=80% the hydration reactions become almost negligible. Thus, as H approaches this threshold, the numerical model practically ceases the local evolution of mechanical properties of concrete (such as E-modulus and tensile strength). In Bazant and Najjar (1972) a quite similar equation to (3.41) is used, where the "5" values are substituted by "7.5".

Based on a set of experimental results concerning concrete at different stages of cement hydration, and under various constant humidity environments, Mjornell (1997) proposed an equation for correcting equivalent age by a coefficient β that is function of water

content W_e, initial water content W_0, cement content C, degree of hydration α_c, and the amount of water in the gel at saturation and complete hydration k_{wg}:

$$\beta = \left[\frac{W_e/C - k_{wg}\ \alpha_C}{W_0/C - 0.19\ \alpha_C - k_{wg}\ \alpha_C} \right]^4 \tag{3.42}$$

This equation leads to a more significant reduction of β when humidity drops at early stages of the reaction (low degree of hydration) than what occurs at later stages. Anyway, it leads to similar results as (3.41), with the same tendency of causing the rate of hydration reaction to become negligible for H<80%.
A description of the approach proposed by Maekawa *et al.* (1999) for the reduction coefficient β is relegated to the next chapter, where such model is used and compared to experimental results.

3.9 Depression in internal moisture content due to self-desiccation

In the cases that the term $\dot{H}_S$ of equation (3.15) cannot be neglected because of relevant early H depression associated to chemical hydration reactions, a mathematical formulation is needed. Few authors have focused on this particular issue; nonetheless, a review of existing approaches follows.
An approach based on a specific experiment conducted by Martinola and Sadouki (1998) for a low w/c mortar resulted in the following equation, which relates the variation of internal humidity H along time t due to the sole effect of autogenous water consumption:

$$\dot{H} = -\frac{0.358}{(43.8+t)^2} + \frac{0.358}{43.8+t} \tag{3.43}$$

Mjornell proposed the following equation for humidity variation due to autogenous water consumption, with basis on available experimental results for several concrete mixes:

$$H = \ln\left[\left(\sqrt{W^2 + 2W\,(K-G) + G^2 + 2GK + K^2} + W - G + K \right) \frac{1}{2K} \right]^{\frac{1}{B}}$$
$$\text{with} \qquad W = W_e/C\ ;\ G = W_{gel}/C\ ;\ K = W_{cap}/C\ ;\ B = b - \alpha_C\ \ 10 \tag{3.44}$$

Where b is a fitting parameter, α_C is the degree of hydration and W_e, W_{gel} and W_{cap} are volumetric water contents (evaporable, gel and capillary, respectively). This model has been further applied by Oh and Cha (2003).
Within the numerical framework DuCOM (Maekawa *et al.* 1999) a sink term Q_{hyd} exists in the moisture field equation that pertains to the rate of fixation of pore water as a chemically combined part of the CSH due to hydration. It is computed as follows:

$$Q_{hyd} = \frac{\partial \left(W_p \, \alpha \, \beta_w \right)}{\partial t} \tag{3.45}$$

where W_p is the weight of power materials (cement and others if applicable) per unit paste volume, t is time and β_ω is the amount of chemically combined water per unit weight of hydrated powder material (obtained based upon the stoichiometric balance of chemical reactions) and α is the degree of hydration. The product $W_p \times \beta_\omega$ corresponds to the chemically combined water per unit paste volume. After multiplying it by α, one obtains the $W_p \times \beta_\omega$ at degree of hydration α.

For the numerical simulations conducted in this thesis the term $\dot{H}_S$ was systematically disregarded due to the consideration of normal strength concrete with relatively high water to cement ratio, which makes the internal H depression associated to hydration negligible.

3.10 Shrinkage induced microcracking

Intrinsically to its nature, drying of concrete occurs progressively from the surface towards the core. So, focusing on an initially sealed concrete prism without external restraints, neither reinforcement, it is plausible to consider that upon sealing removal, evaporation begins and the near surface concrete layers start to have tendency to contract. As the inner concrete has a natural tendency to remain unchanged, compatibility dictates that the surface layer will endure tensile stresses. The order of magnitude of such stresses has been analyzed in a simplified fashion by Sadouki and Mier (1997), and their example is used herein: supposing a linear relationship between the relative humidity change ΔH in the material and the corresponding free shrinkage by a coefficient of hygral expansion α_{sh}, it is possible to postulate that the very near surface fibre of concrete, assumed totally restrained by the subjacent concrete, endures stresses σ according to

$$\sigma = E \, \alpha_{sh} \, \Delta H \tag{3.46}$$

where E is the elastic modulus of concrete/mortar. If the material characteristics are assumed as: E=25GPa and α_{sh} =0.003mm/mm.h, it follows that ΔH=10% leads to a tensile stress of 7.5MPa. This is a very simplified approach that disregards creep and supposes 100% restriction to shrinkage caused by the underlying concrete, however, it allows to recognize that it is plausible to expect that the tensile strength of the material f_{ct} is reached quite easily due to drying shrinkage (even in the absence of external restraint and reinforcement). It is therefore generally expectable that hygral gradients occurring in cementitious materials are most of the times large enough to induce surface cracking. This tendency for surface cracking is corroborated by the hygro-mechanical simulations conducted by Suwito *et al.* (2006), by Granger *et al.* (1996), Benboudjema *et al.* (2005b), Wittmann *et al.* (1980) and Chen *et al.* (2007). Based on a mixed use of experimental results and numerical simulations, Grasley *et al.* (2006) report the existence of a surface layer in which the tensile strength of concrete is reached, in a depth that does not overcome 6mm from the surface. Also, in terms of experimental research, Bisschop

and van Mier (2002a) and Colina and Acker (2000) have reported consistent tendencies of cementitious materials to exhibit small surface cracks associated to self restraint to drying. Regarding this topic, there is a further issue that is quite worth being mentioned, which is the microcracking induced by aggregate restraint. It is understandable that either in the case of drying or autogenous shrinkage, aggregates do not follow the same tendency to shrink as cement paste (having only negligible drying strains). Therefore, the volumetric changes of the paste are internally restrained by aggregates. This restraint has been shown to cause internal microcracking (Bisschop and Van Mier 2002a, Shiotani *et al.* 2003).

3.11 Potential coupling of the moisture field with other fields

3.11.1 Stress field - cracking

It has been stated in the previous section that microcracking is bound to occur even in externally unrestrained specimens, due to the internal restraint of the core wet areas of concrete in regard to those enduring drying near the surface. It would be understandable to expect that cracking could significantly influence the moisture transport capacity of the porous material. In spite of this, and based on experimental evidence, Bisschop and Van Mier (2008) state that the expectable degree of microcracking in practical mortars and concretes is not bound to cause relevant changes in the drying rate (thus moisture diffusion) of the material. These drying induced cracks have been reported to have openings that range from 25μm to 50μm (Bisschop *et al.* 2002b), which are remarkably lower than the 100 μm value of crack opening under which Bazant states that negligible effects exist on drying rates (Benboudjema *et al.* (2005b)). This is further confirmed by Granger (1996) and Benboudjema *et al.* (2005b) that report experimental studies in which non-loaded specimens and loaded specimens in compression (thus closing cracks) dry in the same manner.

Suwito *et al.* (2006) have conducted a numerical study of drying and drying shrinkage, including the effect of cracking on the diffusion characteristics of the material. The results were consistent to what has been stated above, with the small drying cracks having a small accelerating effect on the further rates of drying of the material.

This conclusion of negligible influence of microcracking in drying rates cannot be generalized for larger cracks, such as those usually expected in service life of reinforced concrete structures (with allowable opening limits reaching 0.4mm according to Eurocode 2 (CEN 2004)). In fact, Bazant *et al.* (1987) have reported cracks of 0.1mm to have an appreciable effect on the overall rate of drying (doubling diffusivity in some cases).

The option of neglecting the effect of hygral cracks on the moisture diffusivity characteristics of concrete in the numerical modelling, for the reasons that have been mentioned, was also adopted by Sadouki and Van Mier (1997).

It is considered feasible to establish that the moisture field can influence the stress field through the shrinkage strains, whereas the reverse influence would occur by changes in drying rates associated to shrinkage (or structural) cracking. The approach to be adopted

in the thermo-hygro-mechanical framework of this thesis adopts the former interaction (moisture field → stress field) and disregards the latter (stress field → moisture field), causing the models to be formally de-coupled or, in other words, unidirectionally coupled.

3.11.2 Thermal - hydration field

Thermal and moisture phenomena occur at rather dissimilar time scales, once the thermal diffusivity $k/\rho c$ for concrete is in the order of $10^{-6}m^2s^{-1}$, while the corresponding quantity for moisture flow is within the orders of 10^{-8} and $10^{-10}m^2s^{-1}$ (Jonasson 1994). Moisture fluxes within concrete transport heat energy, as well as the evaporation/condensation of water involved in moisture transport. However, the mentioned differences in diffusivities mean that a variation in temperature due to thermal flux occurs almost instantly within concrete, by comparison with the temperature variations that moisture fluxes would induce. This provides grounds for the simplification assumed in this work of considering that the thermal field is not influenced by the moisture field. However, it should be stressed that this simplification carries limitations to the model associated to surface evaporative cooling as will be described in Chapter 4: loss of thermal energy of the concrete surface associated to the enthalpy of evaporation of water being evaporated from concrete to the environment. This phenomenon only assumes relevance when it occurs at very early ages (with saturated concrete surface and evaporation is not diffusion controlled), or when concrete is significantly hotter than the environment (see Chapter 4), or even when it rains over concrete and the surface becomes saturated. None of these three situations occur in the applications intended for the scope of the implemented numerical framework, since exposure to the environment usually occurs only after the curing time (during which water evaporation is prevented), which usually spans longer than the time that heat of hydration takes to dissipate, and also because rain occurrence is not contemplated at the present stage of development.

It has been shown in section 3.8 of this Chapter that the diminishment of the moisture availability within the pore structure (due to evaporation to the environment or self-desiccation) can conduct to a strong deceleration or even total hindering of chemical hydration reactions. To be able to simulate this deceleration, moisture and thermal/hydration models should be fully coupled. However, because of the fact that the applications presented in this thesis regard to concrete mixes with low self-desiccation, as well as exposure of concrete to evaporation at least a few days after casting (meaning that most heat generation has occurred, and that a great percentage of the hydration has occurred), it is considered feasible to consider the thermal and moisture fields decoupled.

The moisture field is however strongly influenced by the thermal field once the moisture equilibrium in the pore structure strongly depends on temperature; therefore diffusion properties are strongly dependent on temperature. At its present stage of development, the moisture model implemented within the scope of this thesis does not account for this, which is acceptable given that the diffusion parameters were derived for an environmental and concrete temperature of 20°C, and the applications envisaged involve only moisture movements under isothermal conditions. So, this simplification further justifies the decision of decoupling thermal and moisture models.

3.11.3 Carbonation field

Carbonation is a chemical neutralization process of hydration cement products, whose ultimate effect is to replace hydroxyl ions by carbonate ions. Even though these chemical reactions cause a global increase of volume of the reaction products in regard to the reactants (and a consequent decrease in porosity), it has been widely acknowledged, and experimentally demonstrated, that carbonation induces contraction of concrete (Hewlett 2004, Houst 1997). Several mechanisms have been put forward to explain this phenomenon (Houst 1997), however none has full agreement in the scientific community, and the tendency is to believe that this phenomenon may occur as combination of the several factors that have been stated by researchers in this field.

For the purposes regarded in the topic of this research, carbonation shrinkage is a relevant issue, once it has been known to have induce strains as important as those of drying shrinkage (Hewlett 2004). Carbonation may as well change the relative humidity in the pore structure, because of the decrease in porosity and the possible changes in H equilibrium caused by the presence of the reaction products. This is however a phenomenon that usually only has relevance in cover concrete, given the fact that carbonation depth after one year of exposure may vary between 0.05mm and several centimetres (in a worst case scenario) (Granger 1996, Holt 2001).

As a simplifying option, and bearing in mind the small treatment given to this issue in the literature, carbonation and carbonation shrinkage effects were disregarded in the present thesis.

3.12 Numerical implementation of the moisture model

The governing equation to be solved has been illustrated in Section 3.3.1, and is reproduced here:

$$\left(\frac{\partial W}{\partial H}\right)\frac{\partial H}{\partial t} = div\left(D_H \ grad\left(H\right)\right) + \frac{\partial H_S}{\partial t} \tag{3.47}$$

and may be rewritten as

$$\frac{\partial}{\partial x}\left(D_H \frac{\partial H}{\partial x}\right) + \frac{\partial}{\partial y}\left(D_H \frac{\partial H}{\partial y}\right) + \frac{\partial}{\partial z}\left(D_H \frac{\partial H}{\partial z}\right) + \dot{H}_S = \left(\frac{\partial W}{\partial H}\right)\dot{H} \tag{3.48}$$

Neumann's conditions may be applied on boundary Γ_q, rendering

$$D_H \frac{\partial H}{\partial x} l + D_H \frac{\partial H}{\partial y} m + D_H \frac{\partial H}{\partial z} n = h_m \left(H - H_{env}\right) \tag{3.49}$$

where l, m and n are direction cosines.

There are in fact striking resemblances between equations (3.48)-(3.49) and equations (2.61)-(2.62) in Chapter 2 for the thermal field. Therefore, intermediate steps for derivation of the final equations will be skipped, bearing in mind the mutual correspondences shown in Table 3.1.

Table 3.1: Correspondence of entities in the thermal and moisture field equations

Thermal field	Moisture field
T	H
k	D_H
ρc	$\dfrac{\partial W}{\partial H}$
h_{cr}	h_m
T_{env}	H_{env}
$\dot{Q}$	$\dot{H}_S$

So, in analogy to equation (2.67), the field equation may be formulated as:

$$\overline{\boldsymbol{C}}^e\ \dot{\boldsymbol{H}}\ +\ \overline{\boldsymbol{G}}^e\ \boldsymbol{H}\ =\ \overline{\boldsymbol{F}}^e_H\ +\ \overline{\boldsymbol{F}}^e_{aut} \tag{3.50}$$

where the elemental matrices and vectors are

$$\overline{\boldsymbol{C}}^e\ =\ \int_{\Omega^e} \boldsymbol{N}^T \left(\frac{\partial W}{\partial H}\right) \boldsymbol{N}\ d\Omega \tag{3.51}$$

$$\overline{\boldsymbol{G}}^e\ =\ \int_{\Omega^e} \nabla \boldsymbol{N}^T\ D_H\ \nabla \boldsymbol{N}\ d\Omega\ +\ \int_{\Gamma^e_q} \boldsymbol{N}^T\ h_m\ \ \boldsymbol{N}\ d\Gamma_q \tag{3.52}$$

$$\overline{\boldsymbol{F}}^e_H\ =\ \int_{\Gamma^e_q} \boldsymbol{N}^T\ h_m\ \ H_{env}\ \ d\Gamma_q \tag{3.53}$$

$$\overline{\boldsymbol{F}}^e_{aut}\ =\ \int_{\Omega^e} \boldsymbol{N}^T\ \dot{H}_S\ \ d\Omega \tag{3.54}$$

Note: For NSC, $\dot{H}_S \cong 0 \Rightarrow \overline{\boldsymbol{F}}^e_{aut}\ = 0$

Assuming a backward-Euler integration scheme of the form

$$\dot{H}_{n+1}\ =\ (H_{n+1}\ -\ H_n)/\Delta t \tag{3.55}$$

Eq. (3.50) defined for instant n+1 becomes

$$\frac{1}{\Delta t}\ \overline{\boldsymbol{C}}^e_{n+1} \left(\boldsymbol{H}^e_{n+1}\ -\ \boldsymbol{H}^e_n\right) +\ \overline{\boldsymbol{G}}^e_{n+1}\ \boldsymbol{H}^e_{n+1}\ =\ \overline{\boldsymbol{F}}^e_{H,n+1}\ +\ \overline{\boldsymbol{F}}^e_{aut,n+1} \tag{3.56}$$

Using standard assembling procedures one is able to constitute the global $\overline{\boldsymbol{C}}$ and $\overline{\boldsymbol{G}}$ matrices and the $\overline{\boldsymbol{F}}_H$ and $\overline{\boldsymbol{F}}_{aut}$ vectors required for the FE analysis of a moisture structural problem:

$$\left(\frac{\overline{\boldsymbol{C}}_{n+1}}{\Delta t} + \overline{\boldsymbol{G}}_{n+1} \right) \boldsymbol{H}_{n+1} = \overline{\boldsymbol{F}}_{H,n+1} + \overline{\boldsymbol{F}}_{aut,n+1} + \frac{\overline{\boldsymbol{C}}_{n+1}}{\Delta t} \boldsymbol{H}_n \tag{3.57}$$

Due to the dependencies of $(\partial W/\partial H)$ and D_H on the relative humidity H, $\overline{\boldsymbol{C}}$ and $\overline{\boldsymbol{G}}$ are nonlinearly dependent on $\boldsymbol{H}_{n+1}$. Equation (3.57) is thus solved by recourse to an incremental iterative procedure based in the Newton-Raphson method, in order to obtain the nodal relative humidities $\boldsymbol{H}_{n+1}$.
For simplicity of interpretation, equation (3.57) may be rewritten as

$$\widehat{\overline{\boldsymbol{K}}}_{n+1} \boldsymbol{H}_{n+1} = \widehat{\overline{\boldsymbol{F}}}_{n+1} \tag{3.58}$$

$$\widehat{\overline{\boldsymbol{K}}}_{n+1} = \frac{\overline{\boldsymbol{C}}_{n+1}}{\Delta t} + \overline{\boldsymbol{G}}_{n+1} \tag{3.59}$$

$$\widehat{\overline{\boldsymbol{F}}}_{n+1} = \overline{\boldsymbol{F}}_{H,n+1} + \overline{\boldsymbol{F}}_{aut,n+1} + \frac{\overline{\boldsymbol{C}}_{n+1}}{\Delta t} \boldsymbol{H}_n \tag{3.60}$$

The strategy for finite element implementation (shape functions, integration strategy, etc.) of these equations follows the same strategy as that of the thermal model. A brief outline of the overall procedure for the moisture analysis is presented in Box 3.1, where the main parts of the used algorithm for calculation of humidity distribution are shown, with particular focus on the application of the Newton-Raphson method in the iterative procedure.

Box 3.1: Outline of the moisture model

INPUT: n, $\boldsymbol{H}_n$, Δt, t_{end}, *TOLER*

OUTPUT: $\boldsymbol{H}_{n+1}$

(i) Update time $t_{n+1} = t_n + \Delta t$.
Is $t_{n+1} > t_{end}$? NO: Go to step (ii).
YES: Go to step (x).

(ii) Initialize iteration counter i=0 and set $\Delta \boldsymbol{H}_{n+1}^{i=0} = \boldsymbol{0}$.

(iii) Set $\boldsymbol{H}_{n+1}^{i} = \boldsymbol{H}_n + \Delta \boldsymbol{H}_{n+1}^{i}$.

(iv) Compute $\widehat{\overline{\boldsymbol{F}}}_{n+1}^{i}$ and $\widehat{\overline{\boldsymbol{K}}}_{n+1}^{i}$.

(v) Compute the residuals vector $\boldsymbol{\Psi}_{n+1}^{i} = \widehat{\overline{\boldsymbol{F}}}_{n+1}^{i} - \widehat{\overline{\boldsymbol{K}}}_{n+1}^{i} \boldsymbol{H}_{n+1}^{i}$.

(vi) Check convergence:

Is $\left\|\boldsymbol{\psi}_{n+1}^{i}\right\| \leq TOLER$? NO: Go to step (vii).

YES: Go to step (ix).

(vii) Compute $\Delta \boldsymbol{H}_{n+1}^{i+1} = \Delta \boldsymbol{H}_{n+1}^{i} + \left[\widehat{\widehat{\boldsymbol{K}}}_{n+1}^{i} \right]^{-1} \boldsymbol{\psi}_{n+1}^{i}$.

(viii) Update iteration counter $i:=i+1$. Go to (iii).

(ix) Update the step counter $n:=n+1$. Go to (i).

(x) End.

3.13 Validation of the numerical model

Validation pertaining to specific data related to moisture fields was made by replicating simulations performed by Kwak *et al.* (2006b), in regard to experimental results communicated by Kim and Lee (1999). This example consisted of $10\times10\times20\text{cm}^3$ concrete specimens, sealed in five surfaces with paraffin wax, leaving only one $10\times10\text{cm}^2$ surface in contact with the environment (the specimens were initially fully submerged in water, until the age selected for exposure to a drying environment with T=20°C and H=50%). Relative humidity sensors were embedded in the concrete specimens at three predefined depths, measured in regard to the exposed surface as shown in Figure 3.16: 3cm, 7cm and 12cm. From the various specimens reported, a w/c=0.4 concrete specimen, with exposure to the environment at the age of 28 days was selected for the comparison in this thesis. The parameters used for the numerical modelling of moisture diffusivity D_{H^*} according to equation (3.21) were: $D_1=6.17\times10^{-10}\text{m}^2\text{s}^{-1}$, $\alpha_H=0.047$ and $H_C=0.8$. The moisture transfer boundary coefficient was null during the first 28 days (moist curing conditions), and switched to $h_m=5.81\times10^{-9}$ ms^{-1} from then on.

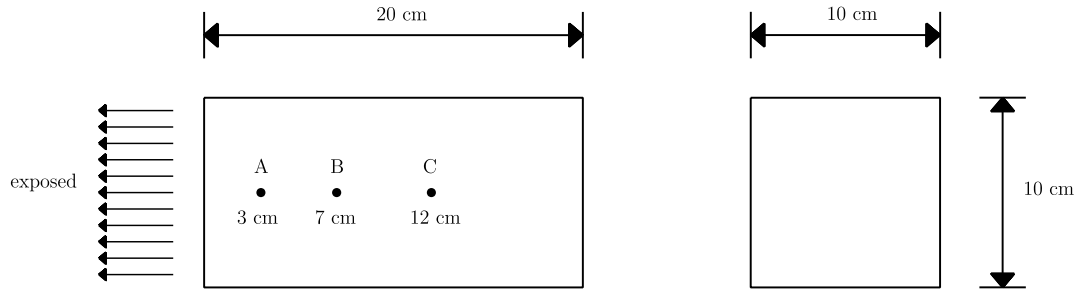

Figure 3.16: Geometry and sensor location in the monitored specimen (Kim and Lee 1999)

Comparison of performance of the two numerical implementations in regard to the experimental values available is made in Figure 3.17. The coherence between the two numerical simulations is evident, and the validation can be considered successful.

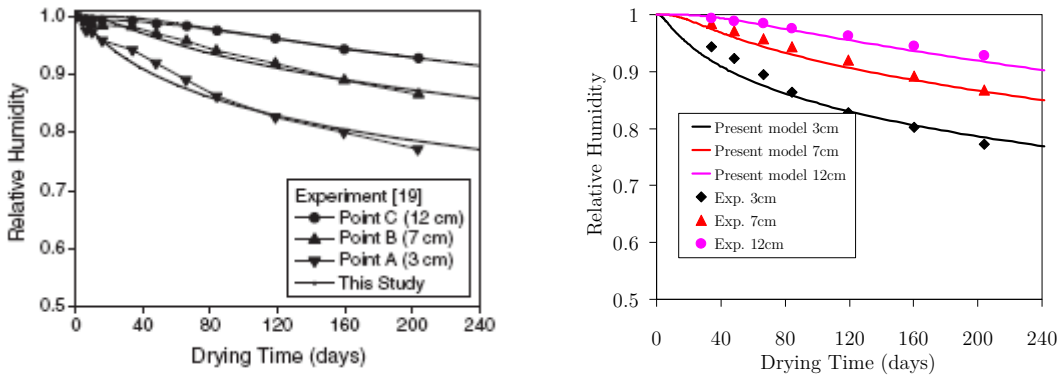

a) b)

Figure 3.17: Validation example for moisture field computation: a) results by Kwak; b) current implementation *versus* experimental results

Further validation of the implemented numerical moisture model was conducted with recourse to several benchmarking examples available in the literature (Manrique 1976) (not included here for conciseness). The set of validation examples includes transient calculations, with nonlinearity in both $(\partial W/\partial H)$ and D_H parcels.

3.14 Moisture analyses of a concrete prism and a RC slab

The present section pertains to the thermal and moisture field simulation of two concrete prisms and a RC slab, accompanied by a brief discussion of results. The results of these analyses are used as inputs to the mechanical analyses to be conducted in Chapter 5, completing a thermo-hygro-mechanical analysis. After an initial presentation of the moisture material properties under consideration (shared by the prisms and the RC slab), details on modelling options are given.

3.14.1 Material properties

As no laboratorial testing was performed for these particular applications, feasible material properties of a normal strength concrete were adopted, to reproduce realistic cases.

In terms of heat of hydration generation, the thermal output of a dosage of 250kg/m^3 of cement type I 52.5R was considered, with the material parameters indicated in Figure 3.18. Other assumed thermal properties of concrete were: k=2.6Wm^{-1}K^{-1} and ρc=2400kJm^{-3}K^{-1}. The boundary transfer coefficient corresponding to contact of concrete with the environment was considered constant and equal to h_{cr}=10Wm^{-2}K^{-1}, whereas the initial temperature of concrete was 20°C.

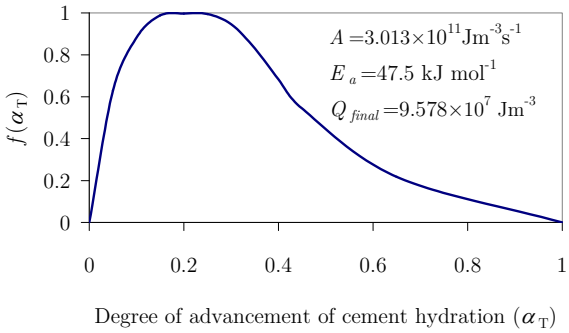

Figure 3.18: Material parameters for heat generation

A moist curing of 28 days was considered in all the calculations for both applications, and the diffusion parameters for D_{H^*} reported above were adopted: D_1=6.17×10^{-10}m^{2}s^{-1}, α_H=0.047 and H_C=0.8. The moisture transfer boundary coefficient was null during the first 28 days (moist curing conditions), and the value h_m=5.81×10^{-9}ms^{-1} was adopted from then on; $\varepsilon_{sh,\infty}$ in equation (3.39) was considered as 500×10^{-6}, which is a feasible value for normal strength concrete. Initial internal relative humidity was considered as H=100%.

3.14.2 Concrete drying shrinkage prism

The thermal and moisture behaviour of a concrete drying shrinkage specimen is studied in this section. Two geometries are considered: 20×20×60cm^3 (named as P200) and 15×15×45cm^3 (named as P150), in accordance to usual specimen sizes in laboratorial research. Each drying shrinkage prism has the three planes of symmetry depicted in Figure 3.19a, thus only one-fourth of it was modelled according to the scheme in Figure 3.19b, where surfaces labelled as "sym" refer to symmetry planes and surfaces "bou" are boundaries in contact with the environment. The sketch of the FE mesh as adopted for both prisms models is represented in Figure 3.19c, where smaller element sizes were placed in the neighbourhood of boundaries, in accordance to the greater thermal and moisture gradients predicted there. Calculations for both temperature and humidity fields were conducted using 8-nodded FE (with 2×2×2 Gauss points), with surface FE to simulate the boundaries (planar 4-nodded FE with 2×2 Gauss points). Time integration was undertaken as follows: 40 steps of 1h, 20 steps of 4h, 20 steps of 16h, 30 steps of 24h and 230 steps of 96h. The total time of analysis reached 968 days (23240h), which was found to be enough for the prisms to attain almost steady-state conditions. Environmental conditions were constant with T=20°C and H=50%.

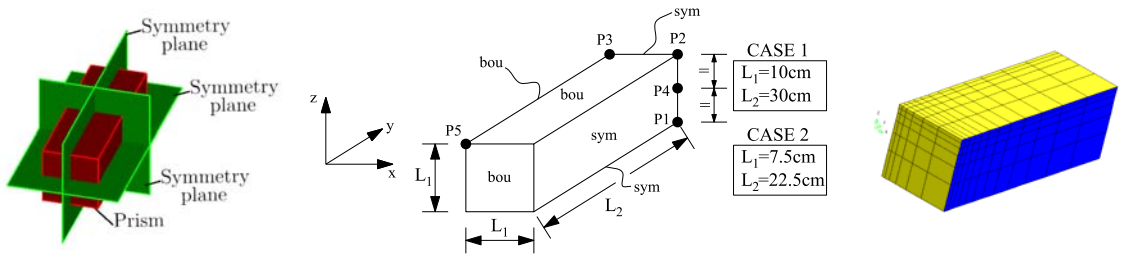

a) b) c)

Figure 3.19: a) Symmetry planes of the prism; b) schematic representation of the model; c) sketch of the FE mesh

Results pertaining to the temperature evolution during the phase of cement heat of hydration release for a selected group of points of the prism P200 (P1 to P5) are depicted in Figure 3.20a. The highest temperature rise occurs at the centre of the prism (point P1), with a value of less than 6°C. Conversely, the lowest temperature rise occurs at the corner of the specimen, in P5, amounting to less than 3°C, with the temperature gradients in the specimen remaining always below 4°C. All temperature gradients cease to exist at approximately 3 days of age, time after which the temperature within the specimen is constant (T=20°C). The temperature rise and gradients are smaller in prism P150, as expected (see Figure 3.20b).

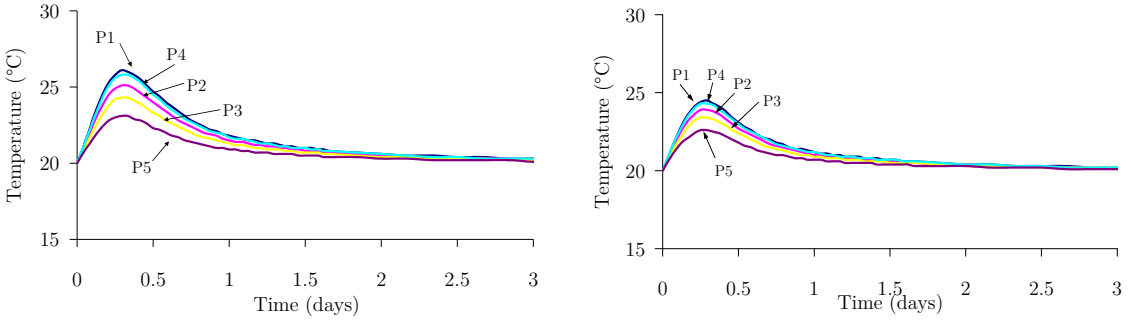

a) b)

Figure 3.20: Computed temperatures for a selected group of points of: a) specimen P200; b) specimen P150

The evolution of H within the specimen P200 occurs in a much slower fashion than it was the case for temperature, as shown in Figure 3.21 in the form of plots for points P1 to P5, and through the distribution fields in Figure 3.22. It is clear that the surface points P5 and P3 dry much faster than the inner points, immediately after exposure at the age of 28 days. H in P1, located at the specimen's centre, is the slowest to converge to the environmental relative humidity of 50%, reaching H=51.8% at the end of the analysis. These relative humidity gradients are responsible for unrestrained potential shrinkage strains, calculated according to equation (3.39), which induce self-balanced stresses.

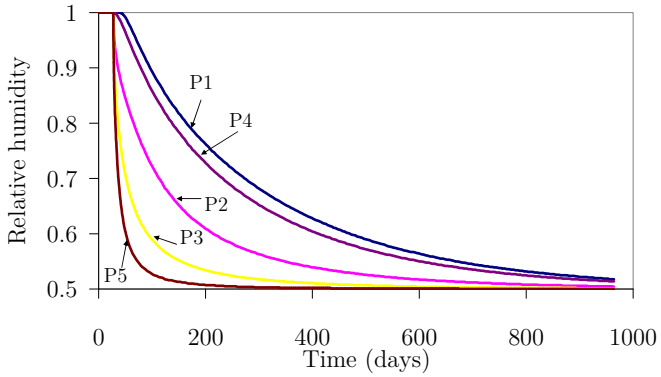

Figure 3.21: Computed H for a selected group of points of specimen P200

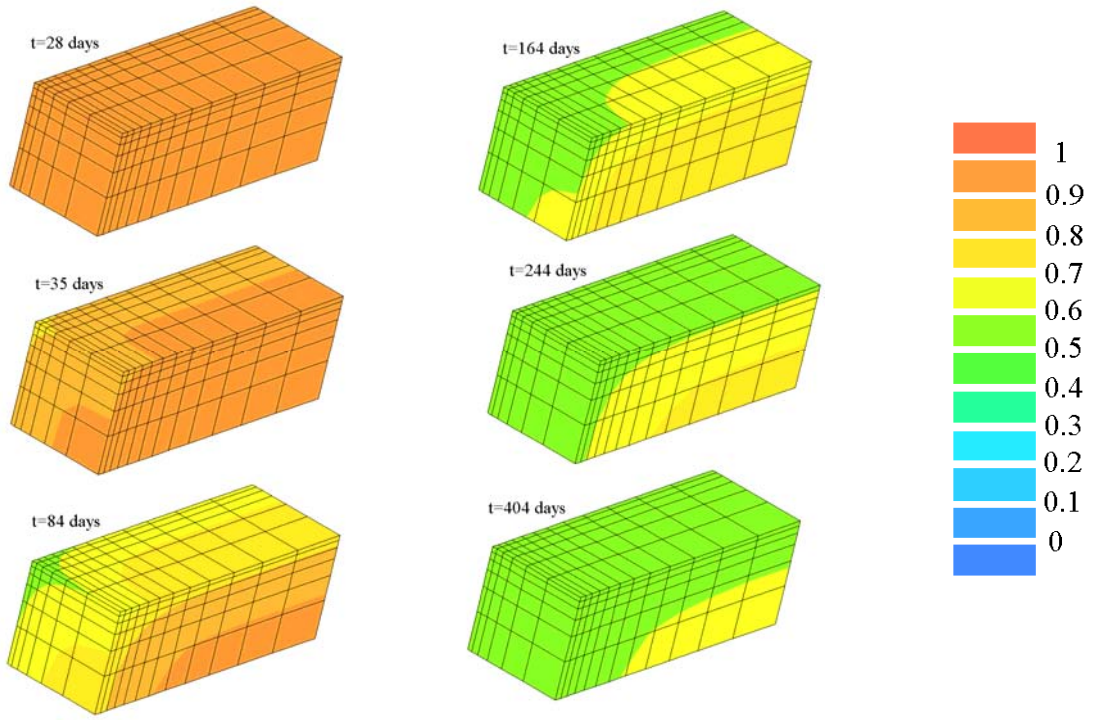

Figure 3.22: Evolution of the H field in specimen P200

After interpretation of results for the specimen P200, some comparisons of moisture field results for specimen P150 are performed for the control points P1 (inner core) and P3 (edge point located on the ZX plane of symmetry) – see Figure 3.23. Point P3 endures quite similar evolutions for both P200 and P150, even though in the case of P200 H remains slightly higher due to the higher internal supply of humidity (associated to the fact that this is a thicker specimen). In point P1, the differences are much more noticeable, with slower moisture losses in the thicker specimen, as expected. As a consequence, specimen P150 has lower H gradients than in P200, the latter being thus prone to the development of higher stresses.

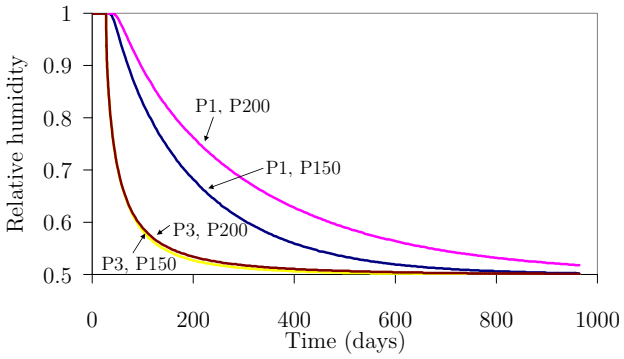

Figure 3.23: Comparison between computed H for specimens P200 and P150

3.14.3 RC Slab

The example to be discussed is a 25cm thick RC slab. For both thermal and hygral analysis, interactions with the environment are considered to occur only through the bottom and top surfaces of the slab, with one dimensional heat and moisture fluxes perpendicular to the slab's middle-plane. Even though the considered geometry is different from that of specimens P200 and P150 (Section 3.14.2), the same type of 3D FEM elements are used, and the thermal properties, as well as boundary transfer coefficients have the same values. Exposure to drying is considered to occur also at 28 days, with an external environment with T=20°C and H=50%.
The small thickness of the slab, as well as its relatively low cement content (250kg/m^3 as mentioned in Section 3.14.1), contribute to a small temperature rise in concrete due to heat of hydration. In fact, upon observation of Figure 3.24, where the temperature evolution is plotted, one can conclude that both the maximum temperature (~32°C) and maximum thermal gradient (~2.3°C) occur at the same time (~10h age). Bearing these results in mind, it is highly unlikely to expect significant stresses to be associated with the heat of hydration release.

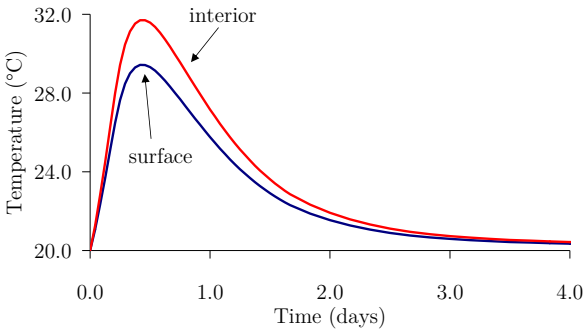

Figure 3.24: Thermal model: surface and core temperatures

Computation of moisture fields yielded the results depicted in Figure 3.25. After the age of 28 days, until which the slab remained at H=100%, exposure occurred, followed by a sudden drop in the H of the near-surface FE. The decrease in humidity progresses towards the core of the slab along time, causing it to be almost uniformly in equilibrium with the environmental H at the age of 3000 days (~8 years). The H gradient within the cross-section increases from 0 to a maximum of ~20% at the age of 88 days, and remains relatively constant until about the age of 200 days, time after which it decreases to a value of 1% at 3000 days.

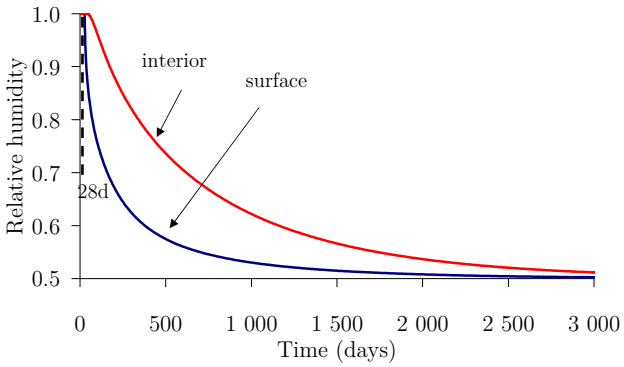

Figure 3.25: Moisture model: surface and interior H

The potential free shrinkage evolutions that result from the computed H, which will be used as inputs to the mechanical model, are shown in Figure 3.26. The well known tendency of concrete to progressively shrink from the surface towards the core can be confirmed by the observed curve evolutions.

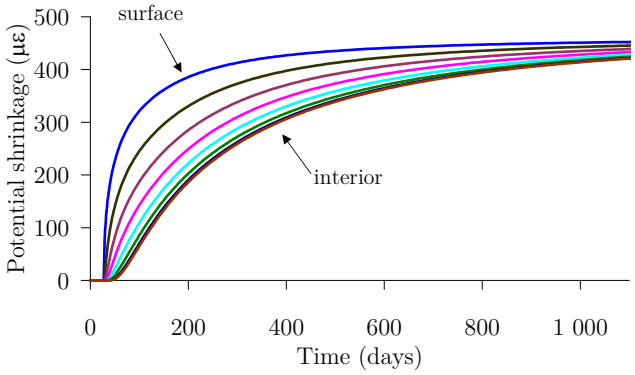

Figure 3.26: Potential drying shrinkage for all FE elements along the slab thickness

Chapter 4

Early age concrete as affected by environmental issues: use of a multi-scale model

4.1 Introduction

Although the main scope of this thesis is to develop a macro-level thermo-hygro-mechanical numerical framework, a part of its research concerning boundary condition formulations was conducted by using the multi-scale FE package DuCOM, developed at the Concrete Laboratory of the University of Tokyo, with a multi-component approach for hydration, concrete micropore structure development, as well as moisture transport. The conducted research involved laboratory experiments and numerical simulations, with the purpose of improving the DuCOM's boundary formulation for operation under arbitrary environmental conditions (temperature, relative humidity, wind speed). DuCOM is further used with the purpose of validating its capabilities of predicting near surface hindering of hydration reactions associated to moisture losses, as well as extending its aptitudes in simulating the phenomenon of evaporative cooling from cementitious materials.

The present chapter begins with a general description of the DuCOM framework, followed by some remarks on the current state of knowledge on evaporation from porous media (with particular emphasis on evaporation of plain water from water pans). After that, the experimental campaign on moisture losses from mortar at early ages is described, with focus on the effect of environmental factors (temperature, relative humidity and wind speed), age of sealing removal (i.e. the age at which concrete is exposed to drying), as well as the effect of the evaporative cooling phenomenon. Based on experimental evidence and

on the conducted literature review, an alternative boundary condition formulation for DuCOM is proposed.
With basis on the improved confidence on the predictive capacities of DuCOM, several sensitivity analyses are described, which in turn allow conclusions to be extracted with relevant utility for supporting several simplifications adopted in the thermo-hygro-mechanical numerical framework developed in the scope of this thesis.

4.2 The DuCOM numerical framework

4.2.1 Overview

Given the fact that all the numerical simulations reported in this chapter were conducted by using DuCOM, with implementation of a novel boundary condition formulation (proposed in Section 4.5), some remarks are made first regarding the overall outline of the numerical framework.
As stated before, this FE based microstructural model accounts for (*i*) the heat generated by cement hydration and consequent temperature development, (*ii*) the pore structure formation and (*iii*) the internal moisture transport (Maekawa *et al.* 1999, Maekawa *et al.* 2003). Many other phenomena are included in the current state of development of DuCOM, such as conservation of carbon dioxide, oxygen, chloride and calcium (Maekawa *et al.* 2003). However, only the main features of the models that were actually used - (*i*), (*ii*) and (*iii*) - are to be pointed out in the text that follows. It should be remarked that these descriptions are in no fashion intended to be extensive and thorough; rather, they aim to provide general information regarding the range of modelled phenomena and their degree of complexity. For particular information on each formulation, proper references are to be given throughout the descriptions.

4.2.2 Thermal model – multi-component hydration approach

As far as the heat development in cementitious materials is concerned, an equation based on Fourier's law is adopted (Maekawa *et al.* 1999)

$$\rho c \frac{\partial T}{\partial t} = div\left(k \nabla T\right) + \dot{Q} \tag{4.1}$$

where k is the thermal conductivity, ρc is the heat capacity, T is temperature, t is time and $\dot{Q}$ is the internal heat generation rate of the mix (concrete, mortar or cement paste). In DuCOM $\dot{Q}$ is computed upon use of a multi-component model (Kishi *et al.* 1995, Maekawa *et al.* 1999), in which the total heat generated by the cement hydration arises from the contribution of the several clinker components and other heat generating materials involved. This multi-component model comprises therefore four clinker minerals (aluminate C_3A, alite C_3S, ferrite C_4AF and belite C_2S), as well as other blending materials (fly ash FA and slag SG), which are included as pseudoclinker mineral components. Two further components exist in the model with regard to the heat contribution, due to the formation of ettringite from C_3A and C_4AF reactions with the

gypsum: C_3AET, C_4AFET. Computation of the heat generation rate of cement $\dot{Q}_C$ is performed by summing the heat generation rate of each of the considered components $\dot{Q}_i$, according to their corresponding mass ratio p_i in the mix (such that $\sum_i p_i = 1$):

$$\begin{aligned}\dot{Q}_C &= p_{C_3S}\,\dot{Q}_{C_3S} + p_{C_2S}\,\dot{Q}_{C_2S} + p_{SG}\,\dot{Q}_{SG} + p_{FA}\,\dot{Q}_{FA} \\ &+ p_{C_3A}\left(\dot{Q}_{C_3AET} + \dot{Q}_{C_3A}\right) + p_{C_4AF}\left(\dot{Q}_{C_4AFET} + \dot{Q}_{C_4AF}\right) = \sum_i p_i \dot{Q}_i\end{aligned} \tag{4.2}$$

The heat generation rate of each of the considered components, as well as the temperature dependent character of the chemical reactions, may be expressed by a modified Arrhenius Law of the form:

$$\begin{aligned}\dot{Q}_i &= \beta_i\,\mu\,\varepsilon\,\gamma\,s_i\,\dot{Q}_{i,T_0}\left(Q_i\right)\exp\left(-\frac{E_i\left(Q_i\right)}{R}\left(\frac{1}{T}-\frac{1}{T_0}\right)\right) \\ Q_i &= \int_0^t \dot{Q}_i\,dt\end{aligned} \tag{4.3}$$

in which the following coefficients are used to express the interdependence between the several chemical reactions involved: (*a*) the consumption of free water shared by all the components (coefficient β_i); (*b*) the deceleration of cement and slag chemical reactions due to the presence of fly ash or other additions (coefficient γ); (*c*) the dependence of behaviour of pozzolanic materials in regard to the available calcium hydroxide (coefficient ε), and (*d*) the mutual interactions between C_3S and C_2S (coefficient μ). The effect of the relative fineness (Blaine index) of each component is taken into account through s_i. $\dot{Q}_{i,T_0}\left(Q_i\right)$ is the reference heat generation for the i^{th} component at the reference temperature T_0=293 K (~20°C), and for the accumulated released heat Q_i. Proposed values for $\dot{Q}_{i,T_0}\left(Q_i\right)$ can be found in Figure 4.1. The ratios $-E_i(Q_i)/R$ are usually termed the thermal activities, and their plots are depicted in Figure 4.2.

Computation of the heat generation rate of the concrete mix $\dot{Q}$ for application in equation (4.1) is obtained by multiplication of the cement heat generation rate $\dot{Q}_C$ (computed according to equation (4.2)) by the volumetric cement content (C) in the mix.

A further output from the multi-component model is the degree of hydration α, defined as the ratio between the heat generated by cement at a given instant and the total expectable generated heat upon completion of the chemical reactions:

$$\alpha = {Q(t)}\Big/{Q_\infty} \tag{4.4}$$

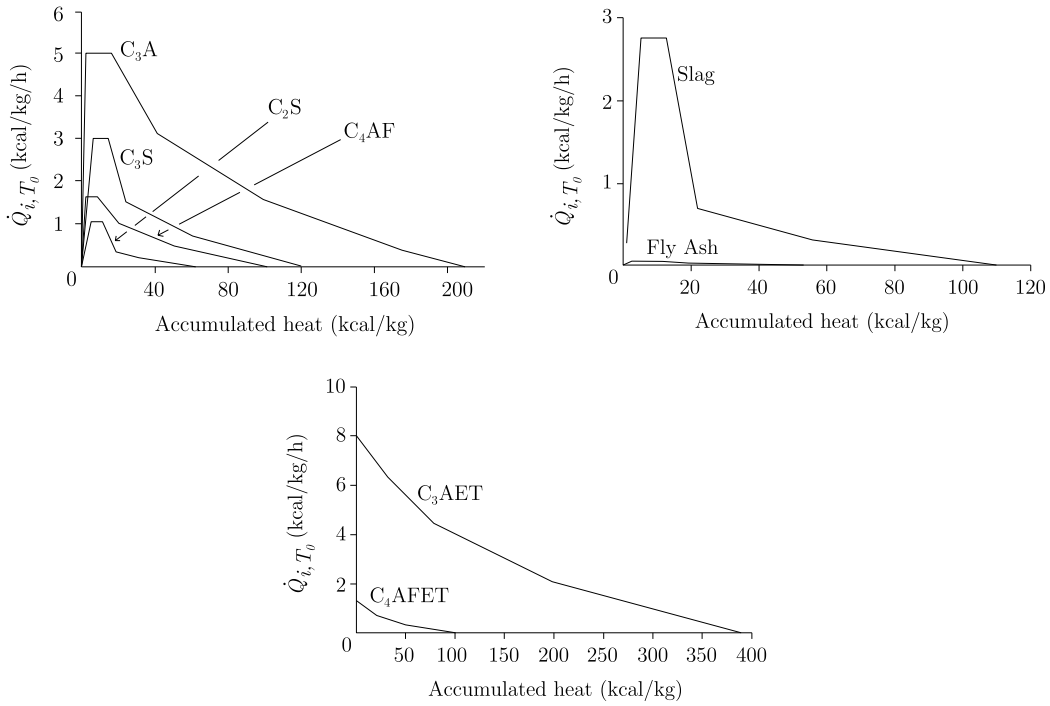

Figure 4.1: Reference heat generation rates for cement and pozzolans (Maekawa *et al.* 1999)

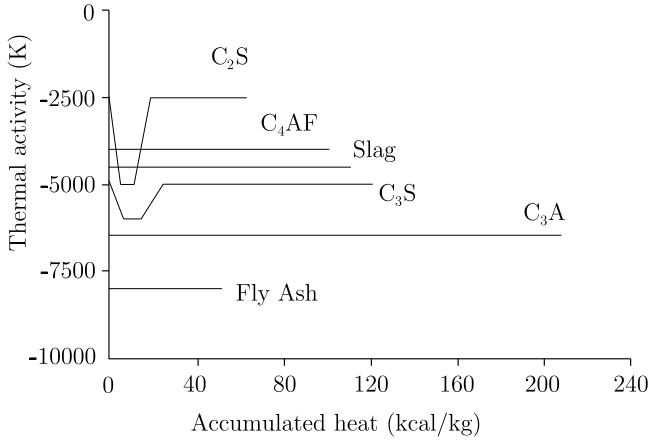

Figure 4.2: Thermal activities of several components (Maekawa *et al.* 1999)

4.2.3 Microstructure development model

Simultaneously with the chemically based computation of the heat generation described in the previous section, a pore structure is computed for the concrete, allowing for the existence of three classes of pores - capillary, gel and interlayer -, whose size distributions evolve during cement hydration. Capillary pores are empty spaces left between partially hydrated cement grains (acting as free space for subsequent precipitation of hydrate products), whereas gel pores are formed as an internal geometrical structure of the CSH grains, which deposit around a hydrating cement grain. Finally, the interlayer pores are located between the layer structure of the CSH gel grains.

The stereological model assumed for hydration in DuCOM assumes that the cementitious material consists of uniformly sized and uniformly distributed spherical particles. During hydration these spherical particles start to dissolve and reaction products precipitate, forming inner and outer products whether precipitation occurs within the boundaries of the initial particle or not – overall scheme of the model is shown in Figure 4.3. The microstructural properties of the inner products are assumed to be constant throughout the process of pore structure formation, and it is considered that hydrates of similar characteristics are formed at all the stages of hydration.

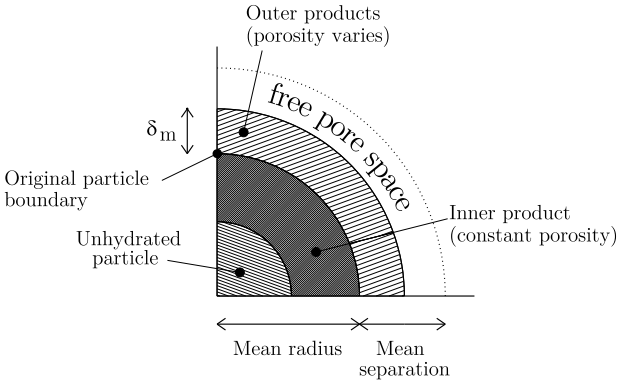

Figure 4.3: Micro pore-structure development model

Based on the mentioned assumptions, and upon knowledge of the degree of hydration α (with basis on the multi-component model described in the previous section), a model is derived that allows computing the capillary porosity ϕ_c, the gel porosity ϕ_g and the interlayer porosity ϕ_l as

$$\phi_c = 1 - V_S - (1-\alpha)\frac{W_p}{\rho_p} \tag{4.5}$$

$$\phi_g = V_S\,\phi_{ch} - \phi_l \tag{4.6}$$

$$\phi_l = \frac{t_w\, s_l\, \rho_g}{2} \tag{4.7}$$

where t_w is the interlayer thickness (~2.8Å), s_l is the specific surface area of interlayer, W_p is the weight of powder materials per unit volume, ρ_p is the density of the powder material, ϕ_{ch} is the gel particle's porosity (assumed as 0.28), ρ_g is the dry density of gel products and ρ_w is the density of chemically combined water (~1.25 g/cm^3). V_S represents the volume of gel products (per unit volume of paste), and it can be obtained at any stage of hydration according to

$$V_S = \frac{1}{1-\phi_{ch}}\left(\frac{\alpha W_p}{\rho_p} + \frac{W_{chem}}{\rho_w}\right) \tag{4.8}$$

where W_{chem} is the weight of chemically combined water per unit paste volume (computed with basis on stoichiometric relations of the hydration reactions).
The overall porosity distribution ϕ as a function of the pore radius r is computed with basis on the assumption of simple Raleigh-Ritz functions for pore size distribution, considering the contribution of the three classes of pores as

$$\phi(r) = \phi_l + \phi_g\left(1 - e^{-B_g r}\right) + \phi_c\left(1 - e^{-B_c r}\right) \tag{4.9}$$

where parameters B_g and B_c represent the peak of the porosity distribution on a logarithmic scale. Calculation of these parameters follows the assumption of cylindrical pore shapes, obtaining them from the computed porosity and surface area values for the capillary and micro-gel regions.

4.2.4 Moisture model

In DuCOM the moisture field within cementitious materials is calculated according to the following equation for mass balance in porous media (Maekawa *et al.* 1999)

$$\rho_L\left(\sum_i \phi_i \frac{\partial S_i}{\partial P}\right)\frac{\partial P}{\partial t} - div\left(k_L \nabla P\right) + Sd = 0 \tag{4.10}$$

where ρ_L is the pore water density, ϕ_i is the porosity of each i^{th} class of pores (interlayer, gel and capillary), S_i is the degree of saturation of the i^{th} class of pores, k_L is the moisture conductivity (for liquid and vapour), P is the equivalent liquid pore pressure and Sd is the sink term (it reflects the internal moisture loss due to water consumption in cement hydration reactions, and the changes in the bulk porosity distribution of the hardened cement-paste matrix).
Without going into specific details (for such purpose see Maekawa *et al.* (1999)), general remarks are made in regard to equation (4.10) and some of the parameters involved that imply by themselves the use of secondary models. Firstly it is pointed out that the selected driving potential for this equation is P (equivalent liquid pore pressure), which corresponds to the pore pressure of condensed water, thus allowing saturated and unsaturated conditions to be covered consistently. The degree of saturation S_i is computed with basis on the calculated porosity distribution, allowing the knowledge of the critical radius of saturation (i.e., the pore radius below which all pores are saturated at a given moisture state), as well as the evaluation of adsorbed water in unsaturated pores through the use of a modified BET (named after S. Brunauer, P.H. Emmet and E. Teller) model (Maekawa *et al.* 1999).
As discussed in detail in Chapter 3, the relationship between water content and the humidity state of the pore structure is not linear, and does not follow the same path in adsorption and desorption (hysteretic behaviour). This effect is taken into account

through the term $\partial S_i/\partial P$ in equation (4.10), which is termed moisture capacity, and has an underlying model that involves the integration of the pore saturation over the entire porosity distribution of the porous media.
The moisture conductivity term k_L comprises two components: (*i*) one pertaining to vapour transport, which is based on the Knudsen diffusion theory, formulated for vacant micro-pores where vapour movement is possible; and (*ii*) the other corresponding to the liquid transport, based on the micro-pore distribution occupied by condensed water. Finally, the sink term *Sd* reflects two main phenomena, the first one being the reduction in porosity associated with hydration of cement, that clearly has an influence on the liquid pressure. The second effect is the moisture consumption associated to hydration. Both terms are computed with information gathered from the hydration and micropore structure models.
It is therefore noticeable that the outputs of the hydration model (spatial distributions of temperature and degree of hydration) and the micropore structure model (calculated porosities) described in the previous section are inputs for several parameters involved in equation (4.10). On the other hand, the moisture variations inherent to equation (4.10) affect the availability of water, which in turn influences the heat generation rate in equation (4.1), with direct consequences on the micropore structure development. Based on this reasoning, the mutual interaction of the three models under several aspects becomes therefore quite clear.

4.3 Remarks on drying of porous media

4.3.1 Prediction of water evaporation

Before a direct application to concrete, some considerations will be made regarding the current state of knowledge on evaporation from free water surfaces. Prediction of water evaporation is an important issue for many fields of science such as hydrology, irrigation, oceanography, meteorology and many more. In the past, much effort has been devoted to the achievement of a water evaporation prediction method, particularly in the last two centuries (Keey 1972, Marek *et al.* 2000), and therefore a very wealthy source of information can be found by literature research.
Evaporation from a water surface to the surrounding air environment (containing water vapour) can be regarded as the balance of the number of molecules that actually evaporate from the water interface, and the number of water molecules in the vapour that condensate in the interface. With basis on the kinetic theory of gases, the evaporation from a water surface to the surrounding air can be expressed by the Hertz-Knudsen equation (Jones 1992)

$$\Phi_0 = \frac{E_v}{\sqrt{0.5\ \pi\ m\ k\ T_S}} \left(e_s - e\right) \tag{4.11}$$

where Φ_0 is the molecular flux (number of molecular impacts per unit area of water surface and per unit time) [kmol m^{-3}], E_v is the evaporation coefficient (non-dimensonal), m is the mass of each water molecule, k=1.38×10^{-6}JK^{-1} is the Boltzman's constant, T_S is

the temperature of the liquid surface, e_s is the saturation vapour pressure [Pa] of water at temperature T_S and e is the vapour pressure [Pa] in the gas medium (environment) at temperature T. About this equation, the following comments are pertinent:

- The driving potential for evaporation of water is the difference in vapour pressure between the water surface and the environment.
- Coefficient E_v is of empirical nature, and to the present date, there is no analytical way to define its value.

The saturation vapour pressure of water is temperature dependent, and it can be calculated by using the Clausius-Clapeyron equation in the following form

$$e_s = p_0 \; e^{-\frac{H_{vap}}{R}\left(\frac{1}{T_S}-\frac{1}{T_0}\right)} \tag{4.12}$$

where p_0=1.01×10^{5}Pa is the reference pressure, T_0=373K is the reference temperature, R=8.314 Jmol^{-1}K^{-1} is the universal gas constant and H_{vap}=40.7×10^3 Jmol^{-1} is evaporation heat of water at the reference temperature.

Upon knowledge of the relative humidity of the environment, the vapour pressure of the air can be calculated by multiplying the relative humidity (H) by the saturated vapour pressure at temperature T:

$$e = e_s \, H \tag{4.13}$$

Generally speaking, for practical purposes equation (4.11) can be represented in a simplified manner by

$$q_S = -E_S \left(e - e_S\right) \tag{4.14}$$

where E_s is the moisture emissivity coefficient [kgm^{-2}s^{-1}Pa^{-1}] and q_S is the moisture flux [kgm^{-2}s^{-1}]. In literature (Bansal *et al.* 1998, Eames *et al.* 1997, Jones 1992, Marek and Straub 2000, Pauken 1999) many empirically based formulas for evaporation prediction (within a micro-climatic scope) can be found, most of them having in common the two facts mentioned above: (*i*) the vapour pressure difference as the driving potential for evaporation, and (*ii*) the existence of a evaporation coefficient that can be dependent of factors such as the geometry of the evaporating surface and the wind speed, among others. Also, in concrete engineering (ACI 2001, Al-Fadhala *et al.* 2001) some similar empirical equations have been forwarded to predict the evaporation of bleeding water over a concrete surface.

A brief overview of some existing equations that relate the moisture emissivity coefficient with the wind speed V (m s^{-1}) is presented.

- From Hinchley and Himus (quoted in (Bansal and Xie 1998, Jones 1992, Pauken 1999)):

$$E_S = 2.777 \times 10^{-10} \left(125 + 75.5 \; V\right) \tag{4.15}$$

- From Bansal and Xie (1998), for V<5m/s :

$$E_S = 2.08385 \times 10^{-6} \times \left(0.002198 + 0.0398\ V^{0.5756}\right) \tag{4.16}$$

- From Menzel (ACI 2001, Al-Fadhala and Hover 2001, Uno 1998), with V measured at the height of 0.5m above the water surface:

$$E_S = 2.08385 \times 10^{-6}\ \times 0.0415 \times \left(0.253 + 0.215\ V\right) \tag{4.17}$$

- From Rowher (quoted in (Pauken 1999)):

$$E_S = 2.777 \times 10^{-10} \times \left(232.5 + 101\ V\right) \tag{4.18}$$

A comparative plot of the results output by equations (4.15), (4.16), (4.17) and (4.18) can be observed in Figure 4.4.

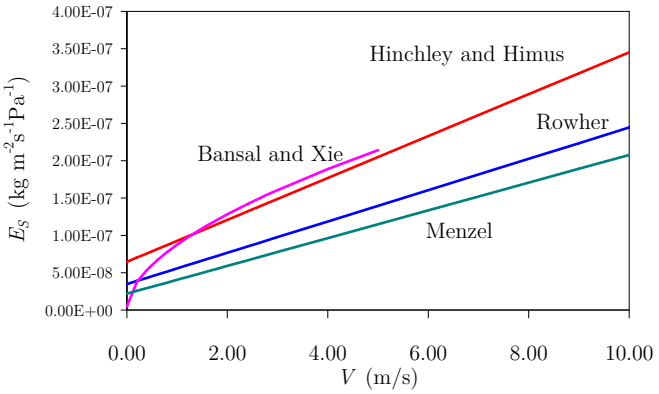

Figure 4.4: Empirical predictions for moisture emissivity

It can be noticed that some differences exist between different prediction formulas, which can be caused by factors related to their basic assumptions and experimental procedures: the size of surface from which tests were conducted, the height at which wind speed measurements were taken, turbulence of the flow, wind speed profile of the free stream, range of tested wind speeds, etc.

An alternative way of defining E_s would be using the Lewis' relationship, based on the similarity approach of the boundary layer theory (heat and mass transfer analogy (Incropera and DeWitt 1996)). The Lewis relationship allows the estimation of convection heat transfer coefficients from moisture emissivity coefficients and vice-versa. The Lewis relationship can approximately be stated as (Chuntranuluck *et al.* 1998)

$$\frac{h_T}{E_S} \approx \frac{29\ c_a\ P}{18} \tag{4.19}$$

where h_T is the convection heat transfer coefficient [Wm^{-2}K^{-1}], c_a is the specific heat capacity of air (1007Jkg^{-1}K^{-1}) and P is the total air pressure (usually around 1.01×10^{5}Pa). By applying equation (4.19) to the empirical formulas for predicting the convection heat transfer coefficients presented in Chapter 2 of this thesis (see Section 2.5.1), and plotting the resulting values against the prediction formulas for moisture emissivity coefficients

(equations (4.15), (4.16), (4.17) and (4.18)), Figure 4.5 is obtained: a good coherence can be observed between Rowher prediction and the Lewis transformed predictions of McAdams, Branco and Silveira. This fact points to a plausible validity in the use of the Lewis's relationship, once either heat or moisture transfer coefficients, or even both, are known.

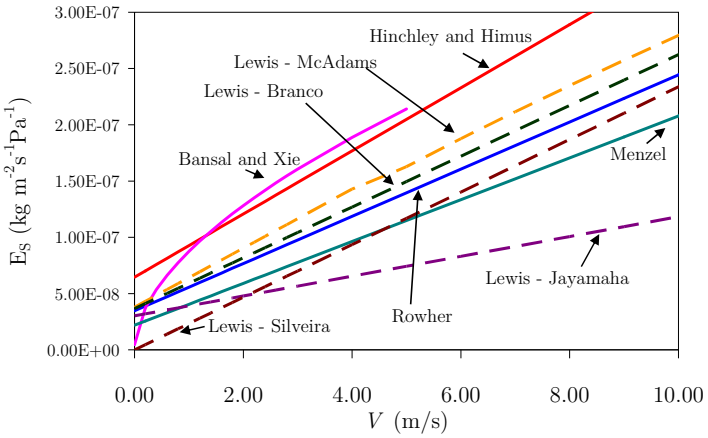

Figure 4.5: Moisture emissivity coefficients based on Lewis's relationship, and on empirical predictive formulas

For evaporation to occur and persist, three basic conditions should be satisfied (Hillel 1998):

1. There should be a supply of heat large enough to reach the latent heat of water. This means that for water to evaporate from the free surface an energy barrier should be overcome. Usually this energy can be obtained by simply cooling the water surface, causing a phenomenon that is usually known as evaporative cooling.
2. The vapour pressure in the air should remain lower than the one at the evaporating surface. This condition can be easily understood by analysing equation (4.11): a pressure gradient is necessary to act as driving potential.
3. There must be a supply of water to evaporate. This is an obvious condition when evaporation from a free water surface is concerned, but if evaporation from a porous body is regarded, this condition may assume critical importance.

Acquaintance of these three conditions is necessary for some considerations that will be made further on this document.

4.3.2 Evaporation in porous media

Until this point some important facts have been discussed about evaporation of water from a free water surface, but for porous media such as concrete, some further considerations have to be made.

Cementitious materials are known to have a wide range of pore diameters within their pore structure, spanning from radiuses as small as 10^{-10}m (gel pores), to radiuses up to 10^{-2}m (air voids). Due to the existence of pores with radius smaller than 1μm, significant lowering of vapour pressure within the pores can occur according to the Kelvin equation (which describes the change in vapour pressure due to a curved liquid/vapour interface).

This kind of pore exhibits energetic retention of moisture, and the porous media where this pore range exists are therefore called hygroscopic.
Along drying of initially saturated porous media four main stages can be distinguished, as depicted in Figure 4.6 (Keey 1972). Firstly (Stage 1) moisture flows as liquid water under hydraulic gradients. In Stage 2, because of drying, some air pockets appear, and water withdraws to the waists of the pores, migrating either by creeping along the capillary walls or by successive evaporation and condensation between liquid bridges. On further drying (Stage 3), the liquid bridges evaporate entirely, leaving only adsorbed moisture behind. In the final Stage 4, moisture just flows as vapour along the dry pores.

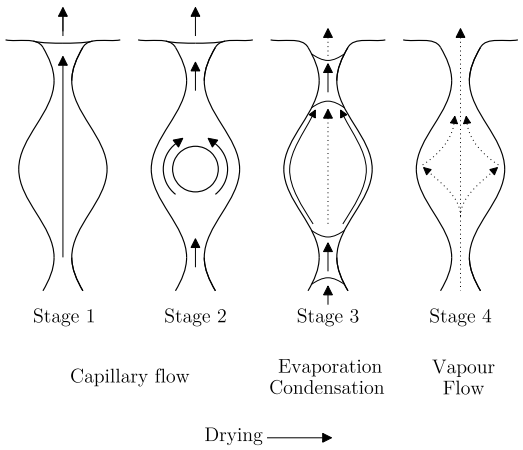

Figure 4.6: Moisture at various stages of drying in a porous material

Therefore, in terms of the global drying of a cementitious solid some distinct behaviours are expectable, according to the general moisture state of the pore structure. Generally speaking, three main distinct phases can be distinguished on the global drying of cementitious solids, and accordingly attention is drawn to Figure 4.7, where a schematic plot of the rate evolution of weight loss of an initially saturated porous solid is depicted. At an initial phase I, superficial moisture is present, and therefore the drying rate is controlled by factors related to the surrounding environment (radiation, wind, air temperature and humidity, etc.), rather than by the moisture profile inside the solid. Therefore the drying rate is constant, performing in a very similar fashion to the drying of a free water surface. In other words, it can be said that during this initial phase the moisture transport in the material is faster than the mass transfer to the atmosphere by the air flow (Pel *et al.* 2002).
As drying proceeds (phase II), the water supply to the surface of the solid by capillary forces becomes insufficient to replace the liquid being evaporated, and the water film that initially existed on the surface starts to be disrupted at some points. As a consequence, the global drying rate decreases during this phase.
Finally on phase III a residual slow drying stage occurs, which may persist as a near steady state condition for long periods of time. This stage apparently occurs when the cementitious surface becomes so desiccated that further conduction of liquid water to the surface is limited to the few small sized pores that remain saturated (or partially saturated) in equilibrium with the surrounding environment. Water transmission through the desiccated layer occurs primarily by the slow process of vapour diffusion. This stage is

usually called diffusion controlled, once the rate of evaporation from the solid is completely governed by the diffusion characteristics of the solid. This is a situation in which the third condition for evaporation mentioned in 4.3.1 has clearly become the key factor for the rate of moisture loss. According to Selih *et al.* (1996), this third stage of drying is reached when the average moisture content decreases below 70-80% of total saturation.

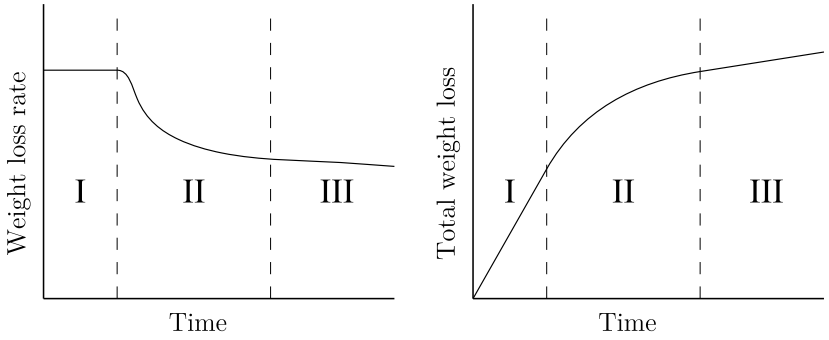

Figure 4.7: Weight losses along drying

In the context of freshly cast concrete surfaces exposed directly to the environment, the transition from phase I to the subsequent phases of drying has been identified by Al-Fadhala and Hoover (2001), that proposed an empirical formula to predict the decrease of the rate of moisture loss from a cementitious surface when compared to the rate of moisture loss from a water pan:

$$\frac{E_C}{E_S} = e^{-\left(\frac{t}{a}\right)^{1.5}} \tag{4.20}$$

Here E_C is the moisture emissivity coefficient for the concrete/mortar, E_S is the moisture emissivity coefficient for the water pan, t is the time after casting [h] and a is a time constant that depends on the mixture (a=3.75h for concrete; a=6.16 for mortar). This equation is not claimed to be of universal application for any composition of concrete/mortar, as it is in fact comprehensible that the evolution of the rate of moisture loss is dependent on many further influences, such as: the water vapour concentration in the atmosphere, the wind speed, the w/c ratio of the concrete/mortar, the geometry of the specimen under consideration, the temperature field created by the exothermic hydration reactions, the age at which the surface is exposed to the environment and the hydration extent. For a more general way of predicting the evolution of the moisture loss from a cementitious material a numerical tool for modelling moisture transport inside the material, with explicit consideration of the evolution of the pore structure at early ages (such as in DuCOM) would be necessary. With the purpose of obtaining validation examples for the numerical models, an experimental campaign that is described in the following section was conducted within the present PhD work.

4.4 Experimental campaign

4.4.1 Introduction

An experimental campaign was undertaken to assess the many influences that affect the moisture removal from mortar specimens, having in mind the considerations related to drying of porous media referred to in the previous section. For all the experiments in this campaign, mortar specimens cast with ordinary Portland cement were used. Two w/c ratios were considered: w/c=0.35 (mixes named as 'H') and w/c=0.55 (named as 'N'), with the compositions reproduced in Table 4.1. The water content in sand was measured immediately before casting, and the proportions of the mortar components were adjusted in order to assure that the w/c ratios were precisely the ones referred above. The general idea of most of the experiments was to study the effect of exposing mortar specimens to different environmental situations (in terms of temperature, relative humidity, wind speed or even age of exposure) on the loss of water out of those porous media. To assure known and constant environmental conditions in terms of T and RH, controlled environment chambers were used. For the experiments to simulate the influence of wind on moisture losses, a wooden wind tunnel and a fan were used. For ages of exposure greater than 0 days, initial sealing of specimens was undertaken. At the end of this section experiments regarding evaporative cooling are also presented, reporting the measured temperature drops that occurred in mortar specimens immediately after the sealing removal.
For most of the tests, two specimens were cast per situation. In addition, and to compare the evaporation from a water surface with the ones from the mortar specimens, containers with water samples were also tested for all the analyzed environmental conditions.

Table 4.1: Composition of the used mortars

	Water (kgm^{-3})	Cement (kgm^{-3})	Sand (kgm^{-3})
w/c=0.55 - N	311	565	1315
w/c=0.35 - H	257	734	1315

4.4.2 Effects of relative humidity and temperature on early water loss

Three combinations of temperature and relative humidity conditions were considered for the two mortar compositions: (i) T=20°C and RH=60%; (ii) T=35°C and RH=30%; (iii) T=60°C and RH=60%. The specimens were cast at a temperature of 20°C into a cylindrical container with an internal diameter of 5cm and a height of 5cm (see Figure 4.8a). After casting, no curing measures (that is, sealing or submersion) were adopted, and the specimens were immediately exposed to the environmental conditions (i), (ii) and (iii). Weightings in a high precision weight scale, with a resolution of 0.001g (see Figure 4.8b) were conducted for all specimens within regular intervals, selected in accordance to the observed gradients of weight losses.

a) b)

Figure 4.8: a) Cylindrical specimen used in the experiments; b) High precision scale

Measurements performed for the described experiments with mortar and water samples are depicted in Figures 4.9, 4.10 and 4.11 for environments (i), (ii) and (iii). From these figures it becomes clear that good coherence was obtained in measurements made for the specimens within each pair. Also, the evaporation rate is very similar for mortar and water specimens during the initial period (phase I of evaporation) for the three environmental conditions, which indicates that during this period the mortar surface is able to remain saturated (or almost) long enough to keep evaporation environmentally controlled. The end of this phase is reached due to shortage of water on the drying surface, as a consequence of the mechanism explained in Section 4.3.2, as well as due to water consumption in the cement hydration reactions. Besides, the increasingly denser pore structure of cement augments the difficulty for the water to migrate from the core to the evaporating surface of the specimen. Bleeding may also influence the transition from the environmentally controlled phase to the diffusion controlled one, as it engenders a supply of water to the surface, maintaining it wet for longer times. In the cases reported in this study, the observed bleeding was small or even negligible, and thus it can be considered to have had a minor contribution to the observed results.

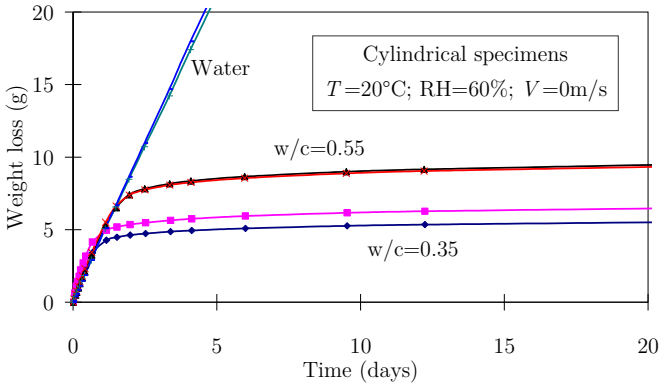

Figure 4.9: Weight losses for environment with T=20°C, RH=60%

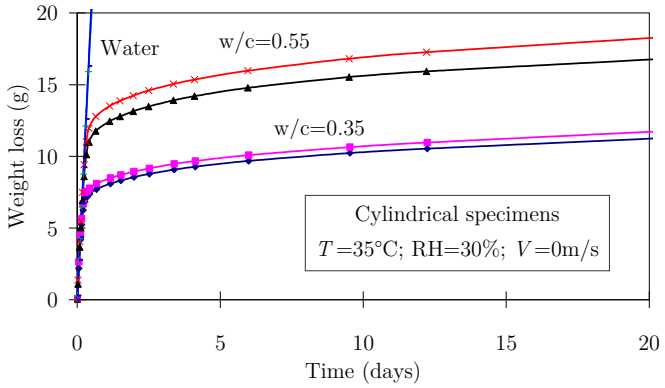

Figure 4.10: Weight losses for environment with T=35°C, RH=30%

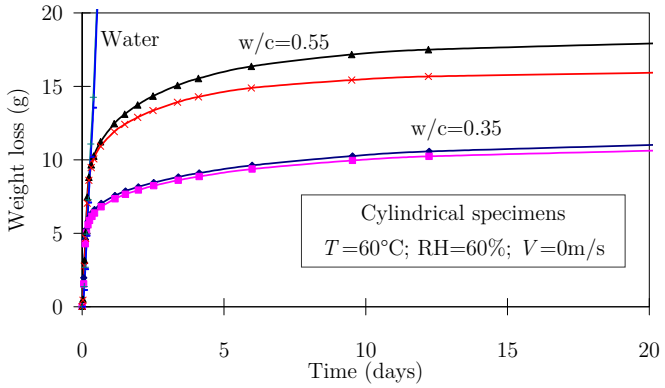

Figure 4.11: Weight losses for environment with T=60°C, RH=60%

Regarding the evaporation rates in the water specimens, some interesting remarks can be made by recalling the prediction equation (4.17) from Menzel (Uno 1998) for the moisture emissivity coefficient, together with equation (4.14) for evaporation fluxes from a water surface. By analyzing equation (4.14) two contributions may be individualized: the moisture emissivity coefficient that is dependent on the wind speed, and the vapour pressure differential between the liquid and the environment. In Table 4.2 a summary is presented of the main experimental observations for the three selected environmental conditions, and respective numerical calculations performed with equations (4.14) and (4.17). It can be observed that the rates of weight loss for environments (ii) and (iii) are much higher than the one measured in situation (i), which can be explained by the very large difference that can be found in the magnitudes of the vapour pressure difference (henceforward referred to as 'driving potential'). Justification of the differences in the evaporation rate for situations (ii) and (iii) is not so straightforward: in fact, taking solely the driving potential into account the expectable evaporation rate for situation (iii) should be greater than for (ii), according to column 5 of Table 4.2. A crucial aspect that should be kept in mind in this comparative study is the following: the chamber adopted for the environmental condition (ii) had more ventilation requirements than the one used to create the environmental condition (iii). Therefore, combination of the moisture emissivity coefficient with the driving potential has led to a higher rate of evaporation for situation (ii). Computing E_S from equation (4.14), together with the driving potentials,

and applying equation (4.17) allowed the estimation of the wind speeds for the three environments as shown in the last column of Table 4.2.

Table 4.2: Evaporation from cylindrical shaped water specimens

Environment	T (°C)	RH (%)	Measured rate of weigh loss (g/day)	e-e_s (Pa)	E_S (kg m^{-2} s^{-1} Pa^{-1})	Estimated V (m s^{-1})
(i)	20	60	4.4	936.3	2.79×10^{-8}	0.33
(ii)	35	30	39.1	3933.1	5.85×10^{-8}	1.97
(iii)	60	60	36.9	7967.3	2.73×10^{-8}	0.29

Referring back to Figures 4.9, 4.10 and 4.11, in the three studied environments the transition from an environmentally controlled evaporation to a diffusion controlled one (identifiable by the change of the shape of the moisture loss behaviour from a straight line to a curved one) occurs later for the 'N' composition than for the 'H' one, and the intermediate period seems to last longer for the 'N' composition. This is probably due to the following combination of factors: lower amount of water available in the 'H' composition; higher cement content in the 'H' composition that increases self-consumption of water; faster build up of a denser pore structure for the 'H' composition. In what concerns to the total weight losses at 20 days, they were higher for environments (ii) and (iii) than for (i). The reason for this is that in situations (ii) and (iii) much higher quantities of water were removed by the environment before the mortar pore structure had the time to become dense enough as to hinder migration of water towards the evaporating surface.

4.4.3 Effect of wind speed on early water loss

To investigate the effect of wind on evaporation from mortar surfaces, tests under three distinct wind speeds were conducted. Dimensions of the mortar prismatic specimens used for these experiments were $7.3\times5.1\times3.0\text{cm}^3$, and drying was allowed solely by the top surface, with dimensions $7.3\times5.1\text{cm}^2$ (see Figure 4.12a). Casting, curing and weight measurement procedures were the same as mentioned in Section 4.4.2. The tests were carried out in a controlled environment with T=20°C and RH=60%.

For wind testing, an ordinary fan combined with a hand made wind tunnel (based on the geometry of the one formerly mentioned by Sun and Marrero (1996)) were used (Figure 4.12b), according to the setup and geometry depicted in Figure 4.12c. Three different wind speeds (V) inside the wind tunnel were tested - 1.8m/s, 3.3m/s and 4.2m/s -, which were measured with a hot wire anemometer placed 130mm above the exposed surface of the specimens. Detailed description about the assembly and calibration of wind speeds in the wooden wind tunnel may be found in Azenha *et al.* (2005). Since only a single wind tunnel was available, the three wind speed situations were not tested simultaneously. Therefore, as the experiments were started immediately after casting, three mortar batches (mixed at different dates) were necessary. Simultaneously with the evaporation

tests under each wind speed, control specimens not subject to forced wind were also monitored. With this strategy repeatability of the mortar casting and mixing operations, as well as of experimental conditions was checked.

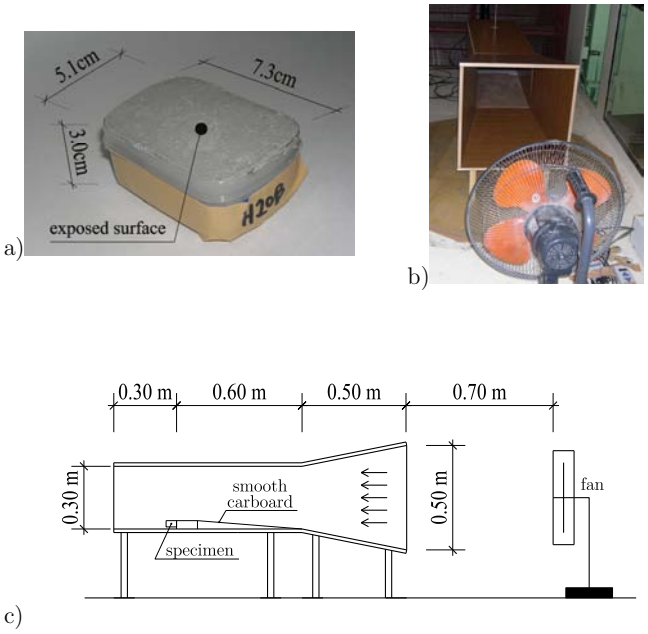

Figure 4.12: a) Prismatic specimen; hand-made wind tunnel: photo (b) and scheme (c)

Results of the experimental campaign are depicted in Figures 4.13, 4.14, 4.15 and 4.16, which report the weight losses from the freshly cast prismatic specimens as a function of time for each wind speed. Once again, good coherence was found on the results within each pair of specimens. Also, consistency of results between the various tests conducted for the stagnant air situation confirms the good repeatability of the adopted experimental procedures.

For all experiments with V>0m/s the initial rate of evaporation from the water samples matched the one from mortar specimens during the environmentally controlled phase. In the case of the stagnant air tests (Figure 4.13) this match was not observed, unlike it happened in the set of experiments described in Section 4.4.2 for the same environment (yet with cylindrical specimens - see Figure 4.9). No explanation for this faster evaporation when cement is present could be found in the bibliographic review that was made for this research. Having ruled out the possible effect of temperature rise due to heat of hydration (the measured temperature rises were very low and cannot account by themselves for the observed differences), the observed tendency may be due to an acceleration of the evaporation rates of the water present in mortar due to the chemical reactions of cement that occur at early stages (which may be more noticeable for the cases of stagnant air than for those where V>0m/s).

As expected, the initial evaporation rates increased with the wind speed in a quite consistent manner, when compared to the predictable tendencies that would be obtained by using equation (4.17). Yet, in what concerns the overall trends of the moisture loss curves it is evident that there are more important differences when the stagnant air situation (Figure 4.13) is compared to the forced wind situations (Figures 4.14, 4.15 and

4.16), than between the forced wind situations themselves. This can be confirmed by comparing the total weight losses at the age of 8 days for w/c=0.55: 15g for V=0m/s; 18.4g for V=1.8m/s; 20g for V=3.3m/s and 19.6g for V=4.2m/s. The unexpected slightly larger moisture loss for V=3.3m/s than for V=4.2m/s leads to the conclusion that at this level of wind velocities the real differences in the overall moisture losses are small enough to be overcome by the inevitable dispersion of the experimental campaign results.
The tendency for earlier transition to diffusion controlled evaporation (i.e. threshold between phase I and phase II, identifiable by deviation of the moisture loss curve from the initial straight line) in the 'H' mortar, when compared to the 'N' mortar, is also confirmed in Figures 4.13, 4.14, 4.15 and 4.16. Furthermore, such transition occurs sooner for increasing wind speeds.

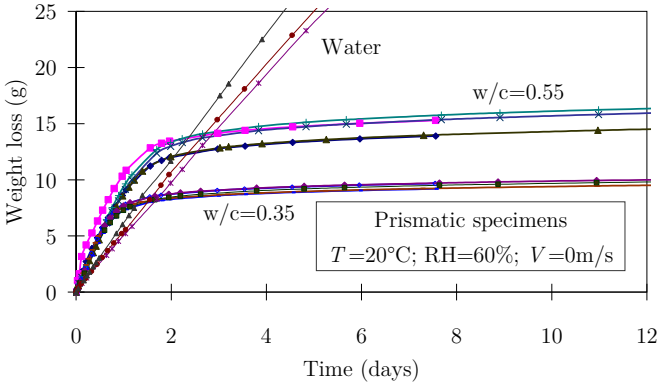

Figure 4.13: Weight losses for wind speed V=0m/s

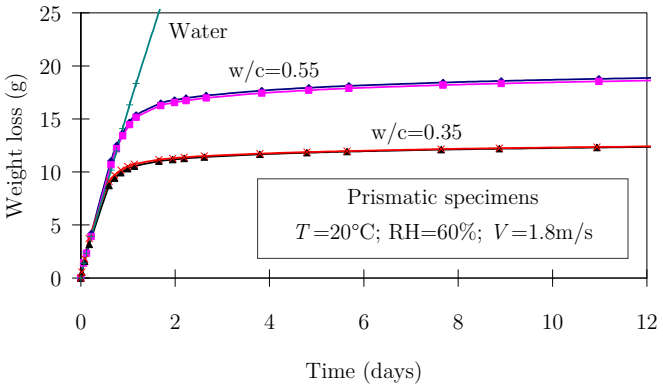

Figure 4.14: Weight losses for wind speed V=1.8m/s

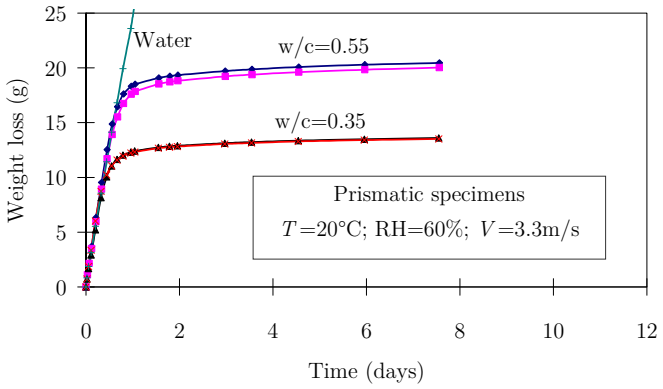

Figure 4.15: Weight losses for wind speed V=3.3m/s

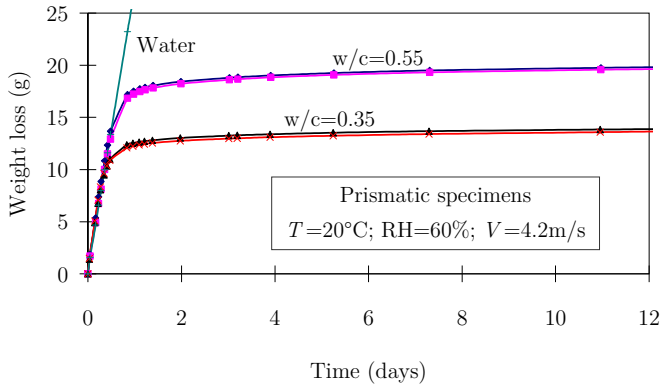

Figure 4.16: Weight losses for wind speed V=4.2m/s

Assuming completion of stage I of drying, that is, when evaporation from mortar specimens starts to deviate from what is observed in water samples, duration of this phase as a function of the wind speed is plotted in Figure 4.17 for the two mortar mixes under study. It is interesting to observe that the duration of such phase is shortened as the wind speed increases, and that the ratio between the duration of phase I for mortars 'N' and 'H' is always about 1.6, which is also the quotient between their w/c ratios. This points to the duration of the drying phase I to be linearly dependent on the available water in the mix.

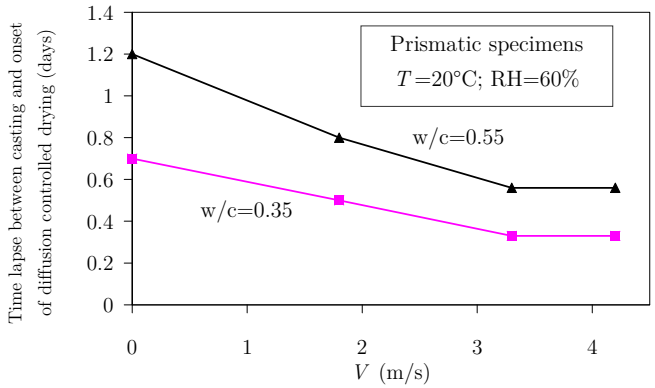

Figure 4.17: Onset of diffusion controlled drying as a function of wind speed

4.4.4 Effect of sealing period on early water loss

In this set of tests the specimens, with the same prismatic geometry described in Section 4.4.3, were sealed immediately after casting and maintained that way until the following ages: 1 day, 3 days and 7 days. Upon sealing removal, which exposed solely the top 7.3×5.1cm^2 specimen surface, the water drops observed in some cases for this surface were removed with the aid of a moist cloth. All tests were conducted with the 'N' mortar composition, under an environment with T=20°C and RH=60%. In terms of wind speed, three conditions were considered: V=0m/s, V=1.8m/s and V=4.2m/s. The number of tested specimens per environmental situation is summarized in Table 4.3. For the V=4.2m/s case one specimen out of each pair was placed with the exposed surface vertically, facing the wind stream, in order to investigate the effect of the wind incidence direction on the water loss from the specimen.

Table 4.3: Number of specimens per environmental situation

	V=0m/s	V=1.8m/s	V=4.2m/s
1 day removal	3	2	2*
3 days removal	2	2	2*
7 days removal	1	-	-

*one of the specimens with the evaporating surface in vertical direction, facing upstream

Figures 4.18, 4.19 and 4.20 report the monitored weight loss evolutions, taking also into account the relevant wind speeds. From these figures it is noticeable that water losses from the mortar specimens are reduced as sealing removal occurs later. This tendency can be confirmed by comparing the average water losses 9 days after sealing removal for the cases with V=0m/s: for a removal age of 1 day the water loss is about 8.2g (Figure 4.18), for 3 days it reaches 6.3g (Figure 4.19) and for 7 days it becomes about 5.1g (Figure 4.20). Also, onset of diffusion controlled evaporation seems to occur sooner for later sealing removal – see Figure 4.21. These trends are most probably due to the fact that upon later sealing removal a denser pore structure exists, and less water is likely to be available after a higher cement hydration level is achieved.

All mortar specimens appear to exhibit the same trend as that of the companion water samples, in what concerns the rate of evaporation immediately after sealing removal (see Figures 4.18, 4.19 and 4.20).

For sealing removals occurring after the age of 1 day the effect of wind speed on the evaporation seems to be much smaller than what happened in the case of exposure right after casting. This is a consequence of the mentioned anticipation of onset of the diffusion controlled evaporation that takes place when specimens are initially sealed: from then on wind speed has no effect on the evaporation rate. So, the small differences in the weight losses under different wind speeds are mostly due to the evaporation that occurred during stage I, rather than during the diffusion controlled phase.

According to Figure 4.18 and Figure 4.19 it is also possible to observe that the two pairs of mortar specimens that were placed in different positions in relationship to the wind stream direction for V=4.2m/s exhibit almost the same weight losses during the whole experiment. This result points to a possible independence of the water loss from cementitious materials with respect to the wind direction, as a consequence of the predominance of the diffusion controlled water loss mechanism in the partially hydrated paste.

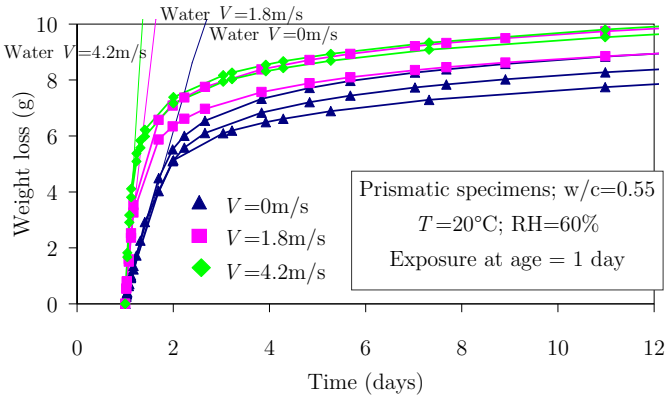

Figure 4.18: Weight losses for sealing removal at 1 day of age (w/c=0.55)

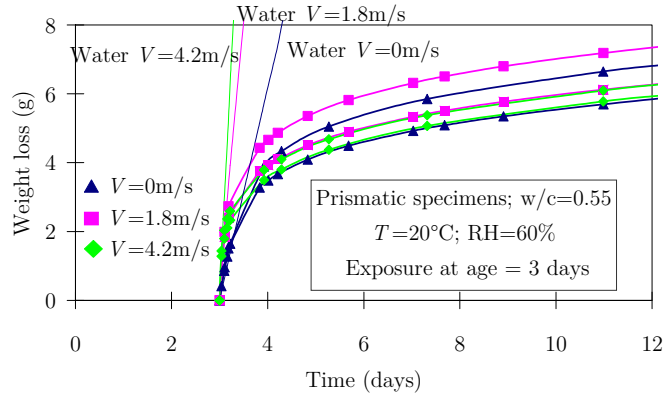

Figure 4.19: Weight losses for sealing removal at 3 days of age (w/c=0.55)

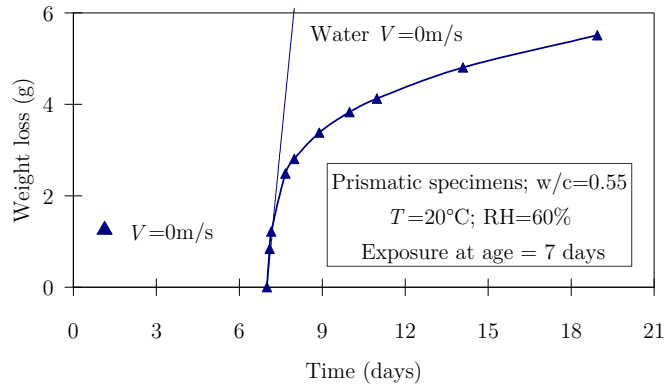

Figure 4.20: Weight losses for sealing removal at 7 days of age (w/c=0.55)

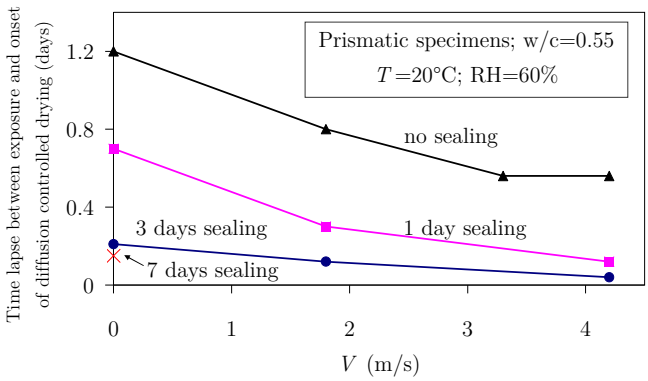

Figure 4.21: Onset of diffusion controlled drying as a function of wind speed (w/c=0.55)

4.4.5 Effect of evaporative cooling

As mentioned in Section 4.3, one of the necessary conditions for evaporation to occur is the supply of a minimum energy to promote the phase change. This energy is called '*latent heat of vaporization*', and when provided by the liquid or solid from where water is evaporating, a phenomenon of '*evaporative cooling*' is said to occur. This phenomenon has been reported for concrete by Kovler (1995), and seems to be significant in hot and dry climates, as strong temperature reductions on the concrete surface are felt almost simultaneously upon formwork removal. Kovler measured the evaporative cooling in a laboratory specimen, as well as the corresponding volumetric changes, observing that few hours after the evaporative cooling shock temperature returns to balance with the environmental temperature. Schindler *et al.* (2003) included the effect of evaporative cooling in their numerical model for temperature development in concrete, but did not show any experimental validation of such implementation. In the literature review made for this research only few documents were found with reference to evaporative cooling in cementitious materials, and so a small experiment was conducted in for this thesis, described herein.

Using prismatic specimens with the same geometry adopted in Sections 4.4.3 and 4.4.4, and a mortar composition 'N', two specimens were cast with two embedded thermocouples, one 0.5cm below the exposed surface, and the other at a depth of 2.0cm (see Figure 4.22). Moreover, two additional specimens were cast to monitor the rates of evaporation via weight measurements, and water samples were also used. All specimens were cast in a T=20°C environment and immediately sealed; afterwards they were placed in a controlled environment chamber at T=36.4°C and RH=30%. The choice of such a high temperature and low humidity environment is due to the purpose of obtaining a high (yet feasible) surface temperature variation due to evaporative cooling. After 1 day of sealed curing measurement of temperatures started, and sealing was removed from the top surface of the mortar specimens.

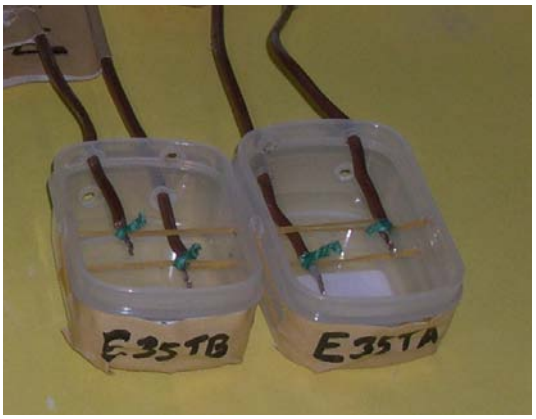

Figure 4.22: Forms and thermocouples used for the evaporative cooling experiment

Results from the tests concerning evaporative cooling are depicted in Figures 4.23 and 4.24, which reproduce the global weight loss and temperature evolutions in the specimens. The rates of evaporation from the mortar specimens match the one from the water sample in the instants just after sealing removal – during 0.025 days (35 minutes) -, as it can be confirmed in Figure 4.23. Temperature near the mortar surface (see Figure 4.24) suffered a sudden drop, from 37°C at the instant of sealing removal to 28.7°C about 35 minutes later (when the rate of evaporation from mortar started to deviate from that of the water sample – see Figure 4.23).

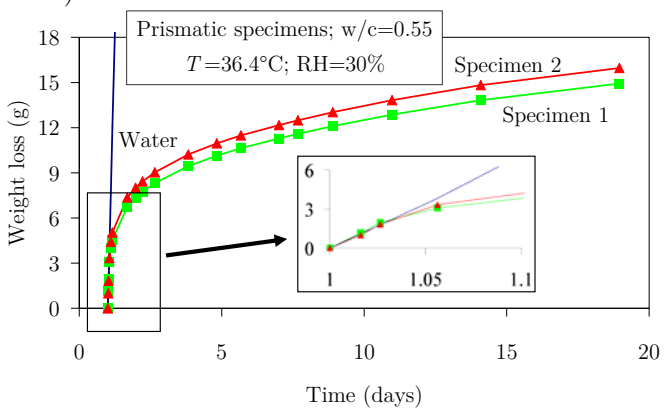

Figure 4.23: Weight losses: evaporative cooling tests (w/c=0.55)

The mortar temperature reached equilibrium with the environmental one about 8 hours later, as illustrated in Figure 4.24. According to this figure temperatures within the specimens are rather homogenous, even though the amplitude of the measured temperature drop is larger in the thermocouples located nearer the top surface.
The results obtained in this experiment suggest that the temperature drop lasts until evaporation from the mortar surface ceases to be completely environmentally controlled. The observed temperature development confirms that formwork removal should be carefully planed in construction sites, as the volumetric changes associated with this kind of thermal shock may induce cracks due to hindered deformation.

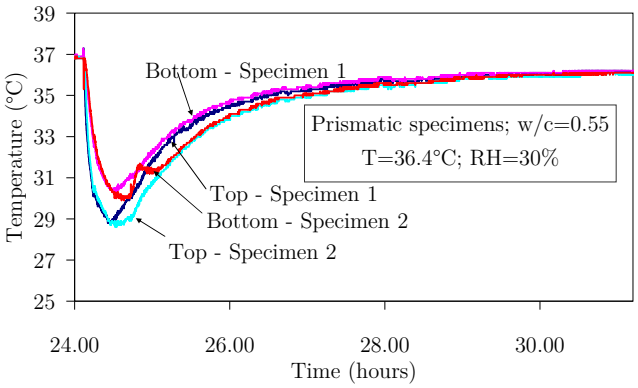

Figure 4.24: Measured temperatures: evaporative cooling tests (w/c=0.55)

4.5 New boundary condition formulation for DuCOM

4.5.1 Moisture boundary conditions

An accurate prediction of the moisture interactions between cementitious materials and the surrounding environment should involve the determination of moisture fields in both media, i.e., the numerical simulation of the external air/vapour flow and the mass balance inside the cementitious material. Being the aim of the numerical analysis for this thesis to predict the moisture field inside the cementitious material, a simplification is proposed here, based on the definition of appropriate moisture boundary conditions using mass transfer coefficients, as in Masmoudi and Prat (1991).

It has been observed by several authors (ACI 2001, Al-Fadhala and Hover 2001, Uno 1998), and confirmed in the experimental campaign reported in Section 4.4, that the evaporation from a freshly cast concrete or mortar surface and from a free water surface are identical for a limited time, after which rates of evaporation from cement/mortar start decreasing. This observation is consistent with the three phases of drying rate of porous media, described in Section 4.3.2.

The moisture boundary conditions approach of the present research is based on the hypothesis that initially the potential for water evaporation from the surface of a freshly cast (wet) cementitious material can be computed with the same formulas as for a water pan. The subsequent reduction of evaporation rates should therefore be a consequence of the densification of the material pore structure, which leads to a diffusion controlled evaporation. This effect is accounted for by the moisture model of DuCOM, and it depends on many factors such as: the water vapour concentration in the atmosphere; the wind speed; the w/c ratio; the geometry of the specimen; the temperature field inside the cementitious material due to the hydration reactions; the age at which the surface is exposed to the environment, the hydration extent, etc. An empirical methodology has been put forward by Al-Fadhala and Hoover (2001), to predict the decrease of the rate of moisture loss from a concrete surface when compared to the one from a water pan. Yet, this equation fails to account for the influencing factors that have just been described, and therefore its scope of application is limited. Selih *et al.* (1996) reported experimental and numerical research on moisture fields in concrete, where the boundary conditions

were simulated as imposed moisture fluxes on the surfaces, based on the measured evolving fluxes from the specimens in their experiments. This kind of approach is not adequate nor suitable for moisture field prediction in arbitrary environmental conditions.
The methodology to be proposed herein relies on the evaporation rate equation (4.14), conveniently backed by the current state of knowledge about water evaporation (Jones 1992). The definition of E_S in this equation is not consensual, and many empirical approaches have been put forward, as shown in Section 4.3.1, most of them function of the wind speed. In fact, the applicability of those empirical equations for water evaporation is quite dependent on the exact replication of the original conditions under which they were derived (Nilsson 1996). Yet, a simple procedure can be adopted (in both laboratory and construction sites), and it is proposed here: to characterize the evaporation potential of the testing environment by the use of a simple water pan, exposed to the studied environment (with known temperature and water vapour pressure) and regularly weighted. From the data collected with this simple and reliable test, the moisture emissivity coefficient for water in equation (4.14) can be determined, once all the other involved variables are known. However, in real structural applications care should be taken in what regards the coefficients E_s to be adopted, as due to microclimatic effects they can exhibit great variations in space and time (Nilsson 1996).
Furthermore, the proposal here made to reproduce the mass transfers that influence the drying induced moisture losses from cementitious materials to the environment is to apply equation (4.14) directly as a boundary condition to the moisture field problem described in equation (4.10). Therefore, it is assumed that the near-surface exposed pores of cementitious materials can exchange moisture with the environment in accordance to their water vapour pressure (which replaces e_s in equation (4.14)), computed on the base of the average pore relative humidity.

4.5.2 Effect of evaporative cooling

A description of a novel boundary condition for simulation of the effect of evaporative cooling in cementitious materials is made in this section. The basic idea is to account for the additional heat flux that occurs at the boundaries of the cementitious material, as a consequence of the moisture flux that occurs just after formwork removal. This additional heat flux may be computed by multiplying the moisture flux by the latent heat of vaporization of water (which is a measure of the energy barrier that needs to be overcome for evaporation to occur). In other words, the proposed methodology may be explained as follows: at a given time step the additional surface heat flux q_{ec} [Wm^{-2}] that occurs at the interface between the cementitious material and the environment, as a consequence of the moisture evaporative flux q_s (calculated from equation (4.14)), can be obtained based on the latent heat of vaporization of water h_l [Jkg^{-1}] (Chuntranuluck *et al.* 1998), that is,

$$q_{ec} = q_S \quad h_l \tag{4.21}$$

where

$$h_l = 2500 \times 10^3 - 2500 \times \left(T_S - 273.15\right) \tag{4.22}$$

(T_S in Kelvin). The effect of evaporative cooling is then superimposed to the other heat boundary conditions, so that the total heat flux q at the boundary is the sum of the heat fluxes due to convection, irradiation, solar radiation and evaporative cooling (Azenha *et al.* 2005, Schindler *et al.* 2003).

4.6 Performance of the new boundary condition formulation

By using the methodologies described in Section 4.2 (DuCOM), numerical simulations of the experiments reported in Section 4.4 will be presented in order to check the adequacy of the proposals here made to reproduce the moisture boundary conditions and the evaporative cooling phenomenon in cementitious materials. The numerical simulations of this section are presented in the same order as the corresponding experiments reported in Section 4.4.

4.6.1 Effect of T and RH on early water loss

The 5cm diameter and 5cm tall mortar cylinders referred to in Section 4.4.2 were modelled in DuCOM with the mesh depicted in Figure 4.25, comprising 3D 8-nodded finite elements. In terms of boundary conditions, three situations occur: on the top exposed surface both moisture and heat transmissions were allowed; in the lateral and bottom form surfaces thermal fluxes were considered, but no moisture exchanges were permitted; in the remaining two FE surfaces heat and moisture fluxes were prevented (axisymmetric condition). The moisture emissivity coefficient involved in equation (4.14) for the boundary condition of the mortar top surface in each environmental condition was evaluated by following the water evaporation experiment outlined in Section 4.5.1. The obtained values for this coefficient were already presented in Table 4.2. Numerical analyses were conducted according to a time integration scheme whose first step had a length of 0.0002 days (approximately 17.3 seconds), and from then on time steps were successively increased by a factor of 1.05, until the age of 28 days.

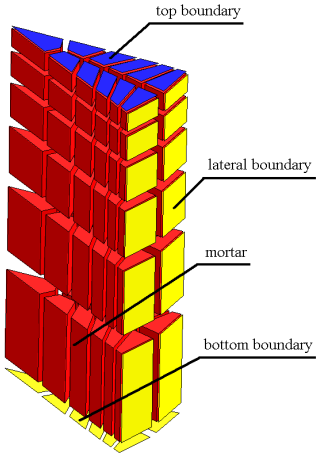

Figure 4.25: FE mesh for the cylindrical mortar specimens

Predictions from the numerical model for evaluating the influence of T and RH on the weight losses are compared to the experimental results in Figures 4.26, 4.27 and 4.28 (solid lines refer to numerical predictions). The numerical proposal for reproducing the moisture boundary conditions has a good performance both for mortars 'H' (w/c=0.35) and 'N' (w/c=0.55): the ascending branches of the weight loss curves are correctly reproduced, and both the transition and the diffusion controlled phases are also fairly reproduced (with a slight exception for the case of the 'N' composition for T=60°C and RH=60% - see Figure 4.28). It is important to remark that the overall agreement of the numerical predictions against the experimental observations is a consequence of an appropriate simulation of the thermal and moisture boundary conditions, as well as of a good prediction of the internal evolution of the material pore structure and respective moisture field under arbitrary internal temperature conditions (for further details see Ishida *et al.* (2007)).

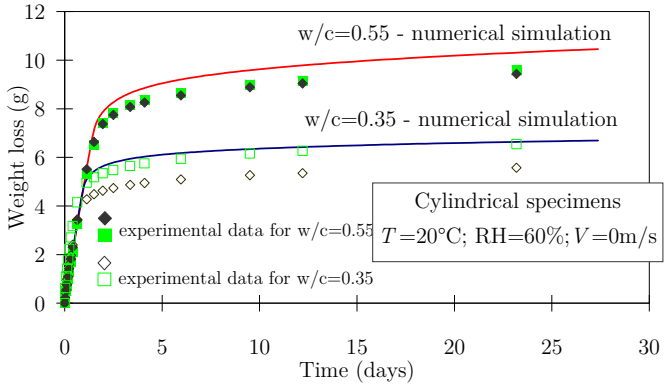

Figure 4.26: Weight losses for T=20°C and RH=60%

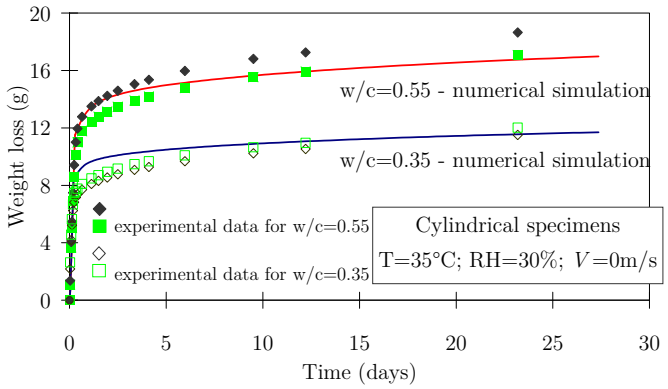

Figure 4.27: Weight losses for T=35°C and RH=30%

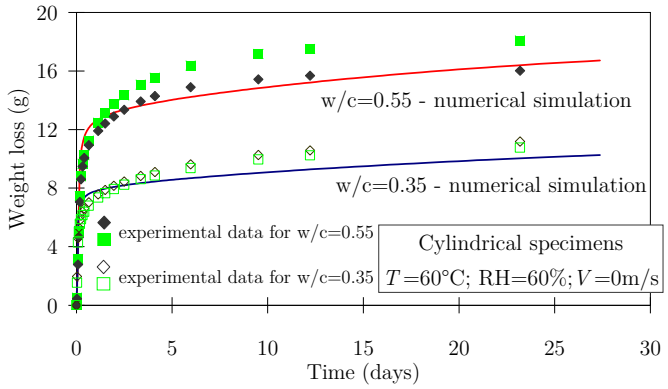

Figure 4.28: Weight losses for T=60°C and RH=60%

In Figure 4.29 numerical results regarding the evolution of both the weight loss of mortar 'N' and the pore relative humidity at depths of 0.6mm, 2.4mm and 9.3mm from the exposed surface are represented for the environmental case of T=20°C and RH=60%: it can be observed that the drop in the rate of moisture loss from the sample approximately coincides with a strong decay of the pore relative humidity in the vicinity of the surface (roughly saying, until 2.4mm deep). This observation points to the conclusion that the transition to diffusion controlled evaporation from mortar is intimately related to the desiccation of the zones near the exposed surface.

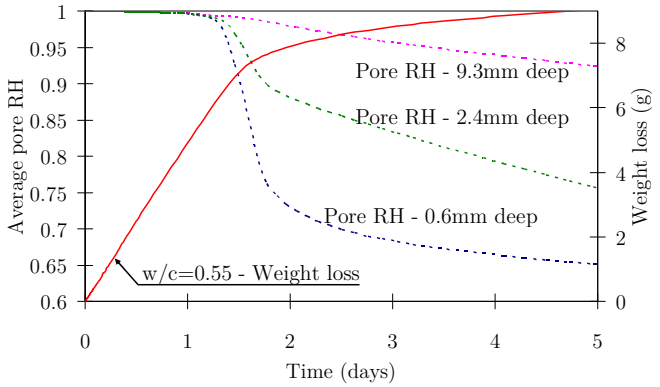

Figure 4.29: Evolution of pore RH and weigh loss for T=20°C and RH=60% - numerical simulation

4.6.2 Effect of wind speed on early water loss

The prismatic 7.3×5.1×3.0cm^3 mortar specimens mentioned in Section 4.4.3 were modelled in DuCOM with 3D 8-nodded FE, according to the mesh of one quarter of the specimen depicted in Figure 4.30. The adopted boundary conditions were: in the top exposed surface heat and moisture fluxes were allowed, while in both the lateral and bottom boundaries (corresponding to contacts with the form surfaces) only thermal fluxes were allowed. In symmetry planes (that correspond to the two vertical surfaces that cannot be seen in Figure 4.30) all fluxes were prevented. The environmental conditions considered where T=20°C and RH=60%.

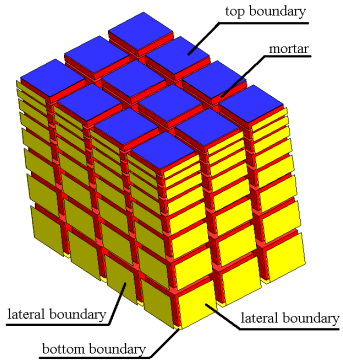

Figure 4.30: FE mesh for the prismatic mortar specimens

To numerically simulate the tests concerned with the influence of wind speed on the weight losses of specimens 'H' and 'N', for V=0m/s, V=1.8m/s, V=3.3m/s and V=4.2m/s, the experimentally determined values of E_S (according to equation (4.14)) for water specimens with the same geometry are listed in Table 4.4. The time steps and the total period of analysis for the present numerical simulations are the same as in Section 4.6.1.

Table 4.4: Moisture emissivity coefficients (prismatic specimens)

V (m/s)	E_S (kg m^{-2}s^{-1} Pa^{-1})
0	2.00×10^{-8}
1.8	4.92×10^{-8}
3.3	7.66×10^{-8}
4.2	9.09×10^{-8}

Numerical predictions (solid lines) are compared to the experimentally measured weight losses in Figure 4.31 (V=0m/s), Figure 4.32 (V=1.8m/s), Figure 4.33 (V=3.3m/s) and Figure 4.34 (V=4.2m/s). For the cases of V=1.8m/s and V=3.3m/s, a quite satisfactory agreement between simulations and experiments is observed. For the case of V=0m/s, the initial slope of the computed moisture loss curve slightly underestimates the experimental observations, whereas for the case of V=4.2m/s some non-negligible discrepancies are found on the shape of the computed moisture loss curves during the transition from phase I to phase II of drying. In spite of the observed differences between experiments and simulations, it can still be considered that the overall coherence is reasonable, which once more points to the validity of the adopted numerical model and moisture boundary conditions approach.

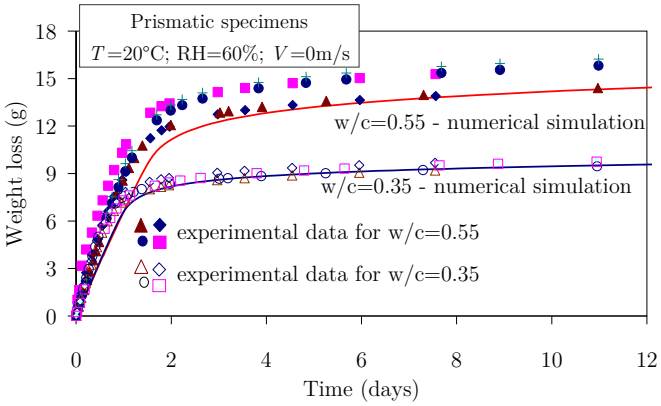

Figure 4.31: Weight losses for V=0m/s

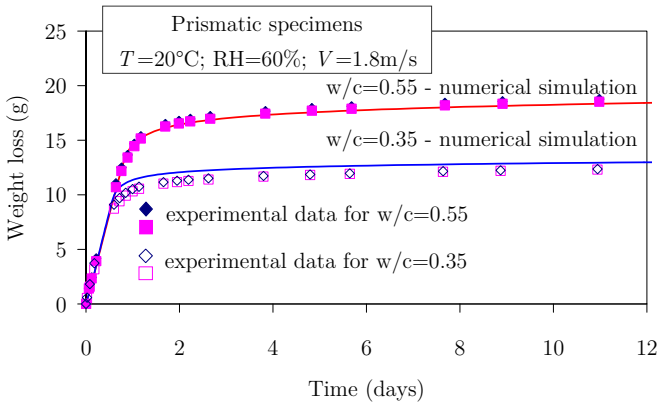

Figure 4.32: Weight losses for V=1.8m/s

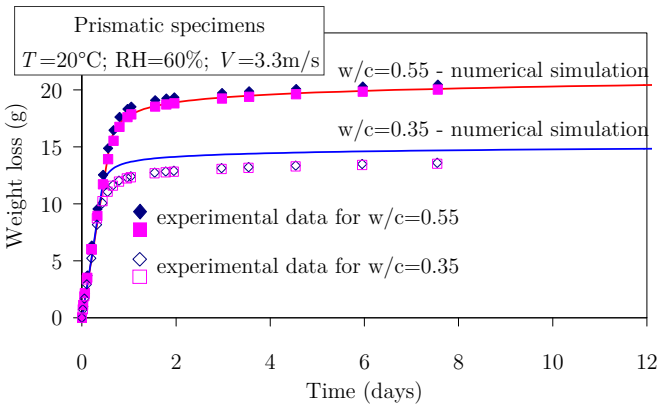

Figure 4.33: Weight losses for V=3.3m/s

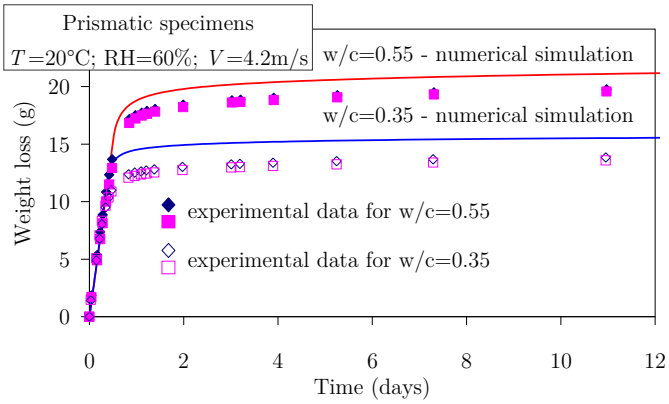

Figure 4.34: Weight losses for V=4.2m/s

At this point, and by just performing numerical simulations, it is interesting to check the overall effect of variable wind speed on the evolution of the weight losses from the mortar samples. Figure 4.35 reproduces the predicted weight losses for the tested wind speeds and for the two studied mortars: it becomes clear that the linear ascending branch of the weight loss, associated to the environmentally controlled evaporation, has the same slope for both mortars, provided the same wind speed is considered. The transition for diffusion controlled moisture loss occurs sooner for w/c=0.35 than for w/c=0.55, and the final weight losses for the 'H' mortars are lower than for the 'N' ones.

Dependency of the final weight loss at t=13.8 days on V is depicted in Figure 4.36: it is interesting to note that the ratio between the weight losses in the two mortars is almost constant, with an average value of 1.42 (which fairly resembles the quotient between the w/c ratios: 55/35=1.57). In addition, in this figure the plotted dashed lines represent the expectable weight losses if the relationship with V was linear: it can be concluded that as V increases the effect of wind speed on the water removal from mortar reduces.

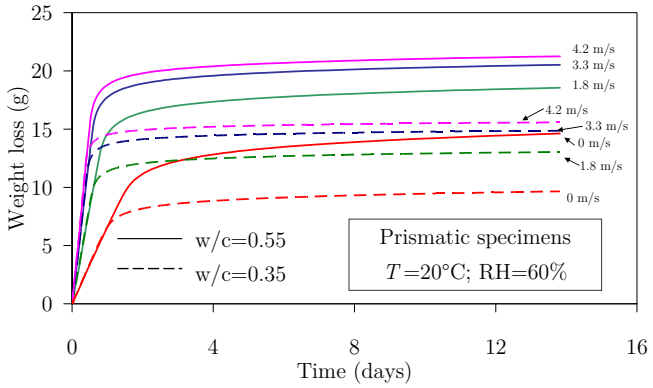

Figure 4.35: Weight losses under variable wind speed - numerical simulations

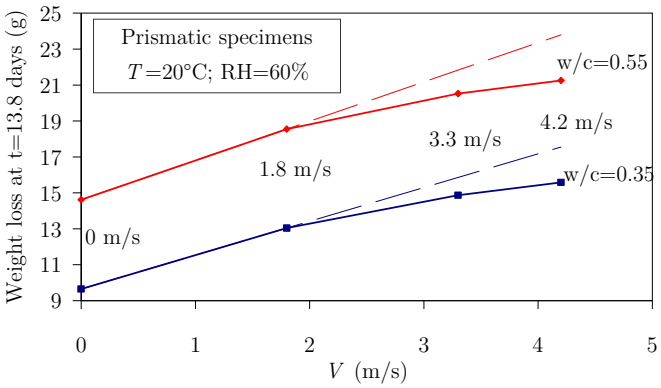

Figure 4.36: Final weight loss (at t=13.8 days) as a function of wind speed – numerical simulations

Another interesting point to discuss at this stage is the comparison, made in Figure 4.37, of the computed moisture emissivity coefficients E_S for water, based on the experimentally observed evaporation with the expectable values for E_S that would be obtained upon the use of the empirical models mentioned in Section 4.3.1. There appears to be a good coherence between the experimental results and the Menzel equation predicitons. Nevertheless, it must be said that the wind speed measurement inherent to the Menzel proposal was taken at 0.5m above the evaporating surface; in the case of this actual experiment, wind speed measurements were considered at 0.13m, and the wind speed profile is surely much different than the one in the Menzel's experiments (wooden wind tunnel *vs.* outdoor conditions). Also, in Al-Fadhala and Hover (2001) it is mentioned that Menzel equation failed to provide accurate predictions for wind speeds lower than 5m/s. It is believed that more tests should be carried out before it can be said that the coherence between these experimental results and the Menzel equation was more than a mere coincidence. Nevertheless, for the time being, the Menzel and Rowher equations appear to be the most appropriate for predicting water evaporation under variable wind speeds.

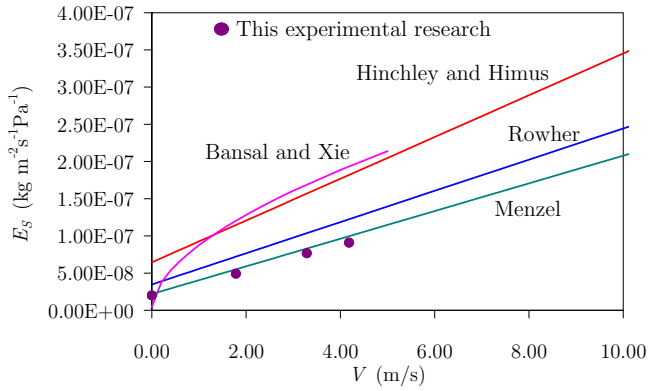

Figure 4.37: Values of the moisture emissivity coefficient: conducted experiments and empirical formulas

4.6.3 Effect of sealing period on early water loss

In the numerical analyses of this section, concerning the influence of the age of sealing removal on the weight losses of the mortar samples will be checked. Mesh geometry, boundaries, time steps and material characteristics are the same as the ones mentioned in the previous section, except for the age at which the moisture boundary conditions are activated (in this case considered as 1, 3 or 7 days). The environmental conditions were also the same, with T=20°C and RH=60%, whereas the only mortar composition considered here is 'N'. In regard to wind speeds three conditions are evaluated: V=0m/s, V=1.8m/s and V=4.2m/s

The numerical predictions and the experimental measurements of the weight losses in the cases of sealing removals at the ages of 1, 3 and 7 days are plotted in Figures 4.38, 4.39 and 4.40. From observation of Figure 4.38 it can be noticed that the numerical simulations clearly over predict the final weight losses as a consequence of having longer ascending branches than the ones verified in the experiments. This difference may be in part attributed to the experimental procedure: upon sealing removal at the age of 1 day the use of a moist cloth to remove drops of what appeared to be bleed water may have resulted in an excessive removal of surface moisture. Yet, the numerical predictions for sealing removal at the ages of 3 and 7 days seem to be reasonably good when compared to the experimental results (Figure 4.39 and Figure 4.40).

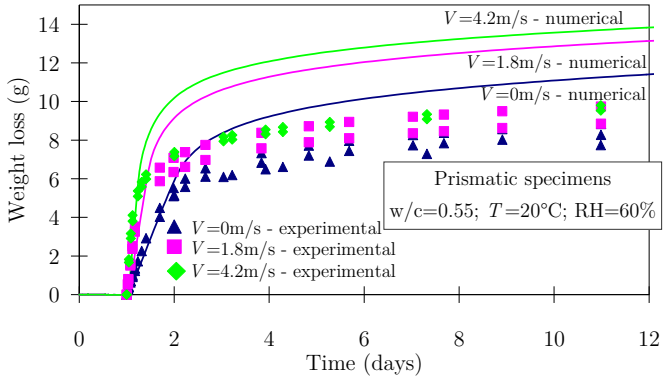

Figure 4.38: Weight losses for a sealing removal at the age of 1 day

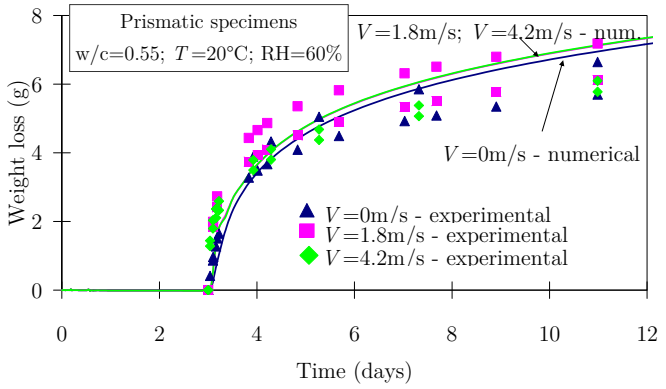

Figure 4.39: Weight losses for a sealing removal at the age of 3 days

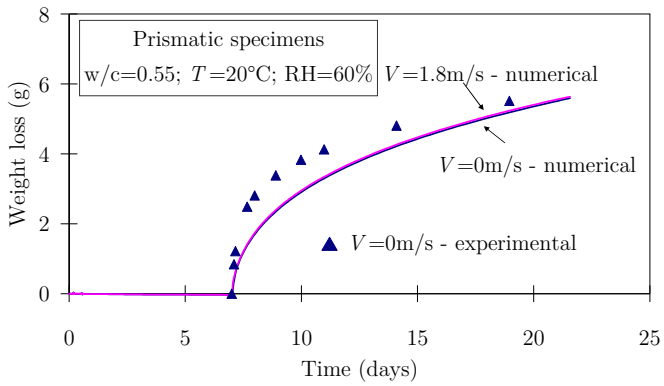

Figure 4.40: Weight losses for a sealing removal at the age of 7 days

For an overall comprehension of the relative importance of wind speed and age of sealing removal on the mortar weight losses, the numerical results depicted in Figure 4.41 are invoked: it is quite evident that the effect of wind speed is much stronger for earlier ages of sealing removal (around 1 day), becoming almost negligible for later ages (3 and 7 days); moisture losses clearly diminish with later sealing removal.

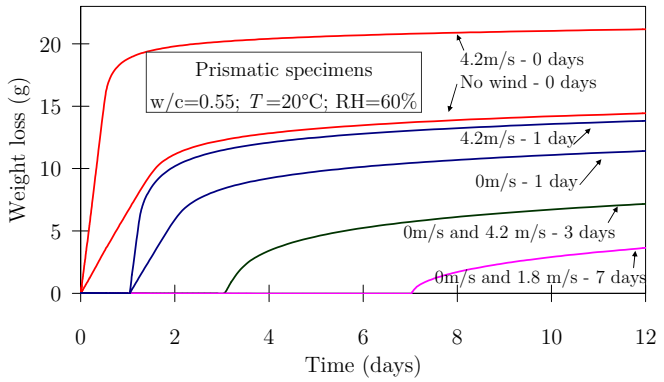

Figure 4.41: Weight losses as a function of wind speed and age of sealing removal – numerical simulations

4.6.4 Effect of evaporative cooling

The numerical strategy pursued to simulate the evaporative cooling experiment reported in Section 4.4.5 is essentially the same as adopted in the previous two sections, except that the environmental conditions are now T=36.4°C and RH=30%. In accordance to the measurements made in water specimens under these environmental conditions, the value of 5.0×10^{-8}kgm^{2}s^{-1}Pa^{-1} was adopted for E_S. In regard to heat convection coefficients, firstly a value of 5Wm^{-2}K^{-1} was adopted on all the mortar surfaces to account for the heat shielding effect provided by the sealing material; upon sealing removal the convection/radiation coefficient on the exposed surface was increased to 11.6Wm^{-2}K^{-1}, to reproduce the direct contact with the environment. The numerical predictions (solid lines) are compared to the experimental results in terms of the evolutions of both the weight loss (Figure 4.42) and the temperature evolution (Figure 4.43). Figure 4.42 demonstrates that the numerical model predicts fairly well the moisture fluxes from the mortar specimen, which is a good starting point for the evaporative cooling prediction, as such

fluxes are used for estimation of the heat removal (see equation (4.21)). Temperature evolution of the mortar specimen is depicted in Figure 4.43, where the experimental results are only plotted immediately exposure at the age of 1 day, while the numerical results are plotted since casting at T=20°C and later placement in the environmental chamber at T=36.4°C. The temperature drop prediction upon sealing removal matched quite well the measured one. Yet, return of mortar temperature to equilibrium with the environmental one was slightly slower in the numerical model than it actually happened in the experiment.

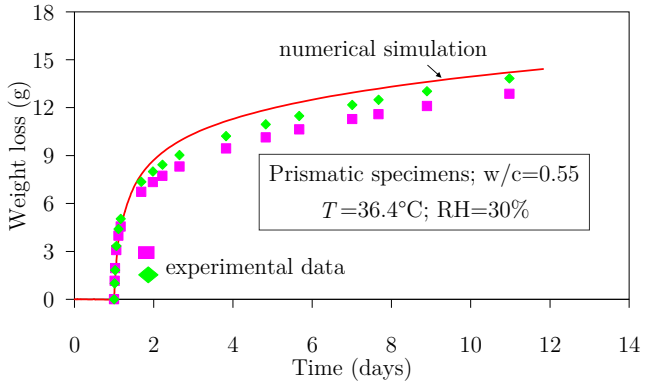

Figure 4.42: Weight loss during the evaporative cooling test

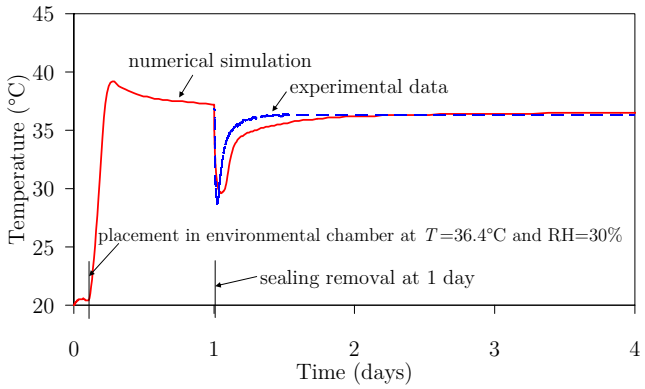

Figure 4.43: Temperature evolution during the evaporative cooling test

4.7 Numerical sensitivity analyses regarding the effects of environmental conditions

4.7.1 Overview

Taking advantage of the confirmed capabilities of DuCOM numerical framework to simulate the heat and moisture fields inside cementitious materials at early ages, three sensitivity numerical analyses concerning influences of boundary conditions on moisture losses as well as internal pore humidity distribution are presented in the sections that follow.

4.7.2 Influences of E_S and of the moisture driving potential

This sensitivity analysis aims to clarify the differences in the behaviour of two identical mortar specimens ('N' composition, with w/c=0.55) when subject to dissimilar environmental conditions, which would nonetheless yield the same moisture fluxes in water pans (i.e., under both dissimilar environmental conditions, the drying induced weight loss from a glass filled with water would be the same): one moist environment with V>0m/s, and another environment with less humidity and stagnant air conditions (V=0m/s). The reasons for a different drying behaviour of the mortars are clarified.
Considering the same geometry of the mortar specimens of Section 4.6.3 ($7.3\times5.1\times3.0\text{cm}^3$), and an age of sealing removal of 3 days, two rather different environmental conditions were considered, listed in Table 4.5 as Conditions 1 and 2.

Table 4.5: Environmental conditions for the sensitivity analyses

Condition	T (°C)	RH (%)	e (Pa)	e_s (Pa)	V (m/s)
1	20	60	1404	2340	0.88
2	20	30	702	2340	0.00

In both situations the environmental temperature is T=20°C, but with dissimilar RH (60% and 30% for Conditions 1 and 2, respectively). In Condition 1 a wind speed of 0.88m/s was considered, while in Condition 2 V=0m/s. The environmental and the surface vapour pressures were calculated by the use of equation (4.12), considering the multiplication by the relevant relative humidity (in the wet mortar surface, RH=100% was considered at the beginning of exposure). Considering that the Menzel formula for moisture emissivity coefficient (equation (4.17)) is applicable in the hypothetical wind conditions of these tests, the computed moisture emissivity coefficients are $3.83\times10^{-8}\text{kgm}^2\text{s}^{-1}\text{Pa}^{-1}$ and $2.19\times10^{-8}\text{kgm}^2\text{s}^{-1}\text{Pa}^{-1}$ for Conditions 1 and 2, respectively. Using equation (4.14) the calculated moisture fluxes in the boundaries for both situations are virtually the same, that is, $\sim3.58\times10^{-5}\text{kgm}^{-2}\text{s}^{-1}$, which means that two water pans left in these two environmental conditions would have the same moisture losses. In the case of mortar the situation is not quite like that: considering two mortar specimens under the mentioned environmental conditions, and with the top sealing removed at the age of 3 days, moisture loss rates just after formwork removal would be identical (as in the case of water pans). Yet, as soon as the surface humidity starts dropping below the total saturation, the moisture boundary flux for Condition 2 (RH=30%) will take place at higher rates than for Condition 1 (RH=60%). For example, when the surface relative humidity becomes 90% the calculated moisture boundary fluxes would be

$$\begin{aligned} q_{Cond1} &= 3.83\times10^{-8}\left(0.9\times2340-0.6\times2340\right)=2.69\times10^{-5}\text{kg m}^{-2}\text{ s}^{-1} \\ q_{Cond2} &= 2.19\times10^{-8}\left(0.9\times2340-0.3\times2340\right)=3.07\times10^{-5}\text{ kg m}^{-2}\text{ s}^{-1} \end{aligned} \tag{4.23}$$

that is, they would have become 75.1% and 85.5% of their original values for Conditions 1 and 2. As the surface moisture content decreases, this difference in the moisture loss rates

increases. This reasoning can be further consubstantiated by the observation of the numerical results for both conditions in terms of the moisture fluxes and weight losses depicted in Figure 4.44. In fact, it is noticeable that the moisture flux decreases almost immediately after sealing removal, but the decrease is stronger for Condition 1 (RH=60%) than for Condition 2 (RH=30%), particularly during the first day after exposure. In spite of these differences in the rates of moisture loss, it is only after the end of the first day of exposure that the total weight loss differences for the two conditions become noticeable. Also, attention is drawn again to Figure 4.44, where it can be confirmed that the final weight loss for Condition 2 is clearly higher than the one for Condition 1.

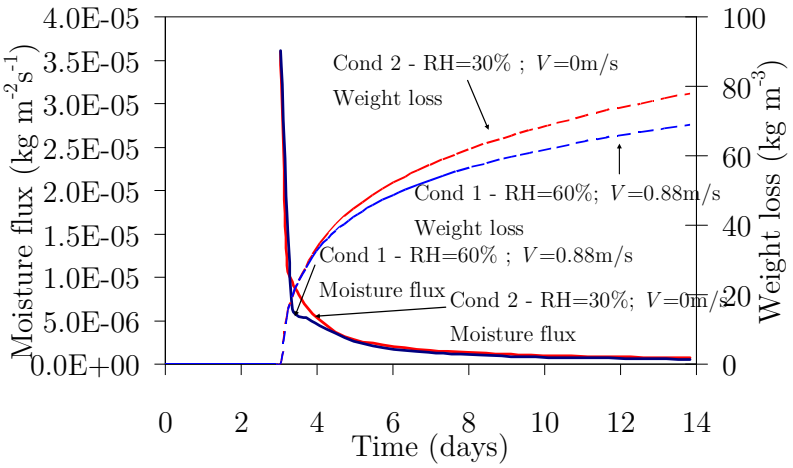

Figure 4.44: Moisture fluxes and weight losses for Conditions 1 and 2 – numerical simulations

In Figure 4.45, which depicts the evolution of RH in the mortar pore structure near the exposed surface, it can be seen that the moisture content drop is faster for Condition 2 than for Condition 1, as a consequence of the higher moisture loss rate. In addition, it can be seen that after some time mortar surfaces will be in quasi-equilibrium with the respective environmental conditions: at 14 days the surface RH of specimen 1 is very near 60%, and for specimen 2 the surface RH≈30%. Nevertheless, even at the end of the analysis (t=14days), the rates of water evaporation in Condition 2 are higher than the ones for Condition 1. The reason for this is relatively easy to understand: at this stage loss of water from mortar is no longer controlled only by environmental conditions, since it has become diffusion controlled. Yet, the moisture gradients between the saturated mortar cores and the surface (in quasi-equilibrium with the environment) are higher for the case where the environment has RH=30%, and therefore the internal moisture transport will be faster.

As a conclusion, this sensitivity analysis puts into evidence the preponderance of the driving potential (i.e., the vapour pressure difference) over the moisture emissivity coefficient in the process of drying of concrete-like materials.

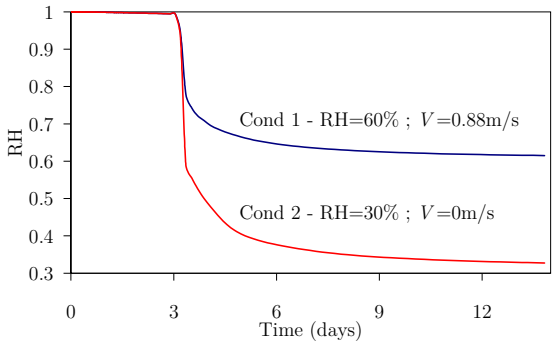

Figure 4.45: Evolution of near surface (at 0.2mm depth) RH for Conditions 1 and 2 - numerical simulations

4.7.3 Influence of age of sealing removal and of environmental conditions on evaporative cooling

4.7.3.1 Effect of age of sealing removal

Considering the situation as described in Section 4.6.4 (evaporative cooling test in a prismatic specimen under T=36.4°C and RH=30%), two further scenarios were numerically analyzed: sealing removal at the ages of 3 and 7 days. The comparative plots of both the moisture losses and the temperature evolutions are depicted in Figure 4.46. As expected, the later the sealing removal occurs, the lower becomes the moisture loss rate and the evaporative cooling temperature drop (~7.6°C for a sealing removal at the age of 1 day; ~3.5°C at the age of 3 days and ~2.7°C at the age of 7 days).

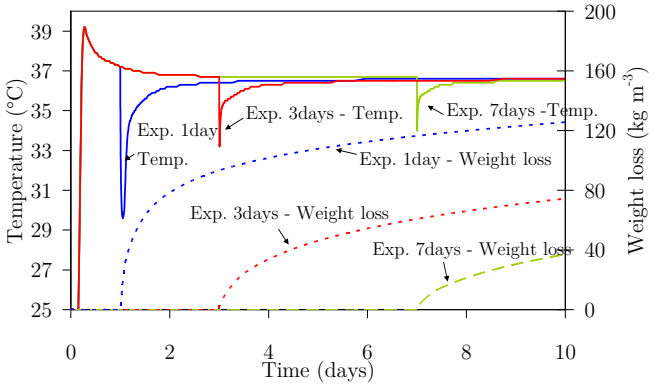

Figure 4.46: Evaporative cooling for sealing removals at the ages of 1, 3 and 7 days – numerical simulations

4.7.3.2 Effect of environmental conditions (T and RH)

Another issue that is dealt with in this sensitivity analysis is the numerical prediction of the evaporative cooling that occurs on a specimen at the age of exposure of 1 day, under the following possible conditions:

a) T=36.4°C; RH=30% (original situation described in Section 4.6.4);
b) T=36.4°C; RH=60%
c) T=20°C; RH=20%
d) T=20°C; RH=60%

An initial comparison is made between conditions a) and b), with the corresponding temperature evolution and total weight losses being shown in Figure 4.47. The moisture loss rate for condition b) is rather smaller than the one for situation a); as a consequence, so is the evaporative cooling temperature drop, which is of about 7.5°C for situation a) and 4.4°C for situation b).

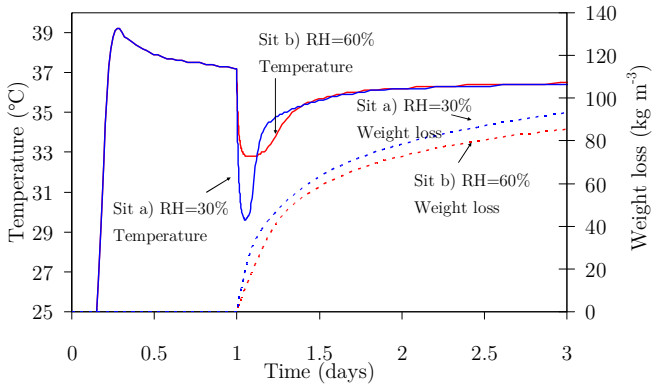

Figure 4.47: Temperature evolution and weight loss for situations a) and b) – numerical simulations

In what regards to situations c) and d), a graphic representation of the numerical predictions is presented in Figure 4.48 in the same format as for the previous figure (Figure 4.48 also reproduces situation a), for reference). Due to the lower environmental temperature of situations c) and d), the vapour pressure difference between the cement paste and the environment is smaller for T=20°C than for T=36.4°C. Consequently the moisture losses vary in accordance and the evaporative cooling temperature drop becomes attenuated: it reaches ~7.5°C for situation a); ~4.0°C for situation c) and ~2.3°C for situation d).

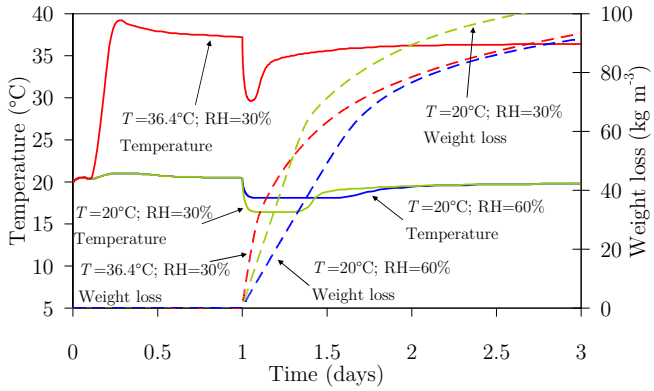

Figure 4.48: Evaporative cooling tests at T=20°C and T=36.4°C, for a sealing removal at the age of 1 day – numerical simulations

4.7.3.3 Effect of specimen size, environmental temperature and heat of hydration

Relevance of the evaporative cooling when using a real size concrete member, instead of a small laboratorial specimen, is discussed in this section. A 0.40m thick and infinite concrete slab is considered, with the concrete composition shown in Table 5.1. Heat and moisture boundaries were only considered in the top and bottom surfaces of the slab,

causing 1D flows to occur, perpendicularly to the middle plane. Formwork (i.e., moist seal and thermal transmission reducer) is removed at the age of 1 day.

For reference, a calculation was performed in which the effect of evaporative cooling was neglected. Also, three possible scenarios for evaporative cooling were considered. The four studied situations can be summarized as follows:

e) T=20°C ; RH=30% (evaporative cooling not considered); (V=0m/s)
f) T=20°C ; RH=30% ; stagnant air (V=0m/s)
g) T=20°C ; RH=30% ; wind with V=5m/s
h) T=20°C ; RH=60% ; stagnant air (V=0m/s)

Regarding the heat transfer coefficients, before/after formwork removal the values of $3.5 Wm^{-2}K^{-1}$/$11.6 Wm^{-2}K^{-1}$ were considered for V=0m/s, and the values of $4.3 Wm^{-2}K^{-1}$/ $30.0 Wm^{-2}K^{-1}$ were adopted for V=5m/s. Moisture transfer coefficients were considered null during the first day, and after formwork removal, they were computed according to each wind condition by using the Rower formula (quoted by Pauken (1999)), resulting in moisture emissivity coefficients of 2.8×10^{-8} $kgm^{-2}s^{-1}Pa^{-1}$ for V=0m/s and $14.0\times10^{-8} kgm^{-2}s^{-1}Pa^{-1}$ for V=5m/s.

Due to the relatively high thickness of the slab and the strong heat generation potential of the concrete mix, a temperature rise of more than 35°C can be observed even in the near surface, as depicted in Figure 4.49 for situation e). The peak temperature is reached at about 0.68 days (~16 hours), instant after which temperature starts decreasing. At the age of formwork removal (1 day) the abrupt change in the surface heat transfer coefficient causes the surface heat flux to increase strongly, and therefore a discontinuity is observable in the derivate of the temperature evolution curve. It should however be stressed that this temperature drop is not related at all with the evaporative cooling, as the analysis in question (situation e)) does not take such phenomenon into account.

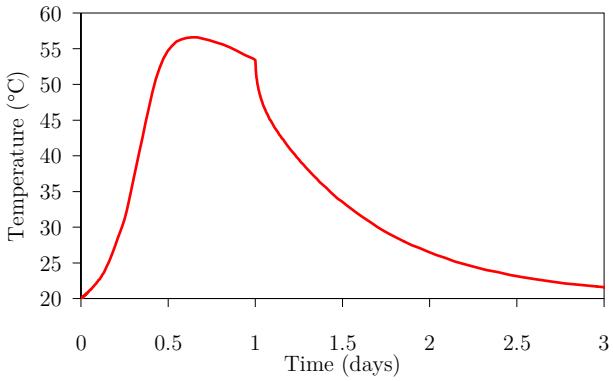

Figure 4.49: Temperature evolution near the surface for situation e)

Comparison of the temperature evolutions for situations e), f), g) and h) can be found in Figure 4.50. It appears that all the three situations in which the evaporative cooling phenomenon is considered render very similar results: in opposition to situation e) where the temperature loss after formwork removal was gradually accelerated, in situations f), g) and h) the corresponding temperature losses are quite abrupt, reaching 9°C. Explanation of this resemblance for the last different situations can be easily provided with basis on Figure 4.51, which depicts the temperature evolution and weight loss for the 1.2 hours (0.05 days) immediately after formwork removal. It is clear that the weight loss rate

becomes very similar for all situations within the first hour (0.04 days), which is related to the preponderance of the effect of the elevated temperature of the surface of concrete on the evaporative rates, coupled with the density of the pore structure that results from much accelerated hydration reactions (due to self-activation by temperature).

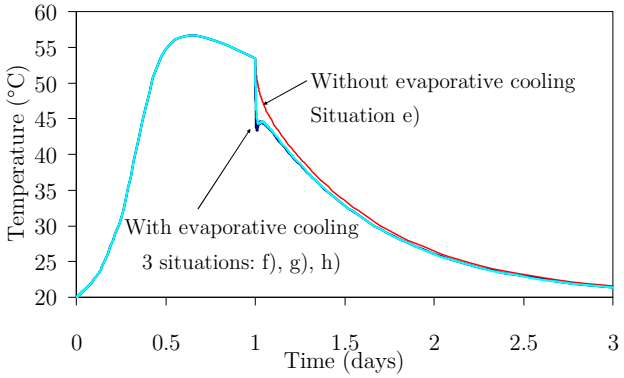

Figure 4.50: Temperature evolution on the surface for situations e), f), g) and h)

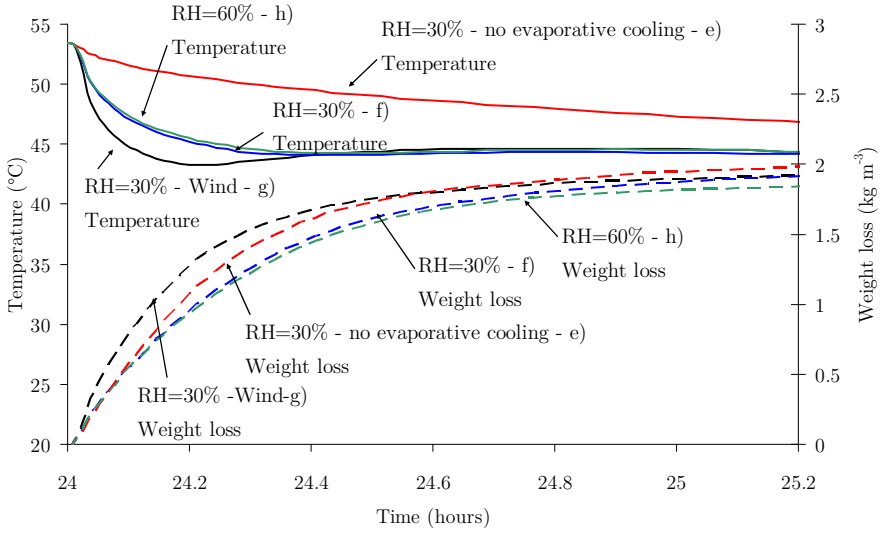

Figure 4.51: Temperature evolution and weight loss for the first 1.2 hours after formwork removal – situations e), f), g) and h)

It can be concluded that for this real size structure, the effect of hydration heat supersedes the effects of different environmental conditions. This is an interesting indicator about the importance of the evaporative cooling phenomenon in real structures: as a matter of fact it has been noticed that a combination of factors has to be taken into account to accurately interpret the magnitude of this phenomenon. The tendency for strong evaporative cooling upon formwork removal in real structures where heat of hydration causes concrete to be at higher temperatures than the surrounding environment has been shown.

Another key point to be analyzed is the actual effect of the evaporative cooling in the temperature evolution at locations far from the concrete surfaces exposed to the environment. In Figure 4.52 the temperature evolutions in the middle plane of the slab for situations e) and f) can be observed: the curves are very similar for these two situations, even though near the surface different scenarios are observed. From what has been

exposed it can be seen that the evaporative cooling phenomenon is mostly felt near the surfaces, and its significance is strongly related to the sudden temperature differential that is caused between the hot interior and the rapidly cooled surface.

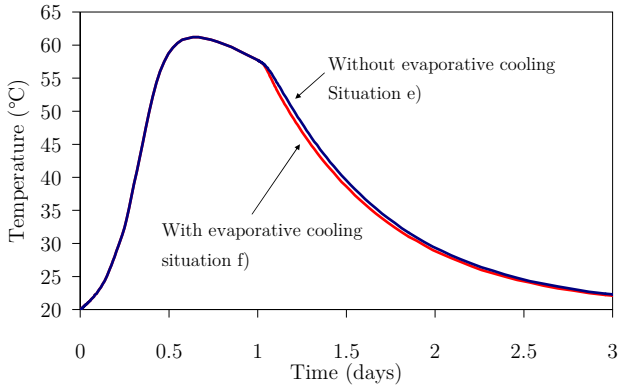

Figure 4.52: Temperature evolution in the slab middle layer – situations e) and f)

After the analysis of a real sized example in which formwork is removed while concrete is still much hotter than the environment, it seems reasonable to make another analysis with the same geometry, but with a formwork removal at the age of 7 days (when concrete temperature is quite similar to the environmental temperature). The same set of environmental situations e), f), g) and h) are analysed, and the temperature evolutions near the surface are depicted in Figure 4.53. It is clear that the magnitude of cooling due to evaporation is much smaller than the one observed for formwork removal at 1 day of age The observed temperature differences for formwork removal at the age of 7 days are irrelevant from the structural point of view, which makes it reasonable to conclude that for this example the effect of evaporative cooling becomes negligible for longer ages of formwork removal (when heat of hydration has been totally or almost totally dissipated) regardless of the environmental conditions to which the surface is subject to.

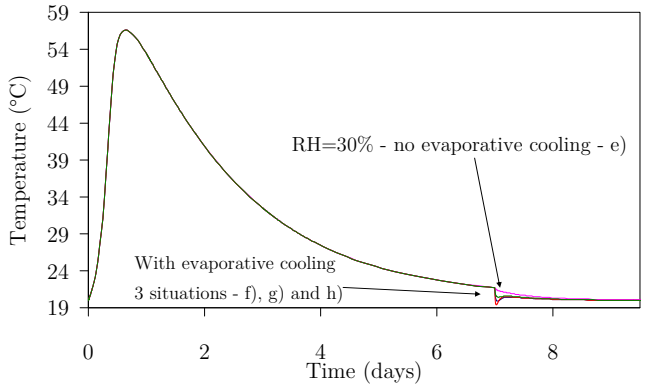

Figure 4.53: Temperature evolution near the surface for a formwork removal at the age of 7 days – environmental conditions corresponding to situations e), f), g) and h)

Another point that should be addressed is the hypothesis put forward by some authors that the evaporative cooling phenomenon might cause temperature disturbances large enough to diminish the evaporation rates (Hasanain *et al.* 1989). From the numerical analyses conducted within the scope of this research, such effect appears to be negligible: the combination of the period of time and magnitude of the evaporative cooling

phenomenon did not prove to be significant enough to affect the overall rates of evaporation. When the temperature drop is high, the period during which it subsists is usually small, and therefore does not have any tangible effect on the evaporation rate.

4.8 Prediction of near surface physical and mechanical properties for cementitious materials

4.8.1.1 Validation of DuCOM with experimental results

From what has been stated in precedent sections, it can be considered that DuCOM simulates the water loss from cementitious materials with a reasonable accuracy. Even though moisture profiles inside concrete were not measured, coherence of the numerical simulations with the experimentally obtained weight measurements under so many different environmental situations points to a probably good numerical approximation of the real moisture profile inside the specimens.

In regard to durability issues and structural effects (thermal and shrinkage cracking), physical and mechanical properties of the concrete surface should be known and quantified within a certain degree of confidence. It is the intention of this section to check whether DuCOM is correctly estimating the properties of concrete surfaces.

In this numerical framework, one of the most important couplings between the moisture transport model and thermal models, is the fact that the chemical reactions of the clinker materials (computed inside the thermal model) are de-accelerated by the shortage of free water (computed in the moisture transport model). Such deceleration is taken into account by the use of a reductive coefficient β_i in the calculation of the heat generation of each clinker material (Maekawa *et al.* 1999), as shown in equation (4.3). The equation that is used for estimating β_i is of empirical nature, and it was derived with basis on the observation of the water shortage related reactivity drop of low w/c ratio samples in adiabatic rise temperature tests

$$\beta_i = 1 - e^{-5\left(\frac{w_{free}}{100\,\eta_i}\right)^{2.4}} \tag{4.24}$$

where w_{free} is the available free water and η_i is the nondimensional thickness of the cluster (see Maekawa *et al.* (1999) for further details). This coefficient was actually developed for the interior areas of concrete, and no experimental verification of its validity for surface properties of concrete has been made so far.

In a paper related to the matters concerned in this section, Patel *et al.* (1988) report experiments using $3\times20\times28\text{mm}^3$ cement paste specimens exposed to the relative humidites of 33%, 49%, 69%, 81%, 91%, 97% and 100%, after a saturated curing period of two days. Degrees of hydration (estimated by three techniques: thermogravimetric analysis; quantitative X-ray diffraction; and loss on ignition) and total porosities were measured at the ages of 2, 14 and 90 days. Performance of DuCOM on predicting surface properties of cement paste was evaluated by comparing its results with the ones reported by Patel *et al.* (1988). The properties considered for the cement paste are reported in Table 4.6.

Table 4.6: Properties considered for the cement paste of the experiments by Patel *et al.* (1988)

Property	Value
w/c ratio	0.59
Weigth percentage of Portland cement	100
Effective Blaine value of cement (cm^2g^{-1})	3300
Weight percentage of C_3A	5.5
Weight percentage of C_3S	68
Weight percentage of C_4AF	7
Weight percentage of C_2S	13.5
Weight percentage of CS_2H	4.5
Specific gravity of OPC cement	3.16

The experimental procedure of Patel *et al.* (1988) started with the initial casting of a cement paste block with $20\times28mm^2$ cross section, which was cut in 3mm slices at the age of 1 day into specimens sized $3\times20\times28mm^3$. For that reason, and bearing in mind that the numerical model concerned only one slice, two different kinds of boundary conditions were considered: one for the parts of the slice that were in contact with the form immediately after casting, and another for the parts of the slice that only became exposed after slicing of the block. Basically, the difference between the two kinds of boundaries is essentially related with the heat boundary conditions, as specimens remained moist cured until the age of two days. The FE mesh used for this simulation is depicted in Figure 4.54, showing the cement paste in red, and the two boundary conditions in yellow and blue. Numerical analysis was conducted for a period of 90 days, in correspondence with the experimental procedure.

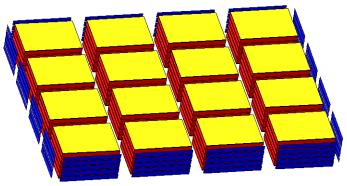

Figure 4.54: Adopted FE mesh for specimens

It could be somehow argued that even though the specimens are rather thin (3mm), there could be some relative humidity gradient inside them, which would make conclusions harder to draw. For this reason, an analysis of the RH distribution along the thickness of the specimen was carried out, particularly for the case of environment with RH=33%. In Figure 4.55, time evolution of internal pore RH along the specimen's thickness is plotted. The time span of the graphic is limited to the interval between 1.9 days (immediately before exposing the specimen to the environment with RH=33%) and 2.5 days. Basically, the important conclusions that can be drawn from the analysis of this graphic are twofold: firstly, the time that it takes for the specimen to become fully balanced with the environment relative humidity is very small (in fact, at 10 hours after exposure all the

specimen seems to have reached the 33% relative humidity); secondly, there appears to be a gradient of RH inside the specimen when it is exposed, with the surface drying faster than the interior, but this situation only persists for a very small interval (less than 10 hours), so, within the time scope of the present analysis, the consequences of this fact may be considered as negligible.

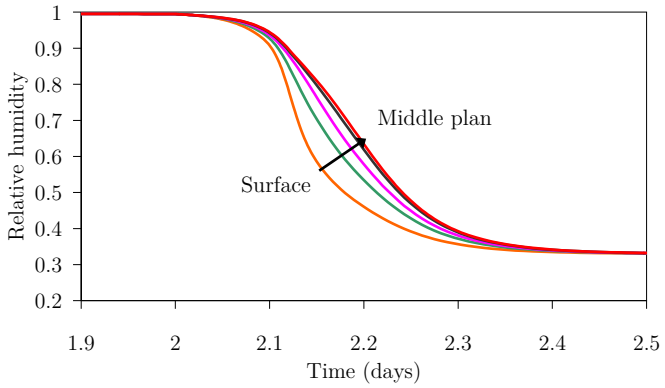

Figure 4.55: Time evolution of RH along the specimen's thickness – Env. RH=33%

A set of results is depicted in the following pictures, with emphasis on the comparison between the DuCOM numerical predictions and the experimental results. In Figures 4.56 and 4.57 the degree of hydration measured on each specimen (averaged within the specimen) at the ages of 14 and 90 days, is plotted against the environmental RH. A relatively large scatter is found between the three measurement techniques that were used for the degree of hydration. Yet, all these techniques exhibit the same trends, i.e., as the environmental relative humidity gets higher, the attained degree of hydration increases. This degree of hydration increase seems to have significant values only for environmental relative humidities above 80%. If the environmental RH is lower than 80% the evolution of the hydration reactions appears to become stagnant: this is particularity easy to conclude by comparison of Figure 4.56 and Figure 4.57. This observation somehow confirms the '80% rule' (that states that cement hydration is virtually impossible if the RH conditions are under 80%) already mentioned by other authors (Neville 1995, Spears 1983). The DuCOM prediction for the degree of hydration seems reasonably coherent with the experimental results (particularly at the age of 90 days), at least if the scatter between different experimental techniques is taken into account. The trends to reach increased degree of hydration for RH above 80% were very well reproduced numerically. This is a good indication in regard to the applicability of equation (4.24) to predict of the effect of water shortage due to evaporation.

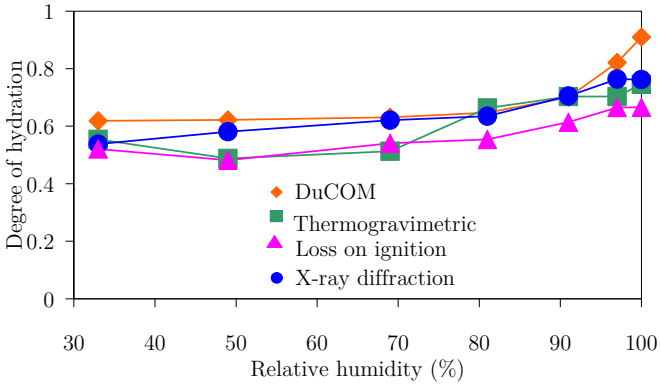

Figure 4.56: Degree of hydration as a function of environmental RH – age of 14 days

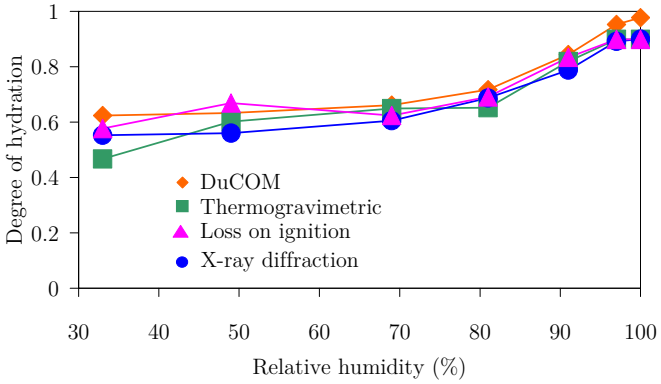

Figure 4.57: Degree of hydration as a function of environmental RH – age of 90 days

If the numerical results of DuCOM are considered to be valid for this case, it will be interesting to compare the degree of hydration evolution for the various environmental RH situations in question. Such comparison is depicted in Figure 4.58: it becomes clear that the evolution of the hydration reactions until the age of 90 days becomes almost negligible if the environmental RH is lower than 80%. Only for relative humidities higher than this threshold do reactions assume a significant evolution after the curing period. Yet, it is still interesting to observe the differences that occur in the evolution of the hydration reactions when RH ranges between 91% and 100%: this points to the fact that for best curing effectiveness, the moisture levels in the surface of concrete should be kept at 100%, and not just near 100%.

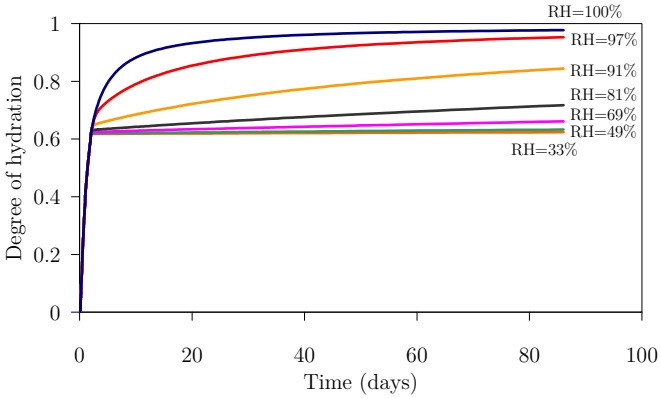

Figure 4.58: Time evolution of degree of hydration for various environmental RH – DuCOM simulations

The total porosities under the studied environmental conditions at the ages of 14 days and 90 days are depicted in Figures 4.59 and 4.60. Even though at 14 days it is not noticeable, at 90 days the experimental data show that for environmental RH higher than 80% the porosity reduces after curing is finished; for RH's under 80% such evolution is almost negligible. These experimental results, in accordance to the ones mentioned for the degree of hydration evolution, are also captured by DuCOM, especially for the case of 90 days of age.

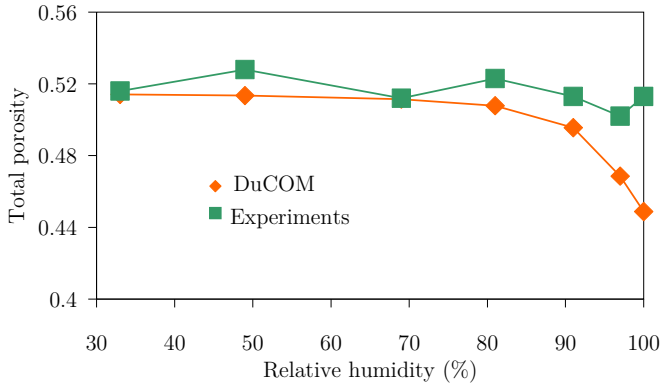

Figure 4.59: Total porosity as a function of environmental RH – age of 14 days

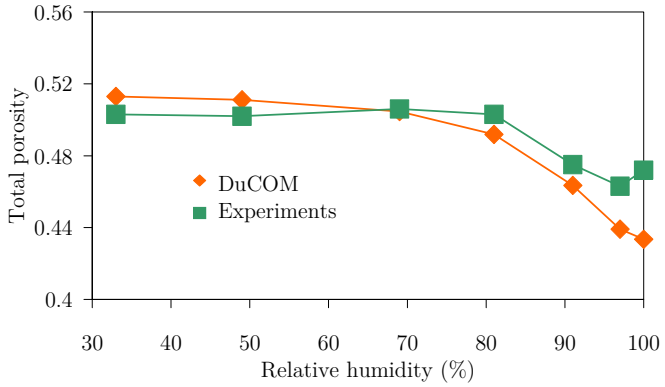

Figure 4.60: Total porosity as a function of environmental RH – age of 90 days

The observed coherence between the experimental results and the numerical predictions of DuCOM yield confidence on the possibility of using this framework for the prediction of concrete near surface properties. This points to the feasibility of actually using DuCOM as an evaluation tool for the most adequate curing time necessary for a given structure.

4.8.1.2 Potential usage for decision-making in formwork removal or finishing curing procedures

Having verified the capabilities of DuCOM to predict moisture interactions between cement-based specimens and the environment, as well as to predict the hydration and total porosity evolution in the near surface of the material, it is necessary to define what kind of criterion should be used to decide the most adequate age for formwork removal or finishing curing procedures (i.e., the age at which artificial maintenance of moist conditions at the surface of concrete is interrupted, and exposure to drying conditions is started). Prevention of thermal or shrinkage cracking at early ages is not enough to

guarantee a good durability performance of concrete. It is also necessary to assure that further characteristics of the surface (like porosity of permeability) are good enough to withstand the effects of time and environmental actions during the predicted structural life span. It is known that the rates of hydration and micro-structure development of the concrete surface may strongly decrease at the instant of exposure to the environment, even in environmental conditions with RH as high as 90% (Patel *et al.* 1988, Snyder *et al.* 2004).

One possible criterion for such decision about the age of formwork removal or finishing curing procedures could be based on the degree of hydration in the following way: "the exposure of concrete to drying environment, and therefore probable stagnation of hydration reactions on its surfaces, should be considered reasonable when the rate of hydration of the sealed/moist cured specimen reaches the rate decrease-phase". Another possible degree of hydration based criterion could be the definition of a minimum value for the degree of hydration, such as 0.7 or 0.8. Yet, some fundamental problems with these criteria of decision can be recognized: at the same degree of hydration, concretes with high and low w/c ratios have different properties (e.g. durability is distinct). So, any criterion based solely on the degree of hydration would not be a warranty of similar durability performance.

Capillary pores are known to be the main responsible ones in the processes of water transport within hardened cement (Neville 1995). So, as durability of structures is intimately related to the transport of water and ions from the surface to the interior of concrete, the assurance of a low value for capillary porosity could be considered as a strong candidate to be the criterion for curing interruption (Neville 1995, Snyder and Bentz 2004). Consequently, a limiting value for capillary porosity should be adopted as a target to achieve by curing. All surfaces that achieve a given level of porosity would then be expected to have the same kind of durability performance, in regard to imperviousness to external agents.

From the percolation theory, it is known that the transport phenomena inside porous media are strongly influenced by the interconnectivity of the porous system (Bentz *et al.* 1991): if the pores within the pore structure have a high degree of connectivity with each other, transport phenomena will happen easier and faster than in a situation where connectivity is low. Bearing this in mind, a zero level of interconnectivity on cover concrete would be desirable for the guarantee of an optimum durability performance. According to Bentz and Garboczi (1991), the degree of connectivity can be related to the capillary porosity of the C_3S paste, and this relationship is independent of the w/c ratio of the mix. It has been concluded by those authors that the percolation threshold for capillary porosity (i.e., the value of capillary porosity under which the pore structure interconnectivity is negligible) is 0.2. In Figure 4.61, the results reported in Bentz and Garboczi (1991) can be observed, showing that even though the relationship between degree of hydration and interconnected pore fraction is quite distinct between different w/c ratio pastes (see Figure 4.61a), the relationship between capillary porosity and interconnected pore fraction seems to be independent of the mix (see Figure 4.61b), and confirming the described threshold of ~0.2 for capillary porosity.

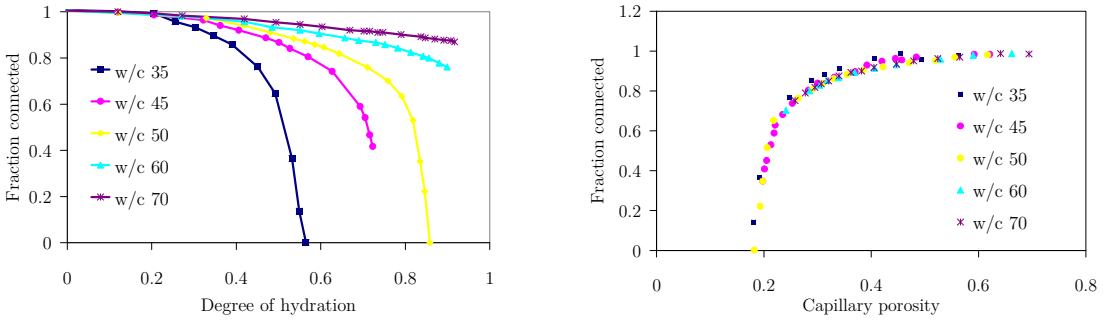

a) b)

Figure 4.61: Neat C_3S pastes a) fraction connected capillary porosity *vs.* degree of hydration; b) fraction connected capillary porosity vs. total capillary porosity (adapted from Bentz and Garboczi (1991))

Neville (1995) cites experimental results that show the relationship between the permeability of the cement paste and its capillary porosity – Figure 4.62. It can be confirmed that at capillary porosities near 0.2 the permeability is very small, which is an indication that the percolation threshold may really be around such value.

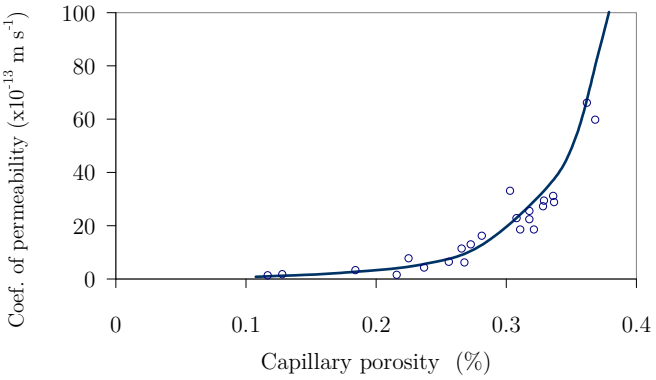

Figure 4.62: Relationship between permeability and capillary porosity of a tested cement paste (adapted from Neville (1995))

In Snyder and Bentz (2004) some recommendations are made for curing in practical conditions, which are based in an experimental campaign on small sized disc shaped cement paste specimens (with a 25mm diameter and 1.6mm thick). A new methodology to check microstructure development based on the determination of freezable water is proposed, and its final results appear to concur with predictions based on the 0.2 percolation threshold. Yet, conclusions of the mentioned research should not be extrapolated directly to practical site curing recommendations. In fact, the temperature increase due to heat of hydration in the small disc shaped specimens is very small or even negligible, which leads to assume that temperature was almost constant and equal to the curing temperature of the experiment, i.e. 25°C. In real structures member dimensions are always rather more significant, and therefore during hydration temperature increases within concrete as well as near the surfaces, where in some cases the temperature increase can be quite significant. Therefore, as cement hydration reaction is strongly activated by

temperature, in actual structures the development of microstructure will be much faster than in the reported experiments. Therefore, the age for curing measures interruption should be based not only on the composition of the mix, but also on the geometry of the member, and its expected environmental thermal conditions. As a consequence, it is most likely that the recommended curing times would not be so severe as the ones indicated by Snyder and Bentz (2004). It would be of great scientific value to conduct similar experiments with curing temperatures that would simulate the fact that surface concrete is part of a mass of concrete that self activates its chemical reactions.

Just for the sake of sensitivity, a simple example will show the combined effect of temperature development and mix proportions. Two fictitious situations are analyzed:

Situation 1 – Infinite slab 0.40m thick; w/c=0.45; moist sealed conditions

Situation 2 – Infinite slab 0.25m thick; w/c=0.55; moist sealed conditions

For both cases, the hypothetical age of curing operations is discussed with base on the results obtained in DuCOM for the capillary porosity and degree of hydration evolution near the surface (plotted in Figures 4.63 and 4.64). For situation 1 (lower w/c ratio and higher slab thickness), it can be seen that the degree of hydration developed very fast during the first day, and that capillary porosity dropped to the intended value of 0.2 at about 1 day of age. This would mean that curing measures could be finished at this point from a durability point of view. For Situation 2 (higher w/c ratio and smaller member thickness), the development of the degree of hydration is slower and so is the capillary porosity, which only after 180 days approaches the intended value of 0.2. This means that for the same durability performance as Situation 1, the concrete of Situation 2 should be cured until 180 days. It should however be stressed that the target of 0.2 for the capillary porosity should not be dogmatically considered; in fact, as it has just been observed, for high w/c ratios the achievement of this porosity may not be possible due to practical limitations. Therefore, one should just be aware that for whichever smaller curing time that is carried out, the durability performance will be less, and the degree of distance to the desired levels of quality can be quantified. For example, in Situation 2, a curing time of 7 days would yield a surface porosity of 0.3, which according to Figure 4.61b) would correspond to very high capillary pore structure connectivity (about 0.8).

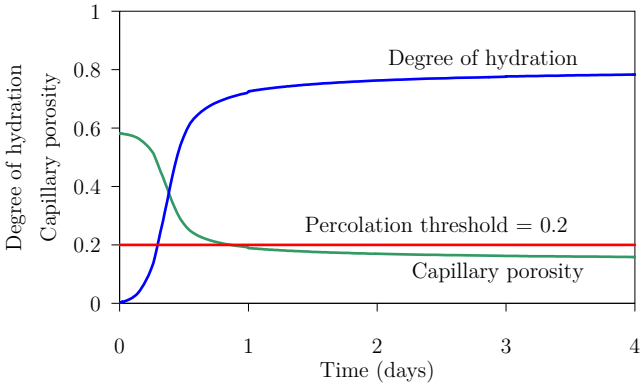

Figure 4.63: Capillary porosity and degree of hydration evolution for Situation 1

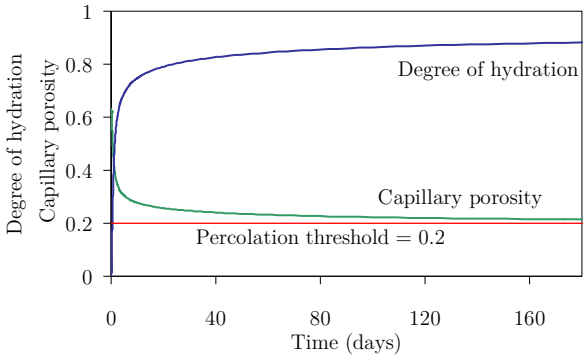

Figure 4.64: Capillary porosity and degree of hydration evolution for Situation 2

4.9 Final remarks

The present chapter is a relatively closed one, given the fact that the DuCOM is not to be used extensively further. Its purpose was to disclose the research conducted using DuCOM, and to use the corresponding conclusions to back a set of simplifications and assumptions made for the macro-approach of the thermo-hygro-mechanical framework. This section highlights the main conclusions obtained.

4.9.1 Moisture boundary condition formulation

It was confirmed that the proposed boundary condition formulation for moisture losses in cementitious materials, using the vapour pressure as the driving potential, and based on moisture emissivity coefficients taken from evaporation measurements in water surfaces, supersedes the previously existing one in DuCOM, which was based in the environmental relative humidity and a fixed moisture emissivity coefficient. It is however important to remark that DuCOM's simulation capacity of moisture losses at early ages is a consequence of an appropriate simulation of the thermal moisture boundary conditions, as well as of a good prediction of the internal evolution of the pore structure and respective moisture field under arbitrary internal temperature conditions.

The performed experiments and corresponding numerical simulations led to the conclusion that the value of the moisture emissivity coefficient (which expresses influence of wind) ends up being irrelevant for cementitious materials as soon as the moisture removal becomes diffusion controlled (phases II and III of drying process in terms of weight losses). In other words, it may be stated that the moisture losses from cementitious materials in which evaporation has already become diffusion controlled is only marginally influenced by the wind speed. Furthermore, it was observed that when the end of moist curing procedures (or age of removal of sealing in the performed experiments) occurs for ages of 7 days or higher, moisture losses from the cementitious material become almost instantly diffusion controlled right after exposure to the environment.

The observations made in the two preceding paragraphs allow for the conclusion that a numerical approach to the moisture field that does not aim to simulate moisture exposure to the environment at ages lower than 7 days may consider it valid to assume that drying rates can be regarded as independent of wind. Therefore, in the simulations regarding the moisture model that have been presented in Chapter 3, the adopted simplification of

using a constant value for the moisture emissivity coefficient, regardless of the wind conditions, may be considered valid.

4.9.2 Evaporative cooling phenomenon

The evaporative cooling phenomenon, associated to the sudden evaporation that occurs upon formwork (or sealing) removal from concrete, was investigated both experimentally and numerically. It was observed that environments with elevated temperatures and low relative humidity provide the necessary conditions for very strong evaporation upon formwork removal, which engenders a temperature decrease on the concrete surfaces. An example of this situation was the 7.6°C temperature drop observed under environmental conditions with T=36.4°C and H=30%.

Sensitivity analyses allowed the conclusion that under environmental conditions considered typical of Western Europe (T=20°C; H=60%), formwork removal from concrete structures in periods at which their surface temperature resembles that of the surrounding environment is likely to only cause very slight (or even negligible) evaporative cooling effects.

The evaporative cooling phenomenon may become quite relevant in cases where formwork removal occurs at stages in which the surface temperature of concrete is significantly higher than the environmental temperature. The resulting sudden surface temperature decay can be quite large (~9°C in the performed numerical simulation), and therefore induce a significant cracking risk on the concrete surface upon formwork removal. Taking the above conclusions into consideration, it may be deemed valid to ignore the evaporative cooling phenomenon in most of the applications that do not involve early formwork removal, or wetting/drying cycles, or extreme environments (low H and high T).

4.9.3 Surface physical and mechanical properties

The ability of DuCOM to simulate the hindering of cement hydration near the paste surface, related to the pore humidity drop associated to drying, has been demonstrated by successfully reproducing the experimental results reported by Patel *et al.* (1988). A possible methodology for quantifying the necessary duration of the moist curing period was presented, in view of fulfilling a concrete durability target. Such methodology is based on the percolation threshold concept (which many authors tentatively recommend to be 0.2) for assuring sufficient imperviousness of the concrete cover. Through numerical simulation of the evolution of the concrete pore structure in two exploratory examples, the potential of the methodology based on the percolation threshold concept was outlined in regards to concrete durability. Regardless of the conclusions that have been stated about the hindering of hydration reactions associated to depressions in the pore H, it was decided to exclude this phenomenon in the approach that has been presented in Chapter 3. This option was taken because exposure to drying conditions usually occurs for ages higher than 7 days, when relevant properties, such as concrete tensile strength have already attained relevant values, and therefore the effect of hydration hindering on overall surface mechanical properties development is diminished (even though the threshold of 0.2 in capillary porosity may not have been achieved).

Chapter 5

Thermo-hygro-mechanical framework

5.1 Introduction

Chapters 2 and 3 dealt with the simulation of the temperature and moisture fields in concrete since early ages. These scalar fields have been recognized to be of importance in regard to volumetric changes of concrete, namely through the thermal expansion coefficient and the hygral driven volume variations (usually referred to as shrinkage). Based on the knowledge of the temperature and moisture fields, together with the corresponding expectable volume variations, it is possible to compute the resulting stresses in concrete.

However, calculation of stresses since the early ages of concrete demands for some specific issues to be tackled, particularly for the thermal stresses that usually occur within the first days after casting. These issues relate to the great variations on the mechanical properties of concrete since it is cast (solid suspension, with no bearing capacity), until it reaches its hardened stage. During this period properties such as concrete E-modulus, tensile and compressive strength, as well as creep behaviour and the thermal expansion coefficient suffer relevant variations, which need to be considered in the numerical simulations.

Regarding the stresses caused by moisture variations in concrete, and bearing in mind what was stated in Chapter 3, only drying shrinkage is envisaged in this thesis, so the period of relevance of this phenomenon does not pertain to the early ages of concrete. Rather, it corresponds to the period past ~7 days after casting, when usually formworks are removed and curing procedures stop taking place: therefore, phenomena occurring at these stages can be generally considered to develop later than all the relevant thermal changes associated to cement heat of hydration have dissipated. Generally speaking, the

effects of drying shrinkage only start having relevance after thermal stresses are fully developed, and thus, the drying shrinkage stresses occur subsequently to those previously generated by heat of hydration (principle of superposition).
The present chapter begins with a brief discussion on two possible approaches to account for the evolution of concrete properties at early ages (degree of hydration, and equivalent age concepts), with the capacity of accounting for the accelerating influence of increased temperature. Afterwards, a review on existing knowledge on the evolution since early ages of the relevant mechanical properties of concrete is presented. A following subsection deals with the adopted strategy for the thermo-hygro-mechanical numerical model, which involves the combined use of the FEM code described in Chapters 2 and 3, together with the DIANA software adopted to perform the mechanical analyses.
Three distinct experimental procedures devised for a better understanding of the phenomena involved in modelling concrete at early ages and under restrained shrinkage are discussed. Firstly, a pilot experiment is described to check validity of strain measurements in concrete, during the early age development of thermal gradients, in which the performance and suitability of vibrating wire strain gages is evaluated. Numerical modelling of this pilot experiment was conducted, allowing an interesting clarification of issues involved. Secondly, an experimental campaign regarding the use of the restrained ring test, which has the interesting capability of measuring stresses in a concrete ring whose free shrinkage is restrained by an inner steel ring. By monitoring the strains in the steel ring it is possible to infer the stresses developing in concrete. The use of numerical models (with parameters obtained from a parallel characterization campaign of the concretes under use), and subsequent comparison with the obtained results from the ring test, allows verification of their capabilities in predicting the observed stresses. Thirdly, an innovative method for monitoring E-modulus evolution of cementitious materials since early ages is presented. This method involves the use of a hollow acrylic beam, inside which concrete/mortar/cement paste is cast. By monitoring the changes in the 1st resonant frequency of the composite beam (through modal identification, using only natural environmental excitations for such purpose), it is possible to assess the evolution of the E-modulus of the hardening material right after casting. Two distinct experimental campaigns are detailed in regard to this technique: one devised for concrete characterization, and the other for testing cement paste samples.
As a final application of this Chapter, a set of thermo-hygro-mechanical analyses are carried out, namely for concrete prisms and a RC slab, showing the potential of the numerical framework to simulate concrete structural behaviour since early ages.

5.2 Degree of hydration and equivalent age concepts

In regard to numerical models that aim to quantify the effect of temperature on the rate of chemical of physical processes that occur during hydration (i.e., the influence of temperature/time history in the development of concrete properties), two fundamental approaches are most usual nowadays: the degree of hydration approach (DOH) and the equivalent age concept (EA). It is the purpose of the present section to show that both approaches have the same basic definition, and explain why the equivalent age concept

has been selected as most suitable for the numerical simulation of concrete structural behaviour since early ages.

The definition of DOH has been dealt with in Chapter 2, but it must however be re-stressed that most numerical models dealing with early age heat of hydration compute DOH with basis on the heat liberation, which has been acknowledged to be a simplification of reality, as it disregards the later reactions of hydration and polymerization (Thomas *et al.* 2006), which represent significant changes in the hydration products (and consequently cement properties) without causing relevant heat generation.

It is possible to show that the EA concept can be directly derived from the degree of heat liberation concept (which is often called degree of hydration).

The line of thought that will be carried out in the text that follows considers the formulation for $\dot{Q}$ shown in equation (2.23) of Chapter 2, and bears in mind that the DOH is $\int \dot{Q}/Q_\infty \, dt$. Let's consider two batches of the same concrete, one subjected to a constant temperature T_{ref}, and the other subjected to a generic temperature history $T(\tau)$. Both mixes achieve the same degree of heat liberation α at different stages in time, here considered t_{eq} for T_{ref} and t for $T(\tau)$. Therefore, for the degree of heat liberation α, it can be stated that:

$$\alpha_{T_{ref}} = \alpha_{T(\tau)} \Leftrightarrow \int_0^{t_{eq}} \frac{\dot{Q}\left(T_{ref}\right)}{Q_\infty} d\tau = \int_0^{t} \frac{\dot{Q}\left(T\left(\tau\right)\right)}{Q_\infty} d\tau \Leftrightarrow \int_0^{t_{eq}} \dot{Q}\left(T_{ref}\right) d\tau = \int_0^{t} \dot{Q}\left(T\left(\tau\right)\right) d\tau \tag{5.1}$$

By introducing equation (2.23) into equation (5.1), one obtains

$$\int_0^{t_{eq}} A\, f\left(\alpha\right) e^{\frac{-E_a}{RT_{ref}}} \, d\tau = \int_0^{t} A\, f\left(\alpha\right) e^{\frac{-E_a}{RT(\tau)}} \, d\tau \tag{5.2}$$

and, if $A\ f(\alpha)$ is assumed to be removable in both sides of the equation, the following is obtained:

$$\int_0^{t_{eq}} e^{\frac{-E_a}{RT_{ref}}} \, d\tau = \int_0^{t} e^{\frac{-E_a}{RT(\tau)}} \, d\tau \Leftrightarrow t_{eq}\, e^{\frac{-E_a}{RT_{ref}}} = \int_0^{t} e^{\frac{-E_a}{RT(\tau)}} \, d\tau \tag{5.3}$$

which finally provides the well known equation for equivalent age:

$$t_{eq} = \int_0^{t} e^{\frac{-E_a}{R}\left(\frac{1}{T(\tau)} - \frac{1}{T_{ref}}\right)} \, d\tau \tag{5.4}$$

This shows that two concretes of the same degree of heat evolution have the same equivalent age. However, the equivalent age keeps evolving along time, whereas the degree of heat development tends to stop its progression as heat liberation becomes residual. So, the equivalent age concept is more adequate for the purposes envisaged in this research which in some applications transcend the strict scope of concrete at early ages.

5.3 Concrete properties for structural analysis

5.3.1 General remarks

Bearing in mind that the structural analyses envisaged in this thesis include the early age behaviour of concrete, it is especially important to discuss the issue of the evolution of concrete mechanical properties. The sections that follow provide a brief review of some of the most used approaches for application in numerical simulations.

5.3.2 Time zero

For the purpose of numerical modelling of concrete stresses, time zero (t_0) can be defined as the duration between the instant when water comes in contact with cement and the time at which concrete has developed sufficient structure to enable tensile stress transfer (Weiss 2001). According to this definition, time zero roughly coincides with the beginning of hydration stage II, as identified in Figure 1.2, with typical occurrence between 5h-12h for a casting temperature of 20°C. It should be remarked that for formulations based on degree of hydration, the same concept of an initial threshold may be idealized in the form of an initial degree of hydration α_0.

Unsatisfactory identification of instant t_0 may cause non-negligible errors to occur in concrete stresses estimation as it will be shown in the parametric analyses of Section 5.8.2. Prediction of t_0 is difficult not only because of issues related to the casting temperature, but also due to the very frequent presence of admixtures with accelerating or retarding effects, whose behaviour is quite difficult to predict before testing. Therefore, the most advisable approach is to use a t_0 value that results from experiments conducted on the actual concrete mix used in the envisaged application. Several methods exist to achieve this goal, none of which actually directly measuring the stiffness of the material: (i) the Vicat needle; (ii) evaluation of rate of heat evolution (as stated above, provides information regarding the transition between hydration stages I and II); (iii) electrical testing (Beek 2000); (iv) ultrasonic testing or similar (Voigt 2004) and (v) from extrapolation of mechanical properties evolution. A method that allows measurement of stiffness since casting (thus including the determination of t_0) will be proposed in Section 5.7.

5.3.3 Compressive strength, tensile strength and E-modulus

Due to similarities in the formulations usually adopted for numerical modelling of evolutions of f_c, f_{ct} and E_c, these properties are dealt with in the same section. Regardless of the approach used for estimating the relative evolution of these properties (based on degree of hydration or on equivalent age), it is known that typically E-modulus evolves faster than f_{ct}, which in turn evolves faster than f_c, as may be confirmed from Figure 5.1 for both degree of hydration and equivalent time domains.

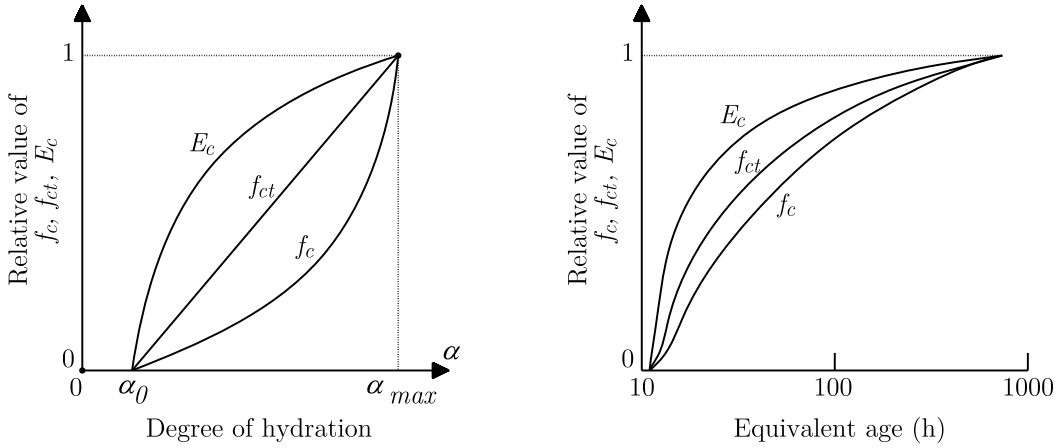

Figure 5.1: Relative evolution of E_c, f_{ct} and f_c along hydration (left – Rostásy *et al.* (2001)) and along equivalent time (right – Kanstad *et al.* (2003))

Evolutions of these three mechanical properties may be expressed by a general equation as the one indicated and experimentally validated by Rostasy *et al.* (2001) for the general property X_i (which may be f_c, f_{ct} or E_c), at a degree of hydration α as a function of the hypothetical value of X_i upon full hydration development X_{i1} (α=1), the initial degree of hydration α_0 and a parameter η_i (with the recommended values of η_i=1.5 for f_c; η_i =1.0 for f_{ct}; η_i =0.5 for E_c):

$$X_i(\alpha) = X_{i1}\left(\frac{\alpha - \alpha_0}{1 - \alpha_0}\right)^{\eta_i} \tag{5.5}$$

The formulation of MC1990 (CEB-FIP 1993) used together with the equivalent age concept can be applied for the general property X_i at the equivalent age t_e (in days) as a function of the property's value at the equivalent age of 28 days (X_{28}), involving parameters s (ranging from 0.2 to 0.38 according to the type of cement) and n (with the recommended values of n=1 for f_c; n=1/2 for E_c; no recommended value for f_{ct}):

$$X_i(t_e) = X_{28}\left[e^{s\left(1-\sqrt{\frac{28}{t_e}}\right)}\right]^n \tag{5.6}$$

This formulation was adapted by Kanstad *et al.* (2003) to include the fact that stresses and mechanical properties only start developing in concrete after t_0 by substituting t_e in equation (5.6) by (t_e-t_0), resulting in equation (5.7).

$$X_i(t_e) = X_{28}\left[e^{s\left(1-\sqrt{\frac{28}{t_e - t_0}}\right)}\right]^n \tag{5.7}$$

With this small modification, Kanstad *et al.* (2003) report that the adaptation of parameter s each concrete mix, as well as n to each concrete property, allows obtaining very good correlations with experimentally obtained properties.

Another important issue regarding the evolution of properties of concrete since casting is the relative diminishment of final values of mechanical properties with the increase in curing temperature. Chanvillard and D'Aloia (1997) point to a loss of about 20% in the final compressive strength for a given concrete mix, when comparing curing regimes at the constant temperatures of 20°C and 40°C. For curing temperatures until approximately 80°C the nature of hydration products does not differ much from what can be observed for lower curing temperatures. However, curing at elevated temperatures causes the reaction products to be denser, thus leading to higher capillarity porosity. As compressive strength is directly related to capillary porosity, the diminishment of ultimate compressive strength with the increase of curing temperature becomes obvious (Breugel 1998). As a simplification, and bearing in mind the range of studied applications, none of the formulations for property evolution mentioned in this thesis is capable of predicting the loss in final strength associated to elevated curing temperatures. Nonetheless, the reader should be aware that predictive equations for this purpose are available (Chanvillard and D'Aloia 1997).

Another issue worth mentioning within the scope of using the equivalent age concept for the prediction of concrete mechanical properties evolutions is the determination of the apparent activation energy for use in equation (5.4). According to extensive experimental work reported in Chapter 2, the apparent activation energy has been determined from calorimetric experiments. The issue of verifying the applicability of using E_a determined from calorimetric experiments in the prediction of mechanical properties has been subject of an extensive experimental campaign conducted by Wirquin *et al.* (2002), showing that the deviations between prediction and measured values were very small.

5.3.4 Poisson's coefficient

Because of the solid suspension state of concrete during the initial period after casting, it is acceptable to consider that Poisson's coefficient ν is equal to 0.5, given the fact that deformation occurs without volumetric changes (De Schutter *et al.* 2001). As ν of hardened concrete is often assumed as 0.2 (CEN 2004), it is presumable that a continuous evolution from 0.5 to ~0.2 of this coefficient occurs during the hardening process, even though some authors advocate it to be constant at the very early ages (Oluokun *et al.* 1991). Based on experimental evidence, De Schutter and Taerwe (1996) proposed the following equation for the evolution of ν along hydration, whose feasibility is confirmed by the results reported by Krauβ *et al.* (2001).

$$\nu(\alpha) = 0.18 \sin\left(\frac{\pi}{2}\alpha\right) + 0.5\, e^{-10\alpha} \tag{5.8}$$

The reader's attention is drawn to the fact that ν according to equation (5.8) starts at 0.5 for α=0 and lowers sharply to a minimum of ~0.11 for α=0.3, finally growing back to its final value of ~0.18 at α=1. The initial sharp drop from 0.5 to values under the final Poisson's coefficient for hardened concrete has also been experimentally observed by Habib *et al.* (2002).

Relevance of Poisson's coefficient along hydration in view of its effect on calculated stresses is to be discussed in the parametric analyses of Section 5.8.3.

5.3.5 Thermal expansion coefficient

The thermal expansion coefficient α_T is a parameter of utmost importance in stress estimation at early ages, as it directly affects the volumetric changes associated to variations in concrete temperature. Experimental research works have shown that concrete α_T endures significant changes at early ages. In spite of some discrepancies encountered in bibliography in regard to the early evolution of this parameter, there seems to be a general agreement on the tendency of the parameter to be higher at early stages (about 20×10^{-6}/°C), immediately lowering to smaller values (in some cases reaching about 90% of its final value upon hydration completion), and finally stabilizing to a final value around 10×10^{-6}/°C. Typical experimental evolutions of α_T during the early ages of concrete found in the literature (Bjontegaard *et al.* 2001a, Cusson *et al.* 2006, Laplante *et al.* 1994, Viviani *et al.* 2007) can be observed in Figure 5.2. The reason for the higher thermal dilation coefficient at the very early ages of concrete is related to the initial state of concrete, when its behaviour is strongly ruled by free water (which has higher thermal dilation coefficient than hardened concrete).

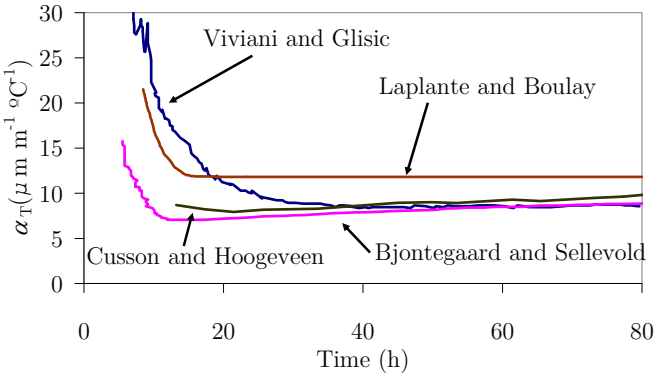

Figure 5.2: Concrete thermal dilation coefficient during cement hydration

One of the main topics of controversy in regard to the experimental determination of the thermal dilation coefficient of concrete is the difficulty in establishing a clear separation between the thermal deformation and the autogeneous shrinkage deformation (Bjontegaard *et al.* 2001b). Another difficulty in the measurement of α_T pertains to the early thermal deformation that appears to be made up of two components (Boulay 2001), one regarding the deformation of solid skeleton and another regarding the water within the pores, causing the overall deformation response to have an instantaneous and a delayed part.

Nonetheless, it is a fact that the actual variation of α_T at early ages is an issue of importance for predicting concrete strains and stresses, and should thus be included in the numerical models. However, the establishment of an analytical formula for the evolution of concrete α_T at early ages stumbles with several complexities, because of the lack of consensus on the experimental procedure for measurement of this coefficient, as well as on the multiplicity of factors that affect it (thermal and moisture conditions, microstructure and pore network, type of cement and aggregates, etc.). Therefore, no general purpose formulation was found in the literature for the evolution of α_T in view of its inclusion in numerical models for prediction of concrete behaviour. Most numerical simulations at

early ages seem to assume the simplification of constant α_T (equal to the reference value for hardened concrete), with the inherent errors in stress estimation being attenuated by the fact that E-modulus of concrete is at its smallest values during the stages at which α_T is higher. As for the value of α_T to adopt for hardened concrete, it roughly corresponds to the volumetric pondered average of the thermal dilation coefficients of the mix constituents (Azenha 2004, FIB 1999, Khan *et al.* 1998). Contribution of reinforcement to the α_T of concrete can be considered negligible for practical engineering applications (Harrison 1992).

5.3.6 Creep

Regarding the viscoelastic behaviour of concrete during the early ages, the Double Power Law (DPL) (Bazant 1988) has been used successfully in the numerical prediction of early age stresses by de Borst and Van den Boogaard (1994), where explicit comparisons between experiments and simulations revealed good coherence. More recently, extensive experimental campaigns devoted to compressive and tensile creep behaviour of concrete at early ages (Atrushi 2003, Ji 2008) have shown good fits of the DPL to experimentally obtained creep curves (basic creep), using either constant loading tests or constant deformation experiments with concrete cast in active restraining frames (Sule 2003). Furthermore, it has been acknowledged by Bazant and Prasannan (1989) that the DPL itself constitutes a particular case of the Solidification Theory for small creep durations. Therefore, it is considered that the use of the DPL is reasonable for the majority of applications in this thesis, and it was adopted by considering the following creep compliance function at time t, for a load applied at instant t' (both times expressed in days)

$$J(t,t') = \frac{1}{E_0(t')} + \frac{\phi_1}{E_0(t')}(t')^{-m}(t-t')^n \tag{5.9}$$

where $E_0(t')$ is the asymptotic elastic modulus (corresponding to short term loads), and ϕ_1, m and n are material parameters, calibrated based on experimental creep tests.

5.3.7 Cracking index

Several numerical simulations conducted within this research pertain only to the evaluation of the risk of cracking of the structure under analysis, rather than evaluating post-cracking stress redistribution or crack widths. This is the case for thermo-mechanical analyses that solely concern the effect of heat of hydration in the stress calculations at early ages: in this kind of simulation, the main purpose is to check whether the risk of thermal cracks is relevant or not, rather than evaluating the consequences of cracking. In case the risk of cracking is considered relevant, the most usual approach is to try a different concrete mix or curing condition in order to establish lower cracking risk.
So, in view of what has been stated, a criterion to define the risk of cracking is necessary. In situations such as the ones dealt with in this thesis, where concrete stresses and tensile strength are actually calculated, a cracking index may be established, such as the one

reported by Emborg (1998) as a maximum stress ratio $\eta_{\max,i}$ at a given point i, and instant t in concrete:

$$\eta_{\max,i} = max\left(\frac{\sigma_{ct}(t,i)}{fct(t,i)}\right) \tag{5.10}$$

with σ_{ct} being the principal tensile stress and f_{ct} the instantaneous average tensile strength of concrete. Safety with regard to cracking is considered assured when $\eta_{\max,i}$ <0.5, which corresponds to a safety factor of 2 in regard to the instantaneous average tensile strength.
As opposed to this deterministic criterion, a probabilistic analysis of the risk of cracking would demand for the knowledge of the probabilistic distributions of both the tensile strength and principal stress of concrete, for which few results exist in early age concrete research.
Several other criteria for evaluating cracking risk exist, with a review comprehending the Danish and Japanese regulations, as well as the iBMB (Institut für Baustoffe, Massivbau und Brandschutz) recommendations, presented in Rostasy *et al.* (2001).

5.3.8 Concrete cracking

None of the applications envisaged in this thesis deals with cracking of reinforced concrete at early ages. This is related to two main reasons: (i) in practical terms early age cracking is a undesirable situation, so at a design stage if cracking is predicted, measures should be taken to avoid it, thus eliminating the necessity for cracking models in most applications; (ii) cracking behaviour at early ages has many added complexities, due to the evolution of concrete fracture properties, as well as reinforcement bond issues, which are still insufficiently studied (Gutsch *et al.* 2001, Ostergaard 2003, Sule 2003), with scarce or none real sized applications reported in the literature.
In some applications, however, cracking will be reproduced through a smeared fixed crack approach, where the total strain $\boldsymbol{\varepsilon}$ is decomposed into an elastic component $\boldsymbol{\varepsilon}^e$ and a crack strain $\boldsymbol{\varepsilon}^{cr}$, that is, $\boldsymbol{\varepsilon} = \boldsymbol{\varepsilon}^e + \boldsymbol{\varepsilon}^{cr}$ (De Borst 1987). A stress-strain model with softening, based on the Crack Band Theory developed by Bazant and Oh (1983), is employed to describe the crack formation and crack growth in plain concrete. Along the direction normal to each crack a stress-strain softening model is adopted, defined by the concrete tensile strength f_{ct}, the fracture energy G_F and the characteristic length h. Figure 5.3a represents the relationship between the normal stress perpendicular to the crack σ_n and the corresponding strain ε_n.
The tension-stiffening effect, related to the behaviour of concrete more closely bonded to rebars, is taken into account by modifying the stress-strain relationship for the concrete surrounding the reinforcing bars, inside an effective cross-sectional area $A_{c,ef}$, which was quantified according to MC90 (CEB-FIP 1993). A constant value was adopted for the average tensile stress carried by the concrete between cracks during the stabilized cracking phase, equal to $\beta_t fct$, according to the approach followed by MC90 (CEB-FIP 1993), Eurocode 2 (CEN 2004) and FIB (1999). Bearing in mind the applications envisaged in the scope of this thesis β_t =0.4 was adopted, in accordance to the

recommendations of MC90. ε_{yc} in Figure 5.3b represents the strain at which steel yields in the crack section, being determined by (Sousa 2004)

$$\varepsilon_{yc} = \varepsilon_{sy} - \beta_t \frac{f_{ct}}{E_s \times \rho_s} \tag{5.11}$$

Where E_s is the E-modulus of steel, ρ_s is the reinforcement ratio in $A_{c,ef}$ and ε_{sy} is the yield strain of steel. For strains greater than ε_{yc} a linear decrease of the retained concrete tensile stresses is adopted, which vanishes when concrete strain reaches ε_{sy}. This approach allows modelling the behaviour of a reinforced concrete member in pure tension along its length (in average terms), after cracking is initiated (Walraven 1999).
An elastic-perfectly plastic diagram was adopted for the reinforcing steel, with a Young's modulus E_s and a yield stress f_{sy}.

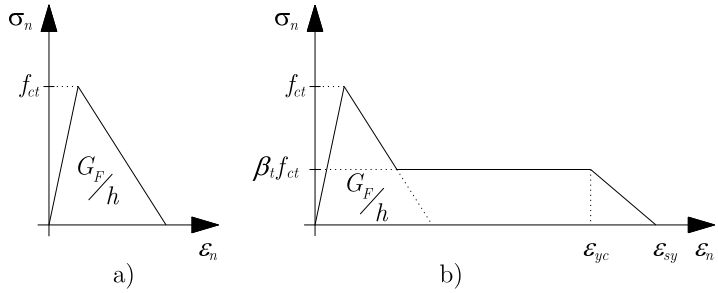

Figure 5.3: Stress-strain diagram of concrete: a) outside $A_{c,ef}$; b) inside $A_{c,ef}$

5.4 Numerical modelling of the mechanical problem, influenced by the thermal and moisture fields

The present section pertains to the numerical modelling strategy adopted within the scope of this thesis for the mechanical field and also to its integration with the thermal and moisture models described in the preceding chapters.
The adopted strategy in regard to mechanical properties, their evolution along time, as well as to creep and cracking, fits within the capabilities of DIANA software (TNO-DIANA-BV 2007). Therefore, and given the fact that no further models were to be implemented in the scope of the present research, it was decided to use DIANA for stress fields computations. Nevertheless, whenever numerical simulations of the mechanical field are described in this document, general information is given on the used models and parameters.
The thermo-hygro-mechanical numerical framework adopted is described in the text that follows, with support on the scheme depicted in Figure 5.4. Three models are involved: the thermal and moisture ones, developed within the scope of this thesis and implemented in MATLAB, and the mechanical model with basis on DIANA. The use of the numerical framework involves the deliberate uncoupling of thermal and moisture fields, due to their scope of application and the adopted simplifications. Therefore, the calculations start with the simultaneous computations regarding the thermal and moisture models, which after being fed with the necessary geometrical information and material parameters, allow

obtaining relevant results for use in the mechanical field simulation. The thermal model yields the temperature field that inflences the mechanical model by causing volumetric changes in concrete mainly associated to heat of hydration release. Equivalent age fields are computed by the thermal model and exported to be used as inputs in the mechanical model. At its present stage of development, the moisture model results relevant for use as mechanical model inputs are the infinitesimal local shrinkage strains, calculated with basis on the moisture fields. These infinitesimal local shrinkage strains represent the material local shrinkage that concrete would tend to endure if no mechanical restraint existed. The actual macroscopic shrinkage strains, which in turn produce internal self-balanced stresses, are to be calculated in the mechanical model, as a consequence of internal or external restraints to the free deformation.

The relevant results of the thermal and moisture models are then put together into a DIANA input file, and the following equivalent age dependent mechanical properties of concrete are updated: tensile strength, compressive strength, stress-strain relationship, E-modulus, coefficient of thermal expansion, and creep parameters according to the Double Power Law. Calculations are then performed by the DIANA engine, allowing evaluation of concrete stresses since the early ages (mainly associated to hydration heat), and along service life of the structure, with proper allowance for the non-uniform drying shrinkage self-induced stresses, as well as for eventual external applied loads.

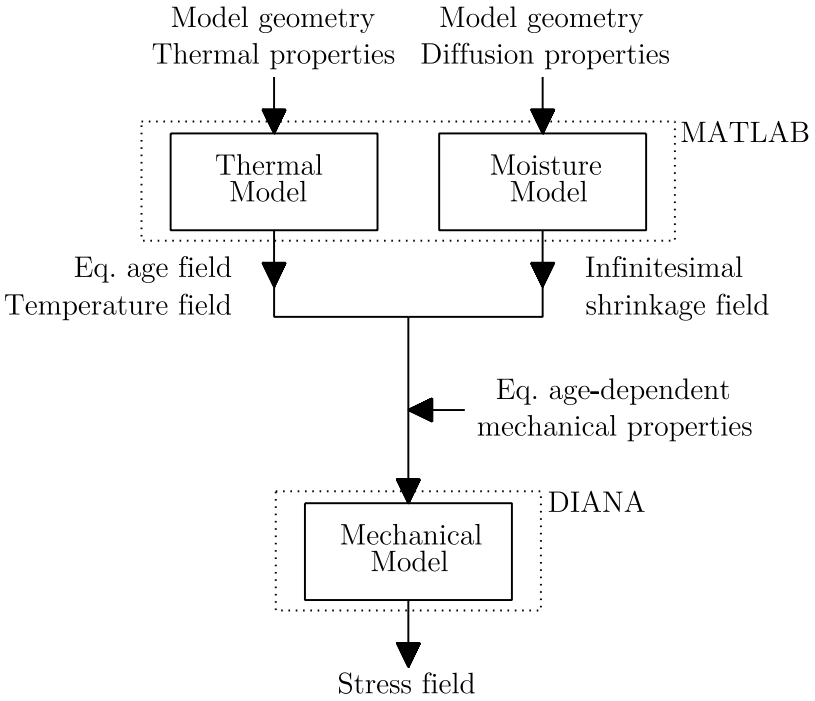

Figure 5.4: Overall workflow of the numerical framework

Having presented the main characteristics of the used numerical framework, some remarks are now made in regard to the underlying simplifications, and their consequences in the range of applicability of the overall methodology:

Coupling between thermal and moisture models

The thermal and moisture fields are fully decoupled at the present stage of development. This was an explicit option at the beginning of the implementation, in view of the final purpose of the numerical framework: the study of ordinary concrete structures since early ages in service life conditions. One of the main reasons for the feasibility of uncoupling the models is the difference in the time scales at which the main involved phenomena are occurring; in most structures the hydration heat related volume changes occur within the first week after casting, whereas the drying shrinkage phenomena (envisaged in the calculations of the moisture model) only start occurring after curing procedures have stopped, which can roughly be considered to occur later than one week after casting, i.e., at an age when heat of hydration effects can be considered negligible for non-massive concrete structures.

Also, the coupling of these phenomena at early ages would bring about considerable model complexities and difficulties, with potential necessity of extending some of the model formulations (with analogy to some of the formulations that were briefly described in Chapter 4 for DuCOM). This would violate one of the basic principles of the intended framework, which was to keep the models as simple as possible in order to make their use feasible in real-sized structures.

This decoupling of thermal and moisture models limits the ability of the present framework in regard to:

- The prediction of the hindering effect of diminishing pore RH in the development of hydration reactions (whose importance has been highlighted in Section 3.8). This is not so important when curing conditions are properly assured, as such hindering occurs at very late stages of reaction. Thus, this simplification just limits the scope of the framework to adequately cured concrete.
- Evaporative cooling is not considered. However, it has been acknowledged in Chapter 4 that this phenomenon only assumes importance in non-massive concrete structures in cases of extreme environmental conditions, or if exposure of concrete to the environment is made at very early ages, when its surface is still wet. Both these situations lay outside the intended scope of application of the present numerical framework, providing one further reason for not coupling the thermal and moisture models.
- The moisture model loses validity under non-isothermal conditions, which is the case in most real applications, subject to daily and season temperature variations. However, this is not considered a relevant handicap: parametric simulations conducted with DuCOM (that accounts for non-isothermal phenomena in moisture losses) have shown that computing moisture losses with annual average temperatures, or with actual hourly temperature variations lead to final quite similar results in terms of moisture loss evolution.

However, it must be stressed that even though the present strategy involves the uncoupled solution of each of the thermal and moisture field equations, the MATLAB implementation was devised to easily allow interchange of data between the two models, given the fact that both are computed step by step simultaneously, and both have non-linear solving procedures which can accommodate sudden property changes that may be

motivated by a strong coupling of the models (which would occur in case evaporative cooling or surface reaction hindering are introduced in the formulations).

Coupling between the mechanical and the thermal and moisture models

The numerical framework is devised in such fashion that mechanical simulations are performed after both heat and moisture fields have been computed, without the possibility of thermal/moisture fields being influenced by the mechanical one. In fact there can be some situations where such influence may occur. Two main situations that are only known after mechanical computations may be considered to possibly effect some influence on both heat and moisture models: volumetric changes can cause concrete to separate from boundaries such as formworks, and cracking may change the kinetics of heat and moisture transfer. Both these subjects have been discussed for the case of moisture transfer in Chapter 4, where they were considered to have negligible importance. For the heat model, this reduced importance is even clearer, once the geometrical relevance of both separation from formworks and cracking is too small to have a relevant effect on heat transfer, and has thus not been subject of any scientific study so far, according to the bibliographic review made in the scope of this thesis.

Remarks about the framework strategy

The simplifications assumed in this numerical framework allow it to be simple enough to conduct straightforward interpretations of results, with a strong focus on the physical meaning of the phenomena involved, and their structural consequences. The assumed set of models and their interactions are, however, complex enough to provide the numerical framework with the capacity to analyze the structural effects off self-induced stresses (due to heat of hydration and drying shrinkage) combined with the effects of external loadings, since early ages. This is in fact a clear strong point of the present approach, since most of the softwares and numerical frameworks that reach this degree of complexity in material modelling are usually not applied to real scale structures, or at least not interpreting their service life behaviour, thus not allowing relevant practical lessons to be learnt. Also, even though many thermo-mechanical or hygro-mechanical numerical frameworks exist, few are the works that actually devote attention to the integration of the three sub-models (thermal, moisture and mechanical), to handle complex practical applications looking at the response of a structure that has endured self-induced stresses due to heat of hydration at early ages, shrinkage-induced stresses, both of these combined with the effects of external applied loads.

5.5 Laboratorial pilot experiment for monitoring early age strains in concrete

5.5.1 Main objective

The purpose of validating the adopted numerical models (thermal and mechanical), together with an extensive characterization of the evolving material properties of concrete

demand for comparisons to be made between numerically predicted temperatures, stresses and strains and the corresponding monitored values. This section focuses mainly in stresses and strains, as temperatures have been subject of this kind of study in Chapter 2. Monitoring stresses in concrete has been attempted in the past by using stress meters (Kawaguchi *et al.* 1996). However, this technique is expensive and demands for relatively large sensors, which make them only suitable for massive concrete applications where the intrusion of the sensor can be considered negligible. Therefore, a basic option for in-situ verification of the numerical models was the use of strain gages. Several authors have attempted to measure strains in early age concrete structures, but with limited success, given the fact that measured strains during the initial phase while concrete is solidifying are frequently found to be inconsistent between different measuring techniques (e.g., electrical strain gages glued to reinforcement, or embedded in a ceramic matrix and vibrating wire strain gages), and between experimental and numerical model strains (Anson *et al.* 1988, Cusson 2002, Faria *et al.* 2006, Heimdal *et al.* 2001, Morabito 2001a, O'Moore *et al.* 2004). Fiber optic has recently arose as an interesting alternative to previous techniques in strain monitoring (Glisic *et al.* 2000, Habel *et al.* 1997, Slowik *et al.* 2004, Wong *et al.* 2007), but it is still a developing and expensive technique.

After an extensive review and based on previous experience (Faria *et al.* 2006), it was decided to invest in the use of vibrating wire strain gages, which present robust construction, have great reliability, are negligibly affected by electric disturbances in the field, and have a well-defined effect of temperature on measured strains.

One of the fundamental problems in the interpretation of strain gage measurement outputs in early age concrete is related to the doubts about the instant at which the sensor actually is able to reproduce material deformations. Solidarization of the strain sensors to concrete is a fundamental dilemma within the early age monitoring context, depending mostly on the ratio of stiffnesses between the concrete and the sensor. Solidarization is here defined to occur when the strain gage is capable of reproducing variations in concrete deformations, that is, when concrete stiffness is sufficiently high to ensure the sensor to be perfectly attached. Bearing the solidarization issue into consideration, the main topic of research related to strain monitoring was to evaluate the performance of two kinds of vibrating wire strain gages. One of the kinds of sensors selected for this research was the vibrating wire strain gage with a metallic casing, because of its robustness in what concerns to *in-situ* applications (where mechanical injuries induced by concrete vibrators are frequent). In order to identify the instant of solidarization to concrete of this metallic housed strain gage, a vibrating wire strain gage with a plastic (and thus less stiff) casing was also used. The experiment is conducted with a concrete prism in which the mentioned strain gages, as well as temperature sensors were embedded, and started measuring right after casting. Conclusions withdrawn from the experimental results to be described were further elaborated with basis on simulations using a thermo-mechanical numerical approach. It should be stressed that within this section concrete deformations refer to 'total strains', that is, the sum of the 'mechanical' and 'thermal' components.

5.5.2 General description of the experiment

The intended experimental monitoring campaign for measuring early age temperatures and strains on a concrete prism was carried out, fulfilling the following requisites: (i) the prism should have a geometry allowing for an easy and accurate numerical discretization, with dimensions compatible with the laboratory work, and at the same time, (ii) it should engender a heat generation potential high enough to cause significant temperature and strain gradients. The concrete prism geometry, whose dimensions are $0.60\times0.30\times0.60\text{m}^3$, is presented in Figure 5.5. Lateral faces and base of the prism were insulated with 6cm thick polystyrene plates and 2.1cm thick plywood formworks. The mix composition of the concrete was: 1134kgm^{-3} of calcareous gravel, 263kgm^{-3} of recycled concrete sand, 264kgm^{-3} of natural sand, 400kgm^{-3} of cement type I 42.5R and 200kgm^{-3} of water. Concrete casting and experimental procedures took place inside a climatic chamber with a constant temperature T=20°C and relative humidity RH=50%; data acquisition started at the end of the casting operations.

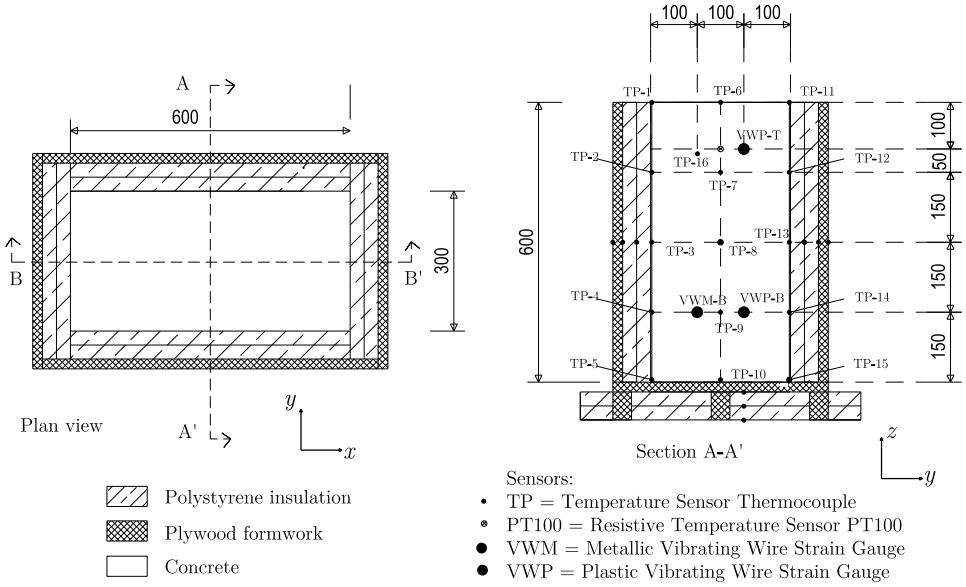

Figure 5.5: Experimental set-up: concrete and sensors location

Regarding the experimental monitoring measurements, different types of sensors were placed at symmetrical positions in relationship to plane B-B' of Figure 5.5 (where identical temperatures and strains were to be expected), in order to compare their performances. Concerning the temperature sensors, two types were adopted: the thermocouple type K (TP), very easy to use and economical, but with a low precision of ±2.2°C, and resistive temperature sensors (PT100), with a high precision of ±0.1°C. As far as the strain sensors are concerned, two types of vibrating wire strain gages with rather dissimilar casings were used: one with a metallic and stiffer housing (VWM) and the other with a plastic and less stiff casing (VWP). Vibrating wire strain gages have internal resistive temperature sensors, so they are able to monitor strains and temperatures at the same time and location. All these strain gages were embedded into concrete.

Sensors location is schematically represented in Figure 5.5. Temperature sensors were placed in the lateral faces and base of the concrete prism, as well as between polystyrene layers, in order to validate the thermal boundary conditions of the numerical model; in the concrete element itself sixteen TP and two PT100 were placed at different heights. The experimental set-up, reproduced also in Figure 5.6, includes the following strain sensors located at two levels along the height: (i) on the top level (0.10m from the top surface) a VWP sensor named as VWP-T was sited; (ii) on the bottom level, 0.15m above the base, the vibrating wire strain gages VWM-B and VWP-B were placed (Figure 5.6b). These nomenclatures of "top" (-T) and "bottom" (-B) levels will also be used later, for discussion of the experimental and numerical results.

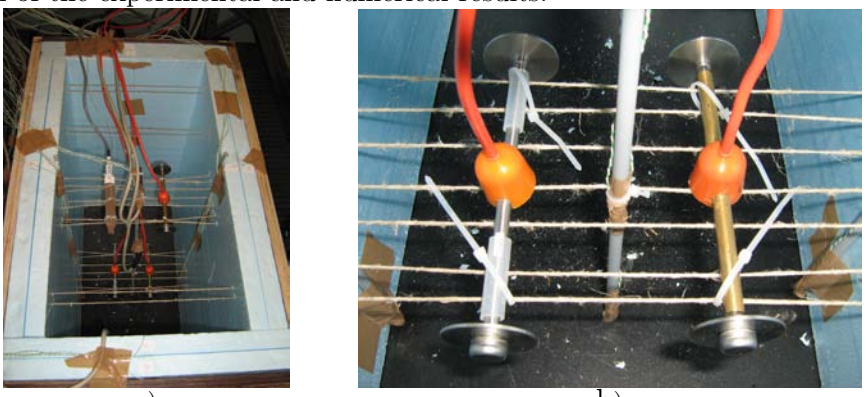

a) b)

Figure 5.6: a) Overview of polystyrene insulation and sensors; b) sensors VWM-B (left) and VWP-B (right)

One should be aware that the thermal deformation of the vibrating wire ($11\times10^{-6}K^{-1}$, according to the manufacturer's specification) must be withdrawn from the gage response to reflect the sensor total deformation: all the strain measurements reported here have been previously corrected for this effect.

In addition, a preliminary experiment was carried out to compare the responses of the two types of vibrating wire strain gages when subjected to temperature variations in free regime, that is, not embedded into concrete. These responses reflect the free thermal deformations of the sensor casings, which is a relevant information concerning the interpretation of the sensor output prior to solidarization to concrete. For such purpose the strain gages with metallic and plastic casings were placed inside a climatic chamber, with prescribed temperature variations. The corresponding measured strains were $46.24\times10^{-6}K^{-1}$ for sensor VWP, and $4.55\times10^{-6}K^{-1}$ for sensor VWM, showing clearly that sensor VWP is more influenced by temperature variations than VWM. Nevertheless, when these strain gages are embedded into hardened concrete the responses to equal temperature variations must be the same, as total strains are prescribed by the concrete deformation.

5.5.3 Experimental results

Temperatures measured in the concrete prism by the thermal sensors integrated on the vibrating wire strain gages are presented in Figure 5.7a. One can notice that, as expected, the sensors of bottom level recorded higher temperatures (64°C, at the age of 17h) than

the one of the top level (55°C at 11h). It is also important to remark the high coincidence on the responses of the two bottom level sensors VWM-B and VWP-B. In Figure 5.7a it can also be noticed that the heating period starts right after the concrete placement, and lasts for about 20h; it is then followed by the cooling period, and after 160h thermal equilibrium is reached between the concrete element and the climatic chamber temperature.

In Figure 5.7b measurements from the thermocouples TP placed along the lateral boundaries of the specimen (as shown in Figure 5.5) are presented. One can observe the thermal insulation provided by the polystyrene placed on the lateral and bottom faces: as it was expected, the areas near the non-insulated top surface reached lower temperatures. It is also worth remarking the strong coherence of temperatures measured by the TP placed symmetrical along the two vertical boundaries (TP1 and TP11, TP2 and TP12, and so on, up to TP5 and TP15) of the concrete.

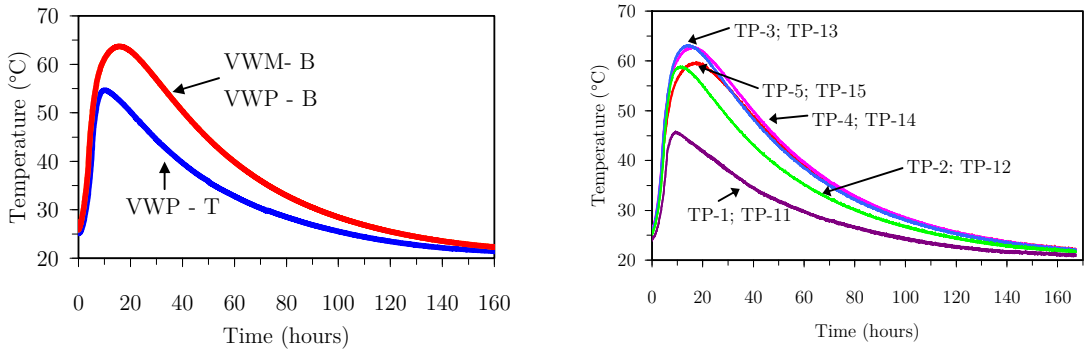

a) b)

Figure 5.7: Temperatures measured by: a) the vibrating wire strain gages; b) the thermocouples on the lateral boundaries

In regard to the monitored deformations, Figure 5.8a reproduces the total strains measured by the various sensors embedded in the concrete element: VWM-B and VWP-B at the bottom level, and VWP-T at the top level. The expectable tendency that the total strains should be superior at the bottom level (because it reached higher temperatures that led to larger expansions) than at the top level, was confirmed by the VWP-T and VWP-B curves on Figure 5.8a. Focusing on the bottom level, the strain gages recorded different peak expansions (see Figure 5.8a), which can have two main sources: (i) VWP-B stiffness is much lesser than that of VWM-B, thus solidarization of the plastic sensor to the early age concrete occurs before than for the metallic one, engendering higher final deformations on sensor VWP-B; (ii) before solidarization to concrete sensor VWP-B reveals a greater sensitivity to temperature variations than VWM-B (according to the free regime characterization mentioned in the previous section), therefore recording higher thermal deformations at the heating phase. During the cooling phase (after the age of 20h) both strain gages present identical evolution tendencies. Hence, it is interesting to notice that both types of vibrating wire strain gages are adequate to measure strains during the cooling phase, a stage whilst concrete presents a reasonable stiffness, assuring a perfect solidarization to both types of sensors. These results are coherent with previous findings reported on literature (Anson and Rowlinson 1988, Heimdal and Kompen 2001, Morabito 2001a, O'Moore *et al.* 2004).

Bearing in mind that the low stiffness of the plastic vibrating wire strain gages allows them to solidarize to concrete sooner than the metallic ones, that instant of solidarization may be defined, in a simplified way, as the one when the response evolutions for both strain gages exhibit the same trends. In Figure 5.8b a detail of the strains recorded by both types of vibrating wire strain gages (VWP-B and VWM-B) until the age of 4h is represented, where the plastic sensor graph was vertically translated until its peak became coincident with the one related to the metallic sensor; temperature evolution for the location of these strain sensors is also represented. Concerning the plastic sensor, one can notice a change on the derivative sign of the evolution trend signal at the age of 0.83h, being reasonable to consider this the instant of solidarization of sensor VWM-B to concrete. It is also possible to observe that beyond the age of 2.3h both the metallic and the plastic vibrating wire strain gages provide the same total strains, corresponding that instant to the one at which the metallic sensor solidarizes to concrete. With reference to the temperature variations (ΔT) that the vibrating wire strain gages experienced between the instant of concrete placement and the instants of solidarization, it can be remarked that: (i) the plastic strain gage was subjected to ΔT=1.5°C, which corresponds to a free thermal deformation of the sensor casing of about 69×10^{-6}; (ii) the metallic strain gage experienced a ΔT=5.7°C, which corresponds to a free thermal deformation of 26×10^{-6} for the sensor casing. This thermal sensitivity values are merely indicative of the difference between the two types of vibrating wire strain gages, since in the pre-solidarization phase the sensor casings are not totally free to deform thermally.

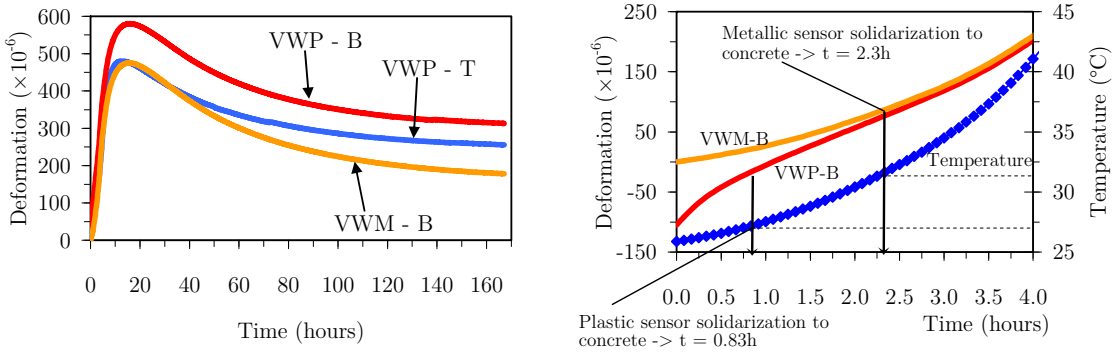

a) b)

Figure 5.8: a) Total strains measured in concrete; b) Solidarization instants of the plastic and metallic vibrating wire strain gages

As the solidarization instant for a metallic vibrating wire strain gage was already determined (though approximately), it is possible to adjust the corresponding signal of measured strain by vertically shifting the graph, so as to cancel the deformations registered prior to solidarization (see Figure 5.9). In this way, the original signal of VWM-B may be considered as an upper-bound of the total strains in concrete, and the corrected graph a lower-bound. It is important to remark that the upper-bound can be erroneous if the concrete total deformations that took place in the pre-solidarization period are greater than the recorded sensor temperature sensitivity. Nonetheless, it can be considered that the real concrete total strains should lie within the interval defined by the upper and lower-bounds in Figure 5.9: in one hand, the upper-bound possibly will overestimate the concrete total strains, due to the gage sensitivity to the temperature

variations that occurred prior to solidarization; and in the other hand, the lower-bound does not consider the total strains that occurred in concrete during the interval while solidarization evolves. In comparison to the plastic housed strain gage, the lesser thermal sensitivity of the metallic cased sensor during the period prior to full solidarization is an interesting feature in what concerns measurements of early age concrete strains, in spite of a later solidarization. Nevertheless, plastic vibrating wire strain gages are quite useful for the definition of the instant of solidarization of the metallic housed sensors.

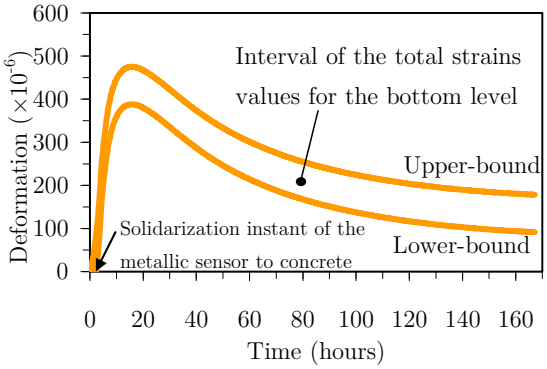

Figure 5.9: Responses on sensor VWM-B: upper-bound (original graph) *versus* lower-bound (after signal deletion until solidarization to concrete)

5.5.4 Interpretation of the experimental results with the numerical model

The concrete prism used for the experimental campaign was discretized with 3D FE. Figure 5.10a illustrates the double symmetry adopted in the numerical model, as well as the assumed thermal boundary conditions. As far as the model geometry is concerned, the following considerations are presented:

- Both the polystyrene insulations and the concrete were explicitly discretized with FE, and modelled according to their corresponding thermal and mechanical properties.
- Between the external boundaries and the environment a convection-radiation coefficient equal to $8 Wm^{-2}K^{-1}$ was considered, reproducing a stagnant air condition. Solar radiation was disregarded, as the experiment occurred indoors, on a climatic chamber. The initial temperature of concrete during the casting operations was considered to be 25°C, in correspondence to the first temperature measurements.
- Plywood formwork was simulated in two ways: (i) at the vertical faces via an equivalent convection-radiation coefficient h_{eq}=$4.2 Wm^{-2}K^{-1}$, reproducing the heat flux to environment (Azenha 2004, Jonasson 1994); (ii) at the base, and since formwork was placed between the concrete and the insulation, it was explicitly discretized with FE.

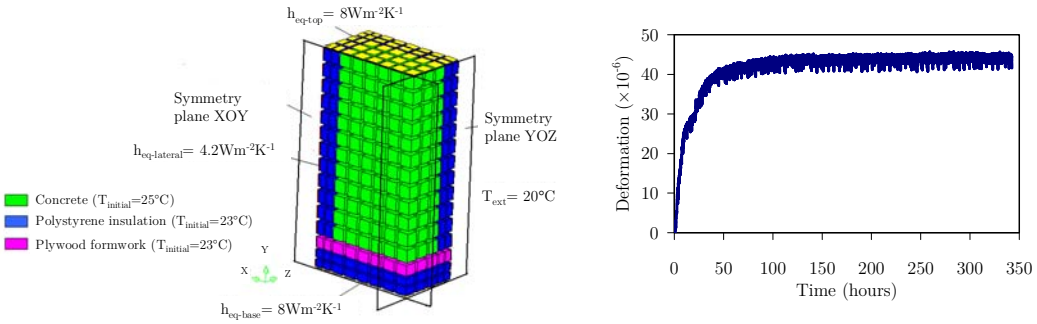

a) b)

Figure 5.10: a) Concrete prism: mesh, symmetries and thermal boundaries; b) Concrete autogenous shrinkage evolution

Regarding the mechanical boundary conditions, the following displacements were assumed to be null (see Figure 5.10a): (i) along direction X on the symmetry plane YOZ, (ii) along direction Z on the symmetry plane XOY, and (iii) along direction Y on the bottom plane. As there is no relevant mechanical adherence between concrete, insulation or formwork, mechanical properties of the polystyrene and plywood were considered negligible.

In regard to the thermal model the properties considered for each material were the following: (i) concrete: k=2.6Wm^{-1}K^{-1} and ρc=2.4×10^{6}Jm^{-3}K^{-1}; (ii) polystyrene: k=0.035Wm^{-1}K^{-1} and ρc=2.84×10^{4}Jm^{-3}K^{-1} and (iii) plywood: k=0.15Wm^{-1}K^{-1} and ρc=8.544×10^{5}Jm^{-3}K^{-1}. The Arrhenius Law was characterized through isothermal calorimetry, and the results from the tests performed at the temperatures of 20°C, 30°C, 40°C, 50°C and 60°C allowed to determine the following parameters for the used concrete mix: E_a=44.71kJmol^{-1}, A_T=1.2066×10^{11}Wm^{-3}, Q_∞=1.43121×10^{8}Jm^{-3} and function $f(\alpha)$ as shown in Figure 5.11.

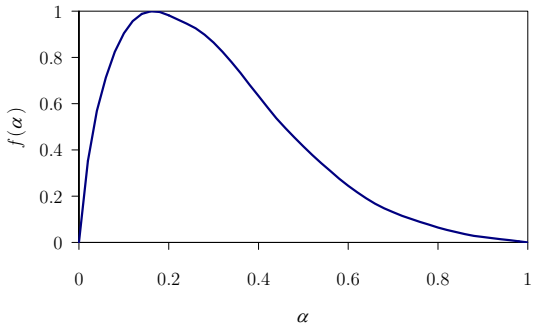

Figure 5.11: Function $f(\alpha)$ for the mix used in the prism

Concerning the concrete mechanical characterization, compression tests at the ages of 1 and 3 days were performed, rendering the following coefficients for the DPL: ϕ_1=0.6, m=0.15 and n=0.20; the E_0 values were assumed to be 40% greater than the static elastic modulus at each age of loading. For defining the concrete elastic modulus $E_{cm}(28)$, compressive tests were performed at the age of 28 days, resulting on the value of 39GPa. For expressing the evolution of E-modulus with the equivalent age, equation (5.6) was used, with s=0.2. The thermal dilation coefficient was taken as α_T=8×10^{-6}, corresponding to a volumetric weighted average of the thermal dilation coefficients of the concrete mix components (Khan *et al.* 1998); Poisson's coefficient was assumed as ν=0.20. In the time window concerned with this early age study of concrete (less than 7 days)

drying shrinkage was negligible, and so disregarded in the numerical model. However, autogenous shrinkage played an important role, and accordingly it was measured on a $0.15\times0.15\times0.60\text{m}^3$ prismatic specimen, free to deform but insulated against moisture variations with paraffin, rendering the evolution curve depicted in Figure 5.10b (imposed strains in the numerical model).

With reference to the thermal analysis, the mesh presented in Figure 5.10a corresponds to prismatic 8-noded FE, whereas for the mechanical problem 20-noded FE were used (both types of FE have coinciding corner nodes). The thermo-mechanical analysis was carried out until the age of 7 days, with a time-step of 0.25h.

The results obtained with the numerical model are compared to the experimental ones, firstly in regard to temperatures, and then to strains.

Distribution of temperatures at the instant when the maximum was reached (15.8h) is reproduced in Figure 5.12a, showing a significant coherence to the sensors measurements (see Figure 5.7, for comparison).

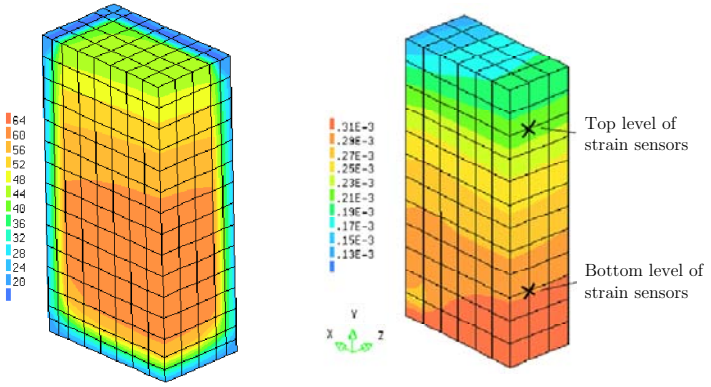

Figure 5.12: Numerical results for t=15.8h: a) temperatures (°C); b) total strains ε_x

Relating to the temperatures on the strain sensors positions, a direct comparison between the experimental measurements and the numerical results throughout time is made in Figure 5.13a. In addition, and to check the adequacy of the presumed thermal boundary conditions, the numerical and experimental temperatures on the interfaces close to the vertical boundaries are presented in Figure 5.13b. In both figures a very good agreement between the numerical and the experimental results can be observed, which validates the assumed simulation hypotheses.

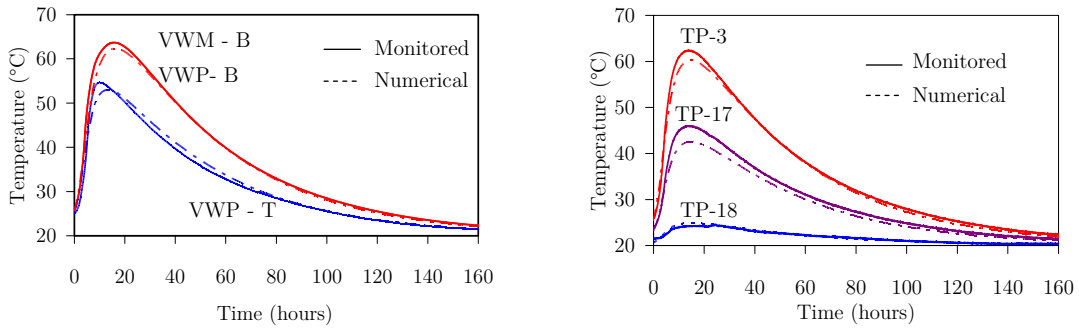

Figure 5.13: Temperatures: a) on the strain sensors positions; b) on several interfaces close to the vertical boundaries

Since the thermal model was well succeeded, there is some confidence to go into the mechanical problem. Accordingly, disagreements on the numerical total strains in relationship to the experimental ones are to be considered due to insufficiencies of the mechanical model, or misinterpretation of the monitoring results.

Adopting the same strategy as for the thermal analysis, numerical and experimental early age concrete total strains will be compared. Concrete total strains ε_x computed numerically for the instant of maximum temperature (15.8h) are presented in Figure 5.12b. Is it interesting to notice the strain gradients between the top and bottom of the concrete prism, in correspondence to the two levels of strain sensors, and already identified on the experimental results discussion presented before. As far as the computed concrete tensile stresses are concerned, they remained always below the threshold of 0.5MPa, pointing to an almost negligible cracking risk, which is consistent with the strain gage measurements (otherwise their graphs would have to show sudden hops).

Comparison of the total strains measured experimentally and the corresponding numerical predictions is made in Figure 5.14a, for both top and bottom levels of strain gages: considerable discrepancies on the numerical peak values in relationship to the experimental results are observed. However, and as previously remarked, results obtained directly from the vibrating wire strain gages are upper-bounds of the real total strains. After performing the vertical correction of the vibrating wire strain gages signals, as described for Figure 5.8b and Figure 5.9, the expectable total strains interval for the bottom level sensors and the corresponding numerical results are depicted in Figure 5.14b: it is straightforwardly noticeable that although the numerical peak value is fairly under the assigned interval, evolution of the numerical curve is significantly similar to the upper- and lower-bound ones from the monitoring campaign. Consequently, and within the normal errors acceptable for this kind of applications, it can be remarked that during the post-peak phase the numerical model provides highly coherent evolutions of concrete total strains, when compared to the experimental ones.

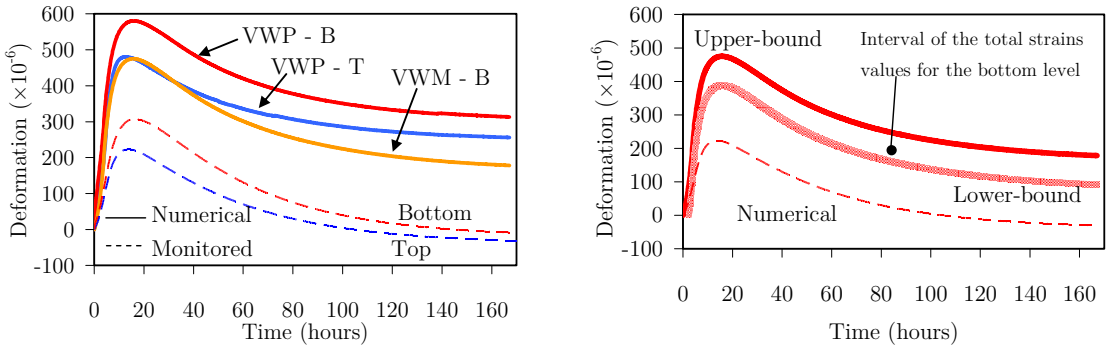

a) b)

Figure 5.14: a) Numerical and monitored total strains ε_x; b) Total strains ε_x at the lower level

Among the reasons that may explain the differences on the peak total strains obtained from the experimental campaign or from the numerical model, one could refer to the following:

- Possible incorrectness of the assumed early E_{cm} evolution might be plausibly argued as leading to misleading results. In present research evolution of the elastic modulus of

concrete was numerically simulated by using the expression from EC2, which clearly is not devised for very early ages, nor does it contemplate the dormant stage whilst concrete stiffness should be considered as zero. Recently a new method for monitoring the early age concrete stiffness (right after casting) has been devised at the Faculty of Engineering of the University of Porto (presented in Section 5.7). The results obtained with this method for a very similar concrete to the one used in this application (same cement type and content) allowed a realistic early E_{cm} curve to be obtained that, after convenient scaling, was only significantly different from the EC2 one during the first few hours after casting. The use of that realistic E_{cm} curve on the numerical model for the present application yielded almost the same strains as the one from EC2. The reason for this is that the temperatures that develop within the concrete prism are relatively uniform (see Figure 5.12a), and restraints induced by neighbouring parts of the prism at different temperatures are relatively small. Thus, as there is no external restraint to the deformation, and the internal restraint is relatively small, influence of changing the concrete elastic modulus is negligible given the fact that deformations are being commanded by thermal dilation.

- Insufficiencies of the creep model with regard to the viscoelastic behaviour of concrete could also be argued to be the reason for the observed discrepancies. Nonetheless, according to what has been stated above, as stiffness evolution of concrete seems to have small effect in this thermal dilation driven phenomenon, so does creep. The small influence of creep modelling was confirmed by conducting parametric analyses with drastic changes in the creep laws (doubling and halving all parameters of the DPL), which led to negligible changes in the computed strains of the application envisaged in this section.
- In regard to the strain calculation, the remaining mechanical parameter that might be responsible for the observed differences is the thermal dilation coefficient α_T, which is not constant during the cement hydration process, as for simplification it was assumed in the present simulation, furthermore being also a property of rather complex experimental characterization. Evolution curves for α_T with the equivalent age of concrete are shown in Figure 5.2: the discrepancy is notorious, not only because of the differences on the analyzed concretes, but specially due to the different methodologies used to measure the thermal dilation coefficient, as there is no consensus within scientific community in this concern. In this figure it stands out that at the first 5h (corresponding to a concrete development stage during which the role of the liquid phase is of major importance) α_T assumes values around 20×10^{-6} (Viviani *et al.* 2007) or even higher, decreasing for less than half with the advancement of the concrete hardening process (increasing relevance of the solid phase).

In order to evaluate the influence of the α_T reduction during hydration on the early age concrete total strains, a new thermo-mechanical numerical analysis was carried out by implementing the experimental evolution of α_T reported by Bjontegaard and Sellevold (2001a), and depicted in Figure 5.2. The corresponding numerical predictions for the concrete total strains ε_x at the bottom level are depicted in Figure 5.15. Now the numerical predictions are considerably more coherent with the experimental measurements, during both the cooling and heating phases, and it can be also observed

that the numerical total strains fall within the interval of expectable strains provided by the two types of vibrating wire strain gages (with metallic and plastic casings). Relevance of explicitly including concrete α_T reduction throughout the first hours of cement hydration is therefore highlighted, which calls for the urgent need of an adequate set-up to experimentally determinate this property, with a huge relevance for early age concrete behaviour.

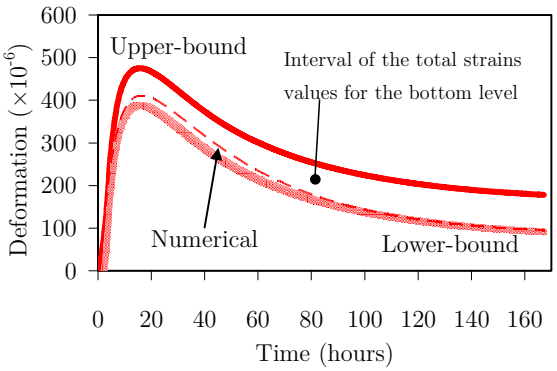

Figure 5.15: Total strains ε_x at the bottom level assuming reduction of α_T along hydration

5.6 The restrained concrete ring test for evaluation of shrinkage induced stresses

5.6.1 Background

The restrained concrete ring test, which has been used since the 1940's by several researchers (Vaysburd *et al.* 2001), essentially consists of a concrete hollow cylinder cast around a steel ring: shrinkage (both autogenous and drying) causes concrete under contraction to radially compress the inner steel ring (setup is represented schematically in Figure 5.16). Circumferential stress in the steel ring can be monitored, which allows the gathering of valuable information in regard to the evolution of the pressure exerted by concrete, and the instant of cracking (if it happens). This kind of test has been widely used with the purpose of qualitatively comparing the cracking potentials of different concrete mixes, induced by shrinkage. In 1998 the American Association of State Highway Transportation Officials (AASHTO) issued a provisional standard where the restrained ring test was contemplated (AASHTO 1998). More recently, Hossain and Weiss (2004) proposed a different geometry than the AASHTO one, in order to get higher shrinkage rates, more uniform moisture profiles inside concrete and easily comparable results; the specimens used in the experimental campaign described in the present section are inspired on this latter geometry.

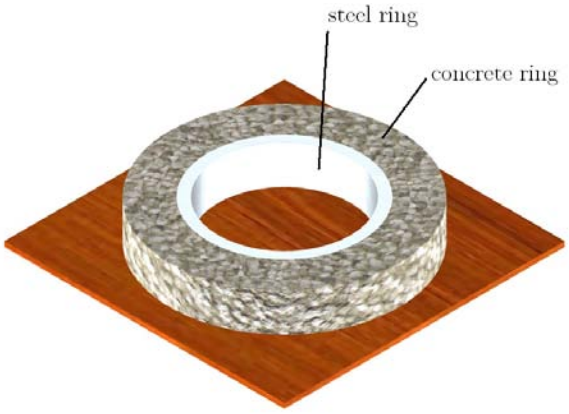

Figure 5.16: Illustration of a restrained concrete ring test

Besides the concrete ring test being quite economic (since re-usable), it has a strong potential for the practical characterization of concrete shrinkage and partial dissipation of its effects through creep. In fact, many concrete compositions may be tested simultaneously, in opposition to what happens with other kinds of tests that use complex and expensive systems, such as the linear restraint experimental setups described in Kovler (1994) and Pigeon *et al.* (2000).

Because of its very simple geometry, within the domain of Theory of Elasticity (Timoshenko *et al.* 1970) the restrained ring test has exact solutions for determination of the strain and stress fields. Yet, because of concrete creep, such solutions are not applicable to both materials of the experimental setup, but indeed they can be applied to the steel ring alone. In the following it will be shown that based solely on the strains measured in the inner face of the steel ring, it is possible to determine the hoop stress acting on concrete in the interface steel/concrete. A similar approach has been used in the past for the restrained ring test (Hossain and Weiss 2004).

For derivation of the concrete stress formula, nomenclature presented in Figure 5.17 is adopted: the concrete ring is the outer ring, and the steel ring is the inner one; exerted pressures on the faces of the rings are presented as arrows.

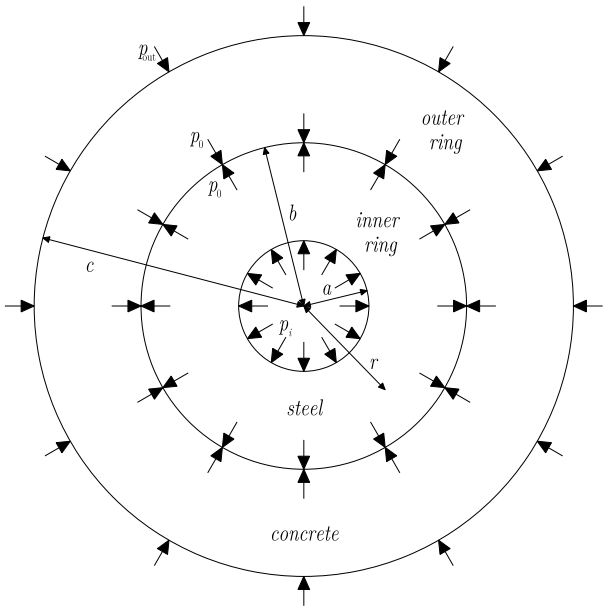

Figure 5.17: Scheme of the ring system

Considering the above geometrical definitions for the steel ring, the following formulas are forwarded in Timoshenko and Goodier (1970) for both hoop (σ_θ) and radial (σ_r) stresses, as well for the hoop strain (ε_θ):

$$\sigma_r = \frac{a^2 b^2 \left(p_0 - p_i\right)}{b^2 - a^2} \frac{1}{r^2} + \frac{p_i\, a^2 - p_0\, b^2}{b^2 - a^2} \tag{5.12}$$

$$\sigma_\theta = -\frac{a^2 b^2 \left(p_0 - p_i\right)}{b^2 - a^2} \frac{1}{r^2} + \frac{p_i\, a^2 - p_0\, b^2}{b^2 - a^2} \tag{5.13}$$

$$E_s\, \varepsilon_\theta = \sigma_\theta - \nu_s\, \sigma_r \tag{5.14}$$

Where E_s and ν_s are respectively the E-modulus and Poisson's ratio of steel, r is an arbitrary distance from the centre of the rings, a and b are the inner and outer radius of the steel ring, and p_i and p_0 are the inner and outer pressures acting on the steel ring.
Considering that p_i=0 and substituting equations (5.12) and (5.13) into equation (5.14), the following is obtained:

$$p_0 = \frac{\varepsilon_\theta \left(a^2 - b^2\right) r^2\, E_s}{b^2 \left(a^2 + r^2 + \nu_s\, a^2 - \nu_s\, r^2\right)} \tag{5.15}$$

If the strain ε_θ=$\varepsilon_{\theta,a}$ refers to the inner face of the ring (r=a), then equation (5.15) transforms to:

$$p_0 = \frac{\varepsilon_{\theta,a} \left(a^2 - b^2\right)\, E_s}{2\, b^2} \tag{5.16}$$

As the outer concrete ring has an internal radius b and an external radius c (see Figure 5.17), the hoop component of stress according to equation (5.13), making the necessary arrangements may be established:

$$\sigma_{c\,\theta} = -\frac{b^2 c^2 \left(p_{out} - p_0\right)}{c^2 - b^2} \frac{1}{r^2} + \frac{p_0\, b^2 - p_{out}\, c^2}{c^2 - b^2} \tag{5.17}$$

where p_{out} is an external pressure exerted on the concrete ring. As in the experiment p_{out}=0, the previous equation simplifies to:

$$\sigma_{c\,\theta} = \frac{p_0\, b^2}{c^2 - b^2} \left(1 + \frac{c^2}{r^2}\right) \tag{5.18}$$

By analysis of this equation, it can be noticed that the maximum hoop stress in concrete happens when r=b, i.e., at the interface between the concrete and the steel rings:

$$\sigma_{c\,\theta,\max} = \frac{p_0\left(b^2 + c^2\right)}{c^2 - b^2} \tag{5.19}$$

Therefore, upon knowledge of the strain in the inner face of the steel ring, it is possible to compute the concrete hoop stress in the interface between concrete and steel by substituting (5.16) on (5.19):

$$\sigma_{c\,\theta,\max} = \frac{\varepsilon_{\theta,a}\left(a^2 - b^2\right)E_s}{2\,b^2}\,\frac{\left(b^2 + c^2\right)}{c^2 - b^2} \tag{5.20}$$

With this simple equation, the maximum hoop stress in concrete at any instant may be calculated directly upon monitoring the strains in the inner face of the steel ring.

5.6.2 Experimental setup

The steel rings used in the experimental campaign were obtained from commercially available thick walled pipes with an external diameter of 30cm, cut in 7.5cm tall rings, and machinated to their final wall thickness: 0.5cm, 1.0cm and 2.0cm. The outer mould for the concrete ring was obtained through calendering of thin brass plates. This outer mould has an internal diameter of 45cm, and is 7.5cm tall. In conjunction with the inner steel rings, this external mould assures that all concrete rings have the same geometry: 7.5cm by 7.5cm cross section, and an inner diameter of 30cm. The inner steel ring and the outer mould were placed over a wooden plate with 60cm×60cm, which acted as a bottom formwork. The correct relative positioning of the three parts involved was assured by a set of eight holes on the wooden plate, in which nails could be placed to lock positions (4 outside of the outer mould and 4 inside the steel ring). The whole set that has been described can be observed in Figure 5.18a. Also in this figure, the set of used extensometers can be seen: 4 extensometers monitored hoop strains at mid-height of the inner face of the steel ring, equally spaced at 90° angles. The extensometers were resistive ones, with a 350Ω resistance, having the commercial reference Vishay CEA-06-250UW-350.

a) b)

Figure 5.18: Appearance of the restrained ring test: a) before casting; b) after casting

Before casting, surfaces to be in contact with concrete were painted with a demoulding oil used in construction. This paint helps both the demoulding operations and the slipping between concrete and steel along the experiment. During casting operations care was taken to avoid the inner surface of the steel ring to be disturbed by drops of cement paste. Right after casting, the exposed concrete surface was covered with plastic foil, to avoid moisture exchanges with the environment before demoulding – see Figure 5.18b. At the age of 24h, this plastic foil was removed, as well as the outer brass mould of the concrete ring. The outer surface of the concrete ring exposed upon mould removal was covered with a bituminous paint and then re-covered with aluminium foil to prevent moisture losses– see Figure 5.19. In order to allow moisture exchanges with the environment from both top and bottom surfaces of the concrete ring, the setup was placed over plastic mats with ribbed patterns, as shown in Figure 5.19b. Strain gage measurements were performed at each 5 minutes and recorded by a DATATAKER DT505 datalogger. All the restrained ring experiment occurs in a climatic chamber with controlled temperature (T=20°C) and relative humidity (RH=50%).

a) b)

Figure 5.19: a) Application of the bituminous paint on the external surface of the concrete ring; b) Experiment after sealing and placement over final support system

5.6.3 Experimental campaign

The conducted experimental campaign involved the use of a self-compacting concrete with the mix proportions defined in Table 5.1, and it was extended for a total period of 55 days.

Table 5.1: Concrete mix for the restrained ring experimental campaign

Material	Dosage kgm^{-3}
Cement (CEM I 42.5R)	374
Filler	270
Gravel	809
Natural sand	737
Water	168.6
Superplasticizer	6.438

Three concrete rings were cast, with two active strain gages per ring. In order to characterize the concrete used in regard to shrinkage, a prismatic specimen with the same

cross section as the concrete ring ($60\times7.5\times7.5cm^3$) was cast, with its strains being monitored. At the age of 24h this specimen was demoulded and isolated to humidity exchanges in all faces except for the top and bottom ones, as already described for the concrete rings. This way the unrestrained prismatic specimen had the same cross section and was monitored under the same moisture conditions as for the concrete rings. Therefore, the shrinkage measurements on the prismatic specimen were used for characterization purposes, namely for the numerical analyses to be presented later. Concrete cubes and cylinders were cast in order to assess the compressive and tensile strengths and the Young's modulus at the ages of 1 day, 3 days, 7 days, 21 days and 28 days. Compressive creep tests were also performed at the ages of 1 day, 3 days, 8 days and 23 days, using prismatic specimens with dimensions $45\times15\times15cm^3$, and with an applied stress corresponding to 20% of the compressive strength of concrete at the age of loading. Except for the cubes and cylinders, which were kept at T=20°C and RH=100%, all specimens were kept inside a climatic chamber at a constant T=20°C and a RH=50%. All specimens were covered with a plastic foil during the first 24h of age.
The linear shrinkage test yielded the strains depicted in Figure 5.20. The overall result appears to be logical, except for some apparent shrinkage recoveries (such as the one that is evident at about 13.6 days) that are probably not real, and might be attributed to electrical disturbances in the measuring system.

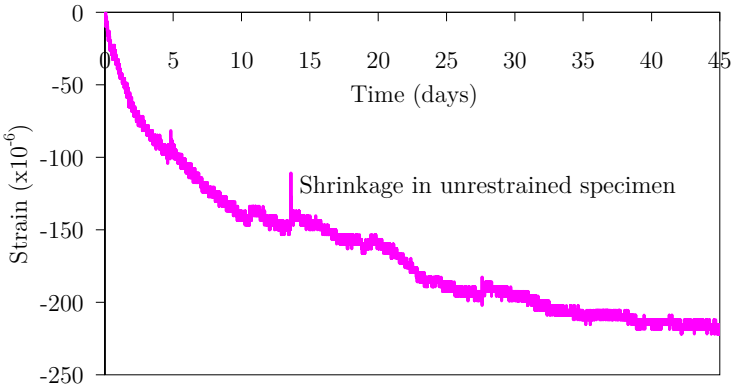

Figure 5.20: Strain evolution in the shrinkage prismatic specimen

Shrinkage induced strains measured in pairs of strain gages placed in each one of the three monitored steel rings can be observed in Figure 5.21. Results of each pair of extensometers appear to mutually validate themselves, fact that gives confidence to the measured strains in the steel rings. The strain in the steel can be considered as almost matching the strains in the inner surface of the respective concrete ring. Therefore, some comparisons can be made between the results of the concrete restrained rings themselves, and between them and the strains on the concrete shrinkage prism. As expected, thicker steel rings provide higher restraints to concrete deformation, and therefore the measured strain is smaller. In addition, the measured strains in the restrained concrete rings are obviously lower than the ones measured for the shrinkage prism: at 45 days after casting, the less restrained concrete ring has a measured strain of about 110×10^{-6}, while at the same age the shrinkage prism reaches a strain of about 220×10^{-6}.

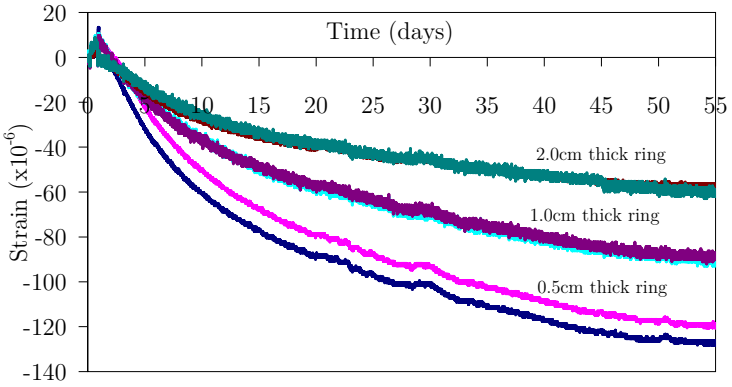

Figure 5.21: Shrinkage induced strain evolution in the steel rings

The measured temperature evolution in the unrestrained concrete shrinkage prism is shown in Figure 5.22. After a dormant period of about 0.2 days, a small hydration induced temperature rise of 2.7°C happened: this was expectable in view of the very small cross section of the monitored prism. This early temperature development is the probable explanation for a part of the initial swelling that can be noticed in the measured strains on the steel rings (see Figure 5.21).

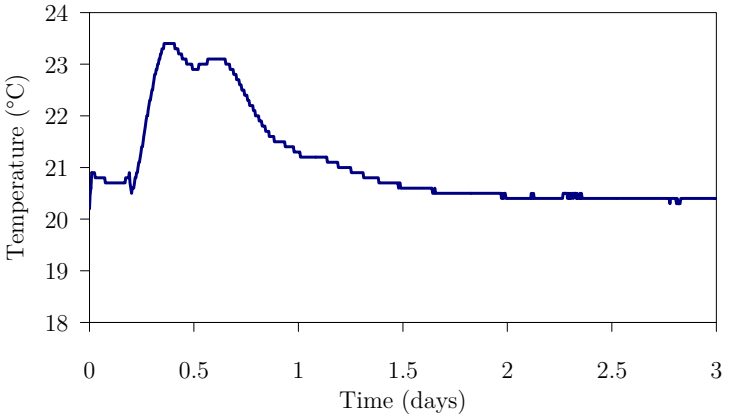

Figure 5.22: Temperature evolution in the unrestrained prismatic specimen

Results of the conducted creep tests are depicted in Figure 5.23. In this figure, the line named as $1/E_c$ corresponds to the inverse of the elasticity modulus obtained by compressive tests. LVDT and CLIP measurements are identified. The results of creep tests with age at loading of 1 and 8 days seem very reasonable and coherent with the $1/E_c$ curve. In addition, at the 8 days test, measurements of the two systems (CLIP and LVDT) seem to be quite coherent with each other. In the tests at 3 days and 23 days, responses of the used measuring systems appear to be extremely stiff. The reason for this may have been related to the fixation of the sensors to the specimen (slack) or some eccentricity in the application of the load. In the same figure, the creep parameters used for fitting creep data using the Double Power Law are identified.

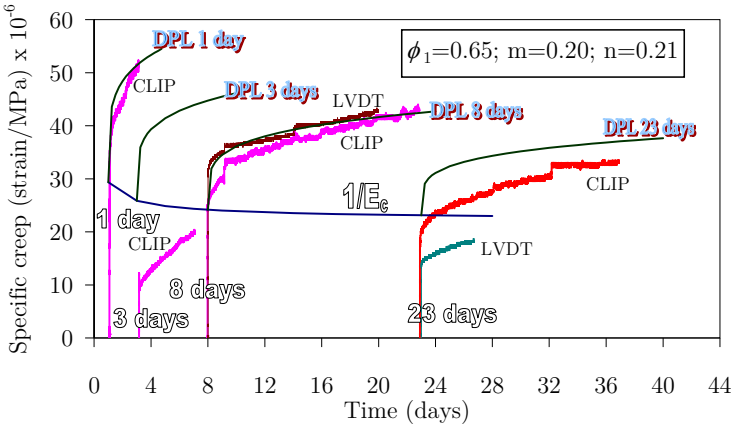

Figure 5.23: Creep test results and DPL creep parameters

The results of the mechanical characterization tests performed on the concrete cubes and cylinders can be observed in Figures 5.24 and 5.25. The evolution of these mechanical properties fell within the expectable tendencies and values. There were some problems in the Young's modulus testing at the age of 1 day. For that reason, the results for such age are omitted in Figure 5.25.

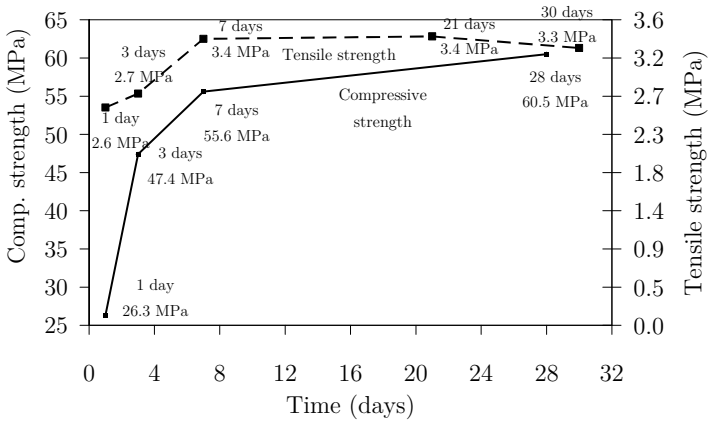

Figure 5.24: Evolution of concrete strengths: tensile and compressive

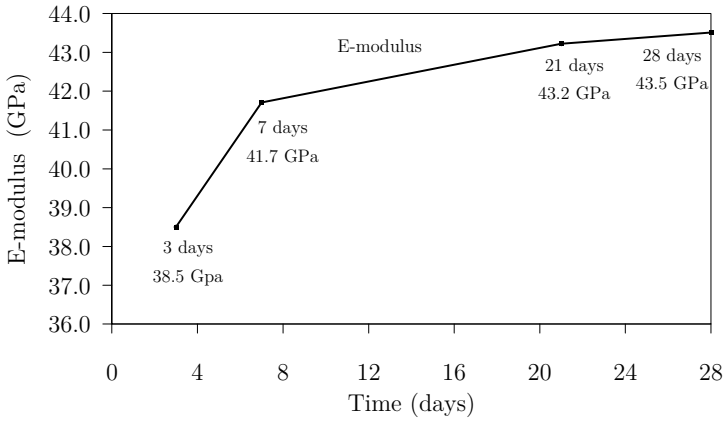

Figure 5.25: Evolution of Young's modulus

Upon knowledge of concrete tensile strength evolution, it is interesting to evaluate its relationship to the evolution of stresses on concrete at the interface steel/concrete for the three restrained rings, calculated using equation (5.20), as depicted in Figure 5.26.

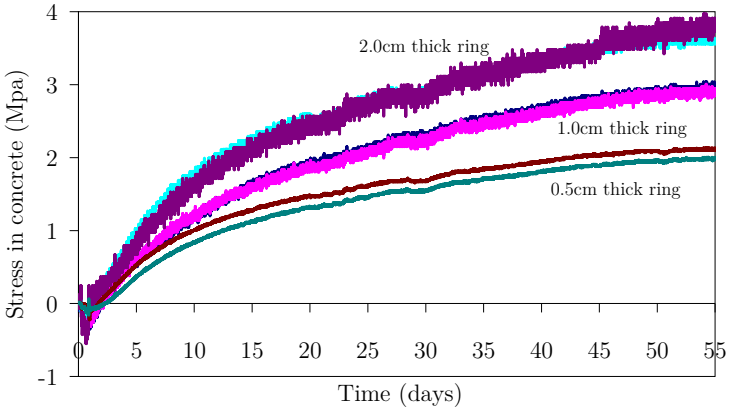

Figure 5.26: Tensile stresses in concrete computed from the steel strains

It can be observed that the tensile stresses in concrete are rather different according to the restraint provided by the steel rings. At the end of the experiment (t=55 days), the measured stresses are of 3.7MPa, 2.9MPa and 2.0MPa for the ring thicknesses of 2.0cm, 1.0cm and 0.5cm, respectively. In the case of the 2.0cm thick steel ring, cracking was probably imminent once the recorded value of 3.7MPa was already slightly above the last recorded tensile strength of 3.4MPa (at the age of 30 days). Cracking is difficult to achieve in the restrained ring test for concrete, given the combination of relatively small shrinkage strains compared to the restraint provided by the used steel rings. Nevertheless, this is not an indication that thicker rings should be used; in fact, if thicker steel rings were used, the measured strains would become too small in regard to the precision of the strain gage. Thus, there is a balance to be observed: either there is much restraint and limited measuring capacity, or there is good measuring capacity with limited restraint.

5.6.4 Interpretation of results through numerical modelling

The present section pertains to the numerical simulation of the three restrained concrete rings under study, allowing a better understanding of the experiment, as well as a validation of the capabilities of the numerical simulation tools. Firstly, a thermal analysis of the temperatures developed in the monitored shrinkage concrete prism was conducted. The thermal analysis considered a plane model of the cross section of the specimen (with the simplifying assumption that heat transfer in the longitudinal direction is negligible): geometry adopted for this model is schematized in Figure 5.27a. The four boundaries of the model (P1-P2, P2-P3, P3-P4 and P4-P1) are considered as direct contact with the air, reproducing the conditions of the experiment: initial temperature of 20°C was considered for concrete, and the environmental temperature was constant during the whole test (T=20°C). The thermal properties adopted in the model can be observed in Table 5.2. For the characterization of the heat of hydration generation, the DuCOM model was used, with basis in the cement type and dosage. For the finite element discretization, 4 nodded

FE with 2×2 integration points (nodal) were used in a FE mesh with 4 by 4 elements. The thermal analysis was conducted in 32 steps of 1 hour each.

The numerically obtained temperature matched the experimental measurements reasonably well – see Figure 5.27b. From the numerical results it was also possible to observe that the temperature gradients within the cross-section were almost negligible. For the sake of simplicity, and given the very small strains that this temperature rise represents (less than 25με), the temperature effect is to be neglected in the mechanical analysis that follows.

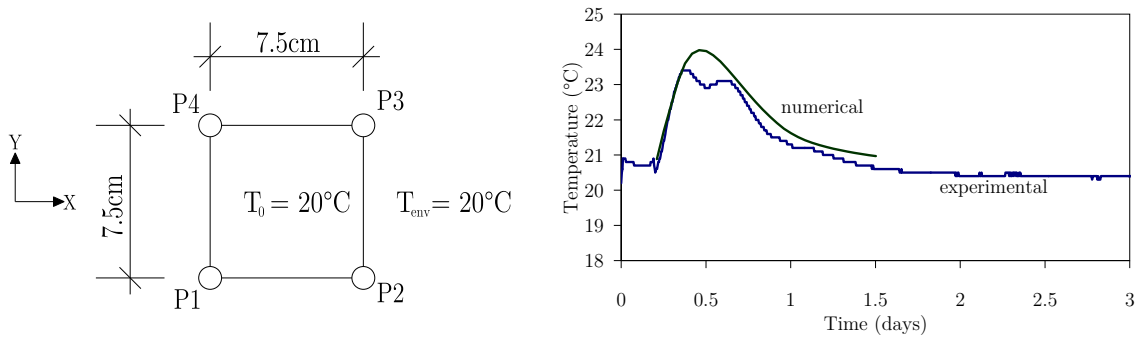

a) b)

Figure 5.27: Thermal model: a) Geometry adopted; b) Temperatures

Table 5.2: Thermal properties

Property	Value
Concrete thermal conductivity	k=2.6Wm^{-1}K^{-1}
Concrete volumetric specific heat	ρc=2400kJm^{-3}K^{-1}
Convection coefficient in boundaries	h=4.5Wm^{-2}K^{-1}

For the restrained rings, a structural analysis was undertaken in an axi-symmetric model, considering both steel and concrete – see Figure 5.28a. Because steel and concrete are not adherent along vertical direction (P2-P5), and shrinkage will simplified to occur uniformly in all concrete (explanation follows), only a 1cm strip of each ring was considered in the FE model, with no transmission of vertical stresses in the interface P2-P5. In terms of supports, line P1-P3 was restrained in the Y direction. In terms of FE mesh refinement, 8 nodded finite elements with 2×2 integration points were used. The adopted mesh for the concrete ring restrained by the 1cm thick steel ring is depicted in Figure 5.28b (steel elements shaded). The analysis was conducted using time steps of 3h during a total of about 47 days.

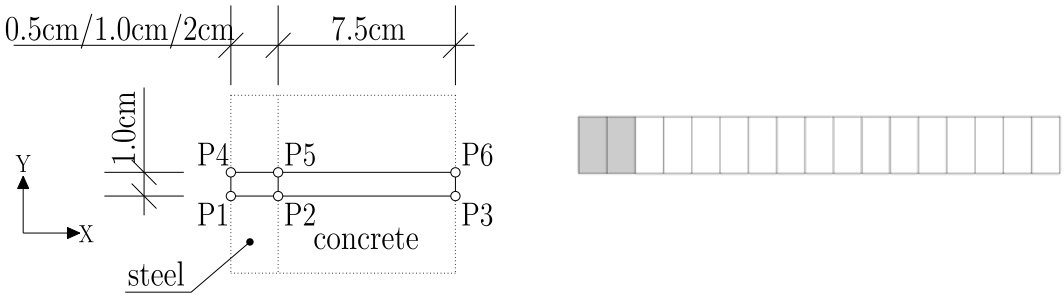

a) b)

Figure 5.28: a) Schematic representation of the model for the structural analysis of the rings; b) Typical FE mesh (steel elements shaded)

For the evolution of concrete elasticity modulus to be used in the numerical model, an equation of the type suggested in Model Code 90 (CEB-FIP 1993) was used, which fitted the experimental results:

$$E_c(t) = 43.5\left(e^{0.19\left(1-\sqrt{\frac{28}{t}}\right)}\right)^{0.3} \quad \text{(in GPa)} \tag{5.21}$$

This experimental campaign did not involve any characterization of the moisture diffusion coefficient of concrete, nor its desorption isotherm. Shrinkage strains input for the numerical simulation were therefore considered uniform along the concrete cross-section, according to the evolution depicted in Figure 5.20. Other mechanical properties for both concrete and steel are shown in Table 5.3.

Table 5.3: Mechanical properties used in the numerical model

Property	Value
Concrete Poisson's ratio	$\upsilon = 0.18$
Steel Poisson's ratio	$\upsilon = 0.30$
Thermal dilation coefficient (concrete and steel)	$\alpha_T = 10\times10^{6}\ \mathrm{K}^{-1}$
Steel – Young's modulus	195 MPa

The mechanical model that has just been described led to the results depicted in Figure 5.29, where a comparison is made to the experimental measurements of strains in the steel rings; Figure 5.30 provides a similar comparison in terms of concrete stresses. The strains and stresses in the the experiments and numerical calculations show a relatively good coherence. Nevertheless, the numerical model seems to underpredict the steel strains and the concrete stresses after 10 days from the beginning of the experiment. This deviation is probably related to the fact that there might have been a monitoring problem in the shrinkage prism, whose measurements exhibited an unexpected deceleration at such age. Therefore, based on the reliability of the source data, and the complexity of phenomena

involved (concrete creep, and evolving mechanical properties) the numerical simulation may be considered reasonably successful.

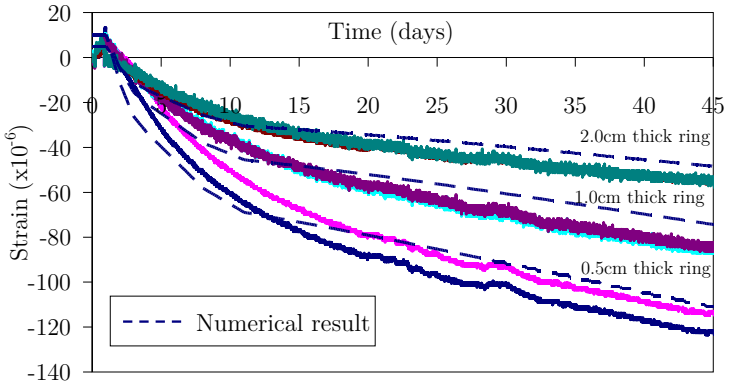

Figure 5.29: Strain evolution in the steel rings: numerical *versus* experimental

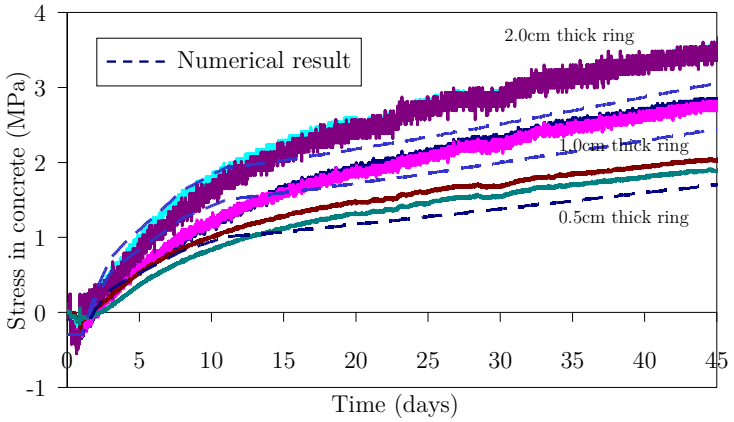

Figure 5.30: Stresses in concrete: numerical *versus* experimental

For sensitivity analysis, the calculated strain and stress profiles at the age of 47 days depicted in Figures 5.31 and 5.32, will be discussed further. It can be seen that strains are minimum at the interface between concrete and steel, which is coherent with what would be expectable by the use of Elasticity Theory. The strain profile within concrete is almost linear (see Figure 5.31), yet a larger strain gradient between the inner and outer surfaces of the concrete ring can be found in thicker rings. In terms of stresses, as expected, the steel rings are subjected to compressive stresses and the concrete rings are subjected to tensile stresses, with stresses in concrete being more uniform for the 0.5cm steel ring (thinnest). Parametric analyses regarding alternative geometries for the ring test in terms of thickness of the steel ring, thickness of the concrete ring and the diameter of the whole system can be found in Azenha *et al.* (2006).

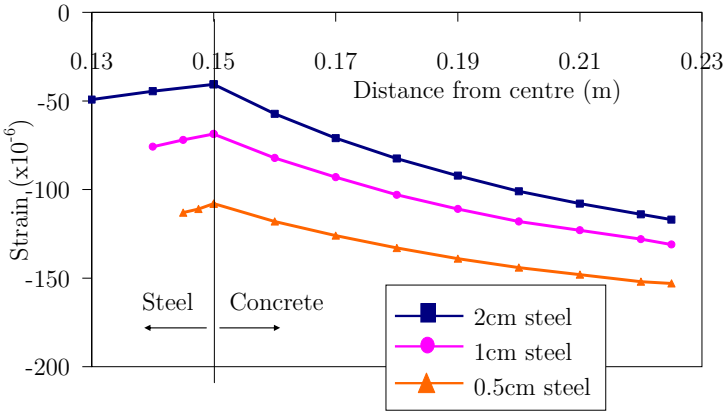

Figure 5.31: Computed strain profiles at 47 days of age

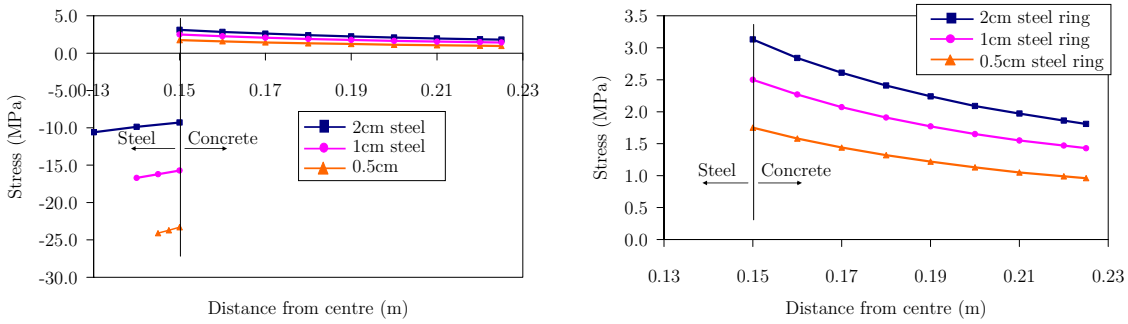

a) b)

Figure 5.32: Computed stress profiles at 47 days of age: a) steel and concrete; b) concrete

5.7 New method for continuous monitoring of concrete E-modulus since casting

5.7.1 Introduction

The knowledge of how concrete E-modulus evolves since casting and along hydration reactions is of paramount importance for many fields of material science, namely for prediction of stress development in hardening concrete at early ages, when important volumetric changes are known to occur. It is therefore quite important to know the structural setting time (time at which the material starts to bear structurally relevant stresses, also known as "mechanical threshold" (Torrenti *et al.* 2005)), as well as the concrete stiffness increase along time.

Non destructive techniques for the determination of concrete E-modulus are used for quite some time. Two dominant techniques exist: the resonant frequency methods and ultrasound techniques. The resonant frequency methods basically consist of impacting concrete specimens with hammers, measuring their fundamental transverse, longitudinal and torsional frequencies, which in turn are related to the E-modulus of concrete. It is usually applied to cylindrical specimens, and its usage is widely spread, including in

ASTM standards (ASTM 2002). These methods require a mechanical shock to create an excitation and therefore it is mandatory that the concrete specimen is demouldable (i.e. has hardened enough to be removed from its form). This requirement makes this technique inadequate to evaluate concrete E-modulus evolution since the early ages just after casting, as well as the mechanical threshold. The earliest evaluations of E-modulus with this technique found in literature were 5 hours after casting (Nagy 1997) and 8 hours after casting (Jin *et al.* 2001).

Ultrasound techniques are based on the velocity of propagation of artificially generated sound waves in concrete, relating it to its E-modulus. If adequate experimental setups are adopted, with the acoustic emitter and receptor embedded in the specimen's formwork, it is possible to evaluate the wave speed continuously right after casting. External disturbances that may cause wave motion in the specimen, such as jackhammers, should be avoided during the test (Malhotra *et al.* 2004). Because of the geometric scales at which these tests are usually conducted (small specimens such as cubes, or small distances between emitter and receiver), this technique is quite sensitive to local effects caused by aggregates, and thus many authors dismiss its capability to actually quantifying the E-modulus in concrete, advocating the technique as being rather more qualitative than quantitative (Neville 1995).

The present study aimed to create a variant to the traditional resonant frequency methods, allowing continuous concrete E-modulus measurement right after casting. Development of the method comprised two phases: (i) a first one, in which a pilot experiment using a concrete specimen was performed, and (ii) a second, in which the methodology was adapted to fit systematic characterization of E-modulus of cement pastes. Regardless of the cementitious material under study (concrete, cement paste or other), the experimental setup consists of an acrylic glass hollow beam (i.e. a tube), filled with the material to be characterized, constituting a composite beam with known support conditions. The first natural flexural frequency of this composite beam is thereafter identified along time using ambient vibration based identification techniques. As the concrete or cement paste starts with no stiffness, the natural frequency at the beginning of the test corresponds to that of the acrylic tube alone, carrying the mass of the unhardened sample. During concrete hardening the beam endures composite behaviour, and the first flexural natural frequency increases in correspondence to the growth of the hardening material elastic modulus. So, by determining the first natural frequency, and regarding the geometrical and material conditions of the setup, it is possible to directly obtain the E-modulus of the hardening material at each instant. The proposed method is entirely passive, in the sense that it avoids the necessity of providing external vibration sources. In fact, the ambient vibrations are enough: people walking nearby, mechanical equipment vibrations, wind acting on buildings, and so on. Another important point regarding the experimental procedure proposed is that measurement of the Young's modulus is made through a test that actually mobilizes structural performance of the specimen, in an analogous fashion to what actually occurs in real concrete structures.

After a brief description of the principles of ambient vibration based modal identification techniques, the two versions of the devised methodology will be described, and their experimental results are presented and cross-validated with other experimental techniques.

5.7.2 Ambient vibration tests: theory and use for the current application

The technique of ambient vibration for modal identification of civil engineering structures has been widely used since the 1980's. This technique relies on the environmental vibrations to provide excitation for the structures, thus allowing the identification of their natural frequencies. In view of recent works conducted at FEUP in the field of ambient vibration applied to civil engineering structures (Cunha *et al.* 2007, Magalhães *et al.* 2008), the application envisaged in the proposed methodology, involving a composite beam with known support conditions, is a relatively simple one. The selected methodology for identification of the resonant frequencies is the Peak-Picking method, in its 'output only' version (Bendat *et al.* 1980). This method assumes that excitation of the structure under study can be idealized as a white noise, i.e., a stochastic process with constant spectral intensity in all frequencies. Because of this assumption, the peaks of the response spectra coincide with the peaks of the frequency response function, which in turn permit the identification of the structure's natural frequencies. A brief outline of the overall acceleration measurement and data processing procedure adopted in the proposed experimental technique follows:

- Accelerations at a selected point of the studied composite beam are measured during the whole range of the experiment using an accelerometer, and stored in a data logger. As all the frequencies to be measured were below 100Hz (both in the case of concrete and cement paste specimens), it was considered enough to monitor frequencies under 200Hz.
- The response record of accelerations along time collected during the experiment is divided in several parts with 15 minutes duration each. For each of these parts, resonant frequencies are identified by applying the Welch procedure (Welch 1967): the 200Hz measured acceleration 15 minute long time series are divided in a group of smaller time segments (of 4096 points each), with 50% overlapping. In order to minimize leakage effects, Hanning windows (Maia *et al.* 1997) are applied to each one of these 4096 point time segments. The windowed time series are then processed using a Discrete Fourier Transform (DFT), which results in a group of auto-spectra. These auto-spectra are then averaged, and the averaged auto-spectrum for the 15 minute period under analysis is obtained.
- All the N averaged auto-spectra (PSD) obtained are then normalized by dividing them by the sum of all the spectral ordinates per angular frequency w, according to Eq. (5.22). The reason for this necessity is the fact that the averaged time series collected along the experiment correspond to distinct 15 minute periods, for which the ambient vibration may have had dissimilar intensity, thus conducting to distinct energy content in the spectra.

$$NPSD(w) = PSD(w) \Big/ \sum_{i=1}^{N} PSD(w_i) \tag{5.22}$$

- The resulting normalized auto-spectra $NPSD(w)$ are then included side-by-side in a colour map with frequency *versus* time axes - see Figure 5.33a -, the colours being proportional to the intensity of the power spectra.
- In order to obtain, with a simple and fast procedure, an automatic estimate of the resonant frequency of the first vibration mode of the composite beam, an average is made with the frequencies corresponding to the 40 points of higher energy of each spectrum, using the energy intensity as a ponder factor. By applying this to all averaged spectra, a graphic of resonant frequency *versus* time is obtained, such as the one represented in Figure 5.33b.

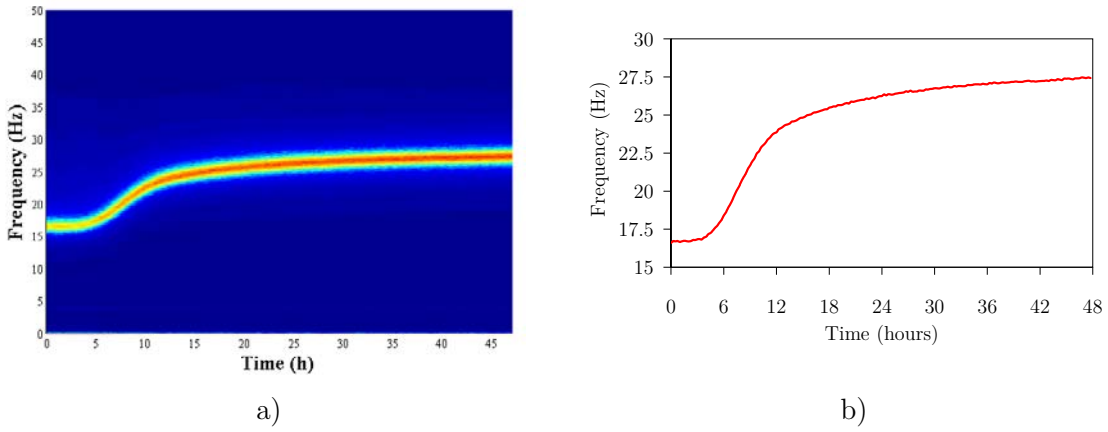

a) b)

Figure 5.33: a) Colour map containing the several NPSD(w) side by side; b) Automatic estimate of the corresponding resonant frequency

5.7.3 Pilot experiment in concrete

5.7.3.1 Geometry and procedure

The experiment consists of casting a concrete specimen bounded by an acrylic formwork, working as a horizontal simply supported beam. The basic component of the experiment is a 2m long acrylic hollow cylinder, with an internal diameter of 92mm and an external one of 100mm, as depicted in Figure 5.34. Holes with 5mm diameter were drilled in the cylinder (symmetrically in regard to its midspan) for several purposes: 2 horizontal holes at 10cm distance from the edges, in order to insert steel rods and materialize simple supports; vertical holes at the distances of 40cm, 70cm and 100cm from the extremities of the beam, to install steel rods acting as connectors (improving solidarization between acrylic and concrete). Two horizontal threaded steel rods (effective diameter 4mm, E=180GPa) materialize the pinned supports at both extremities of the beam, trespassing it completely and spanning over the flanges of a steel profile (15cm wide between axes of flanges), as schematized in Figure 5.34 and reproduced in Figure 5.35 (photo of the experimental setup).

Because the horizontal rods have to span 15cm above the steel profile, this arrangement led to a 2.5cm long steel bar cantilever at each side of the acrylic beam, whose flexibility played a role in the results obtained in this experiment, as to be discussed later.

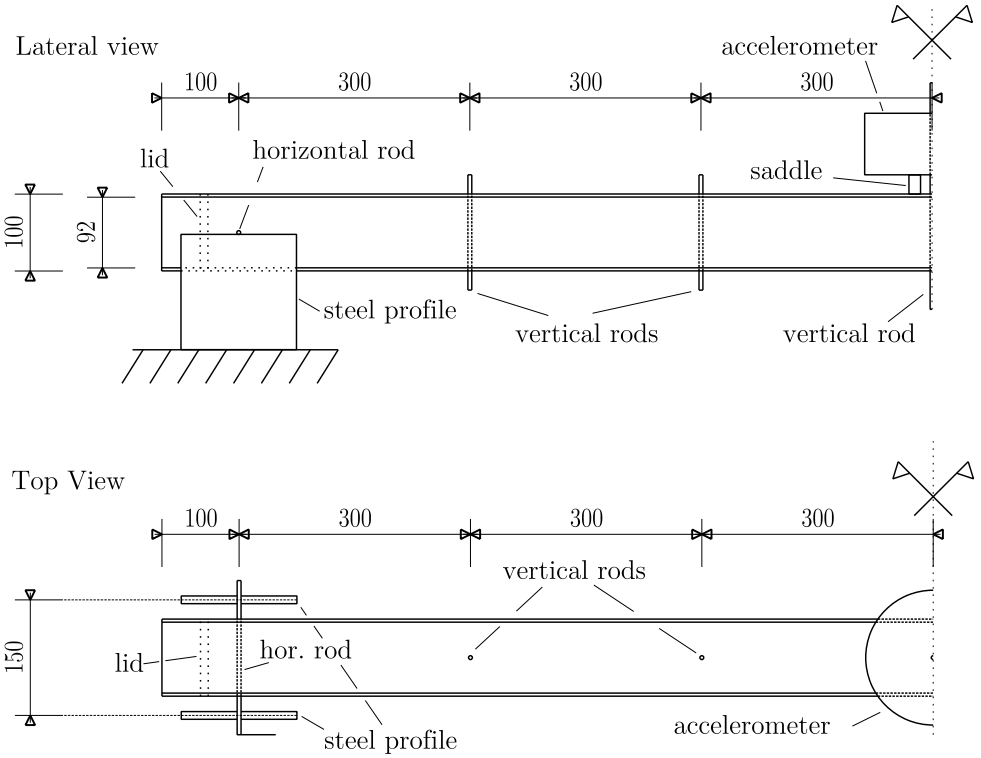

Figure 5.34: Geometry of the acrylic tube and experimental setup (dimensions mm)

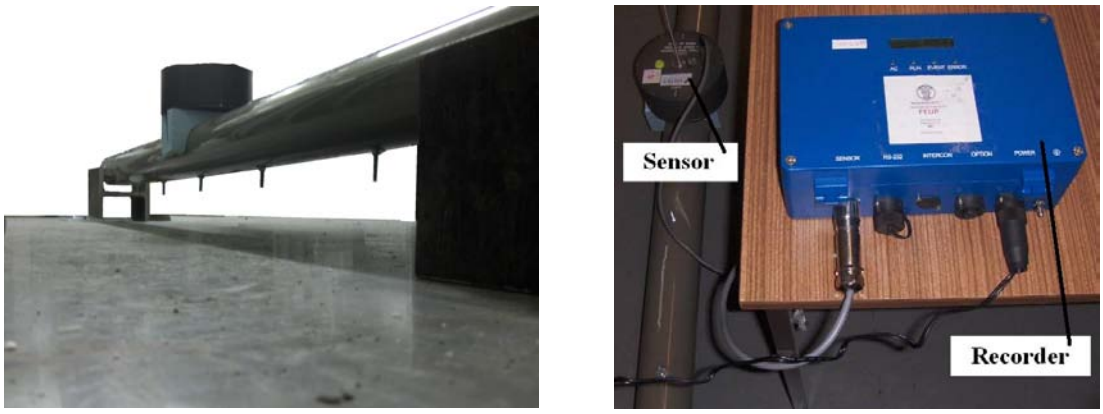

a) b)

Figure 5.35: a) Photo of the experimental setup; b) accelerometer and recorder used in the experiment

A CMG-5T force balance accelerometer from Guralp, weighting 2.27kg, was used, allowing measurement of vertical accelerations at mid-span within the frequency band from DC to 100Hz, with a sensitivity of 5V/g and a noise floor around 2μg (g being gravity's acceleration). This sensor was connected to a GSR-24 recorder from Geosig that performs the analogue to digital conversion of the measured signals using a 24-bits board and stores the collected data in a memory card. The accelerometer was placed at midspan on top of the beam, using the existing vertical steel rod for fixation, together with two

symmetrically placed polystyrene saddles (see Figure 5.35, and a detail in lateral view of Figure 5.34).
Concrete casting started with the acrylic cylinder inclined at a 45° angle with the horizontal, ending with the tube in vertical position for placement of the closing lid (see Figure 5.34 – lateral view). The time elapsed between onset of casting and the start of acceleration acquisition was less than 15 minutes. During the whole monitoring period, which extended for 14.9 days since casting, the composite beam remained untouched inside a climatic chamber, under a constant T=20°C and RH=50%. Bearing in mind the observed effect of the supporting rods on the measured frequencies (to be described later), at the age of 14.9 days the experiment was interrupted, and the supporting conditions were changed by suppressing the 'small cantilevers' referred before, thus enforcing from then on vertically rigid pinned supports (see Figure 5.36).

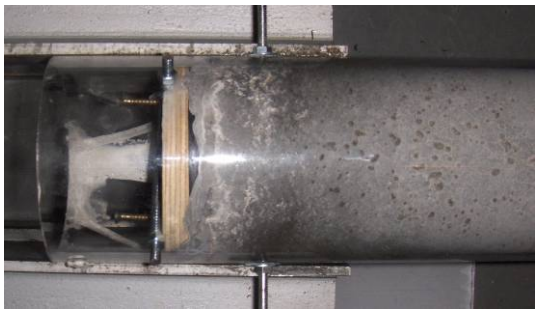

Figure 5.36: Final arrangement of the pinned support (changed at t=14.9 days – view from top)

After this support condition was changed some periods of ambient vibration measurement were performed until the age of 15.08 days. The experiment was then interrupted and left untouched, and at the age of 28 days additional experiments were performed (without any further change to the support conditions). Firstly, a time series of 15 minutes duration was recorded in order to evaluate the beam frequency f at this age. Then a static loading test was performed, which consisted of sequentially placing steel plates with known mass on top of the accelerometer (at mid-span), and recording the corresponding mid-span deflections with Linear Variable Differential Transducers (LVDT). After this static test, which was conducted with loads well below the cracking load of the beam, nine time series of 15 minutes duration each were recorded, in order to check that f remained the same, and that no damage was induced to the composite beam.
In parallel to the beam tests, and for comparison purposes, E-modulus of the concrete was also evaluated at the ages of 0.75, 1, 2, 3, 7 and 28 days through compressive tests performed on standard cylinders (15cm diameter, 30cm tall), cast with the same concrete batch, and using three specimens per age. Prior to testing all specimens were maintained in a T=20°C and RH=100% environment.

5.7.3.2 Materials

For the pilot experiment a self-compacting concrete with w/c=0.42 was selected, with the mixture proportions provided in Table 5.4. River sand and crushed granite stone were used, and the maximum aggregate size was 16mm.

The acrylic used for the formwork was obtained by extrusion, and a summary of its main properties can be found in Table 5.5. The threaded steel rods used as connectors and supporting devices for the beam have a nominal diameter of 4mm and an E-modulus of 180GPa.

Table 5.4: Mixture proportions of the studied concrete

	Quantity (kgm^{-3})
Cement type I 42.5 R	419.8
Mineral adition (calcareous filler)	179.3
Superplasticizer	6.7
Sand 1 (fine)	416.2
Sand 2 (coarse)	315.3
Gravel	848.5
Water	174.5

Table 5.5: Properties of the used extruded acrylic

	Value
E-modulus (GPa)	3.3
Poisson's coefficient	0.39
Density (kgm^{-3})	1190.0
Thermal conductivity ($Wm^{-1}K^{-1}$)	0.19
Specific heat ($Jg^{-1}K^{-1}$)	1.47

5.7.3.3 Results

i) Period 0-14.9 days (flexible supports)

Results obtained for the period starting just after concrete casting and extending until the age of 14.9 days were divided in two parts: an initial one pertaining to the first 72h of monitoring, and a second related to the remaining period. The colour map regarding the spectra of frequencies for the composite beam until the age of 72h is depicted in Figure 5.37: as far as the first vibration mode is concerned, it can be observed that the initial value of f is of circa 7.8Hz until the age of ~3h, instant after which a very steep frequency ascending branch occurs, rapidly reaching 23.3Hz at the age of 14h. After this strong evolution the increase in f occurs very slowly, reaching 25.5Hz at 72h and 26Hz at 357h (see Figure 5.38). As the ambient excitation cannot be classified as a white noise (which would require equal energetic participation of all frequencies of the excitation spectrum), beyond f and the natural frequencies of higher order modes some further frequencies are identified in Figure 5.38 – for example at 18.6Hz, 32Hz and 38Hz –, as expressed by the extra horizontal lines (dashed or continuous). These lines are related to the frequency content of machines working in neighbouring laboratory areas, namely the device used in the climatic chamber to control the environmental temperature and relative humidity. However, and as far as identification of the first beam resonant frequency f is concerned,

this is not a real problem, as it is actually quite well defined in both Figure 5.37 and Figure 5.38.

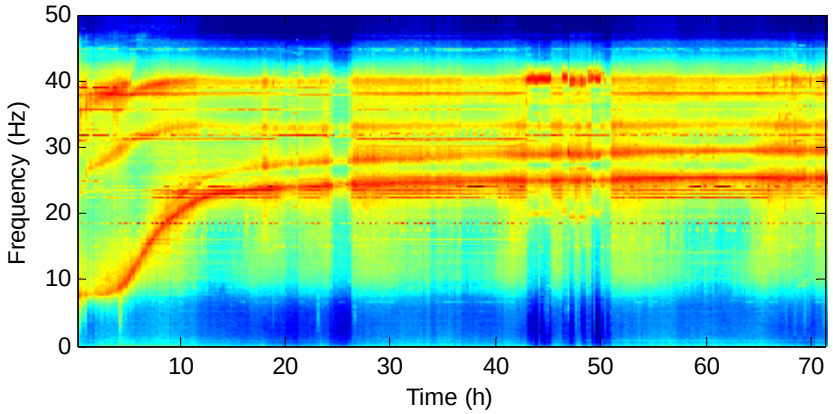

Figure 5.37: Measured frequencies during the first 72 hours of test (flexible supports)

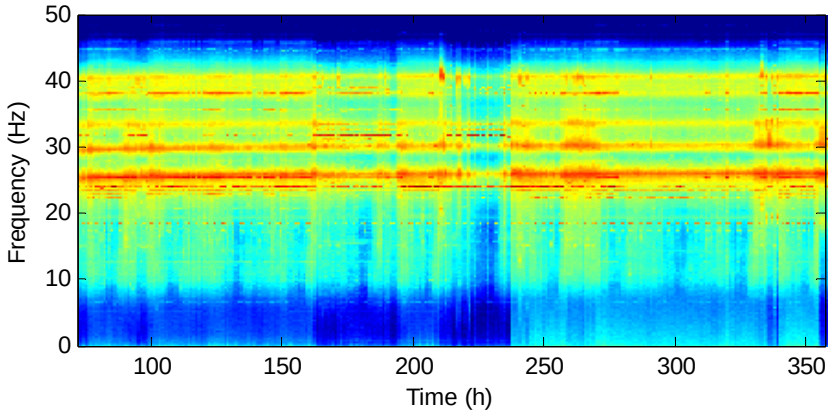

Figure 5.38: Measured frequencies between 72h and 357h (flexible supports)

ii) Period 14.9 d-15.08 days (rigid simple supports)

As mentioned in Section 5.7.3.1, at the age of 357h (14.9 days) the support conditions for the composite beam were changed, eliminating the 'small cantilevers' associated to the flexible rods, and switching to an arrangement where the pinned supports performed as infinitely rigid along vertical direction (rigid simple supports – see Figure 5.36). Henceforward ambient vibration tests were pursued by recording one time series of 15 minutes per hour, resulting in the frequency power spectra reproduced in Figure 5.39: in the three presented spectra a maximum occurs for 38.3Hz, being therefore this value associated with the natural frequency of the beam with the rigid supports, rather different from the value of 26.1Hz measured 1h before the change of support conditions from flexible to rigid. Given the fact that during this period hardening of concrete is almost negligible, this rise in f should be related only to the added stiffness of the whole system, caused by elimination of the 'small cantilever' rods flexibility. For this reason, determination of concrete E-modulus during the first 357h will have to explicitly reproduce those supporting rods on the structural system for the composite beam, as it will be discussed in next section.

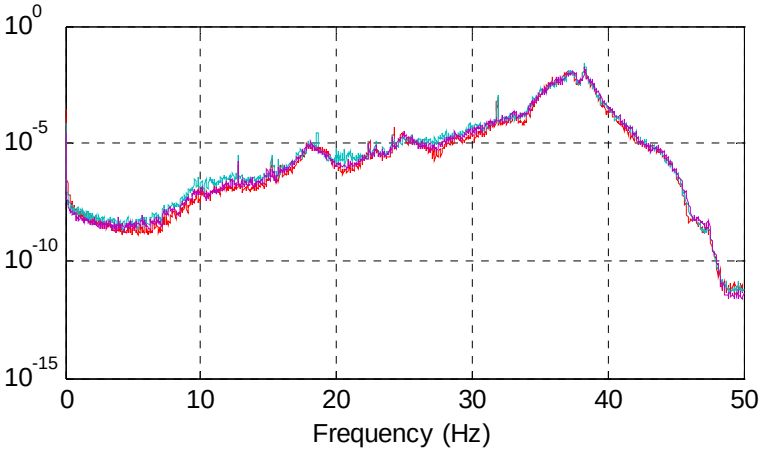

Figure 5.39: Power spectra in the period 358h-362h (rigid supports)

iii) Ambient vibration and static test at the age of 28 days (rigid simple supports)
Ambient vibration tests with one 15 minute time series were performed just before the static loading experiment, and with nine 15 minute time series, distributed in 9h, after it. As it can be seen in Figure 5.40, before the static test at the age of 28 days f was 38.4Hz, which is rather similar to what had been recorded at the age of 15 days (see (*ii*)), revealing that the composite beam stiffness evolved negligibly along the 15-28 days period. Also, f kept constant after the static loading test, indicating that no cracking damage was induced to the concrete.

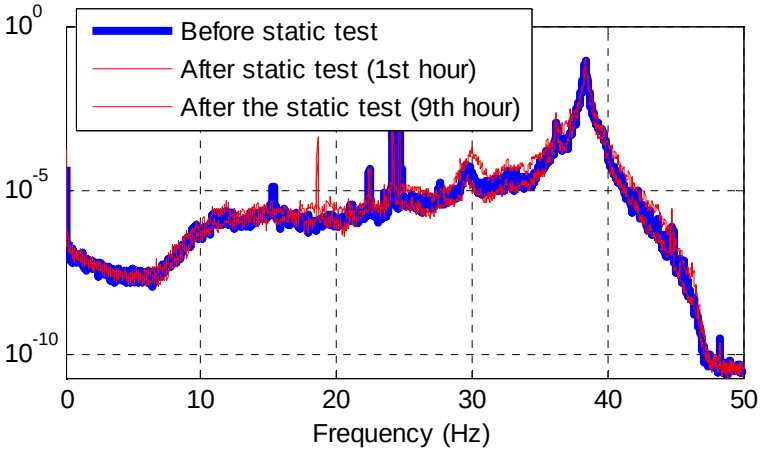

Figure 5.40: Power spectra before and after the static loading test

The composite beam with rigid simple supports was statically loaded by using a succession of masses with 5kg each, applied on top of the accelerometer located at mid-span, ensuring concrete tensile stresses to remain well below the tensile strength, and that linear behaviour could be preserved everywhere. Deflections at mid-span were measured using two LVDTs, placed at the lower face of the composite beam. These mid-span deflections, along with the applied masses, are depicted in Figure 5.41: it can be observed that proportionality existed between the accumulated mass and the corresponding deflection, and that both LVDTs yield quite similar results (i.e. coherent with each other). Also some creep effects during the small periods of load application can be seen, which is particularly evident after the final unloading of the beam, where there is a residual deformation tending asymptotically to 0 along time.

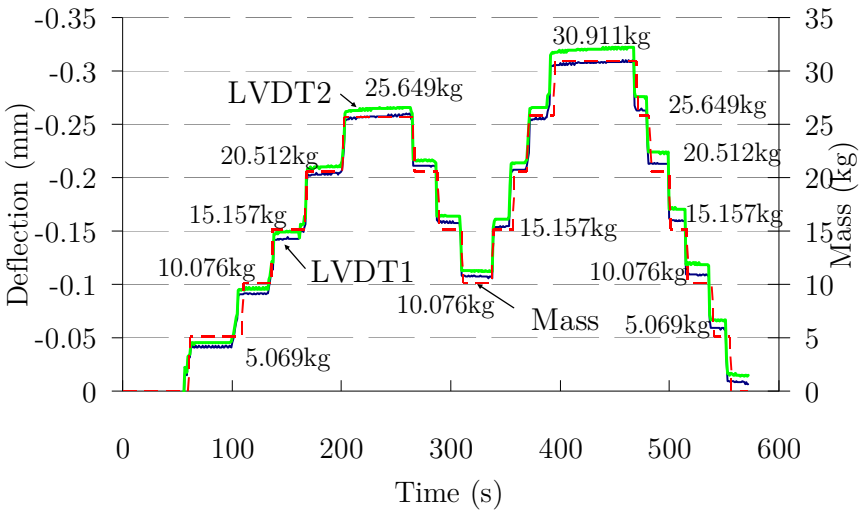

Figure 5.41: Mid-span masses and deflections during the static test

As the purpose of this static loading test was to obtain a reference value for the E-modulus of concrete, in Figure 5.42 the mid-span deflections observed per each kilogram of applied mass are plotted for each of the 18 loading/unloading events reproduced in Figure 5.41.

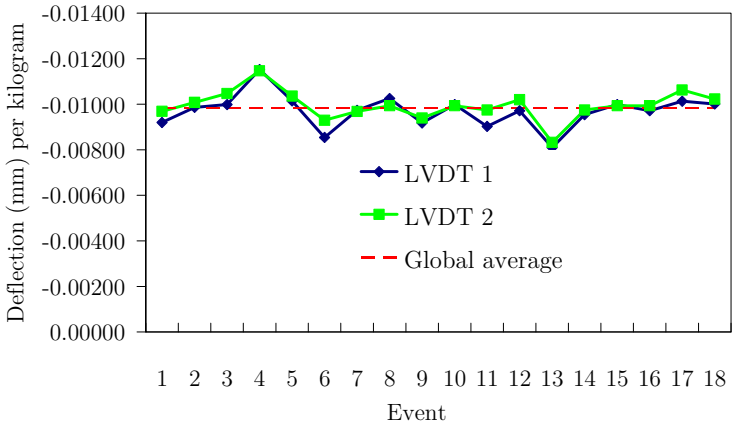

Figure 5.42: Deflections per kg of applied mass during the static test events

iv) Concrete E-modulus evolution measured from compressive tests

Results for the evolution of concrete E-modulus, obtained in compressive tests performed in cylinders cast with the same concrete batch used for the composite beam, are reproduced in Table 5.6. It becomes evident that E-modulus evolves from an average value of 27.7GPa, at the age of 19h, up to 33.4GPa at the age of 28 days, showing that the fastest evolution takes place within the first 19h.

Table 5.6: Evolution of E-modulus – compressive tests of cylinders

Age	E-modulus (GPa) 3 specimens	Average E-modulus (GPa)
19 hours	29.0, 26.7, 27.4	27.7
24 hours	26.8, 27.5, 27.0	27.1
2 days	29.1, 27.8, 28.3	28.4
3 days	29.7, 28.5, 26.8	28.3
7 days	30.5, 31.7, 30.9	31.0
28 days	33.4, 33.6, 33.1	33.4

5.7.3.4 Discussion

Concrete E-modulus at the age of 28 days

The experiments performed allow to determine concrete E-modulus at the age of 28 days by three dissimilar methods: ambient vibration, static loading (with the composite beam), and compressive testing (with cylinders). According to Table 5.6, the latter method provided an average value for the concrete E-modulus of about 33.4GPa.

Regarding the static loading test in the composite beam, and bearing in mind results plotted in Figure 5.42, global average of the mid-span deflection per unit of applied mass is 0.0098mmkg^{-1}. With due account to standard elastic formulae relating mid-span deflections on a simply supported composite beam with a concentrated load, one gets a E-modulus for concrete at the age of 28 days equal to 33.3GPa, quite consistent with the value provided by the compressive testing of cylinders.

Concerning the results obtained with ambient vibration tests at the age of 28 days, which led to a resonant frequency of 38.4Hz for the composite beam, an analytical formulation relating f with the concrete E-modulus will be presented. Taking advantage of the symmetry of the beam, the considered geometry is depicted in Figure 5.43. In this figure $\phi(x)$ is the vertical deflection mode, x denotes the abscise along the beam length, $\overline{m}$ is a uniformly distributed mass, m_p is a concentrated mass applied at mid span, k is a spring constant (related to vertical stiffness of the 'small cantilevers' on the supports), L is half of the span and $\overline{EI}$ is the distributed flexural stiffness of the composite beam.

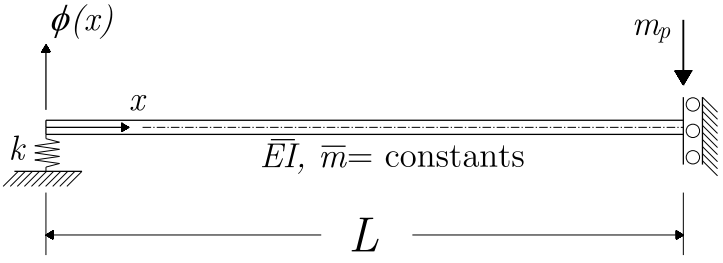

Figure 5.43: Scheme of half of the composite beam

Along time t the free vibration equation for the beam is (Clough *et al.* 2003):

$$\overline{EI}\,\frac{\partial^4\left(\phi(x)Y(t)\right)}{\partial x^4}+\overline{m}\,\frac{\partial^2\left(\phi(x)Y(t)\right)}{\partial t^2}=0 \tag{5.23}$$

where $Y(t)$ represents the amplitude of the transversal displacement, expressed in relationship to the deflection mode $\phi(x)$. After some mathematical manipulation of Eq. (5.23) (Clough and Penzien 2003) it is possible to express $\phi(x)$ as a function of four real constants A_1, A_2, A_3 and A_4, in the form,

$$\phi(x)=A_1\cos(a\,x)+A_2\sin(a\,x)+A_3\cosh(a\,x)+A_4\sinh(ax)$$
$$\text{, with } a=\sqrt[4]{\frac{w^2\overline{m}}{\overline{EI}}} \tag{5.24}$$

where w=2πf. At this stage boundary conditions need to be applied to Eq. (5.24): for the present beam, with a vertical spring on the left and a vertical sliding support on the right, one has

$$\begin{array}{lll}\text{At } x\text{=}0: & \overline{EI}\,\phi''(0)=0 & \overline{EI}\,\phi'''(0)=-k\,\phi(0)\\ \text{At } x\text{=}L: & \overline{EI}\,\phi'''(L)=-w^2\,\phi(L)\,m_1 & \phi'(L)=0\end{array} \tag{5.25}$$

(symbol (.)´ means derivative of (.)). Introducing these boundary conditions into Eq. (5.24) a set of equations is obtained, whose eigenvalues w may be computed according to:

$$\begin{aligned}&-1/(2k)\Big[\ \overline{EI}\,a^3\sin(a\,L)^2\,w^2\,m_p+2\cosh(a\,L)\,k\,w^2\,m_p\,\sin(a\,L)+\cosh(a\,L)^2\,w^2\,m_p\,\overline{EI}\,a^3\\&+2\left(\overline{EI}\right)^2a^6\sin(a\,L)\cosh(a\,L)-\overline{EI}\,a^3\sinh(a\,L)^2\,w^2m_p+2\cos(a\,L)\left(\overline{EI}\right)^2a^6\sinh(a\,L)-\\&4\cos(a\,L)\,k\,\overline{EI}\,a^3\cosh(aL)+\cos(a\,L)^2\,w^2m_p\,\overline{EI}\,a^3+2\cos(a\,L)\,w^2\,m_p\,\overline{EI}\,a^3\cosh(a\,L)-\\&2\cos(a\,L)\,k\,w^2\,m_p\sinh(a\,L)\ \Big]=0\end{aligned} \tag{5.26}$$

Bearing in mind that at the age of 28 days the composite beam is sustained by vertically rigid pinned supports, k turns infinite then after. Furthermore, for the beam considered one has: (i) L = 0.9m, (ii) $\overline{m}$ = 17.0176kgm^{-1} (uniformly distributed mass computed based on the geometry of the acrylic tube and on the densities of the materials involved, the latter being 2344kgm^{-3} for concrete and 1190kgm^{-3} for acrylic) and (iii) m_p=1.135kg (half of the accelerometer's mass). Regarding the value of $\overline{EI}$, it may be expressed based on the values E_aI_a and EI referring to the acrylic cylinder and to the concrete, respectively:

$$\overline{EI}\ =\ E_aI_a+EI\ =\ 3.3\times10^9\,\frac{\pi\left(0.1^4-0.092^4\right)}{64}\ +\ E\,\frac{\pi\,0.092^4}{64}\quad\text{[in Pa]} \tag{5.27}$$

Introducing all these data into Eq. (5.26), and having in mind the measured frequency f=38.4Hz that leads to w=241.3rads^{-1}, the concrete E-modulus at the age of 28 days is computed as E = 33.6GPa, remarkably coherent with the 33.4GPa and 33.3GPa values

obtained with the previously mentioned methods. This coherence led to a great confidence in the results obtained with the performed ambient vibration tests.

Concrete E-modulus evolution during period 0-14.9 days

The validated analytical model of the beam was used together with the information collected from the ambient vibration test conducted at the age of 15 days (358h-362h): ~38.3Hz. The corresponding calculated concrete E-modulus is 33.4GPa, which is almost the same as the one at 28 days (33.6GPa). This evolution was not confirmed at this age with compressive E-modulus tests, but the very similar results obtained for this age and 28 days are quite consistent with usual observations in this concrete property.

As mentioned previously, a drastic change in the resonant frequency was identified with the ambient vibration technique when at the age of 14.9 days the vertical supports of the composite beam were changed from flexible (f=26.1Hz) to infinitely rigid (f=38.3Hz). Since concrete E-modulus at this age has just been established to be 33.4GPa, it is possible to adequately fit the value of k in the analytical model to correctly reproduce the supporting conditions during the period 0-14.9 days (whilst flexible rods apply). Furthermore, instead of being really centred with the supporting flanges (Figure 5.44a), during the experiment it was detected that the composite beam was slightly deviated to one flange (in both extremities), as reproduced in Figure 5.44b. Based on the resulting rod lengths of 23 and 31mm, and on the stiffnesses of the correspondent 'small cantilevers' involved, the estimated stiffness spring constant k for the analytical model would be:

$$k = \frac{3 \times 180 \times 10^9 \ \pi \ 0.004^4}{64} \left(\frac{1}{0.023^3} + \frac{1}{0.031^3} \right) = 785507 \text{Nm}^{-1} \tag{5.28}$$

By using this spring constant together with E=33.4GPa, the predictable frequency using equation (5.26) would be 26.37Hz (at the age of 14.9 days), which is quite similar to the 26.1Hz obtained from the ambient vibration modal identification. To achieve a perfect match a slight correction to the estimated spring constant k was further introduced, thus finally resulting $k = 756600 \text{Nm}^{-1}$.

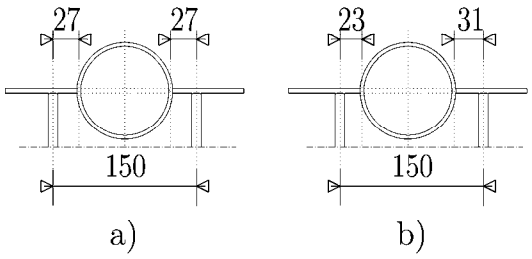

Figure 5.44: Cross section of the beam at the supports – a) original plan; b) actual placement (units: mm)

At this stage, the analytical model together with the adopted parameters are considered valid for the initial period of monitoring. With the experimental data collected via the ambient vibration tests, it is then possible to relate the identified f for the composite beam with the elasticity modulus of concrete, and thus draw the evolution of concrete E-modulus along time, since the instant of casting. The procedure for relating f with E is

the same as described for the age of 28 days: (i) using f as identified from the ambient vibration test, w is obtained; (ii) Eq. (5.26) is used to estimate $\overline{EI}$ and (iii) the corresponding E is calculated from application of Eq. (5.27). The calculated evolution of concrete E-modulus along time, together with the E-modulus obtained from the compressive tests performed on concrete cylinders, are plotted in Figure 5.45 and in Figure 5.46.

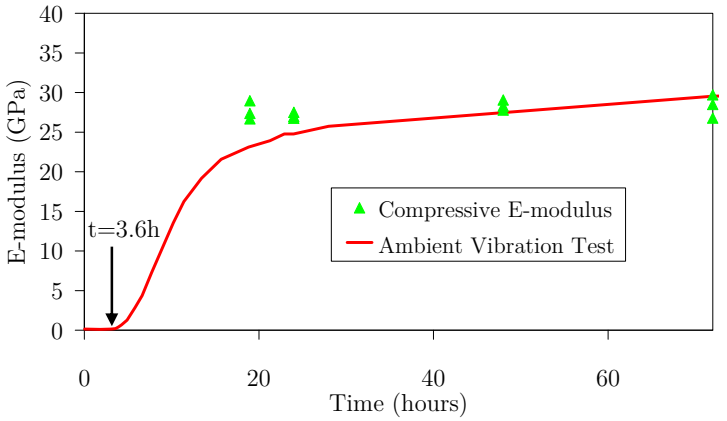

Figure 5.45: Evolution of E-modulus until 72h

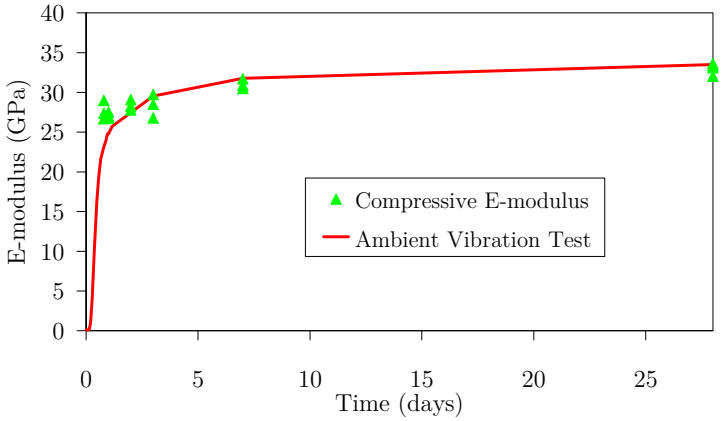

Figure 5.46: Evolution of E-modulus until 28 days

Coherence between the ambient vibration predictions and the one obtained from compressive testing on cylinders is quite satisfactory, particularly for the ages of 2, 3, 7 and 28 days. However, for the ages of 0.8 days and 1 day the ambient vibration test identifies lesser values for the concrete E-modulus. But here the reader should be aware that specimens with different sizes and curing conditions are being used: the ambient vibration test pertains to a concrete specimen that is a cylinder with a diameter of 92mm, cured inside a 4mm thick acrylic formwork, whereas compressive E-modulus testing regards to greater diameter cylindrical specimens (150mm), cured inside a 26mm thick plastic formwork. Therefore, these differences in size and boundary conditions lead for more heat development to occur in the compressive cylinders than in the composite beam, and thus to a faster development of the material microstructure, which is more evident at the first hours and fades as concrete ages.

Still regarding to Figure 5.45, it is noteworthy to mention the clear ability of the ambient vibration test to identify the instant at which structural setting occurs, and stiffness starts developing at a fast rate: at the age of about 3.6h, for the present concrete application. This structural setting time, as well as the early evolution of stiffness, are known as being rather important information to actually determine when concrete starts to hold stresses and the subsequent stress development, which represents information of paramount importance for numerical simulation of concrete structures at early ages.

5.7.4 Variant experimental setup for cement paste characterization

5.7.4.1 Introduction

The pilot experiment described in Section 5.7.3 allowed concluding that the E-modulus measured with the proposed technique matched those obtained from standard compressive tests in cylinders and from static loading of the composite beam. Confidence in the measurement principle gained in the pilot experiment led to further research in the field, with the purpose of devising a smaller scale experiment, easier to carry out, and suitable for cement pastes and mortars. This variant to the original setup points its main utility to material science research, namely the study of additives and additions for cement, as well as partial substitutions of cement. By monitoring the continuous evolution of the material E-modulus since casting, it is possible to extract quantitative information about the structural setting time, as well as the changes in the reaction kinetics from a stiffness point of view.

The experimental procedure proposed in this section pertains to a 55cm long hollow acrylic tube with 16/20mm internal/external diameter, inside of which the cementitious material was cast. The cantilever was then fixed in one of the extremities, assuring a cantilever structural system with a 45cm span. At the free end of the cantilever a light weight accelerometer was placed, which recorded accelerations due to ambient vibrations and allowed estimates of the E-modulus of the cementitious material.

5.7.4.2 Geometry and procedure

A schematic representation of the experimental setup used for testing cement pastes or mortars, as well as a photo, are reproduced in Figures 5.47 and 5.48. The basic component of the setup is an acrylic tube 55cm long (the length having an error less than 1mm), inside which mortar will be filled. An important concern in the setup design was to devise it in such fashion that the cantilevered composite beam would have its weight uniformly distributed, and that at the supported end a clamping condition would be enforced as much as possible.

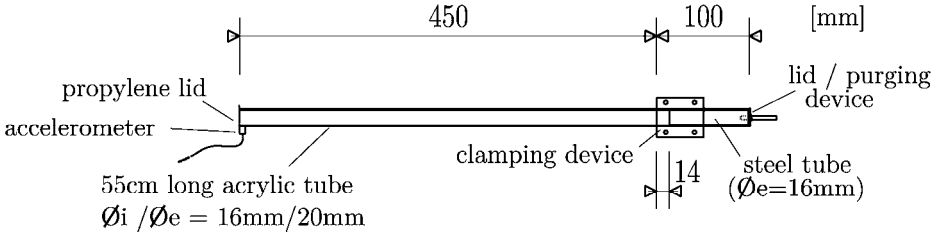

Figure 5.47: Scheme of the experimental setup

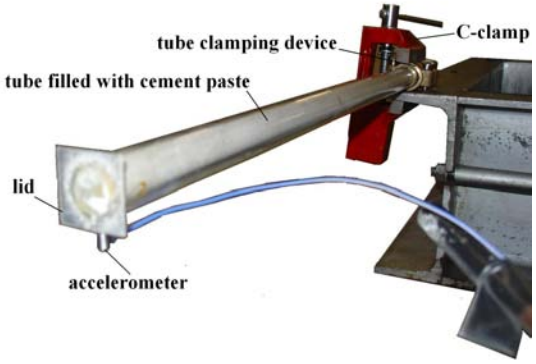

Figure 5.48: Photo of experimental setup

To minimize disturbances on the weight distribution, very light solutions were adopted for the lid and accelerometer placed at the cantilever free end: the lid was made out of propylene, resulting quite rigid but weighting less than 0.35g; the accelerometer is a very light model, weighting only 0.7g, with the weight of its wire being partially distributed to a nearby support planned for this purpose. The clamping device was adapted from a pipe fastening component, with an internal diameter equal to the outer diameter e of the acrylic tube, and fastened with screws to assure complete fixation of the cantilever. To allow applying the maximum fastening force possible to the clamping device screws without fearing damage to the acrylic tube, a steel tube (8.5cm long) with an outer diameter equal to the inner diameter ϕ_i of the acrylic tube is fitted inside. As it can be observed from Figure 5.47, this steel tube does not extend along the entire length of the acrylic one embraced by the clamping device, rather leaving a 14mm interval. The purpose of this was to avoid any disturbance of the cementitious material that fills the acrylic tube right at the clamping vicinity, thus assuring the same cross-section for the composite beam along all its free span.

Regarding technical specifications of the measurement system, a PCB 352A10 accelerometer was used together with an amplifier/signal conditioner PCB 480E09 and a NI DAQ data logger. The frequency of acquisition was 2000Hz; however as the frequencies to be measured were all under 100Hz, it was considered enough to store in hard disk data pertaining to frequencies under 200Hz (after appropriate filtering of the 2000Hz data, to avoid mirroring of high frequencies).

5.7.4.3 Computation of E-modulus with basis on measured natural frequencies

After having measured the resonant frequencies using the ambient vibration methodologies, the conversion of frequencies into E-modulus of cementitious material is made based on the free-vibration equation for a bar of length L with uniformly distributed mass $\bar{m}$, whose mode shape $\phi(x)$ equation has been shown in equation (5.24). In the case concerned in this application, a cantilever system is considered, thus, considering that the support exists at x=0, two boundary conditions arise: $\phi(0) = 0$; $\phi'(0) = 0$. Regarding the free end of the cantilever, the masses of both accelerometer and lid are taken into account as a concentrated mass m_l at the extremity of the cantilever, whose rotary mass moment of inertia is neglected. The presence of this mass causes a

shear force to occur in this boundary, and after performing force and moment equilibrium, the resulting boundary conditions are

$$\overline{EI}\,\phi'''(L) = -w^2\,\phi(L)\,m_1 \quad \text{and} \quad \overline{EI}\,\phi''(L) = 0 \tag{5.29}$$

providing a total of 4 boundary conditions that may be applied to (5.24). The four resulting equations can be put into matrix notation in regard to the 4 unknown A variables, leading to a unique solution only if the corresponding determinant is null. By performing the necessary mathematical operations on this, the frequency equation is obtained:

$$a^3\left[\cosh(aL)\cos(aL) - 1\right] + \frac{w^2 m_1}{\overline{EI}}\left[\cos(aL)\sinh(aL) - \cosh(aL)\sin(aL)\right] = 0 \tag{5.30}$$

With due account for the first frequency w identified, as well as for masses $\overline{m}$ and m_1, the sought value of $\overline{EI}$ can be extracted from Eq. (5.30) using an iterative solving technique, which naturally requires a feasible starting approximation for the cantilever stiffness. As m_1 is relatively small compared to the cantilever mass, w is relatively near the first natural frequency of the cantilever alone (i.e. disregarding the masses m_1), that is (Chopra 2006),

$$w = 1.8751^2\sqrt{\frac{\overline{EI}}{\overline{m}\,L^4}} \tag{5.31}$$

and accordingly, the first estimate of $\overline{EI}$ for solving equation (5.30) is obtained:

$$\overline{EI} = \frac{\overline{m}\,L^4\,w^2}{1.8751^4} \tag{5.32}$$

Once Eq. (5.30) has been solved for $\overline{EI}$, the Young's modulus E_{cm} of the cementitious material can finally be obtained from

$$\overline{EI} = E_a\frac{\pi\left(\phi_e^4 - \phi_i^4\right)}{64} + E_{cm}\frac{\pi\,\phi_i^4}{64} \qquad \Rightarrow \qquad E_{cm} = \left[\overline{EI} - E_a\frac{\pi\left(\phi_e^4 - \phi_i^4\right)}{64}\right]\frac{64}{\pi\,\phi_i^4} \tag{5.33}$$

where E_a is the acrylic Young's modulus.
Both this equation for computing the paste E-modulus and the frequency identification procedures were implemented in a MATLAB algorithm, so that the whole set of operations is imperceptible to the final user, who gets an E-modulus *versus* time curve at the end of each experiment.

5.7.4.4 Experimental campaign

To check performance of the proposed method to monitor evolution of E-modulus of cementitious materials, a set of experiments was conducted, using two types of cement: (i) the CEM I 52.5R and (ii) the CEM IV/A 32.5R (fly ash - FA). Furthermore, (a) a

retarding admixture (Sika Plastiment VZ, with recommended dosage of 0.2 to 0.5% of the cement weight) and (b) an accelerating admixture (Sika Rapid 1, with recommended dosage of 0.5 to 1.5% of the cement weight) were also considered. A total of eight batches of cement paste was prepared with a constant water to cement ratio w/c=0.5, combining the different types of cement and admixtures, the latter used in their maximum recommended dosage for increased effects. Characteristics of these batches, namely nomenclature, mixture proportions, density of paste, density of the acrylic tube and mass at the cantilever extremity, are provided in Table 5.7. Most of the experiments were conducted for a period of 72h, while some of them lasted only for 48h.

Table 5.7: Mixes under study and measured densities/weights for each experiment

Mix	Cement type	Accel. admix. (%)	Retard. admix. (%)	Paste density (kgm^{-3})	Acrylic density (kgm^{-3})	Mass at extremity (g)
P5.1	CEM I 52.5	0	0	1838.5	1160.4	1.52
P5.2	CEM I 52.5	0	0	1843.8	1144.1	1.50
P3.1	CEM IV/A 32.5R (FA)	0	0	1756.5	1143.2	1.49
P3.2	CEM IV/A 32.5R (FA)	0	0	1750.0	1158.1	1.60
P5.r	CEM I 52.5	0	0.5	1837.3	1124.4	1.59
P5.a	CEM I 52.5	1.5	0	1825.3	1155.6	1.88
P3.r	CEM IV/A 32.5R (FA)	0	0.5	1753.0	1156.0	1.59
P3.a	CEM IV/A 32.5R (FA)	1.5	0	1722.7	1157.8	1.49

5.7.4.5 Results and discussion

A quite relevant issue to be checked first is the experiment repeatability, in the sense that measurements made on different applications to the same paste mixture, under the same conditions, should render similar results. For this purpose results concerning batches P5.1 and P5.2, conducted by the same operator, are depicted as colour maps of frequency spectra versus time in Figure 5.49.

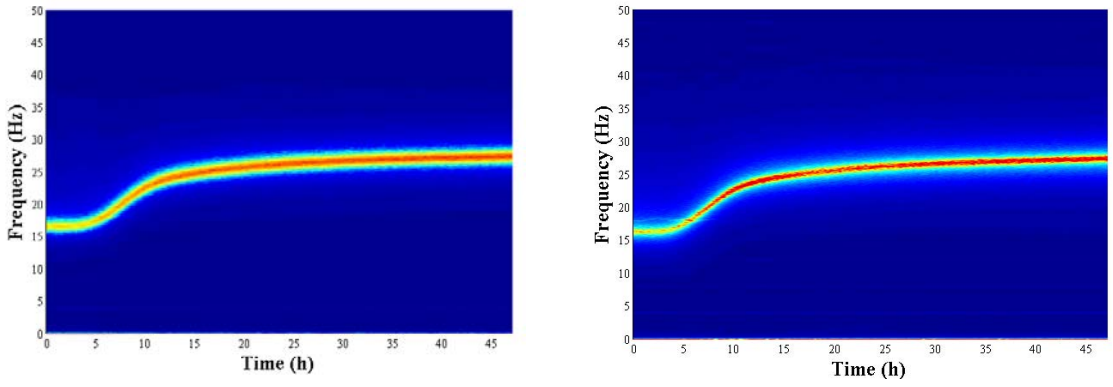

a) b)

Figure 5.49: Colour map of measured frequency spectra along time for mix a) P5.1 and b) P5.2

Both colour maps of this figure are remarkably similar, with the two batches exhibiting an initial measured resonant frequency of circa 16.5Hz, which maintains a constant value

until ~3.5h of age, instant after which a steep increase of frequency occurs until ~12h of age, showing a lower rising tendency then after. However, a more reliable comparison of results can only be achieved by superposition, and therefore, using the identification method presented in Section 5.7.2, the evolution of the resonant frequencies along time for batches P5.1 and P5.2 are depicted in Figure 5.50a, where the ratio between the two measured frequencies is also plotted, for completeness. Resonance frequencies in the two batches are quite coherent, with the ratio between the P5.1 and the P5.2 frequencies always very near unity, reaching a maximum value of 1.02 in the beginning of the experiment.

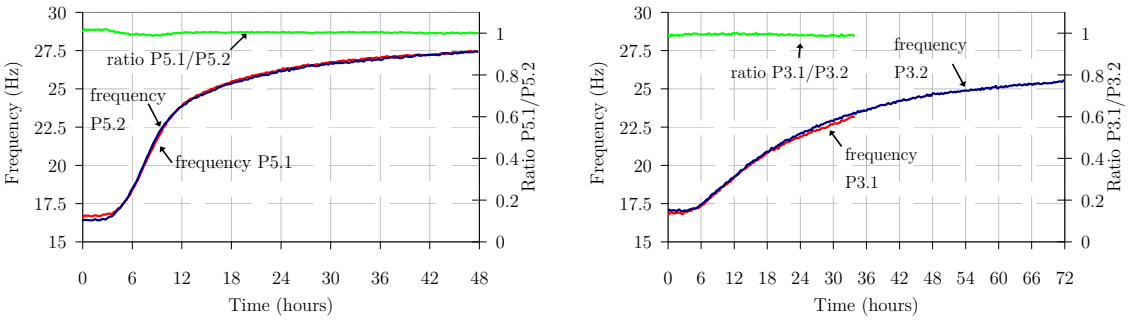

a) b)

Figure 5.50: Measured resonant frequencies and ratio between first and second experiment for: a) P5.1 and P5.2; b) P3.1 and P3.2

Issue of reproducibility regarding the experiment ability to yield similar results when replicated by different operators was tested with batches P3.1 and P3.2, where setup implementations and measurements were undertaken by independent persons (P3.1 having however a smaller duration of ~34h). Superposition of corresponding resonant frequencies, as well as their ratios, is depicted in Figure 5.50b: coherency between results obtained by distinct operators is remarkably high, with frequency ratios always under 1.014, emphasizing the good reproducibility of this kind of experimental setup and procedures.

At this point, and by comparing the results of Figure 5.50a and Figure 5.50b, an interesting consideration may be stated also: frequency enhancement beyond the initial value occurs sooner for P5.1 and P5.2 mixes (~3.5h) than for P3.1 and P3.2 mixes (~5h).

Further data pertaining to measured resonant frequencies for the mixes P5.1, P5.r and P5.a, which use cement CEM I 52.5R, are shown in Figure 5.51a. It can be observed that admixtures clearly affect duration of the initial dormant stage, and that this phenomenon is fully captured by the measurement methodology here proposed: (i) the dormant period lasts ~3.5h for mix P5.1, (ii) it extends up to ~10.5h for batch P5.r with the retarding agent, and (iii) it reduces to ~2.7h for batch P5.a with the accelerating admixture. For this cement type kinetics of the frequency growth is also affected by admixtures, as evidenced by the slightly different shapes of curves in Figure 5.51a. In regard to the mixes containing CEM IV/A 32.5R (FA), influence of admixtures on the measured resonant frequencies can be observed in Figure 5.51b: (i) while the accelerating admixture had a small effect on the dormant stage duration, (ii) the retarding agent led to a huge elongation of the dormant stage, which lasted about 42h. Both accelerating and retarding

agents have also visible effects on the shapes of the frequency development curves, pointing to interferences on the cement hydration kinetics.

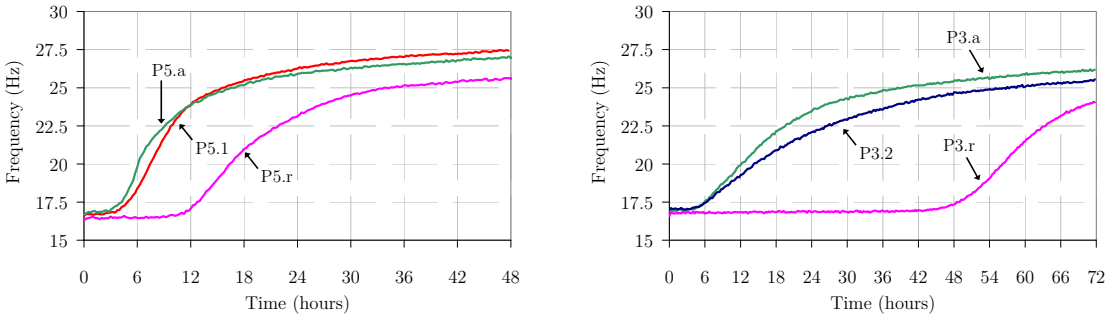

a) b)

Figure 5.51: Measured resonant frequencies for plain paste, paste with retarder admixture and paste with accelerator admixture: a) P5.1, P5.r and P5.a; b) P3.1, P3.r and P3.a

After having shown the measured frequencies, the estimated E-modulus using the methodology put forward in Section 5.7.4.3 is presented henceforward. For such purpose the E-modulus of acrylic needs to be defined beforehand, and accordingly an experiment was devised, in which the tube was filled with water and tested in the same fashion as for the cement pastes. That way, by using water one can guarantee that no relevant stiffness is added to the system, and that the global mass is well known (the uniformly distributed mass for the acrylic tube was 0.1275kgm^{-1}, that related to the water was 0.195kgm^{-1}, and the concentrated mass at the free end was ~1.62g). Considering $\overline{EI}$ as the unknown in Eq. (5.30), and solving Eq. (5.33) with E_{cm}=0, one gets E_a = 3.86GPa.

By using this E_a reference value for all acrylic tubes, the E-modulus evolutions for the cement pastes P5.1, P5.2, P3.1 and P3.2 were computed, leading to the curves depicted in Figure 5.52. From this figure it can be confirmed that all pastes exhibit near zero E-modulus after casting, which is consistent with their fluid-like behaviour. The end of the dormant stage, after which pastes start to exhibit structural stiffness, is clearly identified, as already commented upon resonant frequency analysis. Still regarding Figure 5.52, and bearing in mind the evolution of E-modulus along time, it is clear that the stiffening of pastes P5.1 and P5.2 is much faster than that of pastes P3.1 and P3.2, which is consistent with the characteristics of the cements under study (finer for mixes P5.1 and P5.2, and with partial substitution by fly ash for mixes P3.1 and P3.2). In fact, at the age of 48h differences in the E-modulus of the two families of pastes are indeed remarkable: 9.7GPa for batches P5.1 and P5.2, and 6.3GPa for batch P3.2.

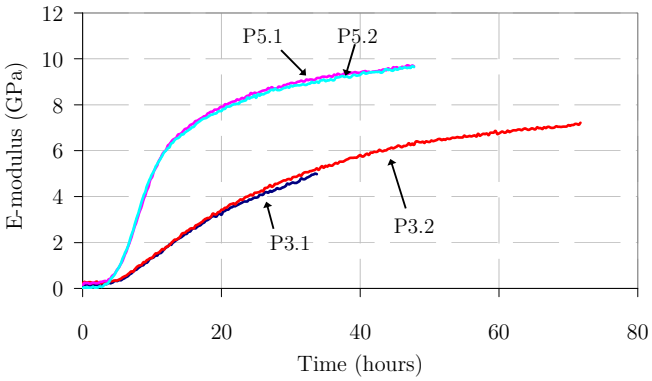

Figure 5.52: Estimated elasticity modulus for the plain pastes 5.1, 5.2, 3.1 and 3.2

Estimated E-modulus for pastes with admixtures (P5.1, P5.r, P5.a, P3.2, P3.r and P3.a) are depicted in Figure 5.53. By analysing this figure it is concluded that the proposed method is rather feasible and efficient, showing clearly that influence of the retarding agent is far more dramatic than that of the accelerating one, as far as the duration of the dormant stage is concerned (as already commented for Figure 5.51). The accelerating agent in the P5.a mix had its strongest effect at the age of 6.2h by increasing the cement paste E-modulus to 2.8MPa, in comparison to the value of 1.6MPa measured for the P5.1 mix. However, the effect of this admixture was detrimental for ages greater than 11.5h, leading to slightly lower stiffnesses than those in mix P5.1. The retarding agent seems to have caused solely a translation of the E-modulus curve in time, as it can be observed in Figure 5.53a for mixes P5.1 and P5.a: both curves have similar configurations, apart from the rather dissimilar dormant periods involved. Analysing Figure 5.53b for mixes P3.2, P3.r and P3.a, the accelerator agent (P3.a mix) causes stiffness development kinetics to differ somewhat from that of P3.2 mix, leading to values of the cement paste E-modulus always greater than those of the plain paste. The retarding admixture (P3.r mix) causes both the elongation of the dormant period, and a change in the shape of the E-modulus *versus* time curve, as compared to what is observed for the P3.2 mix.

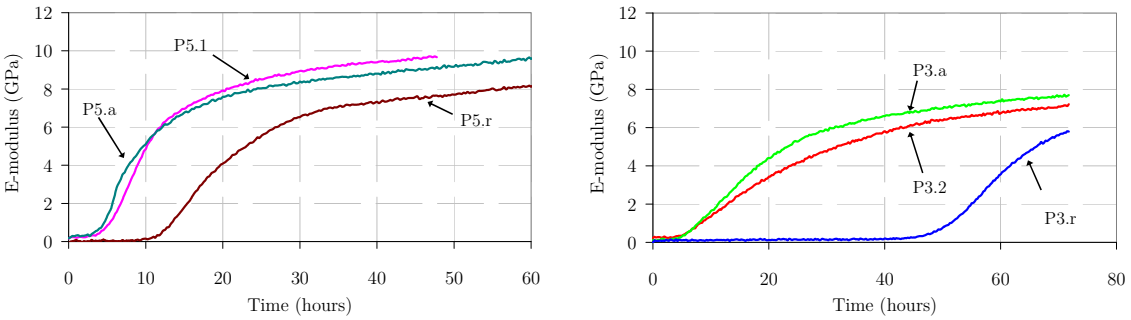

a) b)

Figure 5.53: Estimated E-modulus for plain paste, paste with retarder admixture and paste with accelerator admixture: a) P5.1, P5.r and P5.a; b) P3.1, P3.r and P3.a

5.8 Sensitivity analyses on mechanical input parameter choices

5.8.1 Motivation and description of reference models

In order to clarify the sensitivity of numerical results in regard to several input parameters of the mechanical model, it was decided to carry out a set of analyses on a concrete structure with simple geometry, so that interpretation is fast and easy. Thermo-mechanical analyses are to be conducted with the basic geometry and thermal parameters adopted in the analysis named as "1ref" in Section 2.8.1: a $1 \times 1 m^2$ concrete element in which only the two vertical boundaries allow thermal exchanges with the surrounding environment. The mechanical analyses of this section are conducted by collecting temperature and degree of heat development information from the thermal model "1ref". The FE mesh for mechanical analysis has the same vertexes as the one used for thermal calculations, but instead of 4 node elements, 8 node elements are used. The concrete element is assumed to be 1m thick in the direction perpendicular to the plane of the model. Two basic reference models are considered, as depicted in Figure 5.54: (i) model sup13Ref on the left, where both bottom (*L1*) and top (*L3*) boundaries have their vertical movements hindered; (ii) model sup1Ref on the right, where only the bottom (*L1*) boundary has vertical simple supports. The reason for the choice of these two support conditions was to devise a model in which external restraint to deformation would be the major stress causing effect (model sup13Ref), whereas in the other model (sup1Ref) the main restriction to deformation would occur at a cross-sectional level.
Regarding mechanical properties, all the parameters initially adopted in the analysis shown in Section 5.5.4 were considered. Cracking was disregarded to simplify interpretation of results.
Analyses of results are to be performed in regard to two specific finite elements of the models: the core element (located at the geometric centre of the model) and a surface element, located at mid height of *L4* (both locations identified in Figure 5.54).

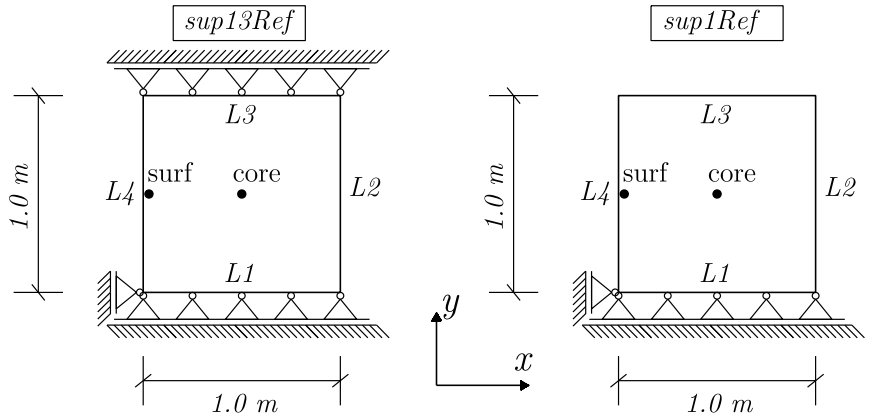

Figure 5.54: Scheme for the sensitivity analyses on mechanical input parameters

A preliminary discussion is made regarding the numerical simulations of models sup13Ref and sup1Ref for the two elements under consideration (core and surface), with basis on

the plots of normal stresses (σ_y) shown in Figure 5.55 (tensile stresses represented as positive).

As far as the sup13Ref model is concerned (Figure 5.55a), due to the fact that vertical movements are hindered on both top and bottom boundaries, the thermal expansion associated to the early temperature rise is totally hindered, and thus compressive stresses arise in concrete. As expectable, these compressive stresses are higher in the core (where higher temperatures occur) than in the surface. During the cooling stage, and because the temperature drop in the core is higher than in the surface, the corresponding stress change is also higher. At the end of the analysis the whole model is under tensile stress. This can be explained by the fact that upon cooling the E-modulus of concrete is higher than during the initial temperature rise.

Regarding the sup1Ref model, whose stress developments are depicted in Figure 5.55b, the typical behaviour of externally unrestrained concrete is observed: during the temperature rise, because of the higher tendency of the core to expand (due to its higher temperature when compared to the surface), it endures compressive stresses, whereas the surface endures tensile stresses. When concrete starts cooling the tendency is reversed, and the surface endures compressive stresses in opposition to tensile stresses in the core. As the cross-sectional restraint in sup1Ref is much smaller than the support restraint in sup13Ref, the magnitude of calculated stresses is also much smaller, with peak tensile stresses of about 1MPa, in opposition to 6MPa in the case of sup13Ref. The evolution of stresses in the surface is also dramatically different, with these two reference calculations representing two extreme scenarios in terms of restraint.

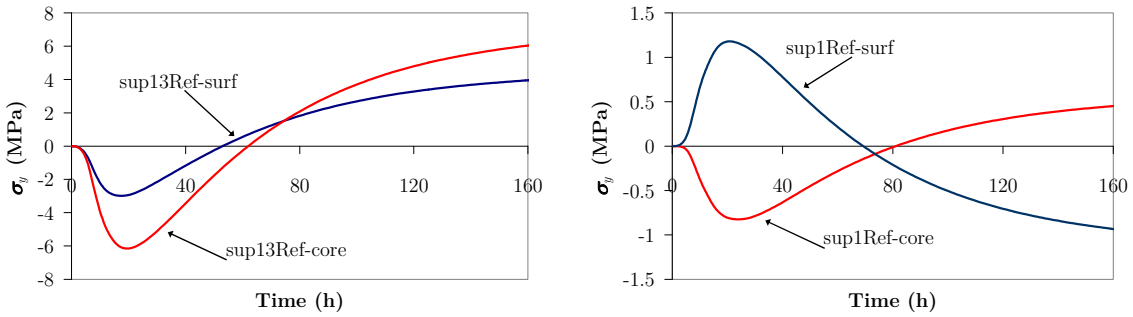

a) b)

Figure 5.55: Computed σ_y stresses for models: a)sup13Ref; b)sup1Ref

5.8.2 Evolution of concrete E-modulus

In order to investigate the effect of considering the evolution of concrete E-modulus according to the realistic curves obtained in the ambient vibration tests in opposition to the use of the EC2 curves as considered in the reference calculations, two further models were calculated. They involve the use of an adapted version of the realistic E-modulus evolution reported in Figure 5.45 and Figure 5.46, adequately scaled so that the E-modulus at the age of 28 days matches the one used in the reference models (sup13Ref and sup1Ref used the EC2 approach for E-modulus evolution– see Section 5.5.4): comparison of the two evolution curves for E-modulus is depicted in Figure 5.56. If one focuses on the overall evolution along the period 0-28 days, both curves seem quite similar, indicating that the EC2 curve is quite feasible. However, if focus is given to the very early

age stiffness evolution (ages lower than 1 day), as shown in Figure 5.56b, it can be confirmed that the two approaches for E-modulus input to the numerical model are quite different, mainly due to the effect of the initial dormant period, clearly not accounted for in the EC2 curve, which consequently strongly overestimates concrete E-modulus until the age of ~0.6 days.

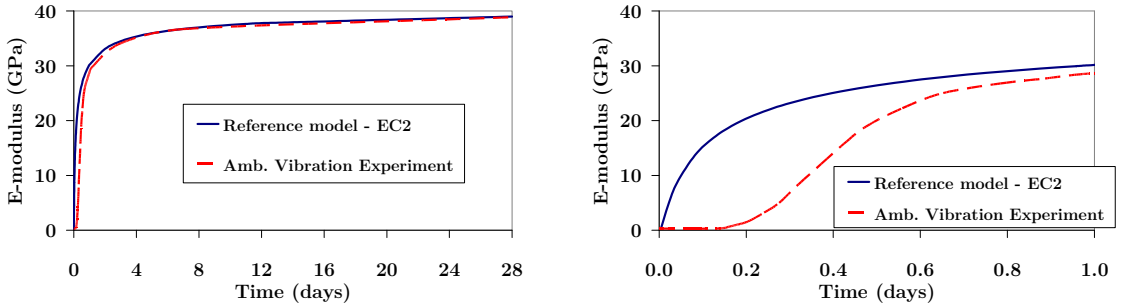

Figure 5.56: E-modulus evolution: a) until 28 days; b) until 1 day

Considering the formulation for E-modulus evolution based on ambient vibration tests, two new calculations were performed with basis on sup13Ref and sup1Ref, by changing solely the used E-modulus evolution (i.e., using the results from the ambient vibration experiment represented by the dashed line in Figure 5.56, instead of the EC2 approach). The resulting models are named as sup13Eamb (based on sup13Ref) and sup1Eamb (based on sup1Ref).

The computed σ_y stresses for the core and surface of the model obtained in model sup13Eamb, and their comparison to the computed ones from sup13Ref, are depicted in Figure 5.57. It can be observed that the early dormant stage introduced by using the E-modulus obtained from the ambient vibration experiment leads to stresses of lower absolute values (compressive) during the heating stage, both in the surface and in the core. As a consequence, during the cooling stage (at which both the E-modulus evolutions used are almost matching), the tensile σ_y stresses become higher.

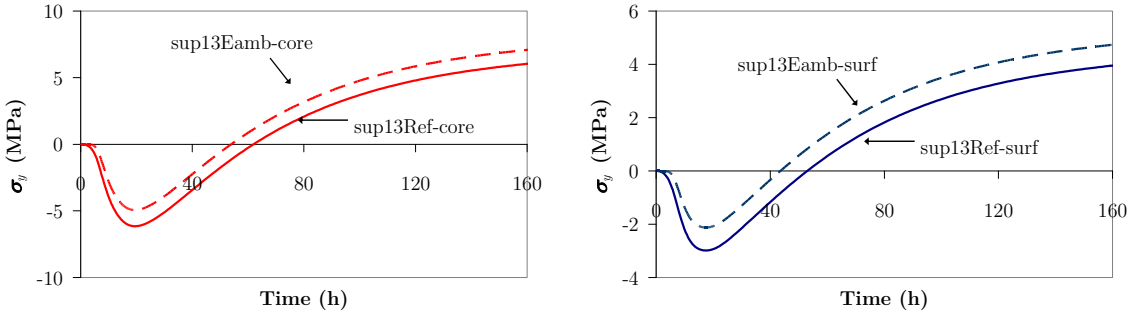

Figure 5.57: Comparison of σ_y stresses developed in sup13Ref and sup13Eamb: a) core; b) surface

Regarding models sup1Ref and sup1Eamb, where no external restraint to deformation exists, the effects of using the E-modulus evolution based on ambient vibration (thus more realistic) are not so straightforward. With basis on the plots of σ_y stresses in Figure

5.58, it can be seen that the changes in stress development on the core FE are qualitatively similar to those reported for the externally restrained case (sup13Ref *versus* sup13Eamb – see Figure 5.57a). The stress development in the surface element that had an initial tendency of enduring tensile stresses during the temperature rise stage for the sup1Ref model, in the sup1Eamb model undergoes lower tensile stresses associated to the lower initial E-modulus – see Figure 5.58b. As a consequence, the final compressive σ_y stresses have greater absolute values in sup1Eamb model than it was the case in sup1Ref. It can therefore be stated that there is no fashion of making a categorical statement regarding the consequences of using the E-modulus evolution based on ambient vibration experiment in the numerical modelling of concrete stress evolution at early ages. While in the case of the sup13Ref/sup13Eamb models it appeared to be prejudicial (by increasing the final tensile stresses, which are the critical ones in concrete), in sup1Ref/sup1Eamb the apparent early diminishment of cracking risk on the surface during the heating phase carries the consequence of higher tensile stresses in the core during the cooling phase. So, the final conclusion is that the use of this more realistic curve for E-modulus that includes the early dormant stage for concrete is considered important, because of the fact that it may introduce non-negligible changes in the stress development either if the concrete element has strong or none external restraint to deformation.

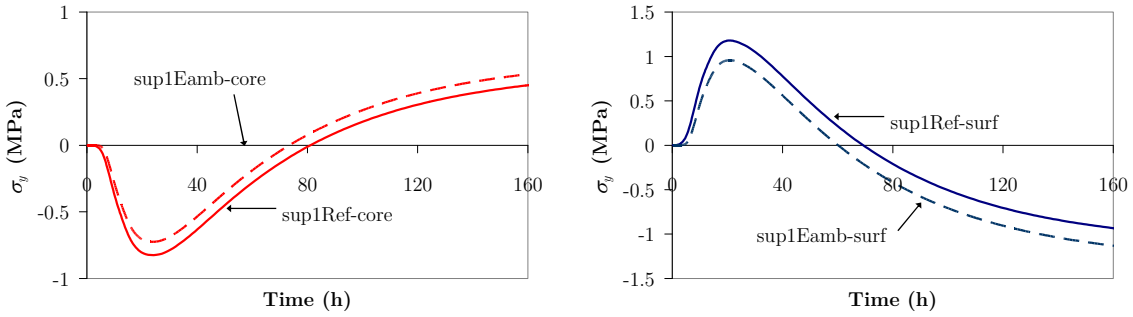

a) b)

Figure 5.58: Comparison of σ_y stresses developed in sup1Ref and sup1Eamb: a) core; b) surface

Still regarding the modelling options for E-modulus evolution along hydration, there is an important topic to address: how does using the alternative formulation (based on results from ambient vibration tests) affect the strain evolution of the concrete specimen? This is an important point because of the fact that monitoring concrete behaviour in concrete structures is frequently made with recourse to strain gages, which are in turn used as validation tools for the numerical models. To try to answer this question, the computed ε_y strains in models sup1Ref and sup1Eamb are compared in Figure 5.59: the obtained strains on both models are so similar that the corresponding curves overlap almost perfectly. This strong resemblance shows that in the case of a structure with the geometry and restrictions of sup1Ref/sup1Eamb, the early evolution of E-modulus causes no relevant changes in the strain evolution, even though it has already been shown to cause non-negligible effects on stress development. It can thus be concluded that strain monitoring results should be analyzed with great care when trying to validate calculated stresses.

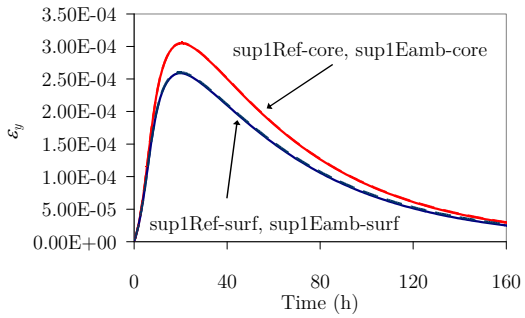

Figure 5.59: Calculated ε_y strains for sup1Ref and sup1Eamb models

5.8.3 Poisson's coefficient

As stated in Section 5.3.4, Poisson's coefficient of concrete has been reported to endure evolutions since ν=0.5 in the fresh state of concrete until ν=0.2 in the hardened stage. Numerical models usually disregard this evolution, and consider this parameter as constant and equal to the hardened stage value. Within the bibliographic review performed within the scope of this thesis, no reference was found dealing with the consequences of this simplification in view of the actual variations reported by several authors. So, it was decided to perform a set of simple sensitivity analyzes regarding the effect of changing this parameter. By using sup13Ref and sup1Ref as reference calculations, a variable value of Poisson's coefficient according to the measurements reported by Krauβ *et al.* (2001) for German HPC was input to new models, named sup13Poi and sup1Poi, respectively. The resulting calculated stresses for the variable Poission's coefficient models are almost the same as those of the reference models, with less than 1% deviation. A further extreme scenario case was conducted by performing the same calculation models, but with a constant Poisson's coefficient of 0.49. The obtained results still differ less than 1% from the original reference models, indicating that the sensitivity of stress development at early ages to Poisson's coefficient is very small, and can thus generally be disregarded with negligible effects on the accuracy of obtained results.

5.8.4 Creep parameters

In order to clarify the influence of creep parameter variations of the DPL on the computed stresses, and thus provide a sustained opinion on the importance of proper creep characterization, a set of creep related sensitivity analyses was conducted. The reference creep parameters were the same as those in all the previous analyses. It must be stressed that these creep parameters were fitted from experimental results on compressive creep tests at the ages of 1 day and 3 days, obtaining a creep coefficient ϕ_1=0.6. The good fit of this parameter choice when compared to the results obtained in the compressive creep experiments for the ages of loading of 1 day and 3 days can be seen in the specific creep curves depicted in Figure 5.60a and Figure 5.60b, where the static elastic modulus curve is also represented. The present parametric analyses were made with basis on the sup1Eamb model (realistic E-modulus evolution and absence of external restraint to deformation), and three scenarios were chosen: no creep considered in the model (model

sup1Nocr); creep parameter ϕ_1 halved (model sup1Fi0.3); creep parameter ϕ_1 doubled (model sup1Fi1.2). The specific creep for the halved and doubled ϕ_1 is also depicted in Figure 5.60, where it can be confirmed that strong deviations occur in regard to the experimentally obtained specific creep curve.

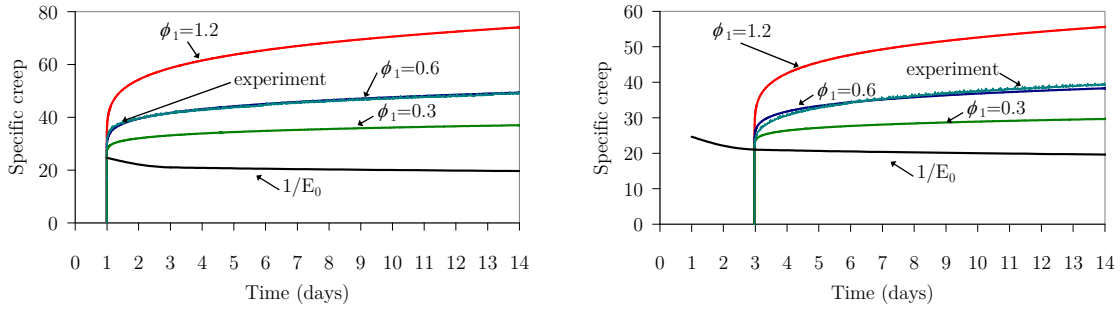

a) b)

Figure 5.60: Specific creep curves for compressive load applied at the ages of: a) 1 day; b) 3 days

The computed σ_y stresses for all the situations envisaged in the intended parametric analyses are depicted in Figure 5.61 for the reference FE of the core and the surface. It can be seen that the computed stresses of the sup1Nocr model are radically different from all the ones obtained with the other models, which on the other hand rely within a relatively narrow interval. So, two main conclusions are to be withdrawn in regard to these parametric analyses:

- Not considering the effect of creep can lead to extremely different stress predictions, which are bound to be erroneous.
- Drastic variations in the creep parameters do not reflect in the same dramatic fashion in the computed concrete stresses, indicating that the parameter choice in creep behaviour may not be a critical issue for the quality of stress estimations, as long as the specific creep curves of the used model fairly resemble the ones pertaining to the mechanical characterization of the material.

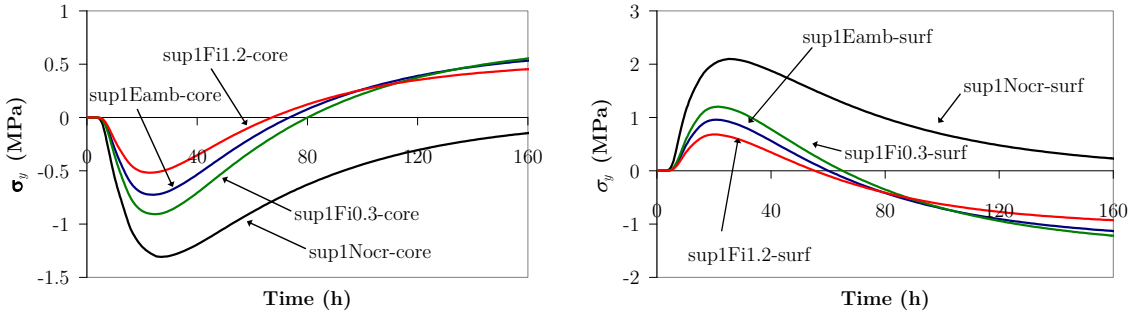

a) b)

Figure 5.61: Computed σ_y stresses for the creep parametric analyses: a) core; b) surface

5.9 Application of the thermo-hygro-mechanical framework

Methodologies for practical analysis and design of reinforced concrete structures comprise several simplifying assumptions, namely in what concerns to the stress state induced by heat of hydration and drying shrinkage. Actually, due to the exothermic nature of cement hydration reactions concrete bodies endure non-uniform internal temperature distributions, usually with higher temperatures in the core and lower close to the external boundaries. Total or partial restrictions to the volumetric deformations associated to these temperatures induce internal stresses in concrete, whose importance is frequently disregarded by designers, most of the times without a quantitative notion of their magnitude. Their quantification is, however, possible with recourse to thermo-mechanical methodologies such as the one described in this thesis..

Regarding drying shrinkage, and according to regulation dispositions (CEB-FIP 1993, CEN 2004), its structural effects are usually taken into account by using a reference shrinkage strain (based on the geometry of the concrete body, environmental relative humidity, age of exposure and concrete strength class), which in turn is applied uniformly to the structure to ascertain the corresponding stresses. This is clearly a simplification for practical calculations, since drying occurs non-uniformly in concrete, as well as the corresponding drying strains, which generate stresses in the presence of any kind of restraint (be it external, caused by reinforcement or even by cross-sectional effects). Quantification of the differential drying shrinkage calls for the necessity of knowing the moisture fields within concrete, as well as the relationship between moisture losses and the corresponding volumetric variations. As most generally concrete structures suffer effects of both heat of hydration and drying shrinkage, it is important to have numerical simulation tools that allow computation of the thermal, hygral and mechanical fields, to appropriately compute concrete stress states during service life.

Several authors have conducted research in the field of numerical simulation of self-induced stresses during service life of concrete. Kwak *et al.* (2006a, 2006b) have studied non-structural cracking in RC walls using an approach similar to the one adopted in this thesis, with explicit consideration of non-uniform temperature and moisture distributions, with the aim of evaluating post-cracking concrete behaviour. Bernard and Brühwiler (2003) and Martinola *et al.* (2001) have explicitly calculated moisture fields and corresponding drying shrinkage in the evaluation of debonding potential between concrete layers cast at different ages. Grasley *et al.* (2006) monitored internal relative humidity in concrete specimens, and evaluated the self-induced stresses in both linearly restrained and free specimens. Oh *et al.* (2003, 2006) have established a numerical framework for analysis of thermal, hygral and mechanical fields, applying it to the study of concrete decks of composite bridges. Chen and Mahadevan (2007) have used a thermo-hygro-mechanical framework for the cracking analysis of a $1\times1\times0.5\text{m}^3$ concrete block using a smeared crack approach. Granger *et al.* (1996) used a hygro-mechanical approach to evaluate skin micro-cracking of concrete with recourse to contact analyses. Gawin *et al.* (2007) devised a numerical framework for thermo-hygro-mechanical analysis in which stresses due to creep and shrinkage are calculated using the effective stress concept.

None of the above mentioned works have specifically focused on the use of these advanced numerical modelling techniques in evaluating service life behaviour of ordinary RC structures, and the correspondence in results with existing concrete codes such as Model Code 1990 (CEB-FIP 1993), in view of evaluating possible implications on how structures are designed nowadays. This is the purpose of this section, which involves the numerical framework that has been described. In terms of selected applications, two separate examples are considered. A first example, concerning the evaluation of stresses in a free drying shrinkage prism, showing that, even in this case, the self-induced stresses can be quite relevant. The second example to be explored regards the behaviour of a RC concrete slab under several situations, where the influence of considering self-induced stresses due to heat of hydration and drying shrinkage is to be evaluated: (i) one performing as a tension tie, evaluating the tension-stiffening effect; (ii) and another working as a flexural member, under imposed curvatures applied at various ages. The descriptions and results related to the thermal and moisture analyses of these examples have been done in Chapter 3, whereas this section deals with the corresponding mechanical simulations.

5.9.1 Material properties

For the mechanical analyses, the following properties of concrete were adopted: f_{ctm}=2.6MPa, G_F=0.085N/mm, α_T=10^{-5} and ν=0.2. Evolution of concrete E-modulus as a function of the equivalent age at the reference temperature of 20°C is represented in Figure 5.62 (E-modulus considered constant for t>28 days). Creep parameters for the DPL were obtained with basis on experimental results reported by Atrushi (2003): ϕ_1=1.88, m=0.2 and n=0.125. When it exists, reinforcement is characterized by a Young's modulus E_s=200GPa, a yield stress f_{sy}=500MPa and a thermal expansion coefficient of 10^{-5}.

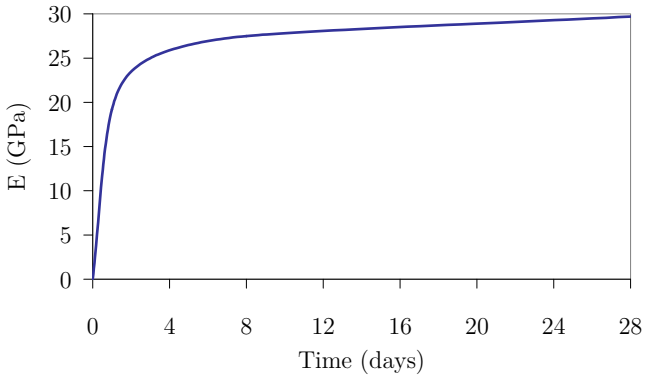

Figure 5.62: E-modulus evolution

5.9.2 Concrete drying shrinkage prism

The structural behaviour of a concrete drying shrinkage specimen is studied in this section considering the two geometries P200 and P150 referred to in Chapter 3. If self-weight effect is disregarded, each drying shrinkage prism has the three planes of symmetry, as considered for the thermal and moisture models. Mechanical calculations

were conducted with the same time integration and FE mesh as described for the thermal and moisture models.

The computed stress field resulted in the principal stress vectors depicted in Figure 5.63a, whereas normal stresses in the Y direction (longitudinal to the specimen) are shown in Figure 5.63b (red colour representing maximum tensile stresses). During the first 28 days only thermal stresses occur, as the specimen is moist cured. Therefore, the first representation of stresses in Figure 5.63 at the age of 27.9 days can have its interpretation based only in the temperature field evolution: the specimen is cast at 20°C; then temperature rises non-uniformly (higher temperatures in the core than in the surface); after the maximum temperature is reached, the specimen starts cooling (faster on the surface than in the core). As a consequence of cooling from a higher temperature, the core tends to contract more than the surface. Therefore, at the age of 27.9 days the surface becomes compressed and the interior endures tensile stresses (see Figure 5.63). Since the thermal gradients observed in the early ages are less than 4°C, the resulting tensile stresses at the core are small, amounting to ~0.05MPa. Such low stresses allow to consider that the specimen begins to dry at a stress-free state. One of the first computed results after the specimen is exposed to drying is shown in Figure 5.63 for t=28.1 days: right after exposure surface areas suffer a quite sudden desiccation in accordance to Figure 3.21, which induces strong potential shrinkage strains in these areas, while the interior remains at high humidities, consequently having no tendency to shrink. As a result, the surface endures tensile stresses while the interior gets compressed. Given the fact that the desiccated depth at the beginning of drying is very small, its relative stiffness in relationship to the internal non-shrinking concrete is very small. It is therefore understandable that high tensile stresses occur at the surface, being higher in the vicinity of the specimen's edges (once drying is stronger in these zones), and reaching values as high as 1.5MPa at t=28.1 days. This tendency for tensile stresses at the surface is intensified until concrete tensile strength f_{ctm}=2.6MPa is reached, and cracking starts occurring at the edges of the specimen at t=30 days, as can be confirmed in the σ_y stress evolution reproduced in Figure 5.64, and in the crack strain vectors of Figure 5.65. The very low maximum crack strain observed (1×10^{-4}), together with the small depth of the cracked zone visible in Figure 5.65, indicates the existence of non-visible cracks, which is consistent with the findings by Granger *et al.* (1996) and Bisschop and Van Mier (2002a). This process keeps intensifying until the age of approximately 42 days, when crack opening is maximum (see Figure 5.65) and tensile stresses are generalized on the surface (see Figure 5.63). After this, due to the progression of drying towards the interior of the specimen, the stress distribution tends to reverse, with the maximum tensile σ_y stresses migrating progressively towards the specimen's core (see Figure 5.63 from t=42 days towards t=964 days). This tendency can be confirmed in Figure 5.64, where the surface points P2 and P3 that experience strong tensile stresses at t=42 days, see their σ_y stresses reduced along time, until they are actually reversed into compression at t≈400 days, stabilizing at the end of the analysis at approximately σ_y =-0.5MPa (compression). The opposite process occurs in the core points P1 and P4, which reach the end of the analysis under σ_y =0.5MPa (tension). Point P5, located in the corner of the specimen, endures almost negligible stresses due to the very low restraint to deformation in this region. The mentioned process of stress reversal in the specimen is also visible in the calculated cracks

(Figure 5.65), with the crack opening decreasing since approximately t=42 days, and even closing right after t=324 days. This tendency of surface shrinkage cracks to close along drying was also documented for similar conditions by Granger *et al.* (1996).

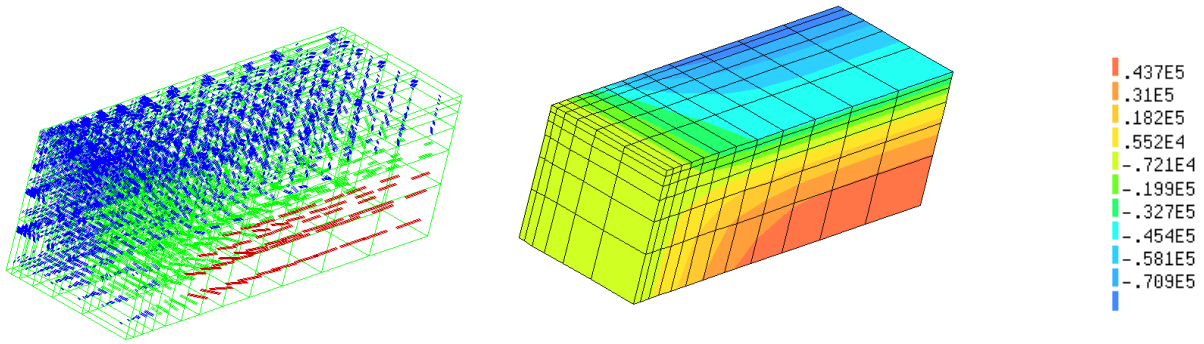

t=27.9 days

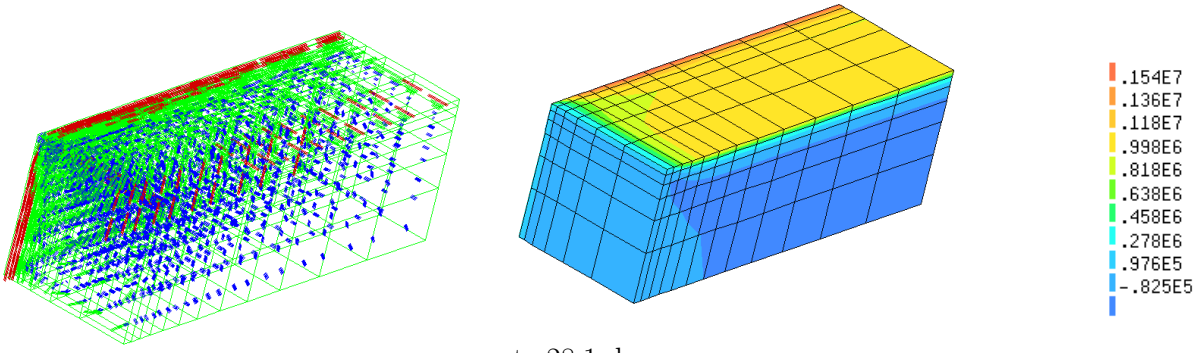

t=28.1 days

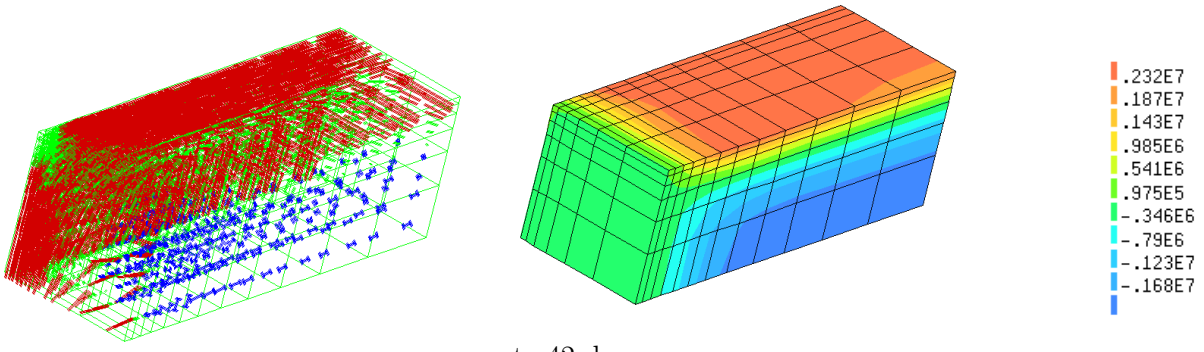

t=42 days

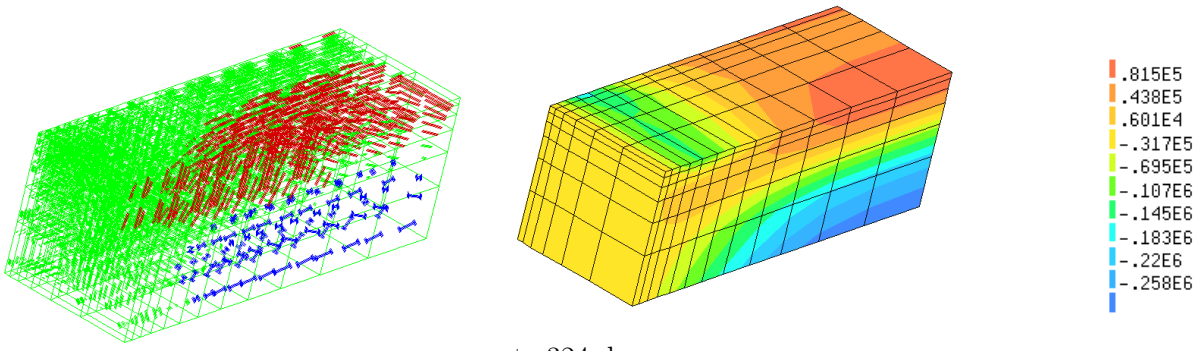

t=324 days

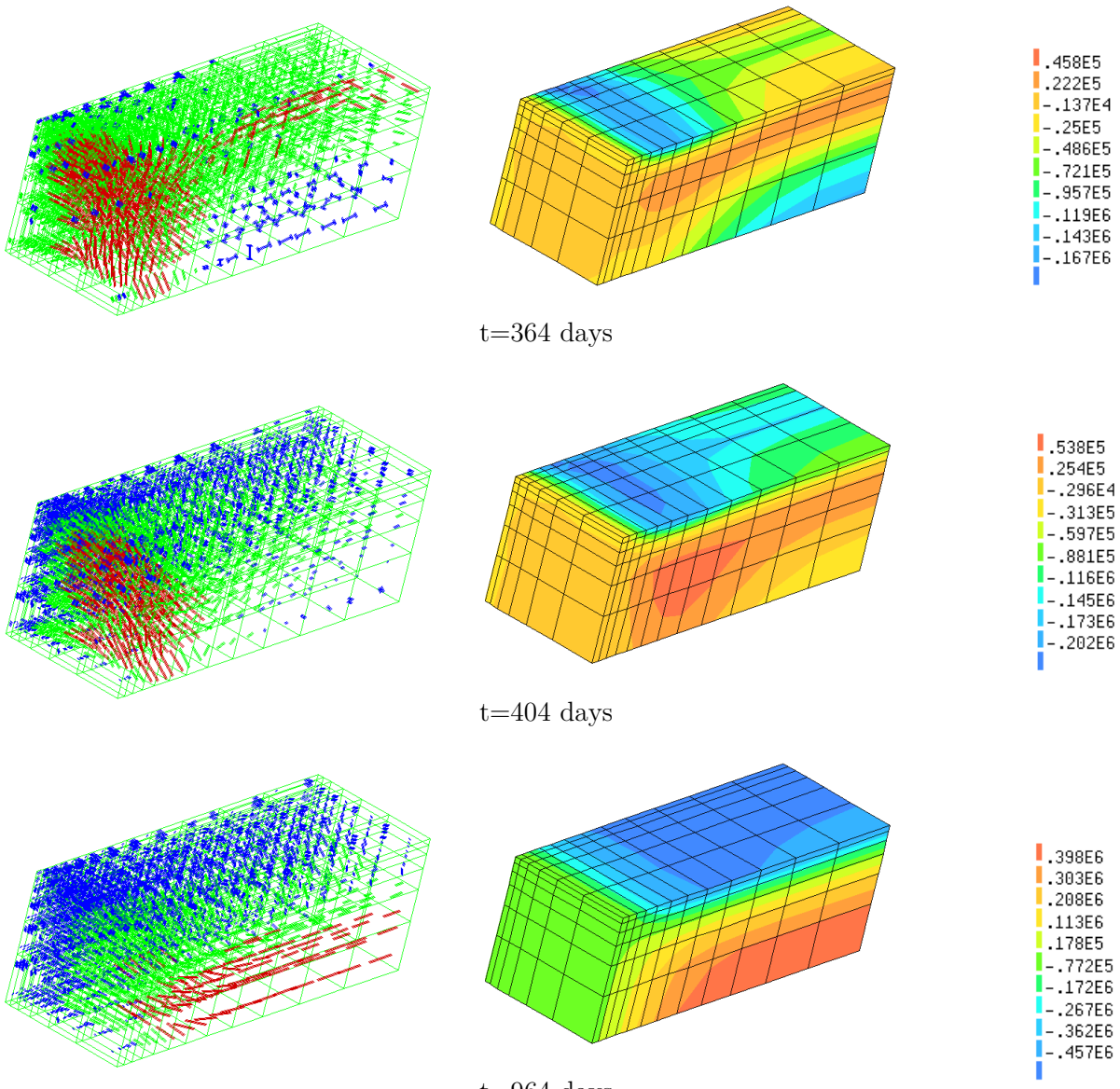

Figure 5.63: a) Vectors of principal stresses in specimen P200, with red colour corresponding to tensile stresses; b) longitudinal stresses σ_y (right column - Pa)

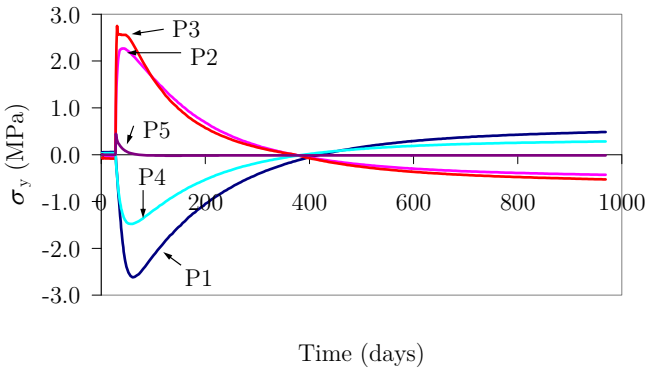

Figure 5.64: Calculated stresses σ_y in specimen P200

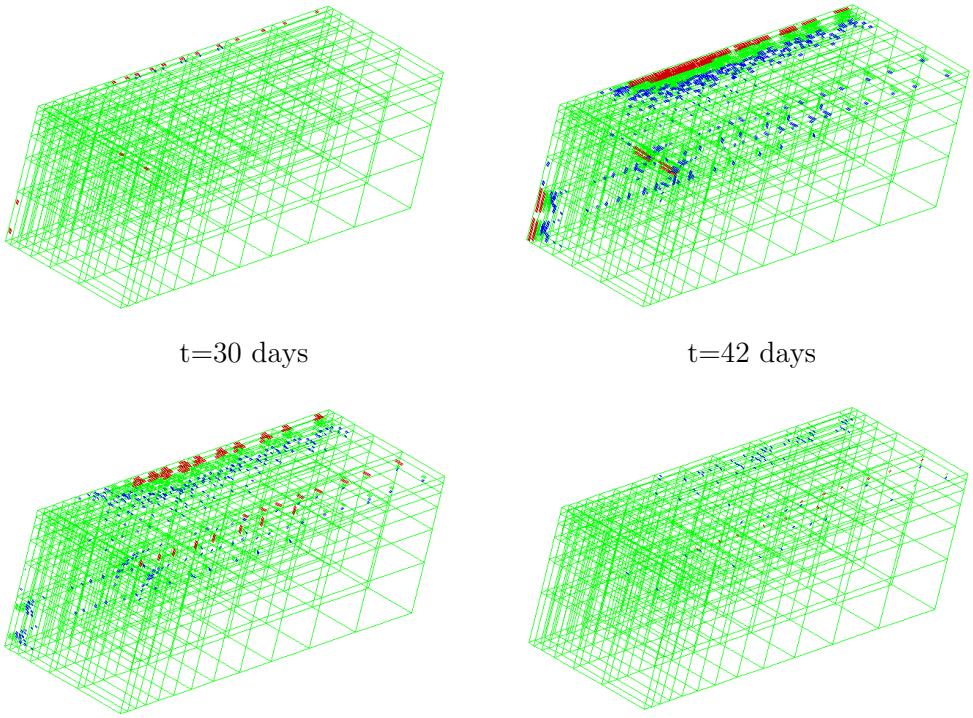

Figure 5.65: Cracking patterns for specimen P200 at selected instants (vectors perpendicular to cracks, with length proportional to the crack opening)

After the detailed interpretation of results obtained for the specimen P200, some comparisons with results for specimen P150 are performed for the control points P1 (core) and P3 (edge point located on the ZX plane of symmetry – see Figure 3.19b), in terms of evolutions of stress σ_y (Figure 5.66). It has been pointed out in Section 3.14.2 that specimen P200 has higher H gradients than P150, and is thus prone to the development of higher stresses of drying origin. The difference in these stresses is attenuated by cracking, which is more significant in P200, and releases the restraint to deformation, as can be confirmed in Figure 5.66. The residual stresses at the end of the analysis are quite similar for both specimen sizes.

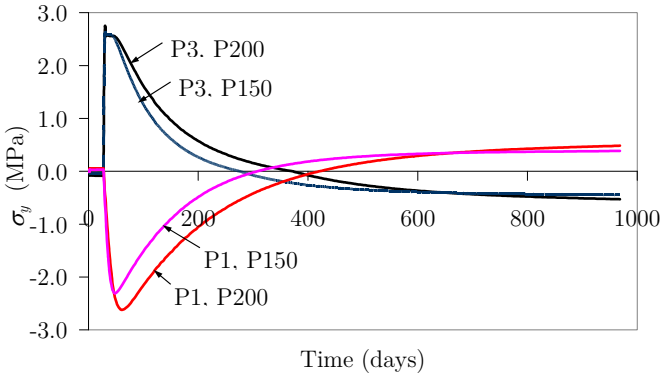

Figure 5.66: Comparison between normal stress σ_y for P200 and P150

To conclude the discussion of results obtained for specimens P200 and P150, their feasibility is tested by comparing the computed shrinkage strains at the specimens' centres with those that would be obtained upon application of Eurocode 2 (EC2). The predictive formula for drying shrinkage as a function of time in EC2, $\varepsilon_{cd}(t)$, comprises the multiplication of a time dependent factor $\beta_{ds}(t,t_s)$ by the final shrinkage value $\varepsilon_{cd,\infty}$. For the present comparison of results, the same final shrinkage is assumed in both the thermo-hygro-mechanical analysis and in the simplified approach of EC2. Therefore, the value of $\varepsilon_{cd,\infty}$ was obtained by multiplying the adopted 500×10^{-6} (see Section 3.14.1) by the remaining part of equation (3.39) - $f_s(H)$ -, using H=50% and thus obtaining the predictable final shrinkage at this environmental humidity to be used in the EC2 formulation: $\varepsilon_{cd,\infty}=459.4\times10^{-6}$ (for the two geometries under study). This comparison should not grant an exact match in any way, since EC2 just provides reference values for the evolution of strains that clearly depend on many more parameters than the ones considered. Therefore, this comparison just aims to verify if the shapes of the curves are similar, to confirm the feasibility of the numerical simulations performed. The predictable strain evolution obtained from application of EC2, together with the computed strains at the core of the specimen, are depicted in Figure 5.67. It can be concluded that the resemblance of tendencies provides grounds to the feasibility of the adopted methodology for calculation of self-induced stresses due to drying shrinkage.

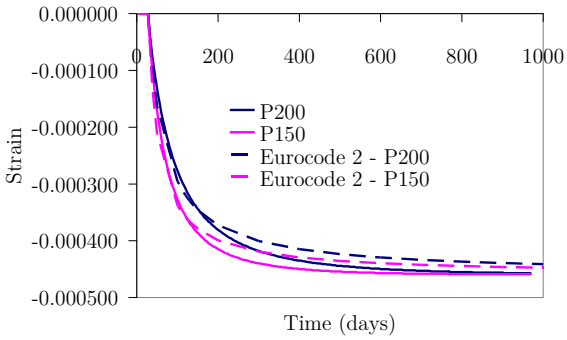

Figure 5.67: Computed strains at the specimens centres *versus* predictions using EC2

According to the presented analyses, it was also possible to quantify the stress fields in the specimens (usually applied for shrinkage measurements), which have relevant variations along time, thus not negligible as often assumed.

5.9.3 RC slab

5.9.3.1 General description

The example to be discussed is a 25cm thick RC slab (1.8m long, and infinite in the perpendicular direction), symmetrically reinforced (top/bottom), and without external restrictions to displacements along its middle plane (i.e., not restrained by supporting columns or walls). Thermal and moisture conditions for the slab have been described in Section 3.14.3.

Mechanical analyses are conducted for the slab whose stress and strain field evolutions resulting from the combined action of self-induced stresses (heat of hydration and drying

shrinkage) and external loads (imposed axial deformations or imposed curvatures) are to be studied. The main purposes of these analyses are:

- To determine the stress profile of self-induced normal stresses within the slab's cross-section.
- To determine the effect of the self-induced stresses when the slab is subject to an axial force or bending moment after an initial period in which the slab was left to shrink without external restraints. The effects under study mainly regard the cracking load, as well as the post-cracking slab's behaviour.

An outline of the analyses to be conducted can be found in Figure 5.68 and in the text that follows.

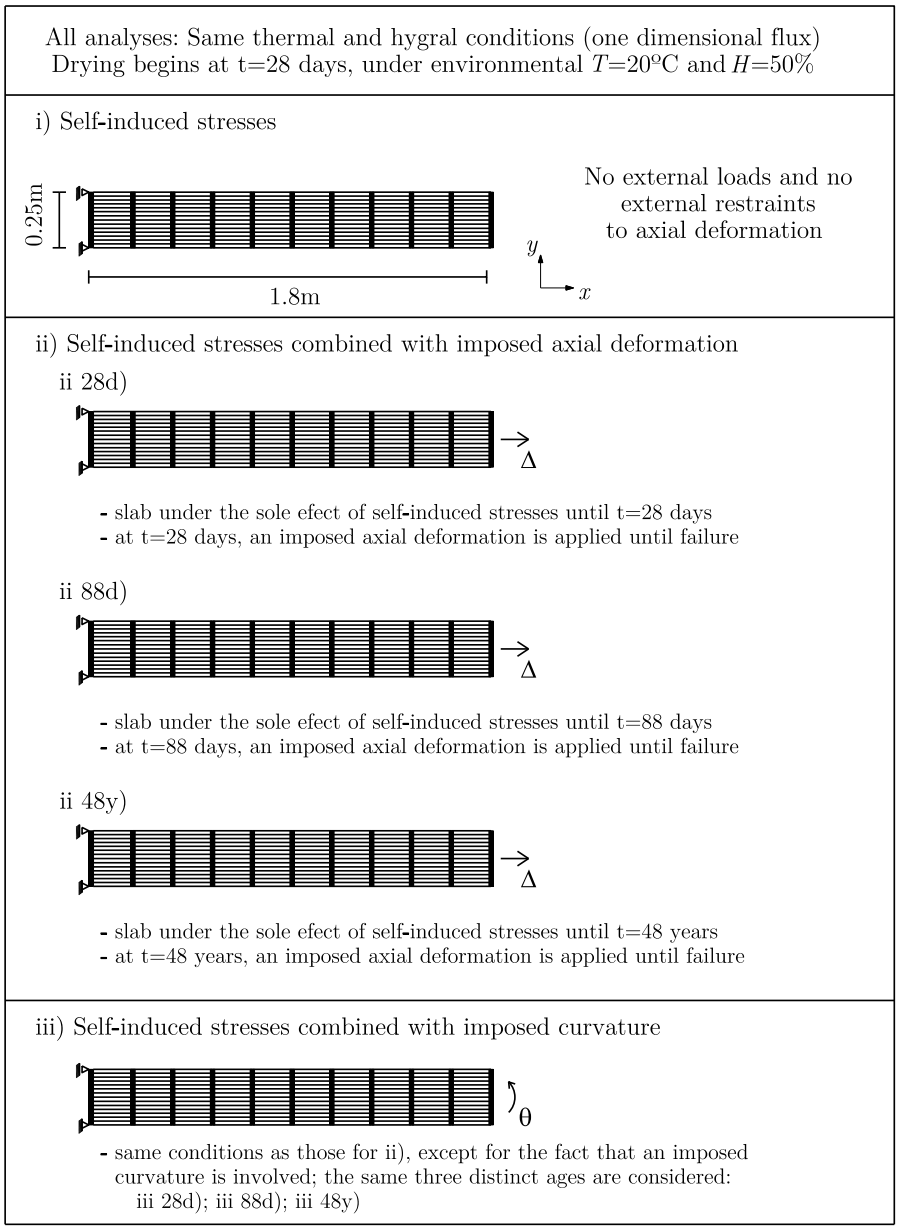

Figure 5.68: Outline of the analyses conducted for the RC slab

All analyses were conducted with the same thermal and hygral conditions, with differences residing only in the mechanical calculations. The first analysis named as i)

pertains to the study of the sole effect of self-induced stresses, combined with the existence of internal reinforcement. For this analysis no external restraint is considered. The set of analyses ii) regards the study of the effect of self-induced stresses in the behaviour of the slab when tested as a tension tie until failure. The slab is left undisturbed until a specified age (which can be 28 days, 88 days or 48 years), and then an axial load is applied. Interpretation of differences in the structural behaviour can be accounted by the thermal and hygral stresses built up until the age of testing. The set of analyses iii) is quite analogous to ii), except for the fact that instead of an axial deformation, an increasing curvature is imposed to the slab, so the aim of the study is to check influence of the self-induced stresses in the slab working as a flexural element.

5.9.3.2 Modelling parameters and strategy

In the mechanical analysis 4-noded quadrilateral isoparametric plane stress elements (1m thick perpendicularly to the plane of the model) were used, with 2×2 Gauss points. Rebars are discretized with 2-noded bar finite elements. In the FE mesh, represented in Figure 5.69 the length of each FE longitudinally to the model is 17.9cm, which coincides with the average crack spacing $s_{r,m}$ (in stabilized cracking phase), for a rebar diameter ϕ_s=12mm and an effective reinforcement ratio $\rho_{s,ef}$: $s_{r,m} = 2/3 \ \phi_s / (3.6 \ \rho_{s,ef})$ (according to MC90). The use of finite elements with a length equal to the average crack spacing is coherent with the adopted models for simulation of tension-stiffening, since the considered σ–ε relationship corresponds to an average behaviour between cracks. In regard to the average stress endured by concrete in the length between cracks, a β=0.4 value is adopted in all the analyses. Reinforcement elements are represented in red in Figure 5.69, at a distance of 3.5cm from the nearest concrete surface. The area of reinforcement considered in each surface is 10.83cm^2/m.

Along the slab thickness, the following discretization strategy was adopted: near both top and bottom surfaces five 1.75cm tall FE correspond to the effective area around the reinforcement (total height=8.75cm); the remaining 7.5cm of the slab's height was modelled with 4 FE. For reference purposes, the vertical alignments of the FE are numbered from Alignment 1 to Alignment 10 as shown in Figure 5.69.

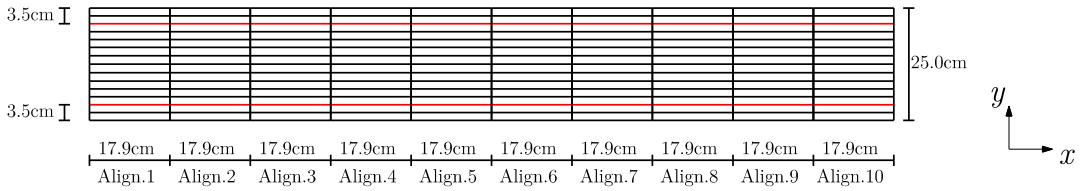

Figure 5.69: FE mesh adopted for the mechanical simulation

In regard to the external supports, shown schematically in Figure 5.70, horizontal x displacements are prevented at the left-hand side of the FE model. Furthermore, linear contraints are imposed in all vertically aligned nodes, assuring that plane sections before deformation remain plane after deformation, in accordance to Bernoulli's hypothesis. By using these linear constraints, the used FE model avoids sectional distortion, allowing nonetheless the imposed strains associated to the temperature and shrinkage fields, as well

as the calculated maturity of concrete, which vary nonlinearly across the thickness of the slab.

All analyses were conducted since the instant of casting until the age of 48 years, with the following time integration strategy: 6 steps×1 hour + 3 steps×2 hours + 9 steps × 4 hours + 6 steps × 8 hours + 34 steps × 1 day + 6 steps × 10 days + 12 steps × 20 days + 24 steps × 30 days + 36 steps × 120 days + 34 steps × 360 days.

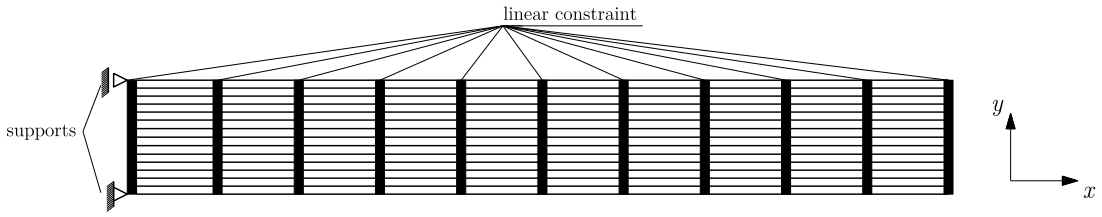

Figure 5.70: Supports and constraints for the mechanical model of the slab

5.9.3.3 Discussion of results

Based on the thermo-higrometric results that have been presented in Section 3.14.3, the three mechanical analyses labelled as i), ii) and iii) were conducted, and the main results are described in the following.

i) Self-induced stresses

In this analysis, including solely influences of the hydration-induced temperatures and the drying shrinkage, the developed longitudinal σ_x stresses on two layers of the analyzed slab strip can be observed in Figure 5.71 until the age of 4000 days. As the temperature rise and decrease associated to the heat of hydration occur within the first 4 days of age, their contribution to the stress development may be commented separately from that due to the drying shrinkage (which is only activated at the age of 28 days). During the hydration heat release phase temperatures in the core are higher than in the surface, and so the former tends to expand more than the latter; accordingly, the slab core becomes compressed and the surface endures tensile stresses (Figure 5.71a). This tendency occurs until the age of 10h, and is inverted from then on, once the core will cool more than the surface. This causes a sign reversal of stresses, with compression in the surface and tension in the core. Due to the very low gradients of temperature within the cross-section, as well as the absence of external axial restraints, the developed thermal σ_x stresses are quite low (less than 0.1MPa), as can be seen for t=28 days (before shrinkage is activated) in Figure 5.72 (where stress profiles within the cross-section are depicted for several ages – continuous lines). Therefore, it can be concluded that heat of hydration plays a negligible role in this example, and therefore it will be generally disregarded hereinafter.

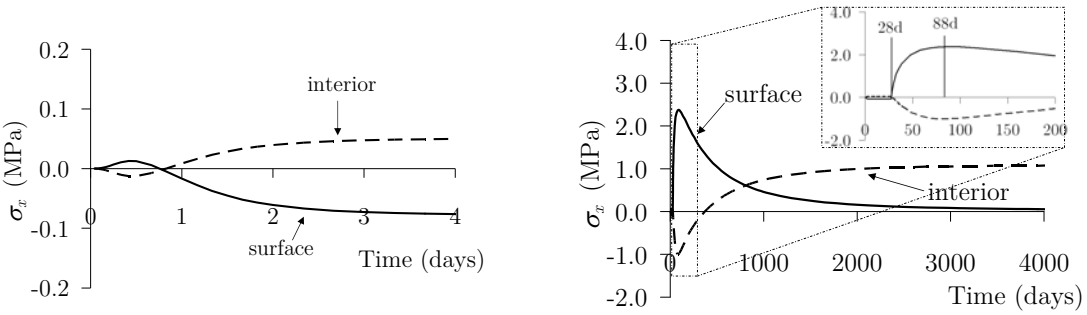

a) b)

Figure 5.71: Concrete longitudinal self-induced σ_x stresses: a) until 4 days of age; b) until 4000 days of age

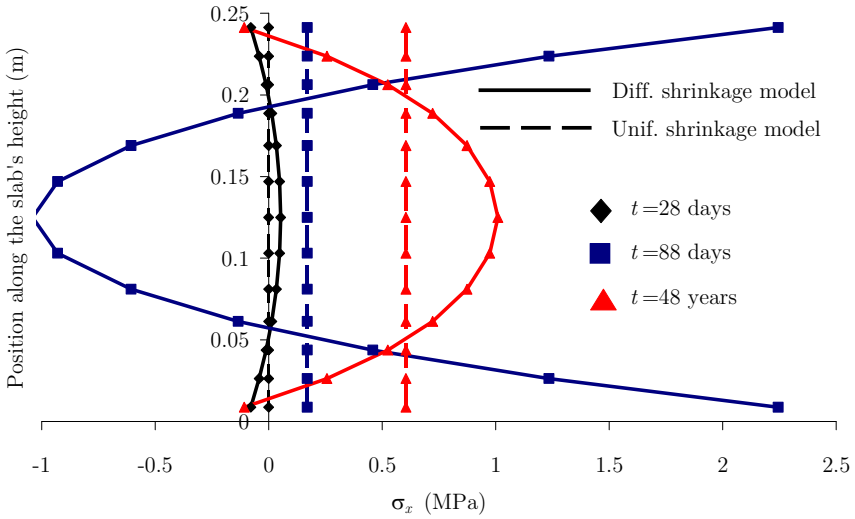

Figure 5.72: Self-induced concrete σ_x stresses, considering both differential (continuous lines) and uniform (dashed lines) drying shrinkage situations

Still looking at the stress evolutions depicted in Figure 5.71b, it is interesting to have some insight on the stress developments between the age of exposure (28 days) and the time at which H gradients reach their maxima within the cross-section (88 days): the surface that was slightly compressed due to the initial temperature development, goes into tension due to the rapid increase in surface potential shrinkage right after exposure, and the core becomes compressed. This tendency is kept until the age of 88 days, when the surface longitudinal tensile stress reaches a maximum of 2.3MPa, as it may be confirmed in Figure 5.72 (continuous line – 88 days). After 88 days the process is reversed: the humidity gradient within the cross-section starts decreasing, and the moisture loss is steeper in the core than in the surface areas. Consequently the surface tension is alleviated, and the core's compression diminishes until it becomes also under tension. This tendency is such that at the age of 2000 days (~5.5 years) the surface σ_x is almost 0MPa and the tensile σ_x in the core reaches 1MPa (Figure 5.71b). At the end of the analysis (48 years), and according to Figure 5.71b, it can be seen that the stress changes are small in regard to the age of 5.5 years. This would be expectable, as the potential drying shrinkage at the age of 2000 days is almost completed.

In order to check the consequences of the detailed analysis of self-induced stresses that has been described, an analysis disregarding the effect of heat of hydration and prescribing drying shrinkage as a uniform strain (customary practice in standard design of RC structures) on the slab cross-section was carried out also. The imposed strains to simulate shrinkage uniformly where obtained in such a way that in a plain concrete slab of the same thickness, both differential and uniform shrinkage models would yield the same average strain within the cross-section. The comparative results of the two analyses can be found in Figure 5.72, where the stress profiles for the differential shrinkage model (including thermal stresses) are depicted in continuous lines, and the stress profiles for the simplified uniform shrinkage model are depicted in dashed lines. It can be concluded that the obtained stresses are clearly different, and large enough to be considered not negligible, particularly at the age of maximum humidity gradient (88 days).

ii) Self-induced stresses combined with increasing axial deformations

The present section regards three distinct numerical simulations of the slab, subjected to self-induced stresses until a certain age, and from then on submitted to growing axial deformations imposed on the rightmost part of the slab until failure. Three distinct ages for imposing axial deformation are considered:

- 28 days, before shrinkage is activated
- 88 days, instant at which the gradient of self-induced stresses associated to drying shrinkage reaches its maximum
- 48 years, corresponding to a long term situation where the slab is in higrothermal balance with the environment

In experimental tensile tests of RC ties with imposed deformations (Jaccoud 1987) it has been observed that the last crack is formed for a load approximately 30% higher than that of the first crack. Therefore, in the numerical modelling concerned in this research, the f_{ct} values were considered to vary within the range [2.6MPa; 1.3×2.6MPa]. To ease the interpretation of results, the same f_{ct} value was considered in all the FE of each vertical alignment (see Figure 5.69), but f_{ct} was assumed to grow linearly from alignment 1 (2.6MPa) to alignment 10 (3.38MPa).

The calculated relationships N-ε_m (axial force *versus* average axial strain) for imposed deformations applied at the three ages under consideration may be observed in Figure 5.73, where the straight dashed lines representing the stiffness in state 1 (tie with uncracked concrete) and state 2 (tie totally disregarding contribution of concrete) are also represented. The shape of the obtained graphics is coherent with the typical ones obtained in experimental works of similar situations (Farra 1995, Jaccoud 1987). The apparent cracking load (here defined as the N value that corresponds to the beginning of the first descending branch of the N-ε_m diagram) is lowered as the age of imposed axial deformations advances. For imposed axial deformations at the age of 28 days, the cracking load computed with the numerical model is practically coincident with the one obtained through $N_{cr}=f_{ct}\times A_c\times(1+\alpha\rho)$=688kN (with α being the homogenization coefficient, and ρ being the reinforcement ratio).

It is noteworthy to mention that when axial deformations are imposed at the age of 88 days, the effect of self-induced stresses is almost enough to cause surface cracking on the FE alignment 1 with f_{ct}=2.6MPa (see Figure 5.72). Nonetheless, the axial force rises until

560kN due to the internal redistribution of normal stresses acting on concrete. However, the first branch of the N-ε_m is clearly non-linear (see Figure 5.73b – deformation applied at the age of 88 days), due to the process of crack formation that follows the internal normal stress redistribution within the cross-section. The concept of apparent cracking load is defined here as the load at which the cracks cross the whole slab thickness for the first time (useful for the interpretations that follow). Still regarding the imposed deformation applied at 88 days, Figure 5.74 depicts the vectorial representation of the maximum crack strain ($\varepsilon_{cr,max}$) for two consecutive increments: immediately before and immediately after the apparent cracking load is reached. The adopted vector scales for a) and b) are different, with $\varepsilon_{cr,max}$ =0.165×10^{-3} for a) and $\varepsilon_{cr,max}$ =0.506×10^{-3} for b). In Figure 5.74a, cracks are propagating inwards along the slab thickness, with all cracked elements still working within the softening branch of their σ–ε relationships. In Figure 5.74b the crack on alignment 1 is fully formed, with the softening branch of the σ–ε diagram having been overcome, thus mobilizing the tension-stiffening effect. The above interpretation helps understanding the reason for using the above defined expression "apparent cracking load": in fact, long before the apparent cracking load is reached, the cross section of the slab exhibits cracks associated to the self-induced stresses. However, the fully cracked behaviour is only attained when the imposed deformation is applied, being influenced by the previous state of surface cracking.

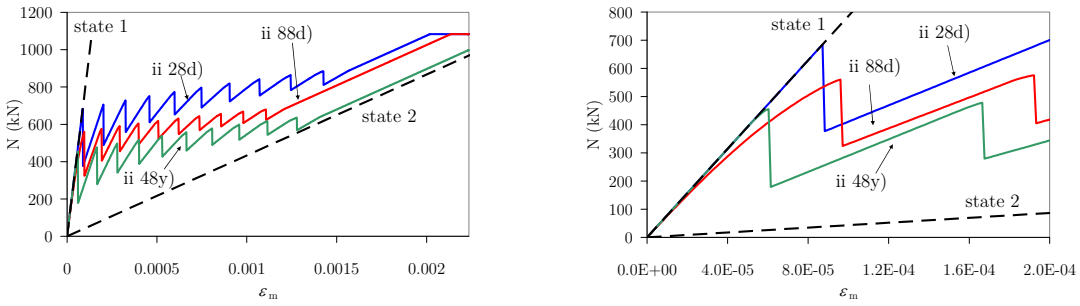

a) b)

Figure 5.73: N-ε_m relationship for imposed deformation tests at the ages of 28 days, 88 days and 48 years: a) representation until stabilized cracking; b) early stages (apparent cracking)

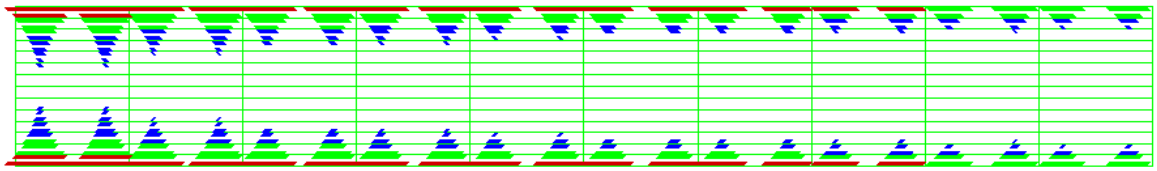

a) immediately before the apparent cracking load is reached (t=88 days)

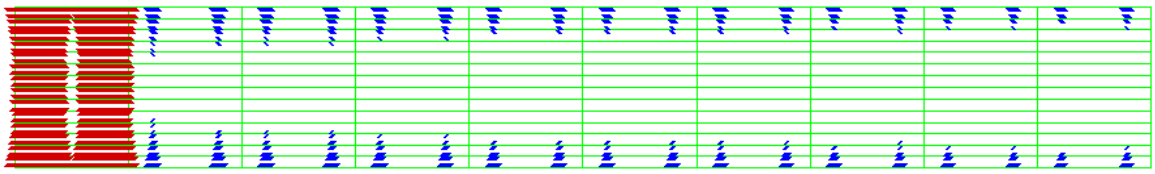

b) immediately after the apparent cracking load is reached (t=88 days)

Figure 5.74: Vector representation of $\varepsilon_{cr,max}$ for imposed axial deformation at 88 days

Focusing attention on Figure 5.73b, it is noticeable that the apparent cracking load for imposed deformations applied at the age of 48 years is lower than that which results of loading at 28 days or 88 days, even though at 48 years there are slight surfacial compressions as a result of drying shrinkage. The apparent cracking load results lower for loading at this later age because the global effect of drying shrinkage causes the resultant of normal stresses acting on the cross-section to be a higher tensile force, as may be confirmed from observation of the stress profile in Figure 5.72.

Still regarding Figure 5.73, it is important to remark that in the phase of stabilized cracking the N-ε_m diagram tends to approach the straight line that represents the stiffness in state 2 as the loading is applied at later ages, with an apparent less contribution of the concrete between cracks (tension-stiffening). This behaviour, which has already been reported by Bischoff (2001), is related to the shrinkage that occurs prior to the load application.

Figure 5.75 allows a comparison between the previous results with those that arise from an analysis in which drying shrinkage is considered as a uniform imposed strain. As expected, the apparent cracking load is higher for this new case, regardless the age of loading (except for the case of loading at the age of 28 days, when the results practically coincide, once drying shrinkage is not active yet, and the small differences are due to the residual stresses associated to heat of hydration). The lower apparent cracking load for the cases where self-induced differential stresses are considered is related to the fact that cracking occurs in surface elements for much lower loads, due to their prior self-induced tensile stresses mainly associated to drying shrinkage. In Figure 5.75 it can be also observed that during the stabilized cracking phase the results obtained with both drying shrinkage modelling approaches are coincident.

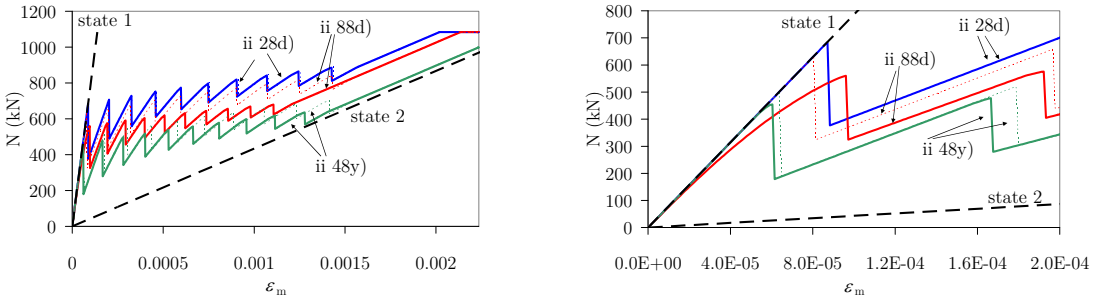

a) until stabilized cracking b) early stages (apparent cracking)

Figure 5.75: N-ε_m relationships for imposed axial deformations at different ages for the model considering differential drying shrinkage (continuous lines) *versus* model considering uniform drying shrinkage (dashed lines)

iii) Self-induced stresses combined with increasing imposed curvatures

The present section is related to the discussion of results obtained when increasing curvatures are applied to the slab's rightmost edge, at the three ages under study (28 days, 88 days and 48 years), superimposed to the previously existing self-induced stresses. The calculated M-χ_m (bending moment *versus* average curvature) diagrams are shown in Figure 5.76.

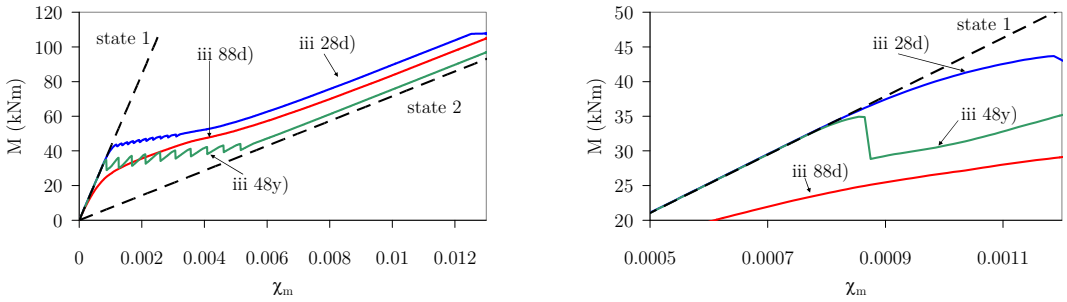

a) representation until stabilized cracking b) early stages (apparent cracking)

Figure 5.76: M-χ_m relationship for imposed curvature tests at the different ages of 28 days, 88 days and 48 years

For the case of imposing curvatures at 28 days, it is verified that the teeth-shaped part of the M-χ_m diagram is rather smooth. The reason for this is the following: the existence of a descending branch (during the crack propagation phase) in the M-χ_m diagram does not correspond to the appearance of a new crack in the slab; in fact, when the apparent cracking moment of 43kNm is reached, cracking already exists throughout the whole slab's length, but the cracks do not cross the whole depth of the slab area in tension. Thus, the appearance of a descending branch in the M-χ_m diagram just corresponds to a slight increase in the depth of cracking, which causes a smooth teeth-shaped pattern.

For the case of imposing curvatures at 88 days, the M-χ_m diagram does not exhibit descending branches during the crack propagation phase. Moreover, by the time the theoretical cracking moment M_{cr} is reached, the M-χ_m diagram already shows a strong non-linear trend. The fact that the diagram does not have descending branches in the crack propagation phase is a consequence of the fact that no new cracks are being formed in the longitudinal direction of the slab; in fact, the existing cracks by the time the theoretical cracking moment was reached are simply progressing inwards the slab. Actually, before curvatures applied, there was already cracking in the two leftmost FE alignments of lower tensile strength, and for a very low bending moment (8kNm, in this case) surface cracking already occurred in all FE alignments. It is thus observed that for loads applied at instants with important pre-existing self-induced stresses (with strong surface tensile stresses), the structural response of the slab is significantly different from that without those self-induced stresses.

For the case in which loading is applied at 48 years, there is a larger height of the teeth-shaped part of the M-χ_m diagram. This is a consequence of successive crack formation along the slab's length, which in turn is motivated by the self-induced stress profile in the cross-section before the curvature is applied (compressive stresses near the surface and tensile stresses in the core of the slab). Therefore, the increase in depth of cracks occurs in a more abrupt way than it was the case for the other two analyzed ages of imposed curvatures.

The previously presented M-χ_m diagrams are now compared with those resulting from a simplified analysis of drying shrinkage effects by considering the latter as a uniform strain – see Figure 5.77. For the case of curvatures applied at 28 days, the two approaches yield similar results, as expected.

By looking at the results obtained with the simplified approach alone, there seems to be a consistent tendency of the M-χ_m diagrams to evolve in the same manner as imposed curvatures are applied at later ages:

- The apparent cracking load is lowered for later loading ages, as a consequence of the normal tensile stresses previously installed in concrete, which is in turn related to the cross-sectional restraint to free concrete shrinkage caused by reinforcement.
- The height of the teeth-shaped part of the M-χ_m diagrams increases for later ages of loading.

There is no evidence in the simplified calculations of general behaviour changes of the M-χ_m diagrams for curvatures applied at intermediate ages (such as 88 days), unlike what occurred for calculations with consideration of drying-shrinkage induced stresses. For the case of loading applied at 48 years the apparent cracking bending moment is smaller when computed with the simplified shrinkage model than with the differential one, which is the opposite trend to that observed at the age of 88 days. This is due to the fact that in the long term the differential shrinkage model leads to the appearance of compressive stresses in the surface areas at 48 years, which retard the process of crack formation.

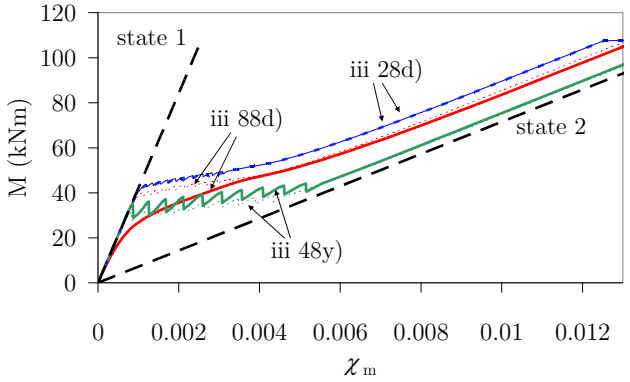

Figure 5.77: M-χ_m relationships for imposed curvatures at different ages: model considering differential drying shrinkage (continuous lines) *versus* model considering uniform drying shrinkage (dashed lines)

Final considerations

The analysis of the RC slab, with consideration of tension-stiffening effects, as well as softening behaviour of plain concrete, associated to cracking, allowed interesting conclusions to be drawn in regard to the effect of self-induced stresses on the load/deformation behaviour of the slab. It was observed that for loads applied at instants when important self-induced stresses were already installed (with strong self-induced surface tensile stresses), the structural response of the slab is significantly different from that corresponding to the absence of self-induced stresses, or even that corresponding to a simplified approach of considering uniform shrinkage strains. Also, for loads applied at high ages (48 years), an unexpected beneficial effect of surface self-induced compressive stresses was found to increase the cracking load in regard to that obtained at earlier ages.

The overall plausibility of the results obtained provides good expectancies in regard to the capacities of the adopted methodologies, which are to be experimentally validated in future research. Upon further validation, there is a great potential for the use of this kind of numerical tools for analysis of real structures (with consideration for external restraints

to the free shrinkage of the element), conducting to possible important savings when it comes to evaluating reinforcement needs in order to control shrinkage cracking (together with externally applied loads) in service life of structures.

Chapter 6

Field applications

6.1 Introduction

Throughout the present thesis, many concrete related aspects have been pointed out regarding several physical phenomena involved in the cement heat of hydration development, as well as drying shrinkage, and their consequences in the stress development in real structures. It is the aim of the present chapter to show practical application of these methodologies to real size concrete structures, and evaluating stresses along time. Two field applications are to be presented, involving both in-situ monitoring of temperatures and stresses, and their corresponding numerical simulation. Because of the types of structures involved, and the practical limitations in monitoring moisture structures in concrete, moisture fields where not measured neither simulated in the scope of the present chapter.

The first example is related to a RC foundation of a steel wind tower. Due to its massivity (~16×16×2m^3), the foundation is bound to have strong self-induced stresses associated to temperature variations due to cement hydration heat release. This example regards a study ordered by the owner of the wind tower, who wished to be aware of the magnitude of self-induced stresses associated to heat of hydration in the zone where the steel mast is anchored in the concrete foundation. This case study involved temperature monitoring of the structure, which allowed validation of the performed thermo-mechanical analysis.

The second application is related with the phased thermo-mechanical analysis of a gravity concrete dam, and corresponding monitoring of temperatures and strains during the construction phase. The analysis focuses on a specific part of the dam, where the openings caused by internal galleries are significant. The study of a concrete dam with such a number of internal singularities has not been object of recent studies, according to the conducted bibliographic review. So, it was decided to evaluate the influence of such

singularities on the stresses that develop in the structure. Due to the relatively long time of construction, and thus analysis, several aspects that are usually disregarded in other shorter term thermo-mechanical analyses had to be dealt with, such as: explicit modelling of solar radiation, effect of evaporative cooling and effect of night sky radiation.

6.2 RC Foundation of a wind tower

6.2.1 Intoduction

The recourse to onshore wind tower electricity generators is proving to be a valid solution to partially circumvent the depletion of conventional energy resources that presently worries humanity. Nowadays the use of wind towers with horizontal turbines that may stand up to 100m above the ground, with turbine blades reaching lengths of 50m, is becoming a routine. These huge dimensions do necessarily lead to large drag forces on the entire system, demanding for specific needs when it comes to the foundation, usually made up of reinforced concrete, with in plan dimensions that may reach $20\times20\text{m}^2$, and thicknesses of about 2m. As these RC foundations are usually cast in a single run, and bearing in mind the significant volumes of concrete involved, large amounts of heat release due to the exothermal nature of the cement hydration reactions are expected.
The restraints to which concrete is subjected, together with the differential temperatures that usually arise within the foundation, may lead to early age thermal stresses capable of inducing premature cracks, or at least to create a stress state of imminent concrete cracking. Most commonly early age thermal cracking poses durability problems related to an increased susceptibility of concrete to degradation phenomena (such as corrosion or carbonation), rather than causing structural concerns. Yet, in the RC foundation to be analyzed, the possible occurrence of early age cracking was mainly checked due to concerns related to the operational performance of the wind tower, and eventually to the reduction of its safety in later stages. In fact, the tower itself is a circular hollow section steel mast, with a diameter of 4m at the base, and for the perfect clamping of the tower onto the RC foundation there is a 2.3m tall steel ring, partially cast inside concrete, as depicted in Figures 6.1 and 6.2. The concrete around the bottom steel ring flange is of utmost importance for the stability of the wind tower, and so on this anchorage domain it is important to prevent formation of gaps above and below the flange, as well as the initiation of cracks on the adjacent concrete, which could engender undesirable oscillations on the tower. As a possible origin of such cracking one should check the early age tensile stresses that will develop in concrete, as a consequence of restrictions to the thermal deformations induced by the heat released during cement hydration.

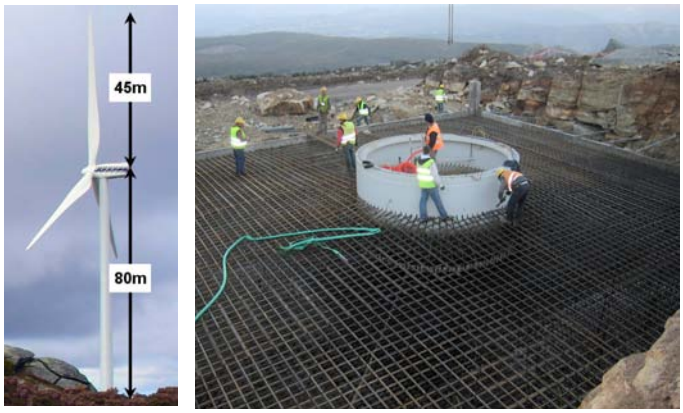

Figure 6.1: Wind tower and RC foundation

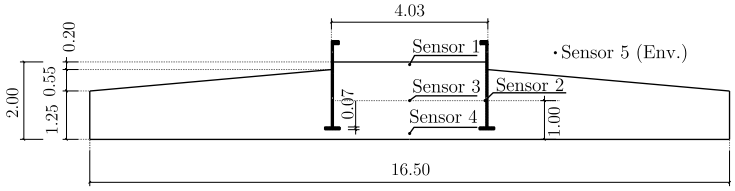

Figure 6.2: Dimensions of the RC foundation

Another source of early age cracking may arise due to autogenous and drying shrinkage, yet, for this application the foundation was made up of Normal Strength Concrete, so autogenous shrinkage was negligible, and drying shrinkage was irrelevant during the early age time interval; consequently the analyses disregarded influences of both shrinkage types.

The tools, modelling approaches and parameter estimation techniques that have been described in Chapters 2 and 5 for thermo-mechanical analyses are to be used in this application. Efficiency of the adopted methodology is illustrated, by performing thermal and mechanical analyses of the above referred R/C foundation, which was monitored for temperatures during the first weeks after casting. Particular attention is drawn to the modelling options and numerical strategies adopted (namely the assumption of a 2D FE discretization), validating the overall assumptions by comparing the numerically predicted temperatures with the in field monitored ones. Evolution of the concrete stresses, particularly the tensile ones, and their relationship with the early age cracking risk to be expected on the foundation, is also subject of concern.

6.2.2 Geometry and materials

The wind tower mast is made up of steel, with a rotor machine standing 80m above the foundation and with blades 45m long, as reproduced in Figure 6.1. In this figure it is also possible to see the bottommost steel ring onto which the tower mast will be bolted, as well as the top reinforcement mesh of the foundation. The relevant dimensions of the foundation, with a square $16.5 \times 16.5 m^2$ insertion in plant, as well as of the flange of the steel ring that anchors the wind tower, are reproduced in Figure 6.2.

As explained before, the scope of the present study was to check whether early age tensile stresses would be expectable on the concrete region around the steel flange, as a

consequence of restrictions to the thermal strains induced by cement heat of hydration, and if they would be large enough as to induce cracking. To make this check a thermo-mechanical simulation will be performed to predict the temperatures and stresses that will develop in concrete during the first 30 days after the pouring and setting phases. Due attention will be also devoted to the evolution of the environmental temperatures and those on the granite massif (onto which the concrete foundation is poured). Concrete grade class for the foundation was C25/30, and grade class for the wind tower steel ring was S355, according to Eurocodes 2 and 3.
Most of the numerical analyses were undertaken assuming axisymmetry conditions, for greater commodity in handling the numerical model and visualization of results. A 3D thermal analysis was also carried out in order to validate the axisymmetry assumption.

6.2.3 Monitoring campaign results

As the intended analyses were centred on a real field application, a judicious calibration of the numerical model was performed. Accordingly, a monitoring campaign was undertaken to measure relevant temperature evolutions using 5 PT100 sensors, placed according to the sketch reproduced in Figure 6.3a. Remarks are made about sensor 5, concerned to the environmental temperature, and about sensors 1 and 4, located respectively 7cm and 15cm apart form the nearest concrete surface. Sensor 3 was placed at half height of the foundation (1m) at its geometrical centre, whereas sensor 2 was placed at the same height, connected to the embedded steel profile. The monitoring campaign started at the day in which the foundation was cast (6th December 2005) and was maintained for a total of 20 days, with constant measurement intervals of 10 minutes. Final placement of sensors 3 and 4 may be observed in Figure 6.3b. A steel bar was used to support the sensors; however, in order to minimize the disturbances in measurements caused by the high thermal conductivity of steel, a polystyrene spacer (thermal isolation) was used between the sensors and the supporting bar.

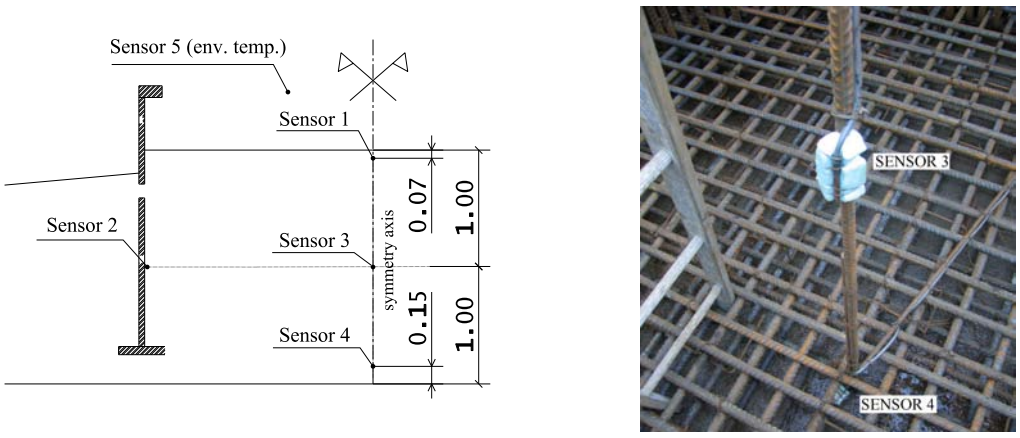

a) b)

Figure 6.3: a) Sensor placement detail; b) Photo of sensors 3 and 4

The measured temperatures by the five temperature sensors between 7:30h and 19:30h of the day in which the foundation was cast are shown in Figure 6.4. Based on the temperature variations measured by each sensor (sudden temperature increases in regard

to the environmental temperature), it is possible to determine the time at which each sensor was reached by the rising concrete surface: the beginning of casting operations took place minutes before 9:00h, time at which sensor number 4 was reached (located 15cm from the bottom surface of the foundation); casting operations have ended around 15:30h, when sensor 1 was reached.

Bearing into account that the progressive casting operation is not explicitly modelled in the numerical analyses regarded in this study, it was considered that the time of casting was 12:30h (6th December 2005), with an initial concrete temperature of 15°C (in correspondence to the data collected for sensor 3, at half height of the foundation).

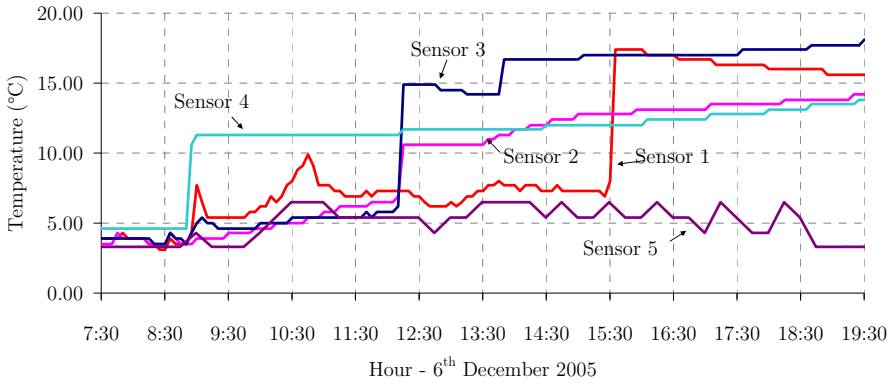

Figure 6.4: Temperatures in the first hours of measurements

The measured temperatures throughout the whole monitoring campaign are shown in Figure 6.5. It can be observed that the maximum temperature was of about 49°C in sensor 3 between 4:40h and 22:35h of the 8th December 2005 (40 to 59h after casting). It is possible to elaborate some qualitative considerations about the temperature values recorded by the various sensors:

- As expectable, the maximum temperature is reached in sensor 3, located in the foundation core, and therefore subject to the smallest thermal energy dissipation to the surrounding air and underlying granite.
- The recorded temperatures for sensor 2 are always lower than those of sensor 3, even though they are both located at the same level in the foundation. The fact that sensor 2 is in physical contact with the steel ring (with strong thermal conductivity and partially exposed to the external environment) causes its temperature rise to be lower than in sensor 3, with the latter being more thermally isolated.
- The temperature elevation for sensor 4 is slower than for sensors 2 and 3. This tendency is justifiable by the proximity of this sensor to the lower extremity of the foundation: the underlying granite with lower temperature than concrete acts as a thermal drain, thus diminishing the temperature of sensor 4 in comparison to sensors 2 and 3. Furthermore, when the two latter sensors begin recording post-peak temperature drops associated to the decrease in cement hydration rates, the lower part of the foundation is still being warmed by the heat accumulated in the granite, causing sensor 4 to record the highest temperatures in the phase of cooling of the foundation.

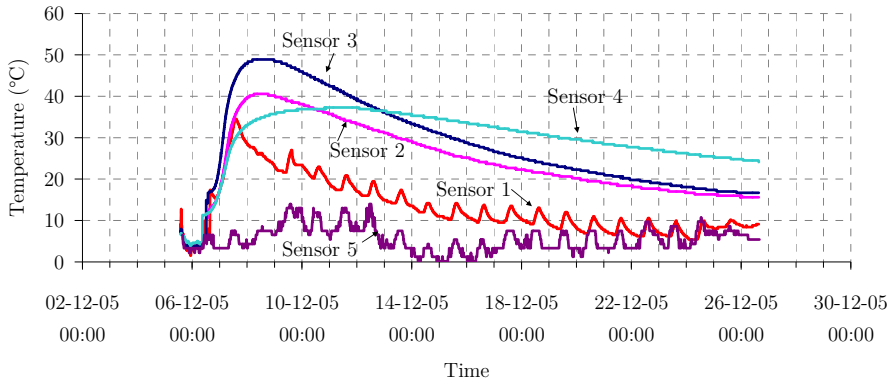

Figure 6.5: Measured temperatures throughout the monitoring period

6.2.4 At-rest temperatures inside the granite massif

For a realistic analysis the thermal field inside granite previously to construction of the wind tower foundation should be characterized somehow. Since measurements along depth and inside the massif are difficult, an estimation of the distribution of temperatures was made based on the predictive methodology indicated on Popiel *et al.* (2001). According to this methodology the upper layer of a rock massif is affected by the daily and seasonal variations of the ambient temperature; yet, for layers standing beyond a certain depth temperature does not change significantly, and it coincides with the average annual ambient temperature. The equation that allows estimating the evolution of temperatures T (in °C) along depth x, and for time t (in days), is

$$T = \overline{T} - 1.07\, v\, a\, e^{-31552\times10^{-8}\, x/\sqrt{d}} \cos\left(2/365\left(t - t^{*} + 0.018335\ x/\sqrt{d}\right)\right) \qquad (6.1)$$

where $\overline{T}$ is the average annual ambient temperature, v is a factor characterizing the density of vegetation, a is the semi-amplitude of the average monthly temperatures, d is the thermal diffusivity of granite, and t^* is the phase of the air temperature wave (units: day). For the present application, taking into consideration the site for construction of the wind tower, the air temperatures registered on sensor 5 and the information provided by the national climatologic agency, it was possible to define $\overline{T}$ =9.5°C and a=4.3°C. For the other parameters the following values were considered: d=1.37×10^{-6}m^{2}s^{-1} and v=0.5. Through application of Eq. (6.1) for the months of March, July and December, the obtained temperature profiles along the granite depth are illustrated in Figure 6.6. It is rather evident that temperatures inside the massif become almost constant during the entire year for depths greater than ~5m, resembling quite closely the average annual ambient temperature. As for preparing the bedding layer to the RC foundation the granite cover was removed until a depth of ~4m, in the analyses it was assumed as rather plausible that the at rest granite temperature below the foundation was constant along depth, and equal to $\overline{T}$.

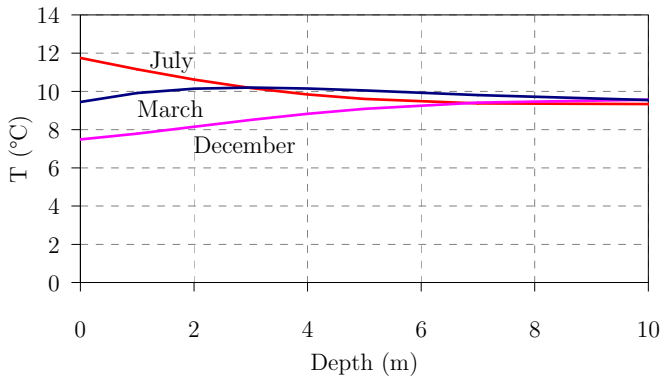

Figure 6.6: Temperature profiles in the granite massif

6.2.5 Material characterization

In view of the intended early age analyses, and as no experimental calorimetric characterization of the cement was available at the time, the heat released by the concrete used in the foundation was estimated with the DuCOM model (Maekawa *et al.* 1999), considering the following mix composition: (i) sand - 765 kgm^{-3}, (ii) gravel - 1065 kgm^{-3}, (iii) cement type II/A-L 42.5R - 220 kgm^{-3}, (iv) fly ash - 105 kgm^{-3}, (v) superplasticizer - 3.2 kgm^{-3} and (vi) water - 162.5 kgm^{-3}. The temperature evolution in a perfectly insulated volume of this concrete mix was simulated in correspondence to the predictable output of an adiabatic test, rendering the curve depicted in Figure 6.7 for an initial temperature of 20°C. With such curve, and assuming E_a=50$kJmol^{-1}$, the necessary data to express the heat generation rate $\dot{Q}$ (see eq. (2.23)) was obtained.

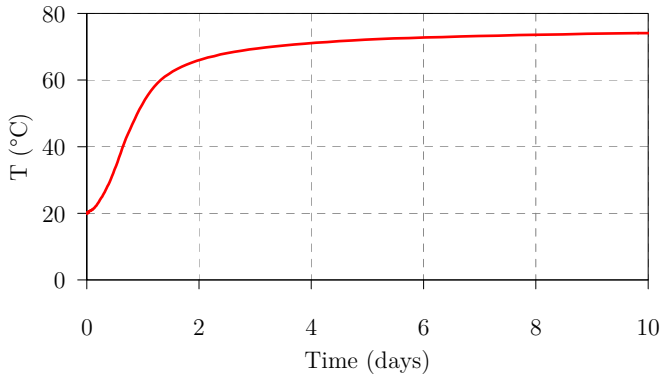

Figure 6.7: Adiabatic temperature rise

As far as the thermal conductivity of concrete is concerned, and bearing in mind that the aggregates are mainly composed of granite, a recommended value of k_c=2.6$Wm^{-1}K^{-1}$ was adopted. For the specific heat of concrete, not greatly affected by the aggregates mineralogical composition, an average value of $(\rho c)_c$=2400$kJm^{-3}K^{-1}$ was considered. The value of 10^{-5} was adopted for the thermal dilation coefficient of concrete. Concrete creep was numerically simulated via a Double Power Law with the following parameters: ϕ_1=0.65, m=0.2 and n=0.21; for the asymptotic elastic modulus the dependency E_c=43.5×$\alpha^{0.5}$GPa on the degree of hydration α was assumed. Following Eurocode 2, for a C25/30 concrete grade class the average tensile strength at 28 days of age is 2.6MPa;

during hydration the average tensile strength of concrete was assumed to evolve linearly with α: $f_{ct} = 2.6 \times \alpha$ MPa.

The explicit simulation of the embedded reinforcement was disregarded in the thermal simulation, as the layers of rebars are generally perpendicular to the main directions of the heat fluxes, which minimizes their effect on the thermal field (see Section 2.8.2). Concerning the mechanical analysis, and bearing in mind the scope of cracking risk prevention of the intended simulations, the option to disregard the influence of reinforcement is also plausible, and accordingly it was assumed in this application.

The steel ring was modelled with the following properties, based on Eurocode 3 recommendations: $k_s = 54 \mathrm{Wm^{-1}K^{-1}}$, $(\rho c)_s = 3270 \mathrm{kJm^{-3}K^{-1}}$, $\alpha_{Ts} = 1.2 \times 10^{-5}$, E_s=210GPa and ν_s=0.3.

According to Silveira (1996) the thermal and mechanical properties of granite were assumed as follows: k_g=2.79 $\mathrm{Wm^{-1}K^{-1}}$, $(\rho c)_g$=2040$\mathrm{kJm^{-3}K^{-1}}$, $\alpha_{Tg} = 10^{-5}$ and E_g=8GPa

6.2.6 Boundaries and FE Mesh

As referred the analyses were performed assuming the hypothesis of axisymmetry, which although not entirely true for a square foundation, deviates not really much on the concrete vicinity to the steel ring. A scheme regarding the areas of the foundation being disregarded by adopting the axisymmetry simplification can be seen in Figure 6.8a: it can be concluded that the overall volume of the foundation is not significantly affected by this simplification. The geometry adopted for the global model after several exploratory analyses is reproduced in Figure 6.8b, which includes the steel ring, the concrete foundation and the granite massif up to a 5m depth.

Concerning the thermal model three boundaries (see Figure 6.8) were considered:

- Boundary 1, where all materials (steel ring, concrete and granite) are assumed in direct contact with the air. Regarding the on site average wind velocity near the ground (lower than $5 \mathrm{kmh^{-1}}$), and the fact that a geotextile membrane remained over concrete after pouring, a convection radiation coefficient h=$10 \mathrm{Wm^{-2}K^{-1}}$ was adopted.
- Boundary 2, concerning the metallic formwork adopted on the foundation vertical faces, where $h = 7.5$ $\mathrm{Wm^{-2}K^{-1}}$ was adopted.
- Boundary 3, limiting the granite volume included in the numerical model, and defining a surface where temperature changes induced by concrete were supposed to be negligible; across this boundary heat flux was assumed to be null.

For the environmental temperatures around boundaries 1 and 2, and during the monitoring campaign, direct measurements from sensor 5 were taken as inputs to the numerical model; from then on the environmental temperatures were assumed to follow the trend exhibited at the beginning of the monitoring campaign. Moreover, during the pouring operations the initial temperatures were taken as 15°C for the concrete (as recorded by the temperature sensors right after being in contact with the fresh concrete), 9.5°C for the granite and 5.6°C for the steel ring (the latter coincides with the average air temperature at the time of casting). On concrete interfaces with the steel ring and granite a direct thermal connection was considered, with heat exchanges being ruled by conduction.

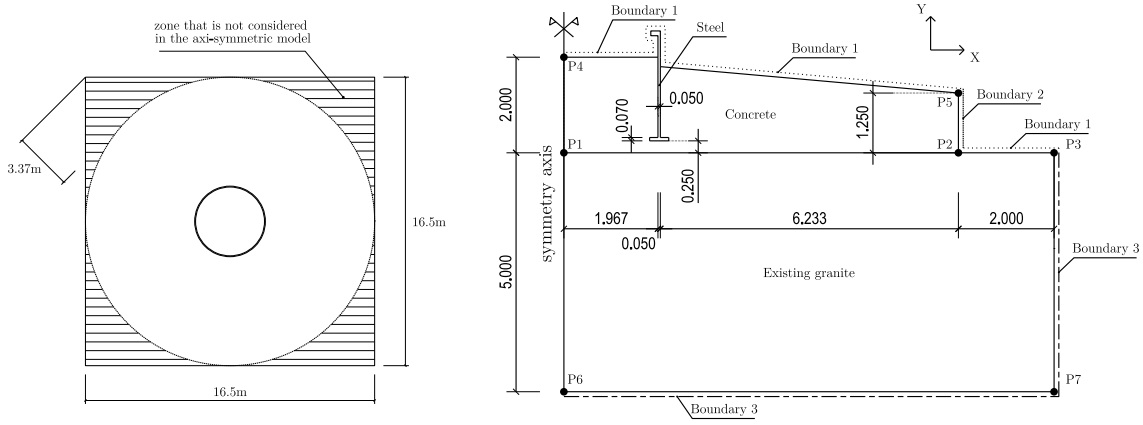

a) b)

Figure 6.8: a) Scheme regarding the axi-symmetry simplification; b) Axi-symmetric model of the foundation and granite (units: m)

With regards to the mechanical boundary conditions, the descending vertical displacements were restrained in all points of baseline P6-P7 of Figure 6.8b. Besides, on the concrete/ring and concrete/granite interfaces special contact elements were adopted that permit only normal compressive stresses, allowing separation and sliding, but preventing interpenetration. An additional mechanical restraint was considered in regard to the reinforcement that passes through the holes in the steel ring: to simulate the connection provided by such rebars, shown in Figure 6.9, the horizontal displacements in the concrete elements located on both sides of the steel rings at the height of the reinforcement were compatibilized.

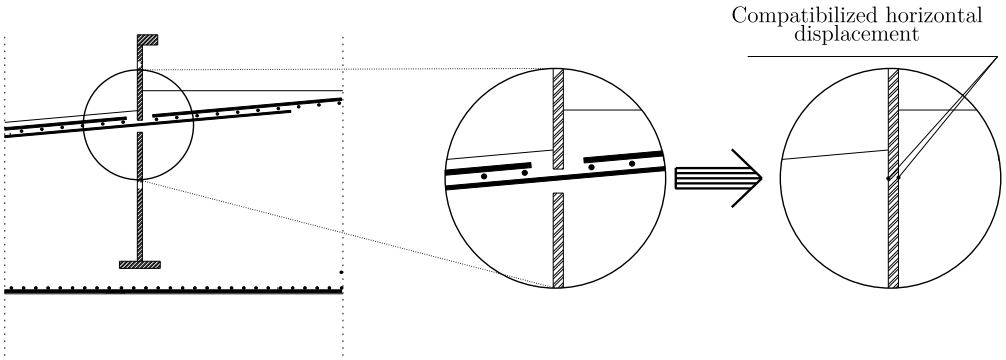

Figure 6.9: Nodal compatibilization due to reinforcement passing through the steel ring

Thermal analyses were performed with a FE mesh comprising 4-noded elements (see Figure 6.10), whereas for the mechanical problem a discretization with 8-noded FE's was adopted; both meshes overlap perfectly, as they have the same number of rectangular FE's, with coinciding corner nodes. The thermo-mechanical analyses covered a total period of 800h (about 33 days), with a time-step equal to 1h.

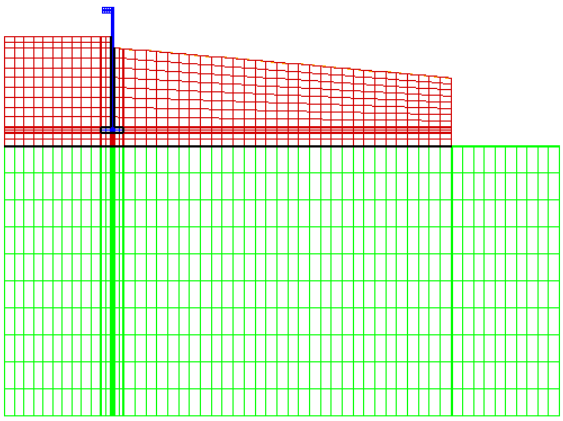

Figure 6.10: Axi-symmetric FE mesh

6.2.7 Calculated concrete temperatures

Evolution of early age temperatures predicted numerically for the foundation is reproduced in Figure 6.11, where it is possible to observe that the peak value reaches 53°C at the age of 2.3 days (Figure 6.11c), on the centre. A peculiar effect to be pointed out in Figure 6.11a-b-c-d is the remarkable cooling influence of the ring, whose top part is in direct contact with the air, which provides an easy path for the heat in the concrete core to exit, as a result of the high thermal conductivity of steel. According to Figure 6.11a-b-c-d it is also noticeable that the concrete heat losses towards the air are larger than those to the underlying granite: in fact, during the heating phase of concrete the rock massif absorbs part of the thermal energy (performing as a heat storage), which is partially sent back during the cooling phase, so that at the age of 9.0 days (Figure 6.11e) the peak temperature already occurs at the concrete/granite interface.
For validation purposes, temperatures obtained in this numerical simulation are compared in Figure 6.12 to the ones monitored on sensors 1 to 4. For the case of sensor 1 (Figure 6.12a), a reasonable coherence is observed; nevertheless, there is an error larger than 5°C in the peak temperature value, and the instant of maximum temperature was not correctly predicted. The differences in computed and measured temperatures for this sensor are probably a consequence of not considering the effects of solar radiation and night cooling in the numerical simulations, which may act as an additional energy input during the day, and as a heat drain during the night. The non consideration of these radiation effects has relevant consequences on the quality surface temperature simulation, but does not affect significantly the quality of predictions in the more interior sensors, as will be discussed in the text that follows. In what regards to the temperatures in sensors 2, 3 and 4 (Figure 6.12), the numerical predictions agree fairly well with the field assessment measurements, with deviations that never overcome 4°C. Therefore, bearing in mind the absence of a complete thermal testing campaign for characterization of the various materials involved, as well as the inherent difficulties in reproducing the true boundary and thermal conditions of the real engineering problem under study, it can be said that the numerical model predicted quite reasonably the *in situ* measured temperature fields, and that the validation purposes of the monitoring campaign were successfully achieved.

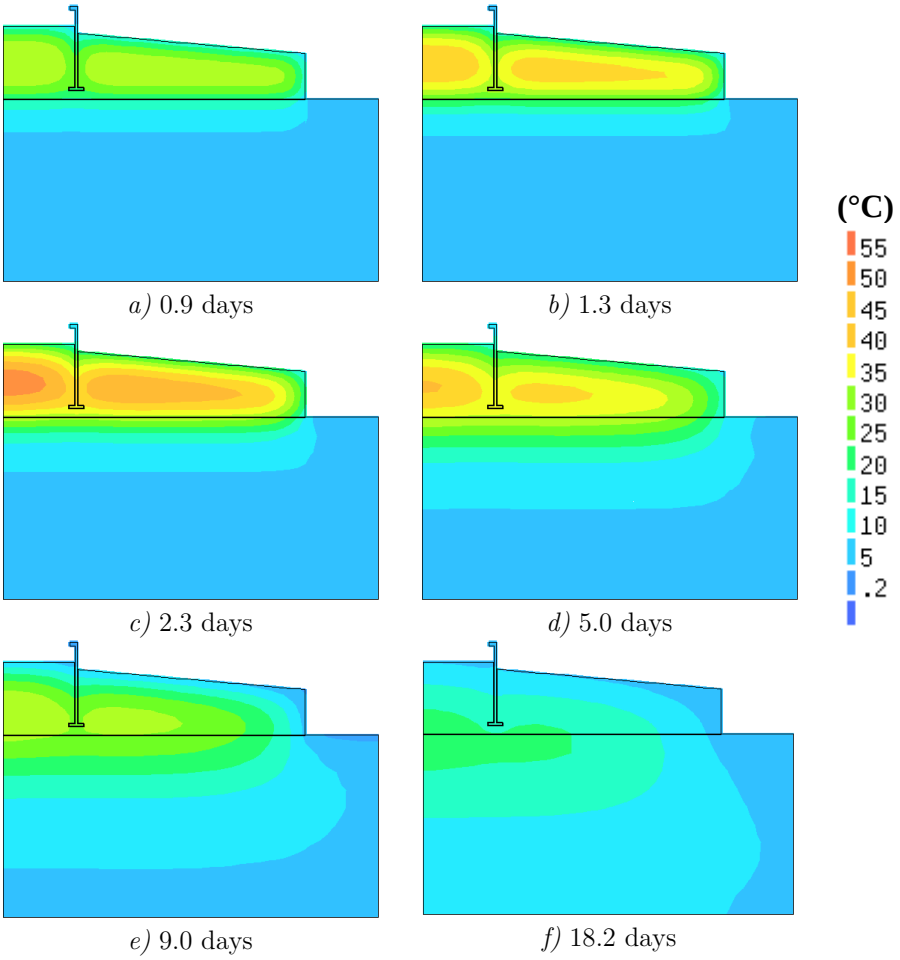

Figure 6.11: Evolution of calculated temperatures

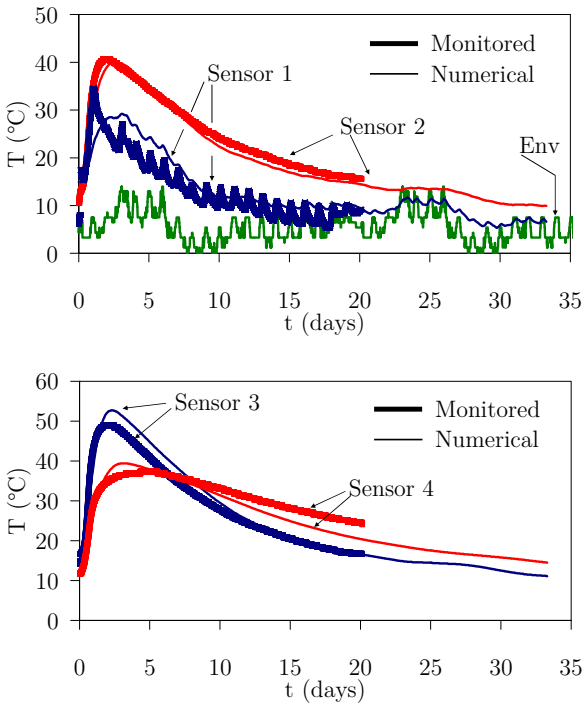

Figure 6.12: Comparison of the numerical and monitored temperatures on sensors

At this stage it is also pertinent to provide information about the distribution of degree of heat development obtained in this simulation. At the instant of maximum temperature – approximately at 56h -, the degree of heat development α_T field is depicted in Figure 6.13. It can be seen that the inner parts of the foundation (with a record of higher temperatures) exhibit a degree of heat development around 0.8, whereas some of the surface areas have α_T ~0.5. To further illustrate the differences in time evolution of degree of heat development on two distinct parts of the structure, the corresponding plots for sensor 1 and 3 (representing a surface and an interior part of the foundation, respectively) are depicted in Figure 6.14. It is clear that hydration reactions occur much faster in the surroundings of sensor 3 (hotter region). Nevertheless, by the end of the simulation period it can be observed that the degree of heat development assumes very similar values in both regions under consideration.

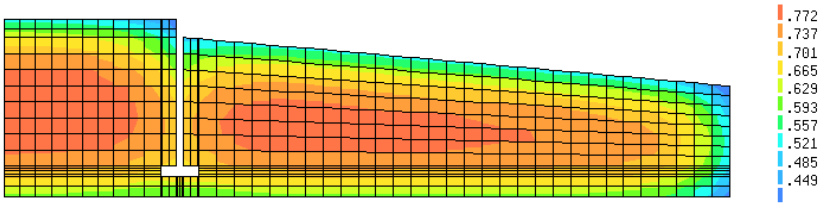

Figure 6.13: Degree of heat development field at t=56h

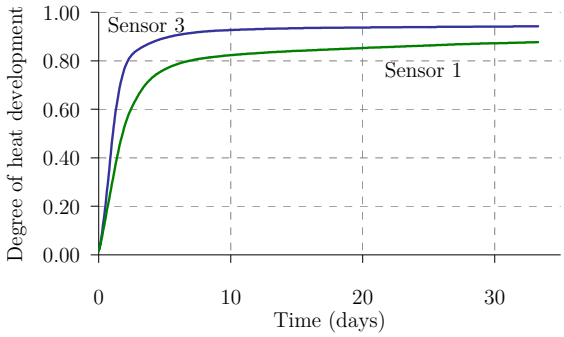

Figure 6.14: Evolution of degree of heat development in the areas of sensors 1 and 3

6.2.8 Calculated concrete normal stresses

The discussion of the numerical results from the mechanical model will be made by analyzing the normal stresses that develop through time along the following three directions of the axisymmetric FE mesh: OX (radial), OY (vertical) and OZ (circumferential) – axes defined in Figure 6.8b. It should be remarked that due to the geometry of the RC foundation, stresses σ_X and σ_Z are of utmost relevance, with greater values (both in tension and compression) than σ_Y. The evolution of stresses σ_X can be observed in Figure 6.15a: during the heating phase (between pouring and the age of 2.3 days), and due to the fact that the thermal volumetric expansion of the foundation core is significant larger than that of the surface areas, tensile stresses arise near the concrete surfaces, particularly in the upper ones, in direct contact with the air. After 2.3 days (onset of the cooling phase) this process is reversed: the volumetric contraction of the foundation core becomes larger than that of the surface areas (due to the higher

temperatures that occurred in the core); accordingly compressive stresses develop in the surface and tensile stresses occur in the core, with the latter reaching about 2 MPa at the age of 33.1 days. A detailed analysis of the stress sign inversions and their relations with the locally developed temperatures is possible through observation of Figure 6.16, which reproduces the calculated evolutions of the principal stresses and temperatures for sensors 1 (surface) and 3 (core). Another interesting point to discuss is the influence of the steel ring on the calculated stresses: the analysis of the spatial distribution of the tensile stresses σ_X (Figure 6.15a) leads to the conclusion that the local conditions for the concrete standing close to the steel ring are very similar to the ones that apply for the concrete close to the metallic formwork (boundary P2-P5 of Figure 6.8b), with no significant development of tensile stresses.

Interpretation of the developed normal stresses σ_Z can be made analogously to what was made for stresses σ_X, because the respective volumetric restraints to deformation are quite similar, particularly for the areas near the axis of symmetry. This resemblance is reflected in the very similar distributions of σ_X and σ_Z depicted in Figure 6.15, as well as on the almost coincident evolutions of the principal stress pairs (σ_1,σ_2) or (σ_2,σ_3) reproduced in Figure 6.16. Nevertheless, on the foundation zones farther from the axis of symmetry the volumetric restraints along direction Z are larger than those along direction X (see Figure 6.15), and so on the foundation periphery normal stresses σ_Z are greater than σ_X. However, even in the most unfavourable instant of analysis tensile stresses σ_Z do not reach 2 MPa.

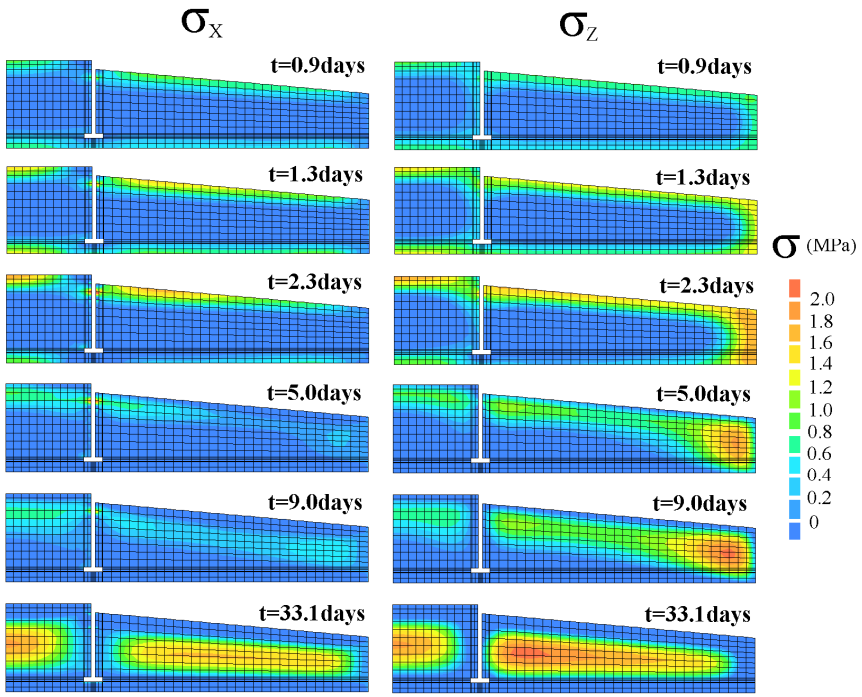

a) *b)*

Figure 6.15: Evolution of normal stresses: a) σ_x (radial); b) σ_z (circumferential)

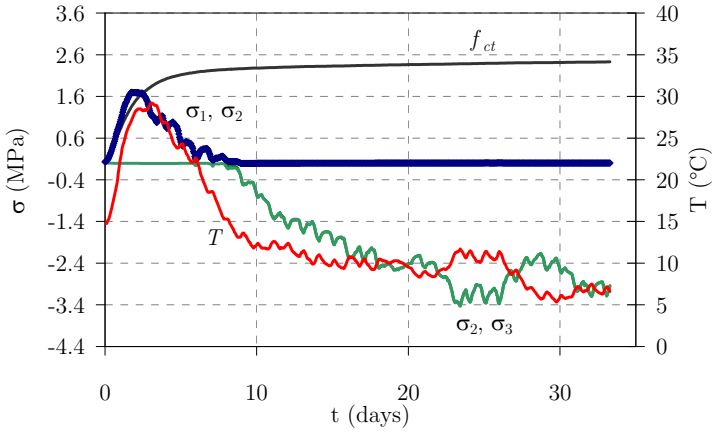

a) Sensor 1

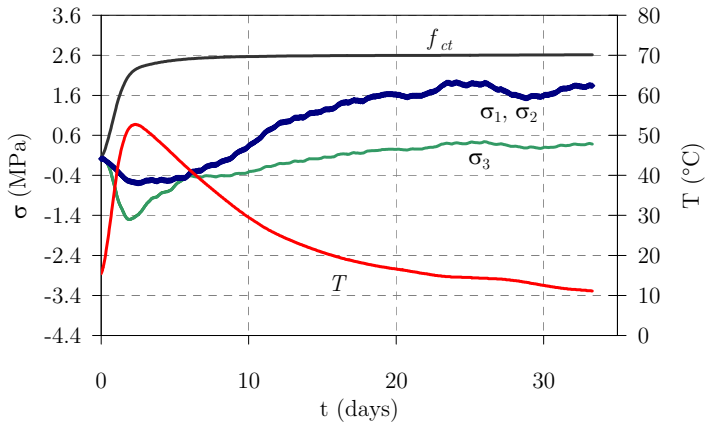

b) Sensor 3

Figure 6.16: Evolution of principal stresses and temperatures close to sensors 1 and 3

6.2.9 Cracking risk

In what concerns the evaluation of the concrete cracking risk in the foundation, attention is once more drawn to Figure 6.16, where the numerically estimated evolution (along hydration) of the concrete tensile strength f_{ct} is directly compared to the predicted principal stresses σ_1, σ_2 in the neighbourhood of sensors 1 and 3. Near the top surface (sensor 1) the tensile principal stresses σ_1 and σ_2 that develop during the heating phase reach the estimated tensile strength, thus pointing to a significant cracking risk at this location; nevertheless, after the ages of 7-8 days the stress state is already of compression (all the three principal stresses become negative), which greatly minimizes that problem, closing the cracks that might have opened before. On the other hand, in the foundation core (sensor 3) the calculated tensile principal stresses are always lower than the estimated tensile strength f_{ct}, leading to the conclusion that the cracking risk at this location is significantly lower than that in the surface area. With these concerns it is worth remarking that a possible way of minimizing the near surface cracking risk would be to diminish the temperature gradients on top of the RC foundation, namely by recovering this concrete surface with temporary thermal insulations (e.g., polystyrene plates). In the concrete areas near the steel ring (the very first motivation of the present study) no significant cracking risk is detected, which points to the conclusion that no

relevant problems concerned with the anchorage zone of the wind tower mast should be feared, as far as the early age thermal behaviour of concrete is concerned.

6.2.10 3D thermal analysis

The 3D analysis had the main purpose of confirming the plausibility of the initially adopted simplification, that consisted in assuming an axisymmetric geometry for the foundation. Because of the complex and time consuming character of the 3D analysis, only the thermal model is calculated with the purpose of comparing its results to the axisymmetric model.
According to the double symmetry of the problem, only one fourth of the foundation and corresponding portion of underlying granite massif was explicitly reproduced in the numerical model. Essentially, the material and boundary conditions coincide with those mentioned in the axisymmetric analysis. A less refined mesh was adopted for the 3D model (see Figure 6.17) than the one that had been used for the 2D model. The used brick FE have 8 nodes and 2×2×2 integration points. Surface elements with 4 nodes and a 2×2 integration scheme were adopted for simulation of the convection/radiation boundaries.

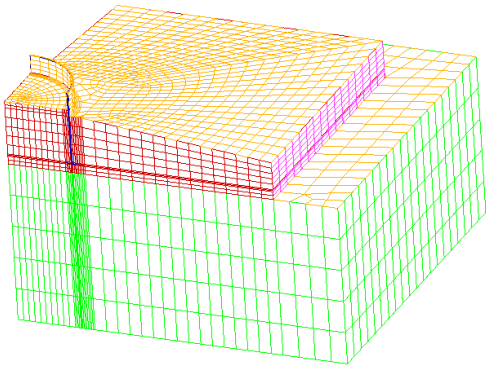

Figure 6.17: 3D model – finite element mesh

The calculated temperature field at the age of 56h is depicted in Figure 6.18. The comparison of computed temperatures by the 2D and 3D analyses for the areas corresponding to the temperature sensors 1 to 4 used in the monitoring campaign can be seen in Figure 6.19: it is noticeable that the predicted temperature evolution with the two modelling approaches is quite similar.

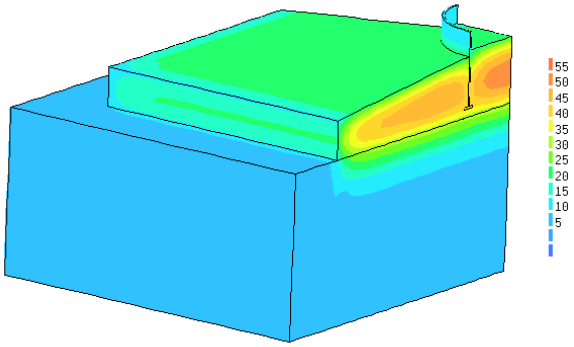

Figure 6.18: 3D temperature field at the age of 56h

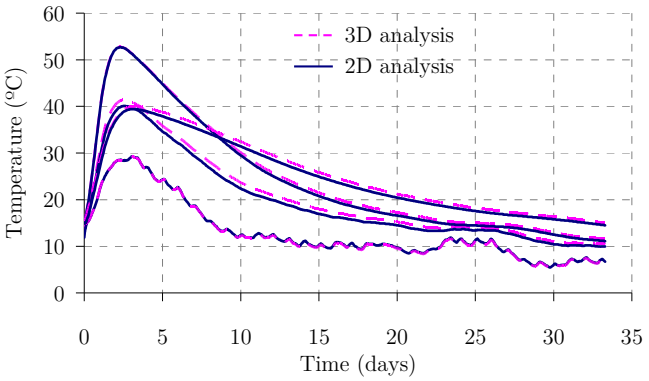

Figure 6.19: Calculated temperatures in the sensor regions: 2D and 3D analyses

In order to allow an evaluation of the relevance of calculated temperature differences in the farthest areas (in plan) from the geometrical centre of the foundation, Figure 6.20 depicts the computed temperatures at 56h by both modelling approaches for cross-sections 1-1 and 2-2: the 2D and 3D models. It can be observed that the temperature fields computed by using the two approaches (along section 2-2 in which the geometry of both models are the same) are very similar, both in the centre and on the foundation edges. Still regarding the same figure, and in concern to section 1-1 and section 2-2 of the 3D analysis, it is evident that there is a clear geometry difference (the length of the foundation along section 1-1 is 1.4 times longer than along section 2-2). Nonetheless, this does not seem to induce significant differences in the maximum reached temperatures, nor in their distribution along the foundation. It may just be stated that there is a slightly lower temperature gradient in the right edge of the foundation for the case of section 1-1, when compared to section 2-2. This difference is not considered relevant for the resulting stress field, particularly if it is beard in mind that the purpose of the conducted analyses was to check cracking risk in concrete surrounding the steel ring, which is clearly far away from the rightmost edge of the model of the foundation.

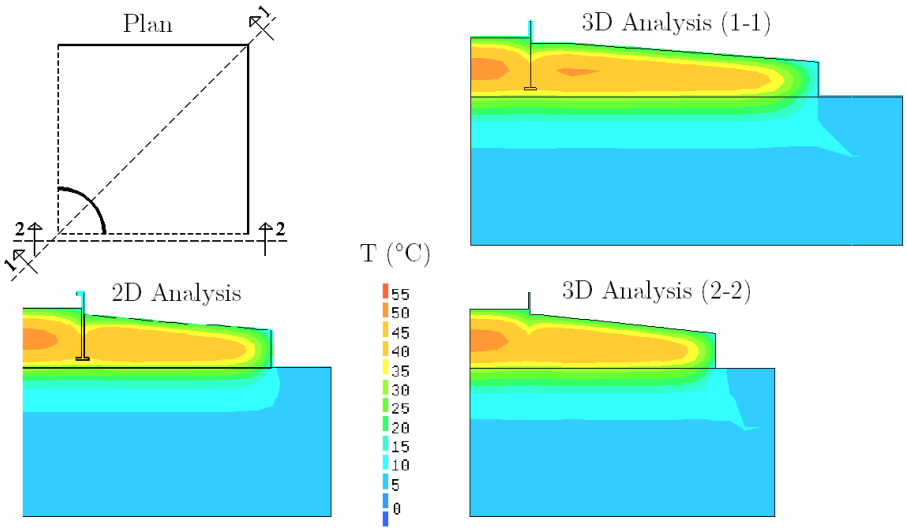

Figure 6.20: Calculated temperatures at 56h for cross-sections 1-1 and 2-2; 2D and 3D analyses

From the analysis of the results of the 2D and 3D models it is therefore concluded that for the purpose of predicting the temperature fields during early ages in the areas neighbouring the steel ring, it is plausible to accept the axisymmetry simplification adopted in the 2D analysis.

6.3 Gravity dam

6.3.1 Introduction

The present section intends to document the experimental campaign and numerical simulation conducted in regard to the structural behaviour a concrete dam built in the north of Portugal. Issues related to the construction phasing and the thermal stresses developed at early ages are to be discussed. This Section comprises the description of the experimental in-situ and laboratorial campaign, as well as the detailed portrayal of the numerical simulations conducted and the comparison with the experimental results.

6.3.2 Motivation

For the construction of concrete dams a construction phasing is usually adopted, which consists of casting parts of the dam in an alternate fashion so that: (*i*) the concrete volumes are compatible with the capacity of the ready-mix concrete central; (*ii*) the volumes involved are small enough to prevent the development of high temperatures within the dam due to cement heat of hydration, and therefore to avoid early thermal stresses that could result in detrimental cracking of concrete. The capability of predicting thermal fields due to the heat of hydration in concrete dams, taking into account the construction sequence, the energy balances with the environment (convection, radiation, solar radiation, conduction of heat to the foundation, among others), and the consequent stress development in concrete, is a valuable asset when, at the design stage, it comes to decide on the phasing of construction. In fact, minimizing the number of phases of construction allows strong scheduling benefits, with consequent financial profits to both the contractor and the owner. Another strong motivation for this study is its temporal coincidence with the beginning of the design phase of several dams in Portugal, such as: Gouvães, Padroselos, Alto Tâmega, Daivões, Pinhosão, Girabolhos, Fridão, Alvito and Almourol, among others.
The dam under study in this section has added interest because of the relatively large volume occupied by internal galleries, which creates discontinuities that may be responsible for increased cracking risk. The numerical modelling reported here explicitly accounts for these galleries, unlike previous studies reported for dams.

6.3.3 Description of the dam and the studied block

6.3.3.1 Location

The studied dam is located near Pretarouca (north of Portugal) in river Balsemão. It is a concrete gravity dam with a maximum height of 28.5m above the foundation. In full

service the reservoir should flood an area of 43.4ha, having a retained water volume of 3 219 000m^3.

6.3.3.2 Geometrical aspects

The dam is divided in 20 blocks transversally to the river, each one of them cast in layers of about 1.2m height. The plan and elevation views of the dam are depicted in Figure 6.21, where the numbering of the separate blocks can be found. The flood spillway is materialized in the two central blocks, with numbers 9 and 10, with recourse to a stepped downstream surface for energy dissipation. A photo of the dam in an advanced phase of construction is shown in Figure 6.22, where the steps associated to the flood spillway can be clearly identified.

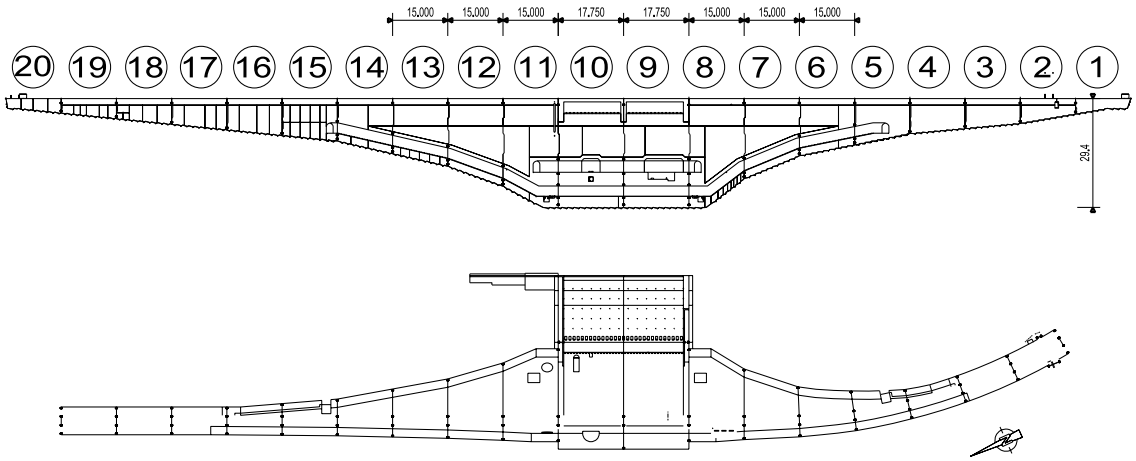

Figure 6.21: Plan view and elevation of the dam

Figure 6.22: Photo of the dam (April 2008)

The subject of this study is block number 9, one of the central ones, having therefore large pours of concrete. The cross section of the dam through this block and its elevation are presented in Figure 6.23 where the construction phases are also numbered from 1 to 24. The presence of several galleries is clear, a complicating feature for the analysis, but also relevant for evaluating influences of these discontinuities on the thermal behaviour of

the structure, since previous studies (De Araujo *et al.* 1998, Fairbairn *et al.* 2004, ICOLD 2004, Leitao *et al.* 2007, Malkawi *et al.* 2003, Noorzaei *et al.* 2006) have clearly focused on areas of dams undisturbed by galleries (or at least have ignored their effect).

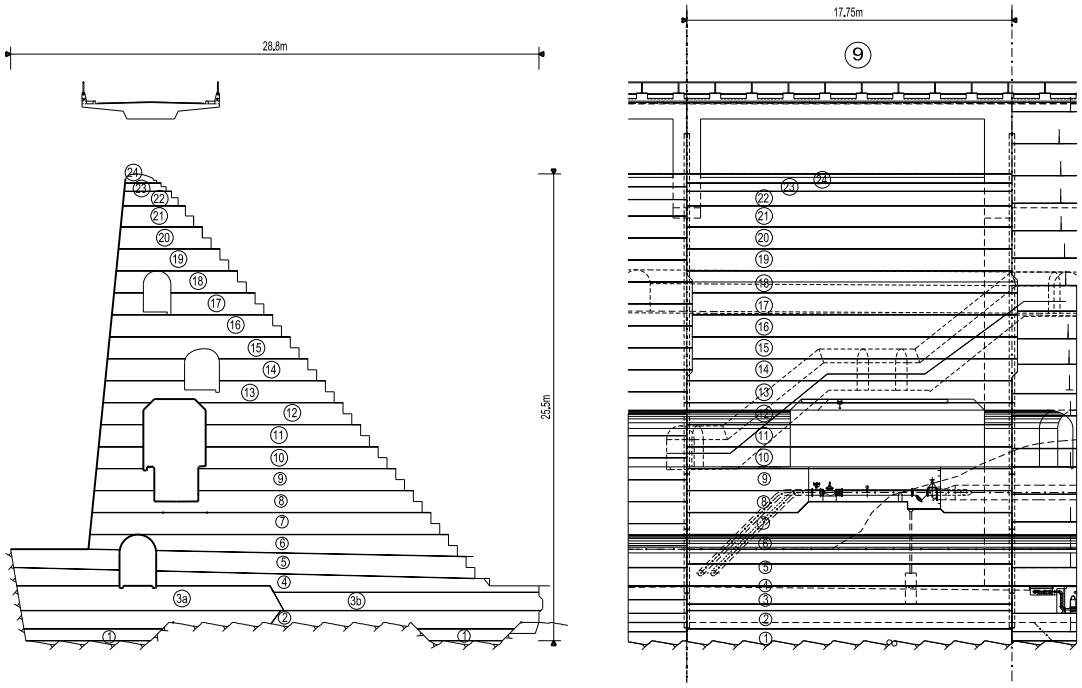

Figure 6.23: Cross-section and elevation of the dam in block 9

The time lapse of each construction phase for block 9 is represented in Table 6.1. It should be stressed that the times represented for each phase correspond to the end of its casting operations.

Table 6.1: Construction phasing of block 9

Phase number	Time	Days from beginning	Phase number	Time	Days from beginning
1	20-11-2007 18:22	0	13	27-02-2008 17:15	99
2	26-11-2007 18:30	6	14	05-03-2008 19:30	106
3	29-11-2007 18:30	9	15	11-03-2008 16:45	112
4	06-12-2007 20:41	16	16	17-03-2008 19:10	118
5	26-12-2007 14:00	36	17	25-03-2008 17:20	126
6	07-01-2008 22:37	48	18	31-03-2008 19:40	132
7	15-01-2008 19:45	56	19	03-04-2008 18:20	135
8	23-01-2008 21:18	64	20	15-04-2008 18:20	147
9	30-01-2008 19:41	71	21	20-04-2008 18:20	152
10	06-02-2008 20:15	78	22	25-04-2008 18:20	157
11	13-02-2008 16:45	85	23	30-04-2008 18:20	162
12	21-02-2008 15:15	93	24	05-05-2008 18:20	167

6.3.3.3 Concrete and reinforcement

The concrete adopted for the greatest part of the dam is referenced as D200.S1.D40, with the mixture proportions shown in Table 6.2. River sand was used (of siliceous nature) and the gravel was mostly granite. In the downstream face associated to the dam spillway a 1.6m thick layer of concrete C16/20 was used for improved mechanical characteristics (composition in Table 6.2). Geometrical distribution of both concrete types is shown in Figure 6.24. Before the initiation of casting operations of a new phase, a 1cm thick layer of a rich mortar was placed in the interface to improve the connection of the concretes with different ages. Even though it is an unreinforced concrete gravity dam, in the parts of concrete near singularities such as galleries and steps, S500 reinforcement was used.

Table 6.2: Mixture proportions for the concretes used in the dam

	Dosage (kgm^{-3})	
	D200.S1.D40	**C16/20**
Sand 0/4	730	770
Gravel 4/12	340	460
Gravel 12/20	240	685
Gravel 14/40	695	-
CEM II/A-L 42.5R	140	185
Fly Ash	60	75
Plasticizer	2.4	2.3
Water	70	112.9

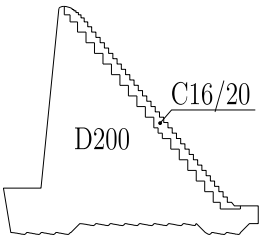

Figure 6.24: Areas with different concrete types in block 9

6.3.3.4 Foundation

According to the geotechnical report elaborated for this dam, the substrate to the dam is a relatively homogeneous granite massif until at least 40m depth. The massif has a relatively low level of alteration (W2-1), and the overall mechanical properties considered in the design of the dam are summarized in Table 6.3.

Table 6.3: Material properties of the granite massif

Parameter	**Value**
Volumic weight (kNm^{-3})	26
Geological Strength Índex (GSI)	55
Deformability modulus (MPa)	8000
Cohesion (kPa)	390
Friction angle (°)	60

6.3.4 Monitoring campaign

6.3.4.1 General remarks

As the purpose of this study was to check the capacity of the numerical framework to successfully simulate temperatures and stresses that occur in the dam, one preliminay fundamental issue was obtaining measurements of temperatures and strains, in order to allow comparisons.

Even though this is a relatively small dam, there were many possible places in which monitoring could be focused. However, the greatest interest would be the bodies of the dam with higher concrete volumes, namely blocks 9 and 10. Another important point should be stressed out at this stage: this monitoring campaign was not initiated at the beginning of construction. In fact, knowledge about this dam's construction only came about by mid January 2008, instant at which blocks 9 and 10 had already begun construction, and were around their 9^{th} and 11^{th} phases respectively. At these stages, the dam was already narrowing and affected by the existence of several internal galleries. Anyway, it was decided to monitor temperatures and strains in block 9 (less advanced construction), with the initiation of the monitoring campaign occurring at phase 12.

It is known that accuracy of temperatures (and consequently stress) calculations of a given construction phase are strongly influenced by knowledge of the temperatures on the previous stage. Therefore, the monitoring campaign involved two stages:

1. A first one in which several temperatures were monitored in phase 12 of block 9;
2. A second stage in which temperatures and deformations were monitored in phase 13, while several instrumentation points of phase 12 were maintained active.

Monitoring of temperatures and deformations was continued for 3 months after the beginning of the monitoring campaign, so that the effect of heat of hydration dissipation (which is a rather slow process in these massive structures) could be captured.

6.3.4.2 First monitoring stage – phase 12

Phase 12 corresponds to a 1.2m tall slice of the dam between levels 905.8m and 907.0m. In this stage of monitoring, only temperatures were measured since casting. Two sets of temperature sensors were used: 12 k-type thermocouples (labelled T1 to T12) and 5 PT100 sensors (labelled P1 to P5). Placement of these sensors is discussed with basis on both the plan of the dam (at level 905.8m) – see Figure 6.25 - and the elevation of the concerned concreting phase – see Figure 6.26. In order to monitor temperature development in the predictably hotter regions, and bearing in mind that at this level the dam is separated in two bodies due to the existence of the gallery (a downstream body and an upstream body – see Figure 6.26), the centre of the downstream body was selected for monitoring. Because there was no reinforcement in this area, there was the necessity of creating support devices for the temperature sensors. As monitoring temperatures and strains in phase 13 would also require the need for support elements in this area, a system of three 75mm diameter vertical PVC tubes 2.4m tall were anchored to the concrete at phase 11, according to the arrangement that can be observed in Figure 6.25 (tubes 1, 2 and 3). A photo of these tubes some days after phase 11 was cast, and before casting

operations of phase 12, is shown in Figure 6.27. After this stage, the tubes were filled with mortar to increase their stiffness, and braced to each other.

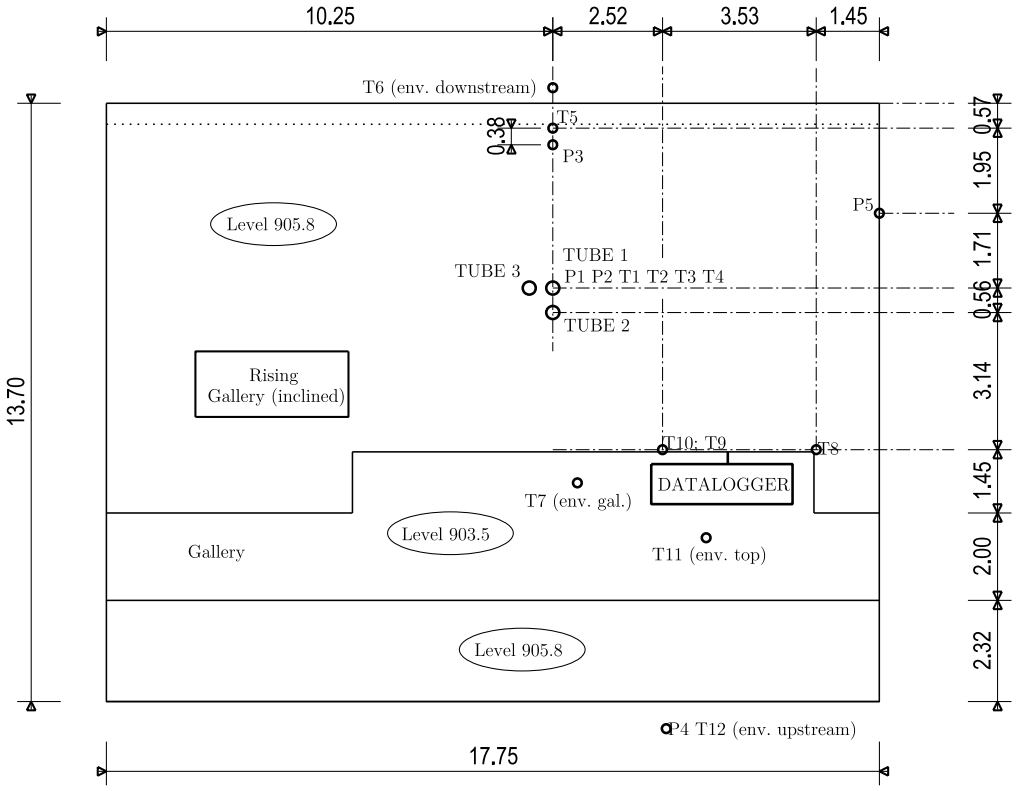

Figure 6.25: Plan at level 905.8m (base of phase 12) – location of temperature sensors

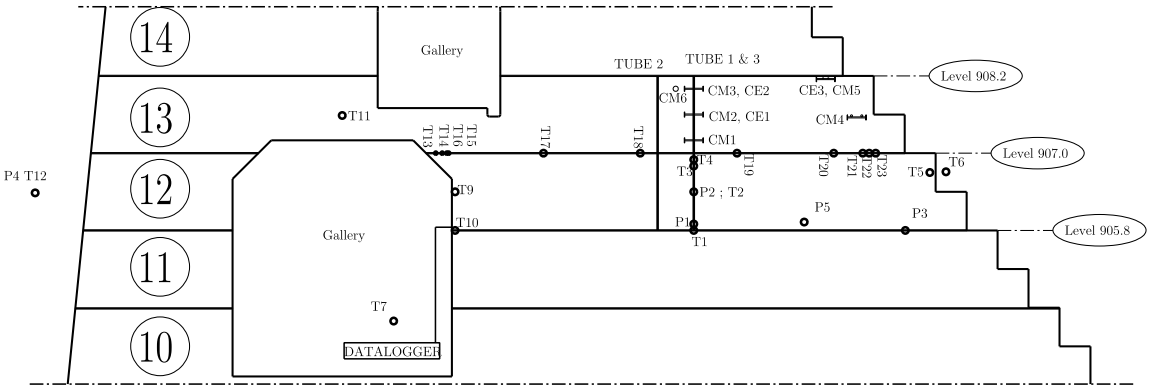

Figure 6.26: Elevation of phases 12 and 13 – location of temperature and strain sensors

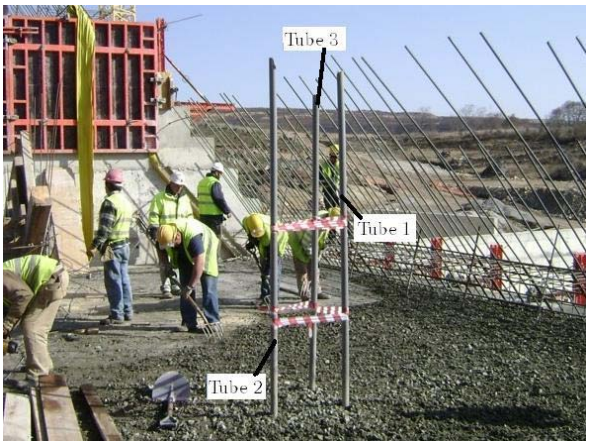

Figure 6.27: PVC tubes partially embedded in phase 11

Temperature sensors were placed along the height of tube 1 according to the sketch and photo presented in Figure 6.28. A vertical temperature profile was intended, and therefore sensors were distributed vertically with smaller spacing near the boundaries. At mid-height two sensors were placed together, P2 (PT100) and T2 (thermocouple), to check coherence and performance of their measurements.

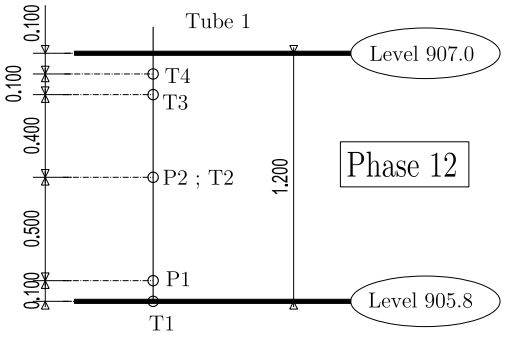

a)

b)

Figure 6.28: Placement of temperature sensors along tube 1 (phase 12): a) scheme; b) photo

Temperatures next to the gallery were monitored using sensors T9 and T10. These sensors were attached to the surface reinforcement (at about 5cm from the formwork): sensor T9 was placed at a height of 0.6m relatively to the basis of phase 12, while sensor T10 was put in contact with the base concrete (see Figure 6.26 and Figure 6.29a).
In order to measure the temperature near the downstream boundary, sensor T5 was placed on the interior part of the reinforcement mesh (at about 9cm from the adjacent vertical surface), in accordance to Figure 6.25 and the photo in Figure 6.29b. On the outer side of the downstream formwork, environmental temperature was measured using a thermocouple T6. Environmental temperature was also measured inside the gallery (sensor T7), outside the upstream formwork (sensors P4 and T12), and above the final level of phase 12 (sensor T11).

a) b)

Figure 6.29: Placement of sensors: a) T10 (bottom) and T9 (top); b) T5

Measurement of concrete temperatures also included sensor P3 in the basis of phase 12, at a horizontal distance of 0.38cm from sensor P5 (see Figure 6.25 and Figure 6.26).
Since the instant of casting of phase 12 until the date of casting of phase 13, all the temperature sensors just described were connected to a datalogger, which stored the data every 10 minutes. The datalogger was placed inside the gallery, according to the pictures of Figure 6.25 and Figure 6.26, being protected by a rigid impermeable box (Figure 6.30).

Figure 6.30: Datalogger system installed in the gallery

6.3.4.3 Second monitoring stage – phase 13

Phase 13 corresponds to a 1.2m tall slice of the dam between levels 907.0m and 908.2m. It is noteworthy to mention that in this phase a new geometrical issue appears due to the passage of a new gallery that rose from the left-hand part of phase 12 (see Figure 6.25). This gallery also represents an opening on the basis of phase 13 (where it is still rising) and eventually becomes horizontal (with is base level 0.7m above the base level of phase 13), making a slight right turn, as can be confirmed from the observation of Figures 6.25, 6.26 and 6.31.
In this casting phase, both temperatures and strains were measured in concrete. In what regards to temperature sensors, a set of thermocouples T13 to T23, supported by a cable and placed at level 907.0m (basis of phase 13), were prepared at the laboratory with predefined distances (except for the sensors near the extremity of the cable) – see location

in Figures 6.26, 6.31 and 6.32. The basic intention was to provide a temperature profile in the downstream/upstream direction. However, due to difficulties in the connection of the cable to the reinforcement, as well as difficulties in tensioning the cable (which ended up being somehow loose), some uncertainty remains in what regards to the position of sensors T13 to T23 in the extremities.

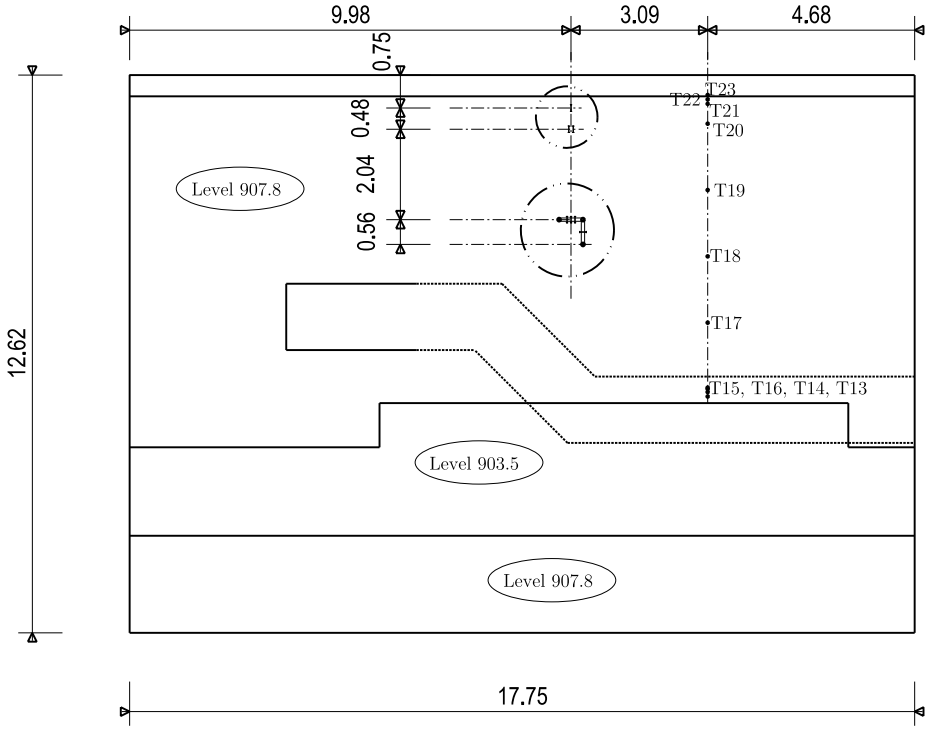

Figure 6.31: Plan at level 907.0m (base of phase 13) – location of temperature and strain sensors (units: m)

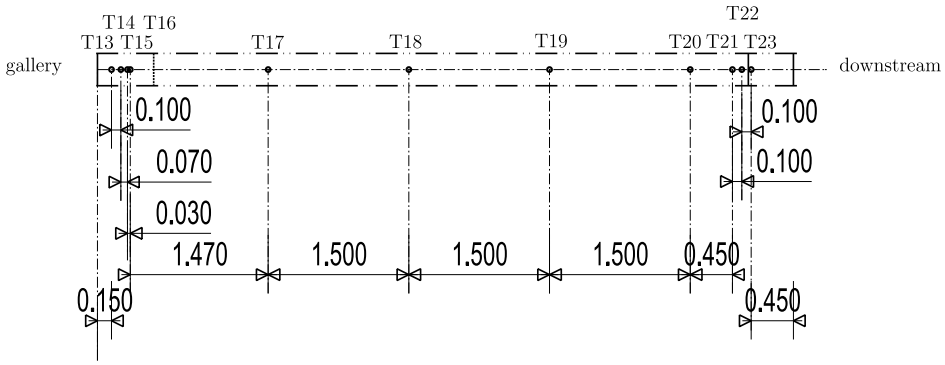

Figure 6.32: Detail of sensor location T13 to T23 (plan view) - (units: m)

In what concerns to strain measurements, vibrating wire gages were used with a reference length of 14cm between anchoring heads. Two types of vibrating wire strain gages were used: one with a metallic casing, and another with a plastic casing, in view of confirming the findings reported in Section 5.5 of this thesis. Due to limitations of budget and number of measuring channels available in the datalogger, only 6 metallic gages (named CM1 to CM6) and 3 plastic ones (named CE1 to CE3) were used in this monitoring

campaign. Their positioning within the dam corresponded to two main zones: one in the centre of the volume under study, and another near the downstream face. Regarding the centre of volume, the same three tubes used in phase 12 were used to hold the strain gages: horizontal steel bars between tubes were placed in order to support each strain gage in two points, as reproduced in Figure 6.33a. The schematic position of these sensors is depicted in Figure 6.34, and the photo of the sensors at their final positions is shown in Figure 6.33b. The aim of positioning most sensors in the same direction was to obtain a vertical strain profile in the downstream/upstream direction, which is the direction in which the thermal gradients will be steeper. For control purposes, one of the strain gages (CM6) was placed in an orthogonal orientation.

a) b)

Figure 6.33: a) Fixation of the strain gages; b) photo of sensors positioned in the tubes

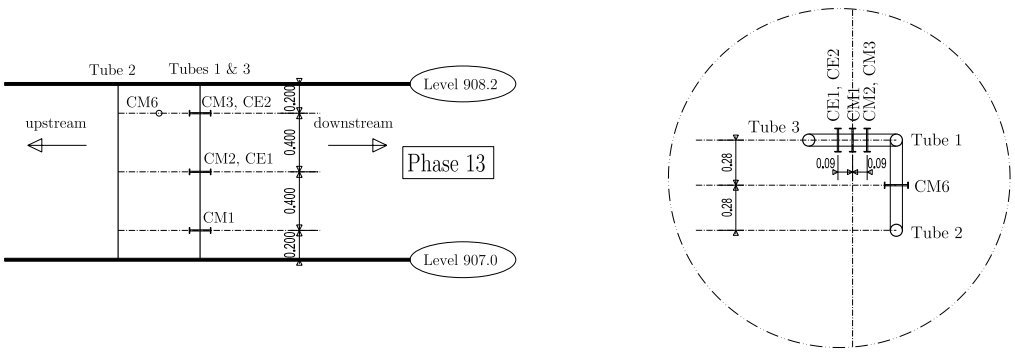

a) b)

Figure 6.34: Schematic representation of strain gages positioning in the tubes: a) elevation; b) plan (units: m)

Three strain gages were positioned near the downstream surface, according to the arrangement depicted in Figure 6.35 and the photo in Figure 6.36. The positioning of these sensors was essentially related with the purpose of knowing the strain development in a cooler region (due to higher proximity of the downstream boundary) than the central region already monitored around the tubes.

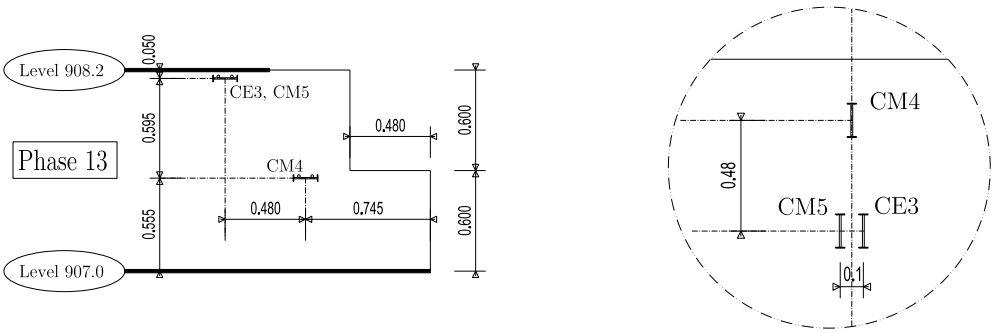

a) b)

Figure 6.35: Schematic representation of strain gages near the downstream surface: a) elevation; b) plan (units: m)

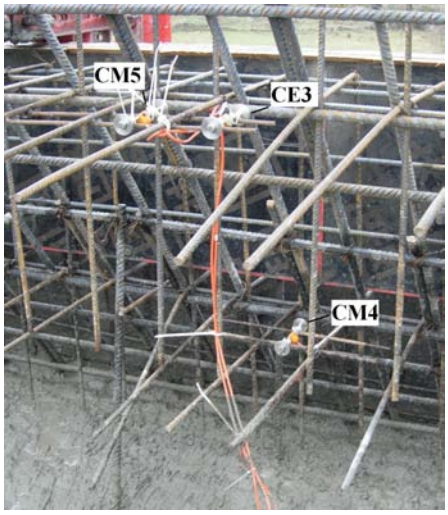

Figure 6.36: Photo of sensors positioned near the downstream surface

In what regards to data logging, ideally all the measurements from phase 12 should have been carried on during phase 13. However, this was not possible due to limitations in the number of simultaneous acquisition channels in the data logger. Therefore, some of the sensors of phase 12 were disconnected, and some of the temperature sensors that were placed in the cable on phase 13 were also not connected (due to their great proximity, and the relevance of keeping some of the sensors of phase 12 functioning). Bearing in mind what has just been stated, the sensors that were active from the beginning of phase 13 were the ones listed in Table 6.4.

Table 6.4: List of active sensors after casting of phase 13

Phase 12	T1, T2, T3, T4, T5, T6, T7, P1, P2, P3, P4, P5
Phase 13	T11, T12, T13, T14, T15, T17, T18, T19, T21, T22, T23 CM1, CM2, CM3, CM4, CM5, CM6, CE1, CE2, CE3

Each vibrating wire gage allowed the simultaneous recording of local strain and local temperature. Thus, when referring to strain measurement the name indicated for the gage is used; when referring to temperature a suffix "T" is added to the sensors reference.
At this point, and before actually analyzing the results provided by this monitoring campaign, it is noteworthy to mention the need for special care during casting operations around the sensors, especially for the case of the vibrating wire strain gages. In fact, due to the low workability of the D200 concrete applied in the major part of the dam, there was the necessity of a heavy duty vibration device with 100mm diameter. Direct contact between such a device and a strain gage would probably result in damage. To protect these sensors from impacts during casting, usually metallic wire meshes (of prismatic shape, involving the sensor) are used to encapsulate them, and they are cast around with mortar. However, for this application, the process adopted was to place the strain gages in direct contact with concrete, and advising the contractor to have special attention and care during casting operations.

6.3.4.4 Data collected through the in-situ monitoring campaign

In this section, the data collected through the monitoring campaign (including the sensors placed in phases 12 and 13) is exhibited and discussed in view of coherence between different devices, as well as expectable behaviour. In all graphics that will be presented, there are vertical dashed lines labelled with black boxes containing numbers. These indicate the corresponding casting phase, at the instant of its conclusion.
A first look is taken at the temperature sensors placed on tube 1 and embedded in the concrete of Phase 12: the results are depicted in Figure 6.37. From observation of these results, the following comments can be made:

- After casting of Phase 12, and before casting of Phase 13, it is clear that the highest temperatures are attained in the sensors farthest from the top surface of the dam. Sensors T3 and T4 (near the surface) have registered quite similar temperature developments, with peaks around 24°C. These two sensors exhibit strong influences of the environmental temperature; in fact the several sinus-like waves of temperature corresponding to each day are recognizable in the outputs of T3 and T4. During the same period, sensors P1, P2 and T1 exhibited similar peak temperatures surrounding 30°C (higher than the 24°C registered near the surface).
- The tendency for dropping temperatures at the end of the period comprised between casting of Phase12 and casting of Phase13 is strongly reversed after casting of Phase 13. In fact, the heat of hydration of the concrete of Phase 13 has a clear influence on the temperature development of the concrete of Phase 12. As expectable, this influence is stronger on the sensors near the top surface of Phase 12 (T3 and T4) than for other sensors in that phase.
- Sensor T2, placed together with P2, exhibits an unexpected behaviour with strong variations. No plausible explanation could be found for this fact, except for some electrical problem in the wiring, of even some kind of physical damage occurred during casting, once P2 yields a much more plausible and regular output, which is also coherent and consistent with results obtained by neighbouring sensors. Thus, the results monitored by sensor T2 will be disregarded hereinafter.

- Sensor T1 exhibits slightly higher temperatures than those measured in P1 (with placement at a 10cm higher level). This is consistent with the heat supply from the concrete of Phase 11, which was still liberating heat when Phase 12 was cast; also, the first centimetre or so of each casting phase is composed of a rich mortar, which may be responsible for some additional heat generation. It is noteworthy to mention than sensor T1 was affected by some kind of disturbance (possibly of electrical nature), which resulted in sudden shifts of the measured signal, particularly at the middle of Phases 15-16 and 16-17, end of Phase 17-18 and beginning of Phases 20 and 23.

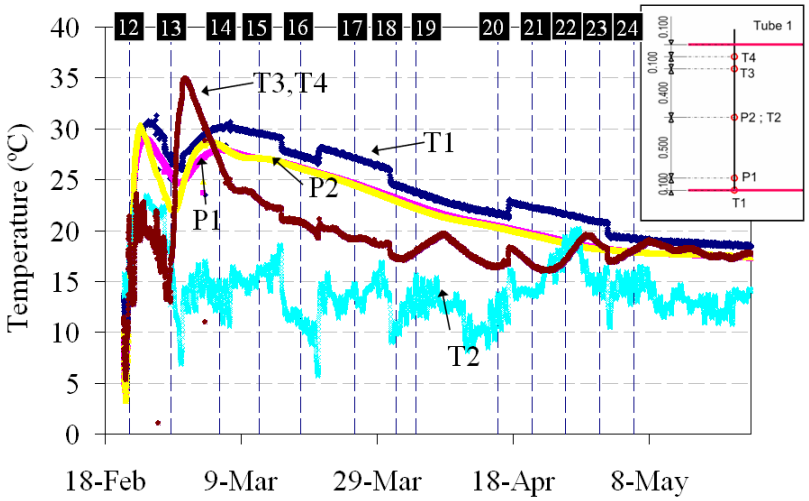

Figure 6.37: Temperature measurements along tube 1 (sensors located in Phase 12)

Regarding the sensors placed near the downstream steps (T5, T6 and P3), the monitored temperatures are depicted in Figure 6.38. The maximum temperature rise was measured in P3. However, in T5, the achieved temperature was quite similar. Once T5 is much nearer the environment, it is much more influenced by daily temperature variations than P3, and its temperature drop (after the peak) is much steeper than that of P3. Regarding T6, which measured environmental temperature in the downstream steps, it was observed to be strongly affected by both solar radiation (measuring temperatures reaching values near 40°C), and radiation losses during night (strong cooling), exhibiting thus high daily thermal amplitudes.

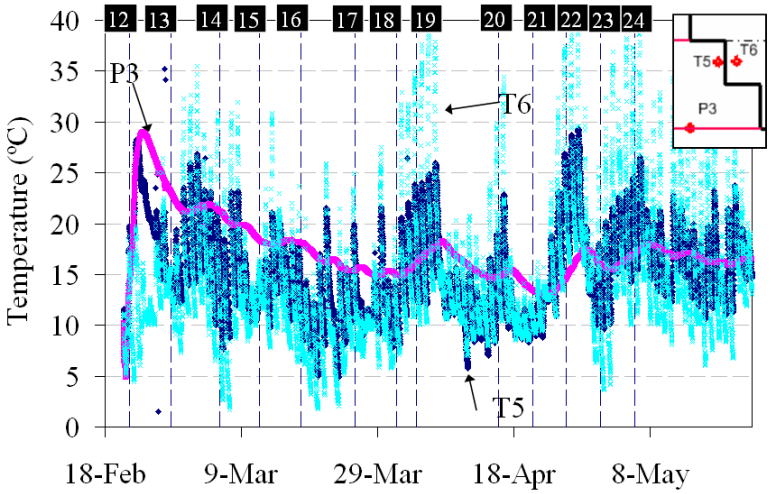

Figure 6.38: Temperature measurements near the downstream steps (Phase 12)

Sensors T9 and T10, placed adjacently to the gallery, yielded the temperature measurements depicted in Figure 6.39. As these plots regard to 7 days of measurement, the time at which concrete reaches each sensor can be individualized by focusing on the instant that the sensor ceases measuring environmental temperatures, and starts exhibiting typical hydrating concrete behaviour. This occurs sooner for T10 than for T9, once the former is placed at a lower level. Regarding the relative behaviour of these two sensors, T9 exhibits a slightly higher temperature peak than T10 due to its location being nearer the core of the phase. However, temperature losses after that are more significant in T9 than T10, probably due to the effect of thermal losses at the top horizontal boundary of the casting phase.

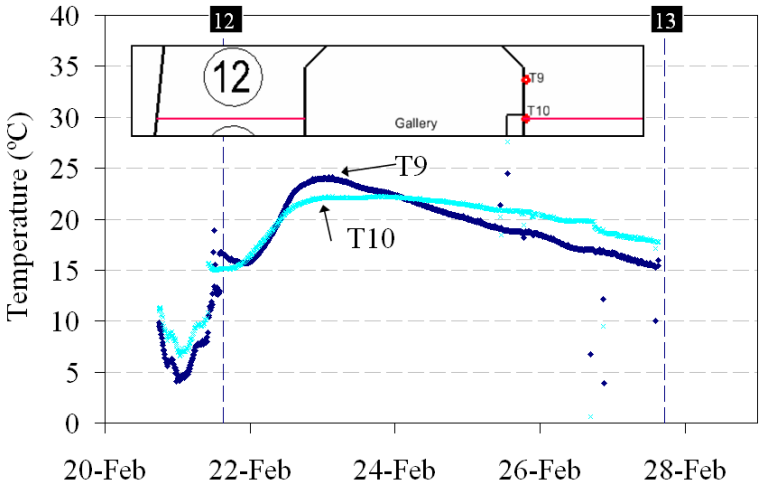

Figure 6.39: Temperature measurements near the gallery (Phase 12)

Sensor P5 was placed in the boundary between blocks 9 (the one under study) and 8, with the purpose of checking temperature evolution in such zone (see Figure 6.25), and therefore to have an idea about the heat losses between the hydrating construction Phase 12 of block 9 and the already built neighbouring block 8, which was still dissipating its heat of hydration. The temperature development for P5 can be seen in Figure 6.40. The temperature rise is not as high as that of P3 (which is actually nearer the downstream

boundary than P5), indicating that temperature losses occur for the previously cast concrete body. However, the heat losses longitudinal to the dam appear to be very small, as the subsequent temperature decay is not stronger than that observed for P3, indicating that most of the heat lost from the dam occurs in the downstream/upstream/top surfaces, rather than between longitudinally adjacent concrete blocks cast at different ages. In view of this, it is admissible to numerically model the temperatures developed in the dam by analyzing the cross-section and considering losses parallel to the longitudinal axis of the dam to be negligible.

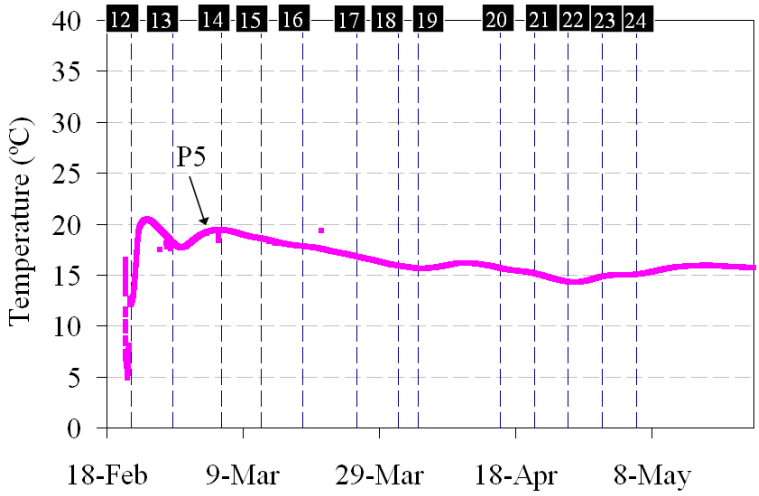

Figure 6.40: Temperature measurements near block 8 (Phase 12)

Environmental temperatures were measured at several points: downstream (T6), upstream (P4, T12), inside the gallery (T7) and above the horizontal surface corresponding to Phase 12 (T11). As mentioned before, sensors T11 and T12 were only active in the period between casting of Phases 12 and 13. The results pertaining to the sensors that were active during the whole monitoring period (P4, T6, T7) are shown in Figure 6.41, while a detail of the environmental temperatures measured during the first 10 days after casting of phase 12 is shown in Figure 6.42 for all environmental temperature sensors. Before analysing the temperatures in the various sensors, it is important to mention the orientation of the dam in terms of cardinal points. The perpendicular to the downstream surface is almost oriented E-SE (less than 2° deviation), therefore, such dam face is exposed to solar radiation for much longer periods than the upstream one. The gallery is not subject to solar radiation, nor subject to night radiation cooling. As a consequence, interpretation of the differences registered in sensors P4, T6 and T7 in Figure 6.41 becomes of quite accessible explanation:

- The highest daily peak temperatures are registered by T6, which is the one that is most exposed to solar radiation.
- Even though to a lesser extent than T6, sensor P4 also shows the effect of solar radiation, with higher heating than in T7 (inside the gallery).
- Sensor T7 has the smallest daily thermal amplitudes: not only the maximum temperature is lower than for sensors T6 and P4, but also the minimum temperature is higher than the ones recorded in those sensors. This difference in lowest temperature is explained by the night cooling radiation. It is worth mentioning that

the night cooling effect is much stronger in the upstream surface than the downstream surface. This may be explained by the fact that the concrete in the downstream surface is consistently hotter than the upstream one, thus, at night, sensor P4 endures lower temperatures associated to radiation cooling, given the lower starting temperature.

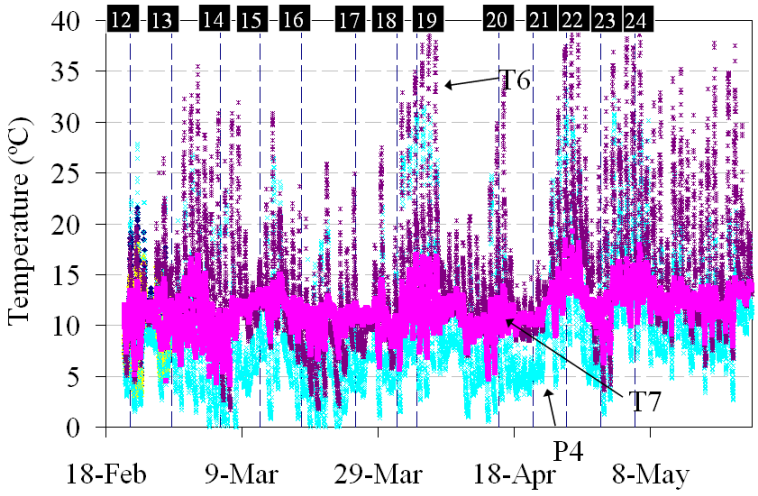

Figure 6.41: Environmental temperature measurements – P4, T6, T7

Regarding Figure 6.42, in which the environmental temperatures between 21st February 2008 and the 2nd March 2008 are plotted, the same conclusions as stated for the previous figure can be withdrawn. Nonetheless, measurements from two additional sensors are depicted: T11 and T12. Sensor T12 was placed together with P4 in the upstream surface, and consequently it has a very similar output to the latter. The slight differences between these two sensors may be explained by the fact that they use different measurement techniques, and they may have dissimilar radiation emisitvity and absorptivity, causing distinct behaviour under radiation. Sensor T11, which is placed over the horizontal concrete surface, has a similar behaviour to P4 and T6, with less heating during the day, probably related to the shadowing effect caused by adjacent concrete blocks (blocks 8 and 10 were already taller than block 9 at the time this monitoring campaign was carried out), or alternatively due to higher heat convection losses associated to wind.

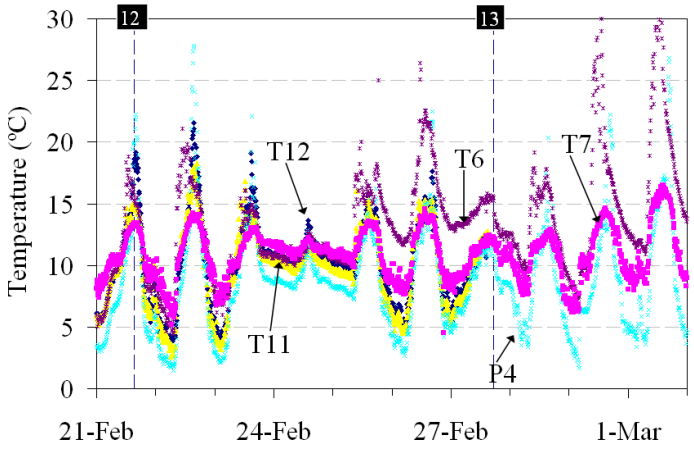

Figure 6.42: Environmental temperature measurements – from 21st February until 2nd March

The temperatures measured by the strain gages positioned in the central tubes of Phase 13 can be observed in Figure 6.43. Except for the case of CE2T, which seems to have malfunctioned, all the results seem rather coherent:

- Highest temperatures are attained in CM1T, which is the sensor farthest from the top boundary.
- Intermediate temperatures are registered by CM2T and CE1T, which are placed at the same height and exhibit rather coherent results with each other.
- The lowest temperatures are measured near the top boundary (CM3T and CM6T), in correspondence to the heat losses near the top surface. A good coherence occurs between these two sensors, which are placed in areas where the same temperature evolution would be expectable. Sensor CE2T, which should endure the same temperature as the two previous ones, clearly evidences a different behaviour, which seems to be an indication of the malfunction mentioned above.
- All sensors undergo a temperature rise right after casting, followed by a tendency to return to temperatures near the environmental ones. However, due to the casting of Phase 14, temperatures are slightly elevated, causing a second peak, after which a monotonic descending temperature branch occurs, with a slow descending tendency that is similar to all sensors.

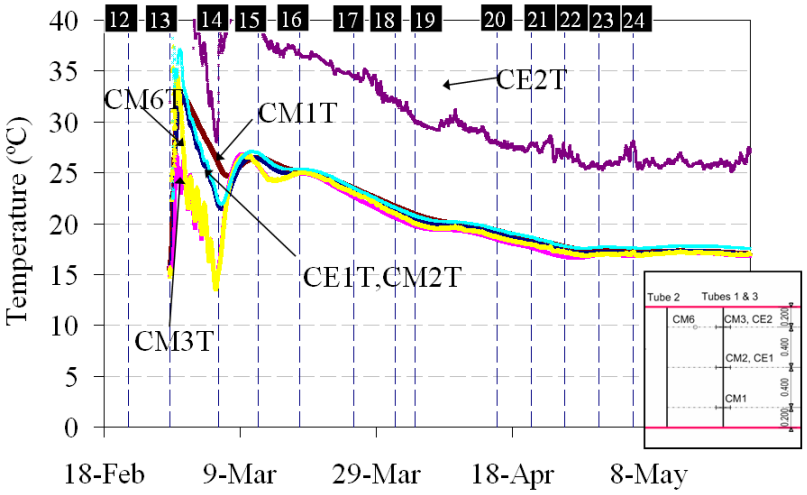

Figure 6.43: Temperature measurements in the strain gages supported by the tubes (Phase 13)

In regard to the registered temperatures of the strain gages positioned near the downstream surface, the corresponding temporal evolutions are shown in Figure 6.44. The following comments may be issued:

- Slightly higher temperatures occur in CM4T, due to its position nearer the vertical centre of this casting sequence.
- The outputs of CE3T and CM5T mutually validate each other, as these sensors relate to locations were the same temperature evolutions would be expectable.
- The effect of casting of Phase 14 is clearly stronger in the sensors near the top: CE3T, CM5T.
- All sensors in Figure 6.44 exhibit a much stronger influence of the daily temperature variation than the case of the sensors depicted in Figure 6.43. This is clearly related

to the vicinity of the downstream surface, which together with the upstream one (and the provisional top surface), end up being the parts of the dam where most heat is lost.

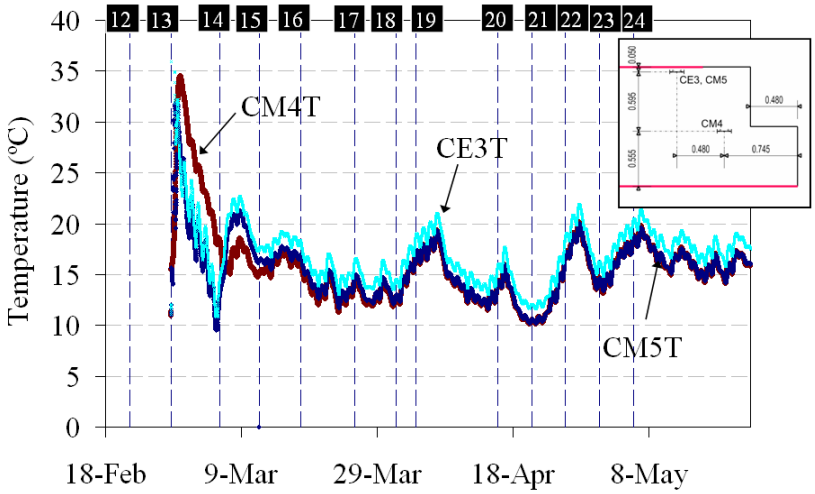

Figure 6.44: Temperature measurements in the strain gages near the downstream surface (Phase 13)

One interesting situation to point out is the comparison of results from sensors T4 (top of Phase 12) and CM1 (bottom of Phase 13), both placed on tube 1. Their proximity would point to a potential strong similarity in their recorded temperatures, which came to be confirmed, as shown in Figure 6.45.

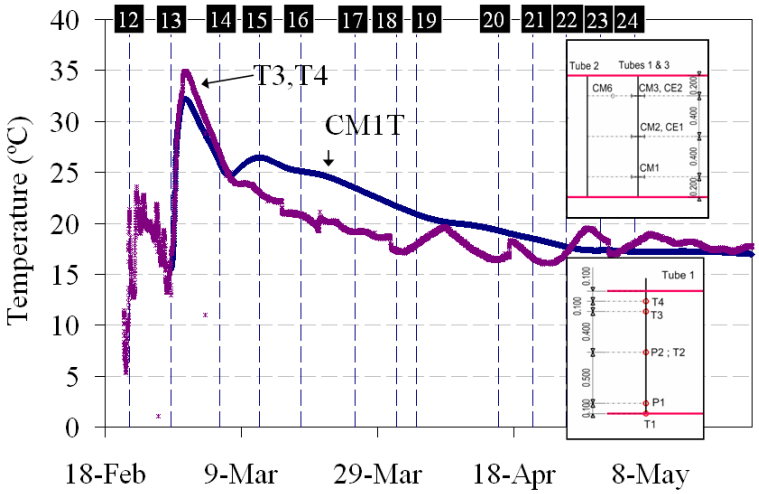

Figure 6.45: Comparison of measured temperatures along tube in T3, T4 (top of Phase 12) and CM1 (bottom of Phase 13)

The obtained results in terms of measured strains for some of the gages concerned in this monitoring campaign (CM3, CM6 and CE2), together with the corresponding measured temperatures, are plotted in Figure 6.46. There is a clear relationship between the measured strains and temperatures, confirming that temperature is the main driving potential for strain generation in the dam at early ages. Specific comments about relative behaviour of the measured strains, as well as the measurements recorded for other strain gages, are to be issued upon comparison with computed strains.

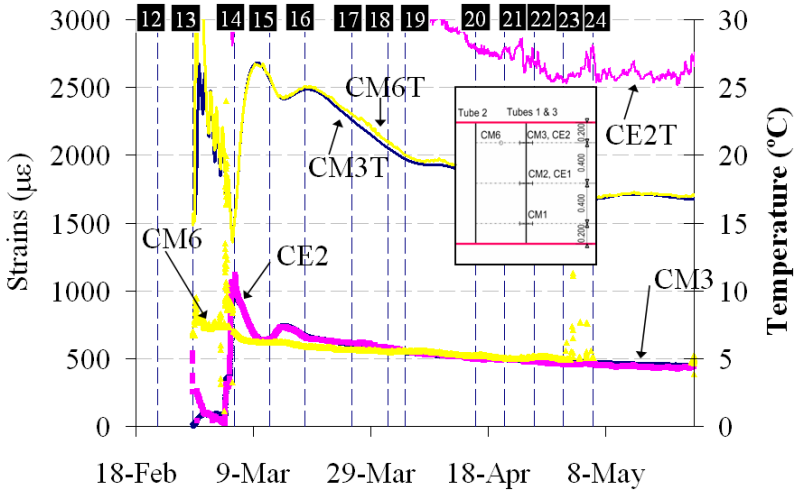

Figure 6.46: Measured strains and temperatures for CM3, CM6 and CE2

6.3.5 Laboratorial characterization of concrete

In 27th May 2008, date of onset of Phase 13, several specimens were cast for mechanical characterization of concrete, as far as creep behaviour, compressive and tensile strengths and drying shrinkage are concerned. Also, samples of the cement, fly ash and plasticizer used in the concretes of the dam were brought to laboratory, in order to perform an isothermal calorimetric characterization of the cement pastes corresponding to the concretes. All specimens were cast with D200 concrete, and covered with plastic foils to assure moist curing. They were kept inside an improvised hut for a period of 1.5 days (subject to outdoors temperature), time after which they were transported to the laboratory at FEUP/LABEST (~150km distance).

Creep behaviour

Four concrete 15×15×60cm^3 prismatic specimens monitored with strain gages for creep testing were cast according to the steel moulds represented in Figure 6.47a. Once arrived to the laboratory, the specimens were demoulded and kept in a climatic chamber at T=20°C and RH=100% until the age of testing. Testing occurred in creep rigs inside a climatic chamber at T=20°C and RH=50%. During testing the specimens were sealed with a plastic foil, in order to assess basic creep. The ages of testing were 1.8 days, 4.75 days, 7 days and 28 days. Forces applied for creep testing were selected to be around one third of the average compressive strength of the concrete (tested in cubes) at the same age. The results in terms of specific creep are depicted in Figure 6.47b (creep at 1.8 days not displayed, because of problems in load application).

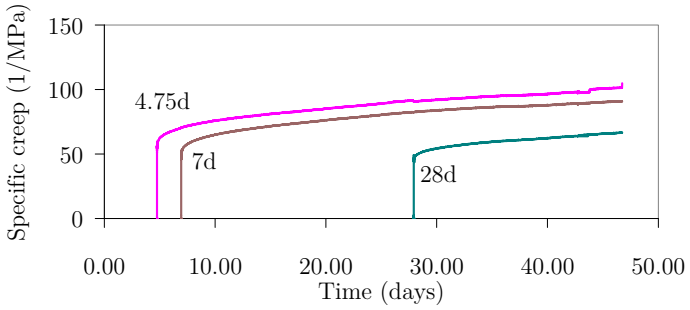

a) b)

Figure 6.47: a) Creep specimen moulds with gages; b) Specific creep – experimental

Compressive strength, tensile strength and E-modulus

For evaluation of the compressive strength evolution of the D200 concrete, eight 15×15×15cm^3 cubes were cast and placed in a climatic chamber (T=20°C and RH=100%), after transportation to the laboratory. Compressive strength tests were conducted in pairs of specimens for each age of 1.5 days, 4.5 days, 7 days and 14 days. The compressive strength at 28 days was determined using a 15cm diameter and 30cm tall cylindrical specimen. The results obtained for compressive strength are depicted in Figure 6.48.

Tensile strength was measured with recourse to the Brazilian splitting test, using nine cylinders (15cm diameter, 30cm tall), tested at the ages of 1.5 days, 4.5 days, 7 days, 14 days and 28 days. The obtained results can be seen in Figure 6.49.

Six cylinders (15cm diameter, 30cm tall) were cast for evaluation of concrete E-modulus evolution at the ages of 7 days and at 30 days. The average E-modulus at the age of 7 days was 26.2 GPa, and at the age of 30 days it reached 31.4 GPa.

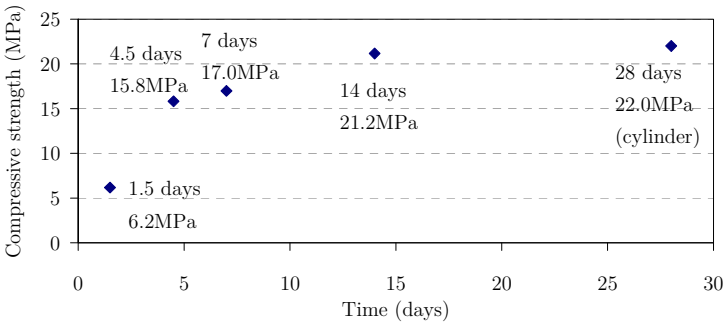

Figure 6.48: Compressive strength evolution

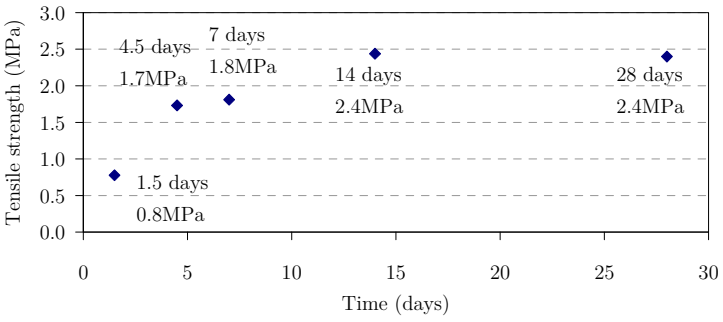

Figure 6.49: Tensile strength evolution

Drying shrinkage

In regard to drying shrinkage, one prismatic specimen (15×15×60cm^3) was monitored with a metallic vibrating wire strain gage, moist cured until the age of ~1.5 days, and after that sealed with paraffin wax except for two opposite 15×60cm^2 surfaces – see Figure 6.50a. The measured shrinkage at the age of 110 days was of about 360×10^{-6}, and its evolution is shown in Figure 6.50b (short period of data between 60 and 68 days lost due to a power loss).

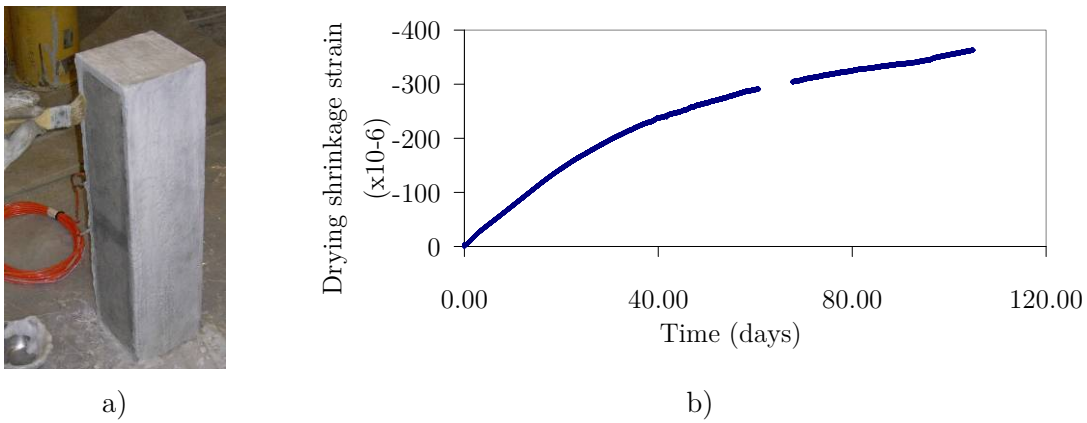

a) b)

Figure 6.50: a) Drying shrinkage specimen during sealing process; b) Drying shrinkage evolution on D200 concrete since age of exposure (specimen 15×15×60cm^3)

Isothermal calorimetry

With the purpose of characterizing the heat generation potential and reactivity of the concretes used in the dam (D200 and C16/20), the technique of isothermal calorimetry was used. Because this technique only allows the characterization of small specimens with maximum solid content of ~30g, the option of characterizing solely the cement paste (including fly ash and plasticizer) corresponding to each concrete was taken. Samples of the necessary ingredients for the experiment were taken from the construction site. Therefore, bearing in mind the original compositions of concretes D200 and C16/20, the necessary adaptations were made to obtain samples reproducing the same cement-based pastes present in both concretes. It is presumed that the absence of aggregates (both fine and coarse) has negligible influence on the heat generation potential and reactivity characteristics. To obtain the composition of the cementitious pastes to be characterized, the following procedure was followed:

- Step 1 - From the original dosage of constituents of concrete (see Table 6.2), the contents in gravel and sand were removed, resulting in a mix that does not totalize one cubic metre, but in fact represents the quantity of each of the present constituents in a cubic metre of the actual concrete. By summing the solid contents of this paste, it is possible to know the solid content of cement-based paste in per cubic metre of the actual concrete.
- Step 2 - From the resulting dosage (weight of all constituents per cubic metre except for sand and gravel), a simple multiplication of all constituents proportions by the same factor is made, to obtain a proportional mix whose solid content is 30g (the weight of the specimen for isothermal calorimetry characterization). The

proportionality constant is also applied to water and plasticizer, thus resulting in a total weight around 45g for w/c ratios of 0.5.

After the above procedure, the mix proportions of the cement-based pastes, as well as the weight of solid content such pastes in their respective original concretes (per cubic metre) are obtained, and summarized in Table 6.5.

Calorimetric tests were conducted for the D200 paste at 20°C, and for C16/20 at 20°C and 25°C – see Figure 6.51 and Figure 6.52. Tests at higher temperatures were not considered necessary, since the range of temperatures that actually occurred in the dam was not much larger than this.

Table 6.5: Constituents of the cement based pastes relative to D200 and C16/20 concretes

	Dosage (g)	
	D200	**C16/20**
Sand 0/4	-	-
Gravel 4/12	-	-
Gravel 12/20	-	-
Gravel 14/40	-	-
CEM II/A-L 42.5R	21.00	21.35
Fly Ash	9.00	8.65
Plasticizer	0.36	0.27
Water	15.30	18.30
Weight of solid content of the paste in $1m^3$ of concrete	200 kg	260kg

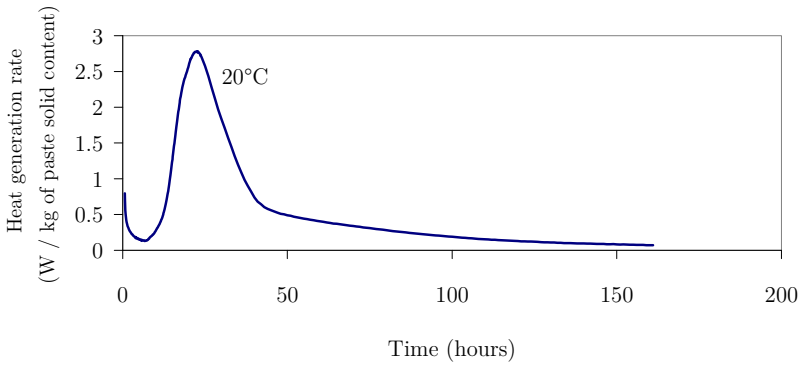

Figure 6.51: Isothermal calorimetry test on the D200 paste

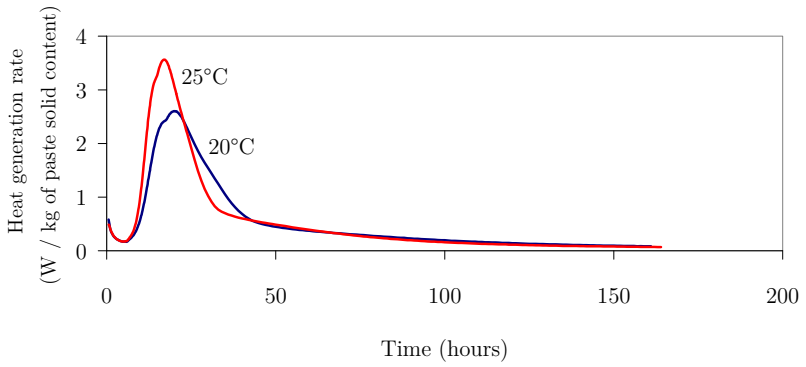

Figure 6.52: Isothermal calorimetry tests on the C16/20 paste

The results obtained from the isothermal calorimeter express the heat generation per kg of solid content of the analyzed paste. Therefore, in order to extrapolate the measured heat generation for one cubic metre of concrete, one has to multiply the obtained result by the solid content of cement-based paste per cubic metre of the actual concrete (obtained at the end of Step 2 of the procedure mentioned above).
For comparative purposes, the heat generation potentials at 20°C for both D200 and C16/20 are shown in Figure 6.53. There is an interesting fact to be pointed out: from observation of the heat generation rate of the cement paste of D200 (maximum of 2.78W/kg in Figure 6.51) and that of C16/20 (maximum of 2.6W/kg in Figure 6.52), it can be seen that the maximum heat generation of D200 is higher than that of C16/20. However, for the case of maximum heat generation per cubic metre of the actual concretes (Figure 6.53) this tendency is reversed because the cement paste content is higher in C16/20 (260kg/m^3) than in concrete D200 (200kg/m^3). Figure 6.53 also allows observing that the dormant phase of chemical reactions of C16/20 is somehow smaller, with sooner start of heat development. This difference ends up attenuated in the construction, due to fact that the C16/20 concrete is cast only after the D200.

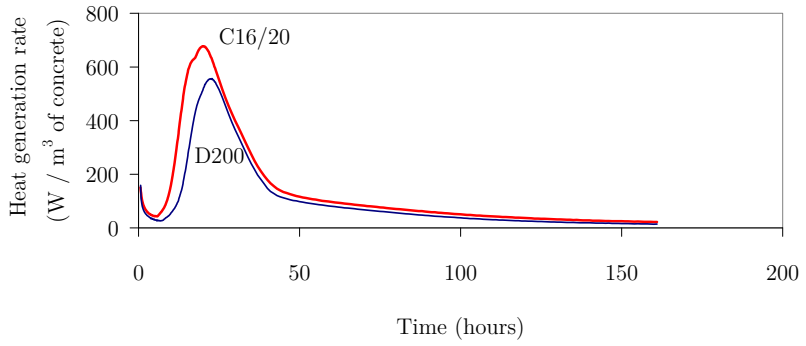

Figure 6.53: Estimated heat generation at 20°C for D200 and C16/20 (W/m^3 of concrete)

6.3.6 Numerical model

6.3.6.1 Overview

For the numerical simulation of the temperature and stress fields of the dam, the DIANA finite element software was used. As the monitoring campaign was centred in the

measurement of strains perpendicularly to the axis of the dam, a plane analysis was conducted concerning the cross-section of the monitored concrete dam block 9. This is a significant simplification, once the galleries within this dam block have a geometry that is non-uniform along the dam's axis. However, the possibility of performing a 3D model with all the singularities pertaining to the actual dam (namely the actual geometry of all galleries, and the construction phasing of block 9 and its adjacent blocks) would yield a too much complex model. The overall methodology for the thermo-mechanical analysis undertaken was the same as adopted for the wind tower RC foundation previously described.

6.3.6.2 Geometry, mesh and time discretization

Having chosen a plane stress simulation for the dam, passing through most of the sensors described in Section 6.3.4 (see Figure 6.54a), four galleries can be identified, two of them influencing Phases 12 and 13. Also, one should bear in mind that the downstream surface of the dam is stepped, representing an additional complexity since an explicit modelling of the influence of solar radiation was intended (thus having different effects in the vertical and horizontal surfaces of the stepped downstream face). Generally speaking, each casting phase had a height of 1.2m, extending all the dam width, except for some singularities occurring in the base of the dam (see Figure 6.54a). The geometry reproduced through the FE method comprised some simplifications, and can be seen in Figure 6.54b. The following remarks can be made concerning the main features of the adopted geometry, in regard to the actual situation:

- The dam geometry near the base was slightly simplified, to avoid inclined lines. This simplification allowed making a structured mesh easier, and did not carry relevant consequences as the overall volume of the simplified regions remained almost unchanged.
- Casting Phases 1 to 6 involved intermediate phasing and non-horizontal limiting surfaces – see Figure 6.54a. The option of removing intermediate phases and turning limits between phases horizontal was taken, resulting in the drawing represented in Figure 6.54b. It is understandable that these simplifications do not represent significant changes to the volumes of concrete, nor to the exposure conditions, which provide confidence that no relevant consequences on the calculated temperatures/stresses are expectable, particularly in the vicinity of the monitored areas (Phases 12 and 13).
- Geometry of the galleries was slightly simplified, avoiding inclined lines, to simplify the implementation of a structured FE mesh. Extra care was put on appropriately simulating the galleries intersecting Phases 12 and 13 that were mentioned.
- The FE mesh was prepared to include the ~1.6m long strips of C16/20 concrete, placed in the stepped areas of the downstream dam surface. Such preoccupation had to be reflected in the adopted geometry for the model, as can be confirmed in Figure 6.54b.
- A limited area of underlying granite was considered in the geometry, in order to simulate heat exchanges between the dam and its foundation massif.

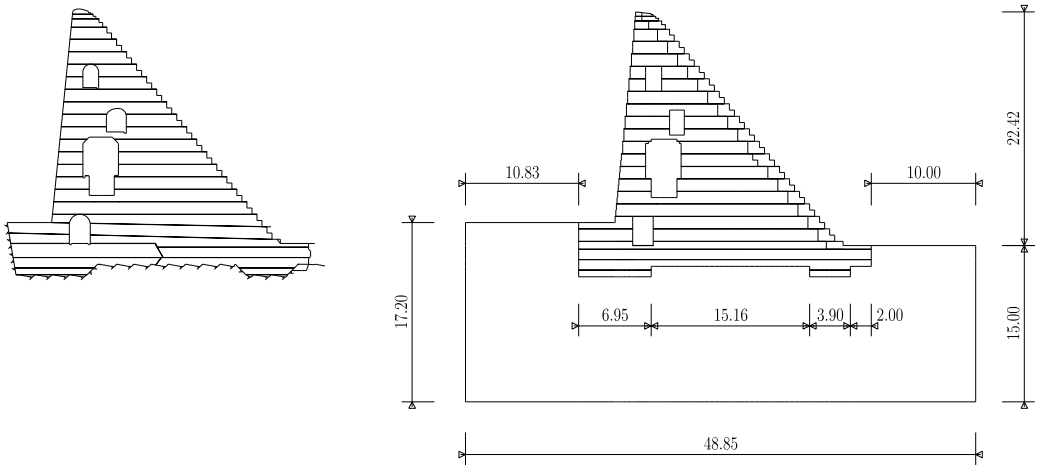

a) b)

Figure 6.54: a) Real geometry of the dam in block 9; b) Geometry adopted for the FE model (units: m)

The final FE mesh adopted is depicted in Figure 6.55 (with D200 concrete represented in green, C16/20 in red and granite in blue). This mesh comprises 4-noded FE for the thermal analysis, and 8-noded FE for the structural analysis, both types of elements with coinciding FE vertex nodes. Throughout the dam body most FE are about 0.20mx0.20m, which represents a compromise between the small sizes that would be necessary for an accurate representation of surface fluxes, and the avoidance great computational effort costs due to excessive discretization. This discretization yielded a numerical model with a total of ~30000 nodes and ~11800 FE. Special boundary elements exist for simulation of convection phenomena in the thermal model (linear elements with two nodes, applied on the boundaries), with a placement to be discussed in detail in Section 6.3.7.

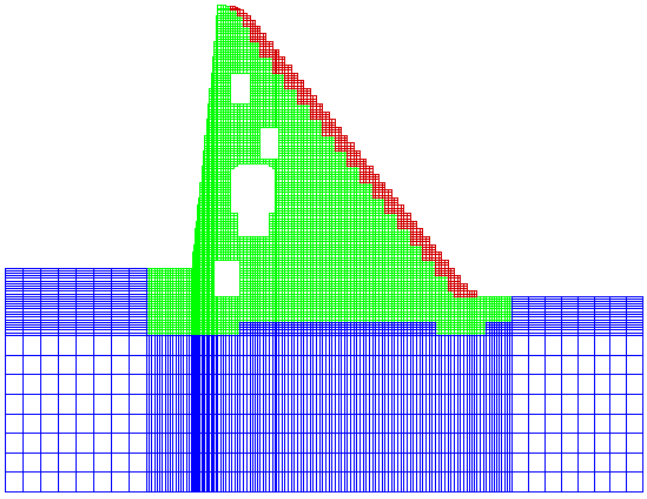

Figure 6.55: FE mesh adopted

This FE mesh is prepared to deal with the phased analysis in correspondence to the construction phasing that actually occurred in site. The analysis was conducted in correspondence to the timings already reported in Table 6.1, starting in the beginning of Phase 1 and ending 27 days after the end of casting of Phase 24. This corresponded to a

total time of analysis of 196 days, performed with a constant time-step of 1 hour. For such a wide time span of analysis this short time-step carried important computational and storage costs which however could not be avoided because of the decision of explicitly considering the contribution of solar radiation and the construction phasing.
The basic principle of the phased analysis is to carry the results of a previous phase (temperatures, maturities, stresses) as initial conditions for the subsequent phase. The input of a new phase of analysis also includes the additional geometry, as well as information about the previously existing geometry or boundaries that remain active. Other than these input specificities, and result superimposition, the procedures for each phase of the analysis are the same of a regular non-phased analysis model.

6.3.6.3 Material parameters

Thermal model

The three materials involved in this numerical simulation are the granite and the D200 and C16/20 concretes.
Regarding granite, and since no experimental characterization was conducted, reference values (Silveira 1996) were adopted: k_g=2.79Wm^{-1}K^{-1} and a $(\rho c)_g$=2040kJm^{-3}k^{-1}. The initial temperature was considered to be the annual average temperature of the site (~13.4°C).
In what concerns to the thermal characteristics of the concretes, the only property that was characterized was the heat of hydration, with the results shown in Section 6.3.5. By considering the mentioned results from isothermal calorimetry and the formulation for heat generation stated in Chapter 2 (see equation (2.23)), the material parameters for each of the considered concretes are reproduced in Table 6.6. The normalized heat generation function $f(\alpha)$ is plotted in Figure 6.56. For thermal conductivity and volumetric specific heat, the same values were adopted for both D200 and C16/20 concretes in correspondence to the usual range of values found in literature (Azenha 2004): k_c=3.0Wm^{-1}K^{-1} and $(\rho c)_c$=2300kJm^{-3}k^{-1}.

Table 6.6: Heat generation parameters (values per cubic metre of concrete)

	D200	**C16/20**
A (Wm^{-3})	7.2237×10^{10}	8.7862×10^{10}
$\mathbf{Q_{final}}$ (Jm^{-3})	6.7939×10^{7}	8.9247×10^{7}
$\mathbf{E_a}$ (kJmol^{-1})	45.507	45.507

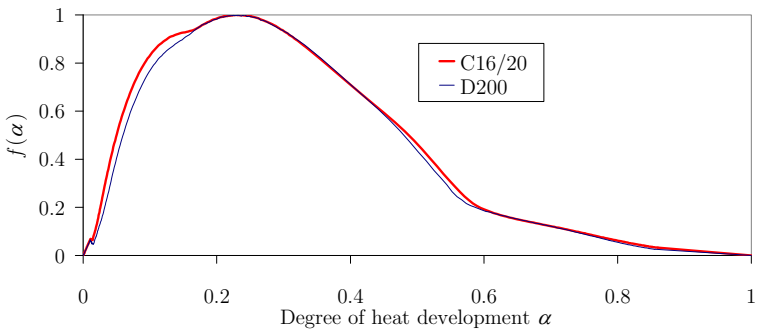

Figure 6.56: Normalized heat generation function $f(\alpha)$

The temperature of concrete during casting varied throughout the several casting phases. However, since this variable was only evaluated for Phases 12 and 13, it was decided to assume a reference value, representative of what happened in these phases: 15.0°C.

Mechanical model

The only material that actually had mechanical characterization was the D200 concrete. The reference evolution of tensile strength depicted in Figure 6.49 was used as an input to the model, to check cracking risk. In the model this evolution can be accelerated of de-accelerated according to the equivalent age concept (as discussed in Chapter 5). E-modulus was also considered dependent on equivalent age accordingly, based on the evolution estimated from the two tests performed at the ages of 7 days and 28 days referred to in Section 6.3.5.

Creep was modelled through the use of the Double Power Law: based on the experimental results documented in Section 6.3.5, the parameters ϕ=0.2246, m=0.2 and n=0.3 were adopted. Poisson's coefficient was taken as 0.2 and the thermal dilation coefficient as $12\text{x}10^{-5}$ $°C^{-1}$, both assumed as constant. The great volume of the dam causes the non-negligible drying shrinkage strains that were measured in laboratory (Figure 6.50) to have an almost negligible influence on the overall concrete stress development. Consequently, due to its foreseeable limited contribution, drying shrinkage was not considered in the numerical model. Autogenous shrinkage was also disregarded in the numerical model due to its predictably very low significance related to the low cement content and high water cement ratio of the mix.

Regarding the C16/20 concrete, and since no specific characterization was performed, the same mechanical properties as those considered for D200 were assumed.

For granite, the following reference material parameters were considered: E_g=8GPa, α_{Tg}=$8\text{x}10^{-5}°C^{-1}$ and ν_g=0.3.

All interfaces between distinct materials (D200 – C16/20 and D200 - granite) were considered to be fully adherent. This consideration is deemed to be valid while stresses in these interfaces had low values.

6.3.7 Boundary conditions and environmental data

6.3.7.1 General principles

The boundary conditions adopted in the numerical model are described in this section. The model in question is quite complex in terms of evolving geometry and boundaries, so, the general principles about the actual modelling options are to be discussed first.

Figure 6.57 provides a schematic representation of Phase 13 of the construction sequence. Discussion of the boundaries used in this case is representative for all other phases. Boundaries are labelled B1 to B6, according to the following:

- B1 represents the limit of the modelled granite. It is considered that no heat is transmitted through this boundary during the whole analysis. Validity of this assumption may be assessed by analysis of the calculated temperatures developed in the granite massif.
- B2 represents the top surface of the granite massif, a boundary that remains unchanged throughout the whole analysis.

- B3 is the upstream dam surface boundary, which grows in size as construction phasing progresses.
- B4 is the downstream dam surface boundary, growing in size as does boundary B3.
- B5 is the top boundary of the last phase built. This is a temporary boundary that applies immediately after casting of its respective phase, and finishes upon beginning of the subsequent construction phase.
- B6 is the boundary relative to the gallery environment, shielded from solar radiation effects and partially shielded from wind effects (since the galleries open to the exterior). This boundary only starts existing upon closure of the top of the gallery; until then it behaves like boundary B5.

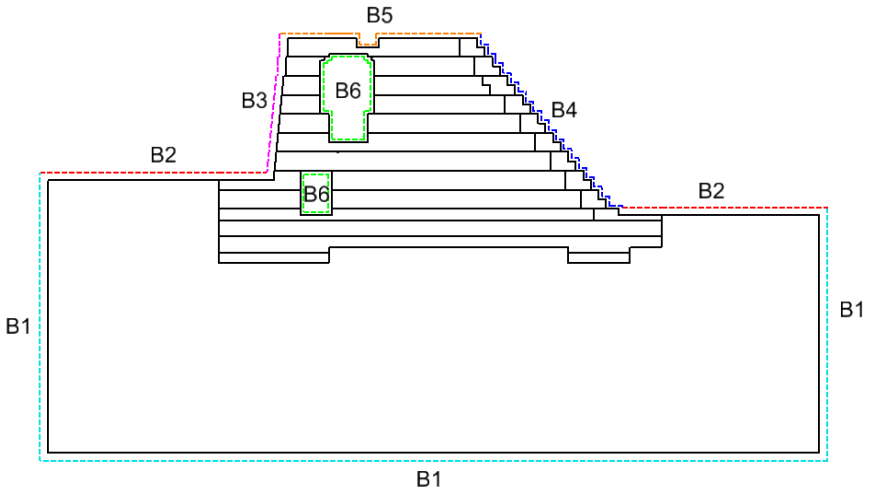

Figure 6.57: Boundary conditions for Phase 13

6.3.7.2 Environmental temperature

The temperature measured by sensor T7 (see Section 6.3.4.4) was selected to be the input representing the environmental temperature to the numerical model. Effects of solar radiation, night cooling and evaporative cooling are added directly to concrete boundaries, according to the sections that follow.

6.3.7.3 Convection/radiation coefficients

A convection/radiation coefficient is adopted to simulate the combined effects of free and forced convection and long wave radiation exchanges with the environment. This lumped coefficient has been dealt with in Chapter 2: it comprises a simplified long wave radiation heat transfer coefficient h_r=5.2Wm^{-2}K^{-1} for an environmental temperature of 20°C (Branco *et al.* 1992).

For the convection coefficient to be combined with h_r, and bearing in mind the application in question, which is outdoors in a river valley (low urbanization area), windy situations are expected, causing the forced convection to contribute more than free convection. The wind is not constant during construction, and no wind speed monitoring was performed in the experimental campaign. So, it was considered that the most feasible option was to adopt constant convection coefficient values replicating a reasonably windy place. These heat transfer coefficients also have to replicate the existence of formwork at some times, and the fact that some boundaries regard to galleries, where lower wind

speeds, thus lower heat transfer coefficients are to be expected. The values of the convection/radiation transfer coefficients adopted in the numerical model are shown in Table 6.7. The maximum value of $22 Wm^{-2}K^{-1}$ corresponds to a convection coefficient of $16.8 Wm^{-2}K^{-1}$, which according to the wind tunnel experiments described in Chapter 2 corresponds to a wind speed lower than $2 ms^{-1}$. As formwork removal was not always made at the same relative time since casting, and no record of formwork striking times was kept, a reference period of 3 days after casting was considered, according to an average estimate provided by the contractor.

The part of radiation that is lumped into the convection/radiation coefficient pertains to radiation exchanges with surrounding environment. Solar radiation and night cooling associated to the fictitious night sky temperature are dealt with in the following sections.

Table 6.7: Adopted convection/radiation transfer coefficients

	Outer environment $Wm^{-2}K^{-1}$	Inside galleries $Wm^{-2}K^{-1}$
h (with formwork)	12	10
h (without formwork)	22	16

6.3.7.4 Solar radiation

Solar radiation plays an important role by inputting relevant amounts of heat to the concrete surface. Such effect has been taken into account in the dam trough the solar models described in Section 2.5.2.4. The only shadowing effects are the ones implicit to the used formulation (considering the position and orientation of the surface as well as its relative position to the sun). Shadowing effects caused by neighbouring objects were disregarded.

Regarding the general naming convention of boundaries presented in Figure 6.57, and bearing in mind the dam orientation according to the plan shown in Figure 6.58, the following distinct solar exposure conditions were considered:

- Boundaries B2 and B5 – horizontal surfaces, where α=0° and ψ=0°.
- Boundary B3 - upstream surface, inclined 84.29° to the vertical, with its normal making an angle of 245.72° with South: α=84.29° and ψ=245.72°.
- Boundary B4 - downstream stepped surface comprising two situations: a) the horizontal part of the steps, which is treated as described for boundaries B2 and B5; b) the vertical part of the steps, which corresponds to α=90° and ψ =65.72°.

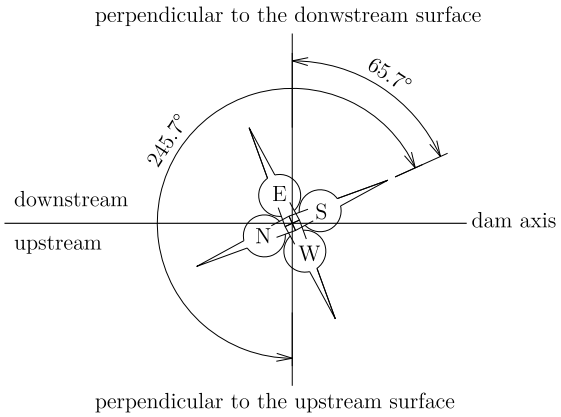

Figure 6.58: Dam orientation diagram

The latitude and longitude of the dam location are 41.03°N and 7.84°W, respectively. Concrete absorvity was considered to be 0.6, and the turbidity factor taken as 4. This allowed the automatic generation of the predicted radiation input to the various dam boundaries. However, not all days were sunny, and atmospheric turbulence, among other factors, are known to affect turbidity. As no monitoring of radiation by the dam was conducted, the predicted values of radiation inciding on a horizontal surface (not considering the effect of absorvity) were compared to the values measured in the nearby weather station of Rio Torto. Two parts of such comparison in distinct periods are shown in Figure 6.59a (Winter 2007) and Figure 6.59b (Spring 2008). It can be observed that the numerical model fairly predicts the global tendency, but since it does not include the aforementioned effects of shadowing by clouds and atmospheric turbulence variations, it fails in days such as 18th December 2007 (quite cloudy day) or 22nd April 2008 (for the same reasons). Other days occurred where no cloudiness existed, and the atmospheric turbulence was less than the value of 4 considered in the model; this occurred for example in 3rd December 2007.

In view of these limitations and the availability of experimental results, it was decided to normalize the predictions of the model by applying a multiplying factor to the prediction of each day. This factor was obtained from the quotient of the maximum measured radiation of the day to the maximum radiation predicted for that day. The result obtained through the period of analysis for this multiplication factor is frequently in values around 1.0 (meaning that the simulation correctly predicted the inciding radiation), but often oscillates to more than 1.5 or even lower than 0.3. This provides a realistic indication about the vital influence of clouding and atmospheric turbulence in the quality of solar radiation simulation.

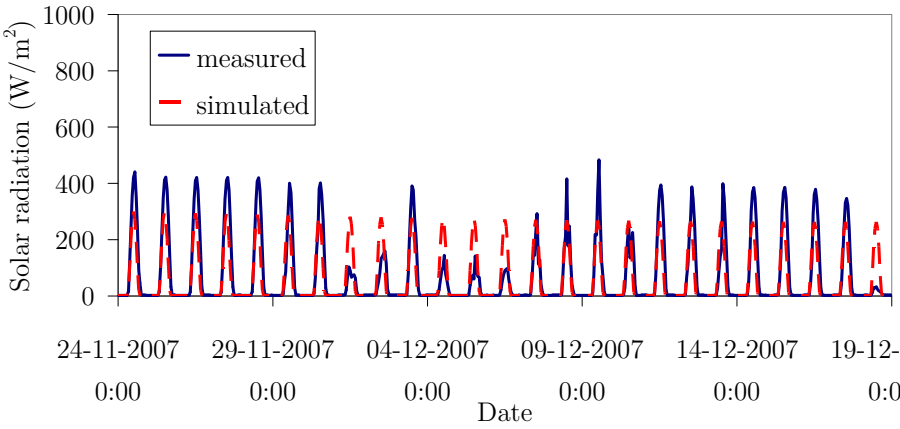

a)

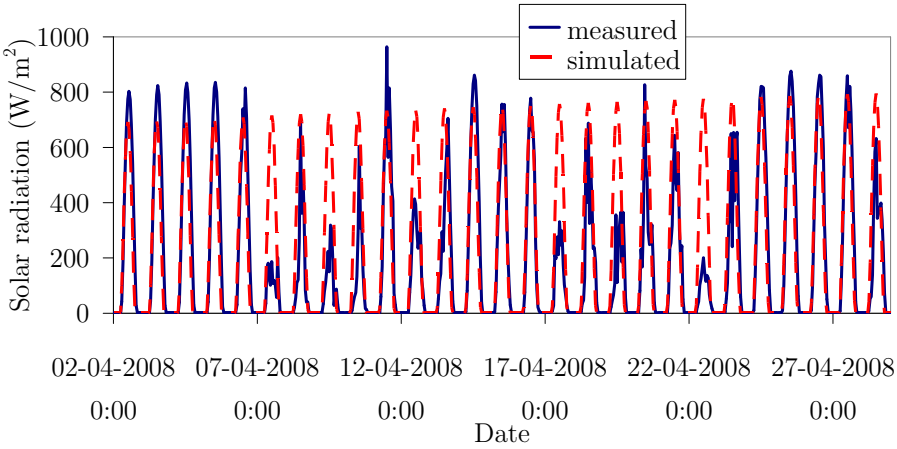

b)

Figure 6.59: Comparison of measured and predicted values of solar radiation on a horizontal surface: a) November/December 2007 ; b) April 2008

A result concerning the normalized radiation actually absorbed by some of the concrete surfaces of the dam is shown in Figure 6.60. It is noticeable that on the 21st November, there was a higher solar attenuation than in the 22nd November. Also, the relative position of each surface determines how sun acts upon it (in the same manner in both days represented):

- The perpendicular to the downstream vertical surface is oriented to ESE, therefore from the three cases represented it is the one that starts being exposed to sun earlier in the day, and as a consequence, is the one that stops receiving solar radiation sooner in the day.
- The upstream inclined surface is oriented towards WNW, therefore receiving more solar radiation at the end of the day, when its effect is smaller.
- The horizontal surface is acted by solar radiation symmetrically in relationship to the solar noon, with intermediate radiation levels.

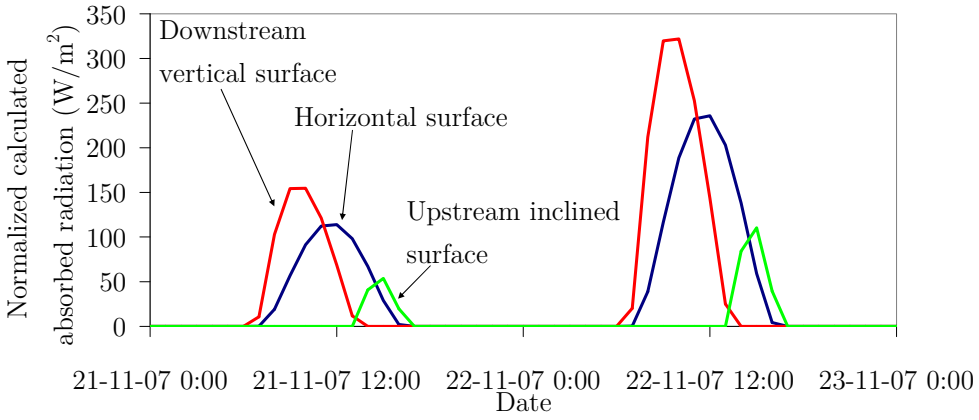

Figure 6.60: Normalized simulated radiation for two consecutive days

6.3.7.5 Night radiation cooling

Being built outdoors, the dam is subject to additional radiation heat fluxes during the night, causing a cooling effect. These additional heat fluxes associated to night cooling can be attributed to the apparent sky temperature, which can be much lower than the environmental temperature itself (assuming values as low as 30°C under the environmental temperature). As the apparent sky temperature depends on relative humidity, cloudiness and presence of dust in the air, among others, it is impossible to conduct an accurate hourly prediction of this phenomenon, since the relevant data is not available. Therefore, it was decided to conduct a rough estimate of the difference between the environmental and the apparent sky temperatures as 15°C, considered also as constant during night periods. Bearing in mind that a simplified radiation exchange coefficient has the value of $5.2 W^{-1}K^{-1}$ (according to Section 6.3.7.3), with an estimated emissivity coefficient for concrete of ε=0.9, the computed additional heat flux due to night radiation cooling according to equation (2.53) becomes:

$$Q_{add} = 0.9 \times 5.2 \times 15 \cong 70 \text{ W m}^{-2} \tag{6.2}$$

This additional flux was applied in the numerical model during the whole period between the end of solar radiation input of a given day until the beginning of the solar radiation of the next day.

6.3.7.6 Evaporative cooling and water run-off

The effect of evaporative cooling and its driving mechanisms have been discussed in detail in Chapter 4 (Sections 4.4.5, 4.5.2, 4.6.4 and 4.7.3). In the case of the dam, the moisture loss by evaporation occurs due to several reasons:

- Water is applied in jets over horizontal surfaces of recently cast bodies. in order to remove loose material and allow casting of the next construction phase. This water accumulates in ponds and thin films, becoming available for evaporation. These jet operations over recently cast parts of the dam occurred some time before the subsequent casting phase (usually less than 1 day).
- After the end of casting, the top surface of a given construction phase is composed of saturated concrete, which tends to lose water to the environment by evaporation. This

tendency is partially compensated by watering (curing) procedures by the contractor, but evaporation occurs continuously, therefore heat removal occurs. At this stage it is important to mention that, even if all the environmental conditions (relative humidity and temperature) and curing conditions were known, the estimation of water losses would involve advanced numerical simulations of water content inside concrete, and its interactions with the environment, such as the ones presented in Chapters 3 and 4. In the absence of detailed information on curing procedures and humidity environmental conditions, the use of such advanced models becomes somehow pointless, and rough estimates as the one that will be presented are preferable.

- Rain is an important source of water for concrete surfaces, as it tends to be accumulated on films or ponds over concrete. This is also water that evaporates and removes heat from concrete. Also, this is a rather difficult aspect to be appropriately accounted for in the numerical model, particularly because there is no information about the amount of rain in the construction site.

In addition to moisture losses that cause evaporative cooling in concrete structures, there is another effect that causes heat losses from concrete: the water run-off. Whichever the origin of water (curing procedures, cleaning water, or rain), at the very instant it touches concrete, there is an energy transfer associated to the fact that their temperatures are different (with concrete's temperature being usually higher due to heat of hydration effects, causing heat losses from concrete).

All the heat fluxes associated to evaporative cooling, as well to water run-off are rather difficult to simulate given the amount of events and environmental parameters that would have to be accounted, and whose parameters are mostly unknown in an outdoor structure this complex, with an intricate and long construction schedule. In fact, from the conducted bibliographic review, only one author (Wojcik 2001) has tried to account for these factors explicitly.

In the absence of data for an accurate estimation of heat losses in concrete due to evaporative cooling, it was decided to use the expectable heat loss from a water pond at 20°C, applied to the horizontal top surface of the dam (in each phase) during the first 24h of the phase (corresponding to the wet surface associated to the saturated concrete and the curing procedures). During the 24 hours preceding the casting operations of the next phase, the same heat losses were considered in order to somehow simulate the evaporative cooling associated to the water input to the structure by the preparation cleaning water jets.

Calculation of the heat loss from a pond at 20°C firstly requires an estimation of the water loss from such pond. The water loss can be estimated analogously to heat losses by convection, through the multiplication of an emissivity coefficient by a driving potential difference according to the findings reported in Chapter 4. At 20°C, the saturated water vapour pressure of water is e_s=2805Pa; considering a RH=60%, the vapour pressure in the air is e=0.6×2805=1683Pa. Taking a moisture emissivity coefficient E_S=4.92×10^{-8}kgm^{-2}s^{-1}Pa^{-1} for water (slight wind conditions, with V=1.8ms^{-1} – See Chapter 4), the resulting evaporative flux can be computed as:

$$evaporative\ flux = E_S \times (e_s - e) = 4.92 \times 10^{-8} \times (2805 - 1683) = 5.52 \times 10^{-5}\,\mathrm{kgm^{-2}s^{-1}} \qquad (6.3)$$

Computation of the evaporative cooling heat flux is now made according to the entalphy of evaporation of water with recourse to equations (4.21) and (4.22) yields:

$$q_{heat,ev.cooling} = 5.52 \times 10^{-5} \times \left(2500 \times 10^{3} - 2.5 \times 10^{3} \times \left(293.15 - 273.15\right)\right) \approx 135\,\mathrm{Wm^{-2}} \qquad (6.4)$$

Knowing that this is no more than a rough estimation of the evaporative cooling losses in the structure, and that the applied period (24 hours in the periods immediately before and immediately after casting in the relevant exposed horizontal surfaces) is bound to overestimate the water losses, it was decided to round the value of the cooling flux to $100\mathrm{Wm^{-2}}$ in the numerical model (which is still probably an overestimation of evaporative cooling).
The calculations above make no reference whatsoever to the effects of heat removal by water run-off. It is assumed that the overestimation of water losses associated to the calculation of water loss due to evaporative cooling covers this effect.

6.3.7.7 Boundary conditions for the mechanical model

The numerical model comprises both the dam and a part of the underlying granite massif. The only boundary conditions for the mechanical model were applied along the lowest horizontal B1 line in Figure 6.57: this line was completely restrained in the vertical direction, and the leftmost node of the line has a horizontal restraint to avoid translation of the whole system.

6.3.8 Results of the thermal model

The present section aims firstly to show the coherence between computed temperatures and the measured ones. In a second part of this section, after having shown the feasibility of the calculated temperatures and the validity of the numerical model, information about the overall temperatures in the dam during the various construction phases is provided.

6.3.8.1 Comparison between numerical and monitored temperatures

The calculated temperatures for points of the dam where temperatures were monitored and the corresponding comparison will be discussed in this section. Firstly, the temperature sensors located along tube 1 in Phase 12 are dealt with: the comparisons between monitored and calculated temperatures are depicted in Figure 6.61 (sensor T1), Figure 6.62 (sensor P1), Figure 6.63 (sensor P2), Figure 6.64 (sensor T3) and Figure 6.65 (sensor T4). The overall results for this group of sensors were quite satisfactory, particularly for the cases of P1, P2 and T3, where deviations between calculated and monitored temperatures generally kept within very low values. The case for sensor T1 was not as satisfactory, with some periods in which temperature differences reached 4°C. These differences may be partially attributed to the existence the rich mortar layer in the interface between each casting phase, being that sensor T1 was actually embedded in this mortar. As this layer was not accounted for in the numerical model, its heat of hydration may have played a role in the observed differences between calculated and monitored values. In the case of sensor T4 (top of casting Phase 12), deviations between calculated and monitored temperatures are more significant, but it must be stressed that they do not

occur in Phase 12 itself (where coherence was actually quite good), but start occurring right after the casting of Phase 13: the temperature peak is missed by about 5°C (below measured values), and the tendency of diminishing temperatures after such peak seem to be underestimated. This would be an important point for discussion, and possible necessity of improvement of the numerical model simulation and parameters, where it not for the good results obtained for the sensors in Phase 13 (see discussion ahead). Therefore, deviations in sensor T4 are considered to be related to a quite local effect (possible accumulation of rich mortar over the sensor during casting of Phase 13, or even a sensor malfunction), thus not constituting an obstacle to the numerical model validation.

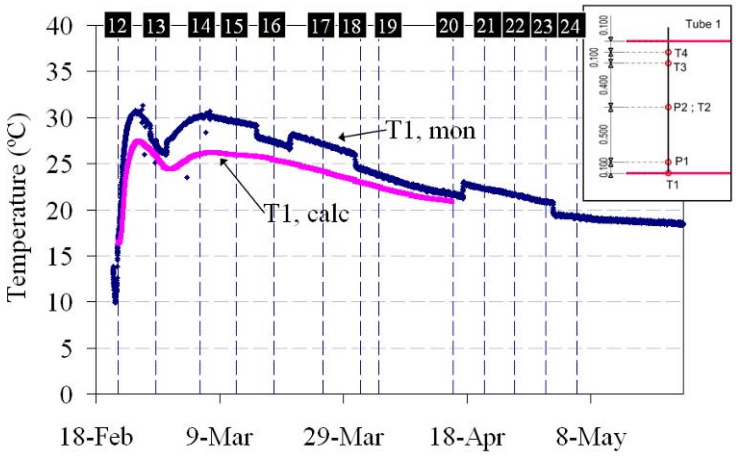

Figure 6.61: Monitored and calculated temperatures for T1

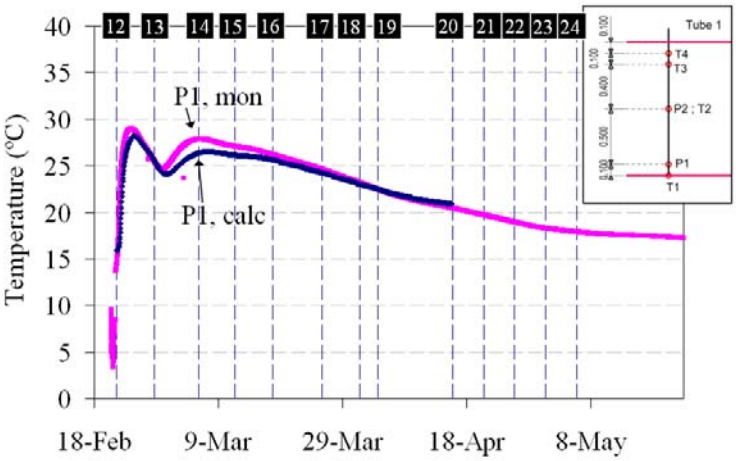

Figure 6.62: Monitored and calculated temperatures for P1

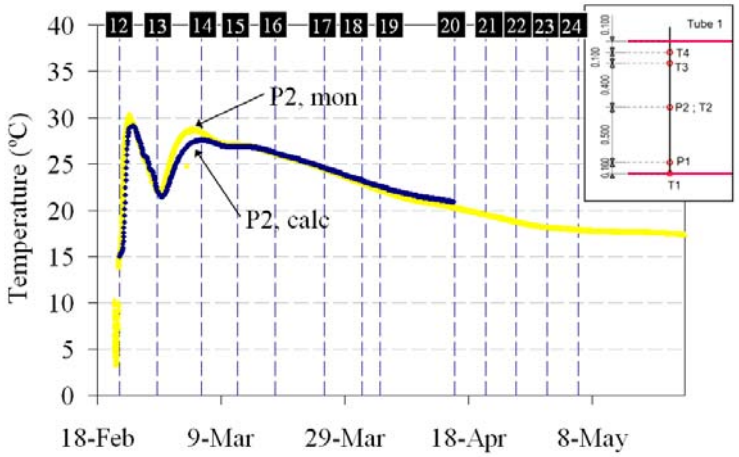

Figure 6.63: Monitored and calculated temperatures for P2

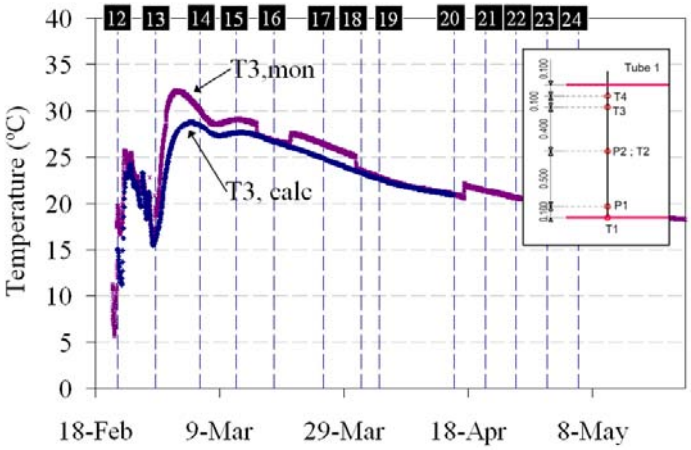

Figure 6.64: Monitored and calculated temperatures for T3

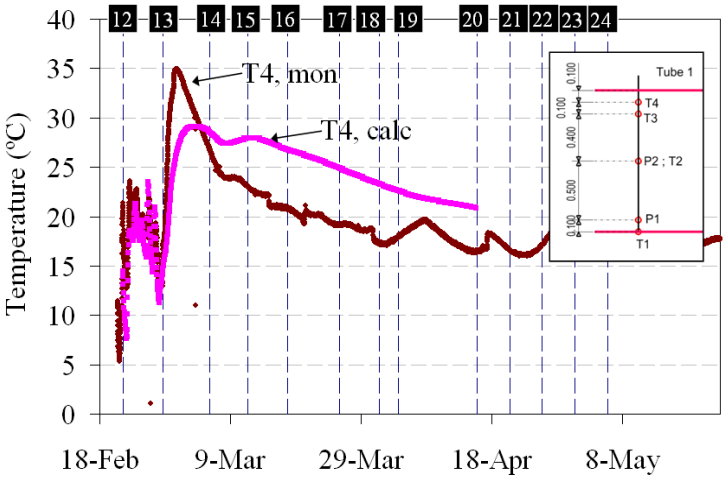

Figure 6.65: Monitored and calculated temperatures for T4

Regarding the sensors located near the downstream surface of Phase 12 – sensor P3 (Figure 6.66) and sensor T5 (Figure 6.67) -, the obtained coherences in results were quite satisfactory. In sensor P3, both the peak and the temperature development along time were reasonably well captured: differences not exceeding 2°C, and quite similar evolution

tendencies were obtained. Sensor T5, which was rather near the concrete surface, also revealed a quite satisfactory behaviour, both during Phase 12 (in terms of heating and cooling phases) and during the period whilst it is mainly influenced by external environmental factors. However, it must be stressed that there are frequent days in which the measured temperature at night fell 4°C under the calculated temperature, indicating a stronger effect of night radiation cooling than the one considered in the numerical model.

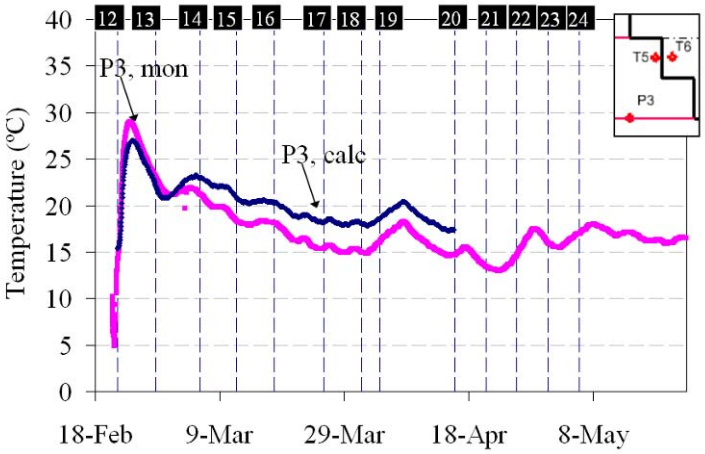

Figure 6.66: Monitored and calculated temperatures for P3

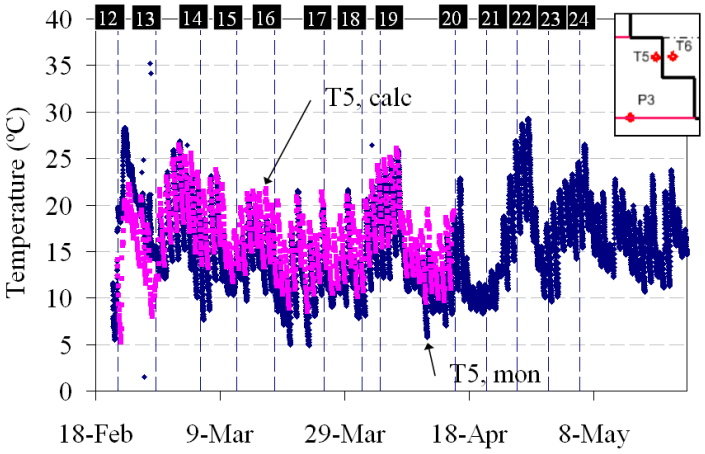

Figure 6.67: Monitored and calculated temperatures for T5

In what concerns to sensors T9 and T10 placed near the gallery in Phase 12, the corresponding results are shown in Figure 6.68. The coherence is clearly not entirely satisfactory, with deviations in peak temperatures of about 5°C (numerical model underestimating the actual temperature development). However, this was tolerated given the uncertainty in the sensors placement during construction: in fact a slight deviation of 3 to 5cm of the considered placement of the sensors in the numerical model would yield very good coherences.

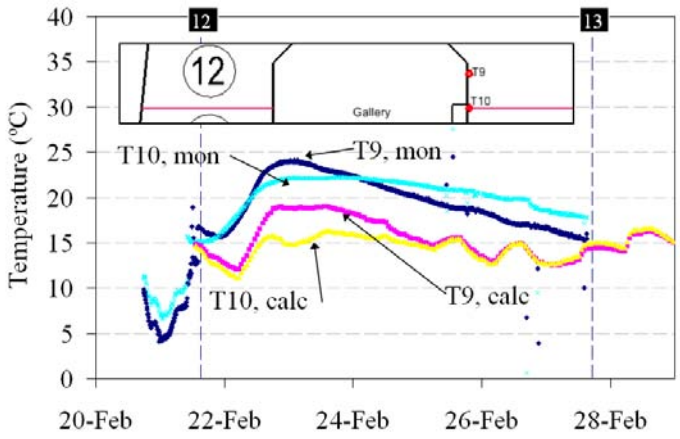

Figure 6.68: Monitored and calculated temperatures for T9 and T10

Figures 6.69 to 6.71 refer to the results obtained in the sensors supported by tubes 1 and 3 in Phase 13. There seems to have been a slight underestimation of peak temperatures in the bottom part of this phase (sensor CM1T), and a slight overestimation in the vicinity of the phase's top surface (sensors CM3T and CM6T). Nevertheless, the overall coherences of temperature magnitude and tendency for this group of sensors seem quite reasonable, bearing in mind the complexities associated to both the dam itself and the corresponding numerical model (with several simplifying assumptions).

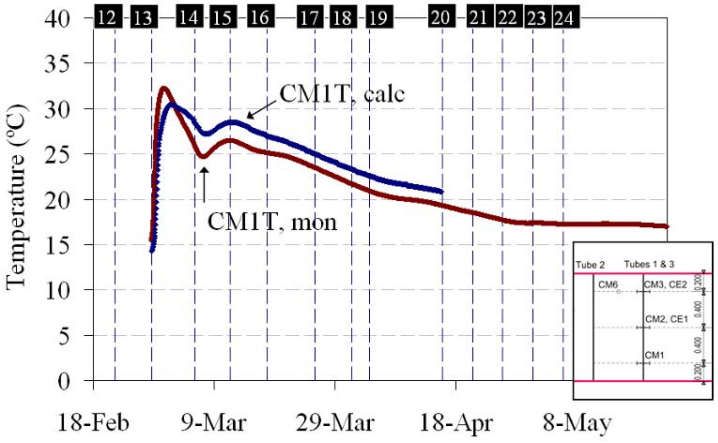

Figure 6.69: Monitored and calculated temperatures for CM1T

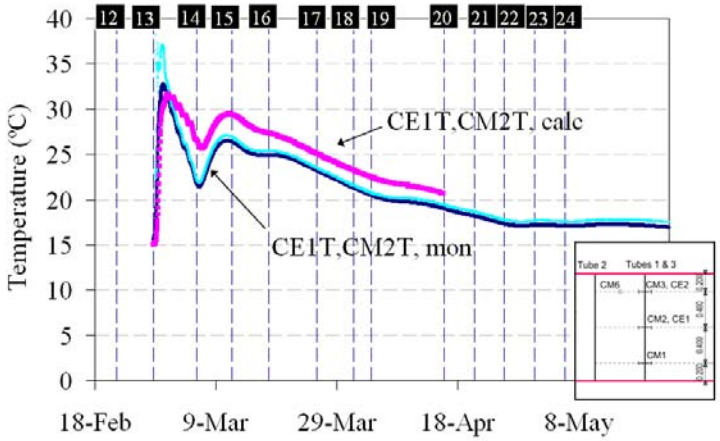

Figure 6.70: Monitored and calculated temperatures for CM2T, CE1T

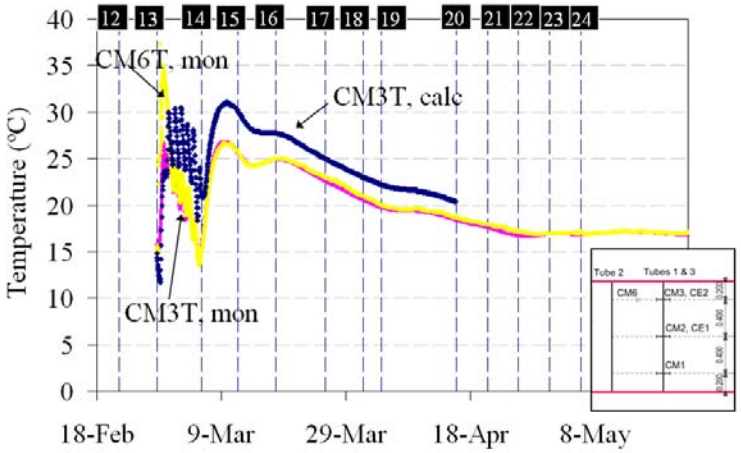

Figure 6.71: Monitored and calculated temperatures for CM3T and CM6T

For the sensors located near the downstream surface of Phase 13 (sensor CM4T - Figure 6.72; sensors CE3T, CM5T - Figure 6.73), quality of the numerical predictions seems quite good, with the exception in the peak temperatures, a few hours after casting, in the case of sensors CE3T and CM5T.

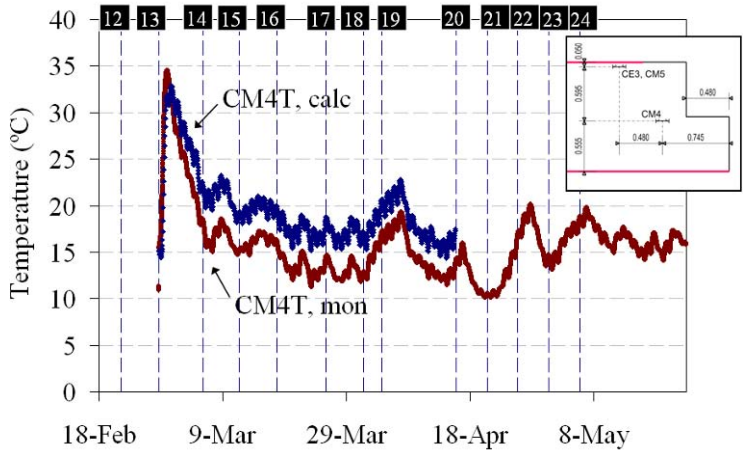

Figure 6.72: Monitored and calculated temperatures for CM4T

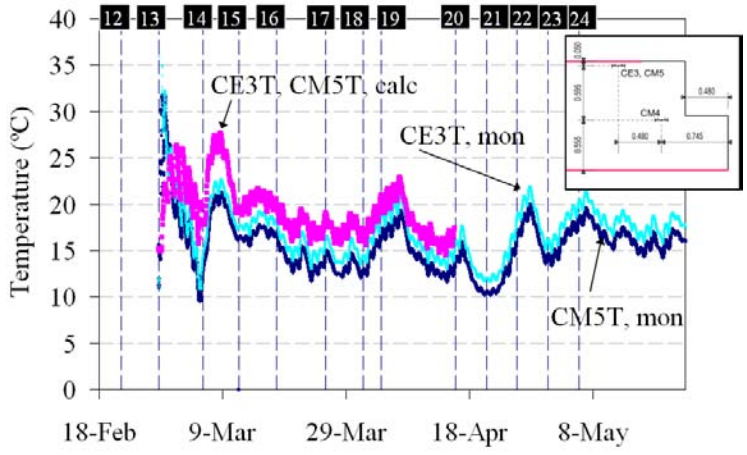

Figure 6.73: Monitored and calculated temperatures for CM5T and CE3T

Finally, regarding the set of sensors stretching along a line in the lower level of Phase 13, only results pertaining to sensors T17 and T18 are presented in Figure 6.74, as there are significant doubts about the precise location of the sensors neighbouring the surfaces, since strong difficulties were encountered in the construction site for their fixation and placement. The numerical predictions for T17 and T18 yielded quite good results, both in terms of peak temperature and temperature development after the peak.

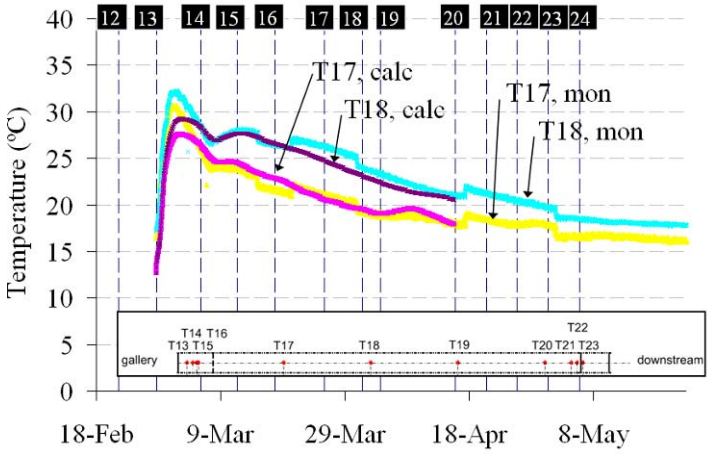

Figure 6.74: Monitored and calculated temperatures for T17 and T18

Generally speaking, the observed coherences between measured and calculated temperatures are considered to be very good, in spite of some local deviations that in some cases even reach 5°C. This relatively high tolerance in differences between calculated and measured temperatures can be explained by the complexity of the example in question: many construction phases and events during each construction phase, for which it was impossible to keep record (such as precise timings for formwork removal, use of equipments on the dam that generate heat, rain, cloudiness, cleaning water jets, slight variations in concrete and mortar composition, etc.). Complexity of the construction itself, summed up to the model complexity (with many parameters that had to be estimated under simplifying assumptions) allow the obtained results of the numerical simulation to be considered successful.

So, since the calculated temperatures are considered validated by the monitored ones, there is enough confidence in the thermal model simulation to use its results as inputs for the stress field simulation, which in turn is to be validated by the in-situ measured strains.

6.3.8.2 Calculated temperatures in the dam during the whole construction period

This section is intended to provide information about the distribution of calculated temperatures in the dam, throughout the whole construction period. Temperature maps can be found in Figure 6.75, pertaining to Phases 5, 8, 12, 13, 15 and 19. Starting on Phase 5, at 46h after casting, which is an instant of near maximum temperature development, it can be seen that the discontinuity corresponding to the first gallery generates two separate bodies that develop temperatures in a similar way, since the main heat fluxes occur in the vertical direction. It can also be observed that highest temperatures are achieved in the vicinity of the downstream surface steps: in spite of being near a boundary which would indicate stronger temperature losses, this area has a

C16/20 concrete with higher heat generation than D200; also, the effect of solar radiation during the day potentiates higher temperatures in the near surface. At 66h of Phase 8, a second gallery discontinuity also occurs, with slightly higher temperatures being developed in the right hand side of the dam, as the left side is disturbed by the presence of the first gallery, to which heat flows (as it can be confirmed by the low temperatures predicted for the vicinity of this first gallery in Phase 8). Also in Phase 8, there seem to exist two temperature bubbles (the word bubble referring to a concentration of higher temperatures in a specific area of the dam) on the right side: one pertaining to the concrete of Phase 8 itself within its 1.2m top thickness, and the other related to the region of accumulated heat of hydration from the previously cast phases (about 3m below the top surface). This effect of two bubbles is more evident at Phase 12 (36h after casting), with the bubble of accumulated heat of the dam rising in height as construction progresses. In Phase 13 (36h after casting) an interesting singularity occurs related to the thin horizontal layer of concrete existing between the second and the third galleries: this layer conducts heat from the adjacent larger parts, and therefore endures a significant temperature rise, but due to its vicinity to two gallery boundaries it is also bound to strongly lose heat, and thus a possible weak point in terms of concrete cracking risk. At the end of Phase 15 (131h after casting), it is seen that a single temperature bubble exists on the right side of the dam (where two bubbles used to exist in the previous phases, which were depicted near their casting), and that a new temperature bubble is being formed on the left hand side of the model. This secondary temperature bubble is bound to disappear due to the fourth gallery to be built over it, which tends to conduct the heat to the environment, as can be seen in Phase 19 (286h after casting), near the end of the analysis, where temperatures are decreasing and approaching the environmental temperature.

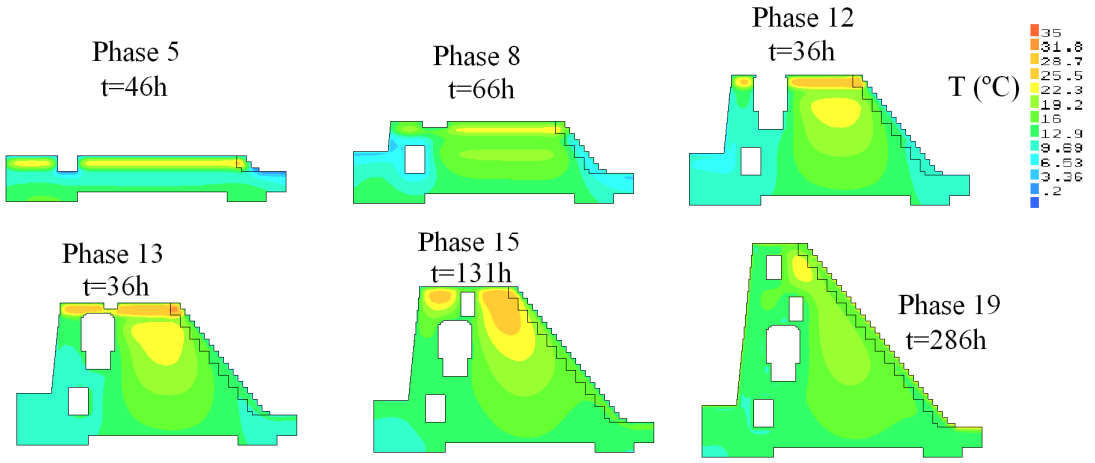

Figure 6.75: Temperature maps in the dam

6.3.9 Results of the mechanical model

6.3.9.1 Comparison between numerical and monitored concrete strains

The results collected from the used vibrating wire strain gages were zeroed at the instant of end of casting procedures of Phase 13, and their outputs were corrected for the effects

of temperature on the measured resonant frequencies of the wire. The resulting strains correspond to actual physical variations in concrete, rather than the case of mechanical strains, actually related to stress development. These techniques of measurement and temperature compensation of the vibrating wire strain gages were described briefly in Chapter 5, and are described in detail in Azenha *et al.* (2009).

The measured strains are then compared with the numerically predicted ones in the sets of figures that follow, all of them pertaining to sensors placed during casting Phase 13. Firstly the sensors supported by tubes 1 and 3 are discussed. Sensor CM1, placed at a lower level, has its strain development depicted in Figure 6.76. It can be observed that during the period between casting of Phase 13 and casting of Phase 14, the numerically predicted strain development is quite coherent with the measured one. Furthermore, in the period between casting of Phase 14 and casting of Phase 15, the coherence is reasonably good, but the numerical result tends to underestimate the strain drop tendency right before casting of Phase 15. Since this instant the numerical model seems to consistently underestimate the strain drops along time. The reason for this underestimation may be related to lower restrictions to deformation caused by the neighbouring concrete or by the underlying granite, or even to different creep behaviour than that input to the model. Justification for these differences cannot actually be found in the temperature development, as the latter was quite coherent with the measured one, particularly for stages after casting of Phase 15, as can be confirmed in Figure 6.69. Despite these deviations, the coherency between numerical and monitored results can be considered to be fairly reasonable, given the complexity of the whole range of events and phenomena involved.

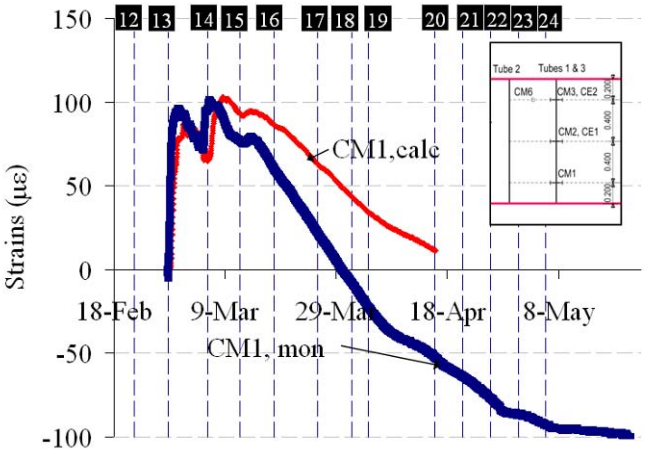

Figure 6.76: Monitored and calculated strains for CM1

The measured strains and correspondent numerical simulations for the middle and upper levels of sensors supported by tubes 1 and 3 are shown in Figure 6.77 (sensors CM2, CE1) and Figure 6.78 (sensors CM3, CE2). At a first look at these figures one may become quite surprised, as the measured strains are generally several times larger than those predicted by the numerical model, particularly since the instants immediately before casting of Phase 14. Before Phase 14, for the case of sensor CM3, the coherence between measured and calculated values was actually quite good. Also, after the major climb of strains immediately before Phase 14, the tendency of descending strains is generally well

predicted by the numerical model for most sensors (with the predicted strains curve fairly parallel to the measured ones). Therefore, one important point remains to be explained: what is the reason for such a strong and sudden change in strains immediately before casting of Phase 14, when no indication of this would be expectable from the monitored temperatures in the area of these strain gages (see Figure 6.70 and Figure 6.71)? The most reasonable explanation for this can be found on an analogy to occurrences observed in laboratory environment shrinkage specimens: it has been more than once observed in LABEST/FEUP that moving a shrinkage prism in laboratory (with small impacts associated to picking up and dropping) may sometimes permanently shift the measured strain in the embedded strain gauge by more than 10$\mu\varepsilon$. It is plausible to postulate that the vibration of the specimen can somehow either re-arrange the internal connection with the strain gage, or alternatively the resonant frequency of the string is changed by the externally induced strong vibration (causing for example a slight modification in the tension of the string, with the consequent change in its resonant frequency even though no length change occurs). So, it would be plausible to consider that an analogous, but much stronger, interference to the sensors in the dam may be occurring due to the activities that occur immediately before and during casting of Phase 14, such as: influence of a diesel powered electricity generator that is usually placed on top of each recently cast surface of concrete to prepare for the next phase in order to power several electrical devices, the water jets that are used to clean the dam's surface, or even the heavy-duty vibrating devices used during casting. This line of thought is corroborated by the fact that sensors nearer the top surface and above tubes 1 and 3 of Phase 13 (over which the diesel generator was placed) being more affected by measured strain shifts than those sensors located near the bottom boundary (CM1) or near the downstream face (CM4, CM5 and CE3 – as shown in the following). The hypothesis that some sensors may have been damaged or misplaced during casting operations because of contact or proximity with the heavy duty vibrating device should not be ruled out. It is thus deemed valid to ignore the strain shifts observed in many sensors in the period surrounding casting operations of Phase 14, for the sake of interpreting the coherence with the numerically simulated strains.

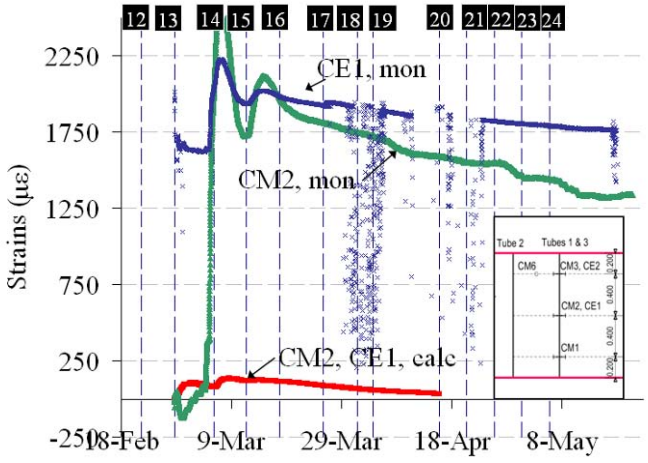

Figure 6.77: Monitored and calculated strains for CM2, CE1

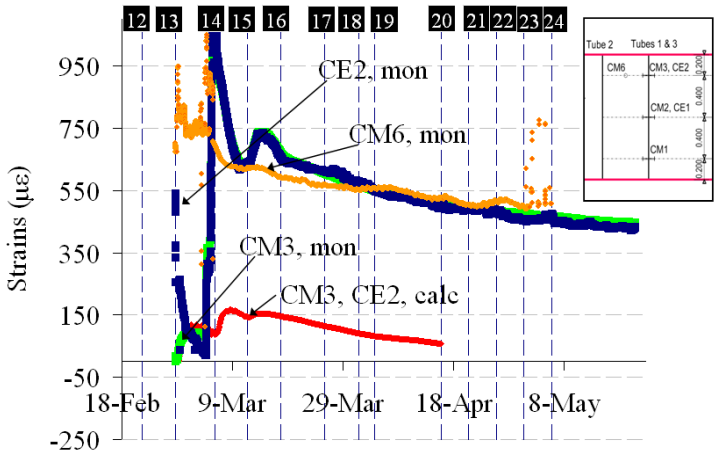

Figure 6.78: Monitored and calculated strains for CM3, CE2

Regarding the strain sensors in the vicinity of the downstream surface of the dam, and focusing initially on the CM4 sensor (Figure 6.79), the observed coherence was excellent, except for the slight underestimation of peak deformation. For the case of sensors CM5 and CE3 (Figure 6.80), the ascending branch of the strain development before casting of Phase 14 was well reproduced by the numerical model, however, the descending branch was underestimated (even though the measured values of CM5 and CE3 are not totally coherent with each other at this stage, they both exhibit a stronger overall strain descending trend than that of the numerical simulation). The highest differences between calculated and monitored strain evolution occur in phases where the differences between calculated/monitored temperatures were already negligible (see Figure 6.73). The quality of coherence with monitored on CM5 and CE3 is actually quite similar to that observed for CM1 (see Figure 6.76), with the reasons for the deviation being probably of the same origin.

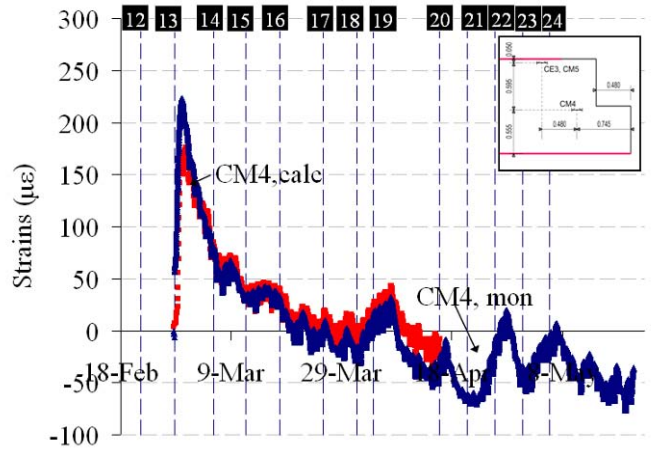

Figure 6.79: Monitored and calculated strains for CM4

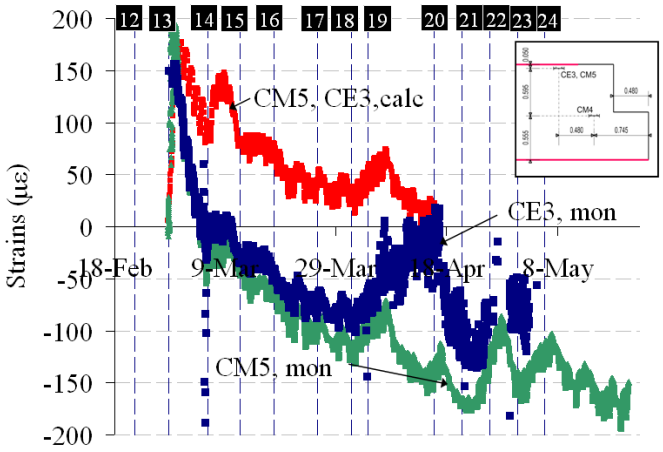

Figure 6.80: Monitored and calculated strains for CM5, CE3

Overall, it is well known that strain measurement is a much trickier issue than temperature measurement. In fact, the confidence in measured strains is lower than the case for temperatures, as there were redundant strain sensors in similar locations meant to validate each other, and instead they ended up casting doubts upon the strain measurements, even on places where only a single strain sensor was placed.

Monitoring doubts apart, the overall strain development tendency has been well captured by the numerical model, and in some cases the whole strain evolutions were very reasonably predicted, as for the case of sensors CM4 and CM1, and the beginning of sensors CM3 and CM5. Bearing in mind the complexity of the construction phasing and phenomena involved, as well as the simplifications underlying the numerical model, it can be argued that a reasonable accuracy has been reached in the numerical simulation, conducting to a good confidence in the stresses calculated from the model.

6.3.9.2 Calculated stresses in the dam during construction

This section focuses essentially on commenting the adequacy of the adopted construction sequence and concrete composition, in view of the environmental conditions encountered on site. For such purpose, and bearing in mind that most of the validations were made for Phases 12 and 13, description of stress development will be centred also in these phases, emphasizing its relationship with the corresponding temperature development. Attention is drawn to Figure 6.81, where temperature and stress σ_x (see axes definition in the figure) maps are depicted for several instants of Phases 12 and 13. The discussion of stress development is also supported by the calculated stress evolution for a set of six points along tubes 1 and 3, as identified in Figure 6.82: three points in Phase 12 (12.b near the bottom of the phase, 12.m at mid-height and 12.t near the top of the phase), and three analogously positioned points in Phase 13 (13.b, 13.m and 13.t). Comments to the mentioned figures are made stepwise in the following:

- Phase 12, t=1h – Concrete of Phase 12 is placed at 15°C. The initial σ_x stresses are 0MPa.
- Phase 12, t=41h – Concrete of Phase 12 reaches temperatures neighbouring 30°C in the interior areas (temperature bubble in Phase 12, as opposed to the temperature bubble that exists in the underlying concrete of the previous phases), causing compressive stresses in the hotter areas, due to the partially hindered expansion, that

reach ~0.7MPa, as it can be observed in points 12.m and 12.b of Figure 6.83. The areas near the top (12.t) do not reach the same temperature levels, thus not having the same level of compression associated to hindered expansion. Tensile stresses arise associated to environmental effects, such as diurnal cycles of solar radiation and night radiation cooling, as well as environmental temperature, as can be seen in Figure 6.83.

- Phase 12, t=71h – Cooling of the concrete of Phase 12 from top causes its temperature bubble to migrate towards temperature bubble of the underlying concrete, and eventually merge with each other. The compressed areas in Phase 12 accompany this migration downwards, as can be confirmed in Figure 6.83: the σ_x stress in point 12.m, which was the maximum compression at t=41h, becomes now lower than the σ_x compressive stress in 12.b. However, both of them have a tendency to become lower because of the cooling process of this casting phase. Point 12.t tends to migrate towards tensile stresses, having however strong daily oscillations, as described previously. The normal stresses developed in this surface layer are more related to external environmental effects (solar radiation, evaporative cooling, night cooling and environmental temperature) than to the heat of hydration phenomenon itself, because the cooling of the inner parts of Phase 12 should conduct the top surface to compressive stresses, which is not the case in this figure.
- Phase 12, t=136h – Last instant of Phase 12, with stress evolutions maintaining the same tendencies reported in the previous commented instant (t=71h). The continuing of diminishment of compressive σ_x stresses in points 12.m and 12.b even induces point 12.m to endure tensile stresses of about 0.2MPa at the end of the phase. The near surface point 12.t endures tensile or compressive stresses according to the environmental effects, having reached a maximum tensile stress of 0.6MPa near the end of Phase 12.
- Phase 13, t=1h - Concrete of Phase 13 is placed at 15°C. The initial σ_x stress is 0MPa. No sudden changes in temperatures and stresses are detected at this stage, as expected.
- Phase 13, t=41h – A very similar process to the one described for Phase 12 at t=41h occurs, with most concrete of Phase 13 enduring compressive stresses associated to the partially hindered expansion (see Figure 6.84). It is now interesting to observe the consequences on the development of stresses in the concrete of Phase 12. The top part of Phase 12 (around point 12.t) endures a temperature increase associated with the heat conduction from Phase 13, while the neighbouring areas of 12.m and 12.b are not being heated and keep the slow process of cooling. For this reason, the σ_x stress development at points 12.b, 12.m and 12.t since the beginning of Phase 13 (Figure 6.83) can be easily understood: 12.t is located in a area of concrete under rising temperature, meaning that it will try to expand. Being this expansion hindered by the underlying concrete (that encompasses 12.m and 12.b), point 12.t will endure compressive stresses, while 12.m and 12.b will endure tensile stresses (more severe in 12.m, with a maximum of ~0.74 MPa). The described process exists during the rising temperature period of Phase 13, from t=0h until t~41h.
- Phase 13, t=171h – End of Phase 13, corresponding to a post-peak temperature period in which some cooling already occurred. The temperature and stress development in Phase 13 until this stage can be described in the same manner it was discussed for

Phase 12. Cooling of the concrete of Phase 13 at a faster rate (and with a higher temperature drop) than that at which the cooling of Phase 12 is occurring causes the stress development tendency at points 12.t, 12.m and 12.b to be towards compressive stresses. As a consequence, at the end of Phase 13 the tensile σ_x stresses at points 12.m and 12.b are almost dissipated, and point 12.t is enduring compressive stress of about 1MPa.

The process that has been described for interaction between different phases occurs in a quite similar fashion throughout the whole construction, with some differences as the environmental conditions are not always the same, nor are the timings for construction. The stress development of the six control points discussed until the end of Phase 19 is shown in Figure 6.85: it can be observed that the σ_x stresses in the control points of Phase 12 are still affected during construction of Phases 14 and 15, even though the influences are quite lower than that of Phase 13. The σ_x stresses of all the six points are relatively stabilized after Phase 16, with tensile stresses lower than 0.4MPa.

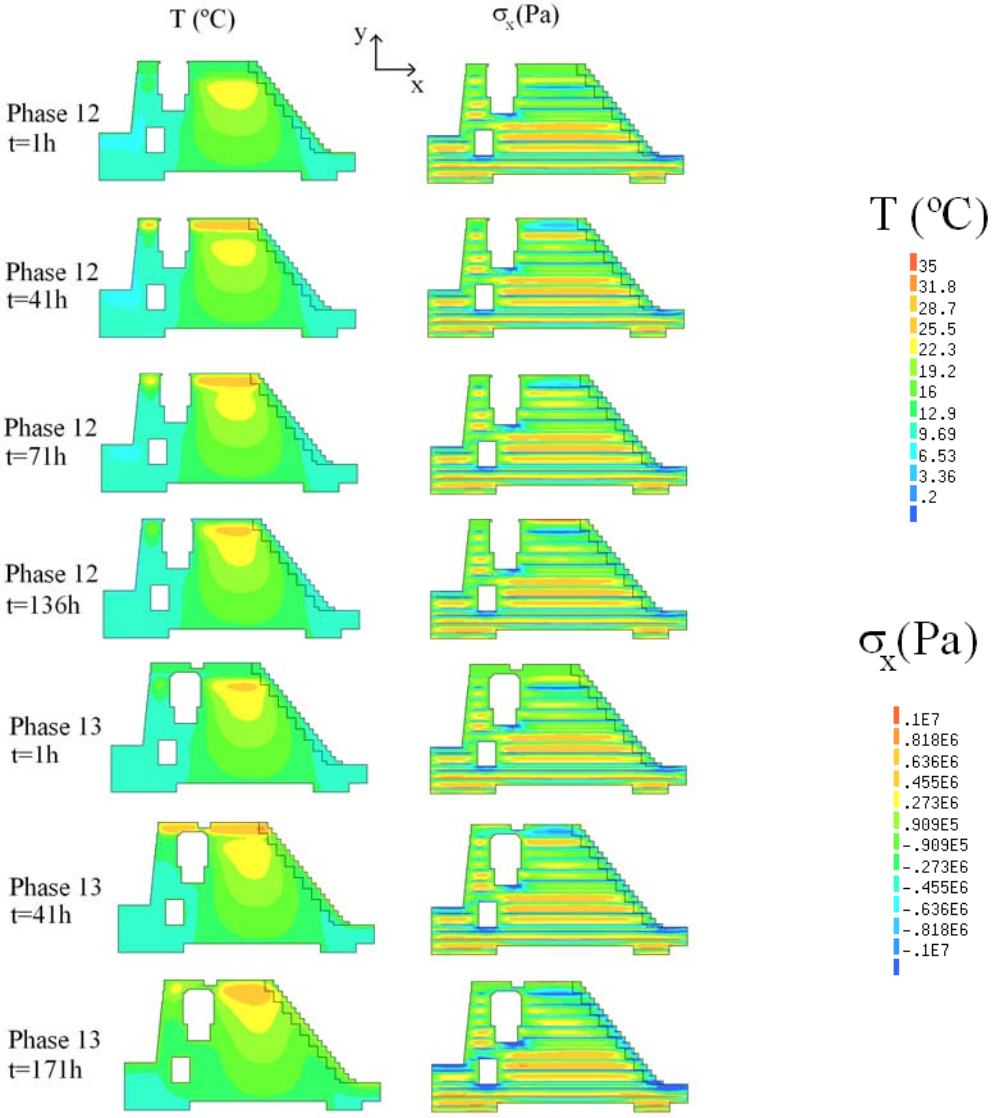

a) b)

Figure 6.81: a) Temperatures and b) σ_x normal stresses at several instants of Phases 12 and 13

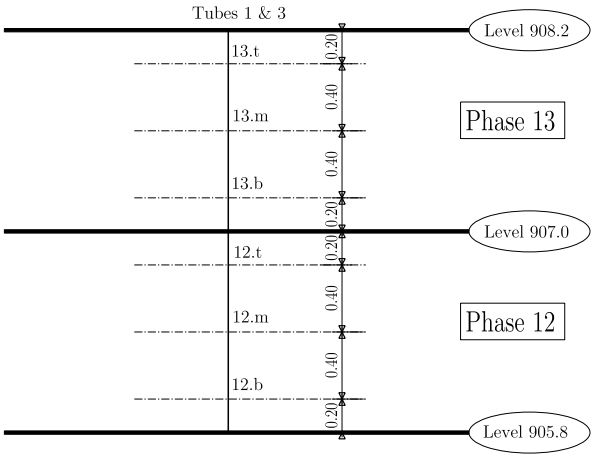

Figure 6.82: Naming convention for the points where stresses are to be discussed

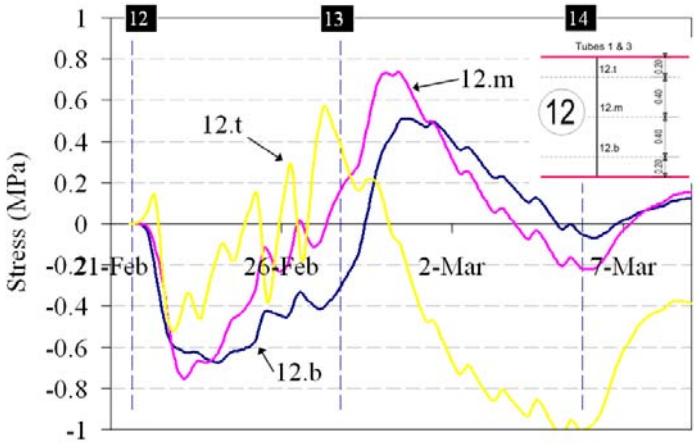

Figure 6.83: σ_x normal stresses for 12.b, 12.m and 12.t until the end of Phase 14

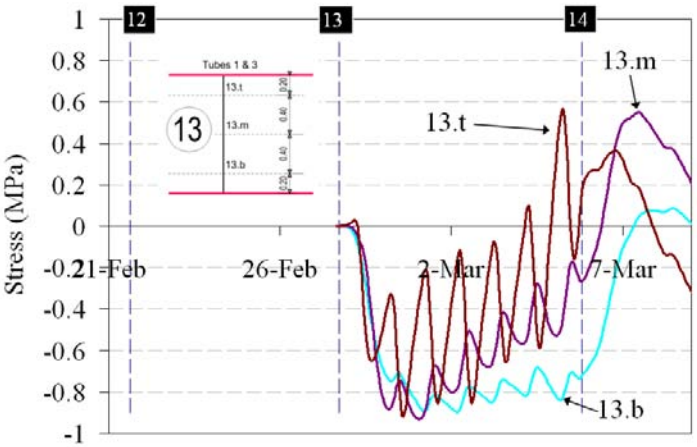

Figure 6.84: σ_x normal stresses for 13.b, 13.m and 13.t until the end of Phase 14

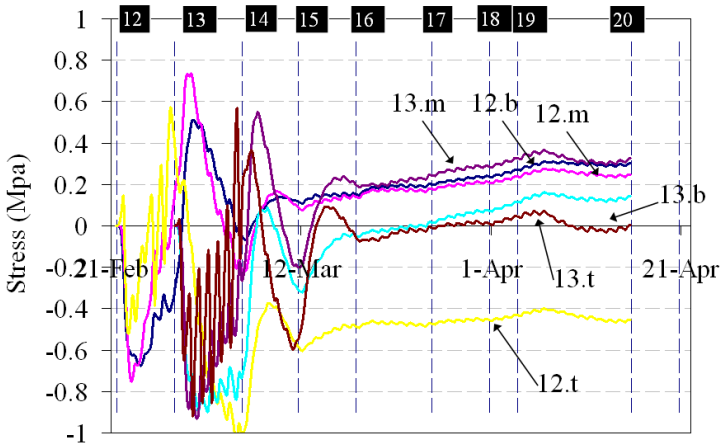

Figure 6.85: σ_x normal stresses for 12.b, 12.m, 12.t, 13.b, 13.m and 13.t until the end of Phase 19

Given the fact that so far the discussion has been centred in σ_x normal stresses in direction X, it is interesting to observe the map for these stresses at an advanced stage of calculation, such as the end of Phase 19 – see Figure 6.86a. Focusing on the tensile stresses, which are particularly interesting for the analysis of cracking risk, it can be seen that the highest stresses are occurring in the boundaries of the first three phases, as well as in the cores of some of the subsequent phases. Particularly high stresses seem to be occurring in Phase 13 at the concrete existent between the two gallery openings. This will be discussed further on when principal stresses are analyzed.

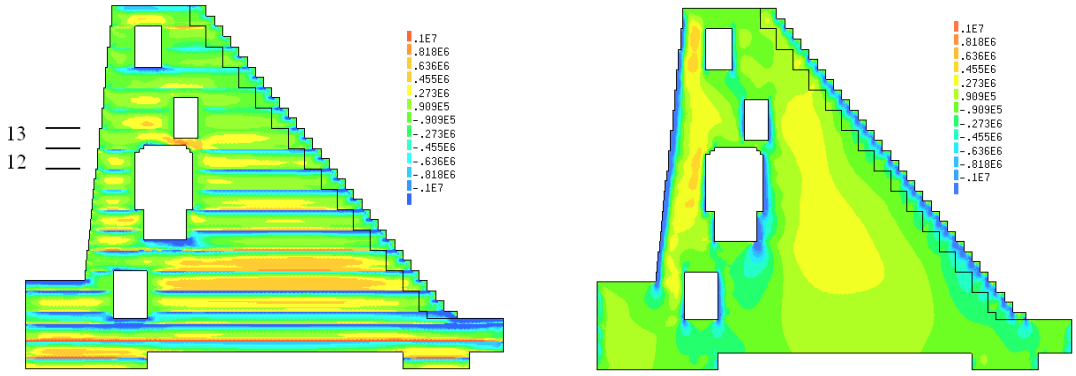

Figure 6.86: Normal stresses the end of Phase 19 (Pa): a) σ_x ;b) σ_y

Attention is now given to the normal stresses σ_y along the Y direction exclusively due to the effect of self-induced thermal stresses (self-weight disregarded). The map of σ_y stresses at the end of Phase 19 is shown in Figure 6.86b, concerning which some interesting observations can be made: outer surfaces are enduring compressive σ_y stresses, while the inner core is generally in tension. Even though these σ_y stresses are rather low (tensile stresses below 0.5MPa, which are partially cancelled by self-weight effects; compressive stresses below 1MPa), it is interesting to analyze the reasons for their development. The observed behaviour is actually consistent with that of a massive concrete body after cooling: the core, which has reached higher temperatures than the surfaces, tends to cool more than the surface, and therefore its contraction is hindered by the lower contraction

of the surface areas. This causes the surface to become compressed, and the core to endure tensile stresses. The fact that surface areas endure compressive stresses associated to heat of hydration in the dam is a favourable effect, as it partially cancels the effect of drying shrinkage.

For evaluation of cracking risk of concrete, the map of maximum principal stresses at the end of Phase 19 is depicted in Figure 6.87. The areas defined by this map clearly reflect the previous maps of stresses σ_x and σ_y, with overall predominance to stresses in the horizontal direction. Maximum tensile stresses are always below 1MPa, which points to a low risk of cracking due to heat of hydration in this structure, as the tensile strength of D200 at 1.5 days is 0.8MPa (age at which concrete in the dam did not yet endure such level of tensile stresses), evolving to 1.7MPa at 4.5 days and 2.4MPa at 28 days. Even though these stresses are relatively low, the development of principal stresses in the point labelled as F in Figure 6.87 is interesting to comment: this point is situated in a part of the dam's concrete between two galleries, in a slice that is only 0.5m thick. The differential development of heat to the left and to the right of this connection could be bound to cause severe stresses in this small area. For interpretation of how stresses develop in point F, Figure 6.88 depicts its maximum principal stress evolution (see also Figure 6.23 where the construction phasing is defined). During Phase 13 point F endures negligible principal stresses, because of the low temperatures achieved, together with the fact that its temperature evolution roughly followed the ones of the dam bodies to the left and to the right of the connection. During Phase 14 a similar interpretation to that of Phase 13 can be made.

However, a dramatic change occurs with the casting of Phase 15 that re-connects the left and right parts of the dam, creating a concrete slice than spans the entire dam's width. Expansion of the concrete block pertaining to Phase 15 is in part hindered by the slice that contains F; this hindering causes tensile stresses to arise during the heating period of Phase 15, reaching almost 2MPa (which represents a non-negligible risk of cracking – see Figure 6.88). The process is slightly reversed when Phase 15 starts its cooling process, but is again intensified after casting of Phase 16, reaching a 2MPa tensile stress again. The effect of further casting sequences becomes more attenuated, and at the end of Phase 19 the calculated principal tensile stress amounts to a mere 1MPa.

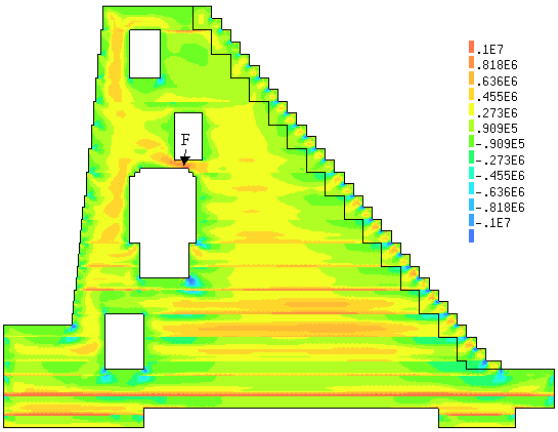

Figure 6.87: Maximum principal stress at the end of Phase 19 (Pa)

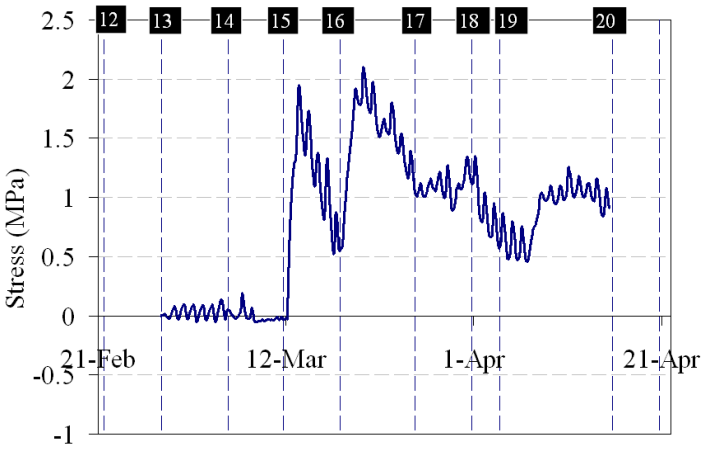

Figure 6.88: Maximum principal stress in point F

In view of what has been discussed, it can be concluded that the part of this dam under study exhibits a relatively low cracking risk, exception made to the thin slice of concrete that has just been discussed.

Final remarks regarding the study of the dam (monitoring campaign and experimental simulations are relegated to the next chapter of this thesis (Conclusion).

Chapter 7

Conclusion

7.1 General remarks

7.1.1 Introduction

In this thesis, a methodology for thermo-hygro-mechanical analysis of real-scale concrete structures has been described, with strong emphasis on the use of feasible material models, as well as a sustainable set of experiments for adequate material characterization. Several experiments, numerical implementations and corresponding simulations were described throughout the thesis, and the present section highlights the main conclusions of the developed work, which are presented chapter-wise as follows.

7.1.2 Thermal problem

The establishment of sustainable parameter estimations for the numerical models led the developed work to significantly invest on one of the most important factors for temperature development in concrete at early ages: the heat generation due to cement hydration. An extensive experimental campaign on several cements produced in Portugal was undertaken, in terms of the hydration heat release, using the technique of isothermal calorimetry (JAF) for hydrating test temperatures ranging from 20°C to 60°C. By using an Arrhenius-type law to reproduce the hydration heat release for each cement paste, the involved parameters were evaluated and their relative importance was discussed. It was found that the total developed heat correlated well to what would be expectable, increasing with the growing cement fineness, and decreasing as Portland cement is partially substituted by fly-ash or limestone.
Evolution of the degree of advancement of hydration was found to be relatively homogeneous for the various cements analyzed, confirming the feasibility of existing empirical equations for this variable.

The normalized heat generation rate was found to be non-unique for each cement. It was in fact temperature dependent, revealing larger variations in experiments performed at temperatures higher than 40°C, and for blended cements. For lower temperatures, and particularly for ordinary Portland cements, it was found to be reasonably constant in the performed experiments.

The apparent activation energy was evaluated within several temperature intervals: [20°C-30°C], [30°C-40°C], [40°C-50°C] and [50°C-60°C]. Consistently with previous researches, it was observed that the activation energy decreased with the reaction advancement, and that at lower temperatures (below 40°C) it was more homogenous than for higher temperatures. Furthermore, blended cements tended to have less homogeneity in this property.

As a general conclusion, fitting the adopted Arrhenius-type law to the experimental results became rather more difficult for temperatures above 40°C, particularly for the apparent activation energy. This should be appropriately taken into consideration when performing numerical predictions of temperatures in concrete structures during hydration using this Arrhenius-type law: if temperatures in concrete surpass 40°C for a significant period of time, accuracy of the numerical results will diminish considerably.

An experiment on a concrete hardening prism was conducted with two main objectives: (i) use of the experimental technique of thermography for monitoring concrete temperatures during hydration of cement, checking its feasibility for this kind of applications; (ii) use of the obtained results for validation of the implemented FE code for prediction of temperature development in concrete structures at early ages, accounting for cement heat of hydration. For the mentioned purposes, a concrete specimen with dimensions 40x40x40cm^3 was cast, and its temperature development was simultaneously monitored by internal sensors, as well as by a thermography camera. Coherence between data collected using the two different measuring techniques allowed strong confidence in the results obtained through thermography for hardening concrete. This technique reveals a strong potential, as the 640x480 pixel image that it collects at each time may be considered as an instant monitoring of temperatures at all the 307200 pixels that compose the image; such richness of information about temperatures cannot be obtained using conventional thermal sensors. The results obtained with the thermography equipment, together with the embedded temperature sensors, were used for validation of the implemented FE thermal code, with the corresponding comparisons allowing increased confidence in the numerical tool.

By using the thermal FE code implemented within the scope of this thesis, a numerical essay on the influence of steel reinforcement on the temperature development of hardening concrete was conducted. In fact, the effect of reinforcement on temperature development is often overlooked without any specific justification. To better clarify this aspect, a numerical model of a slim concrete element with explicit modelling of steel rebars was conducted, confirming that reinforcement has an almost negligible contribution to the temperature development in concrete.

Studies regarding the thermal problem were further deepened, by performing a sensitivity analysis to the effect of considering variable thermal conductivity and specific heat for concrete along hydration, reflecting the evolving nature of concrete during early ages. It was found that the effect of variable thermal conductivity on temperature development

was negligible, whereas variable specific heat had a relevant influence on computed temperatures.
Experiments regarding the effect of solar radiation on the surface temperature of a small concrete cube were conducted, allowing validation of the numerical models for sun radiation implemented in the scope of this thesis. Comparison of numerical results for the same case, with and without consideration of solar radiation, led to the conclusion that disregarding this phenomenon in outdoor structures may lead to significant errors in the temperature estimation near the surfaces of concrete.
Experiments in a wind tunnel were conducted to check feasibility of usually recommended values for boundary coefficients depending on wind speed. It was shown that the obtained coefficients are much dependent on the conditions under which the experiment is conducted, and the height at which wind speed is measured: the phenomenon of convection heat transfer is quite complex, and strongly depends on microclimatic effects related to the air flow streamlines and turbulence around the surface in which heat transfer is under study. Nonetheless, it was confirmed that the observed values lie within general tendencies and scatter reported by other authors on the same subject.

7.1.3 Moisture problem

Models for simulation of moisture fields in concrete are far more controversial than those related to temperature simulation. Furthermore, the experimental procedures for moisture content or internal relative humidity determination are more difficult to conduct, less precise and take longer than temperature measurements in concrete. Because of that, in this thesis there was no experimental work worth mentioning as far as concrete moisture content is concerned. Therefore, the parts of this work devoted to moisture are mostly linked to a critic review of existing modelling strategies, as well as consubstantiating modelling simplifications for the models to be used. A relevant part of the research was also devoted to discussing the relationship that exists between internal humidity of the cementitious material and the corresponding infinitesimal “free” shrinkage, bearing in mind important aspects such as the restraint provided by aggregates and microcracking effects.
The selected model for moisture transport, based on internal relative humidity as the driving potential, was described and implemented in a 3D FE MATLAB code, with its validation being performed against experimental results. It is worth mentioning that self-desiccation related internal moisture losses of concrete were disregarded, limiting the application of the numerical model to Normal Strength Concrete, which in Portugal represents more than 90% of actual construction.

7.1.4 Early age concrete as affected by environmental issues: use of a multi-scale model

Moisture loss from mortar specimens and its sensitivity to several environmental and curing conditions was investigated, as well as the evaporative cooling phenomenon. Experiments on the combined effect of environmental temperature, relative humidity and

wind speed were conducted, revealing the quantitative influence of these factors on the moisture loss from mortar specimens, with and without curing measures.

Similitude of evaporation from a water pan and from a saturated mortar specimen during the first stage of drying, reported in past researches, was also confirmed in this research. Transition from the environmentally to the diffusion controlled evaporation stages in cementitious materials has been identified as a possible criterion to establish the instant when the surface hydration starts to be hindered due to water shortage. For mortar specimens exposed to drying immediately after casting, duration of the environmentally controlled evaporation is strongly dependent on wind conditions: the higher the wind speed, the sooner the transition to diffusion controlled evaporation takes place. Yet, if curing measures are undertaken, such as sealing until specified ages, the pore structure of mortar at the time of exposure becomes denser and more water is already consumed in the hydration reactions, which reduces the influence of wind speed on the mentioned transition. From then on, the water loss from specimens becomes diffusion controlled, and the governing phenomenon is the vapour pressure gradient between the interior of the specimen and the environment. Therefore, after adequate curing, moisture loss and the inherent drying shrinkage can be considered independent of wind speed. Also, considering that after adequate curing the water loss from specimens is diffusion controlled, and bearing in mind the identical results obtained for specimens with exposed surfaces parallel and perpendicular to the wind stream, it was concluded that moisture loss at this stage is not only independent of wind speed, but also seems independent of wind direction.

The evaporative cooling phenomenon from cementitious materials was experimentally confirmed in this research, and the ~8°C temperature drop observed near the surface of the studied specimen just after sealing removal was important enough to justify further investigation on this topic, object of very few studies up to now, but that may be the cause for thermal cracking upon formwork removal in hot and dry environments.

In this thesis, a formulation was proposed to reproduce numerically the boundary conditions between cementitious materials and the environment, applicable for predicting early age drying-induced moisture losses under arbitrary conditions of temperature, relative humidity and wind speed. It expresses evaporation at the boundary as linearly dependent on the water vapour pressure difference between the material exposed surface and the environment, and it uses a moisture emissivity coefficient that accounts for the influence of wind speed. This coefficient can be easily determined by monitoring weight losses from water pans placed on the environmental conditions under study. The computational code (DuCOM) used in this part of the research to determine the thermal and moisture fields on mortar or concrete specimens accounts for the simultaneous densification of the pore structure and the moisture shortage in the near surface areas, due to both autogenous water consumption and evaporation to the environment. So, implementation on that code of the novel moisture boundary conditions developed allows evaporation from freshly cast cementitious materials to be consistently reproduced, including its deceleration as hydration reaction progresses.

In addition, a heat/moisture boundary formulation was proposed to account for the evaporative cooling phenomenon, which occurs just after formwork removal. It basically consists in using the computed evaporative moisture losses to calculate the heat removal from the mortar surface, upon knowledge of the latent heat of evaporation of water. The

computed heat removal is thereafter prescribed as a thermal flux at the boundaries of the DuCOM FE mesh, and so an interaction between the moisture and temperature fields is considered in the numerical simulation of evaporative cooling. Adequacy of the new boundary conditions was checked by reproducing numerically the experiments for cementitious materials reported previously. Agreement between the numerical predictions and the experimental results was fairly good in almost all the situations.
Three sensitivity analyses were then presented. In the first one, concerning the relative importance of wind speed and the water vapour pressure difference between the exposed surface and the environment, it was concluded that the latter driving potential is the dominant issue in long term water losses from cementitious materials, being relevant even when evaporation is diffusion controlled (unlike wind, whose influence becomes almost negligible). In the second sensitivity analysis, relevance of evaporative cooling was numerically investigated under several environmental conditions and ages of exposure, leading to the conclusion that for real concrete structures, the temperature drop due to this phenomenon becomes specially relevant when formwork is removed while concrete is still hotter than the environment.
In view of fulfilling a concrete durability target, a methodology for quantifying the necessary duration of the moist curing period was presented. Such methodology is based on the percolation threshold concept (which many authors tentatively recommend to be 0.2) for assuring sufficient imperviousness of concrete cover. Through numerical simulation of evolution of the concrete pore structure in two exploratory examples (using DuCOM), the potential of this methodology was demonstrated.

7.1.5 Thermo-hygro-mechanical framework

The numerical analyses of stress fields in concrete since early ages were conducted by coupling the mechanical models of DIANA software with two modules created in the scope of this thesis for temperature and moisture field computation.
As a preparation for the in-situ monitoring carried out in Chapter 6, the performances of vibrating wire strain gages with casings of different stiffnesses (metallic and plastic) were evaluated, through measurements on a concrete prism tested in laboratory since the instant of casting. It was shown that the plastic vibrating wire strain gage, of very low stiffness, has the advantage of quicker solidarization to concrete, but exhibits a higher thermal sensitivity in the pre-solidarization phase when compared to the metallic vibrating wire strain gage, leading to higher total strains in the heating period. Therefore, for in-situ monitoring works that involve early age concrete strains it is recommended to use metallic vibrating wire strain gages, as they are more robust and present lower temperature sensitivity. However, the plastic vibrating wire strain gages are important for defining the instant of solidarization to concrete of the metallic vibrating wire strain gages, such instant being defined when the two types of gages start to respond with similar tendencies. Furthermore, the possibility to obtain an upper-bound of the concrete total strains (coincident with the signal directly provided by the metallic sensor), and also a lower-bound (by subtracting to the original metallic gage signal the strains recorded until the solidarization to concrete) was shown.

A well succeeded thermal analysis of the same concrete prism was described, with the temperatures predicted numerically and the ones recorded by the sensors according fairly well. The adopted thermo-mechanical model also predicted the total strains developed in concrete during the early ages. During the cooling period the numerical results showed coherence with the development tendencies observed in the measurements from vibrating wire strain gages. Although the maximum total strains recorded by the sensors during the heating phase were superior to the initial numerical predictions, it was demonstrated that this discrepancy was specially due to the reduction in the concrete thermal dilation coefficient, which takes place during the first 5-10h since concrete casting, a feature that is usually not considered in the numerical simulations, as it is difficult to characterize experimentally.

An experimental campaign using the restrained concrete ring test was described, discussing several aspects related to its practical execution. With the basic information extracted from the experimental ring testing campaign, numerical analyses were undertaken, in order to predict both the temperature and strain evolutions on the monitored steel rings. A good coherence was observed when the numerical results were compared with the actual measured observations. However, additional conclusions could have been drawn if the restrained concrete rings had cracked. The positive outcome of this experimental characterization technique, and the low cost of the entire setup, provide for good perspectives for its practical use in the quantitative evaluation of cracking potential of concrete at early ages.

The work conducted in this research involves a proposal of an innovative technique to monitor the evolution of the E-modulus of cementitious materials since casting, based on the non-destructive technique of ambient vibration testing. Details were provided on the first pilot experiment for a concrete specimen. The basic idea of the experimental technique consists of continuously monitoring the first natural frequency of a simply supported composite acrylic/concrete beam using modal identification techniques. The outcome of the several conducted experiments led to the conclusion that this kind of experiment is quite reliable, and leads to rather satisfactory and promising results, provided that the supporting conditions of the beam are well defined. This experimental technique reveals itself as being a real alternative to currently existing non-destructive techniques for E-modulus evaluation (ultrasound pulse velocity or resonant frequency methods on cylinders), allowing the measurement of E-modulus since casting and providing valuable information about the structural setting instant, as well as clear information about the evolution of E-modulus while concrete is not 'de-mouldable', where classical resonant methods fail.

The experimental technique for continuously monitoring E-modulus of concrete has been further extended for cement paste by changing the geometry of the specimen to a smaller size (less than 2cm diameter and 45cm long) and the structural system, which became a cantilever. By using the analytical equation for the cantilever vibration, the E-modulus of the paste may be computed directly from the identified first natural frequency of the cantilever, which allows obtaining curves E-modulus *versus* time for the studied mixes. In this work eight batches of cement paste were described and tested, in order to ascertain important issues such as the repeatability and reproducibility of the experiment, as well as its capacity to monitor and clearly identify the effects of admixtures (both accelerating

and retarding) in the hardening behaviour of the cementitious materials. Results of the experimental campaign revealed this methodology to be quite promising in materials research, given its capabilities in quantitatively measuring the structural setting time, as well as the stiffness evolution of the material.

The work regarding the mechanical problem was further extended by performing a set of numerical sensitivity analyses, in regard to the effect of mechanical input parameters (concrete properties) on the obtained results. The studied concrete properties were the E-modulus, the Poisson's coefficient and the creep parameters for the Double Power Law. Regarding the E-modulus, comparisons were made between the usage of typical Eurocode 2 evolution curves, or realistic curves as the ones obtained through the ambient vibration tests, which differ essentially in the first hours after casting. It was concluded that the initial over-estimation of stiffness provided by the Eurocode 2 approach ends up introducing non-negligible errors in the initial stresses. Regarding the sensitivity analyses conducted to check the effect of variable Poisson's coefficient along hydration (which is often overlooked in numerical analyses), it was concluded that this parameter has negligible influence on computed stresses and strains at the early ages of concrete. Finally, the following two main conclusions apply to the influence of concrete creep: 1) not considering the effect of creep can lead to extremely different stress predictions, which are bound to be erroneous; 2) the effect of dramatic variations in creep parameters does not reflect itself in the same drastic fashion in the computed stresses, indicating that parameter choice in creep behaviour may not be a critical issue for the quality of stress estimations, as long as the specific creep curves of the used model fairly resemble the ones pertaining to the mechanical characterization of the material.

Two application examples of the thermo-hygro-mechanical framework, accounting for both the self-induced effects due to cement heat of hydration and the development of non-uniform drying shrinkage strains, were presented with the purpose of showing the plausibility of the obtained results, together with its potential for application in real structures: an unrestrained drying shrinkage prism and a RC slab subject to the combined effect of self-induced stresses and externally applied loads. The results obtained with the shrinkage prism allowed for the quantification of the non-uniform residual stresses associated to heat of hydration and drying shrinkage, with significant variations in stress magnitude, including sign reversals. The time evolution of computed strains in the prism revealed quite coherent with the shape of predictive curves of Eurocode 2, thus confirming the plausibility of results. The analysis of the RC slab, with due consideration of cracking and softening behaviour of plain concrete, as well as tension stiffening effects, allowed interesting conclusions to be drawn in regard to the effect of self-induced stresses on the behaviour of the structural element, when load is applied at a certain age (until which the element was only affected by self-induced stresses). It was observed that for loads applied at instants when important self-induced stresses were already installed (with strong self-induced surface tensile stresses), the structural response of the slab is significantly different from that corresponding to the absence of self-induced stresses, or even that corresponding to a simplified approach of considering uniform shrinkage strains. Bearing in mind the overall plausibility of the obtained results, the potential capacities of this framework for assessing actual stresses in concrete (including explicit modelling of

self-induced effects) seem promising for analysis of real concrete structures, with planned validation in near future research.

7.1.6 Field applications

A case study for the cement hydration induced thermal stresses was presented, concerning a large RC foundation for a wind tower, whose temperature development at early ages was monitored. Numerical predictions of the temperatures in the RC foundation since casting until the age of 30 days were corroborated by the monitoring campaign results, which provided confidence in the adopted models and parameters. The importance of the underlying granite supporting the RC foundation was highlighted, and its thermal storage effect was identified, reducing the concrete temperature gradients near the foundation bottom face. Furthermore, the embedded steel ring of the tower, included in the numerical analyses, was shown to have a relevant influence on dissipating the internal heat from the foundation core towards the environment. Thermal stresses in the foundation were interpreted in view of the spatial and temporal evolutions of the temperatures: during the heating phase tensile stresses arose on the foundation surfaces, whereas compressive stresses occurred in the core; conversely, during the cooling phase the surface areas became compressed and the core endured tensile stresses. This pointed to a significant cracking risk in both the top and lateral surfaces of the foundation (whose effects could be minimized by the compressions that arose during the cooling phase), and to a tensile stress build-up in the core, although not enough to induce cracking. In terms of stresses the existence of the embedded steel ring, as well as the underlying granite, proved to be favourable, leading to reduced cracking risks in their vicinities.
The final application in this thesis involved a monitoring campaign and an in-depth material characterization for a concrete gravity dam, with the purpose of validating the numerical predictive models of temperatures and stresses in concrete structures since early ages. These models explicitly considered the heat generation potential of concrete, based on parameters obtained from isothermal calorimetry testing, as well as other phenomena which are often overlooked, such as solar radiation, evaporative cooling and night radiation cooling. The interest of this real-size and complex application was increased by the fact that internal galleries were relevant in the studied cross-section of the dam, which were in turn explicitly considered in the numerical models. The observation of both monitoring results and numerical simulations allowed for the conclusion of the following:

- The numerical models proved to have good capabilities in terms of temperature predictions, particularly if the effects of solar radiation and losses by cooling (evaporation, night cooling and water run-off) are accounted for. However, the complexity and quantity of phenomena and construction phasing involved lead to the conclusion that exact temperature predictions were impossible, due to the unpredictable character of meteorological conditions (along with micro-climatic effects), as well as the unfeasibility of exact quantification of base parameters for a wide range of phenomena (as it is the case for evaporative cooling and the quantity of rainwater). However, even though not exact, the available temperature predictions

have revealed to be quite satisfactory, both in terms of general tendency, as well as peak values.

- Together with the good simulation of the temperature field, the detailed mechanical material characterization conducted allowed for reasonably good predictions for the concrete stresses and strains, reflected in the satisfactory coherence found between monitored and simulated results.
- The risk of thermal cracking of concrete has revealed to be quite low in this particular application, which may point to the possibility of having built this dam with a different construction scheme, with less construction phases.

The confidence in the adopted models allows the conclusion that the adopted methodologies have potential for providing good quality predictions of temperature and stress fields in concrete structures, and may play an important role in the support to decision making in what concerns to construction phasing, or even mixing parameters for concrete.

7.2 Known limitations and prospects for future developments

The work conducted within this thesis represents a contribution to the numerical simulation of concrete structures, with explicit account for self-induced stresses of both thermal and hygral origin. By no means can any of the covered subjects be considered solved or finished, and a list of the acknowledged limitations would be immense. The present section limits itself to the following limitations (and future prospects) considered most relevant:

- Effects of concrete cracking and interface aggregate/matrix have been disregarded in the moisture transport model, as a simplifying assumption. Particularly regarding the influence of cracking on moisture transport, controversial opinions where found in the literature, a reason for which an experimental validation is considered necessary for further progress.
- The moisture transport model adopted in this thesis is based on pore H as the driving potential, assuming a hypothetical isotropic homogeneous material. This is a strong simplification of the actual material, which is composed of a wide range of pore diameters, with water being stored as liquid or vapour, and with simultaneous existence of fully and partially saturated pores. Further experiments are needed to check the possibility of using the H based approach, together with proper material characterization for simulation of moisture transport in actual concrete structures.
- The implementation of the moisture model done in this thesis is valid only for isothermal conditions, which is not realistic in view of real structures. This is a point that requires further improvement, and it may cause a different option to be taken with regards to the driving potential, probably shifting it from pore H to equivalent pore pressure, as the approach used in DuCOM.
- In real outdoor applications, rainfall is known to strongly affect near surface moisture conditions, decelerating the drying process (and consequently the process of drying shrinkage). This effect has not been accounted in the used models, and experimental

work is seen as necessary in exploring this topic, for which no previous research work pertaining numerical modelling was found.

- The thermal effects of night cooling, curing water run-off and rainfall have not been studied experimentally, even though they are acknowledged to be of relevance. This is a topic that deserves further research, in view of improving in-situ temperature predictions for concrete structures.
- The ageing of concrete, which reveals itself as a densification of the pore structure and changes in moisture transport properties, has not been taken into account in the implemented moisture model. This was an option for simplification, which is considered relatively feasible in real structures. In fact, curing procedures and formwork removals usually occur a few days after casting, at a stage where a great deal of the hydration reactions has occurred, motivating that the errors induced by neglecting ageing remain at a relatively low level. However, if moisture losses due to evaporation at very early ages are intended, the implemented model is not valid, thus motivating the necessity for extending its capabilities.
- Based on the lessons learnt from the research work reported in Chapter 4, the situations in which evaporative cooling actually has relevant effect in early temperature development have been established: environments with very high temperature and very low relative humidity, as well as situations in which the formwork is removed while the concrete surface is still much hotter than the surrounding environment. As these situations very seldom occur in European countries, it was decided to leave the phenomenon of evaporative cooling out of the scope of the developed thermo-hygro-mechanical framework.
- Hindering of cement hydration reactions associated to the lack of adequate moisture states in zones near the surface of recently exposed concrete elements has been covered and numerically simulated in Chapter 4. A possible criterion for defining the tie curing procedures has been defined with basis on the percolation threshold concept. This must be considered a preliminary format of the methodology, and proper validations with experiments using durability indexes (such as permeability and corrosion proneness) are necessary in the future.
- The effect of cement hydration hindering mentioned in the previous topic has not been included in the implemented thermo-hygro-mechanical framework. Further experimental work is necessary in this field, to support the implementation of such a model in the macro approach used in the new numerical framework developed for the present thesis.
- Still regarding the differences in properties between the core and the surface areas of concrete, there is an aspect identified in the review conducted by Bentz (2008) that is not usually covered in numerical simulations: the packing of cement particles of freshly cast concrete is different along its thickness due to gravity effects, causing a micro-structural (porosity/density) gradient to occur through concrete elements thickness. This topic deserves further research, in view of assessing the possibility of including its effects in numerical models, with increased realism for cover concrete properties.
- The models, strategies and simplifications adopted throughout this thesis were made in view of Normal Strength Concrete applications. By concentrating only on this type

of concrete, an important simplification could be adopted by disregarding self-desiccation effects in moisture field computations. Future improvements to the moisture model should include experiments and models to account for self-desiccation in the moisture field numerical simulations, thus widening the scope of the framework to High Performance Concrete.

- The field applications concerned in this thesis did not take into account the moisture fields in concrete, with the calculated self-induced stresses being solely related to the heat of hydration. This is not considered a serious flaw because of the types of structures involved: neither the RC foundation nor the concrete dam are usually prone to significant drying shrinkage effects. These drying shrinkage effects are more important in laminar structures such as slabs with strong restraints to deformation (caused by columns or shear walls). It is therefore the future intent of research to apply the thermo-hygro-mechanical numerical framework to an in-situ case of a slab, with the corresponding monitoring campaign including measurements of internal moisture in concrete.
- Regarding the proposed ambient vibration-based technique for continuously monitoring the evolution of concrete E-modulus, it is considered a very promising subject for further developments. Alternative geometries for the experiment are envisaged, as well as further product development for use in both research applications and construction site environment (e.g., as a tool for supporting formwork striking times for concrete, based on stiffness evaluation criteria).
- The variable character of concrete thermal expansion coefficient at very early ages is a subject of great importance for the accuracy of stress predictions. Due to the unavailability of adequate equipment for the study of this parameter, such as active restraint experimental setups with the possibility of imposing temperature to concrete (such as Temperature Stress Testing Machines – TSTM), it was not subject of specific study. However, implementation of a TSTM device for studying this and other relevant issues is intended in the near future.
- The restrained concrete ring test has been conducted for a Normal Strength Concrete. Further tests of the same nature with High Strength Concrete, with higher autogenous shrinkage strains, and eventually leading to concrete cracking, will allow complementary verifications of the numerical tools. Also, a comparison between this cheap and practical passive restraint experiment and the active restraint methods such as the TSTM is intended.
- The numerical simulations performed for the concrete ring test did not take into account the moisture field within concrete. A further step of this study would involve the appropriate additional monitoring tasks to back the choice of parameters for computation of the moisture fields in this test, and their corresponding shrinkage strains.
- The creep model used in stress field computation is a relatively old one: the Double Power Law. It is acknowledged that upon the use of devices such as the TSTM for material characterization, inadequacies might be found in the fits provided by DPL. This topic is to be further studied with recourse to the TSTM to be implemented. Still regarding creep, the topic of temperature dependency is also considered an important issue for future research.

- The extension of the thermo-hygro-mechanical numerical framework to include durability-related issues, such as carbonation, chloride ion ingress, calcium leaching, alkali-silica reactions, among others, seems interesting as a research investment.
- The models for cracking and post-cracking behaviour of concrete under self-induced stresses, associated to thermal and hygral volumetric variations, need to be further clarified and backed by experimental validation. Bond models may be necessary for better simulation of cracking due to self-induced effects.
- The approach adopted for the thermo-hygro-mechanical framework assumes homogenous media. The possibility of investigating the performance of a meso-scale modelling approach that explicitly considers aggregates, and is thus capable of estimating concrete stresses due to aggregate restraint, is intended.

References

AASHTO (1998). Standard practice for estimating crack tendency of concrete. PP34-89.

Ababneh, A., Benboudjema, F. and Xi, Y. (2003). Chloride penetration in nonsaturated concrete. Journal of Materials in Civil Engineering, 15 (2): 183-191.

ACI (2001). Guide to curing concrete. ACI Committee Reports, A. C. Institute, ed.

Akita, H., Fujiwara, T. and Ozaka, Y. (1996). A practical procedure for the analysis of moisture transfer within concrete due to drying. Magazine of Concrete Research, 48 (6): 129-137.

Al-Fadhala, M. and Hover, K. (2001). Rapid evaporation from freshly cast concrete and the Gulf environment. Constr. Building Mat., 15 1-7.

Alberty, J., Carstensen, C. and Funken, S. A. (1999). Remarks around 50 lines of Matlab: Short finite element implementation. Numerical Algorithms, 20 (2-3): 117-137.

Aldridge, L. (1982). Accuracy and precision of phase analysis in Portland cement by Bogue, microscopic and X-ray diffraction methods. Cem. and Concr. Res., 12 381-398.

Almudaiheem, J. A. and Hansen, W. (1987). Effect of specimen size and shape on drying shrinkage of concrete. ACI Materials Journal, 84 (2): 130-135.

Anderberg, A. and Wadso, L. (2008). Method for simultaneous determination of sorption isotherms and diffusivity of cement-based materials. Cement and Concrete Research, 38 (1): 89-94.

Anson, M. and Rowlinson, P. (1988). Early age strain and temperature measurements in concrete tanks. Magazine of Concrete Research, 40 (145): 216-226.

Asamoto, S. (2007). Enhanced multi-scale constitutive model of solidifying cementitious composites and application to cracking assessment of concrete structures., University of Tokyo, Tokyo.

ASTM (1987). C1074-87 - Standard practice for estimating concrete strength by the maturity method.

ASTM (2002). Standard Test Method for Fundamental Transverse, Longitudinal, and Torsional Frequencies of Concrete Specimens.

ASTM (2005). C186-05 - Standard Test Method for Heat of Hydration of Hydraulic Cement.

ASTM (2006). ASTM C341 / C341M - 06 Standard Practice for Length Change of Cast, Drilled, or Sawed Specimens of Hydraulic-Cement Mortar and Concrete. American Society for Testing and Materials

Atrushi, D. (2003). Tensile and compressive creep of early age concrete: testing and modelling. PhD Thesis, Norwegian University of Science and Technology, Trondheim, Norway.

Azenha, M. (2004). Behaviour of concrete at early ages. Phenomenology and thermo-mechanical analysis. (in Portuguese). MSc Thesis, Faculty of Engineering of the Univeristy of Porto.

Azenha, M., Faria, R. and Ferreira, D. (2009). Identification of early age concrete temperatures and strains: monitoring and numerical simulation. Cement and Concrete Composites, 31 (6): 369-378.

Azenha, M., Faria, R. and Maekawa, K. (2007a). Influence of moisture losses at early ages on concrete cover quality: a numerical approach. International RILEM Workshop on Integral Service Life Modelling of Concrete Structures, RILEM Publications.

Azenha, M., Maekawa, K., Ishida, T. and Faria, F. (2005). Heat and moisture transfer between concrete and the environment. LABEST - internal reports.

Azenha, M., Maekawa, K., Ishida, T. and Faria, R. (2007b). Drying induced moisture losses from mortar to the environment. Part II: Numerical implementation. Materials and Structures/Materiaux et Constructions, 40 (8): 813-825.

Azenha, M., Silva, L., Faria, R. and Figueiras, J. (2006). Numerical modelling of the restrained shrinkage in the concrete ring test (in Portuguese). VI Simpósio EPUSP Sobre Estruturas de Concreto, Sao Paulo, Brazil.

Bansal, P. and Xie, G. (1998). A unified empirical correlation for evaporation of water at low air velocities. Int. Comm. Heat Mass Transfer, 25 (2): 183-190.

Baroghel-Bouny, V. (2007). Water vapour sorption experiments on hardened cementitious materials. Part I: Essential tool for analysis of hygral behaviour and its relation to pore structure. Cement and Concrete Research, 37 (3): 414-437.

Baroghel-Bouny, V., Mainguy, M., Lassabatere, T. and Coussy, O. (1999). Characterization and identification of equilibrium and transfer moisture properties for ordinary and high-performance cementitious materials. Cement and Concrete Research, 29 (8): 1225-1238.

Baroghel Bouny, V. (1997). Experimental investigation of self-desiccation in high performance materials - comparison with drying behaviour. Self-desiccation and its importance in concrete technology, Lund, Sweden.

Barreira, E. (2004). The use of thermography in the study of the higrothermal behaviour of buildings (in Portuguese). Faculty of Engineering of the University of Porto.

Bazant, Z. and Baweja, S. (2000). Creep and shrinkage prediction model for analysis and design of concrete structures: Model B3, Adam Neville Symposium: Creep and Shrinkage - Structural Design Effects ACI SP-194.

Bazant, Z. and Najjar, L. (1972). Nonlinear water diffusion in nonsaturated concrete. Materials and Structures, 5 (25): 3-20.

Bazant, Z. and Panula, L. (1982). New model for practical prediction of creep and shrinkage, Designing for creep and shrinkage in concrete structures, Detroit USA.

Bazant, Z. and Prasannan, S. (1989). Solidification theory for concrete creep: I. Formulation. Journal of Engineering Mechanics ASCE, 115 (8): 1691-1703.

Bazant, Z. P. (1988). Mathematical modeling of creep and shrinkage of concrete, Chichester, John Wiley & Sons, Inc., xxii, 459 s.

Bazant, Z. P. and Najjar, L. J. (1971). Drying of concrete as a nonlinear diffusion problem. Cement and Concrete Research, 1 (5): 461-473.

Bazant, Z. P. and Oh, B. H. (1983). Crack band theory for fracture of concrete. Materials and Structures, 16 (93): 155-177.

Bazant, Z. P., Sener, S. and Kim, J.-K. (1987). Effect of cracking on drying permeability and diffusivity of concrete. ACI Materials Journal, 84 (5): 351-357.

Bazant, Z. P. and Thonguthai, W. (1978). Pore pressure and drying of concrete at high temperature. ASCE J Eng Mech Div, 104 (5): 1059-1079.

Bazant, Z. P. and Xi, Y. (1994). Drying creep of concrete: Constitutive model and new experiments separating its mechanisms. Materiaux et constructions, 27 (165): 3-14.

Beek, A. v. (2000). Dielectric properties of young concrete. Doctoral Thesis, Delft.

Benboudjema, F., Meftah, F. and Torrenti, J. M. (2005a). Interaction between drying, shrinkage, creep and cracking phenomena in concrete. Engineering Structures, 27 (2): 239-250.

Benboudjema, F., Meftah, F. and Torrenti, J. M. (2005b). Structural effects of drying shrinkage. Journal of Engineering Mechanics, 131 (11): 1195-1199.

Bendat, J. and Piersol, A. (1980). Engineering applications of correlation and spectral analysis, John Wiley & Sons.

Bensted, J. (1987). Some applications of conduction calorimetry to cement hydration. Advances in Cement Research, 1 (1): 35-44.

Bentz, D. and Garboczi, E. (1991). Percolation of phases in a three-dimensional cement paste microstructural model. Cement and Concrete Research, 21 325-344.

Bentz, D., Lura, P. and Roberts, J. (2005). Mixture proportioning for internal curing. Concrete International, 27 (2): 35-40.

Bentz, D. P. (2007). Transient plane source measurements of the thermal properties of hydrating cement pastes. Materials and Structures/Materiaux et Constructions, 40 (10): 1073-1080.

Bentz, D. P. (2008). A review of early-age properties of cement-based materials. Cement and Concrete Research, 38 (2): 196-204.

Bernard, O. and Bruhwiler, E. (2003). The effect of reinforcement in the new layer on hygral cracking in hybrid structural elements. Materials and Structures/Materiaux et Constructions, 36 (256): 118-126.

Bischoff, P. H. (2001). Effects of shrinkage on tension stiffening and cracking in reinforced concrete. Canadian Journal of Civil Engineering, 28 (3): 363-374.

Bisschop, J. and Van Mier, J. G. M. (2002a). Effect of aggregates on drying shrinkage microcracking in cement-based composites. Materials and Structures/Materiaux et Constructions, 35 (252 SPEC.): 453-461.

Bisschop, J. and Van Mier, J. G. M. (2002b). How to study drying shrinkage microcracking in cement-based materials using optical and scanning electron microscopy? Cement and Concrete Research, 32 (2): 279-287.

Bisschop, J. and Van Mier, J. G. M. (2008). Effect of aggregates and microcracks on the drying rate of cementitious composites. Cement and Concrete Research, doi: 10.1016/j.cemconres.2008.03.015.

Bissonnette, B., Pierre, P. and Pigeon, M. (1999). Influence of key parameters on drying shrinkage of cementitious materials. Cement and Concrete Research, 29 (10): 1655-1662.

Bjontegaard, O. and Sellevold, E. (2001a). Interaction between thermal dilation and autogenous deformation in high performance concrete. Materials and Structures, 34 (5).

Bjontegaard, O. and Sellevold, E. (2001b). Thermal dilation and autogenous deformation, Early age cracking in cementitious systems EAC'01, Haifa, Israel.

Boulay, C. (2001). Determination of coeficient of thermal expansion. In: Early age cracking in cementitious systems. Report 25, A. Bentur, RILEM Publications s.a.r.l.

Branco, F., Mendes, P. and Mirambell, E. (1992). Heat of hydration effects in concrete structures. ACI Materials Journal, 89 (2): 139-145.

Breugel, K. (1980). Artificial cooling of hardening concrete. Concrete Structures, Delft University of Technology, Delft.

Breugel, K. (1991). Simulation of hydration and formation of structure in hardening cement-based materials. Doctoral Thesis, Delft.

Breugel, K. (1998). Prediction of temperature development in hardening concrete. In: Prevention of thermal cracking in concrete at early ages. Report 15, R. Springenschmid, E & FN SPON.

Breugel, K. (2001). Heat of hydration and apparent activation energy. IPACS Document, Subtask 2.1.

Breugel, K. and Koenders, E. (2001). Solar Radiation. Effect of solar radiation on the risk of cracking in young concrete. IPACS Document, Subtask 4.2.

Cano-Barrita, P. F. D. J., Balcom, B. J., Bremner, T. W., MacMillan, M. B. and Langley, W. S. (2004). Moisture distribution in drying ordinary and high performance concrete cured in a simulated hot dry climate. Materials and Structures/Materiaux et Constructions, 37 (272): 522-531.

CEB-FIP (1993). Model Code 90.

CEN (2000). EN197-1. Cement. Composition, specifications and conformity criteria for common cements.

CEN (2003a). EN 196-8 - Methods of testing cement. Heat of hydration. Solution method.

CEN (2003b). EN 196-9 - Methods of testing cement. Heat of hydration. Semi-adiabatic calorimetry.

CEN (2004). EN 1992-1 European Standard Eurocode 2: Design of concrete structures - Part 1: general rules and rules for buildings.

Cervera, M., Faria, R., Oliver, J. and Prato, T. (2002). Numerical modelling of concrete curing, regarding hydration and temperature phenomena. Computers and Structures, 80 (18-19): 1511-1521.

Chanvillard, G. and D'Aloia, L. (1997). Concrete strength estimation at early ages: modification of the method of equivalent age. ACI Materials Journal, 94 (6): 520-530.

Charron, J. (2003). Contribuition à l'étude du comportement au jeune âge des matériaux cimentaires en conditions de déformations libre et restreinte. Laval University.

Chen, B., Clark, D., Maloney, J., Mei, W. and Kasher, J. (1995). Measurement of night sky emissivity in determining radiant cooling from cool storage roofs and roof ponds, Proceedings of the National Passive Solar Conference - 20.

Chen, D. and Mahadevan, S. (2007). Cracking analysis of plain concrete under coupled heat transfer and moisture transport processes. Journal of Structural Engineering, 133 (3): 400-410.

Chopra, A. (2006). Dynamics of Structures: Theory and Applications to Earthquake Engineering Prentice Hall.

Christensen, R. (1979). Mechanics of composite materials, New York, Wiley Interscience.

Chuntranuluck, S., Wells, C. and Cleland, A. (1998). Prediction of chilling times of foods in situations where evaporative cooling is significant - Part 1. Method Development. Journal of Food Engineering, 37 111-125.

Clark, M. R., McCann, D. M. and Forde, M. C. (2003). Application of infrared thermography to the non-destructive testing of concrete and masonry bridges. NDT and E International, 36 (4): 265-275.

Clough, R. and Penzien, J. (2003). Dynamics of Structures, McGraw Hill.

Colina, H. and Acker, P. (2000). Drying cracks: Kinematics and scale laws. Materials and Structures/Materiaux et Constructions, 33 (226): 101-107.

Cunha, A., Caetano, E. and Magalhaes, F. (2007). Output-only Dynamic Testing of Bridges and Special Structures. Structural Concrete - Journal of FIB, 8 (2): 67-85.

Cusson, D. (2002). Field monitoring of the early age performance of concrete structures. In: Early age cracking in cementitious systems. Report 25, RILEM Publications.

Cusson, D. and Hoogeveen, T. (2006). Measuring early-age coefficient of thermal expansion in high-performance concrete, International RILEM Conference on Volume Changes in Hardening Concrete: Testing and Mitigation, Lyngby.

D'Aloia, L. (2001). Early age kinetics: Activation energy, maturity and equivalent age. In: Early age cracking in cementitious systems. Report 25, A. Bentur, RILEM Publications s.a.r.l.

D'Aloia, L. and Chanvillard, G. (2002). Determining the "apparent" activation energy of concrete: Ea - Numerical simulations of the heat of hydration of cement. Cement and Concrete Research, 32 (8): 1277-1289.

Davies, M. (2004). Building heat transfer, Wiley.

De Araujo, J. M. and Awruch, A. M. (1998). Cracking safety evaluation on gravity concrete dams during the construction phase. Computers and Structures, 66 (1): 93-104.

De Borst, R. (1987). Smeared cracking, plasticity, creep, and thermal loading - A unified approach. Computer Methods in Applied Mechanics and Engineering, 62 (1): 89-110.

de Borst, R. and van den Boogaard, A. (1994). Finite-element modeling of deformation and cracking in early-age concrete. J. Engineering Mechanics Div., ASCE, 120 (12): 2519-2534.

De Schutter, G. (2001). Thermal properties. In: Early age cracking in cementitious systems. Report 25, A. Bentur, RILEM Publications s.a.r.l.

De Schutter, G. (2002). Finite element simulation of thermal cracking in massive hardening concrete elements using degree of hydration based material laws. Computers and Structures, 80.

De Schutter, G. and Kovler, K. (2001). Short term mechanical properties. In: Early age cracking in cementitious systems. Report 25, A. Bentur, RILEM Publications s.a.r.l.

De Schutter, G. and Taerwe, L. (1995a). General hydration model for portland cement and blast furnace slag cement. Cement and Concrete Research, 25 (3): 593-604.

De Schutter, G. and Taerwe, L. (1995b). Specific heat and thermal diffusivity of hardening concrete. Magazine of Concrete Research, 47 (172): 203-208.

De Schutter, G. and Taerwe, L. (1996). Degree of hydration-based description of mechanical properties of early age concrete. Materials and Structures, 29 335-344.

Eames, I., Marr, N. and Sabir, H. (1997). The evaporation coefficient of water: a review. Int. J. Heat and Mass Transfer, 40 (12): 2963-2973.

Emborg, M. (1998). Models and methods for computation of thermal stresses. In: Prevention of thermal cracking in concrete at early ages. Report 15, R. Springenschmid, E & FN SPON.

Fairbairn, E. M. R., Silvoso, M. M., Toledo Filho, R. D., Alves, J. L. D. and Ebecken, N. F. F. (2004). Optimization of mass concrete construction using genetic algorithms. Computers and Structures, 82 (2-3): 281-299.

Faria, R., Azenha, M. and Figueiras, J. A. (2006). Modelling of concrete at early ages: Application to an externally restrained slab. Cement and Concrete Composites, 28 (6): 572-585.

Farra, B. (1995). Influence of concrete resistance and its adherence to reinforcement on cracking (in French). PhD Thesis. EPFL - Switzerland.

FIB (1999). Structural Concrete - Texbook on behaviour, design and performance updated knowledge of the CEB/FIP Model Code 1990 - Volume 1, FIB - CEB/FIP.

Gardner, N. (2000). Design provisions for shrinkage and creep of concrete. In: The Adam Neville Symposium: Creep and shrinkage - Structural design effects - SP194, A. Al-Manaseer, American Concrete Institute.

Gawin, D., Pesavento, F. and Schrefler, B. A. (2007). Modelling creep and shrinkage of concrete by means of effective stresses. Materials and Structures/Materiaux et Constructions, 40 (6): 579-591.

Glisic, B. and Simon, N. (2000). Monitoring of concrete at very early age using stiff SOFO sensor. Cement and Concrete Composites, 22 (2): 115-119.

Granger, L. (1996). Comportement différé du béton dans les enceintes de centrales nucléaires. Analyse et modélisation. PhD Thesis, LCPC, Paris.

Granger, L., Torrenti, J.-M. and Acker, P. (1996). Thoughts about drying shrinkage: Experimental results and quantification of structural drying creep. Materials and Structures/Materiaux et Constructions, 30 (204): 588-598.

Granger, L., Torrenti, J.-M. and Acker, P. (1997). Thoughts about drying shrinkage: Scale effects and modelling. Materials and Structures/Materiaux et Constructions, 30 (196): 96-105.

Grasley, Z. C. (2006). Measuring and modeling the time-dependent response of cementitious materials to internal stresses. University of Illionois at Urbana-Champaign.

Grasley, Z. C., Lange, D. A. and D'Ambrosia, M. D. (2006). Internal relative humidity and drying stress gradients in concrete. Materials and Structures/Materiaux et Constructions, 39 (293): 901-909.

Gutsch, A. (2002). Crack control for the massive concrete structures of the new central railway station in Berlin, Germany., International workshop on control of cracking in early age concrete, Sendai / Japan.

Gutsch, A. and Rostásy, F. (2001). Mechanical models of the stress-strain behaviour of young concrete in axial tension and compression. IPACS Document, SubTask 3.3.

Habel, W. R., Hofmann, D. and Hillemeier, B. (1997). Deformation measurements of mortars at early ages and of large concrete components on site by means of embedded fiber-optic microstrain sensors. Cement and Concrete Composites, 19 (1): 81-102.

Habib, A., Lachemi, M. and Aitcin, P.-C. (2002). Determination of elastic properties of high-performance concrete at early ages. ACI Materials Journal, 99 (1): 37-41.

Han, M. Y. and Lytton, R. L. (1995). Theoretical prediction of drying shrinkage of concrete. Journal of Materials in Civil Engineering, 7 (4): 204-207.

Hansen, W. (1987a). Constitutive model for predicting ultimate drying shrinkage of concrete. Journal of the American Ceramic Society, 70 (5): 329-332.

Hansen, W. (1987b). Drying shrinkage mechanisms in Portland cement paste. Journal of the American Ceramic Society, 70 (5): 323-328.

Hansen, W. and Almudaiheem, J. A. (1987). Ultimate drying shrinkage of concrete - influence of major parameters. ACI Materials Journal, 84 (3): 217-223.

Harrison, T. (1992). Early-age thermal crack control in concrete. CIRIA - Construction Industry Research and Information Association.

Hasanain, G. S., Khallaf, T. A. and Mahmood, K. (1989). Water evaporation from freshly placed concrete surfaces in hot weather. Cement and Concrete Research, 19 (3): 465-475.

Hashin, Z. and Shtrikman, S. (1962). A Variational approach to the theory of the effective magnetic permeability of multiphase materials. Journal of Applied Physics, 33 (10): 3125-3131.

Hedlund, H. and Jonasson, J.-E. (2000). Effect on stress development of restrained thermal and moisture deformation, Shrinkage of concrete. Shrinkage 2000, Paris, France.

Heimdal, E. and Kompen, R. (2001). Maridal culvert, Norway - Field Test I. IPACS Report T.5.1.1.

Hewlett, P. (2004). Lea's chemistry of cement and concrete, Elsevier.

Hillel, D. (1998). Environmental soil physics, Academic Press, 771.

Holt, E. (2001). Early age autogenous shrinkage of concrete. VTT Publications, Technical Research Centre of Finland.

Horai, K. i. and Simmons, G. (1969). Thermal conductivity of rock-forming minerals. Earth and Planetary Science Letters, 6 (5): 359-368.

Hossain, B. and Weiss, J. (2004). Assessing residual stress development and stress relaxation in restrained concrete ring specimens. Cem. and Concr. Comp., 26 (5): 531-540.

Houst, Y. (1997). Carbonation Shrinkage of Hydrated Cement Paste. 4th CANMET/ACI International Conference on Durability of Concrete, Canada.

Hua, C. (1992). Analyse et modelisation du retrait d'autodessiccation de la pate de ciment durcissante. Paris.

Hua, C., Acker, P. and Ehrlacher, A. (1995). Analyses and models of the autogenous shrinkage of hardening cement paste. I. Modelling at macroscopic scale. Cement and Concrete Research, 25 (7): 1457-1468.

ICOLD (2004). Thermal analysis of a RCC dam body, 7th Benchmark workshop on numerical analysis of dams, Bucharest, ROMANIA.

Incropera, F. P. and DeWitt, D. P. (1996). Fundamentals of heat and mass transfer, Wiley, New York, 886.

Incropera, F. P. and DeWitt, D. P. (2001). Introduction to heat transfer, New York, John Wiley & Sons, Inc.

Ishida, T., Maekawa, K. and Kishi, T. (2007). Enhanced modeling of moisture equilibrium and transport in cementitious materials under arbitrary temperature and relative humidity history. Cement and Concrete Research, 37 (4): 565-578.

Jaccoud, J. (1987). Armature minimale pour le contrôle de la fissuration des structures en béton., EPFL.

JCI (1985). Thermal stress in mass concrete. Japanese Concrete Institute. State of the art report.

Ji, G. (2008). Cracking risk of concrete structures in the hardening phase: Experiments, material modeling and finite element analysis. Norwegian University of Science and Technology, Trondheim, Norway.

Jiang, Z., Sun, Z. and Wang, P. (2006). Internal relative humidity distribution in high-performance cement paste due to moisture diffusion and self-desiccation. Cement and Concrete Research, 36 (2): 320-325.

Jin, X. and Li, Z. (2001). Dynamic property determination for early-age concrete. ACI Materials Journal, 98 (5): 365-370.

Jonasson, J.-E. (1994). Modelling of Temperature, Moisture and Stresses in Young Concrete. Doctoral Thesis, Lulea University of Technology, Lulea.

Jones, F. (1992). Evaporation of water with emphasis on applications and measurements., Lewis Pub.

Kanstad, T., Hammer, T., Bjontegaard, O. and Sellevold, E. (2003). Mechanical properties of young concrete: Part II: Determination of model parameters and test program proposals. Materials and Structures, 36 226-230.

Kasten, F. (1996). The linke turbidity factor based on improved values of the integral Rayleigh optical thickness. Solar Energy, 56 (3): 239-244.

Kawaguchi, T. and Nakane, S. (1996). Investigations on Determining Thermal Stress in Massive Concrete Structures. ACI Materials Journal, 93 (1).

Keey, R. (1972). Drying. Principles and practice, Oxford ; New York : Pergamon Press, 358.

Khan, A., Cook, W. D. and Mitchell, D. (1998). Thermal properties and transient thermal analysis of structural members during hydration. ACI Materials Journal, 95 (3): 293-303.

Kim, J.-K. and Lee, C.-S. (1998). Prediction of differential drying shrinkage in concrete. Cement and Concrete Research, 28 (7): 985-994.

Kim, J. K. and Lee, C. S. (1999). Moisture diffusion of concrete considering self-desiccation at early ages. Cement and Concrete Research, 29 (12): 1921-1927.

Kim, K. H., Jeon, S. E., Kim, J. K. and Yang, S. (2003). An experimental study on thermal conductivity of concrete. Cement and Concrete Research, 33 (3): 363-371.

Kishi, T. and Maekawa, K. (1995). Multi-component model for hydration heating of portland cement. Concrete library of JSCE - Japanese Society of Civil Engineering, 28 97-115.

Klysz, G. and Balayssac, J. P. (2007). Determination of volumetric water content of concrete using ground-penetrating radar. Cement and Concrete Research, 37 (8): 1164-1171.

Kovler, K. (1994). Testing system for determining the mechanical behaviour of early age concrete under restrained and free uniaxial shrinkage. Materials and Structures, 27 (170): 324-330.

Kovler, K. (1995). Shock of evaporative cooling of concrete in hot dry climates. Concrete International, 17 (10): 65-69.

Krauß, M., Hairiri, K. and Rostásy, F. (2001). Non-destructive assessment of mechanical properties of concrete at very early ages by US techniques - Method, results and modelling. IPACS Document, Task 2 (T2.1/T2.2).

Kwak, H.-G. and Ha, S.-J. (2006a). Non-structural cracking in RC walls: Part II. Quantitative prediction model. Cement and Concrete Research, 36 (4): 761-775.

Kwak, H.-G., Ha, S.-J. and Kim, J.-K. (2006b). Non-structural cracking in RC walls: Part I. Finite element formulation. Cement and Concrete Research, 36 (4): 749-760.

Laplante, P. and Boulay, C. (1994). Evolution du coefficient de dilatation thermique du béton en fonction de sa maturité aux tout premiers âges. Materials and Structures, (27): 596-605.

Lawrence, P., Cyr, M. and Ringot, E. (2003). Mineral admixtures in mortars: Effect of inert materials on short-term hydration. Cement and Concrete Research, 33 (12): 1939-1947.

Lee, Y., Choi, M.-S., Yi, S.-T. and Kim, J.-K. (2009). Experimental study on the convective heat transfer coefficient of early-age concrete. Cement and Concrete Composites, 31 (1): 60-71.

Leitao, N., Batista, A. and Castro, A. (2007). Thermo-mechanical analysis of massive concrete structures. Application to RCC dams. (in Portuguese), Numerical and Computational Methods in Engineering (Portuguese Language Conference), Porto, PORTUGAL.

Lerch, W. and Ford, C. L. (1948). Long-time study of cement performance in concrete. 3. Chemical and physical tests of the cements. Journal, American Concrete Institute; Proceedings, 44.

Lewis, R. and Schrefler, B. A. (2000). The finite element method in the static and dynamic deformation and consolidation of porous media, Wiley.

Lim, S. (2002). Viscoelastic age-dependent analysis of restrained shrinkage development in early-age concrete. Texas A&M University.

Lopez, C., Idiart, A. and I, C. (2007). Analisis meso-estructural de la fisuracion del hormigon debido al efecto de los aridos en la retraccion por secado, CMNE/CILAMCE 2007, Porto, PORTUGAL.

Lura, P. (2000). Autogenous deformation and internal curing of concrete. Doctoral Thesis, Delft.

Lura, P. and Breugel, K. (2001). Thermal Properties of Concrete: Sensitivity studies. IPACS Document, Subtask 2.5.

Maekawa, K., Chaube, R. and Kishi, T. (1999). Modelling of concrete performance, E&FN SPON, 308.

Maekawa, K., Ishida, T. and Kishi, T. (2003). Multi-scale modeling of concrete performance. Integrated material and structural mechanics. J. Advanced Concrete Technology, 1 (2): 91-126.

Magalhães, F., Cunha, A. and Caetano, E. (2008). Dynamic monitoring of a long span arch bridge. Engineering Structures.

Maia, N. and Silva, J. (1997). Theoretical and Experimental Modal Analysis, Research Studies Press Ltd.

Mainguy, M., Coussy, O. and Eymard, R. (1999). Modelisation des transferts hydriques isothermes en milieu poreux. Application au sechage des materiaux a base de ciment., LCPC, Paris.

Malek, K. and Coppens, M. O. (2003). Knudsen self- and Fickian diffusion in rough nanoporous media. Journal of Chemical Physics, 119 (5): 2801-2811.

Malhotra, V. and Carino, N. (2004). Handbook on Nondestructive Testing of Concrete, CRC Press.

Malkawi, A., Mutasher, S. and Qiu, T. (2003). Thermal-Structural Modeling and Temperature Control of Roller Compacted Concrete Gravity Dam. ASCE Journal of Performance of Constructed Facilities, 17 (4).

Manrique, J. (1976). Transferencia de calor, Harla, SA.

Marek, K. and Straub, J. (2000). Analysis of the evaporation coefficient and the condensation coefficient of water. Int. J. Heat Mass Transf., (44): 39-53.

Martin-Perez, B. (1999). Service life modelling of R.C. highway structures exposed to chlorides. University of Toronto, Toronto.

Martinola, G. and Sadouki, H. (1998). Combined experimental and numerical study to assess shrinkage cracking of cement-based materials. Internationale Zeitschrift fur Bauinstandsetzen.

Martinola, G., Sadouki, H. and Wittman, F. H. (2001). Numerical model for minimizing risk of damage in repair system. Journal of Materials in Civil Engineering, 13 (2): 121-129.

Maser, K. R. and Roddis, W. M. K. (1990). Principles of thermography and radar for bridge deck assessment. Journal of Transportation Engineering, 116 (5): 583-601.

Masmoudi, W. and Prat, M. (1991). Heat and mass transfer between a porous medium and a parallel external flow. Application to drying capillary of porous materials. International Journal of Heat and Mass Transfer, 34 (8): 1975-1989.

McAdams, W. (1954). Heat transmission, McGraw-Hill, 532.

Mensi, R., Acker, P. and Attolou, A. (1988). Drying of Concrete: Analysis and Modelling. SECHAGE DU BETON: ANALYSE ET MODELISATION., 21 (121): 3-12.

Mjörnell, K. (1997). Moisture conditions in high performance concrete. Chalmers University of Technology, Göteborg.

Moore, G. E. (1965). Cramming more components onto integrated circuits. Electronics, 38 (8).

Morabito, P. (1998). Methods to determine the heat of hydration of concrete. In: Prevention of thermal cracking in concrete at early ages. Report 15, R. Springenschmid, E & FN SPON.

Morabito, P. (2001a). Sluice gate - Brembo river - Italy - Field test. IPACS Report, T.5.4.

Morabito, P. (2001b). Thermal properties of concrete. Variations with the temperature and during the hydration phase., IPACS Document, Subtask 2.3.

Mulligan, S. (2002). Studies in isothermal heat conduction calorimetry. Drexel University.

Multon, S. and Toutlemonde, F. (2004). Water distribution in concrete beams. Materials and Structures/Materiaux et Constructions, 37 (270): 378-386.

Nagy, A. (1997). Determination of E-modulus of young concrete with nondestructive method. Journal of Materials in Civil Engineering, 9 (1): 15-20.

NEC-SAN-EI-INSTRUMENTS (1991). TH1 101 thermo tracer - operation manual. Japan.

Neville, A. (1995). Properties of Concrete, Prentice Hall, 844.

Nield, D. and Bejan, A. (2006). Convection in Porous Media, Springer.

Nilsson, L.-O. (1996). Interaction between microclimate and concrete - A prerequisite for deterioration. Construction and Building Materials, 10 (5 SPEC. ISS.): 301-308.

Nilsson, M. (2003). Restraint factors and partial coefficients for crack risk analyses of early age concrete structures. Doctoral Thesis, Lulea.

Noorzaei, J., Bayagoob, K. H., Thanoon, W. A. and Jaafar, M. S. (2006). Thermal and stress analysis of Kinta RCC dam. Engineering Structures, 28 (13): 1795-1802.

Norris, A., Saafi, M. and Romine, P. (2008). Temperature and moisture monitoring in concrete structures using embedded nanotechnology/microelectromechanical systems (MEMS) sensors. Construction and Building Materials, 22 (2): 111-120.

O'Moore, L., Baweja, D. and Cux, P. (2004). Investigation of early age tensile stresses, shrinkage strains in pavements and standard drying shrinkage tests. Department of Civil Engineering - Concrete Laboratory, University of Queensland. Internal Report.

Oh, B. H. and Cha, S. W. (2003). Nonlinear Analysis of Temperature and Moisture Distributions in Early-Age Concrete Structures Based on Degree of Hydration. ACI Materials Journal, 100 (5): 361-370.

Oh, B. H. and Choi, S. (2006). Advanced analysis of stresses for controls of transverse cracking in early age concrete decks of composite bridges., Measuring, monitoring and modeling concrete properties, Alexandroupolis, Greece.

Oluokun, F., Burdette, E. and Deatherage, J. (1991). Elastic modulus, Poisson's ratio, and compressive strength relationships at early ages. ACI Materials Journal, 88 (1): 3-10.

Ostergaard, L. (2003). Early-age fracture mechanics and cracking of concrete. Experiments and Modelling., Technical University of Denmark.

Pantazopoulou, S. J. and Mills, R. H. (1995). Microstructural aspects of the mechanical response of plain concrete. ACI Materials Journal, 92 (6): 605-616.

Parker, D. (2005). Theoretical evaluation of the NightCool nocturnal radiation cooling concept. F. S. E. Center, ed.

Parrott, L. (1990). A review of methods to determine the moisture conditions in concrete., British Cement Association.

Parrott, L. J., Geiker, M., Gutteridge, W. A. and Killoh, D. (1990). Monitoring Portland cement hydration: Comparison of methods. Cement and Concrete Research, 20 (6): 919-926.

Patel, R., Killoh, D., Parrott, L. and Gutteridge, W. (1988). Influence of curing at different relative humidities upon compound reactions and porosity in Portland cement paste. Materials and Structures, 21 192-197.

Pauken, M. (1999). An experimental investigation of combined turbulent free and forced evaporation. Exp. thermal fluid science, (18): 334-340.

Pel, L., Landman, K. A. and Kaasschieter, E. F. (2002). Analytic solution for the non-linear drying problem. International Journal of Heat and Mass Transfer, 45 (15): 3173-3180.

Perrin, B., Baroghel Bouny, V. and Chemloul, L. (1998). Methods of determination of the hydric diffusivity of hardened cement pastes. Me?thodes de de?termination de la diffusivite? hydrique de pa?tes de ciments durcies, 31 (208): 235-241.

Persson, B. (1997). Moisture in concrete subjected to different kinds of curing. Materials and Structures/Materiaux et Constructions, 30 (203): 533-544.

Pigeon, M., Toma, G., Delagrave, A., Bissonnette, B., Marchand, J. and Prince, J. (2000). Equipment for the analysis of the behaviour of concrete under restrained shrinkage at early ages. Magazine of Concrete Research, 52 (4): 297-302.

Popiel, C. O., Wojtkowiak, J. and Biernacka, B. (2001). Measurements of temperature distribution in ground. Experimental Thermal and Fluid Science, 25 (5): 301-309.

Prato, T. (1999). Comportamiento del hormigón en edades tempranas. Modelización y aplicaciones. Tesis Doctoral, Universitat Politècnica de Catalunya, Barcelona.

Reinhardt, H., Blaauwendraad, J. and Jongedijk, J. (1982). Temperature development in concrete structures taking account of state dependent properties, Int. Conf. Concrete at Early Ages, Paris, France.

Roelfstra, P. E. (1989). A numerical approach to investigate the properties of concrete : numerical concrete., EPFL, Lausanne.

Roelfstra, P. E., Sadouki, H. and Wittmann, F. H. (1985). Numerical Concrete. LE BETON NUMERIQUE., 18 (107): 327-335.

Roncero, J. (2000). Effect of superplasticizers on the behavior of concrete in the fresh and hardened states: implications for high performance concretes. PhD Thesis, Universitat Politecnica de Catalunya, Barcelona.

Rostásy, F., Gutsch, A. and Krauß, M. (2001). Computation of stresses and cracking criteria for early age concrete - Methods of iBMB. IPACS, Task 3.

Ruiz, J., Schindler, A., Rasmussen, R. and Johnson, T. (2003). Prediction of heat transport in concrete made with blast furnace slag aggregate, 9th conference on Advances in Cement and Concrete, Colorado, USA.

Ruiz, J., Schindler, A., Rasmussen, R., Kim, P. and Chang, G. (2001). Concrete temperature modeling and strength prediction using maturity concepts in the FHWA HIPERPAV software, 7th International Conference on Concrete Pavements, Orlando, Florida, USA.

Sadouki, H. and Van Mier, J. G. M. (1997). Simulation of hygral crack growth in concrete repair systems. Materials and Structures/Materiaux et Constructions, 30 (203): 518-526.

Sakata, K. (1983). A study on moisture diffusion in drying and drying shrinkage of concrete. Cement and Concrete Research, 13 164-170.

Schindler, A., Ruiz, J., Rasmussen, R., Chang, G. and Wathne, L. (2003). Concrete pavement temperature prediction and case studies with the FHWA HIPERPAV models. Cement and Concrete Composites, 26 (5): 463-471.

Selih, J., Sousa, A. and Bremner, T. (1996). Moisture transport in initially fully saturated concrete during drying. Transp. in Porous Media, 24 81-106.

Shiotani, T., Bisschop, J. and Van Mier, J. G. M. (2003). Temporal and spatial development of drying shrinkage cracking in cement-based materials. Engineering Fracture Mechanics, 70 (12): 1509-1525.

Silveira, A. (1996). The influence of thermal actions in the behavior of reinforced concrete bridges (in Portuguese). PhD Thesis, LNEC, Lisbon.

Slowik, V., Schlattner, E. and Klink, T. (2004). Experimental investigation into early age shrinkage of cement paste by using fibre Bragg gratings. Cement and Concrete Composites, 26 (5): 473-479.

Snyder, K. and Bentz, D. (2004). Suspended hydration and loss of freezable water in cement pastes exposed to 90% relative humidity. Cement and Concrete Research, 34 2045-2056.

Song, H., Cho, H., Park, S., Byun, K. and Maekawa, K. (2001). Early-age cracking resistance evaluation of concrete structures. Concrete Science and Engineering, 3 63-72.

Sousa, C. (2004). Structural continuity in bridge decks built with precast beams. Continuity connections in reinforced concrete. (in Portuguese). Master Thesis, Faculty of Engineering of the University of Porto.

Spears, R. (1983). The 80 percent solution to inadequate curing problems. Concrete International, 15-18.

Sule, M. (2003). Effect of reinforcement on early-age cracking in high strength concrete. Doctoral Thesis, Delft.

Sun, S. and Marrero, T. (1996). Experimental study of simultaneous heat and moisture transfer around single short porous cylinders during convection drying by a psychrometry method. International Journal of Heat and Mass Transfer, 39 (17): 3559-3565.

Suwito, A., Ababneh, A., Xi, Y. and Willam, K. (2006). The coupling effect of drying shrinkage and moisture diffusion in concrete. Computers and Concrete, 3 (2-3): 103-122.

Tada, S. and Watanabe, K. (2005). Dynamic determination of sorption isotherm of cement based materials. Cement and Concrete Research, 35 (12): 2271-2277.

Taylor, H. (1989). Modification of the Bogue calculation. Advances in Cement Research, 2 (6): 73-79.

Thomas, J. J. and Jennings, H. M. (2006). A colloidal interpretation of chemical aging of the C-S-H gel and its effects on the properties of cement paste. Cement and Concrete Research, 36 (1): 30-38.

Timoshenko, S. and Goodier, J. (1970). Theory of elasticity, McGraw Hill International Editions.

TNO-DIANA-BV (2007). Diana User´s Manual - Release 9.2. Delft, The Netherlands.

Toma, G. (1999). Comportement des bétons au jeune âge. Laval University.

Torrenti, J. M. and Benboudjema, F. (2005). Mechanical threshold of cementitious materials at early age. Materials and Structures/Materiaux et Constructions, 38 (277): 299-304.

Torrenti, J. M., Granger, L., Diruy, M. and Genin, P. (1999). Modeling concrete shrinkage under variable ambient conditions. ACI Materials Journal, 96 (1): 35-39.

Ulm, F.-J. and Coussy, O. (1995). Modeling of thermochemomechanical couplings of concrete at early ages. Journal of Engineering Mechanics, 121 (7): 785-794.

Uno, P. J. (1998). Plastic shrinkage cracking and evaporation formulas. ACI Materials Journal, 95 (4): 365-375.

Vaysburd, A., Emmons, P., Bissonnette, B. and Pigeon, M. (2001). Some aspects of evaluating cracking sensitivity of repair materials. Early age cracking in cementitious systems, Haifa, Israel.

Viviani, M., Glisic, B. and Smith, I. F. C. (2007). Separation of thermal and autogenous deformation at varying temperatures using optical fiber sensors. Cement and Concrete Composites, 29 (6): 435-447.

Voigt, T. (2004). The application of an ultrasonic shear wave reflection method for nondestructive testing of cement-based materials at early ages: An experimental and numerical analysis. Leipzig University.

Wadsö, L. (2003). An experimental comparison between isothermal calorimetry, semi-adiabatic calorimetry and solution calorimetry for the study of cement hydration., Nordtest report TR 522.

Walraven, J. (1999). 3.3.3 Tension stiffening. In: Structural Concrete, the Textbook on Behaviour, Design and Performance. Updated knowledge of the CEB/FIP Model Code 1990., FIB.

Walton, J., Plansky, R. and Smith, R. (1990). Models for estimation of service life of concrete barriers in low-level radioactive waste disposal. Office of Nuclear Regulatory Research, U.S. Nuclear Regulatory Commission, Washington DC.

Weiss, J. (2001). Experimental determination of the 'time zero' t0 (maturity-zero M0). In: Early age cracking in cementitious systems, A. Bentur, RILEM Publications s.a.r.l.

Welch, P. (1967). The use of Fast Fourier Transform for the Estimation of Power Spectra: a Method based on Time Averaging over short Modified Periodograms. IEEE Transaction on Audio and Electro-Acoustics 15 (2).

West, R. P. and Holmes, N. (2005). Predicting moisture movement during the drying of concrete floors using finite elements. Construction and Building Materials, 19 (9): 674-681.

Wexham (1998). JAF Calorimeter Operation Manual.

Wirquin, E., Broda, M. and Duthoit, B. (2002). Determination of the apparent activation energy of one concrete by calorimetric and mechanical means: Influence of a superplasticizer. Cement and Concrete Research, 32 (8): 1207-1213.

Wittmann, F. H. (1973). Interaction of hardened cement paste and water. Journal of the American Ceramic Society, 56 (8): 409-415.

Wittmann, F. H. (2008). Heresies on shrinkage and creep mechanisms, Creep, Shrinkage and Durability Mechanics of Concrete Structures (CONCREEP 08), Ise-Shima, Japan.

Wittmann, F. H. and Roelfstra, P. E. (1980). Total deformation of loaded drying concrete. Cement and Concrete Research, 10 (5): 601-610.

WMO (1981). Technical note n 172 W. M. Organization, ed., Geneva - Switzerland.

Wojcik, G. (2001). The interaction between the atmosphere and curing concrete bridge decks. PhD Thesis, State University of New York at Albany.

Wong, A. C. L., Childs, P. A., Berndt, R., Macken, T., Peng, G.-D. and Gowripalan, N. (2007). Simultaneous measurement of shrinkage and temperature of reactive powder concrete at early-age using fibre Bragg grating sensors. Cement and Concrete Composites, 29 (6): 490-497.

Xi, Y. (1994a). A model for moisture capacities of composite materials. Part I: formulation. Computational Materials Science, 4 65-77.

Xi, Y. (1994b). A model for moisture capacities of composite materials. Part II: application to concrete. Computational Materials Science, 4 78-92.

Xi, Y., Bazant, Z. P. and Jennings, H. M. (1994a). Moisture diffusion in cementitious materials Adsorption isotherms. Advanced Cement Based Materials, 1 (6): 248-257.

Xi, Y., Bazant, Z. P., Molina, L. and Jennings, H. M. (1994b). Moisture diffusion in cementitious materials Moisture capacity and diffusivity. Advanced Cement Based Materials, 1 (6): 258-266.

Ye, D., Zollinger, D. and Morian, D. (2007). Characterization and analysis of early age concrete pavement behavior at the national airport pavement test facility., Innovative pavement research foundation.

Yuan, Y. and Wan, Z. L. (2002). Prediction of cracking within early-age concrete due to thermal, drying and creep behavior. Cement and Concrete Research, 32 (7): 1053-1059.

Zarr, R. (2001). A History of Testing Heat Insulators at the National Institute of Standards and Technology. In: ASHRAE Transactions 2001, NIST.